

# LAWRENCE TECHNOLOGICAL UNIVERSITY



## **EVALUATING LONG TERM CAPACITY & DUCTILITY OF CARBON FIBER REINFORCED POLYMER PRESTRESSING AND POST TENSIONING STRANDS SUBJECT TO LONG TERM LOSSES, CREEP, AND ENVIRONMENTAL FACTORS, AND DEVELOPMENT OF CFRP PRESTRESSING SPECIFICATIONS FOR THE DESIGN OF HIGHWAY BRIDGES**

Submitted to

MICHIGAN DEPARTMENT OF TRANSPORTATION

Research Administration  
Bureau of Field Services  
Federal Project Number: OR14-024

By

**Nabil F. Grace, PhD, P.E., Project Investigator**  
**Mena Bebawy, PhD, P.E., Co-Project Investigator**

Department of Civil Engineering  
Lawrence Technological University  
Southfield, MI 48075-1058, U.S.A.

Sept. 30<sup>th</sup>, 2019

## TECHNICAL REPORT DOCUMENTATION PAGE

1. Report No. SPR-1690	2. Government Accession No. N/A	3. Recipient's Catalog No.	
4. Title and Subtitle Evaluating Long Term Capacity & Ductility of Carbon Fiber Reinforced Polymer Prestressing & Post Tensioning Strands Subject to Long Term Losses, Creep, and Environmental Factors, and Development of CFRP Prestressing Specifications for the Design of Highway Bridges		5. Report Date Sept. 30 <sup>th</sup> , 2019	
		6. Performing Organization Code N/A	
7. Author(s): Nabil Grace, PhD, P.E.; Mena Bebawy, PhD, P.E., Marc kasabasic; Ernest Al-Hassan; Abinash Acharya; Kerolos Abdo; & Mohamed Mohamed		8. Performing Organization Report No. N/A	
9. Performing Organization Name and Address Center for Innovative Material Research (CIMR) Lawrence Technological University University Advancement Office 21,000 West Ten Mile Road, Southfield, MI-48075		10. Work Unit No. N/A	
		11. Contract or Grant No. LTU 2013-0065 Z2	
12. Sponsoring Agency Name and Address Michigan Department of Transportation (MDOT) Research Administration 8885 Ricks Road P.O. Box 33049 Lansing, Michigan 48909		13. Type of Report & Period Covered Final Report, 10/1/2013 to 9/30/2019	
		14. Sponsoring Agency Code N/A	
15. Supplementary Notes Conducted in cooperation with the U.S. Department of Transportation, Federal Highway Administration. MDOT Research reports are available at <a href="http://www.michigan.gov/mdotresearch">www.michigan.gov/mdotresearch</a> .			
16. Abstract Comprehensive experimental, analytical, and numerical investigations were executed to establish the main design criteria of bridge beams prestressed with carbon fiber reinforced polymer (CFRP) strands. The investigation evaluated the short and long-term performance of CFRP under various environmental and loading conditions. Main CFRP design parameters such as maximum tensile strength, guaranteed strength, environmental reduction factors, relaxation, creep rupture strength, short and long-term prestress loss, and performance at elevated temperatures have been evaluated and documented. The experimental investigation included testing and evaluating unbonded prestressed CFRP strands as well as half-scale CFRP pretensioned decked bulb T-beams. Various test protocols were adopted and included such as testing and evaluating bonded and unbonded CFRP specimens: (1) at ambient temperature and controlled laboratory conditions, (2) under combined fire/loading events, (3) after exposure to cycles of freezing and thawing, (4) after exposure to outdoor harsh Michigan weather conditions for three years, (5) inside an environmental chamber simulating extremely hot and cold weather conditions, and (6) after exposure to elevated temperatures with and without loading. The results from the experimental investigation were implemented in the development of extensive analytical and numerical investigations that addressed the flexural and shear design of full-scale highway bridge beams. Test results were deployed to establish benchmark design criteria, design guidelines, and recommendations in a format similar to that of AASHTO LRFD to facilitate and promote the design and construction of highway bridges with CFRP components.			
17. Key Words CFRP; Prestressed highway bridges; Creep Rupture, Relaxation; Fire; Environmental Conditions; Freeze-Thaw.		18. Distribution Statement No Restrictions. This document is available to the public through the Michigan Department of Transportation (MDOT).	
19. Security Classification (of this report) Unclassified	20. Security Classification (of this page) Unclassified	21. No. of Pages 375	22. Price N/A

## **ACKNOWLEDGEMENTS AND DISCLAIMER**

“This publication is disseminated in the interest of information exchange. The Michigan Department of Transportation (hereinafter referred to as MDOT) expressly disclaims any liability, of any kind, or for any reason, that might otherwise arise out of any use of this publication or the information or data provided in the publication. MDOT further disclaims any responsibility for typographical errors or accuracy of the information provided or contained within this information. MDOT makes no warranties or representations whatsoever regarding the quality, content, completeness, suitability, adequacy, sequence, accuracy or timeliness of the information and data provided, or that the contents represent standards, specifications, or regulations.”

“This material is based upon work supported by the Federal Highway Administration under SPR-1690. Any opinions, findings and conclusions or recommendations expressed in this publication are those of the author(s) and do not necessarily reflect the views of the Federal Highway Administration.”

## TABLE OF CONTENT

LIST OF FIGURES .....	viii
LIST OF TABLES .....	xxvii
EXECUTIVE SUMMARY .....	xxix
CHAPTER 1: INTRODUCTION.....	1
1.1 Overview.....	1
1.2 Research Scope .....	2
1.3 Research Outcome .....	2
1.4 Report Outlines .....	3
CHAPTER 2: ANCHORAGE AND TENSILE STRENGTH .....	4
2.1 Introduction.....	4
2.2 Test Specimens .....	4
2.3 Steel Wedge Anchorage.....	6
2.4 Sleeve Anchorage .....	9
2.5 Results.....	14
2.6 Discussion of Test Results .....	19
CHAPTER 3: CREEP RUPTURE & RELAXATION OF CFRP.....	21
3.1 Introduction.....	21
3.2 Creep Rupture .....	22
3.2.1 Test setup .....	23
3.2.2 Test results .....	28
3.3 Relaxation of CFCC Strands.....	31
3.3.1 Test setup .....	31
3.3.2 Test results .....	34

3.4 Long-Term Monitoring of CFCC Specimens .....	39
3.5 Discussion of Test Results .....	44
3.6 Release and Uni-axial Tensile Test .....	48
CHAPTER 4: ENVIRONMENTAL EFFECTS .....	52
4.1 Introduction.....	52
4.2 Unbonded CFRP Strands .....	54
4.2.1 Test setup .....	54
4.2.2 Test results .....	59
4.3 CFRP Prestressed Decked Bulb T Beams .....	69
4.3.1 Construction of test specimens .....	69
4.3.2 Test setup .....	77
4.3.3 Test results .....	80
4.3.3.1 Beam F1 .....	81
4.3.3.2 Beam F2.....	85
4.3.3.3 Beam H1 .....	88
4.3.3.4 Beam H2 .....	91
4.3.3.5 Beam F2-R.....	94
4.3.3.6 Beam H2-R .....	96
4.3.3.7 Discussion.....	98
4.4 Discussion of Test Results .....	99
CHAPTER 5: FREEZE-THAW EFFECT .....	101
5.1 Introduction.....	101
5.2 Decked Bulb T Beams .....	103
5.2.1 Test setup .....	103

5.2.2 Test results .....	110
5.2.2.1 Uniaxial compressive test of concrete cylinders.....	110
5.2.2.2 Flexural test of decked bulb T beams .....	113
5.3 Freeze-thaw cycles of CFCC specimens .....	129
5.3.1 Test setup .....	129
5.3.2 Test results .....	135
5.4 Discussion of Test Results .....	135
CHAPTER 6: FIRE AND HEAT RESISTANCE .....	137
6.1 Introduction.....	137
6.2 Tensile Strength of CFRP at Elevated Temperatures .....	139
6.2.1 Test setup .....	139
6.2.2 Test results .....	140
6.3 CFCC Prestressed Decked Bulb T Beams Under Fire/Loading Event.....	145
6.3.1 Test setup .....	145
6.3.2.1 Control beam S132-25-1 .....	150
6.3.2.2 Beam C72-14-1 .....	154
6.3.2.3 Beam C100-20-1 .....	159
6.3.2.4 Beam C100-20-2.....	163
6.3.2.5 Beam C100-20-3.....	167
6.3.2.6 Beam C100-20-4.....	171
6.3.2.7 Beam C100-20-5.....	175
6.3.2.8 Beam C132-25-1 .....	179
6.4 Discussion of Test Results .....	183
CHAPTER 7: SPLICING & BOND FATIGUE.....	185

7.1 Introduction.....	185
7.2 Pull-out Test.....	186
7.2.1 Test setup .....	186
7.2.2 Test results .....	191
7.3 Flexural Bond Strength.....	194
7.3.1 Test setup .....	195
7.3.2 Test results .....	201
7.3.3 Discussion of test results.....	217
7.4 Lap-spliced CFRP Stirrups .....	220
7.4.1 Test setup .....	220
7.4.2 Test Setup.....	232
7.4.3 Test results .....	233
7.4.3.1 Control Box-Beam (C-C).....	233
7.4.3.2 Beam (C-10.75) .....	236
7.4.3.3 Beam (C-7) .....	239
7.4.3.4 Beam (C-4) .....	242
7.4.3.5 Control Beam (S-C).....	245
7.4.3.6 Beam (S-10.75).....	248
7.4.3.7 Beam (S-7).....	251
7.4.3.8 Beam (S-4).....	254
7.4.4 Discussion of test results.....	257
<b>CHAPTER 8: LONG-TERM PERFORMANCE OF BEAMS WITH CFRP .....</b>	<b>259</b>
8.1 Introduction.....	259
8.2 Decked Bulb T beams.....	260

8.2.1 Test setup .....	260
8.2.2 Test results .....	275
8.2.2.1 Monitoring of the test beams .....	275
8.2.2.2 Flexural test results .....	281
8.3 Discussion of Test Results .....	297
CHAPTER 9: FLEXURAL AND SHEAR DESIGN OF CFRP PRESTRESSED BEAMS .....	299
9.1 Introduction.....	299
9.2 Flexural Design of CFRP reinforced/Prestressed section.....	300
9.3 Shear Design .....	307
9.3.1 Test setup .....	307
9.3.2 Test results .....	310
CHAPTER 10: SUMMARY & CONCLUSIONS .....	327
REFERENCES .....	332
APPENDIX A: DESIGN GUIDELINES IN LRFD FORMAT .....	A1
APPENDIX B: DESIGN EXAMPLE FOR BEAM WITH CFRP RESINFORCEMENT .....	A2

## LIST OF FIGURES

Figure 2.2-1	Spool of CFCC strands with a diameter of 0.6 in. (15.2 mm) .....	5
Figure 2.2-2	Heat treatment at 140 °F (60 °C) for 15 hours to straighten CFCC strands .....	6
Figure 2.3-1	Applying components of buffer layer around CFCC strands .....	7
Figure 2.3-2	Installing steel-wedge anchorage device on CFCC strand with buffer layer.....	8
Figure 2.3-3	New composite buffer material as a replacement for steel mesh wrap.....	8
Figure 2.3-4	Test specimens prepared using composite buffer layer and wedge anchorage .....	9
Figure 2.4-1	Sleeve-type anchorage for CFCC strands .....	10
Figure 2.4-2	Manufacturing of anchorage device at LTU .....	11
Figure 2.4-3	Preparing the CFCC specimens for sleeve anchorage devices .....	12
Figure 2.4-4	Mixing and placing the HEM inside the steel sockets .....	13
Figure 2.4-5	CFCC specimens with sleeve anchorage device after curing .....	13
Figure 2.4-6	Left: A CFCC specimen in uni-axial test setup. Right, evaluating strain and elastic modulus of CFCC specimen using extensometer (circled) .....	14
Figure 2.5-1	Typical failure mode of CFCC specimens with sleeve type anchorage .....	15
Figure 2.5-2	Uni-axial test setup for test specimens with wedge anchorage devices.....	18
Figure 2.5-3	Failure of test specimens with wedge anchorage devices.....	18
Figure 2.5-4	Establishing elastic modulus of CFCC based on uni-axial test results.....	19
Figure 3.2-1	Test setup for evaluating creep rupture strength of CFRP with high strength steel springs to maintain the load level .....	24
Figure 3.2-2	Stressing creep rupture specimens to 70 % of the average tensile strength of CFCC .....	24
Figure 3.2-3	Creep rupture specimens after stressing showing the compressed steel springs .....	25
Figure 3.2-4	Inline load cells to monitor the force of creep rupture specimens .....	25

Figure 3.2-5	Two sets of creep rupture specimens prestressed to 70 % and 80 % of average tensile strength of CFCC .....	26
Figure 3.2-6	Strand-meter for strain evaluation in creep rupture specimens .....	26
Figure 3.2-7	Creep rupture test setup for stress levels higher than 90 % of the CFCC average tensile strength.....	27
Figure 3.2-8	Creep-rupture test setup for stress level of 94 % of average CFCC tensile strength.....	28
Figure 3.2-9	Force monitoring of CFCC specimens with a load of 48 kip (213 kN) per strand.....	29
Figure 3.2-10	Force monitoring of CFCC specimens with a load of 55 kip (245 kN) per strand.....	29
Figure 3.2-11	Strain monitoring of creep rupture CFCC specimens.....	30
Figure 3.3-1	Relaxation test setup .....	32
Figure 3.3-2	Inline load cells for force monitoring of relaxation specimens .....	33
Figure 3.3-3	Stressing relaxation specimens to an initial load level of 47.5 kip (211 kN) .....	33
Figure 3.3-4	Strand-meters to evaluate the strain in CFCC relaxation specimens.....	34
Figure 3.3-5	Force monitoring in relaxation CFCC specimens.....	35
Figure 3.3-6	Strain monitoring of relaxation CFCC specimens .....	36
Figure 3.3-7	Total loss of the force in CFCC specimens due to anchorage and CFCC relaxation.....	36
Figure 3.3-8	Loss of the force in CFCC specimens due to anchorage relaxation .....	37
Figure 3.3-9	Loss of force in CFCC specimens due to relaxation of CFCC .....	37
Figure 3.3-10	Percentage loss of force in CFCC specimens due to CFCC relaxation only .....	38
Figure 3.3-11	Estimated one-million-hour relaxation rate in CFCC specimens .....	38
Figure 3.4-1	Stressing CFCC specimens for evaluation of long-term properties.....	40

Figure 3.4-2	Long-term monitoring of CFCC specimens in a controlled laboratory environment .....	40
Figure 3.4-3	Long-term monitoring of prestressed CFCC specimens stored outdoors and exposed to Michigan weather .....	41
Figure 3.4-4	Monitoring the level of prestressing force through inline load cells attached to the CFCC specimens.....	41
Figure 3.4-5	CFCC specimens stored outdoors after three years of continuous monitoring ...	42
Figure 3.4-6	Long-term monitoring of CFCC specimens loaded in controlled laboratory environment (indoors).....	42
Figure 3.4-7	Long-term monitoring of CFCC specimens stored outdoors.....	43
Figure 3.4-8	Temperature change in outdoor CFCC specimens .....	43
Figure 3.5-1.	Closed-loop hydraulic system to maintain a constant force in creep test specimen .....	45
Figure 3.5-2	CFCC specimens under constant load to evaluate creep rupture strength.....	46
Figure 3.5-3.	Lowest estimate for one-million-hour creep-rupture strength based on available test results including long-term monitoring CFCC specimens.....	46
Figure 4.2-1	Evaluating prestress loss in CFCC specimens due to temperature increase.....	57
Figure 4.2-2	Heated length of CFCC strand inside the heat chamber .....	57
Figure 4.2-3	Time-temperature curves for thermal test specimens in Phase I .....	58
Figure 4.2-4	Temperature profiles for thermal test specimens in Phase II.....	58
Figure 4.2-5	Load vs. time for TH-S1 in Phase I of thermal testing .....	64
Figure 4.2-6	Load vs. time for TH-S2 in Phase I of thermal testing .....	64
Figure 4.2-7	Load vs. time for TH-S3 in Phase I of thermal testing .....	65
Figure 4.2-8	Load vs. time for TH-S4 in Phase I of thermal testing .....	65
Figure 4.2-9	Load vs. time for TH-S5 in Phase I of thermal testing .....	66
Figure 4.2-10	Load vs. time for TH-S2 in Phase II of thermal testing.....	66

Figure 4.2-11	Load vs. time for TH-S3 in Phase II of thermal testing.....	67
Figure 4.2-12	Load vs. time for TH-S4 in Phase II of thermal testing.....	67
Figure 4.2-13	Load vs. time for TH-S5 in Phase II of thermal testing.....	68
Figure 4.2-14	Uniaxial testing of CFCC specimens in Phase III .....	68
Figure 4.2-15	Failure of CFCC specimens in Phase III.....	69
Figure 4.3-1	Cross section and internal reinforcement details of decked bulb T-beams .....	72
Figure 4.3-2	Assembling the reinforcement cages for decked bulb T beams .....	72
Figure 4.3-3	Placing completed reinforcement cages in formwork .....	72
Figure 4.3-4	Completing the formwork and adding separators between beams .....	73
Figure 4.3-5	Passing prestressing CFCC strands through the reinforcement cages and connecting load cells and end couplers.....	73
Figure 4.3-6	Attaching steel anchorage and applying prestressing force with a hydraulic jack .....	73
Figure 4.3-7	Applying prestressing force using a hydraulic pump .....	74
Figure 4.3-8	Placing concrete in the formwork.....	74
Figure 4.3-9	Slump test measuring 10 in. (254 mm).....	74
Figure 4.3-10	Preparing concrete cylinders for uni-axial compressive strength test .....	75
Figure 4.3-11	Compacting the concrete with electric vibrators .....	75
Figure 4.3-12	Completed decked bulb T beams ready for curing.....	75
Figure 4.3-13	Prestress loss prior to transfer (Strand 1-4).....	76
Figure 4.3-14	Prestress loss prior to transfer (Strand 5-8).....	77
Figure 4.3-15	A decked bulb T beam under three-point loading in the environmental chamber.....	79
Figure 4.3-16	LMTs, LVDTs, and strain gages on the soffit of the beam at mid-span.....	79

Figure 4.3-17	Strain gages on the top surface of the decked bulb T beam.....	80
Figure 4.3-18	Load-deflection curves of Beam F1 due to loading at -40 °F (-40 °C) .....	82
Figure 4.3-19	Load-deflection curves of Beam F1 due to re-loading at ambient temperature .....	82
Figure 4.3-20	Load-deflection curves of Beam F1 during 60-kip (267-kN) load cycle.....	83
Figure 4.3-21	Calculation of the decompression load by evaluating the deviation of the load-deflection curve from the linear un-cracked curve .....	83
Figure 4.3-22	Deviation of load-deflection curves from the linear un-cracked curve in Beam F1 indicating the decompression loads at ambient and -40 °F (-40 °C)....	84
Figure 4.3-23	Close-up view showing the deviation of load-deflection curves from the linear un-cracked curves in Beam F1 and indicating the decompression loads at ambient & -40 °F (-40 °C).....	84
Figure 4.3-24	Load-deflection curves of Beam F2 due to loading at -40 °F (-40 °C) .....	85
Figure 4.3-25	Load-deflection curves of Beam F2 due to loading at ambient temperature .....	86
Figure 4.3-26	Load-deflection curves of Beam F2 during 60-kip (267-kN) load cycle at ambient & -40 °F (-40 °C) .....	86
Figure 4.3-27	Deviation of load-deflection curves from the linear un-cracked curve in Beam F2 indicating the decompression loads at ambient and -40 °F (-40 °C)....	87
Figure 4.3-28	Close-up view showing the deviation of load-deflection curves from the linear un-cracked curves in Beam F2 and indicating the decompression loads at ambient & -40 °F (-40 °C).....	87
Figure 4.3-29	Load-deflection curves of Beam H1 due to loading at 176 °F (80 °C) .....	88
Figure 4.3-30	Load-deflection curves of Beam H1 due to loading at ambient temperature .....	89
Figure 4.3-31	Load-deflection curves of Beam H1 during 60-kip (267-kN) load cycle at ambient and 176 °F (80 °C) .....	89
Figure 4.3-32	Deviation of load-deflection curves from the linear un-cracked curve in Beam H1 indicating the decompression loads at ambient and 176 °F.....	90
Figure 4.3-33	Close-up view showing the deviation of load-deflection curves from the linear un-cracked curves in Beam H1 and indicating the decompression loads at ambient & 176 °F (80 °C) .....	90

Figure 4.3-34	Load-deflection curves of Beam H2 due to loading at 176 °F (80 °C) .....	91
Figure 4.3-35	Load-deflection curves of Beam H2 due to loading at ambient temperature .....	92
Figure 4.3-36	Load-deflection curves of Beam H2 during 60-kip (267-kN) load cycle at ambient and 176 °F (80 °C) .....	92
Figure 4.3-37	Deviation of load-deflection curves from the linear un-cracked curve in Beam H2 indicating the decompression loads at ambient and 176 °F (80 °C)....	93
Figure 4.3-38	Close-up view showing the deviation of load-deflection curves from the linear un-cracked curves in Beam H2 and indicating the decompression loads at ambient & 176 °F (80 °C) .....	93
Figure 4.3-39	Load-deflection curves of Beam F2-R during 60-kip (267-kN) load cycle at ambient and -40 °F (-40 °C) .....	94
Figure 4.3-40	Deviation of load-deflection curves from the linear un-cracked curve in Beam F2-R indicating the decompression loads at ambient and -40 °F (-40 °C).....	95
Figure 4.3-41	Close-up view showing the deviation of load-deflection curves from the linear un-cracked curves in Beam F2-R indicating the decompression loads at ambient & -40 °F (-40 °C) .....	95
Figure 4.3-42	Load-deflection curves of Beam H2-R during 60-kip (267-kN) load cycle at ambient and 176 °F (80 °C) .....	96
Figure 4.3-43	Deviation of load-deflection curves from the linear un-cracked curve in Beam H2-R indicating the decompression loads at ambient and 176 °F (80 °C).....	97
Figure 4.3-44	Close-up view showing the deviation of load-deflection curves from the linear un-cracked curves in Beam H2-R indicating the decompression loads at ambient & 176 °F (80 °C).....	97
Figure 5.2-1	Environmental Chamber at the CIMR .....	103
Figure 5.2-2	Building a steel tank for the freeze-thaw test of bulb T beams .....	104
Figure 5.2-3	Decked bulb T beam placed in the tank for freeze-thaw testing.....	104
Figure 5.2-4	Concrete cylinders from the same batch as the beams placed with the beams and exposed to freeze-thaw cycles. Other cylinders are stored at Lab. conditions .....	105

Figure 5.2-5	Duct work for air freezing and water thawing according to ASTM C666 .....	105
Figure 5.2-6	Decked bulb T beams during freezing and thawing cycles .....	106
Figure 5.2-7	Water thawing of decked bulb T beams .....	106
Figure 5.2-8	Air vs beam core temperature during the freezing and thawing cycles .....	108
Figure 5.2-9	Deterioration of decked bulb T beams after exposure to 300 freeze-thaw cycles.....	108
Figure 5.2-10	Concrete cylinders after exposure to 300 freeze-thaw cycles.....	109
Figure 5.2-11	Testing and failure of cylinders after exposure to freeze-thaw cycles.....	111
Figure 5.2-12	Testing and failure of concrete cylinders after exposure to freeze-thaw cycles.....	111
Figure 5.2-13	Testing and failure of control cylinders .....	112
Figure 5.2-14	Typical failure mode of control cylinders not exposed to freeze-thaw cycles ..	112
Figure 5.2-15	Flexural test setup for control beam C1 .....	116
Figure 5.2-16	Instrumentation of Beam C1 for strain and deflection monitoring.....	117
Figure 5.2-17	Failure of Beam C1 .....	117
Figure 5.2-18	Close-up view showing the rupture of CFCC strands in Beam C1 .....	118
Figure 5.2-19	Load vs. deflection curves for Beam C1 .....	118
Figure 5.2-20	Test setup of Beam C2.....	119
Figure 5.2-21	Failure of Beam C2.....	119
Figure 5.2-22	Rupture of strands and concrete spalling of Beam C2.....	120
Figure 5.2-23	Load vs. deflection curves for Beam C2.....	120
Figure 5.2-24	Test setup of Beam F1 after exposure to freeze-thaw cycles.....	121
Figure 5.2-25	Failure of Beam F1 .....	121
Figure 5.2-26	Close-up picture for CFCC strands in Beam F1 after failure .....	122

Figure 5.2-27	Load vs. deflection curves for Beam F1 .....	122
Figure 5.2-28	Test setup for Beam F2 after exposure to freeze-thaw cycles .....	123
Figure 5.2-29	Failure of Beam F2 .....	123
Figure 5.2-30	Close-up picture for CFCC strands in Beam F2 after failure .....	124
Figure 5.2-31	Load vs. deflection curves for Beam F2 .....	124
Figure 5.2-32	Test setup for Beam H1 after exposure to freeze-thaw cycles.....	125
Figure 5.2-33	Failure of Beam H1.....	125
Figure 5.2-34	Close-up picture for CFCC strands in Beam H1 after failure.....	126
Figure 5.2-35	Load vs. deflection curves for Beam H1 .....	126
Figure 5.2-36	Test setup for Beam H2 after exposure to freeze-thaw cycles.....	127
Figure 5.2-37	Failure of Beam H2.....	127
Figure 5.2-38	Close-up picture for CFCC strands in Beam H2 after failure.....	128
Figure 5.2-39	Load vs. deflection curves for Beam H2 .....	128
Figure 5.3-1	Steel frame to accommodate 4-ft-long CFCC specimens.....	130
Figure 5.3-2	Prestressing CFCC strands and Inline load cell for force monitoring during the test .....	130
Figure 5.3-3	CFCC specimens in the Environmental Chamber along with the beams .....	131
Figure 5.3-4	CFCC specimens during freeze-thaw testing.....	131
Figure 5.3-5	Change in prestressing force with the change in temperature in CFCC strands .....	132
Figure 5.3-6	Removing the CFCC specimens after completion of 300 freeze-thaw cycles...	132
Figure 5.3-7	Releasing CFCC strands after freeze-thaw exposure.....	133
Figure 5.3-8	Preparing CFCC strands for uniaxial tensile test to evaluate residual capacity .....	133

Figure 5.3-9	Loading and failure of CFCC strands .....	134
Figure 5.3-10	Failure of CFCC strands under uni-axial load test setup .....	134
Figure 6.2-1	Test setup to establish tensile strength of CFCC at elevated temperatures .....	139
Figure 6.2-2	Anchorage device passing through a central opening in the heat chamber .....	140
Figure 6.2-3	Typical failure of test specimen at elevated temperature.....	141
Figure 6.2-4	Failure of CFCC specimen at 347 °F (175 °C).....	141
Figure 6.2-5	Failure of CFCC specimen at 392 °F (200 °C).....	141
Figure 6.2-6	Failure of CFCC specimen at 437 °F (225 °C).....	141
Figure 6.2-7	Failure of CFCC specimen at 482 °F (250 °C).....	142
Figure 6.2-8	Failure of CFCC specimen at 527 °F (275 °C).....	142
Figure 6.2-9	Failure of CFCC specimen at 572 °F (300 °C).....	142
Figure 6.2-10	Failure of CFCC specimen at 617 °F (325 °C).....	142
Figure 6.2-11	Failure of CFCC specimen at 662 °F (350 °C).....	142
Figure 6.2-12	Decrease in tensile strength with increase in Temperature for CFCC strands ..	144
Figure 6.3-1	Cross-section of prestressed decked bulb T-beam, all dimensions are in in. [mm].....	146
Figure 6.3-2	Side view of beam with thermocouple locations, all dimensions are in in. [mm].....	147
Figure 6.3-3	Thermocouple location in the beam, top view, all dimensions are in in. [mm].....	148
Figure 6.3-4	Thermocouple location in the beam, underside view, all dimensions are in in. [mm].....	148
Figure 6.3-5	Thermocouple location in the quarter sections, all dimensions are in in. [mm].....	148
Figure 6.3-6	Thermocouple location in the mid-section, typical, all dimensions are in in. [mm].....	149

Figure 6.3-7	Sketch of test set-up, all dimensions are in in. [mm].....	149
Figure 6.3-8	Beam notation .....	149
Figure 6.3-9	Beam S132-25-1 before fire.....	151
Figure 6.3-10	Beam S132-25-1 during fire .....	151
Figure 6.3-11	Beam S132-25-1 after fire .....	152
Figure 6.3-12	Rear view of Beam S132-25-1 after fire.....	152
Figure 6.3-13	Time-deflection curve for Beam S132-25-1 .....	153
Figure 6.3-14	Time-temperature curves for Beam S132-25-1 at the mid-span.....	153
Figure 6.3-15	Time-temperature curves for Beam S132-25-1 at level of prestressed steel strands .....	154
Figure 6.3-16	Beam C72-14-1 before fire .....	155
Figure 6.3-17	Beam C72-14-1 during fire.....	156
Figure 6.3-18	Burning of CFCC stirrups in Beam C72-14-1 during fire .....	156
Figure 6.3-19	Beam C72-14-1 after fire .....	157
Figure 6.3-20	Close-up view of Beam C72-14-1 after failure.....	157
Figure 6.3-21	Time-deflection curve for Beam C72-14-1.....	158
Figure 6.3-22	Time-temperature curves for Beam C72-14-1 at mid-span .....	158
Figure 6.3-23	Time-temperature curves for Beam C72-14-1 at level of prestressed CFCC strands .....	159
Figure 6.3-24	Beam C100-20-1 before fire .....	160
Figure 6.3-25	Beam C100-20-1 after fire .....	160
Figure 6.3-26	Concrete spalling on CFCC stirrups side of Beam C100-20-1 after fire .....	161
Figure 6.3-27	Time-deflection curve for Beam C100-20-1.....	161
Figure 6.3-28	Time-temperature curves for Beam C100-20-1 at mid-span .....	162

Figure 6.3-29	Time-temperature curves for Beam C100-20-1 at prestressed CFCC strands...	162
Figure 6.3-30	Beam C100-20-2 before fire .....	164
Figure 6.3-31	Beam C100-20-2 after fire .....	164
Figure 6.3-32	Concrete spalling of bottom flange of Beam C100-20-2 after fire, bottom side view .....	165
Figure 6.3-33	Time-deflection curve for Beam C100-20-2.....	165
Figure 6.3-34	Time-temperature curves for Beam C100-20-2 at mid-span .....	166
Figure 6.3-35	Time-temperature curves for Beam C100-20-2 at prestressed CFCC strands...	166
Figure 6.3-36	Beam C100-20-3 before fire .....	168
Figure 6.3-37	Beam C100-20-3 after fire .....	168
Figure 6.3-38	Carbon fiber filaments after burning of epoxy adhesive in Beam C100-20-3...	169
Figure 6.3-39	Time-deflection curve for Beam C100-20-3.....	169
Figure 6.3-40	Time-temperature curve for Beam C100-20-3 at mid-span.....	170
Figure 6.3-41	Time-temperature curves for Beam C100-20-3 at prestressed CFCC strands...	170
Figure 6.3-42	Beam C100-20-4 before fire .....	172
Figure 6.3-43	Beam C100-20-4 after fire .....	172
Figure 6.3-44	Concrete spalling of Beam C100-20-4 after fire.....	173
Figure 6.3-45	Time-deflection curve for Beam C100-20-4.....	173
Figure 6.3-46	Time-temperature curves for Beam C100-20-4 in the mid-span .....	174
Figure 6.3-47	Time-temperature curves for Beam C100-20-4 at prestressed CFCC strands...	174
Figure 6.3-48	Beam C100-20-5 before fire .....	176
Figure 6.3-49	Beam C100-20-5 during fire.....	176
Figure 6.3-50	Beam C100-20-5 after fire .....	177

Figure 6.3-51	Time-deflection curve for Beam C100-20-5.....	177
Figure 6.3-52	Time-temperature curves for Beam C100-20-5 at mid-span .....	178
Figure 6.3-53	Time-temperature curves for Beam C100-20-5 at prestressed CFCC strands... 178	
Figure 6.3-54	Beam C132-25-1 before fire .....	180
Figure 6.3-55	Beam C132-25-1 after fire .....	180
Figure 6.3-56	Close up view of mid-section of Beam C132-25-1 just after failure .....	181
Figure 6.3-57	Time-deflection curve for Beam C132-25-1.....	181
Figure 6.3-58	Time-temperature curves for Beam C132-25-1 at mid-span .....	182
Figure 6.3-59	Time-temperature curves for Beam C132-25-1 at prestressed CFCC strands... 182	
Figure 7.2-1	Specimen configuration of pull-out test.....	187
Figure 7.2-2	Formwork for pull-out test specimens .....	188
Figure 7.2-3	CFCC specimens in the formwork before pouring the concrete.....	188
Figure 7.2-4	Pouring concrete and completed pull-out specimen after removal of formwork.....	189
Figure 7.2-5	Test setup for bond specimens .....	190
Figure 7.2-6	Load-displacement curve for static pullout test .....	192
Figure 7.2-7	Stress ratio vs No. of load cycles to failure in CFCC specimens tested for bond fatigue strength.....	194
Figure 7.3-1	Test setup of evaluation of flexural bond splice length .....	195
Figure 7.3-2	Cross section and dimensions of test beams .....	196
Figure 7.3-3	Assembling the reinforcement cages of the test beams .....	197
Figure 7.3-4	Completed reinforcement cage showing the location of the splice and stirrups.....	198
Figure 7.3-5	Placing the reinforcement cages in the formwork .....	198

Figure 7.3-6	Casting the concrete in the test specimens.....	199
Figure 7.3-7	Completed beams and preparing concrete cylinders for uniaxial testing .....	199
Figure 7.3-8	Average compressive strength of concrete over time .....	200
Figure 7.3-9	Setup and Testing of BC-0.5.....	202
Figure 7.3-10	Failure of BC-0.5 .....	202
Figure 7.3-11	Close-up view of BC-0.5 showing the rupture of steel strands .....	203
Figure 7.3-12	Setup and testing of B1-0.5.....	203
Figure 7.3-13	Failure of B1-0.5.....	204
Figure 7.3-14	Close-up view of B1-0.5 showing a large crack at the end of splice.....	204
Figure 7.3-15	Setup and testing of B2-0.5.....	205
Figure 7.3-16	Failure of B2-0.5.....	205
Figure 7.3-17	Close-up view of B2-0.5 showing CFCC slippage at the end of splice.....	206
Figure 7.3-18	Setup and testing of B3-0.5.....	206
Figure 7.3-19	Failure of B3-0.5.....	207
Figure 7.3-20	Close-up view of B3-0.5 showing CFCC slippage at the end of splice.....	207
Figure 7.3-21	Setup and testing of B4-0.5.....	208
Figure 7.3-22	Failure of B4-0.5.....	208
Figure 7.3-23	Close-up view of B4-0.5 showing CFCC slippage at the end of the splice.....	209
Figure 7.3-24	Failure of BC-0.6 .....	209
Figure 7.3-25	Crushing of concrete followed by rupture of CFCC strands in BC-0.6 .....	210
Figure 7.3-26	Setup and testing of B1-0.6.....	210
Figure 7.3-27	Failure of B1-0.6.....	211
Figure 7.3-28	Close-up view of B1-0.6 showing the CFCC slippage at the end of the splice.	211

Figure 7.3-29	Setup and testing of B2-0.6.....	212
Figure 7.3-30	Failure of B2-0.6.....	212
Figure 7.3-31	Close-up view of B2-0.6 showing CFCC slippage at the end of the splice.....	213
Figure 7.3-32	Setup and testing of B3-0.6.....	213
Figure 7.3-33	Failure of B3-0.6.....	214
Figure 7.3-34	Cracking and failure of B3-0.6 at the end of the splice .....	214
Figure 7.3-35	Setup and testing of B4-0.6.....	215
Figure 7.3-36	Failure of B4-0.6.....	215
Figure 7.3-37	Close-up view of B4-0.6 showing CFCC slippage at splice end.....	216
Figure 7.3-38	Load vs. mid-span deflection of beams with 0.5-in. (12.5-mm) CFCC strands .....	216
Figure 7.3-39	Load vs. mid-span deflection of beams with 0.6-in. (15.2-mm) CFCC strands .....	217
Figure 7.3-40	Splice length vs. Maximum load in all test beams.....	219
Figure 7.3-41	Strain versus splice length of the spliced CFCC strands .....	220
Figure 7.4-1	Cross-sections of prestressed box-beam .....	222
Figure 7.4-2	Cross-sections of prestressed box-beam reinforced with spliced stirrups in shear .....	222
Figure 7.4-3	Longitudinal sections of prestressed concrete box-beams.....	223
Figure 7.4-4	Configuration of stirrups in the beam specimens .....	224
Figure 7.4-5	Stirrup dimensions .....	224
Figure 7.4-6	Construction of the formwork for the box beams.....	226
Figure 7.4-7	Preparing and instrumenting the reinforcement cages.....	226
Figure 7.4-8	Prestressing CFCC strands from the live end with load cell on the dead end ...	227

Figure 7.4-9	Prestressing CFCC strands from the live end .....	228
Figure 7.4-10	Prestressing order of CFCC strands .....	228
Figure 7.4-11	Couplers spacing .....	228
Figure 7.4-12	Casting the concrete of the box beams .....	229
Figure 7.4-13	Releasing of prestressed strands .....	230
Figure 7.4-14	Prestressing force prior to transfer .....	231
Figure 7.4-15	Concrete compressive strength .....	231
Figure 7.4-16	Instrumentation and test setup of the box beams .....	232
Figure 7.4-17	Shear test setup of box beams .....	233
Figure 7.4-18	Crack pattern in beam C-C .....	234
Figure 7.4-19	Failure of beam C-C .....	234
Figure 7.4-20	Shear force vs under-load-deflection in Beam C-C for all load cycles .....	235
Figure 7.4-21	Shear force vs under-load-deflection in Beam C-C for last load cycle .....	235
Figure 7.4-22	Crack pattern of beam C-10.75 .....	236
Figure 7.4-23	Failure of beam C-10.75 .....	237
Figure 7.4-24	Shear force vs under-load-deflection in Beam C-10.75 for all load cycles .....	238
Figure 7.4-25	Shear force vs under-load-deflection in Beam C-10.75 for last load cycle .....	238
Figure 7.4-26	Crack pattern of beam C-7 .....	239
Figure 7.4-27	Failure of beam C-7 .....	240
Figure 7.4-28	Shear force vs under-load-deflection in Beam C-7 for all load cycles .....	241
Figure 7.4-29	Shear force vs under-load-deflection in Beam C-7 for last load cycle .....	241
Figure 7.4-30	Crack pattern of beam C-4 .....	242
Figure 7.4-31	Failure of beam C-4 .....	243

Figure 7.4-32	Shear force vs under-load-deflection in Beam C-4 for all load cycles .....	244
Figure 7.4-33	Shear force vs under-load-deflection in Beam C-4 for last load cycle .....	244
Figure 7.4-34	Crack pattern of beam S-C.....	245
Figure 7.4-35	Failure of beam S-C .....	246
Figure 7.4-36	Shear force vs under-load-deflection in Beam S-C for all load cycles.....	247
Figure 7.4-37	Shear force vs under-load-deflection in Beam S-C for last load cycle.....	247
Figure 7.4-38	Crack pattern of beam S-10.75 .....	248
Figure 7.4-39	Failure of beam S-10.75.....	249
Figure 7.4-40	Shear force vs under-load-deflection in Beam S-10.75 for all load cycles .....	250
Figure 7.4-41	Shear force vs under-load-deflection in Beam S-10.75 for last load cycle .....	250
Figure 7.4-42	Crack pattern of beam S-7 .....	251
Figure 7.4-43	Failure of beam S-7.....	252
Figure 7.4-44	Shear force vs under-load-deflection in Beam S-7 for all load cycles .....	253
Figure 7.4-45	Shear force vs under-load-deflection in Beam S-C for last load cycle.....	253
Figure 7.4-46	Crack pattern of beam S-4 .....	254
Figure 7.4-47	Failure of beam S-4.....	255
Figure 7.4-48	Shear force vs under-load-deflection in Beam S-4 for all load cycles .....	256
Figure 7.4-49	Shear force vs under-load-deflection in Beam S-C for last load cycle.....	256
Figure 8.2-1	Longitudinal section of prestressed decked bulb T beam.....	260
Figure 8.2-2	Details of cross section 1-1 (left) & 2-2 (right) of the beam specimen .....	261
Figure 8.2-3	Steel shear reinforcement for end blocks.....	261
Figure 8.2-4	Steel shear reinforcement between end blocks .....	262
Figure 8.2-5	Installing PVC conduits in the end block of the beams .....	263

Figure 8.2-6	Wooden deck supported on adjustable steel chairs and center wall spanning between steel bulk heads.....	264
Figure 8.2-7	Leveling the platform using a laser level.....	264
Figure 8.2-8	Different stages of formwork and cage construction.....	265
Figure 8.2-9	Bottom prestressing installation.....	266
Figure 8.2-10	Layout and prestressing CFCC strands.....	267
Figure 8.2-11	Coupler connections.....	267
Figure 8.2-12	Installed strain gages on longitudinal reinforcement.....	267
Figure 8.2-13	Slump test.....	268
Figure 8.2-14	Placing and curing the concrete of the beams and cylinders.....	269
Figure 8.2-15	Release of steel strands at transfer.....	269
Figure 8.2-16	Prestress loss prior to transfer (Strand 1-4).....	270
Figure 8.2-17	Prestress loss prior to transfer (Strand 5-8).....	271
Figure 8.2-18	Smoothing the surface before installing strain gages.....	272
Figure 8.2-19	Installed VWSG on beams before prestress transfer.....	272
Figure 8.2-20	Instrumentation of decked bulb T beams at mid-span.....	273
Figure 8.2-21	Outdoor beams.....	274
Figure 8.2-22	Indoor beams.....	274
Figure 8.2-23	Test setup of decked bulb T beams.....	274
Figure 8.2-24	Line of best fit for VWSG strain measurements.....	276
Figure 8.2-25	Recorded VWSG strain vs. time for Beam C.....	276
Figure 8.2-26	Recorded VWSG temperature vs. time for Beam C.....	277
Figure 8.2-27	Recorded VWSG strain vs. time for Beam I-1.....	277

Figure 8.2-28	Recorded VWSG temperature vs. time for Beam I-1 .....	278
Figure 8.2-29	Recorded VWSG strain vs. time for Beam O-1 .....	278
Figure 8.2-30	Recorded VWSG temperature vs. time for Beam O-1 .....	279
Figure 8.2-31	Recorded VWSG strain vs. time for Beam I-2 .....	279
Figure 8.2-32	Recorded VWSG temperature vs. time for Beam I-2 .....	280
Figure 8.2-33	Recorded VWSG strain vs. time for Beam O-2.....	280
Figure 8.2-34	Recorded VWSG temperature vs. time for Beam O-2 .....	281
Figure 8.2-35	Cracking load from load deflection curve .....	282
Figure 8.2-36	Load vs. deviation in deflection curve for Beam C .....	282
Figure 8.2-37	Deviation from linearity (Beam C).....	283
Figure 8.2-38	Load vs. deviation in deflection curve for Beam I-1 .....	283
Figure 8.2-39	Deviation from linearity (Beam I-1).....	284
Figure 8.2-40	Load vs. deviation in deflection curve for Beam O-1.....	284
Figure 8.2-41	Deviation from linearity (Beam O-1) .....	285
Figure 8.2-42	Load vs. deviation in deflection curve for Beam I-2 .....	285
Figure 8.2-43	Deviation from linearity (Beam I-2).....	286
Figure 8.2-44	Load vs. deviation in deflection curve for Beam O-2.....	286
Figure 8.2-45	Deviation from linearity (Beam O-2) .....	287
Figure 8.2-46	Cracking pattern of decked bulb T beams from the top: C, I-1, O-1, I-2, and O-2 .....	288
Figure 8.2-47	Failure of Beam C.....	290
Figure 8.2-48	Load vs. deflection curves for Beam C.....	291
Figure 8.2-49	Failure of Beam I-1 .....	291

Figure 8.2-50	Load vs. deflection curves for Beam I-1 .....	292
Figure 8.2-51	Failure of Beam O-1 .....	292
Figure 8.2-52	Ruptured prestressing strands at failure of Beam O-1 .....	293
Figure 8.2-53	Load vs. deflection curves for Beam O-1 .....	293
Figure 8.2-54	Failure of Beam I-2 .....	294
Figure 8.2-55	Ruptured prestressing strands at failure of Beam I-2.....	294
Figure 8.2-56	Load vs. deflection curves for Beam I-2.....	295
Figure 8.2-57	Failure of Beam O-2 .....	295
Figure 8.2-58	Un-ruptured prestressing strands of Beam O-2 at failure .....	296
Figure 8.2-59	Load vs. deflection curves for Beam O-2 .....	296

## LIST OF TABLES

Table 2.2-1	Mechanical properties of CFCC as provided by manufacturer, Tokyo Rope.....	5
Table 2.4-1	Mechanical properties of steel pipes used in anchorage preparation.....	9
Table 2.5-1	Uni-axial test results of sleeve-type anchorage .....	16
Table 2.5-2	Uni-axial test results of wedge anchorage .....	17
Table 3.2-1	Results of creep rupture test performed on CFCC strand specimens with a diameter of 0.6 in. (15.2 mm) .....	31
Table 3.5-1	Summary of CFCC specimens (diameter of 0.6 in. (15.2 mm)) under monitoring.....	47
Table 3.5-2	Test results of creep-rupture strength performed by Tokyo Rope using CFCC strands with a diameter of 0.5 in. (12 mm).....	47
Table 3.5-3	Results of creep-rupture testing on CFCC strands with a diameter of 0.7 in. (18 mm).....	48
Table 3.6-1	Uni-axial test results of indoor specimens with initial load of 47.5 kip (211 kN) .....	49
Table 3.6-2	Uni-axial test results of indoor specimens with initial load of 50.1 kip (223 kN) .....	49
Table 3.6-3	Uni-axial test results of indoor specimens with initial load of 56.5 kip (251 kN) .....	50
Table 3.6-4	Uni-axial test results of outdoor specimens with initial load of 56.5 kip (251 kN) .....	50
Table 3.6-5	Uni-axial test results of outdoor specimens with initial load of 50.1 kip (223 kN) .....	51
Table 3.6-6	Summary of uni-axial test results of unstressed specimens stored for three years .....	51
Table 4.2-1	Summary of observed load loss due to increase in temperature in Phase I .....	63
Table 4.2-2	Results of tensile testing of CFCC specimens .....	69
Table 4.3-1	Concrete mix per cubic yard .....	71

Table 5.2-1	Results of uniaxial compressive test .....	113
Table 5.2-2	Summary of experimental results for decked bulb T-beams .....	116
Table 5.3-1	Summary of experimental results for Post-tensioned CFCC strands.....	135
Table 6.2-1	Summary of test results for tensile strength of CFCC at elevated temperature.	143
Table 6.2-2	Comparison with Manufacturer's test results .....	144
Table 6.4-1	Fire resistance time of CFCC prestressed decked bulb T beam .....	184
Table 7.2-1	Pull-out test results.....	191
Table 7.2-2	Bond fatigue test results.....	193
Table 7.3-1	Properties of reinforcement.....	197
Table 7.3-2	Summary for test results of beam specimens in flexural bond test.....	201
Table 7.4-1	Material properties of shear reinforcement.....	225
Table 7.4-2	Summary of test results of the shear bond test .....	258
Table 8.2-1	Properties of steel shear reinforcement.....	262
Table 8.2-2	Summary of experimental results for decked bulb T-beams .....	297
Table 9.2-1	Nominal moment capacity calculated using different assumptions for the depth of the neutral axis .....	307
Table 9.3-1	Experimental results of test beams .....	311
Table 9.3-2	Experimental vs. calculated shear resistance in beams with CFCC stirrups .....	321
Table 9.3-3	Experimental vs. calculated shear resistance in beams with steel stirrups .....	322
Table 9.3-4	Limits for the shear factors $\beta$ and $\theta$ based on the limits of bottom strain, $\epsilon_s$ ...	323
Table 9.3-5	Nominal shear capacities of test beams using general procedure.....	326

## EXECUTIVE SUMMARY

Successful implementation of carbon fiber reinforced polymer (CFRP) in precast prestressed bridge beam construction requires careful assessment for the short and long-term behavior of the material. Besides, different design parameters need to be evaluated and established before wide range deployment of CFRP in highway bridge design. This report presents the details and results of comprehensive experimental and analytical investigations that were executed with the main objective of establishing the main design criteria of bridge beams prestressed with CFRP strands. The investigations evaluated the short and long-term performance of CFRP under various environmental and loading conditions. The experimental investigation started by evaluating and optimizing the performance of different anchorage devices and selecting a device that was adequate for executing other tasks of the investigation. Second, the mechanical properties of the selected CFRP material such as average tensile strength, maximum strain, elastic modulus, and guaranteed strength were established through testing 49-in. (1244-mm) long CFRP specimens. Third, long-term properties of CFRP strands such as relaxation and creep rupture strength were evaluated by testing multiple sets of similar CFRP specimens exposed to different environmental and loading conditions. Some of the test specimens were loaded and monitored at ambient temperature and controlled laboratory conditions, while other test specimens were loaded and monitored while being exposed to harsh Michigan weather for a period exceeding three years. In addition, multiple sets of test specimens with the same configuration were evaluated for strength and prestress loss under severe exposure conditions. For instance, two sets of test specimens were subjected to elevated temperatures and loads under two different test protocols. Another set was prestressed, exposed to 300 cycles of freezing and thawing in a special environmental chamber, and then loaded to failure in a uni-axial test setup.

Parallel to testing un-bonded CFRP specimens, the experimental investigation also included testing and evaluating half-scale decked bulb T-beams prestressed with bonded CFRP strands. Three sets of CFRP precast prestressed decked bulb T beams were designed, constructed, and tested to failure. The first set included five identical decked bulb T beams that were constructed on the same day from the same concrete batch. Each beam had a span of 26 ft (7.92 m), a depth of 16 in. (406 mm), a flange width of 18 in. (457 mm) and was prestressed with four CFRP strands with an initial prestressing force of approximately 22.5 kip (100 kN) /strand. The first beam served

as a control beam and was tested to failure under four-point-load setup after 28 days of construction. Two of the remaining four beams were preserved in controlled laboratory conditions and were monitored for prestress loss, while the other two beams were stored outdoors where they were exposed to extreme Michigan weather and they were also monitored for prestress loss. After one year, one indoor beam and one outdoor beam were tested to failure under the same four-point-load setup as that of the control beam. The remaining two beams were tested to failure under the same loading setup after two years of construction. The cracking loads, decompression loads, and ultimate loads of the beams were observed and compared to estimate the prestress loss in each beam and assess the effect of environmental exposure on the performance of CFRP prestressed beams.

The second set of decked bulb T beams consisted of eight beams prestressed with CFRP strands and one beam prestressed with steel strands. All beams were identical in cross section and dimensions and had a span of 16 ft (4.87 m), depth of 16 in. (406 mm), and a top flange width of 18 in. (457 mm). Out of the eight CFRP prestressed beams, one beams was prestressed with an initial prestressing force of 72 kip (320 kN) /beam, six were prestressed with an initial prestressing force of 100 kip (445 kN) /beam, and one was prestressed with an initial prestressing force of 132 kip (587 kN) /beam. The steel prestressed beams served as a control beam and was prestressed with an initial prestressing force of 132 kip (587 kN) /beam. All the beams were subjected to a fire event according to ASTM E119 combined with a service loading applied through a three-point-load setup. The test took place inside a large-scale natural-gas fire chamber, where the air temperature, beam temperature, load, and deflection were monitored during the entire test through a special data acquisition system. The test ended when the test beam failed to support the applied service load. Test results were assembled and analyzed to establish fire resistance criteria for beams prestressed with CFRP strands.

To study the effect of seasonal temperature change and the influence of freezing and thawing cycles on the performance of CFRP prestressed bridge beams, a third set of CFRP prestressed decked bulb T beams was designed, constructed and tested. The set included six identical beams with a span of 16 ft (4.87 m), a depth of 16 in. (406 mm), and a top flange width of 18 in. (457 mm). The beams were built from the same concrete batch and were provided with an initial prestressing force of 132 kip (587 kN) /beam. All beams were tested under three-point-load setup

to approximately 67 % of their theoretical load carrying capacity. Two beams served as control beams and were preserved and tested in controlled laboratory conditions. Two beams were tested at hot conditions with air and beam temperatures of 176 °F (80 °C). Then the beams were allowed to cool down and test was repeated at ambient temperature at 68 °F (20 °C). The last two beams were tested at severe cold conditions, where the air/beam temperature was lowered to -40 °F (-40 °C). Then, the beams were allowed to warm up and the test was repeated at ambient conditions. Test results were used to back calculate the effective prestressing force in each beam during the time of the testing and were used to estimate the change of the prestressing force due to seasonal temperature change.

The test also extended to evaluate the performance and residual strength of the beams after exposure to 300 cycles of freezing and thawing according to ASTM C666. The control beams were kept in controlled laboratory conditions, while the remaining four beams were subjected to the freezing and thawing cycles inside a large-scale environmental chamber. After the conclusion of the freeze-thaw cycles, all the beams including the control beams were loaded to failure under three-point-load setup. Parameters such as loss of prestressing force, mode of failure, and residual strength were examined and documented.

Parallel to the experimental investigation, a comprehensive analytical investigation was conducted to examine the test results and develop analytical models for the performance of CFRP materials. The outcome of the analytical investigation was deployed in the development of detailed Mathcad sheets for the design of CFRP precast prestressed highway bridge beams. The Mathcad sheets were calibrated and tested then were used in the design of I-75 bridge beams over Sexton and Kilfoil Drain in Allen Park, MI. In addition, finite element models were generated for a single bridge beam as well as the entire superstructure of the bridge of I-75. The models were analyzed under construction loads, superimposed dead loads, live loads, and also under different seasonal and gradient temperature conditions. Results from finite element analysis were compared with those obtained analytically and were used to further tune the analytical models and the Mathcad sheets.

Test results of the investigation provided valuable information and design parameters that accurately described the short and long-term performances of unbonded and bonded CFRP strands. Those design parameters were deployed to establish benchmark design criteria, design guidelines,

and recommendations that were assembled in a format similar to that of AASHTO LRFD to facilitate the design and construction of highway bridges with CFRP components. The design guidelines as well as the Mathcad sheets for CFRP bridge beam design are attached to this report under the Appendix section.

## CHAPTER 1: INTRODUCTION

### 1.1 Overview

Michigan Department of Transportation (MDOT) pioneers in the deployment of innovative materials such as non-corrosive CFRP to enhance the design, construction, and durability of highway bridge beams. This is influenced by the harsh Michigan weather and the overwhelming corrosion and durability issues associated with steel prestressed beam bridges (Grace et al. 2004 and 2002b). Supported by decades of research and analysis (Grace and Abdel-Sayed 200b), the use of CFRP as a prestressing and reinforcement material has started in Michigan in 2001 with the construction of Bridge street bridge in Southfield, MI. Since then, several bridges have been successfully designed and built with CFRP components. For instance, in 2011, a two-span side-by-side precast prestressed box-beam bridge was constructed to carry Pembroke Rd over M-39 in Detroit, MI. The bridge is transversely post-tensioned with twelve 1.57-in. (40-mm) diameter un-bonded carbon fiber composite cable (CFCC) strands. In 2012, a three-span side-by-side box beam bridge carrying M-50 over NSRR railroad in Jackson, MI was also constructed and transversely post-tensioned using twenty un-bonded CFCC strands. In 2013 and 2014, two simply supported 45°-skewed precast prestressed spread box-beam bridges were constructed to carry the east and west bounds of M-102 over Plum Creek in Southfield, MI. The box-beams are prestressed with 0.6-in. (15.2 -mm) diameter CFCC strands and are provided with CFCC stirrups in the transverse direction. The cast-in-place deck slabs for both bridges are also reinforced with CFCC strands. In 2016, a 102.5-ft (31.2-m) long simply supported bulb T beam bridge was constructed to carry M-86 over Prairie River in Centreville, MI. Each of its seven bridge beams is prestressed with 59 CFCC strands with a diameter of 0.6 in. (15.2 mm). In 2017, the construction of the 137-ft (41.7-m) long I-75 highway bridge over Sexton and Kilfoil Drain in Allen Park, MI marked the construction of the world's longest bridge span prestressed with CFRP strands.

Several other highway bridges with CFCC components are currently in either the design or construction phase. Nevertheless, with the wide deployment of CFRP strands in highway bridge construction, it is crucial to carefully evaluate the short and long-term performance of CFCC material to ensure safety and longevity of the constructed bridges.

## **1.2 Research Scope**

A four-year-old extensive research investigation has recently been completed with the focus on the long-term and durability of CFCC strands in bridge beams. The investigation was executed with the scope of:

1. Reviewing CFRP design guidelines and research reports
2. Develop experimental program to address drawbacks and evaluate long-term performance of CFRP strands
3. Review data collected through field monitoring
4. Perform numerical and analytical investigations as necessary to evaluate and justify experimental results
5. Develop empirical equations, design criteria, and items necessary for developing a guide specification
6. Report results to MDOT along with design examples

## **1.3 Research Outcome**

The outcome of this research can be summarized as:

1. Verifying CFRP design values including creep rupture strength, relaxation, prestress levels, and long-term losses
2. Establishing appropriate levels and strength reduction factors for CFRP strands considering creep rupture strength and long-term losses
3. Experimentally verifying material resistance for: bond fatigue, fire damage, and severe environmental conditions
4. Develop design methodologies, criteria, and empirical equations for inclusion in MDOT Bridge Design Manual (including details for inclusion in MDOT Bridge Design Guide)
5. Develop Mathcad design tools for CFRP prestressed highway bridge beams

6. Develop Design Guide Specifications in LRFD format for the design and construction of highway bridge beams pretensioned with CFRP strands

#### **1.4 Report Outlines**

This report documents the details and the results of the research investigation. Through the report, the work is presented in separate chapters that are split based on the objective of the work. Each chapter starts with an introduction and a brief literature review, if needed, followed by details of the research subject under consideration and finally, a summary for the test results, observations, and recommendations. The final chapter of the report summarizes main findings and recommendations of the research investigation. In addition, based on the findings and recommendations of the report, design guidelines and Mathcad sheets for the design and construction of CFRP precast prestressed highway bridge beams were developed. The design guidelines and the Mathcad sheets are attached to the report under the Appendix section. The chapters of the report are arranged as follows:

Chapter Two:	Anchorage and tensile strength of CFCC strands
Chapter Three:	Creep rupture and relaxation strength of CFCC strands
Chapter Four:	Environmental effects
Chapter Five:	Freeze-thaw effect
Chapter Six:	Fire and heat resistance of CFRP strands
Chapter Seven:	Splicing and bond fatigue of CFRP strands
Chapter Eight:	Long-term performance of beams with CFRP strands
Chapter Nine:	Flexural and shear design of CFCC prestressed beams
Chapter Ten:	Summary and conclusions
Appendix I:	Design guidelines in LRFD Format
Appendix II:	Mathcad sheet for the design of CFCC highway prestressed beams

## CHAPTER 2: ANCHORAGE AND TENSILE STRENGTH

### 2.1 Introduction

An adequate anchorage device is mandatory to establish a successful testing protocol for CFRP materials. Several types of anchorage devices have been recently developed, tested, and implemented in field applications for either post-tensioning or pre-tensioning applications (Grace et al. 2012c, 2011a, 2010a, 2010b, and 2002a). The two most common types of anchorage are sleeve-type anchorage and wedge-type anchorage. Through the investigation provided in this chapter, both types of anchorages were evaluated and tested. A series of 49-in. (1245-mm) long test specimens loaded in a uni-axial test setup to failure using either sleeve or wedge anchorage devices. Test results showed no significant difference in the average tensile strength of the test specimens with regard to the anchorage device. Nevertheless, sleeve-type anchorage appeared to be efficient and adequate for the expedited and consistent construction of the test specimens for the rest of the research investigation and therefore it was selected as the standard anchorage device for the research investigation.

### 2.2 Test Specimens

The strand specimens used in anchorage testing were 47-in. (1194 mm) long 7-wire CFCC strands, manufactured by Tokyo Rope Mfg. Co., Ltd., Japan, with a diameter of 0.6 in. (15.2 mm), cross sectional area of 0.179 in.<sup>2</sup> (115.6 mm<sup>2</sup>), and mechanical properties per lot, reported by the manufacturer, as shown in Table 2.2-1. After installing the anchorage devices at both ends, a uni-axial tensile test was conducted in accordance with ASTM Standard D7205/7205M-06 “Standard Test Method for Tensile Properties of Fiber Reinforced Polymer Matrix Composite Bars.”

The CFCC strands were delivered in spools as shown in Figure 2.2-1 and the test specimens were cut to the required length using power grinder. The cut specimens followed the curvature of the spool and to straighten them, the specimens were stretched in a wooden frame and subjected to a moderate heating at a temperature of 140 °F (60 °C) for at least 15 hours as shown in Figure 2.2-2.

Table 2.2-1 Mechanical properties of CFCC as provided by manufacturer, Tokyo Rope

Strand configuration & Lot No.	1 x 7, G34	1 x 7, G82
Date of testing	8/22/2011	2/23/2012
Diameter, in. (mm)	0.6 (15.40)	0.6 (15.33)
Guaranteed breaking load, kip (kN)	60.7 (270)	60.7 (270)
Effective cross-sectional area, in. <sup>2</sup> (mm <sup>2</sup> )	0.179 (115.6)	0.179 (115.6)
Average breaking load, kip (kN)	76.2 (339)	64.3 (286)
Max. breaking load, kip (kN)	78.7 (350)	64.5 (287)
Min. breaking load, kip (kN)	72.8 (324)	63.8 (284)
No. of test specimens	5	5
Average tensile strength, ksi (GPa)	425 (2.93)	358 (2.47)
Average tensile modulus, ksi (GPa)	21,610 (149)	20,885 (144)
Elongation, %	2.0	1.7



Figure 2.2-1 Spool of CFCC strands with a diameter of 0.6 in. (15.2 mm)



Figure 2.2-2 Heat treatment at 140 °F (60 °C) for 15 hours to straighten CFCC strands

### 2.3 Steel Wedge Anchorage

The steel wedge anchorage device is composed of four high-strength steel wedges that fit snugly around the CFCC strand inside a high-strength steel barrel. As the strand is pulled the wedges slide into the steel barrel and confine the movement of the CFCC strand. To avoid damaging the surface of the strand, a buffer system is used between the wedges and the strand. The buffer system consists of a fine steel mesh confined by a braided steel netting. The process of applying the components of the buffer system is illustrated in Figure 2.3-1 and the installation of the wedge-anchorage device is shown in Figure 2.3-2. In addition, the test extended to address newly developed composite buffer material as a replacement for the steel mesh wrap as shown in Figure 2.3-3 and Figure 2.3-4.



(a) Steel mesh as a buffer material



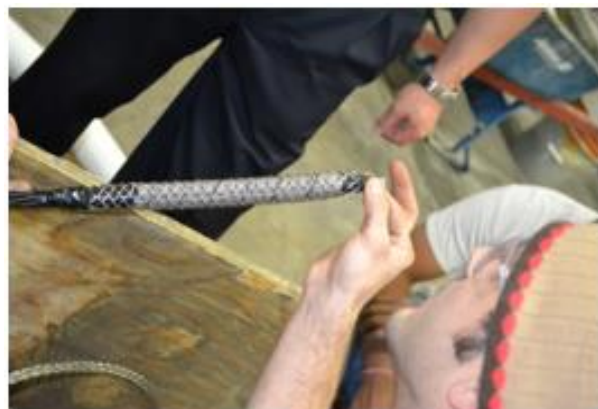
(b) Wrapping steel mesh around CFCC



(c) Securing steel mesh in place with tape



(d) Additional braided steel wire netting



(e) Securing steel wire netting with tape



(f) Preparing four steel wedges

Figure 2.3-1 Applying components of buffer layer around CFCC strands



(a) Sliding steel wedges into barrel



(b) Completed anchorage device

Figure 2.3-2 Installing steel-wedge anchorage device on CFCC strand with buffer layer



(a) New composite buffer material



(b) Confinement with steel wire netting



(c) Steel wedge system



(d) Sliding steel wedges using hand pump

Figure 2.3-3 New composite buffer material as a replacement for steel mesh wrap



Figure 2.3-4 Test specimens prepared using composite buffer layer and wedge anchorage

## 2.4 Sleeve Anchorage

As illustrated in Figure 2.4-1, a sleeve-type anchorage was prepared at Lawrence Technological University (LTU) in collaboration with Tokyo Rope. The anchorage device consisted of an externally threaded socket made of a high-strength steel pipe and a high-strength steel nut. The anchorage device was attached to the CFCC strands using cementitious-based, highly expansive material (HEM). The HEM is a special grout mix that exhibits a high degree of expansion with proper curing and produces a confining pressure of approximately 5800 psi (40 MPa). The mechanical properties of the high-strength steel anchors are given in Table 2.4-1.

Table 2.4-1 Mechanical properties of steel pipes used in anchorage preparation

Type	A53 Grade B
Outer diameter, in. (mm)	1.5 (38)
Inner diameter, in. (mm)	0.875 (22)
Wall thickness in. (mm)	0.3125 (8)
Tensile strength, ksi (MPa)	110 (758)
Yield strength, ksi (MPa)	101 (696)

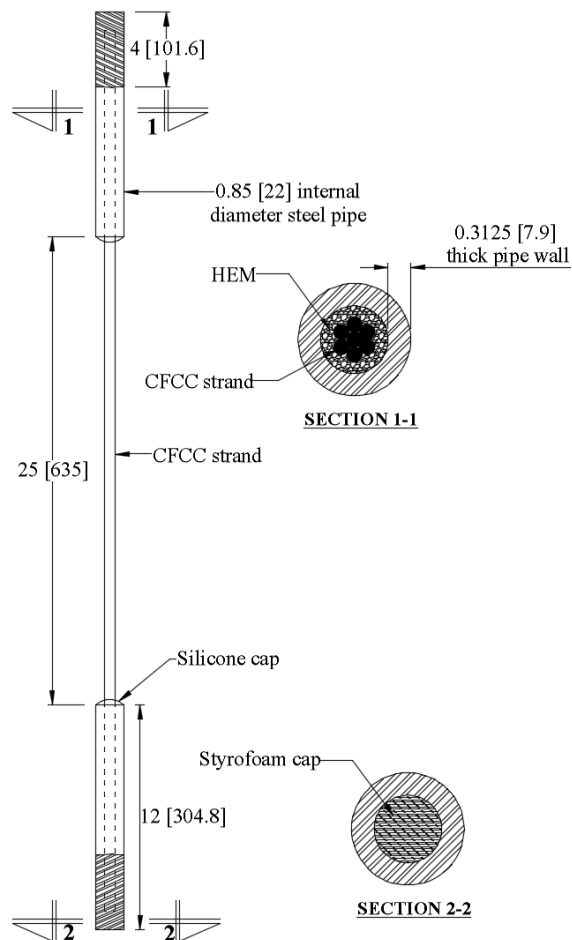


Figure 2.4-1 Sleeve-type anchorage for CFCC strands

The sockets had a length of 12 in. (305 mm) and were externally threaded for a length of 4.0 in. (100 mm) from their ends. After cutting and threading, the sockets were cleaned with compressed air and acetone to remove debris and oil from the cutting and threading process. The strands were centered inside the sockets and were held in place using end caps made of extruded polystyrene foam (Styrofoam) that also prevented the HEM from leaking out of the socket (Figure 2.4-2). The CFCC specimen with steel socket attached on one side were positioned and fastened by plastic ties on an in-house wooden jig as shown in Figure 2.4-3



(a) Threading and cutting steel socket



(b) Preparing end caps from Styrofoam



(c) Cleaning the socket



(d) Center depression for CFCC strand

Figure 2.4-2 Manufacturing of anchorage device at LTU

HEM was mixed with distilled water with a mix ratio of 4:1 by weight until a uniform slurry was obtained. Then, the HEM mix was poured into the anchorage sockets with CFCC strands inside them as shown in Figure 2.4-4. A mechanical vibrator was used to tap the sockets from the outside and ensure proper compaction for the HEM mix inside the sockets. After all sockets were filled, the specimens were allowed to cure at ambient temperature (68 °F or 20 °C) for five hours and at a temperature of 140 °F (60 °C) in an environmental chamber for at least 15 hours. After heat curing, the specimens were allowed to gradually cool down and the specimens were released from the wooden frame. The process was repeated for the other end by rotating the specimens and attaching the anchorage devices through the same process. Figure 2.4-5 shows the CFCC specimens with sleeve anchorage devices after proper curing.



(a) Capping the ends of the steel sockets



(b) Placing specimen in wooden stand



(c) CFCC specimens in wooden stand

Figure 2.4-3 Preparing the CFCC specimens for sleeve anchorage devices

A 220-kip (1000-kN) Material Test Systems (MTS<sup>®</sup>) loading actuator supported by a four-post steel frame was used in the testing and evaluation of different anchorage devices (Figure 2.4-6). Two custom-made steel heads were manufactured to accommodate different CFCC anchorage devices. The steel heads were designed to eliminate any possible eccentricity. Tensile force was applied in a force control mode at a rate of 6.5 kip/min. (29 kN/min) to failure. Tests were conducted in accordance with ASTM Standard D7205/7205M-06: “Standard Test Method for Tensile Properties of Fiber Reinforced Polymer Matrix Composite Bars.”

To evaluate the elastic modulus of CFCC, a set of ten test specimens was loaded in the same uni-axial test setup but the load was stopped at a load level of 60 kip (267 kN). An extensometer was attached to the CFCC strand at the mid-height of the specimen as shown in Figure 2.4-6. The load vs. strain was plotted for each test specimen from a load level of 10 kip (44.5 kN) to 60 kip (267 kN) and the elastic modulus was calculated using the slope of the curve.



(a) Measuring the HEM powder



(b) Adding water and mixing HEM



(c) Pouring HEM to the socket



(d) Vibrating the HEM in the sockets

Figure 2.4-4 Mixing and placing the HEM inside the steel sockets



Figure 2.4-5 CFCC specimens with sleeve anchorage device after curing

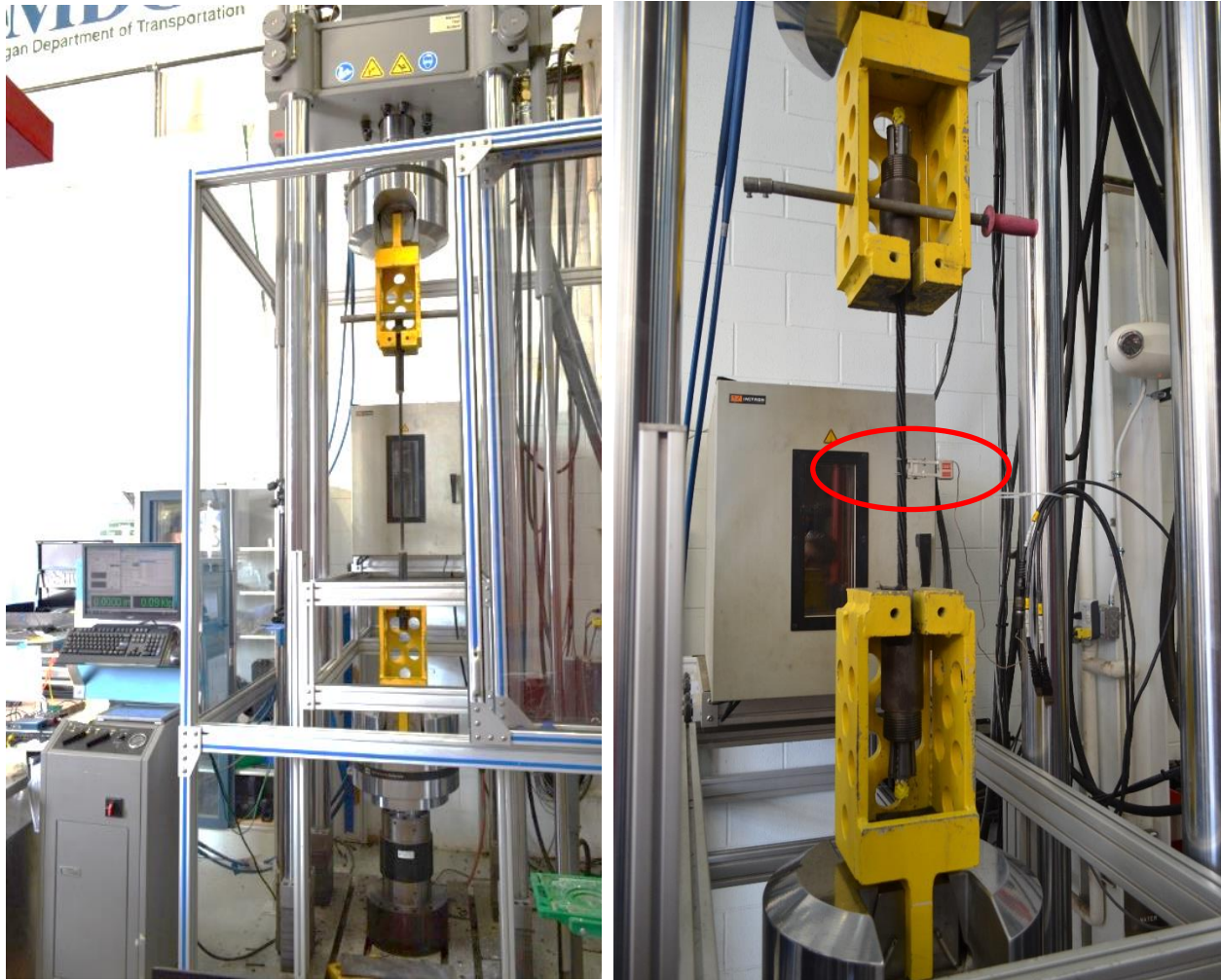


Figure 2.4-6 Left: A CFCC specimen in uni-axial test setup. Right, evaluating strain and elastic modulus of CFCC specimen using extensometer (circled)

## 2.5 Results

Results of testing CFCC specimens with sleeve anchorage are presented in Table 2.5-1. A total of 11 batches were prepared and tested. Batch 1 was prepared specifically for anchorage evaluation. Batches 2 through 11 of test specimens were prepared for other tests included in the experimental investigation such as relaxation, creep rupture strength, and freeze-thaw tests. Before conducting any of those tests, at least two test specimens were tested under a uni-axial test setup to evaluate the tensile strength of the material and the maximum strength of the anchorage device. As shown in the Table, out of a total of 31 test specimens, slippage of the anchorage occurred in six specimens, while the rest of the specimens failed by rupture of CFCC strands. Anchorage slippage

was typically accompanied by a sudden loss in the load while the CFCC strand remained intact. On the other hand, rupture of CFCC strand was an explosive failure that resulted in shattering part or all of the CFCC strand as shown in Figure 2.5-1. It should be noted that post failure inspection showed that some test specimens experienced both slippage and rupture of the CFCC strand nearly at the same time, or at least one type of failure triggered the other type. In addition, nearly all test specimens with strand rupture exhibited the rupture of CFCC strand near the anchorage device. This can be attributed to the effect of the confinement pressure from the anchorage device.

After excluding test specimens with evident anchorage slippage, the average tensile strength of CFCC specimens with sleeve anchorage is approximately 70 kip (311 kN) with a maximum breaking load of 80.2 kip (357 kN), and a minimum breaking load of 66.6 kip (296 kN).



Figure 2.5-1 Typical failure mode of CFCC specimens with sleeve type anchorage

Table 2.5-1 Uni-axial test results of sleeve-type anchorage

Test Group	Failure Load kip (kN)	Failure Mode
Batch 1	67.6 (301)	Strand rupture
	66.6 (296)	Strand rupture
	64.6 (288)	Slippage
	62.4 (278)	Slippage
	66.6 (296)	Strand rupture
	68.2 (303)	Strand rupture
	68.2 (303)	Strand rupture
	71.3 (317)	Strand rupture
	67.8 (302)	Strand rupture
Batch 2	70.7 (314)	Strand rupture
	71.5 (318)	Strand rupture
Batch 3	75.4 (335)	Strand rupture
	80.3 (357)	Strand rupture
Batch 4	68.6 (305)	Strand rupture
	71.1 (316)	Strand rupture
Batch 5	64.1 (285)	Slippage
	67.2 (299)	Strand rupture
Batch 6	64.4 (287)	Slippage
	68.4 (304)	Strand rupture
Batch 7	75.3 (335)	Strand rupture
	60.7 (270)	Slippage
	67 (298)	Strand rupture
	73.9 (329)	Strand rupture
Batch 8	68.6 (305)	Strand rupture
	68.6 (305)	Strand rupture
Batch 9	63.2 (281)	Slippage
	68.3 (304)	Strand rupture
Batch 10	71.8 (320)	Strand rupture
	73.8 (325)	Strand rupture
Batch 11	66.9 (297)	Strand rupture
	66.9 (297)	Strand rupture

Test results of wedge anchorage are shown in Table 2.5-2. Strand rupture was the common mode of failure in all test specimens regardless of the buffer system. The average tensile strength of CFCC specimens with wedge anchorage is approximately 70.1 kip (311 kN) with a maximum tensile strength of 76.4 kip (340 kN) and minimum strength of 65.9 kip (293 kN). Typical test setup and failure of the test specimens with wedge anchorage devices is shown in Figure 2.5-2 and Figure 2.5-3. The average tensile strength from the combined test results of sleeve and wedge anchorage test specimens is approximately 70 kip (311 kN).

Figure 2.5-4 shows the load vs. strain for test specimens loaded to 60 kip (267 kN) and then released. Based on the test results, the average elastic modulus for CFCC strand was calculated approximately as 22,828 ksi (157.4 GPa). It should be noted that the wide range of strain values shown on the Figure was due to the initial stretching of the CFCC specimen when it was first loaded. By correcting the initial reading in all test specimens, the difference in strain diminishes.

Table 2.5-2 Uni-axial test results of wedge anchorage

Test Group	Failure Load kip (kN)	Failure Mode
Steel buffer	69.2 (308)	Strand rupture
	68.4 (304)	Strand rupture
	71.3 (317)	Strand rupture
	72.1 (321)	Strand rupture
	70.5 (314)	Strand rupture
Composite buffer	75.5 (336)	Strand rupture
	72.3 (322)	Strand rupture
	66.8 (297)	Strand rupture
	76.4 (340)	Strand rupture
	65.9 (293)	Strand rupture
	73.3 (326)	Strand rupture
	67.6 (301)	Strand rupture
	66.1 (294)	Strand rupture
	69.4 (309)	Strand rupture
	67 (298)	Strand rupture

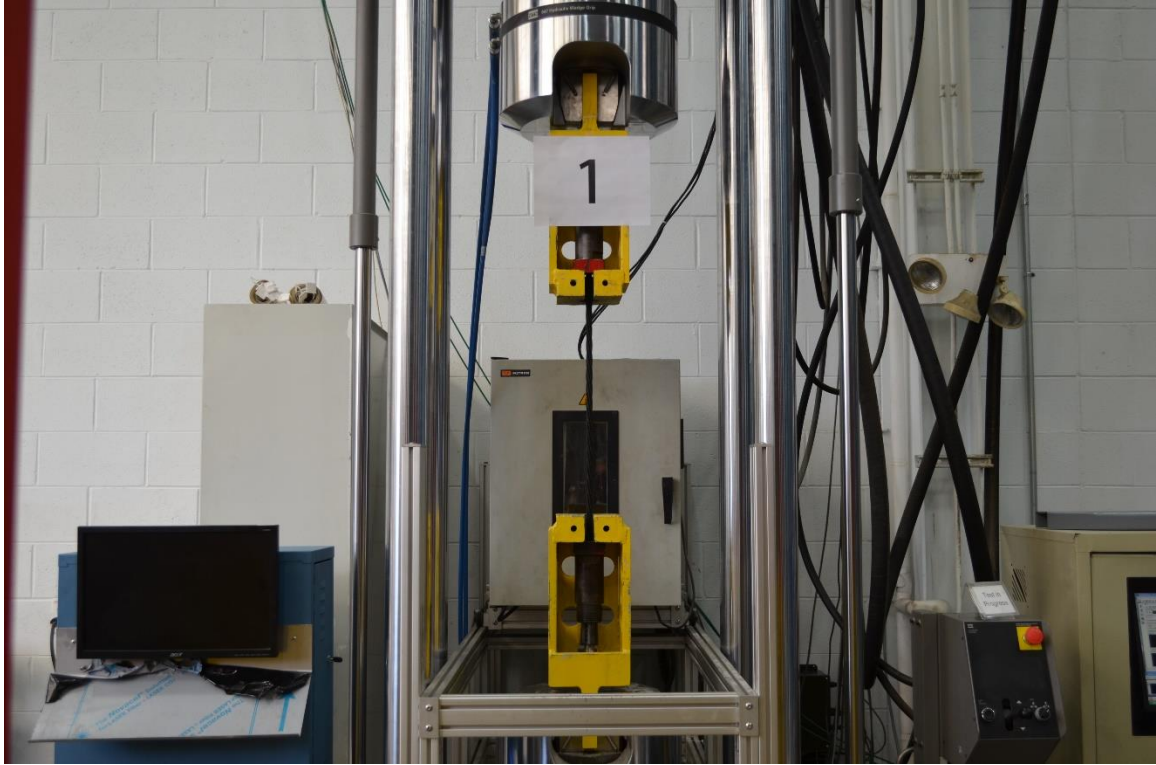


Figure 2.5-2 Uni-axial test setup for test specimens with wedge anchorage devices

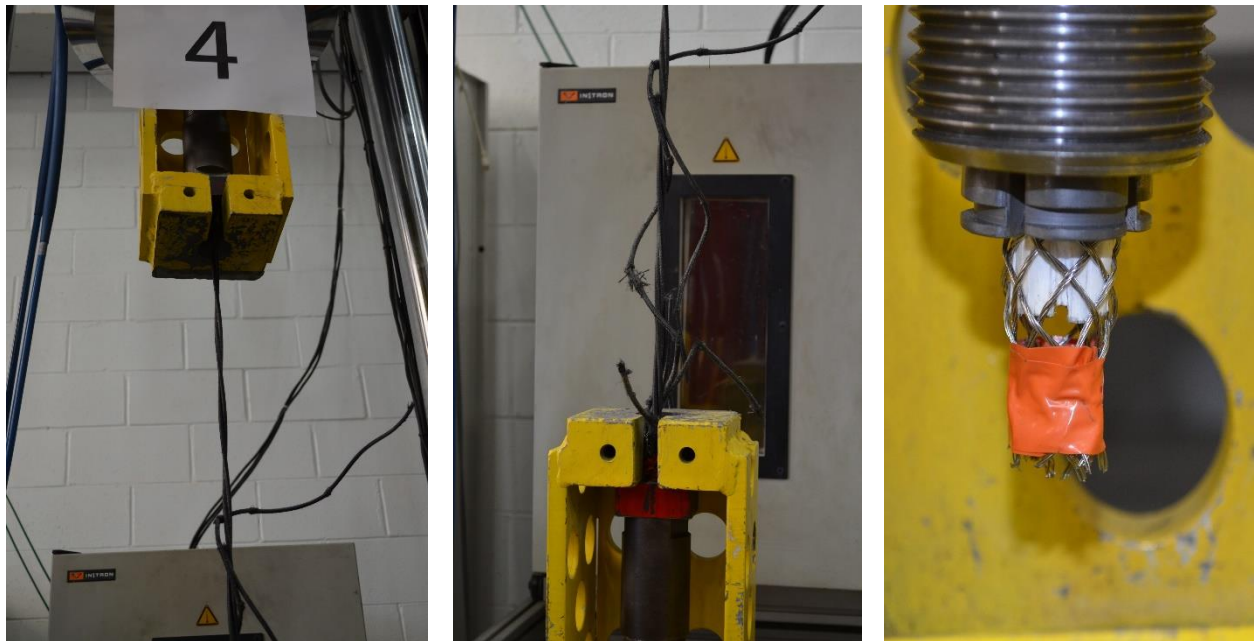


Figure 2.5-3 Failure of test specimens with wedge anchorage devices

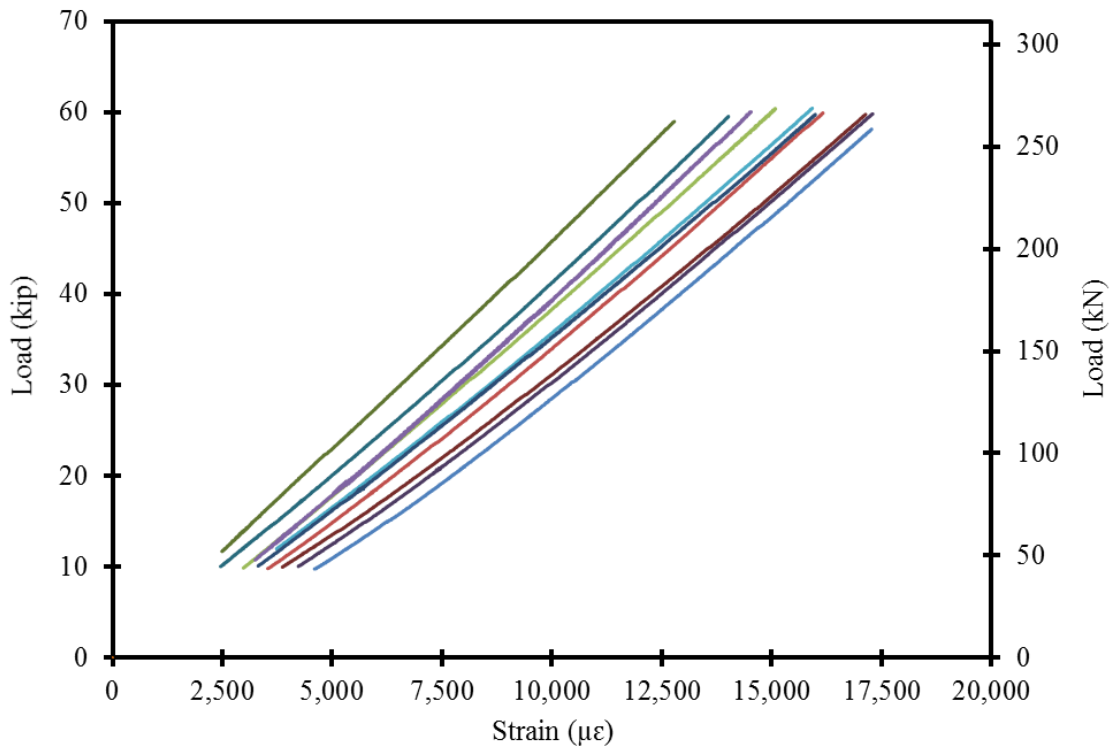


Figure 2.5-4 Establishing elastic modulus of CFCC based on uni-axial test results

## 2.6 Discussion of Test Results

Through the experimental investigation, sleeve and wedge anchorage devices were prepared and tested on CFCC strands with a diameter of 0.6 in. (15.2 mm). Test results showed an average CFCC tensile strength of 70 kip (311 kN), which is approximately 15 % higher than the guaranteed tensile strength recommended by the manufacturer (60.7 kip or 270 kN).

Few of the CFCC sleeve anchorages exhibited failure by anchorage slippage. Nevertheless, none of the test specimens including those with anchorage slippage failed at a load less than the guaranteed tensile strength of the CFCC strand. In addition, failure of the CFCC specimens at the maximum load initiated near the anchorage because of the lateral confinement pressure induced by the anchorage system on the strand. Therefore, test standards and guidelines shall be updated to acknowledge the failure near the anchorage points as an acceptable mode of CFRP strand failure.

CFRP tensile strength test results are highly dependent on the quality control of assembling the anchorage devices. This can be an issue when establishing the guaranteed strength of a CFRP material. For instance, the guaranteed strength is calculated as the average tensile strength minus three times the standard deviation of the test results. Inadequate anchorage handling and assembling can result in dispersed test results and a larger standard deviation, which can impact the calculations of the guaranteed tensile strength. Therefore, when anchorage malfunction is suspected in a certain test result, it may be eliminated from the pool of the test results.

## CHAPTER 3: CREEP RUPTURE & RELAXATION OF CFRP

### 3.1 Introduction

Creep rupture, relaxation, and long-term prestress loss of CFRP strands due to exposure to various environmental conditions are key parameters in the design and construction of CFRP prestressed concrete highway bridge beams.

Relaxation is the loss of stress in a strand or tendon under constant strain (Hollaway 1993) and is affected by factors such as initial imposed stress level, type of fiber, durability factors (Gerritse and Den Uijl 1995), and creep coefficient which is defined as the ratio of creep strain to the initial elastic strain at a particular time. The stress relaxation of FRP composite materials remains a controversial issue within the engineering community because loss of prestressing force overtime in concrete structures reduces camber and could lead to low serviceability cracking loads.

Relaxation of fibers, resin matrix and straightening of fibers are the three main sources of relaxation losses in FRP materials (Oskoue and Taleie 2010). The viscoelastic property of FRP resins causes it to relax when it is stressed and thus lose a portion of its contribution to the load carrying capacity of the fiber. The straightening of incompletely parallel fibers through the resin matrix during loading also results in stress losses. Furthermore, exposure to environmental conditions such as alkaline environment, chloride ions, ultraviolet radiation, moisture and water, and elevated temperatures has a ripple effect on the relaxation characteristics of FRP composite materials. However, each type of FRP responds differently to these exposures. As a result, many design guidelines specify FRP strength reduction factors to account for long-term relaxation losses under severe environments (Ali et al. 2018).

ACI 440.4R-04 (ACI 2004) and Intelligent Sensing for Innovative Structures (ISIS) assumes a general loss in prestressing force of FRPs due to relaxation of 0.6 to 1.2 % and 1 to 2 % for polymer relaxation and fiber straightening, respectively. ACI 440.4R-04 reports that CFRP has almost zero fiber relaxation, which is contradicted by the 1.8 % over a 100-year period reported by ISIS. CAN/CSA S6-06 (2006) provides no provision for the evaluation of losses due to relaxation of FRP in prestressed concrete structures.

(Patrick and Zou (2003) suggest that Carbon FRP exhibits negligible losses due to relaxation when the initial applied stress is equal to or below 50 % of the ultimate tensile strength. This is

due partly to the low creep coefficient under such applied stress. Balazs and Borosnyoi (2001) estimated relaxation of 1.8 to 2 % for CFRP tendons and 5 to 8 % for AFRP over a 1000-hour period. Extrapolated to 50 years, relaxation of GFRP, CFRP and AFRP tendons were estimated as 4 to 14 %, 2 to 10.5 %, and 11 to 25 % respectively, depending on the applied initial stress. Experimental works conducted by Ando et al. (1997) on 0.5-in. (12.5-mm) diameter CFRP and 0.6-in. (15-mm) diameter AFRP at 20 °C, 40 °C and 60 °C for time periods of 3000 hours indicated that higher temperatures facilitate greater relaxation rate and this effect was pronounced in AFRP bars.

This chapter presents test setups and test results of a comprehensive study that was conducted to establish those design parameters. Multiple sets of 4-ft (1.2-m) long CFRP specimens were prepared, provided with sleeve anchorages, and loaded in special steel frames or in a four-post loading frame with a closed-loop MTS® hydraulic actuator. Multiple sets of specimens were tested to establish the creep rupture strength. One set was loaded in a steel frame to establish the one-million-hour relaxation rate of CFRP. Four sets of test specimens were loaded with high initial force levels in steel frames and were subjected to harsh Michigan weather for a period of three years, while similar sets of specimens were kept in a controlled laboratory conditions for the same period.

Test results of this investigation showed that the one-million-hour creep rupture strength of CFCC strands is at least 86 % of their average tensile strength. In addition, the one-million-hour relaxation rate of CFCC was found to be less than 2 %. Furthermore, it appears that various environmental conditions such as moisture, rain, freezing rain, and harsh change in daily and seasonal temperature do not have a significant influence on the strength of CFCC strands and do not lead to accelerated deterioration in the material or significant loss in the prestressing force.

### **3.2 Creep Rupture**

Currently ACI 440.4R-04 limits the jacking strength in CFRP strands to 65 % of their guaranteed strength because of concerns associated with creep rupture failure. Meanwhile, ACI 440.1R-06 acknowledges that higher creep rupture capacities, as high as 85 % of the guaranteed strength, have been documented and reported by CFRP manufacturers and researchers. While a higher creep rupture capacity of CFRP strands will promote a higher jacking strength and a more efficient prestressed member, it is essential that a clear understanding of the creep rupture phenomenon be

established for every CFRP material before it is deployed in highway bridge construction. Besides, limits of prestressing force and jacking strength shall be established based directly on the creep rupture strength, not based on the guaranteed strength because high guaranteed strength does not directly imply excellent creep rupture performance or higher creep rupture strength.

### **3.2.1 Test setup**

A total of thirty CFCC specimens were constructed and tested to determine the one-million-hour creep rupture strength of CFCC strands. The tests were conducted in accordance with JSCE-E 533-1995, “Test Method for Creep Failure of Continuous Fiber Reinforcing Materials”. The CFCC specimens were prepared using sleeve anchorages bonded to the CFCC strands using HEM. The construction process of the specimens followed the same procedures described earlier in Chapter 2.

Two test setups were used in creep rupture evaluation. The first test setup used two custom-made steel frames that accommodated five specimens per frame. The steel frames were fabricated from ASTM A500 Grade B HSS rectangular sections, 13.5 in. (343 mm) × 2 in. (50.8 mm) ASTM A36 plates, and 1.0-in. (25.4-mm) diameter ASTM A193 Grade B7 threaded rods. To avoid excessive prestress loss and maintain a constant level of prestressing force through the duration of the test, high strength steel springs with an outside diameter of 12.5 in. (318 mm) and a linear stiffness of 10 kip/in. (1.75 kN/mm) were attached to the specimens as shown in Figure 3.2-1. The test specimens in the first frame was loaded to approximately 48 kip (213 kN)/strand, while the test specimens in the second frame were loaded to approximately 55 kip (245 kN)/strand. Those load levels represent approximately 70 and 80 % of the average tensile strength of CFCC or 79 and 91 % of the manufacturer’s guaranteed tensile strength. In-line load cells and vibrating wire displacement transducer were attached to each of pre-tensioned CFCC specimen to monitor the prestressing force and the strain, respectively. Load cells were manufactured by OMEGA® with a maximum capacity of 50 kip (222 kN), whereas displacement transducers were Geokon Model 4410 Strand-meter with a range of +3 mm (tension only). All the attached sensors were connected to a data acquisition system the continuously monitor and record the prestressing force and strain in loaded strands. Figure 3.2-2 through Figure 3.2-6 show the steel frames and the instrumentation of the test specimens.



Figure 3.2-1 Test setup for evaluating creep rupture strength of CFRP with high strength steel springs to maintain the load level



Figure 3.2-2 Stressing creep rupture specimens to 70 % of the average tensile strength of CFCC



Figure 3.2-3 Creep rupture specimens after stressing showing the compressed steel springs



Figure 3.2-4 Inline load cells to monitor the force of creep rupture specimens



Figure 3.2-5 Two sets of creep rupture specimens prestressed to 70 % and 80 % of average tensile strength of CFCC



Figure 3.2-6 Strand-meter for strain evaluation in creep rupture specimens

Due to safety concerns, the second test setup used a hydraulic actuator supported by four-post loading frame to apply and maintain load levels higher than 90 % of the CFCC average tensile strength and higher than the manufacturer's guaranteed strength. In this test setup, each CFCC specimen was loaded to the assigned load level and the load was maintained using a closed-loop hydraulic system until the failure of the specimen or 1000 hours, whichever came first. The prestressing force was applied through a hydraulic jacking system at a rate of 6 kip/min (26.7 kN/min). The load was monitored using a load cell attached to the loading actuator, while the strain was monitored in select test specimens using an extensometer attached to the CFCC strand at the mid-height of the specimen. Figure 3.2-7 and Figure 3.2-8 show the test setup for creep rupture testing of CFCC specimens with a load level higher than 90 % of the average CFCC tensile strength.



Figure 3.2-7 Creep rupture test setup for stress levels higher than 90 % of the CFCC average tensile strength



Figure 3.2-8 Creep-rupture test setup for stress level of 94 % of average CFCC tensile strength

### 3.2.2 Test results

Test specimens with 70 % of tensile stress (79 % of the guaranteed strength) were loaded and monitored continuously for 90 days (2160 hours). Figure 3.2-9 shows the load-time history for this set of test specimens. A slight load loss was observed in the first 7 days. Therefore, the specimens were reloaded again to increase the stress ratio back to 48 kip (213 kN). After 90 days, there was no failure in any of the specimens. Therefore, the decision was made to release this set of specimens, while continue monitoring the force in the second set with initial prestressing force of 55 kip (245 kN)/strand. Monitoring of the other set has been going on for over 1200 days as shown in Figure 3.2-10 and Figure 3.2-11 that show the change in force and strain in the specimens with time. As shown in the figures, there was a slight decrease in the load over time but since the decrease in the load was minimal, it was decided not to disturb the specimens as long as the load does not go below 50 kip (222 kN)/strand

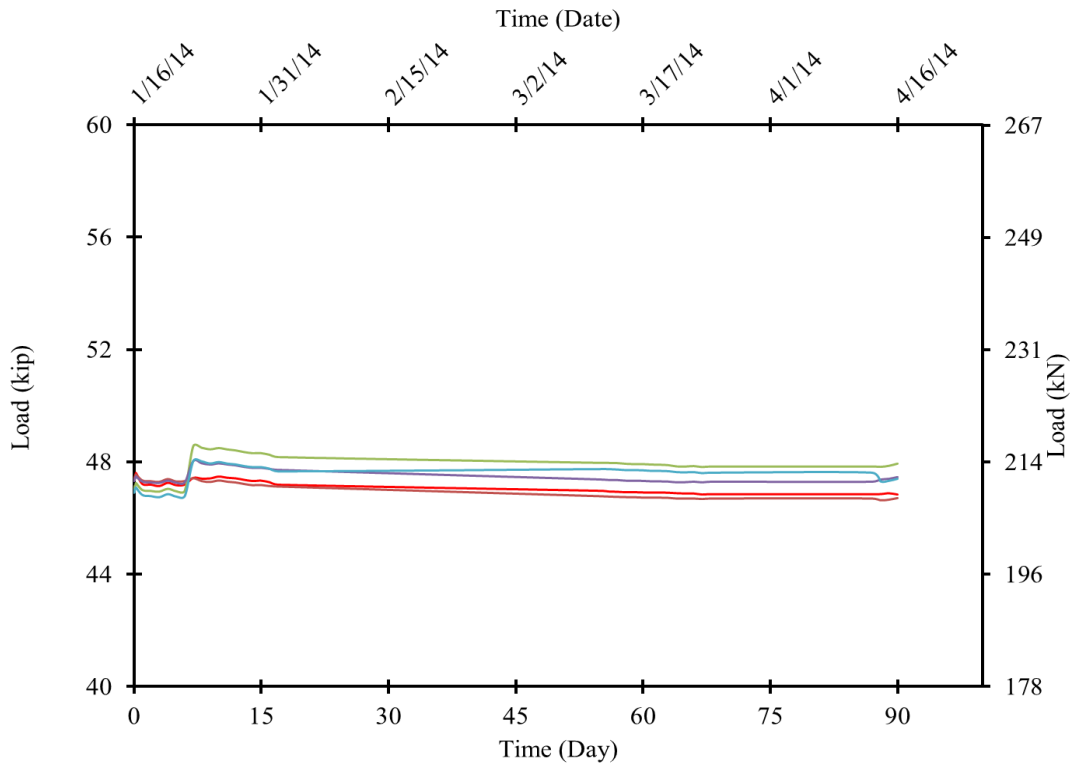


Figure 3.2-9 Force monitoring of CFCC specimens with a load of 48 kip (213 kN) per strand

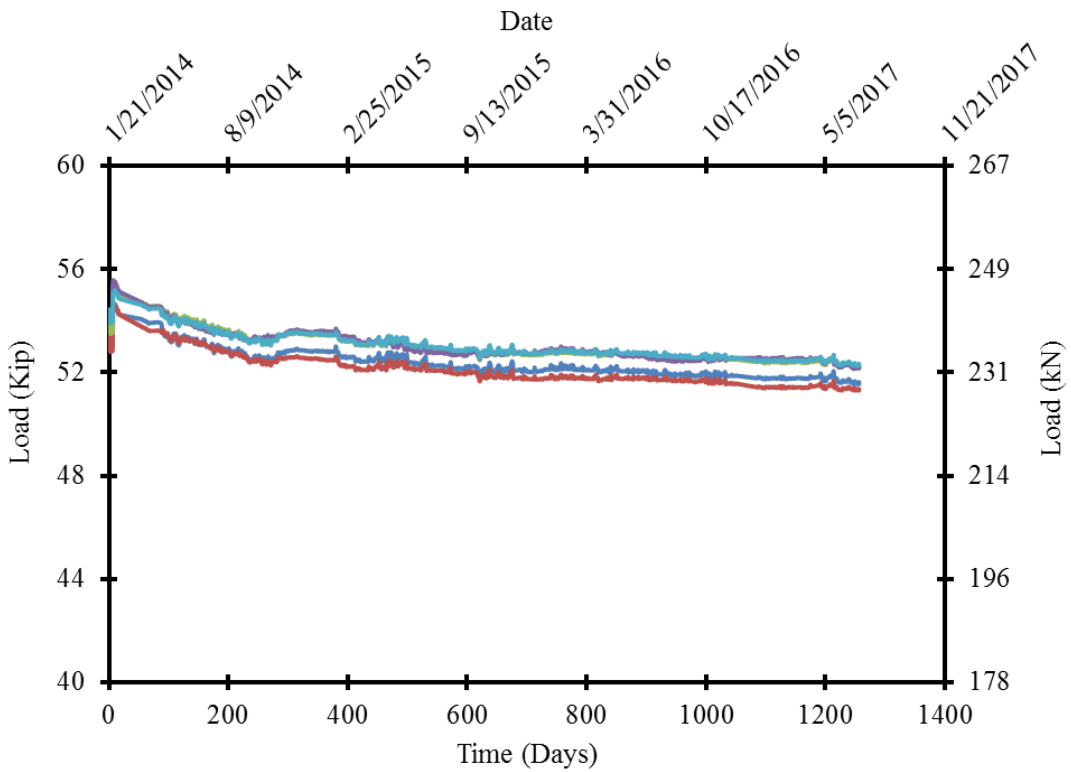


Figure 3.2-10 Force monitoring of CFCC specimens with a load of 55 kip (245 kN) per strand

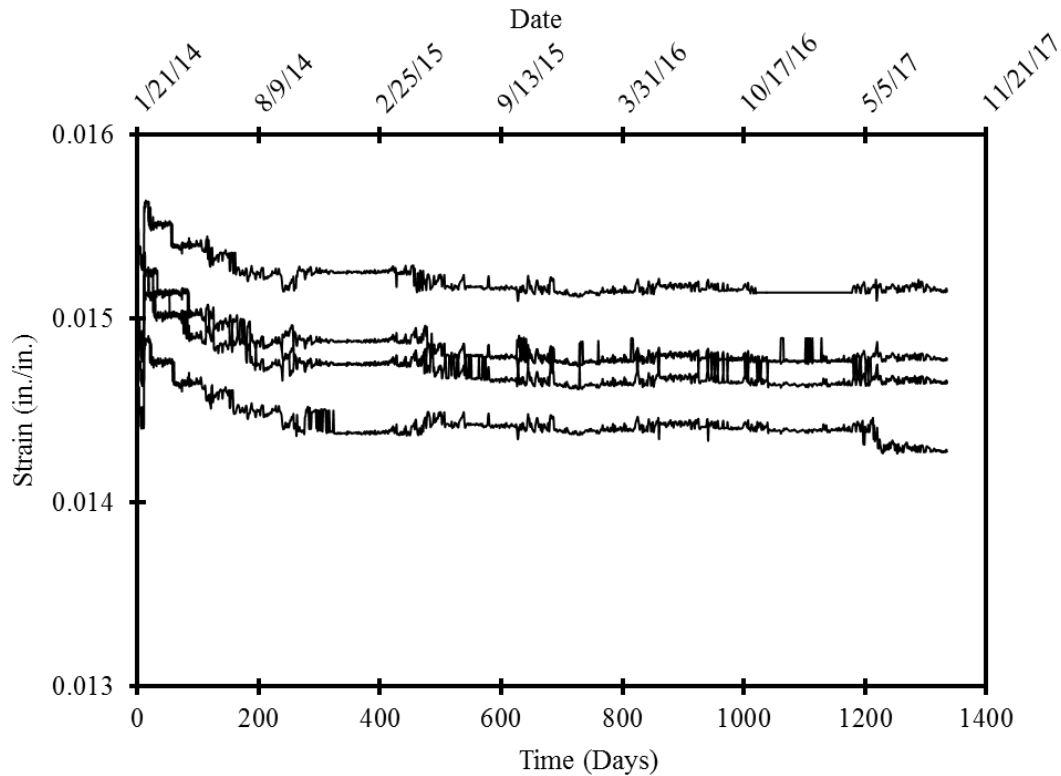


Figure 3.2-11 Strain monitoring of creep rupture CFCC specimens

Test results of the second test setup that was performed in the MTS-four-post loading actuator are summarized in Table 3.2-1. As shown in the Table, test specimens with a load level as high as 94.6 % of the average CFCC tensile strength sustained the applied load for 1000 hours without failure. In addition, it appears that the test specimen either sustained the load or experienced failure within the first 100 hours of loading. It should be also noted that one load level resulted in several outcomes and the results did not seem to follow a certain trend. For instance, Specimen #18 with a load level of 63.71 kip (283 kN) sustained the load for approximately 57 hours before it failed. Specimen # 19, on the other hand, sustained the same load level for 1000 hours, after which it was released. The difference in performance can be attributed to different factors such as preparation and handling of the specimens or curing of the HEM for the anchorage. But overall, it was evident that very high load levels are needed to cause rupture of the CFCC strand and it appears that the rupture was less likely due to a typical creep phenomenon but rather due to the load being very close to the tensile strength of the specimen.

Table 3.2-1 Results of creep rupture test performed on CFCC strand specimens with a diameter of 0.6 in. (15.2 mm)

Test #	Average tensile strength	Sustained load	Load ratio	Duration	Mode
	Kip (kN)	Kip (kN)	%	Hours	
1	≈ 70 (311)	66.84 (297)	95.6	0.073	Failure
2		66.84 (297)	95.6	0.013	Failure
3		66.84 (297)	95.6	5.951	Failure
4		66.80 (297)	95.6	0.000	Failure
5		66.84 (297)	95.6	16.922	Failure
6		66.84 (297)	95.6	0.621	Failure
7		66.13 (294)	94.6	1000	Suspended
8		65.08 (289)	93.1	0.052	Failure
9		65.08 (289)	93.1	38.658	Failure
10		65.08 (289)	93.1	0.026	Failure
11		65.08 (289)	93.1	34.306	Failure
12		65.08 (289)	93.1	0.088	Failure
13		64.39 (286)	92.1	0.011	Failure
14		64.39 (286)	92.1	0.194	Failure
15		64.39 (286)	92.1	0.799	Failure
16		64.39 (286)	92.1	0.005	Failure
17		64.39 (286)	92.1	0.023	Failure
18		63.71 (283)	91.1	57.183	Failure
19		63.71 (283)	91.1	1000	Suspended
20		61.65 (274)	88.2	1000	Suspended

### 3.3 Relaxation of CFCC Strands

#### 3.3.1 Test setup

After releasing the creep test specimens with a load level of 48 kip (213 kN) per strand, the steel frame was used to conduct the relaxation test, where five CFCC specimens were prestressed and monitored for stress loss. The specimens were pretensioned to a force level of 47.5 kip (211 kN), which represented approximately 67 % of the average tensile strength of CFCC. The relaxation test was conducted in accordance with JSCE 534-1995: “Test Method for Long-Term Relaxation of Continuous Fiber Reinforcing Materials”. It should be noted that this load level was higher than the jacking strength recommended by ACI-440-4R-04 (39.5 kip or 175 kN).

As shown in Figure 3.3-1 through Figure 3.3-4, CFCC specimens were connected to load cells and threaded rods at one end (dead end) and fastened at the other end (live end) by a nut and washer. Prestressing force was applied in predetermined sequence at the live end through a hydraulic jack at a rate of 6 kip/min (26.7 kN/min) and monitored through the installed load cells. Strains were monitored using Geokon strand-meters attached to the CFCC strands. The load cells and the strand-meters are attached to data acquisition system and the readings have been recorded for the last three years.



Figure 3.3-1 Relaxation test setup

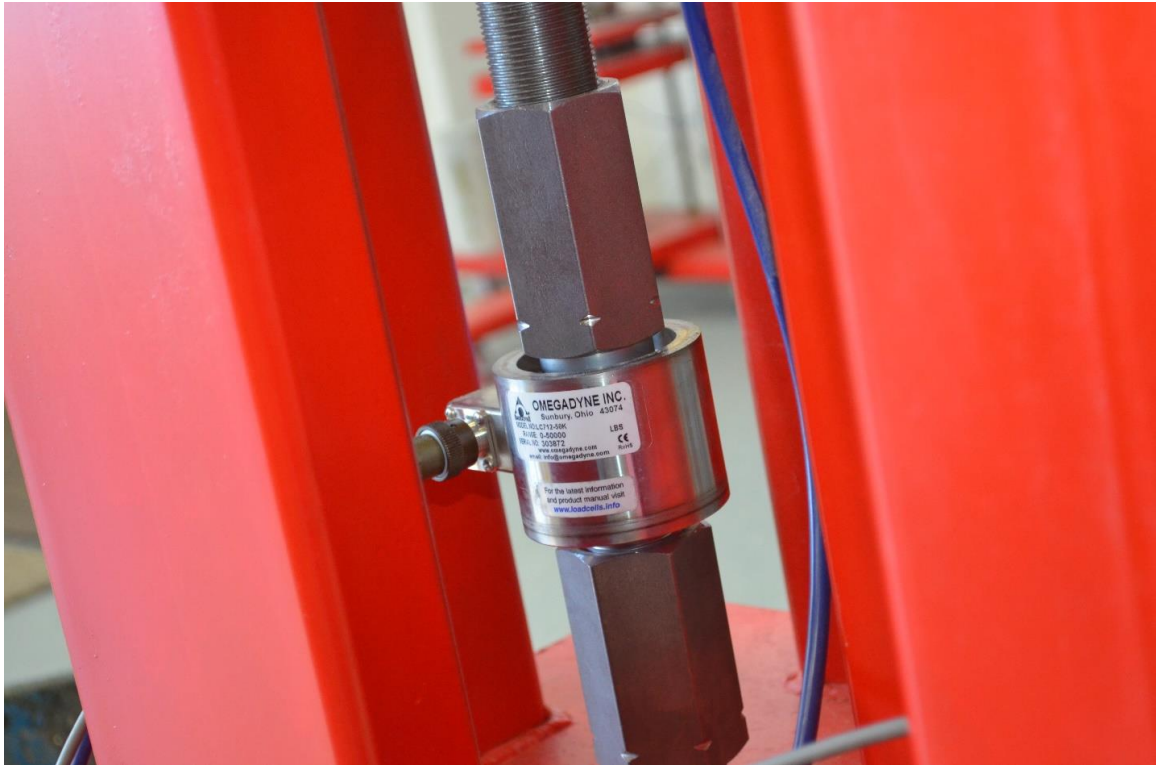


Figure 3.3-2 Inline load cells for force monitoring of relaxation specimens



Figure 3.3-3 Stressing relaxation specimens to an initial load level of 47.5 kip (211 kN)



Figure 3.3-4 Strand-meters to evaluate the strain in CFCC relaxation specimens

### 3.3.2 Test results

Figure 3.3-5 shows the load vs. time curve for the five CFCC specimens. All specimens displayed a bi-linear pattern of load loss with approximate force loss of 4.5 % in the first 4 months (120 days) and additional force loss of 3 % and occurred between 4 and 36 months. The average total loss at the time of writing this report seem to be approximately 7.5 %.

When looking at the strain readings vs. time, shown in Figure 3.3-6, it appears that the loss of the prestressing force was accompanied by a reduction in the strain readings over time. In an ideal situation, where the loss in prestressing force occurs because of strand relaxation only, the strain readings shall be increasing with time, not decreasing. That is because relaxation of the strand leads to strand elongation between the anchor points, which causes the prestress loss. Therefore, the recorded reduction in the strain readings indicated that the loss in the prestressing force was due to a combination between strand relaxation and anchorage relaxation. When anchorage devices relax, they tend to induce a reduction in the strain readings in the CFCC specimens because the strands retract back as the anchorage devices give away finite displacements.

The loss in prestressing force due to strand relaxation and due to anchor relaxation can be mathematically separated by analyzing the strain readings vs. the corresponding load cell reading. If strand relaxation loss is denoted (X) and anchor relaxation loss is denoted (Y), then the attached load cells in the setup measured total relaxation losses (X+Y) from the anchor and the strand. The strand-meter on the strands however measured the net loss due to anchor relaxation and strand relaxation (Y-X). By converting the strain reading to equivalent loss in prestressing force and solving the two equations simultaneously, the loss due to strand relaxation (X) and due to anchorage relaxation (Y) can be determined.

As shown in Figure 3.3-7, the total loss of the prestressing force was approximately 3.6 kip (16 kN) as shown in Figure 3.3-8. The loss due to anchorage relaxation was calculated as 3.1 kip (14 kN), while the loss due to strand relaxation was approximately 0.5 kip (2 kN) as shown in Figure 3.3-9. This loss accounts to approximately 1 % of initial prestressing force as shown in Figure 3.3-10. When plotted on a logarithmic scale, the estimated one-million-hour relaxation loss (relaxation rate) is approximately 1.91 % as shown in Figure 3.3-11.

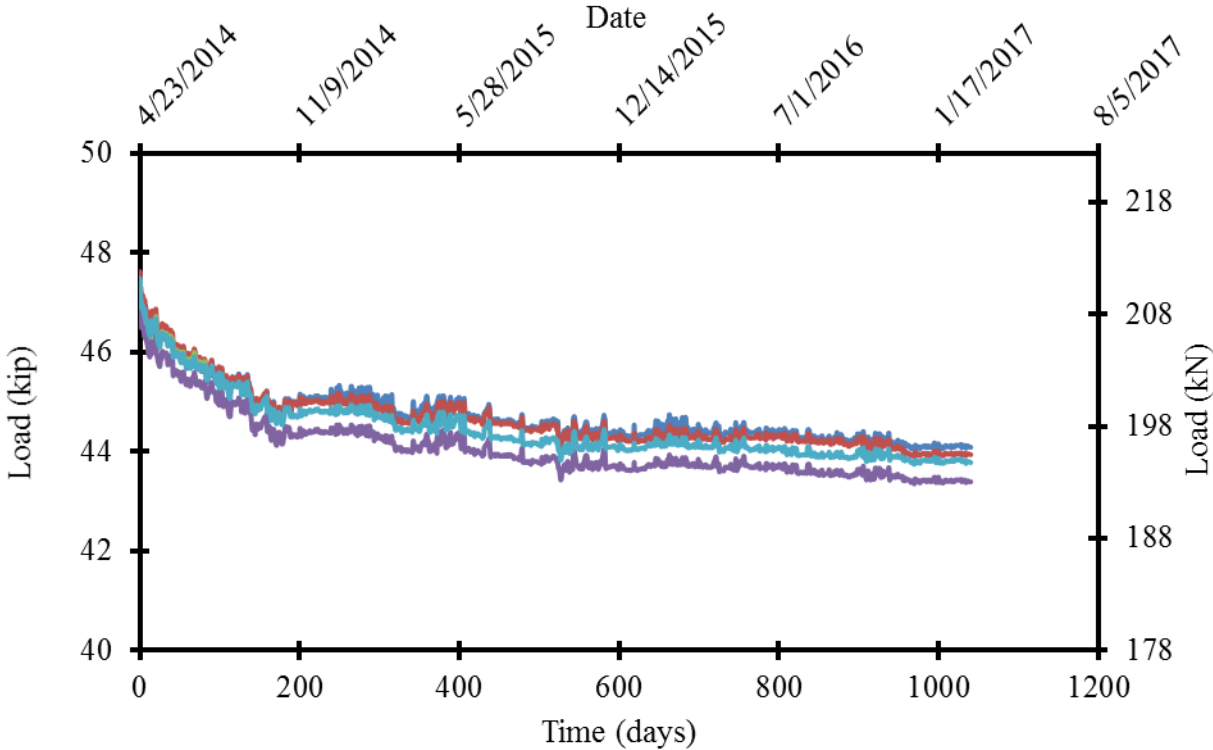


Figure 3.3-5 Force monitoring in relaxation CFCC specimens

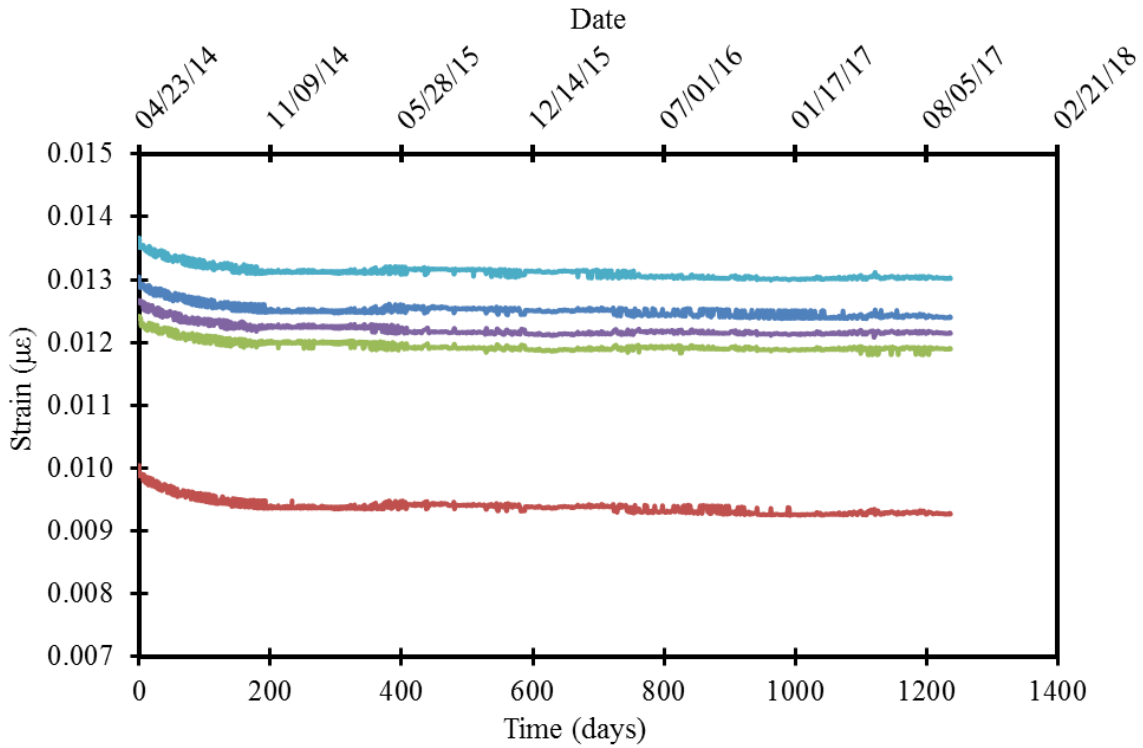


Figure 3.3-6 Strain monitoring of relaxation CFCC specimens

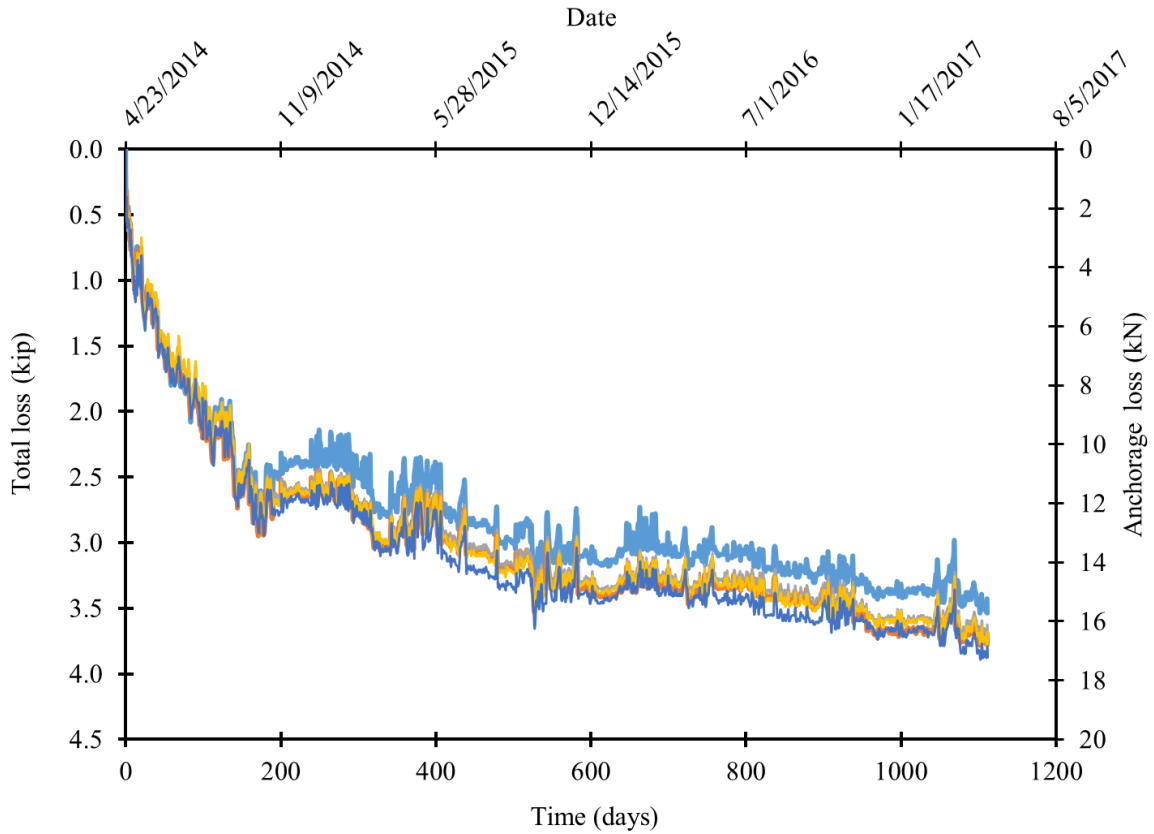


Figure 3.3-7 Total loss of the force in CFCC specimens due to anchorage and CFCC relaxation

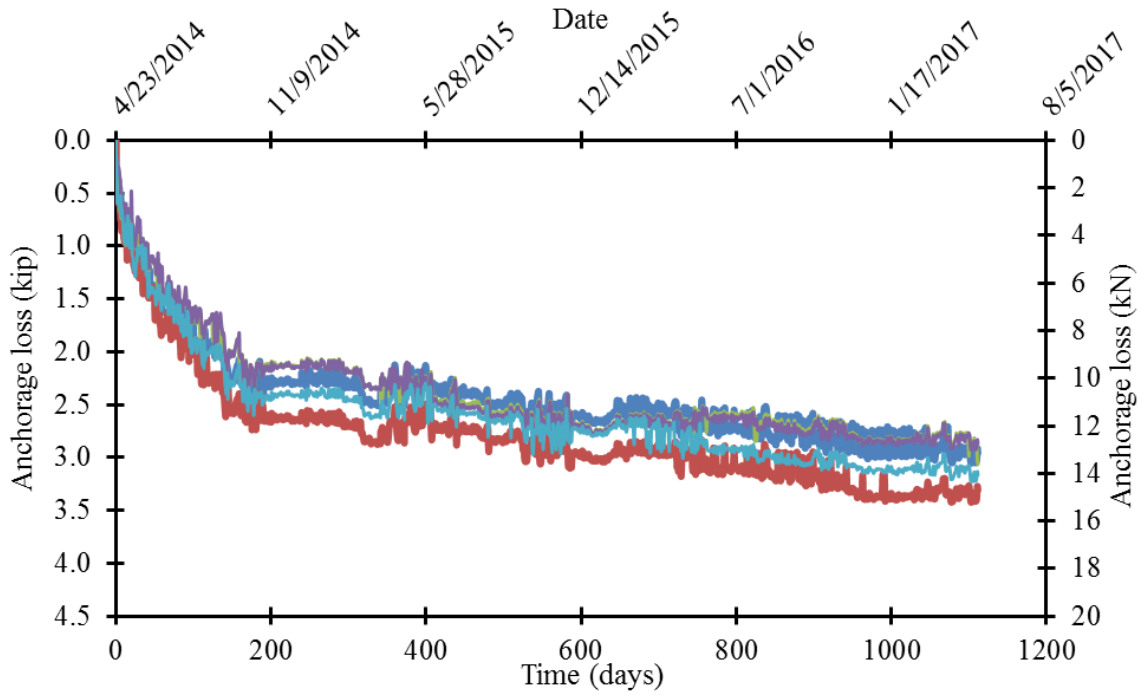


Figure 3.3-8 Loss of the force in CFCC specimens due to anchorage relaxation

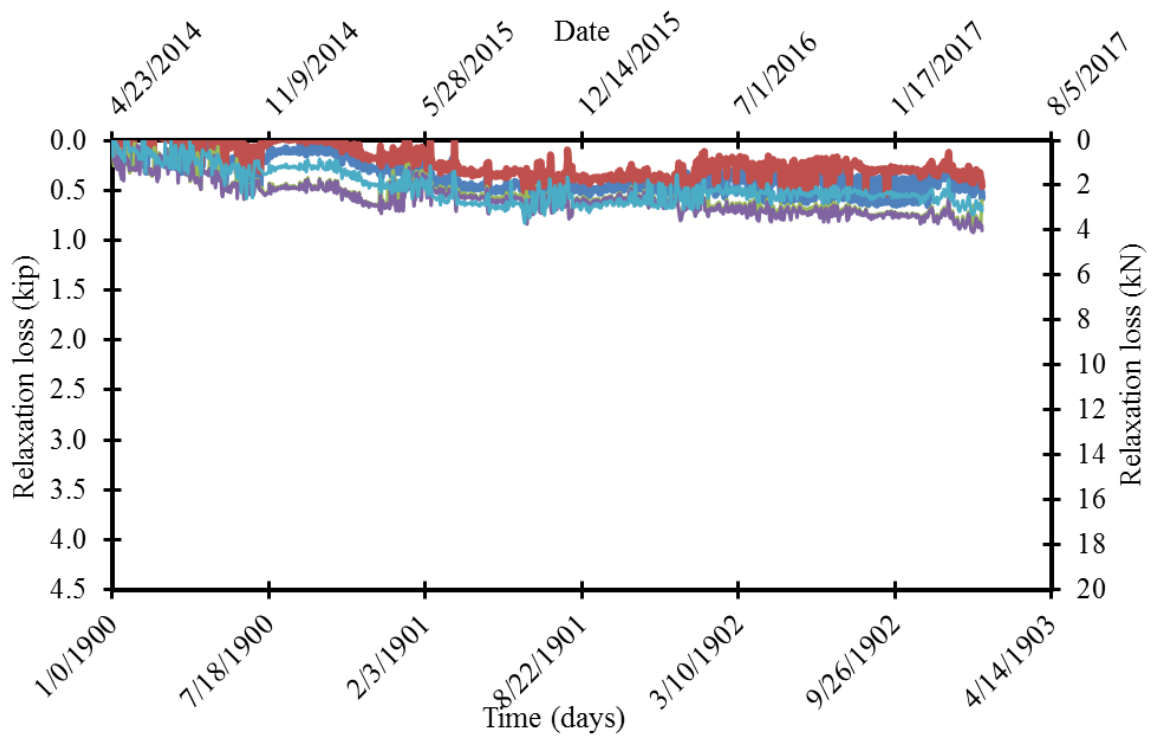


Figure 3.3-9 Loss of force in CFCC specimens due to relaxation of CFCC

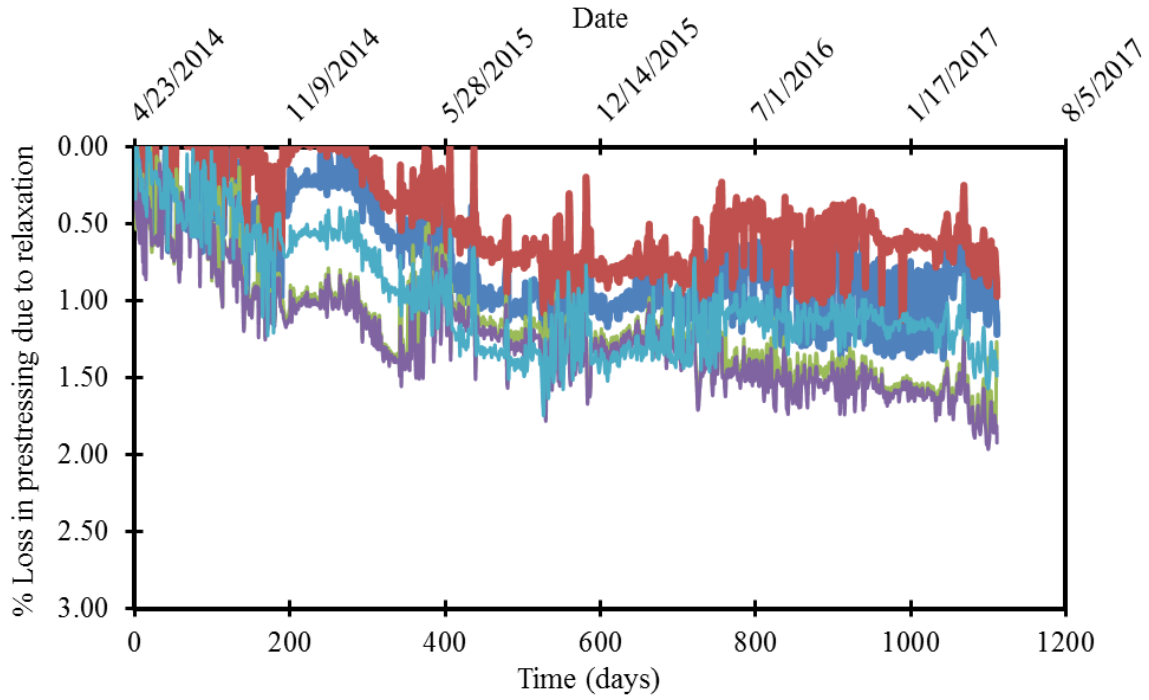


Figure 3.3-10 Percentage loss of force in CFCC specimens due to CFCC relaxation only

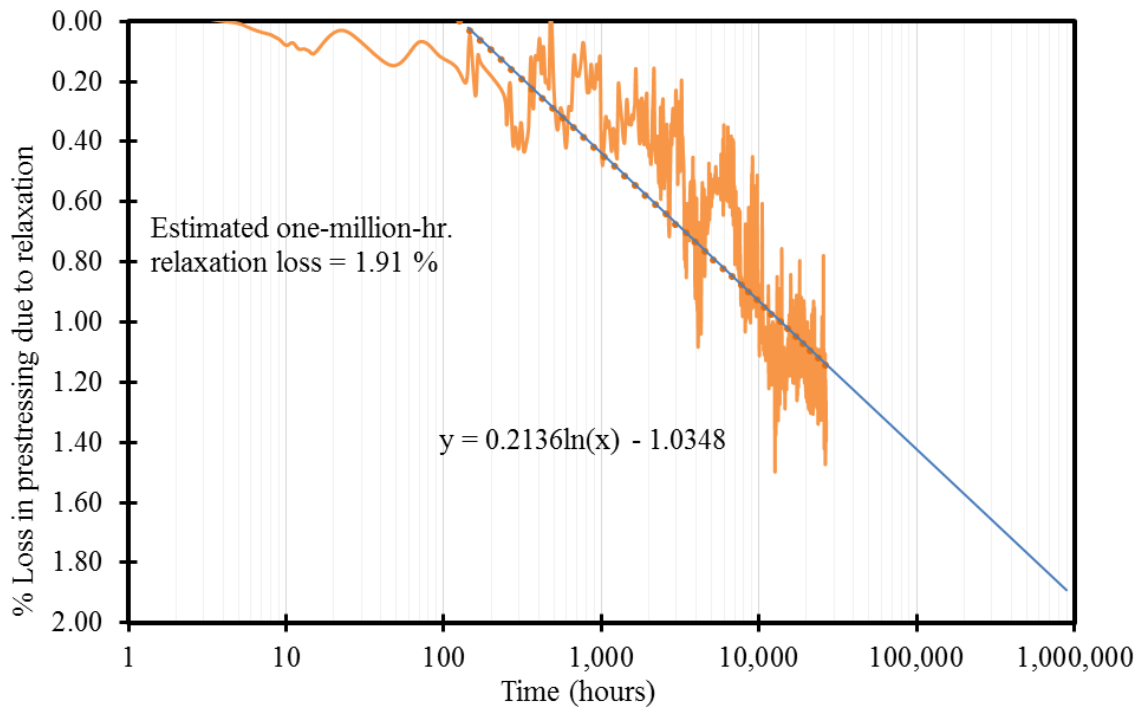


Figure 3.3-11 Estimated one-million-hour relaxation rate in CFCC specimens

### 3.4 Long-Term Monitoring of CFCC Specimens

In addition to the creep rupture test and the relaxation test, multiple sets of CFCC specimens were prepared and prestressed in steel frames as shown in Figure 3.4-1. Five test specimens prestressed to an initial force level of 50.1 kip (223 kN) and ten specimens prestressed to a force level of 56.5 kip (251 kN) were stored indoors in a controlled laboratory environment as shown in Figure 3.4-2. On the other hand, ten test specimens prestressed to a force level of 56.5 kip (251 kN) and ten specimens prestressed to a force level of 50.1 kip (223 kN) were stored outdoors where they have been subjected to severe Michigan weather as shown in Figure 3.4-3. The force in the all test specimens (indoors and outdoors) have been monitored and recorded for the last three years (Figure 3.4-4 and Figure 3.4-5).

Monitoring charts of all CFCC specimens are presented in Figure 3.4-6 through Figure 3.4-8. As seen on the charts, the loss of the prestressing force in indoor specimens was similar to that exhibited in relaxation testing. The outdoor specimens exhibited a fluctuation in the prestressing force associated with the seasonal change in temperature due to the difference in thermal expansion between steel frames and the CFCC strands. However, when corrected for temperature change, the monitoring charts were similar to those obtained for indoors specimens.

Based on the test results available at the time of writing this report, it can be assumed that outdoor specimens did not experience any significant deterioration during the three years of stressing and monitoring. Or at least, it can be assumed that environmental exposure did not cause the strength of the CFCC strand to deteriorate below the level of the highest prestressing force of 56.5 kip (251 kN) otherwise, a strand failure would have occurred. The level of 56.5 kip (251 kN) represents approximately 80 % of the average tensile strength of CFCC. Another remarkable observation is that, current prestressing levels in the indoor and outdoor specimens establishes a benchmark for the minimum creep rupture strength of CFCC strands as discussed in the following section.



Figure 3.4-1 Stressing CFCC specimens for evaluation of long-term properties



Figure 3.4-2 Long-term monitoring of CFCC specimens in a controlled laboratory environment



Figure 3.4-3 Long-term monitoring of prestressed CFCC specimens stored outdoors and exposed to Michigan weather



Figure 3.4-4 Monitoring the level of prestressing force through inline load cells attached to the CFCC specimens



Figure 3.4-5 CFCC specimens stored outdoors after three years of continuous monitoring

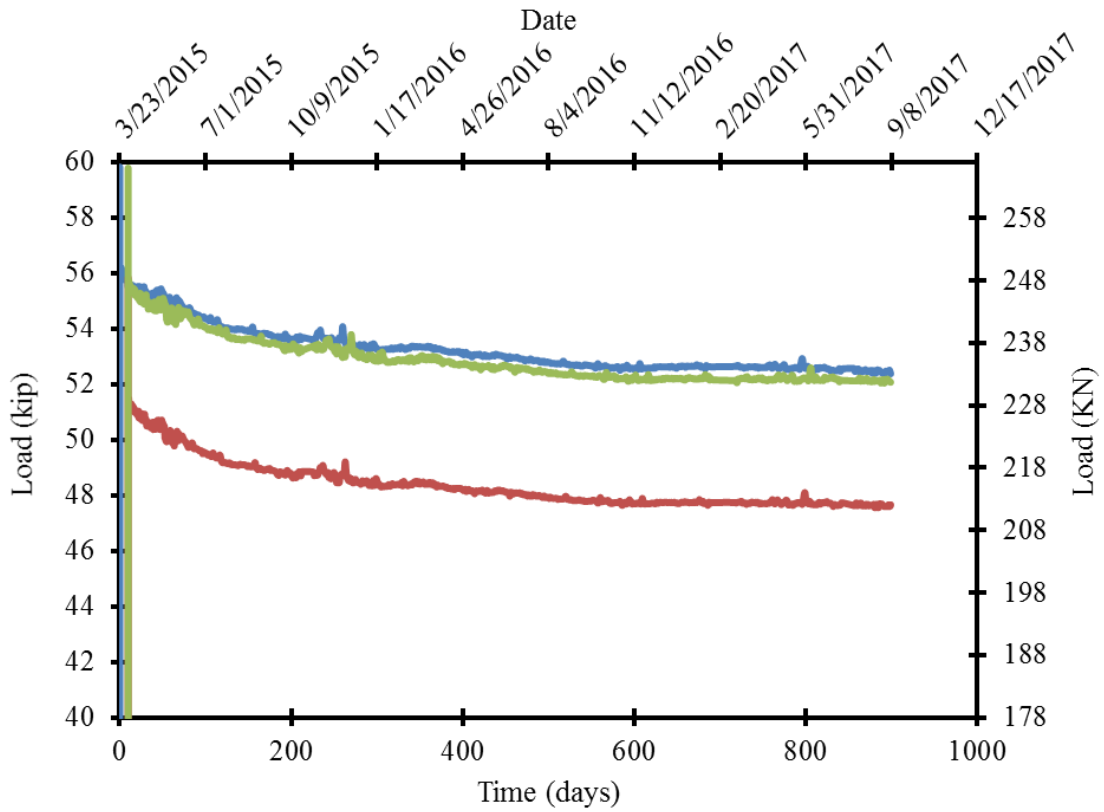


Figure 3.4-6 Long-term monitoring of CFCC specimens loaded in controlled laboratory environment (indoors)

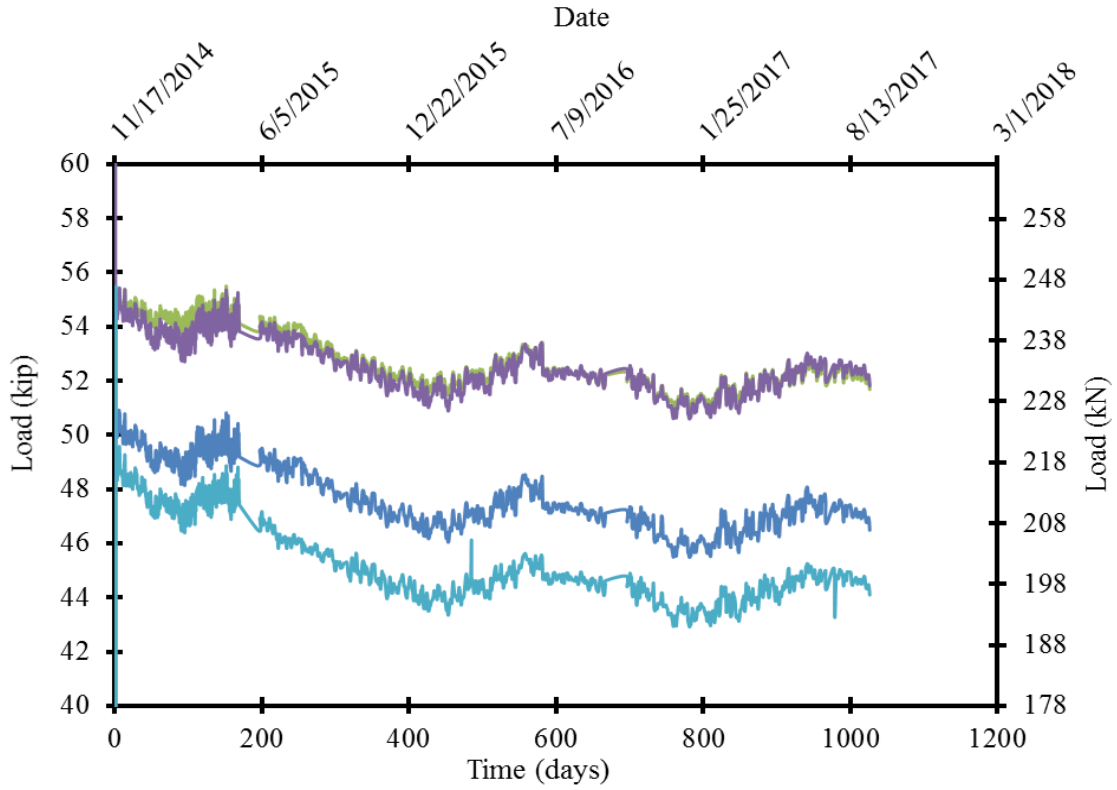


Figure 3.4-7 Long-term monitoring of CFCC specimens stored outdoors

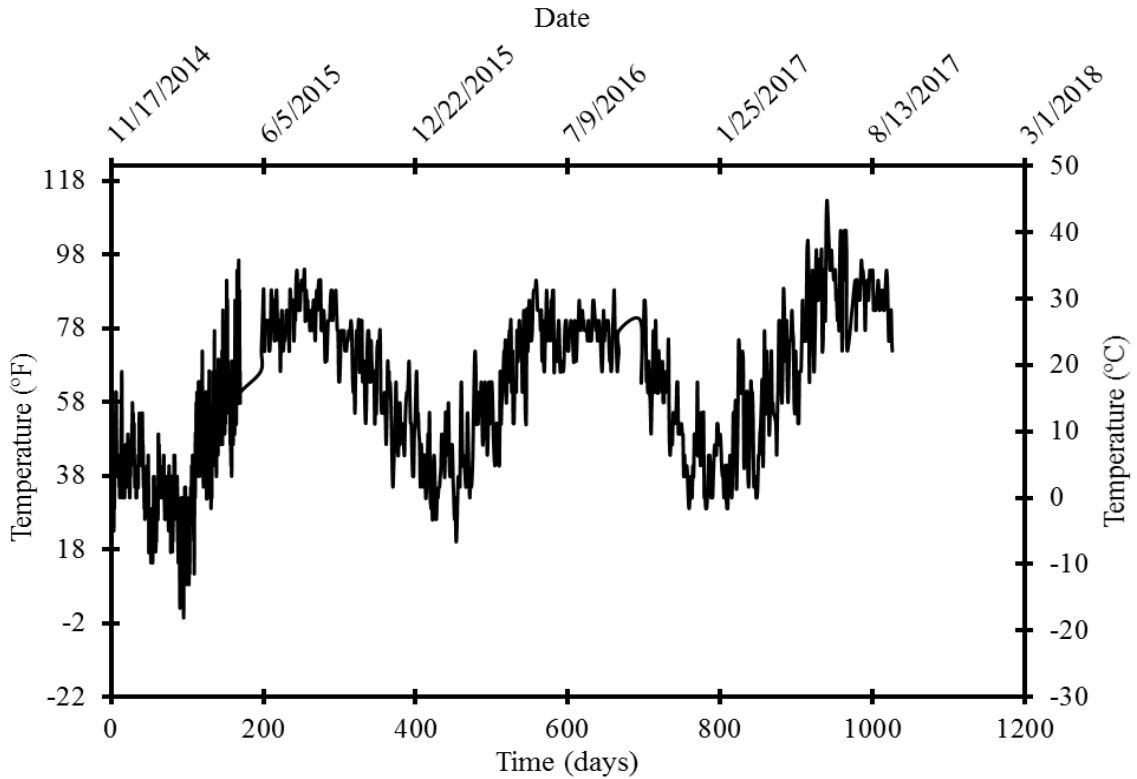


Figure 3.4-8 Temperature change in outdoor CFCC specimens

### 3.5 Discussion of Test Results

Table 3.5-1 shows a summary for the test specimens that have been loaded or currently under continuous monitoring. The pool of specimens includes creep, relaxation, indoor monitoring, and outdoor monitoring test specimens. It should be noted that other than creep specimens, all test specimens were released prior to the end of the project and were loaded to failure under a uni-axial test setup to evaluate the residual strength after exposure to different environmental and loading conditions. Test results of the residual strength are presented at the end of this chapter. The creep specimens were not released with other specimens and at the time of writing this report, the research team were monitoring and recording the load in them. In addition, Table 3.5-2 shows the test results of a creep-rupture test that was performed on CFCC strands with a diameter of 0.5 in. (12.5 mm) by the manufacturer, Tokyo Rope. Furthermore, Table 3.5-3 show the results of a pilot creep-rupture test that was conducted by the research team on CFCC strands with a diameter of 0.7 in. (18 mm).

An extended segment of the project included loading and monitoring additional five 0.6 in. (15.2 mm) CFCC test specimens a load level of 65 kip (289 kN), which represents approximately 92 % of the average tensile strength or 107 % of the strand guaranteed strength. Furthermore, five CFCC test specimens with a diameter of 0.7 in. (18 mm) were loaded to a load level of 95 kip (422 kN), which represented approximately 84 % of the average tensile strength (113.9 kip or 506 kN) or 110 % of the strand guaranteed strength (86.5 kip or 385 kN). Both sets of specimens were loaded in a custom-made closed-loop hydraulic system that maintains a constant level of load in all specimens. At the time of writing this report, the 0.7-in. (18-mm) CFCC specimens were maintaining the assigned load for 18,360 hours, while 0.6-in. (15.2-mm) CFCC specimens were maintaining the assigned load for 11,000 hours.

By plotting the test results for different diameters of CFCC strands as shown on Figure 3.5-3, a one million-hour creep-rupture strength can be estimated by drawing a line separating the failed specimens from those still sustaining the applied load and under continuous monitoring (Table 3.5-1) or those that sustained the load for a period of time and then were released. The failed specimens from different diameters go above the line, while other specimens can go either above or below the line. In other words, this line separates the unsafe stress zone above the line from the

safe stress zone below the line. By extending the line to the end of the graph, an estimate for the one-million-hour creep-rupture strength can be drawn.

Based on available test results at the time of writing this report, the minimum one-million-hour creep-rupture strength for CFCC strands cannot be less than 86 % of the average tensile strength. For instance, for CFCC strands with a diameter of 0.6 in. (15.2 mm) with average tensile strength of (70 kip or 311 kN), the one-million-hour creep rupture strength is approximately 60.2 kip (268 kN). In other words, CFCC strands with a diameter of 0.6 in. (15.2 mm) can be safely loaded to its guaranteed strength of 60.7 kip (270 kN) for 114 years (one-million hour) without experiencing creep rupture. The same can be held true for other CFCC diameters except for the ratio to guaranteed strength since CFCC strands with different diameters have different ratios between the guaranteed and average tensile strengths. Finally, as monitoring for CFCC specimens continues, the points under the line on the figure will continue to shift to the right, while pushing the line upward, which means a higher estimate for the one-million-hour creep-rupture strength.



Figure 3.5-1. Closed-loop hydraulic system to maintain a constant force in creep test specimen



Figure 3.5-2 CFCC specimens under constant load to evaluate creep rupture strength

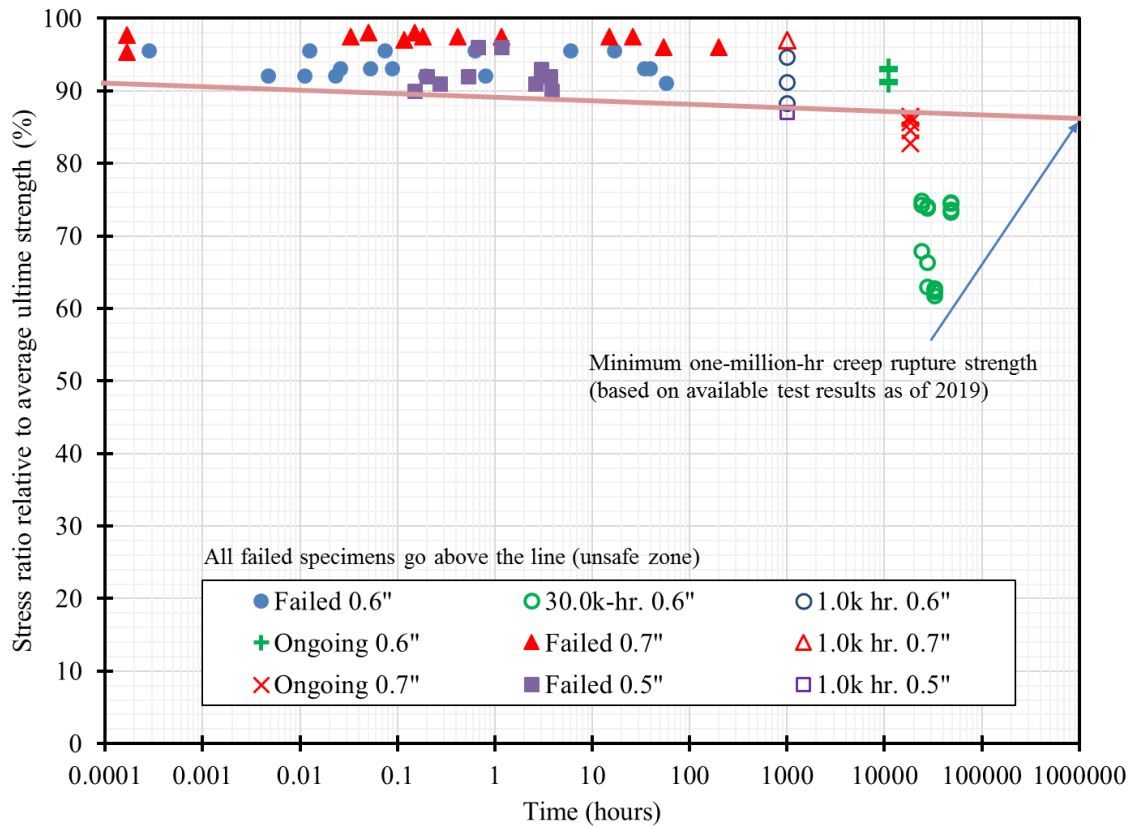


Figure 3.5-3. Lowest estimate for one-million-hour creep-rupture strength based on available test results including long-term monitoring CFCC specimens

Table 3.5-1 Summary of CFCC specimens (diameter of 0.6 in. (15.2 mm)) under monitoring

Test program	Initial load	last load reading	Last load ratio to 70 kip (311 kN)	Time
	Kip (kN)	Kip (kN)	%	hours
Creep (Ongoing)	55 (245)	51.5 (229)	73.6	47,424*
	55 (245)	51.3 (228)	73.3	47,424*
	55 (245)	52.2 (232)	74.5	47,424*
	55 (245)	52.2 (232)	74.5	47,424*
	55 (245)	52.3 (232)	74.7	47,424*
Indoor monitoring	56.5 (251)	52.4(233)	74.8	24,408
	56.5 (251)	52.0 (231)	74.3	23,880
	50.1 (251)	47.6 (212)	68.0	23,856
Outdoor monitoring	56.5 (251)	51.8 (230)	74.0	27,456
	56.5 (251)	51.7 (230)	73.8	27,480
	56.5 (251)	51.9 (231)	74.1	27,480
	50.1 (223)	46.5 (207)	66.4	27,552
	50.1 (223)	44.1 (196)	63.0	27,552
Relaxation	47.5 (211)	43.9 (195)	62.8	32,424
	47.5 (211)	43.8 (195)	62.6	32,424
	47.5 (211)	43.7 194)	62.4	32,424
	47.5 (211)	43.2 (192)	61.8	32,424
	47.5 (211)	43.6 (194)	62.3	32,424

Table 3.5-2 Test results of creep-rupture strength performed by Tokyo Rope using CFCC strands with a diameter of 0.5 in. (12 mm)

Lot #	Test #	Average tensile strength	Sustained load	Load ratio	Time	Mode
		Kip (kN)	Kip (kN)	(%)	(hours)	
0423	1	36.9 (164)	34.4 (153)	93.3	3.00	Failure
	2		33.3 (148)	90.2	0.15	Failure
	3		35.3 (157)	95.7	1.17	Failure
	4		35.3 (157)	95.7	0.67	Failure
	5		32.1 (143)	87.2	1000.00	Suspend
	6		34.4 (153)	93.3	44.00	Suspend
0424	7	34.6 (154)	31.9 (142)	92.2	0.53	Failure
	8		31.9 (142)	92.2	0.20	Failure
	9		31.9 (142)	92.2	3.66	Failure
	10		31.3 (139)	90.3	3.87	Failure
	11		31.5 (140)	90.9	2.61	Failure
	12		31.5 (140)	90.9	0.27	Failure
	13		30.8(137)	89.0	27.00	Suspend
	14		30.8 (137)	89.0	63.50	Suspend

Table 3.5-3 Results of creep-rupture testing on CFCC strands with a diameter of 0.7 in. (18 mm)

Test #	Average tensile strength	Sustained load	Load ratio	Time	Mode
	kip (kN)	Kip (kN)	%	hours	
1	113.93 (507)	111.64 (497)	98.0	0.15	Failure
2		111.68 (497)	98.0	0.05	Failure
3		111.31 (495)	97.7	0.000167	Failure
4		111.04 (494)	97.5	1.166667	Failure
5		111.05 (494)	97.5	0.033333	Failure
6		111.05 (494)	97.5	26	Failure
7		111.05 (494)	97.5	0.416667	Failure
8		111.05 (494)	97.5	15	Failure
9		111.05 (494)	97.5	0.183333	Failure
11		110.53 (492)	97.0	0.116667	Failure
		110.54 (492)	97.0	1000	Suspended
12		109.37 (486)	96.0	54	Failure
13		109.37 (486)	96.0	200	Failure
14		108.63 (483)	95.3	0.000167	Failure

### 3.6 Release and Uni-axial Tensile Test

After completion of the monitoring project, the indoor, outdoor, and relaxation test specimens were released and were loaded under a uniaxial test setup to failure. Test results of the uni-axial testing are given in Table 3.6-1 through Table 3.6-5 for all test specimens. In addition, test results of unstressed test specimens that were constructed at the same time with other test specimens but were kept in controlled laboratory conditions are presented in Table 3.6-6. All test specimens were loaded in a force-control module with a loading rate of 6.5 kip/minute (29 kN/minute).

As shown in the test results, all test groups achieved a higher tensile strength with an average exceeding 80 kip (356 kN). This was a remarkable increase in the tensile capacity from the stated average tensile capacity of 70 kip (311 kN) that was achieved by testing the fresh specimens after construction. The environmental conditions did not seem to have any detrimental effect on the residual tensile capacity of the CFCC strands. Both indoor and outdoor specimens achieved roughly the same average tensile strength. Besides, the stress level in the CFCC strands during monitoring did not seem to affect the residual tensile strength either. Specimen group with the highest average tensile strength was the indoor group with an initial force of 50.1 kip (223 kN),

while the test group with the lowest average tensile strength was also the indoor group with a initial force of 47.5 kip (211 kN) per strand.

Since the unstressed specimens that were kept in laboratory conditions achieved roughly the same tensile capacity, it appears that the increase in the strength is more related to the extended curing of either the epoxy matrix of CFCC strands or the anchorage grout material, or both. However, it can be safely stated that CFCC strands did not experience any loss in strength due to sustained loading of nearly 93 % of the guaranteed strength or due to exposure to severe weather conditions for a period of three years. Therefore, a strength reduction factor that accounts for the durability of CFCC under different environmental conditions may not be necessary in design.

Table 3.6-1 Uni-axial test results of indoor specimens with initial load of 47.5 kip (211 kN)

Specimen	Duration of monitoring (days)	Tensile strength	Strain at failure %
1	1351	83.8 (373)	1.87
2	1351	81.2 (361)	1.80
3	1351	74.8 (333)	1.83
4	1351	80.8 (359)	1.98
5	1351	79.8 (355)	1.61
Average		80.1 (356)	1.82

Table 3.6-2 Uni-axial test results of indoor specimens with initial load of 50.1 kip (223 kN)

Specimen	Duration of monitoring (days)	Tensile strength	Strain at failure %
1	994	82.9 (369)	1.92
2	994	84.5 (376)	1.88
3	994	83.9 (373)	1.94
4	994	83.3 (371)	2.05
5	994	80.4 (358)	1.93
Average		83.0 (369)	1.94

Table 3.6-3 Uni-axial test results of indoor specimens with initial load of 56.5 kip (251 kN)

Specimen	Duration of monitoring (days)	Tensile strength	Strain at failure %
1	1001	82.5 (367)	1.97
2	1001	84.0 (374)	1.96
3	1002	83.6 (372)	2.20
4	1002	83.1 (370)	1.98
5	1002	83.7 (372)	1.95
6	995	85.5 (380)	1.88
7	995	84.0 (374)	1.85
8	995	75.3 (335)	1.50
9	995	84.2 (375)	1.90
10	995	61.9 (275)	1.40
Average		80.8 (359)	1.86

Table 3.6-4 Uni-axial test results of outdoor specimens with initial load of 56.5 kip (251 kN)

Specimen	Duration of monitoring (days)	Tensile strength	Strain at failure %
1	1144	84.5 (375)	1.88
2	1144	82.2 (366)	2.12
3	1144	85.0 (378)	2.25
4	1145	75.3 (335)	1.84
5	1145	74.9 (333)	1.73
6	1145	84.7 (377)	2.03
7	1145	79.9 (355)	1.66
8	1145	79.1 (352)	1.73
9	1145	84.5 (376)	2.11
10	1145	78.5 (349)	1.76
Average		80.9 (360)	1.91

Table 3.6-5 Uni-axial test results of outdoor specimens with initial load of 50.1 kip (223 kN)

Specimen	Duration of monitoring (days)	Tensile strength	Strain at failure %
1	1148	84.1 (374)	1.93
2	1148	77.0 (343)	1.58
3	1148	72.0 (320)	1.66
4	1148	83.8 (373)	1.83
5	1148	84.1 (374)	1.74
6	1148	81.9 (364)	1.82
7	1148	82.0 (365)	1.97
8	1148	84.3 (375)	1.98
9	1148	84.6 (376)	1.83
10	1148	82.9 (369)	1.87
Average		81.7 (363)	1.82

Table 3.6-6 Summary of uni-axial test results of unstressed specimens stored for three years

Specimen	Duration of monitoring, days	Tensile strength, kip (kN)	Strain at failure, %
1	-	80.7 (359)	1.95
2	-	80.4 (357)	1.92
3	-	80.9 (360)	1.96
4	-	79.6 (354)	1.69
5	-	81.48 (362)	1.73
Average		80.6 (359)	1.85

## CHAPTER 4: ENVIRONMENTAL EFFECTS

### 4.1 Introduction

Exposure to fluctuation in temperature is inevitable when CFRP strands are used in highway bridge construction. Starting at the time of construction, CFRP strands are exposed to change in temperature after they are prestressed and before pouring the concrete. While CFRP strands have a negligible coefficient of thermal expansion, the steel strands coupled to them and the steel formwork do not. The difference in the coefficient of thermal expansion between CFCC and surrounding materials leads to a change in the prestressing force that must be calculated and included while establishing the jacking force. In addition, after pouring the concrete and during curing, the temperature of the concrete increases significantly. This increase in temperature could affect the level of the prestressing force in the CFCC strands by producing an additional heat-related relaxation. Furthermore, the daily and seasonal change in temperature, while a CFRP prestressed beam is in service, also affects the level of the prestressing force in the CFRP strands due to the difference in the coefficient of thermal expansion between the CFRP and the surrounding concrete. It should be noted that Laboratory Test Report No. R-5.10\_TOK-JP\_FDOT933.4 by University of Miami Structures and Materials Laboratory averages the glass transition temperature of CFCC samples at 245 °F (118 °C). Test was conducted according to ASTM E1640-13 “Standard Test Method for Assignment of the Glass Transition Temperature by Dynamic Mechanical Analysis”.

Limited experimental data on relaxation of CFRP cables at elevated temperatures are available but are insufficient to suggest certain relaxation loss at different temperatures. Saadatmanest and Tannous (1999) performed a preliminary study on the relaxation of Leadline tendons and CFCC cables at room and elevated temperatures. Twelve CFCC tendons of 16 in. (400 mm) length were tested for relaxation losses in air at temperatures of -30, 25 and 60 °C for a period of 3000 hour, at stress ratios of 0.4 and 0.6. The authors concluded that the percentage loss in the tensile force increased with the increase of the initial stress level and the temperature of the environments. The extrapolated relaxation loss of CFCC were limited to 10 % over a 50-year period.

Enomoto et al. (2009) showed that relaxation and logarithm of passing time can be represented by a linear relationship at room temperature similar to the steel tendons. They reported a one-million-

hour relaxation rate of approximately 2 % of CFRP cables when stressed to 70 % of the guaranteed standard load (average failure load minus three times the standard deviation) at room temperature. In their effort to the study the effect of steam curing of precast members, they carried out relaxation tests of CFRP cables according to JSCE-E 534 (1995) at temperatures of 60, 80 and 100 °C. They found that the relaxation values at 20-80 °C was within the range of 2 %. Whereas, above 80 °C, the estimated relaxation rose sharply due to the softening of the epoxy resin. They also stated the necessity of conducting relaxation tests with temperature as a variable parameter.

Sasaki et al. (2012), in his effort to address the lack of demonstrative data (actual long-term field exposure as opposed to the standard 1000-hour laboratory relaxation test), retrieved and evaluated several properties including relaxation of 17 years old FRP specimens exposed to direct sunlight radiation and salt splash. They concluded that CFRP exhibited a negative response to direct sunlight for relaxation losses unlike AFRP which showed no susceptibility and confirmed the use of the semi-logarithmic plot in a laboratory 1000-hour relaxation test. Apparent relaxation after one-million hours were found to have increased from 10 % for CFRP specimens (prestressed to 70 % of ultimate tensile capacity) not exposed to direct sunlight to between 16 to 19 % for specimens exposed to direct sunlight. The increased relaxation rate was attributed significantly to thermal fatigue resulting from stress induced by sunlight. Possibility of the stress increase resulting from matrix degradation to UV exposure was also not discounted even though earlier tests indicated otherwise.

This chapter addresses the issue of temperature fluctuation and presents detailed results obtained from testing unbonded CFCC strands and CFCC prestressed bulb T beams exposed to a change in temperature. The results showed that unbonded prestressed CFCC strands exhibit a prestress loss with by the increase in temperature. However, recurrent temperature increase, to a certain temperature, does not seem to cause any further loss in the prestressing force. In addition, test results of decked bulb T beams prestressed with CFCC strands showed that seasonal change in temperature leads to a change in the level of prestressing force. However, this change in force is found to be temporary and is reversed once the temperature changes back. Details of test setups and main test results are discussed in the following sections.

## 4.2 Unbonded CFRP Strands

### 4.2.1 Test setup

The main objective of the test was to evaluate the change in the effective prestressing force, as well as the mechanical properties of CFCC at and after exposure high temperatures. To achieve this objective, five CFCC test specimens with prestressing level of 33 kip (147 kN) were monitored for load loss while being subjected to different elevated temperatures. The nomenclatures of the test specimens are: TH-S1, TH-S2, TH-S3, TH-S4, and TH-S5. The thermal test program was executed through three phases; Phase I, II, and III. The temperature matrices and details Phases I and II are discussed in subsequent sections, while Phase III included testing the specimens to failure through uniaxial tensile test to evaluate the residual tensile capacity and elastic modulus of CFCC. The thermal test specimens, shown in Figure 4.2-1 and Figure 4.2-2, consisted of 49 in. (1.2 m) long CFCC strands with two sleeve anchors. Details on CFCC materials and anchorage preparation are presented earlier in this report.

The thermal test of CFCC specimens was performed in an MTS<sup>®</sup> electrically heated environmental chamber as shown in Figure 4.2-1. The internal dimensions of the chamber are 12 in. × 12 in. × 12 in. (305 mm × 305 mm × 305 mm). The chamber is designed to reach temperatures up to 400 °F (204 °C) in less than 15 minutes and is provided with a temperature controller that displays a set point and current temperature. Heating is achieved using electrical heating elements and a circulation fan that ensures uniform temperatures throughout the chamber while also shielding the specimen from direct exposure to radiant heat. Cooling of the chamber is accomplished with liquid nitrogen but was not used in the current study. The chamber is designed to accommodate small scale specimens with two access holes at the top and bottom of the chamber for gripping purposes. Those holes were blocked with thermal blanks during the test to maintain uniform temperature and eliminate any temperature increase of the anchorage devices at the ends of the specimens.

The loading frame used to apply prestressing force to CFCC specimens was manufactured by MTS<sup>®</sup>. This 2-post loading frame shown in Figure 4.2-1 consists of a crosshead that can move along two columns using a crosshead hydraulic actuator with a standard stroke of 6 in. (152 mm). The mounting height of the crossheads varies from 7 in. (178 mm) to 62.5 in. (1586 mm) with a

constant width between the columns of 25 in. (635 mm). The loading frame includes a force transducer (load cell) to measure the axial force applied to the specimen and an LVDT to measure the displacement of the actuator. The tensile load capacity of the loading frame is 55 kip (245 kN). The specimens were only loaded to 33 kip (147 kN).

An MTS FlexTest™ GT Station Manager controls a hydraulic actuator that applies the prestressing load to the test specimens in the loading frame. For this test, the prestressing force was applied to CFCC specimens in a force-control mode with rate of 6.5 kip/min (29 kN/min) until the load reached 33 kip (147 kN). Then, the MTS software automatically switched the mode to displacement-control mode and locked the actuator heads in place.

In Phase I thermal testing, CFCC test specimens were prestressed to 33 kip (147 kN) and were subjected to different elevated temperatures, while the loss in the prestressing force due to the increased temperature was monitored at each temperature range. Specimen TH-S1 served as a control specimen and was loaded to a force level of 33 kip (147 kN) at a room temperature of 76 °F (24 °C) for four hours and then the load was removed without activating the environmental chamber. The loss in the load due to strand and anchorage relaxation was monitored and captured.

The second test specimen (TH-S2) was loaded to a force level of 33 kip (147 kN) at a room temperature. Two hours after loading the specimen, the environmental chamber was activated and the temperature of the heated length of the CFRP specimen increased to 150 °F (65 °C). The temperature was maintained at 150 °F (65 °C) for two hours, then the heat chamber was turned off and specimen was allowed to naturally cool down to room temperature. After one hour, the load was removed. The heating and cooling rates were approximately 20 °F (10 °C) per minute.

The third test specimen (TH-S3) was loaded to 33 kip (147 kN) at room temperature. After two hours, the temperature of the heated length increased to 150 °F (65 °C). After two hours, the temperature increased again to 235 °F (112 °C). After two more hours, the environmental chamber was allowed to cool down to room temperature. An hour later, the load was removed.

The fourth test specimen (TH-S4) was loaded at room temperature for two hours. Then, the temperature increased to 150 °F (65 °C) for two hours, to 235 °F (112 °C) for two hours, and to 316 °F (158 °C) for two hours. After that, the specimen was allowed to cool down and the load was removed an hour later.

The fifth test specimen was loaded to 33 kip (147 kN) at room temperature for two hours. Then, the temperature increased to 150 °F (65 °C) for two hours, to 235 °F (112 °C) for two hours, to 316 °F (158 °C) for two hours, and to 400 °F (204 °C) for two hours. Finally, the specimen was allowed to cool down for an hour, after which the load was removed.

Phase II of the test started after concluding Phase I. In Phase II, the specimens were heated through a single-step heating to their maximum reached temperature in Phase I as shown in Figure 4.2-4 . For instance, fifth specimen (TH-S5) was loaded to 33 kip (147 kN) at room temperature and after two hours, the temperature increased and was maintained at 400 °F (204 °C) for two hours. Then the specimen was allowed to cool down to room temperature and the load was removed after two hours, with total a test duration of 6 hours.

In Phase III. CFCC specimens were placed in a 270-kip (1200-kN) MTS Axial Load Frame for a uniaxial tensile test. Tensile force was applied in a force-control mode at a rate of 2 kip/min (9 kN/min) to failure. The tensile test was conducted in accordance with ASTM Standard D7205/7205M-06: “Standard Test Method for Tensile Properties of Fiber Reinforced Polymer Matrix Composite Bars”.



Figure 4.2-1 Evaluating prestress loss in CFCC specimens due to temperature increase



Figure 4.2-2 Heated length of CFCC strand inside the heat chamber

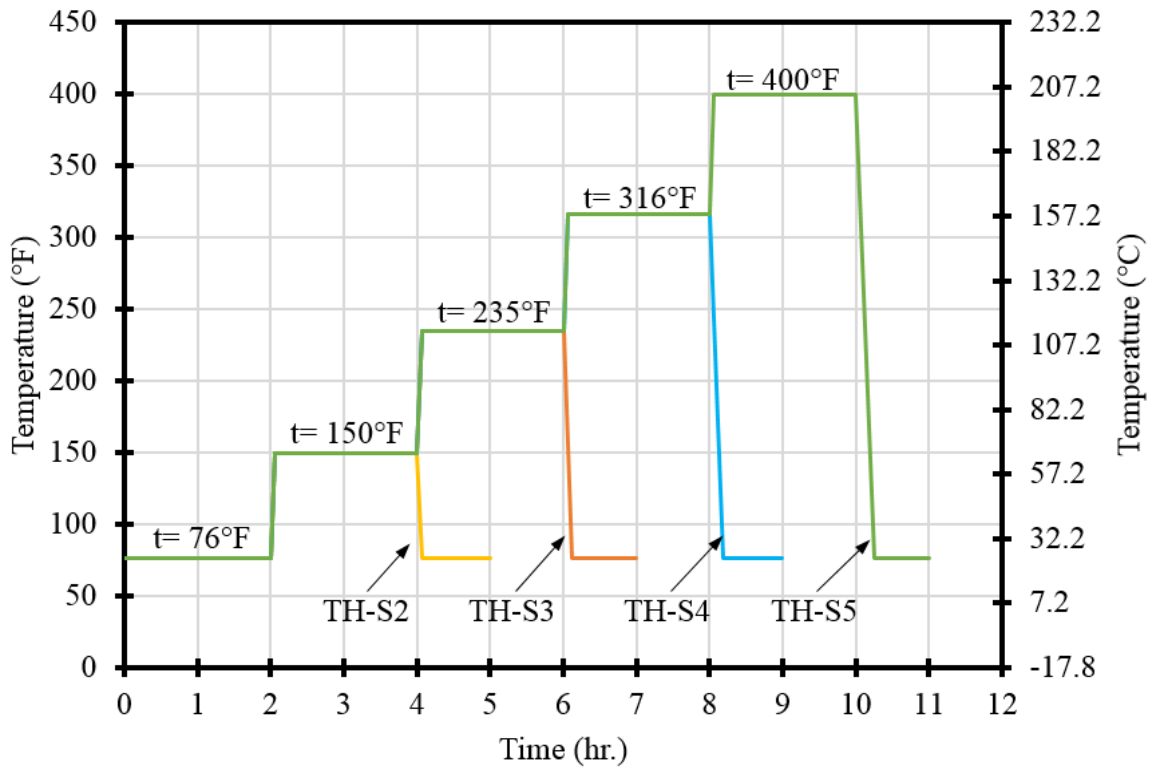


Figure 4.2-3 Time-temperature curves for thermal test specimens in Phase I

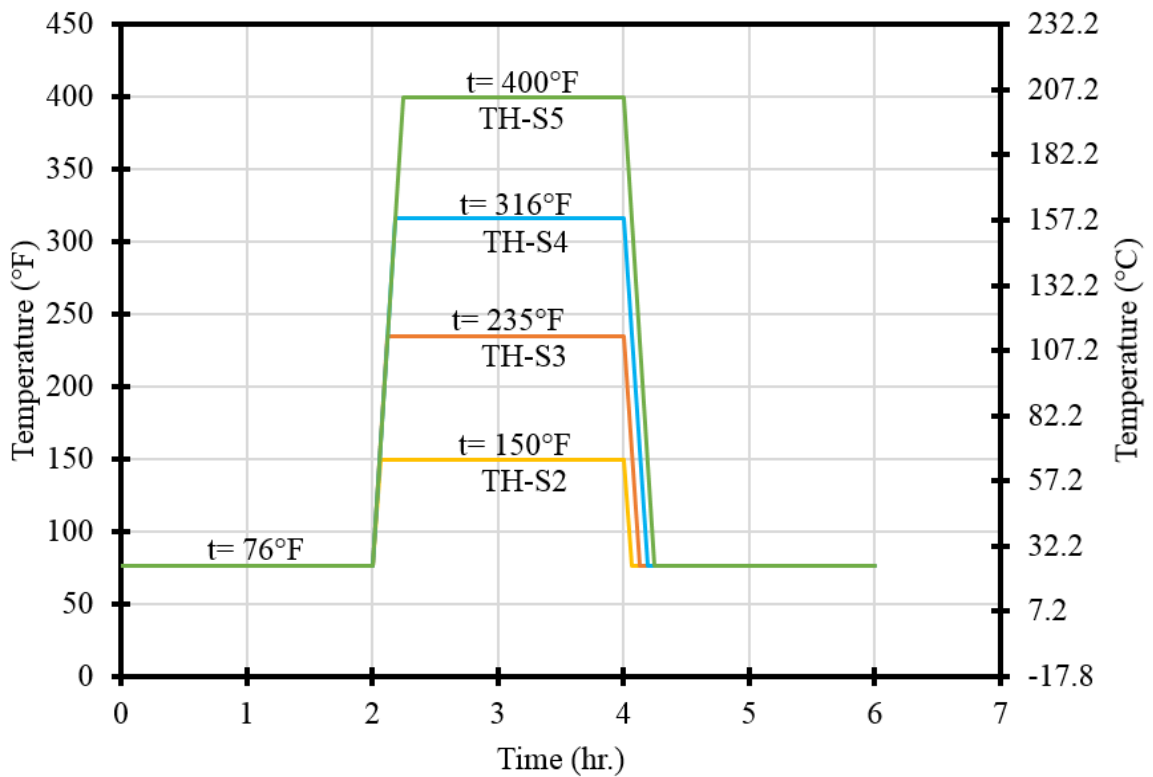


Figure 4.2-4 Temperature profiles for thermal test specimens in Phase II

#### 4.2.2 Test results

The load vs. time curves for all test specimens in Phase I are presented in Figure 4.2-5 through Figure 4.2-9. TH-S1 experienced a typical relaxation loss that was discussed earlier in the report. The prestressing force decreased with the time with a load loss of approximately 0.76 kip (3.4 kN) and 0.84 kip (3.7 kN) after 2 and 4 hrs., respectively with a total prestress loss of 2.5 %.

Specimen TH-S2 displayed the same pattern with a load loss of 0.72 kip (3.2 kN) in the first 2 hrs. (ambient temperature). When the temperature of the specimen was raised to 150 °F (66 °C), there was a step decrease in the load. In order to precisely estimate the load loss that occurred in the specimen due to the thermal change, the slope of the unheated segment was estimated and extended as a linear function between the load and the time. The thermal load loss was determined as the difference between the linear slope and the actual load-time curve. The load loss due to temperature increase was estimated as 0.33 kip (1.5 kN).

TH-S3 was exposed to two temperature increases. With each temperature increase, the specimen exhibited a loss in the load. That is in addition to the initial loss of the load during the first two hours of heating with no increase in temperature. A load loss of 0.67 kip (3kN) was observed in the first 2 hrs with no heat. As shown in Table 4.2-1, a load loss of 0.36 kip (1.6 kN) was associated with the increase in temperature from ambient to 150 °F (66 °C), while a load loss of 0.78 kip (3.5 kN) was associated with the increase in temperature from 150 °F (66 °C) to 235 °F (112 °C).

In addition to the loss in load of 0.73 kip (3.2 kN) before heating, Specimen TH-S4 exhibited a 3-stage loss in load associated with increase in temperature. The recorded losses were, 0.32 kip (1.4 kN), 0.75 kip (3.3 kN), and 0.3 kip (1.3 kN) with the increase in temperatures from ambient to 150 °F (66 °C), to 235 °F (112 °C), and to 316 °F (158 °C), respectively.

Specimen TH-S5 displayed a similar load loss pattern with load losses of 0.67 kip (3 kN) before heating, then a loss of 0.39 kip (1.7 kN), 0.73 kip (3.2 kN), 0.33 kip (1.5 kN), and 0.18 kip (0.8 kN), that corresponded to the temperature increase in the specimen from ambient to 150 °F (66 °C), to 235 °F (112 °C), to 316 °F (158 °C), and to 400 °F (204 °C), respectively.

Load loss in Phase II was significantly less than that observed in Phase I even though the specimens were heated to the same temperature in Phase I. The load vs. time curves for all the specimens

during Phase II is presented in Figure 4.2-10 through Figure 4.2-13. In all the specimens, the increase in the temperature did not result in any significant loss of the load and the drop of the load was almost gradual and similar to a typical load loss that could be observed at ambient temperature. It appears that initial heating of a CFCC specimen to a certain temperature level caused the epoxy matrix to relax and expand. Since the specimen was loaded during the heating period, this expansion/relaxation of the epoxy matrix was converted into a loss in the load. After the specimen was allowed to cool down, the epoxy matrix solidified in its standing shape, which explains the inability of the specimens to regain the lost load when they were allowed to cool down. When the CFCC specimens were heated for the second time in Phase II, the epoxy matrix did not experience any further relaxation since the temperature in the second heating cycle did not exceed that of the first cycle and that explains the minimal loss in the load in Phase II. It should be noted that when the specimens were allowed to cool down at the end of Phase I, the lost load was not recovered, which indicated that the loss in the load was not related to the thermal expansion of the specimens and that the heat relaxation was non-recoverable. This was also confirmed in Phase II since loss of the load due to thermal expansion of the specimens would have been evident during the heating segment in Phase II.

The loss in the load due to the increase in temperature of the test specimens in Phase I was used to calculate the heat relaxation loss and estimate the loss in prestressing force during construction when the concrete is placed around the pretensioned CFRP strands and the heat is generated by concrete hydration. Several studies (Swenson and French 2015; Barr et al. 2005) place the maximum concrete temperature during hydration at 150 °F (65 °C), which is corresponding to a relaxation loss in the heated segment of approximately 287  $\mu\epsilon$  or a prestress loss of approximately 6.75 ksi (46.5 MPa). The calculations of the heat relaxation loss follow the basics of mechanics of materials. For instance, the heated segment of the CFCC specimen was 12 in. (305 mm) and since both heads of actuator were locked in position, the heat relaxation of the heated segment caused the loss in the load. When heating the specimens from ambient to 150 °F (66 °C), the average load loss among all specimens was 0.35 kip (1.56 kN). This loss of the load happened over the entire length of the specimen. In other words, between the two fixed heads of the actuator. The heat relaxation strain in the heated segment of the specimen that caused this loss in the load can be back calculated based on load loss as follows:

$$\Delta\varepsilon = \frac{\Delta L}{L_h} \quad (4.2-1)$$

$$\Delta L = \frac{\Delta P L_T}{EA} \quad (4.2-2)$$

where:

$\Delta\varepsilon$  = heat relaxation strain of the specimen (relative to the heated segment only)

$\Delta L$  = change in length of heat segment due to added heat relaxation, in. (mm)

$L_T$  = length of the specimen between the fixed actuator heads

$L_h$  = heated length of the specimen = 12 in. (305 mm)

$A$  = cross sectional area of the specimen = 0.179 in.<sup>2</sup> (115.4 mm<sup>2</sup>)

$E$  = elastic modulus of CFCC, ksi (GPa)

$\Delta P$  = change in the force due to increase in temperature, kip (kN)

The length of the specimen between the fixed actuator heads ( $L_T$ ) can be challenging to estimate. The total length of the specimen was 49 in. (1244 mm) including two 12-in. (305-mm) long anchorage devices. With a gripping length of 2.5 in. (64 mm) on each end, the specimen length between the fixed heads, from grip to grip, was 44 in. (1118 mm) However, this length had a free strand length of 25 in. (635 mm) and an embedded length inside the anchorage devices of 19 in. (483 mm). Bond mechanism and force transfer in the embedded length complicates the calculations of the elongation in the embedded region.

To avoid the unnecessary difficulty in estimating  $L_T$  along with the need for estimating the elastic modulus of CFCC, Eqn. 4.2-1 can be rewritten using the load-elongation curve of the specimen (from zero loading to 33 kip (147 kN)). The displacement of the actuator was recorded during the loading of the specimen. Therefore, the relationship between the elastic modulus and the length of the specimen can be written as:

$$\frac{L_T}{EA} = \frac{\Delta L_L}{\Delta P_L} \quad (4.2-3)$$

where:

$\Delta P_L$  = change in the load during the loading of the specimen

$\Delta L_L$  = corresponding elongation of the specimen estimated using actuator displacement

From the loading-elongation curves of the five specimens, the average ( $L_T/EA$ ) was 0.00983 in./kip (0.056 mm/kN), calculated based on an observed change in displacement of 0.1081 in. (2.75 mm) over a change in the load from 22 to 33 kip (98 to 147 kN). Therefore, the heat relaxation strain in the CFCC specimen can be calculated as:

$$\Delta L = \Delta P \frac{L_T}{EA} = 0.35 \times 0.00983 = 0.00344 \text{ in.} \quad (4.2-4)$$

$$\Delta \varepsilon = \frac{\Delta L}{L_h} = \frac{0.00344}{12} = 287 \times 10^{-6} = 287 \mu\varepsilon \quad (4.2-5)$$

It should be noted that these calculations are based on a conservative estimate for the heated length of 12 in. (305 mm), which represents the interior height of the heat chamber. The actual heated length of the CFCC strand specimens was slightly longer than 12 in. (305 mm) since the heat radiated beyond the interior cavity of the heat chamber through the top and bottom holes (holes were block with thermal blanket to minimize heat escape). Temperature on the exterior top surface of the heat chamber was approximately 94.5 °F (34.7 °C) when the temperature inside the chamber was 150 °F (65 °C), while the temperature at the bottom exterior surface did not exceed the ambient (76 °F or 24 °C) during the entire test. Therefore, it can be assumed that the temperature dropped linearly from 150 °F (65 °C) to 94.5 °F (34.7 °C) through the 2-in. (50.1-mm) thick ceiling of the heat chamber. Consequently, a more accurate heated length may be taken as 13.5 in. (343 mm) considering an additional 1.0 in. (25.4 mm) of heated length through the top hole and 0.5 in. (13 mm) through the bottom hole, with a resulting additional strain of 254  $\mu\varepsilon$ .

Finally, it should be noted that when the temperature inside the chamber was 400 °F (204 °C), the maximum record temperature at the exterior top surface of the heat chamber was 129 °F (54 °C) and the highest recorded temperature at the bottom of the top anchorage device was 87.5 °F (31 °C). Therefore, it can be safely concluded that the anchorage devices were protected from heat and did not participate in the recorded loss of the load due to temperature increase.

Figure 4.2-14 and Figure 4.2-15 show the testing and failure of test specimens in Phase III. Test results of are also presented in Table 4.2-2. The uniaxial tensile test of the four test specimens at ambient temperature in Phase III revealed an average breaking load of 70.5 kip (314 kN), which is approximately equal to the breaking load of non-heated test specimen. Besides, the average elastic modulus calculated based on uniaxial tensile test at ambient temperature of the four heated test specimens was approximately 23,101 ksi (159 GPa), which is slightly higher than the elastic modulus of non-heated specimen. No noticeable physical difference was observed between the first specimen (non-heated) and the rest of the specimens.

Table 4.2-1 Summary of observed load loss due to increase in temperature in Phase I

Start Temp.	End Temp.	TH-S1	TH-S2	TH-S3	TH-S4	TH-S5
°F (°C)	°F (°C)	kip (kN)	kip (kN)	kip (kN)	kip (kN)	kip (kN)
76 (24)	150 (65)	-	0.33 (1.5)	0.36 (1.6)	0.32 (1.4)	0.39 (1.7)
150 (65)	235 (112)	-	-	0.78 (3.5)	0.75 (3.3)	0.73 (3.2)
235 (112)	316 (158)	-	-	-	0.3 (1.3)	0.33 (1.5)
316 (158)	400 (204)	-	-	-	-	0.18 (0.8)

Table 4.2-2 Results of tensile testing of CFCC specimens

Specimen	Max. Temp.	Failure Load	Elastic Modulus
	°F (°C)	(kN)	ksi (GPa)
TH-S1	76 (24)	71.0 (316)	22,245 (153)
TH-S2	150 (65)	71.2 (317)	22,947 (158)
TH-S3	235 (112)	66.0 (294)	22,967 (158)
TH-S4	316 (158)	70.6 (314)	23,051 (159)
TH-S5	400 (204)	74.1 (330)	23,440 (162)

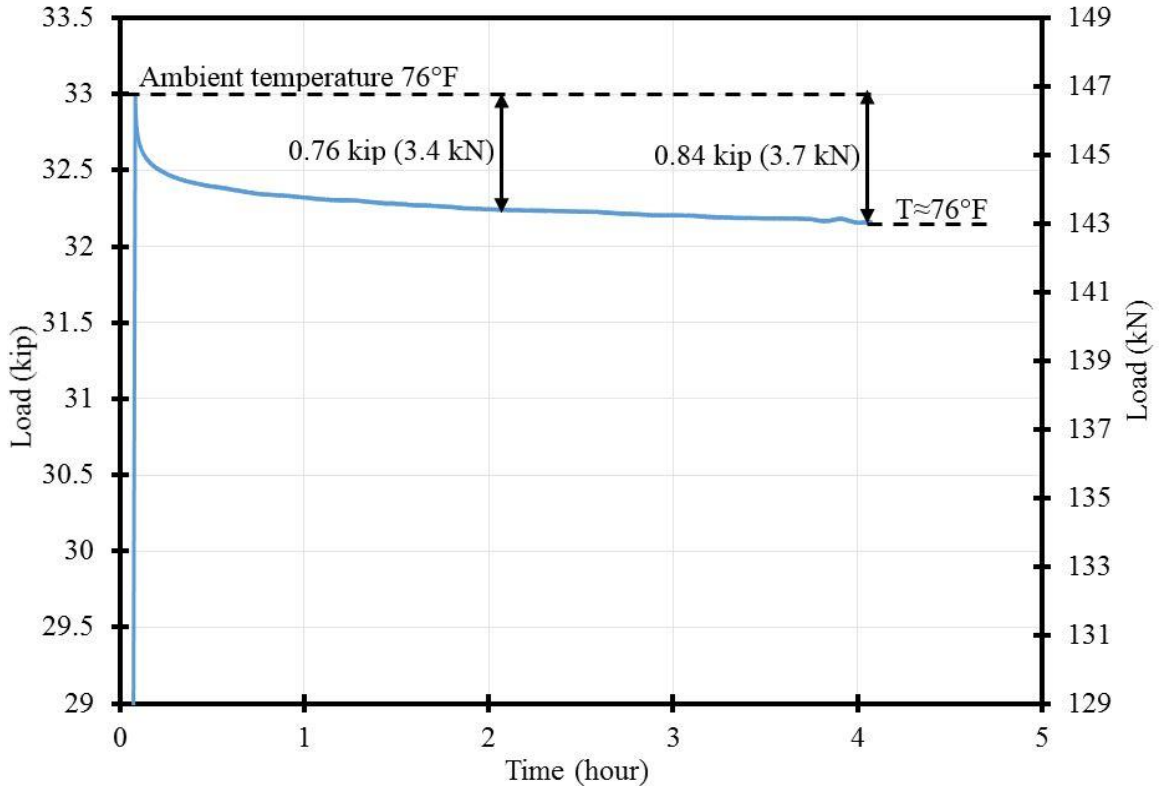


Figure 4.2-5 Load vs. time for TH-S1 in Phase I of thermal testing

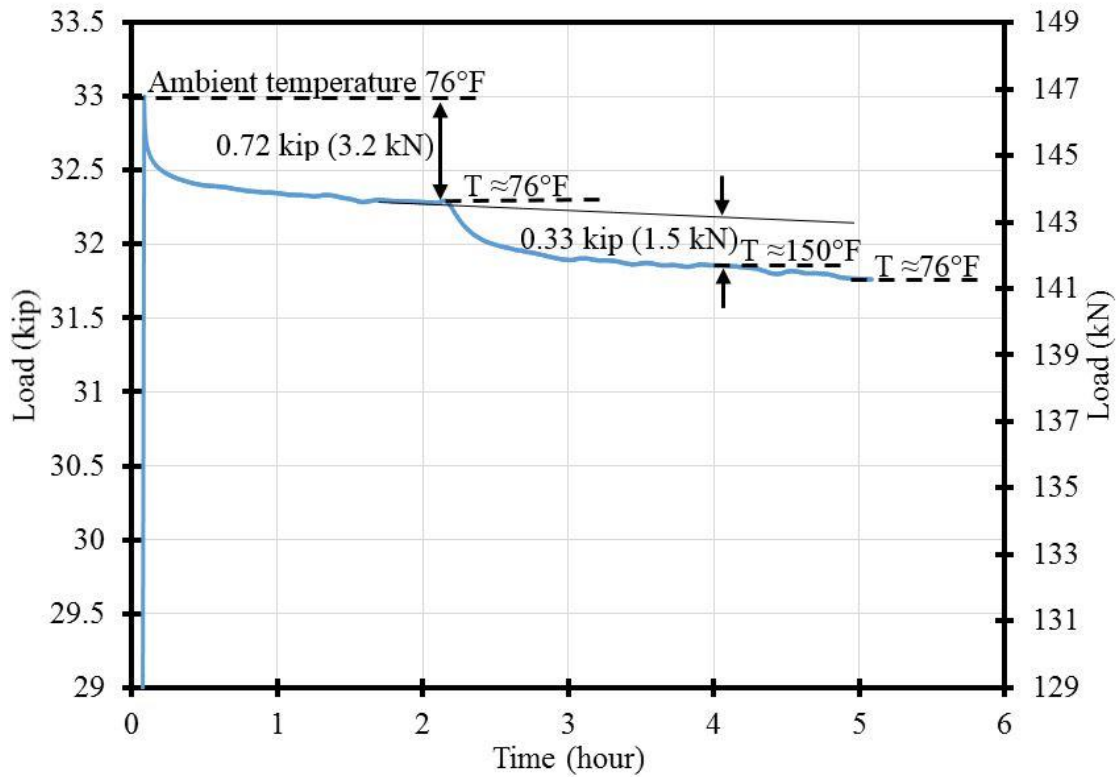


Figure 4.2-6 Load vs. time for TH-S2 in Phase I of thermal testing

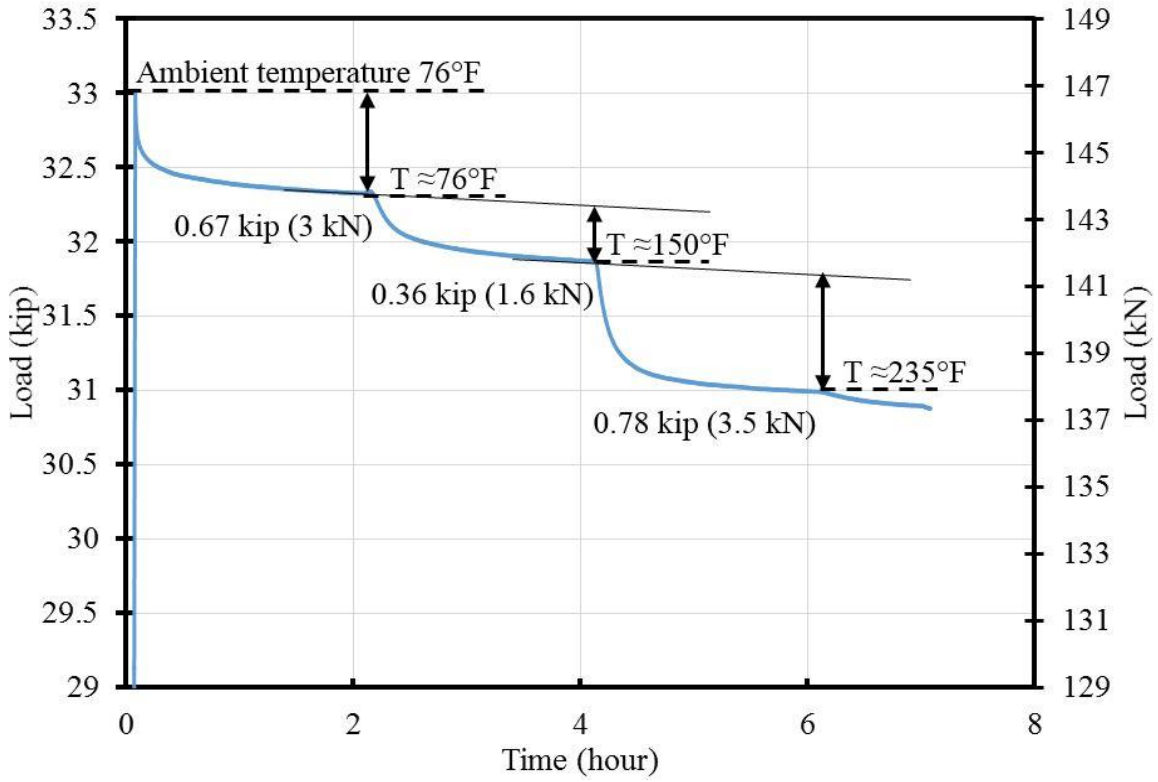


Figure 4.2-7 Load vs. time for TH-S3 in Phase I of thermal testing

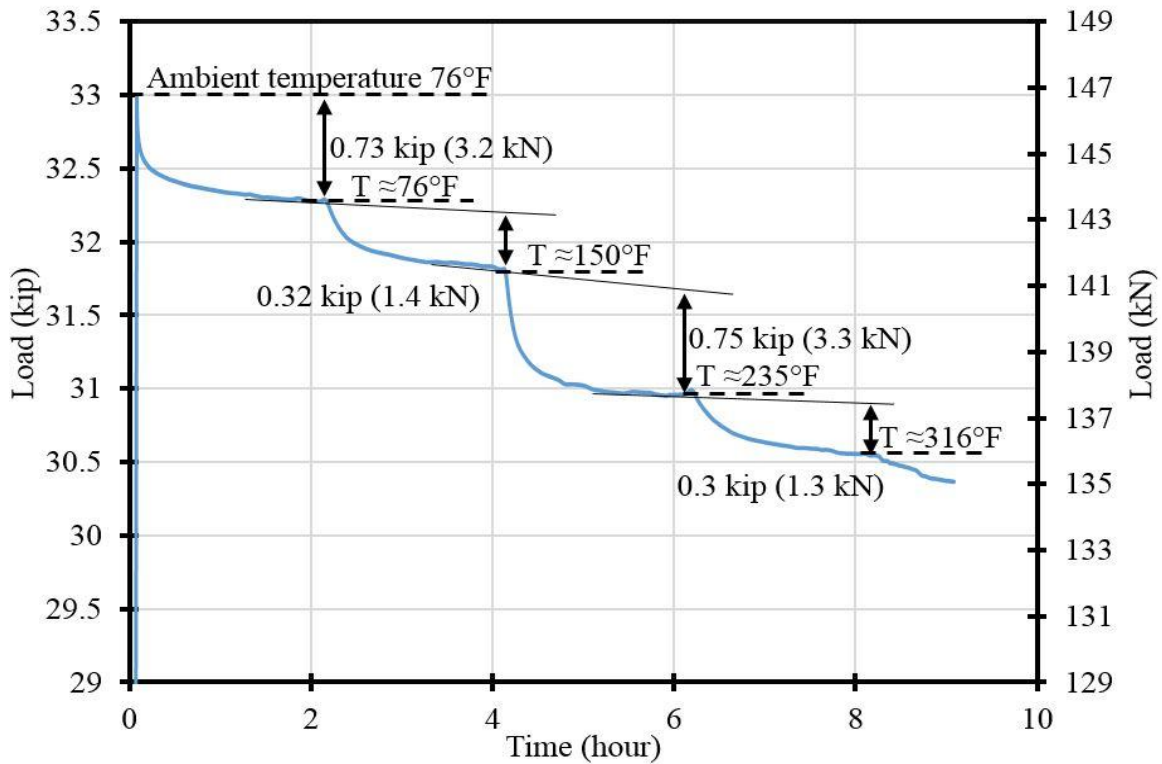


Figure 4.2-8 Load vs. time for TH-S4 in Phase I of thermal testing

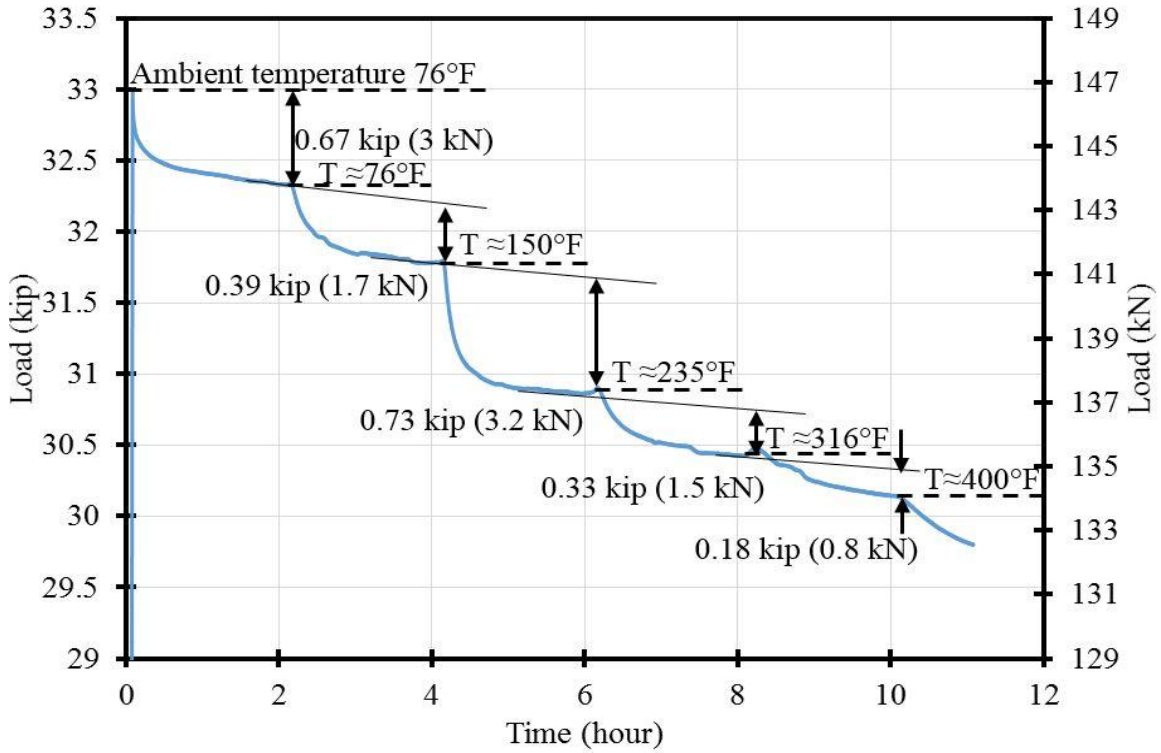


Figure 4.2-9 Load vs. time for TH-S5 in Phase I of thermal testing

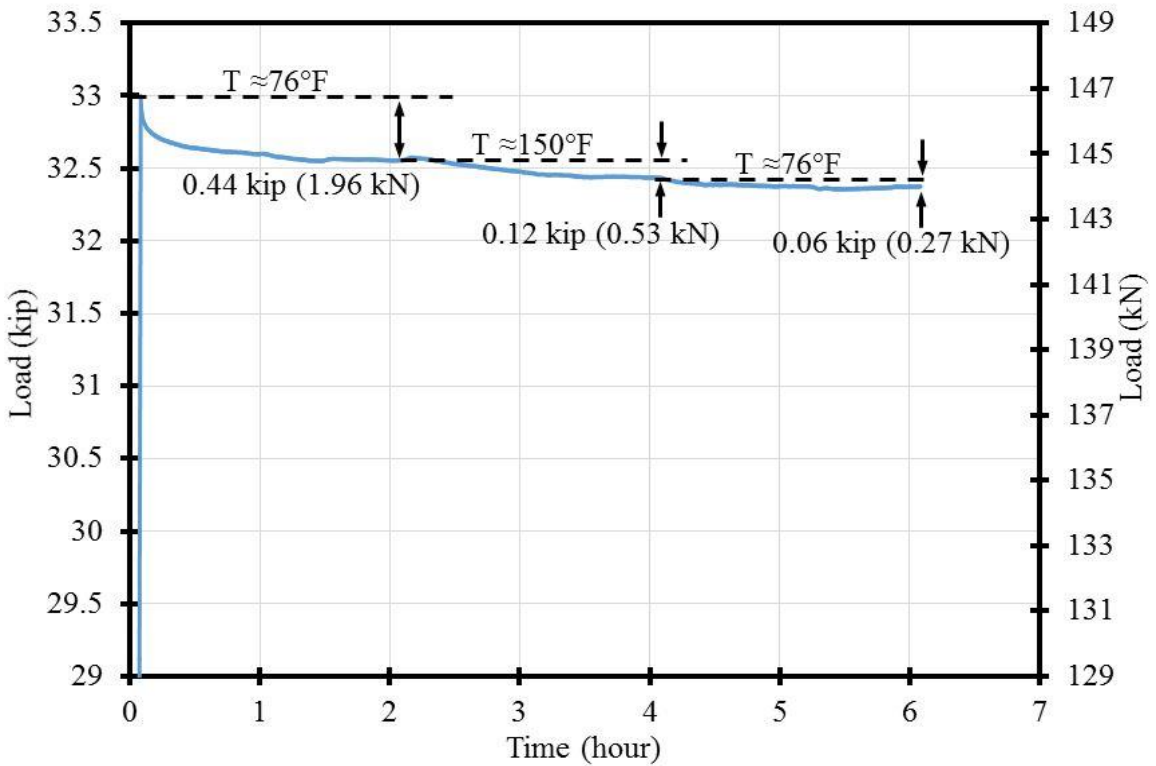


Figure 4.2-10 Load vs. time for TH-S2 in Phase II of thermal testing

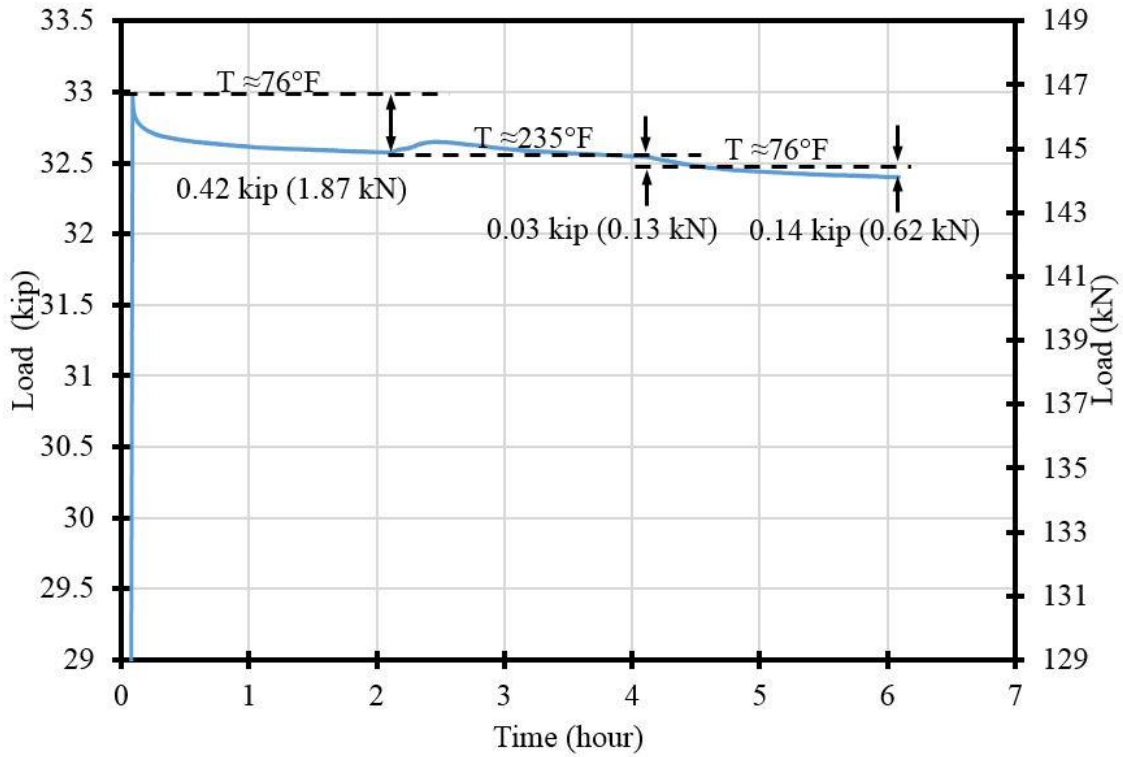


Figure 4.2-11 Load vs. time for TH-S3 in Phase II of thermal testing

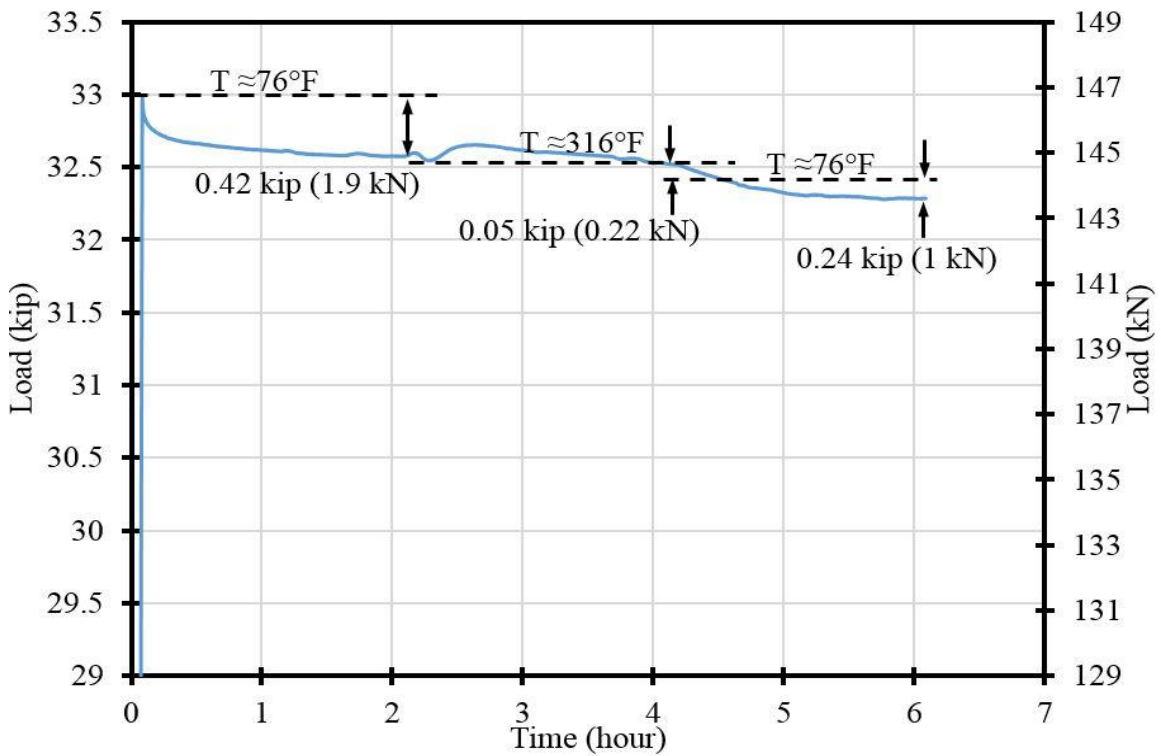


Figure 4.2-12 Load vs. time for TH-S4 in Phase II of thermal testing

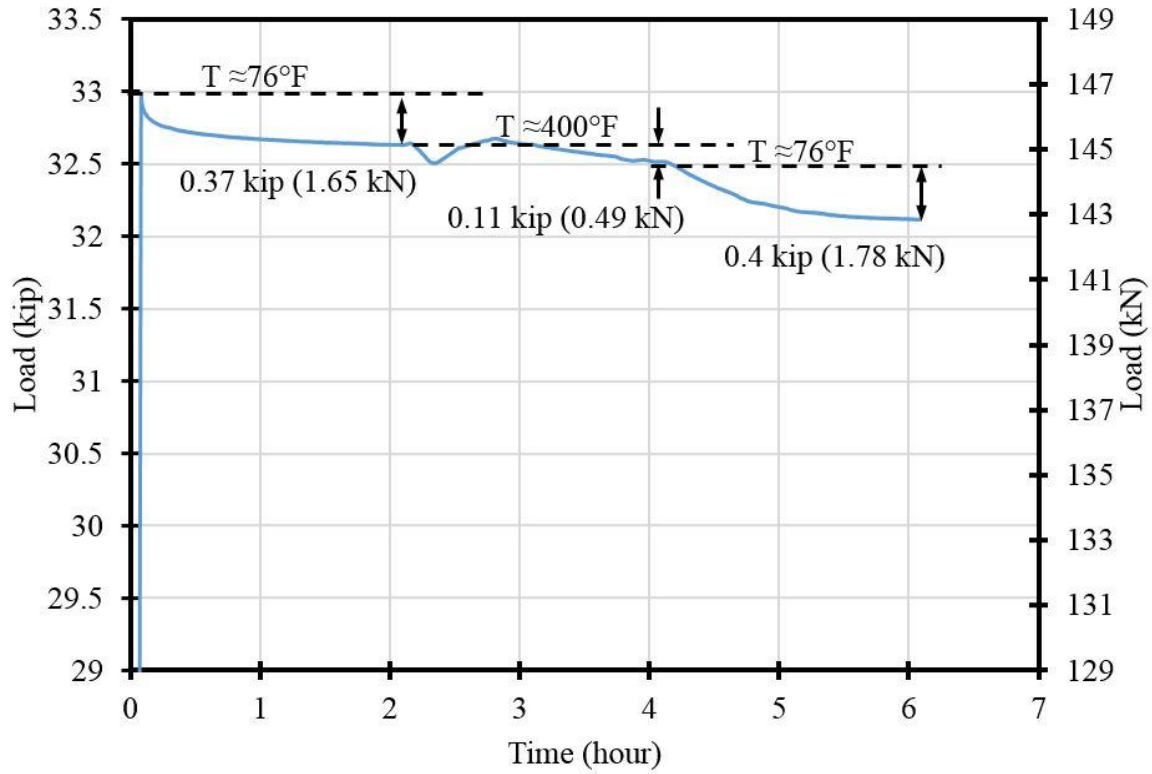


Figure 4.2-13 Load vs. time for TH-S5 in Phase II of thermal testing



Figure 4.2-14 Uniaxial testing of CFCC specimens in Phase III



Figure 4.2-15 Failure of CFCC specimens in Phase III

### 4.3 CFRP Prestressed Decked Bulb T Beams

#### 4.3.1 Construction of test specimens

The coefficient of thermal expansion for concrete is approximately  $6 \times 10^{-6} / ^\circ\text{F}$  ( $12 \times 10^{-6} / ^\circ\text{C}$ ), while CFRP has a coefficient of thermal expansion less than  $0.5 \times 10^{-6} / ^\circ\text{F}$  ( $1 \times 10^{-6} / ^\circ\text{C}$ ). Therefore, concrete beams prestressed with CFRP strands experience a certain loss or gain in the level of prestressing force with the seasonal change in temperature. This experimental study was executed to verify the loss/gain in prestressing level due to thermal changes.

A total of six identical precast prestressed decked bulb T beams were constructed and tested under a flexural loading at different temperatures. The beams had a length of 16 ft (4.87 m), a top flange width of 18 in. (457 mm), and a depth of 16 in. (406 mm). Each beam was prestressed with CFCC strands with a diameter of 0.6 in. (15.2 mm). In addition, each beam was provided with five top non-prestressed CFCC strands in the top flange (Figure 4.3-1). In the transverse direction, the beams were reinforced with No. 3 (10 mm) steel stirrups spaced 4 in. (102 mm) on center.

The decked bulb T beams were constructed at the Structural Testing Lab. (STL), which hosts a prestressing bed that can accommodate beams with a length of 50 ft (15.24 m) and a width of 48

in. (1.22 m). Therefore, there was enough space to accommodate the simultaneous construction of the six beams. The formwork for the beams included a wood platform decking and sides. The decking platform was constructed of plywood and dimension lumber. The sides of the formwork were constructed from layers of plywood and polystyrene (Styrofoam) to form the required bulb T shape and accommodate the end blocks. These layers of polystyrene were pre-cut to shape using a table saw and attached to the plywood using adhesive and wood screws.

The reinforcement cages were assembled from the steel stirrups and the top non-prestressed CFCC strands. The steel stirrups were made of two pieces welded together with tack welds. End blocks were provided with rectangular stirrups every 2.0 in. (51 mm) to resist the bursting force at prestress release. After reinforcement cages were completed, they were moved to the platform decking, where prestressing strands were passed through the cages. Figure 4.3-2 through Figure 4.3-5 show different stages of construction.

To facilitate the prestressing and avoid damaging the CFCC strands, a special coupler system was used to connect the prestressing CFCC strands with conventional 7-wire 0.6 in. (15.2 mm) low relaxation steel strands as shown in Figure 4.3-5. The couplers were provided on both the live and dead ends. Therefore, conventional steel anchorage was used at both bulkheads and the prestressing was executed by tensioning the steel strands. After completing the installation of the coupler system, the steel strands were tensioned from the live end while a set of in-line load cells was attached to the prestressing strands at the dead end. The prestressing was executed using a hydraulic pump and a jacking system, shown in Figure 4.3-6 and Figure 4.3-7. The strands were prestressed in a predetermined sequence to avoid generating a significant eccentricity in the bulkhead. The initial prestressing force was set to 33 kip (147 kN)/strand. The force in each prestressing strand was verified through the readings from the load cells, the readings from hydraulic pump and the measured elongation of the strands. A seating loss of approximately 1.5 kip (6.7 kN) per strand was observed immediately after releasing the pump.

All the beams were cast using a ready-mix concrete with a concrete mix as shown in Table 4.3-1. The concrete mix was designed to achieve a 28-day compressive strength of 7 ksi (48 MPa). The maximum aggregate size was limited to 0.75 in. (19 mm) and a slump of 10 in. (254 mm) was verified before pouring concrete. This concrete mix is a typical concrete mix used in highway bridge beams. After concrete casting, the beams were covered with wet burlap and plastic sheets

to prevent moisture escape and allow for proper curing. In addition, concrete cylinders with a diameter of 6 in. (152 mm) and a length of 12 in. (305 mm) were also cast from the same batch of concrete. The cylinders were allowed to cure under the same conditions of the concrete beams and were tested under uni-axial compressive stress according to ASTM C39/C39M-12a (2012): “Standard Test Method for Compressive Strength of Cylindrical Concrete Specimens.” to determine the compressive strength of concrete after 28 days. Figure 4.3-8 through Figure 4.3-12 document the process of casting the concrete.

Transfer of prestressing forces into concrete beams took place 10 days after casting of concrete and after verifying that the concrete had achieved more than 80 % of its 28-day compressive strength. The prestress release was executed by slowly heating the steel strands using an acetylene/oxygen torch. The camber of the beams was measured at the mid-span of the beam at prestress release. After prestress release, the beams were removed from the formwork and sent to the testing facility. Figure 4.3-13 and Figure 4.3-14 show the change of the prestressing force from the time of prestressing to the time of prestress release.

Table 4.3-1 Concrete mix per cubic yard

Material	Units	Design Quantity per yrd <sup>3</sup>
Limestone Coarse Aggregate (LIA-OTT),	lb (kg)	1762 (801)
Fine Aggregate (2NS-AAR),	lb (kg)	1265 (575)
Type 1 Cement (CMT1-LAA),	lb (kg)	534 (243)
Slag Cement (CMGS-LA),	lb (kg)	288 (131)
Water (WAT1),	gal (m <sup>3</sup> )	31.8 (0.12)
Water/Cement ratio		0.37
Retarding Admixture (0STAB-PR),	oz (kg)	25 (0.7)
High Range Water Reducer (0HRWR-PR),	oz (kg)	53 (1.5)

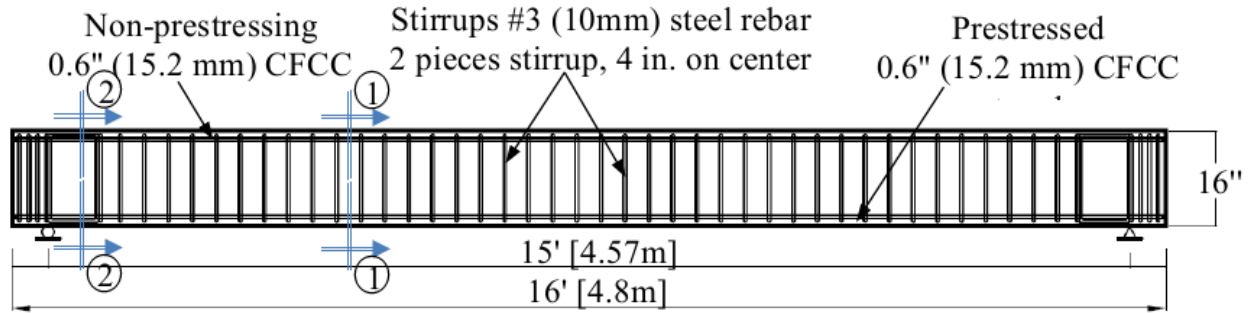


Figure 4.3-1 Cross section and internal reinforcement details of decked bulb T-beams

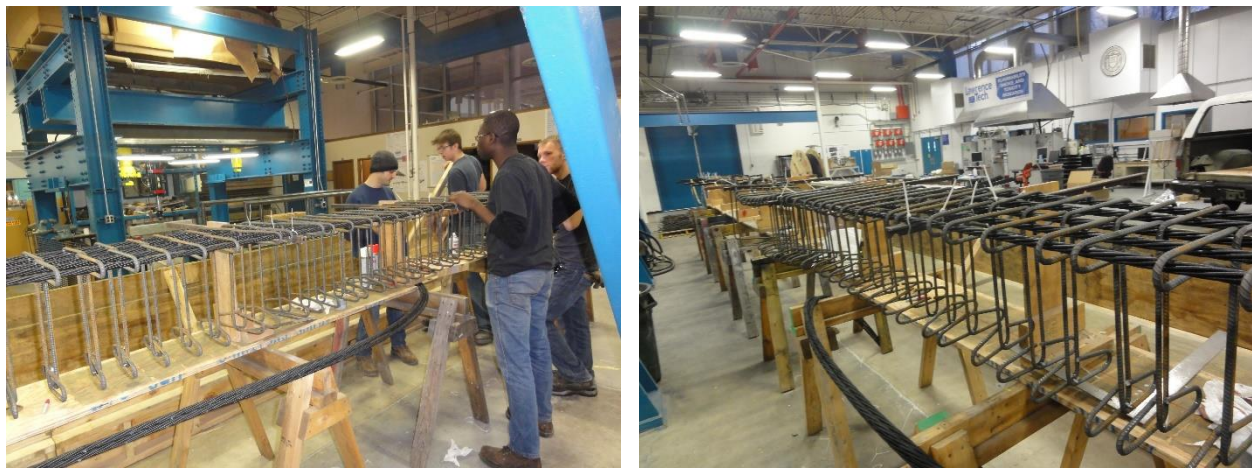


Figure 4.3-2 Assembling the reinforcement cages for decked bulb T beams

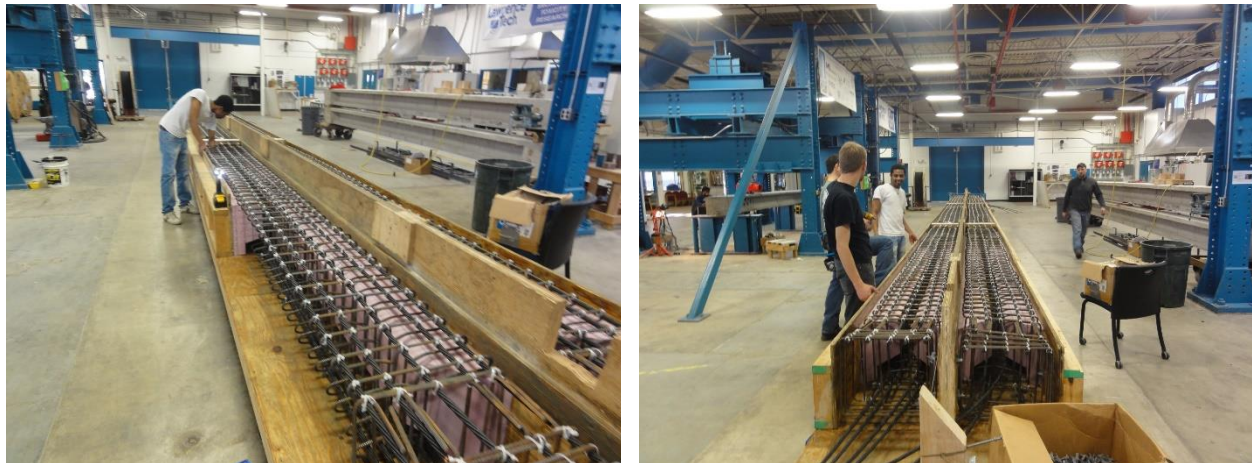


Figure 4.3-3 Placing completed reinforcement cages in formwork

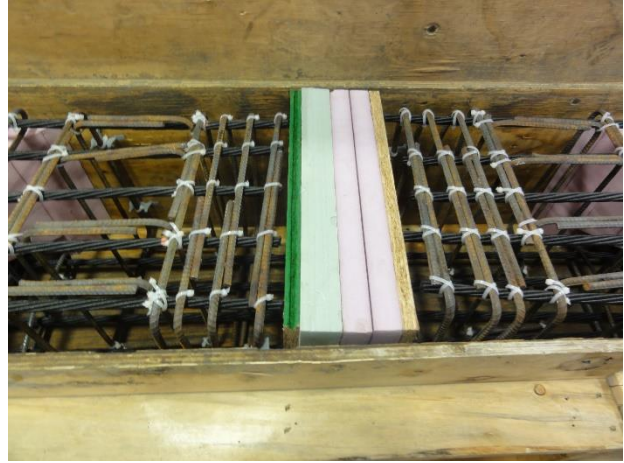


Figure 4.3-4 Completing the formwork and adding separators between beams



Figure 4.3-5 Passing prestressing CFCC strands through the reinforcement cages and connecting load cells and end couplers



Figure 4.3-6 Attaching steel anchorage and applying prestressing force with a hydraulic jack



Figure 4.3-7 Applying prestressing force using a hydraulic pump



Figure 4.3-8 Placing concrete in the formwork



Figure 4.3-9 Slump test measuring 10 in. (254 mm)



Figure 4.3-10 Preparing concrete cylinders for uni-axial compressive strength test

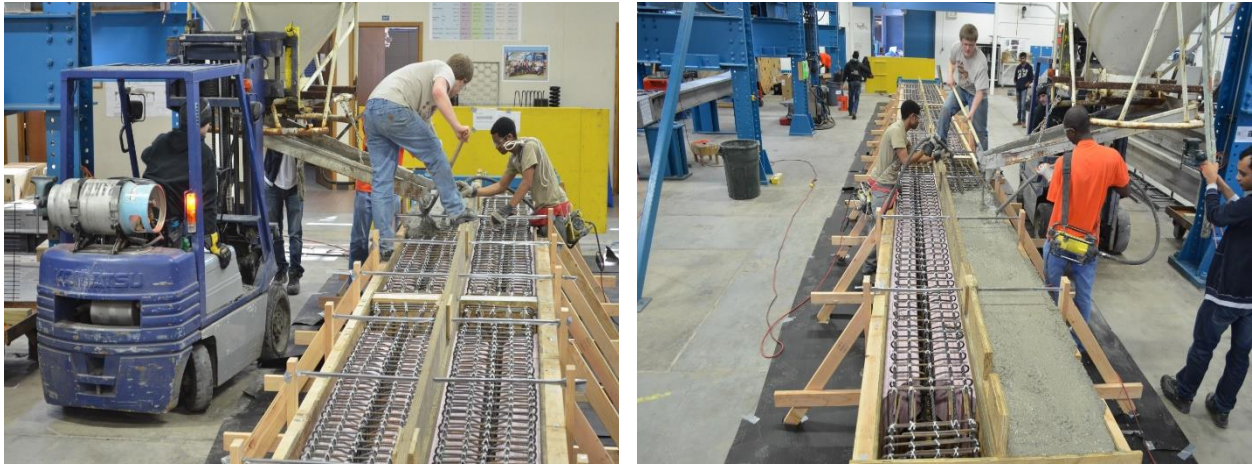


Figure 4.3-11 Compacting the concrete with electric vibrators



Figure 4.3-12 Completed decked bulb T beams ready for curing

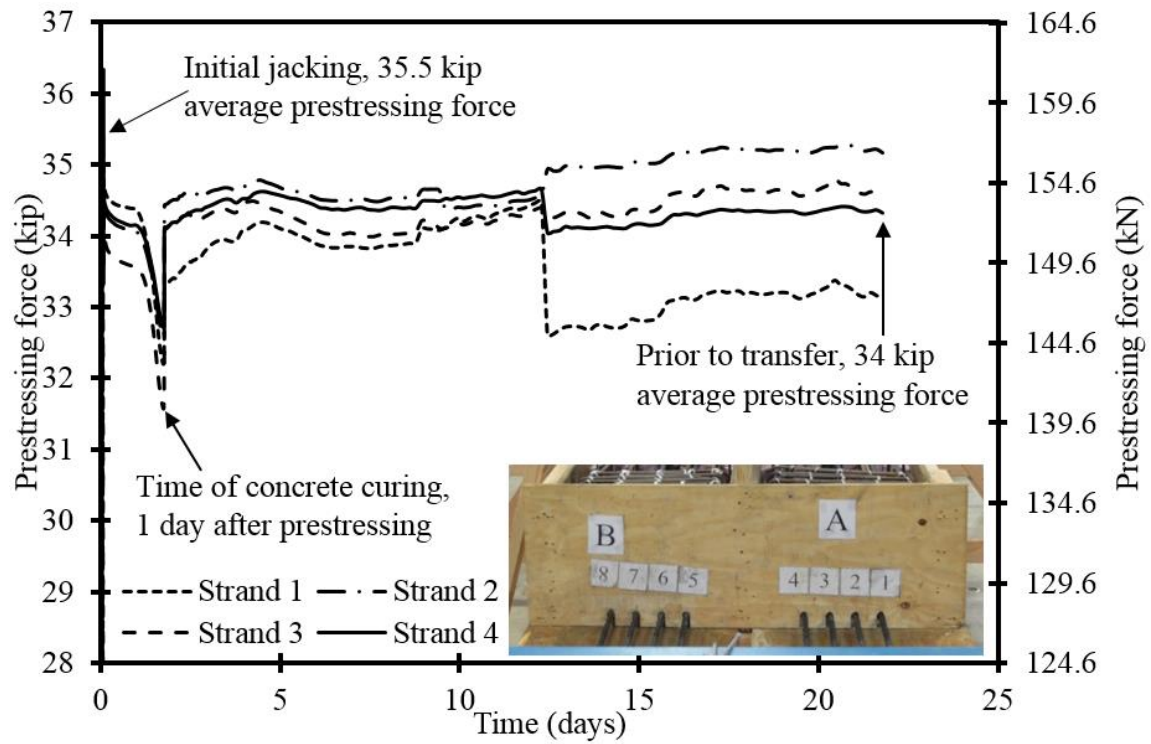


Figure 4.3-13 Prestress loss prior to transfer (Strand 1-4)

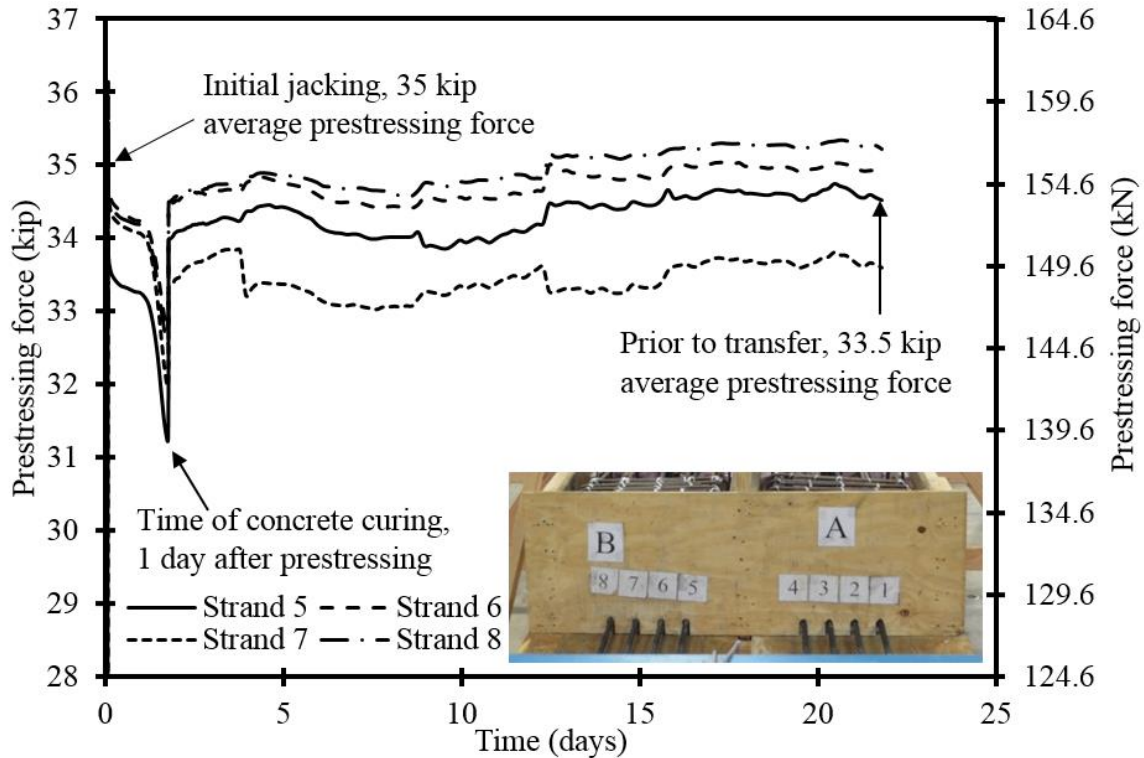


Figure 4.3-14 Prestress loss prior to transfer (Strand 5-8)

### 4.3.2 Test setup

The beams were loaded under three-point loading over an effective span of 15 ft (Figure 4.3-15). Strain gages, load cells, linear variable differential transducers (LVDTs), and linear motion transducers (LMTs) were used to capture the strain, applied load, and deformation of the beams during testing. To monitor the concrete strain, each beam was provided with two strain gages on the top surface at the mid-span section. In addition, two strain gages were provided at the bottom surface of the concrete to capture the onset and development of cracks. LVDTs were used to evaluate the strain at different depths at the mid-span section (Figure 4.3-16 and Figure 4.3-17).

The main objective of the test was to evaluate the prestressing force in the test beams and evaluate the change of that prestressing force due to the change in temperature. However, there is no feasible way of directly measuring the prestressing force in pretensioned beams. Nevertheless, the effective prestressing force can be evaluated indirectly by observing the cracking and decompression loads while loading the beam in flexure. The cracking load can be used to back calculate the effective prestressing force using the stress equation at the soffit of the beam.

However, the cracking load is dependent on the modulus of rupture of concrete and can only be spotted once. In other words, once the beam is cracked, there is no way of verifying the obtained cracking load. The decompression load provides a good alternative for calculating the effective prestressing force once the beam is cracked.

After cracking, the decompression load marks the stage where the flexural cracks start to open under the applied loads. The decompression load is the load required to counteract the effect of prestressing force and cause the stresses in the soffit of the beam to reach zero. The decompression load can be identified by attaching a strain gage next to the flexural crack and capture the reading of the strain in the soffit of the beam while loading. The strain will gradually increase with applying the load. But as the flexural crack starts to open, the strain peaks and then starts to decrease. The load at the peak of the strain is approximately equal to the decompression load.

Another method of calculating the decompression load is by observing the load-deflection curves while loading the beam. Before the load reaches the decompression load, the beam acts as an un-cracked beam and the gross section area resists the load. After the load exceeds the decompression load, the cracks start to open and the section acts as a cracked section with a reduced moment of inertia. This can be clearly observed from the slope of load-deflection curve. Before the decompression load, the curve is represented by a straight line with a steep slope, while after the decompression, the curve is also represented by a straight line but with a much flatter slope. The decompression load therefore can be precisely calculated from the load-deflection curve by estimating the load at which the curve starts to deviate from its linear un-cracked segment.

Out of six beams, two beams were tested under three-point loading setup at ambient temperature (68 °F or 20 °C) as shown in Figure 4.3-15. The test included loading the beam in cycles of loading and unloading to a load level of 60 kip (267 kN). Since the theoretical loading capacity of the beam was approximately 90 kip (400 kN), the beams were not expected to sustain any permanent damage other than the flexural cracks. Two of the remaining four beams were also tested under the same loading setup but at a temperature of 176 °F (80 °C). After concluding the load cycles at high temperature. The beams were allowed to cool down and the load cycles were repeated at ambient temperature (68 °F or 20 °C). The remaining two beams were tested under the same loading setup but at a temperature of -40 °F (-40 °C). After concluding the load cycles at this low temperature, the beams were allowed to warm back to ambient temperature, then the load

cycles were repeated. In addition, the testing scenario (load at 176 °F (80 °C) then ambient or load at -40 °F (-40 °C) then ambient) was repeated for two beams to verify the results. Consequently, it was feasible to precisely relate the change of the decompression load in each individual beam to the change in temperature.



Figure 4.3-15 A decked bulb T beam under three-point loading in the environmental chamber



Figure 4.3-16 LMTs, LVDTs, and strain gages on the soffit of the beam at mid-span



Figure 4.3-17 Strain gages on the top surface of the decked bulb T beam

### 4.3.3 Test results

The following discussion provides the main finding and observations from the test. Four beams were tested and labeled as F1, F2, H1, H2. Beams F1 and F2 were first tested at  $-40\text{ }^{\circ}\text{F}$  ( $-40\text{ }^{\circ}\text{C}$ ) then at  $68\text{ }^{\circ}\text{F}$  ( $20\text{ }^{\circ}\text{C}$ ), while Beams H1 and H2 were first tested at  $176\text{ }^{\circ}\text{F}$  ( $80\text{ }^{\circ}\text{C}$ ) then at  $68\text{ }^{\circ}\text{F}$  ( $20\text{ }^{\circ}\text{C}$ ). In addition, two more sets of test results F2-R and H2-R are obtained by repeating the testing scenario on test Beams F2 and H2, respectively. All beams were kept at the assigned temperature for at least 24 hours before conducting the flexural test. The core temperature of each beam was measured using embedded thermocouples and was verified against the air temperature. The flexural test was executed only after the beams reached the steady state with the core temperature matching the surrounding air temperature.

#### 4.3.3.1 Beam F1

The first phase of testing included loading Beam F1 under three-point loading at a freezing temperature of  $-40\text{ }^{\circ}\text{F}$  ( $-40\text{ }^{\circ}\text{C}$ ). As shown in Figure 4.3-18, the load was applied in cycles of loading and unloading with a load cycle increment of 5 kip (22 kN). The beam was checked for flexural cracks during and after each load cycle. The flexural cracks were observed at the end of the 40-kip (178-kN) load cycle, which suggested a cracking load between 35 (156 kN) and 40 kip (178 kN). The load cycles stopped at a load level of 60 kip (267 kN).

The second phase of testing included loading the beam in load cycles to 60 kip (267 kN) at ambient temperature as shown in Figure 4.3-19. Since the beam was cracked in the previous phase, no cracking load was observed. However, the decompression load was observed in each load cycle of both phases. The load-deflection curves from both test phases for each post-crack load cycle were overlapped as shown in Figure 4.3-20 for the 60-kip (267-kN) load cycle. As shown in the figure, there is a slight difference in the decompression load, but this difference is not visually estimated easily. To precisely estimate the decompression load for each case, the slope of the un-cracked segment was estimated as shown in Figure 4.3-21. Then, using the estimated slope, a straight line was drawn to overlap the un-cracked segment and extended as a linear function between the load and deflection. Finally, the deviation of the actual load-deflection curve from this straight line was calculated by subtracting the theoretical linear deflection from the measured experimental deflection.

The difference in the deflection from the theoretical linear un-cracked load-deflection curve was plotted against the load as shown in Figure 4.3-22 and the close-up view in Figure 4.3-23. As shown on the figures, when this difference is small, the experimental curve follows the linear un-cracked function, or in other words, the section acts as an un-cracked section. Nevertheless, when this difference increases, the experimental curve starts to significantly deviate from the linear un-cracked function, or in other words, the cracks start to open and the section begins to act as a cracked section. Therefore, the decompression load can be easily determined when the difference in deflection increases. As shown in Figure 4.3-24, the decompression load recorded at ambient temperature was higher than that recorded at freezing temperature, the difference tends to be constant and is estimated as 2.5 kip (11 kN).

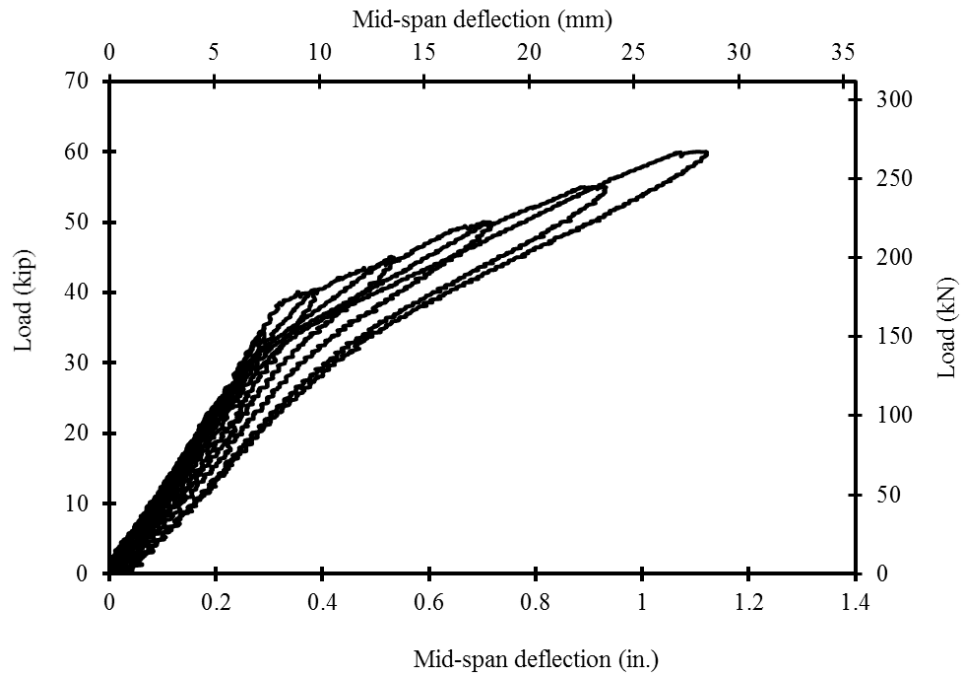


Figure 4.3-18 Load-deflection curves of Beam F1 due to loading at -40 °F (-40 °C)

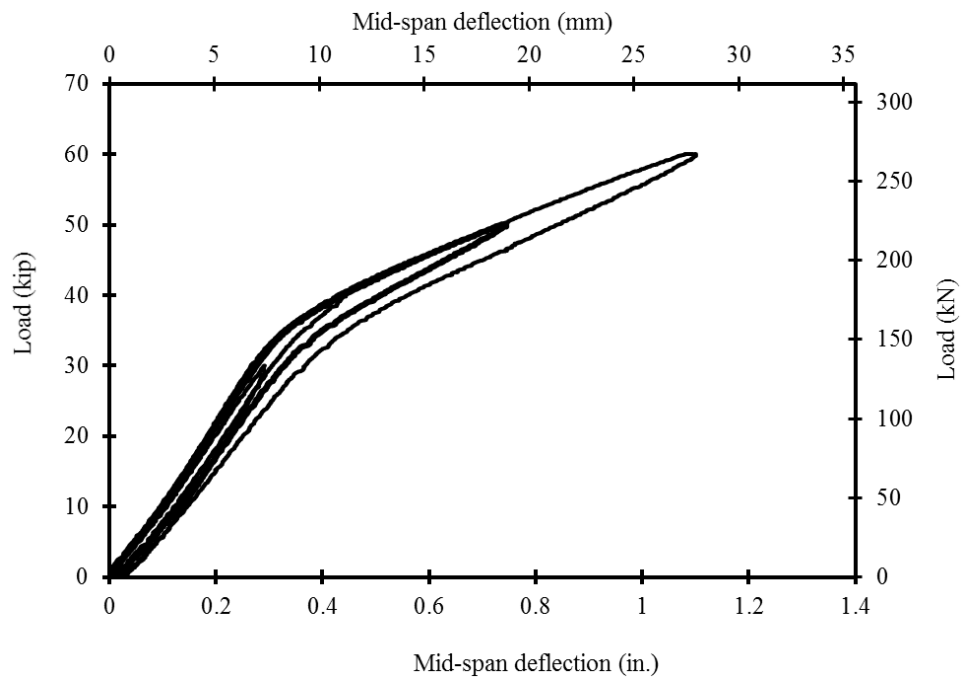


Figure 4.3-19 Load-deflection curves of Beam F1 due to re-loading at ambient temperature

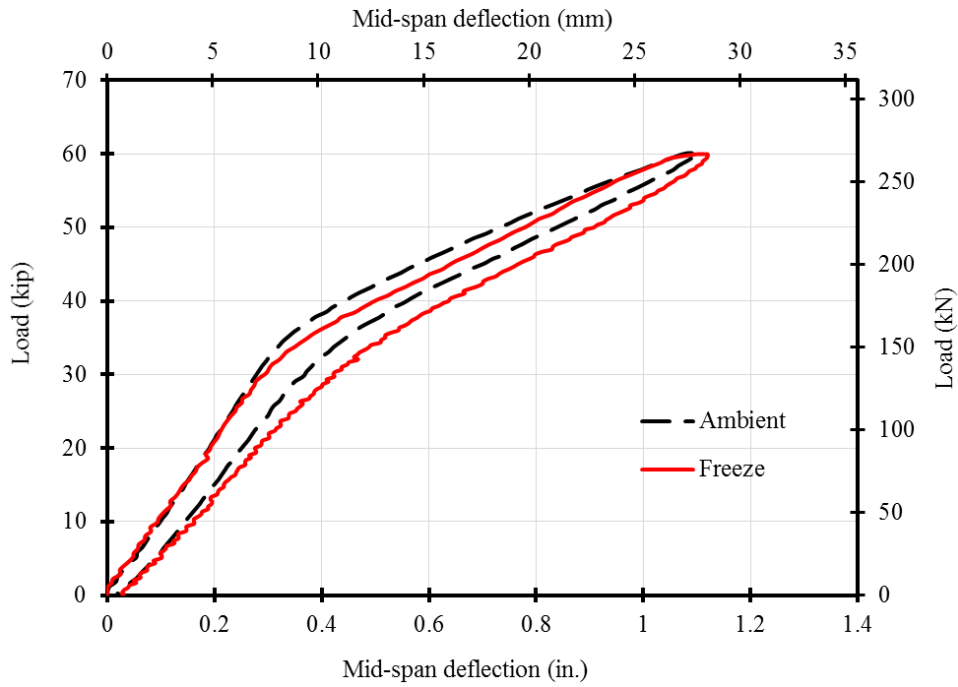


Figure 4.3-20 Load-deflection curves of Beam F1 during 60-kip (267-kN) load cycle

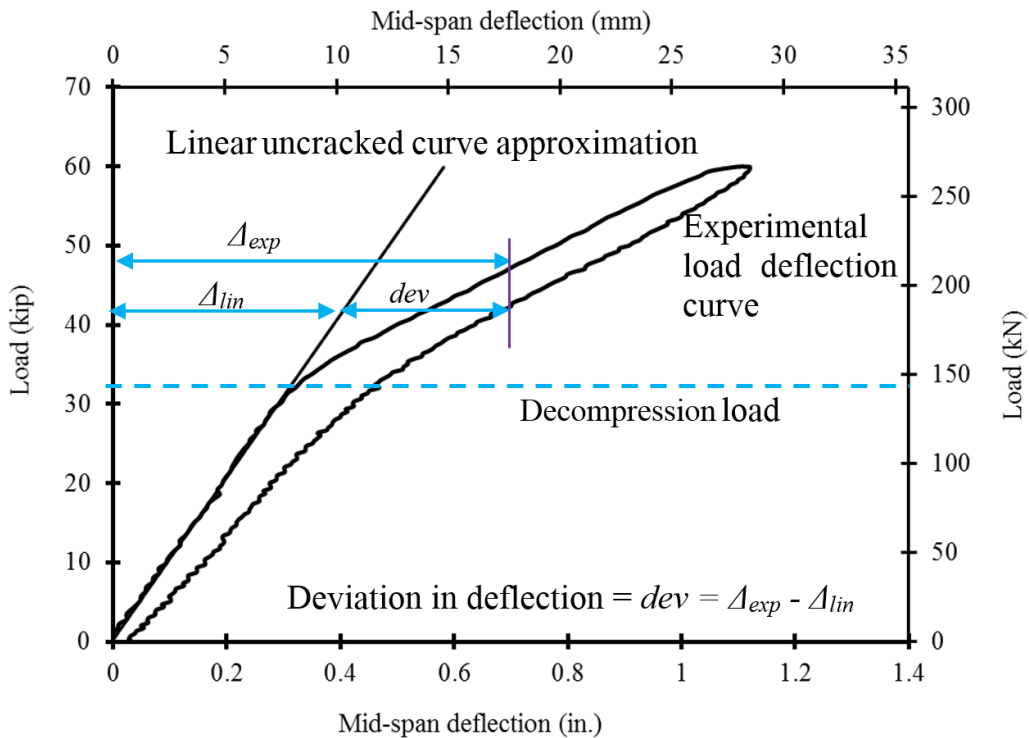


Figure 4.3-21 Calculation of the decompression load by evaluating the deviation of the load-deflection curve from the linear un-cracked curve

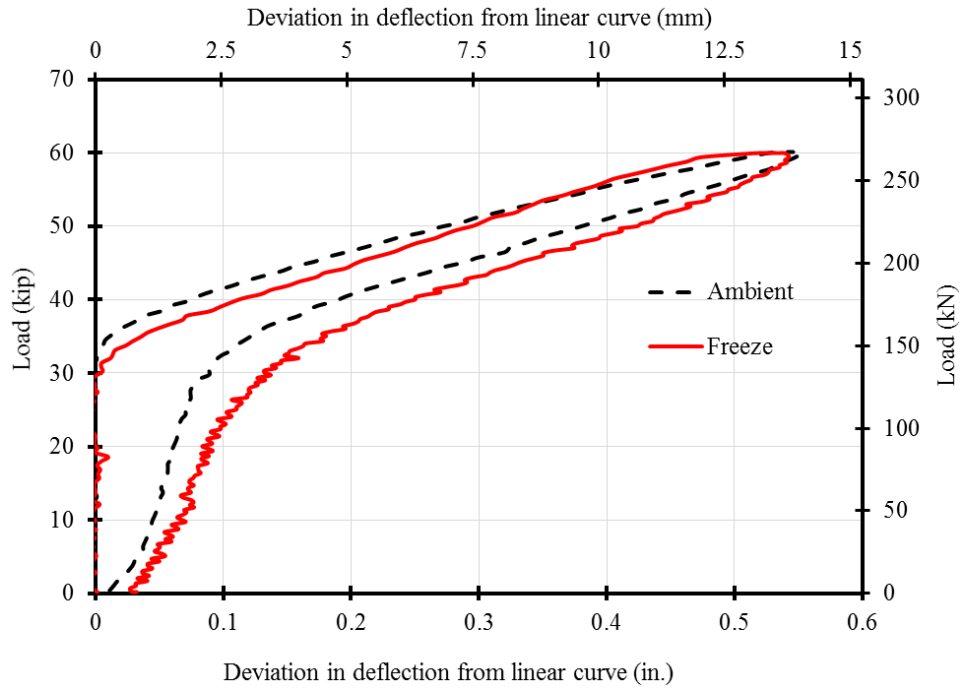


Figure 4.3-22 Deviation of load-deflection curves from the linear un-cracked curve in Beam F1 indicating the decompression loads at ambient and -40 °F (-40 °C)

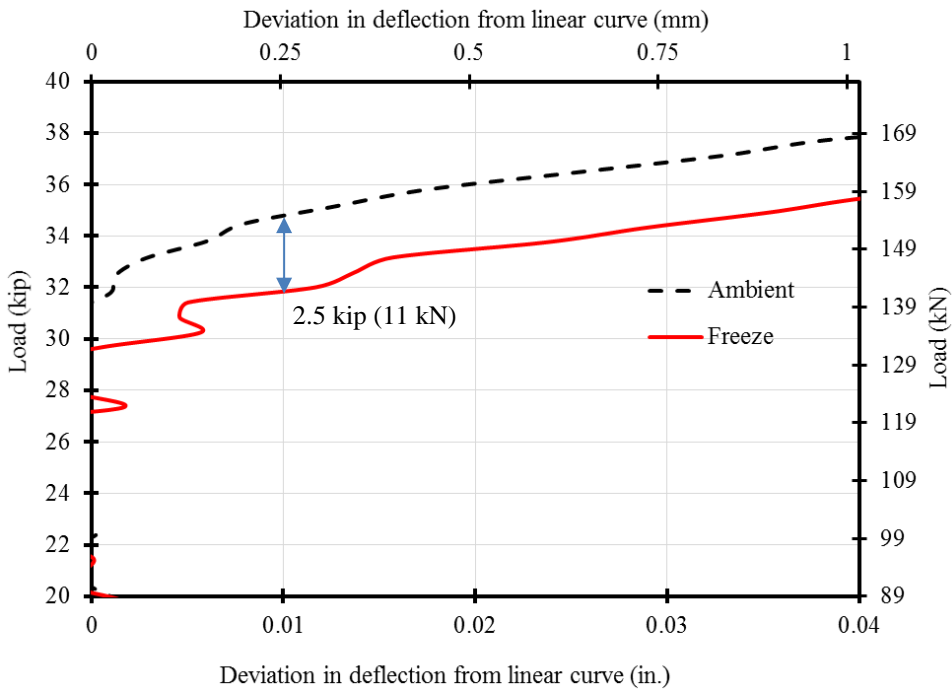


Figure 4.3-23 Close-up view showing the deviation of load-deflection curves from the linear un-cracked curves in Beam F1 and indicating the decompression loads at ambient & -40 °F (-40 °C)

#### 4.3.3.2 Beam F2

Beam F2 was identical in testing conditions to Beam F1. The test was repeated to verify the results through two test specimens. This beam was first saturated at a freezing temperature of  $-40\text{ }^{\circ}\text{F}$  ( $-40\text{ }^{\circ}\text{C}$ ) and then tested under loading and unloading cycles to determine the cracking and decompression loads. After the freezing phase ended, the beam was loaded again at ambient temperature to evaluate the decompression load and calculate the change in prestressing due to temperature change. The load-deflection curves for all load cycles at freezing at ambient conditions are presented in Figure 4.3-24 and Figure 4.3-25, respectively, while Figure 4.3-26 shows the load-deflection curves for the 60-kip (267-kN) load cycles at both freezing and ambient temperatures. As shown in the figure, there is a slight change in the decompression load. To estimate this change with good accuracy, the deviation of the experimental deflection curve from the linear un-cracked curve was calculated for both curves as shown in Figure 4.3-27 with the close-up view shown in Figure 4.3-28. The decompression load at ambient temperature was higher than that at freezing temperature with a difference of approximately 2.3 kip (10 kN).

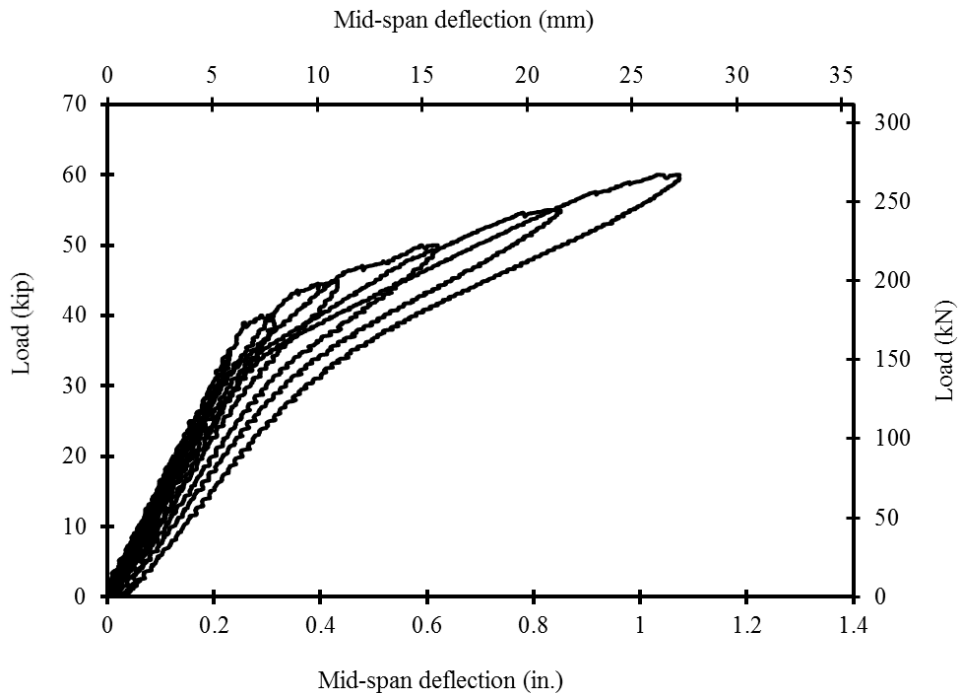


Figure 4.3-24 Load-deflection curves of Beam F2 due to loading at  $-40\text{ }^{\circ}\text{F}$  ( $-40\text{ }^{\circ}\text{C}$ )

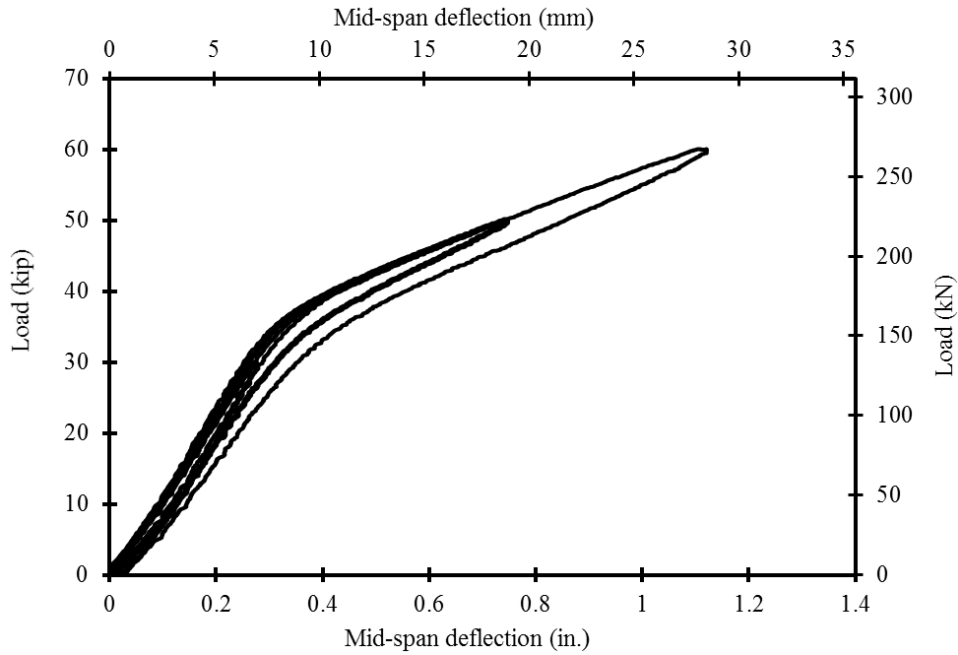


Figure 4.3-25 Load-deflection curves of Beam F2 due to loading at ambient temperature

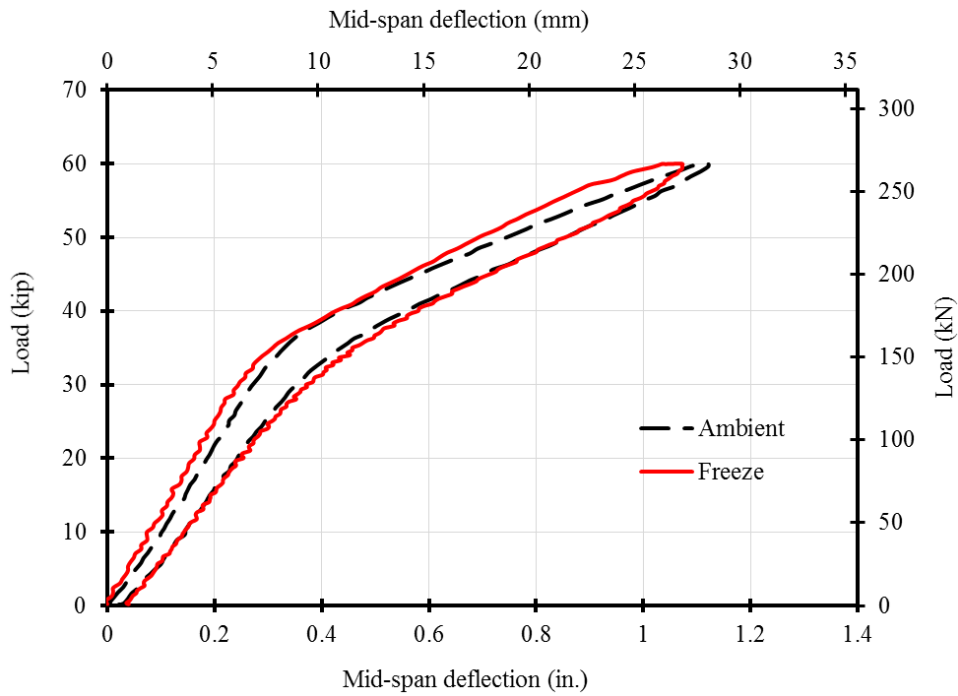


Figure 4.3-26 Load-deflection curves of Beam F2 during 60-kip (267-kN) load cycle at ambient & -40 °F (-40 °C)

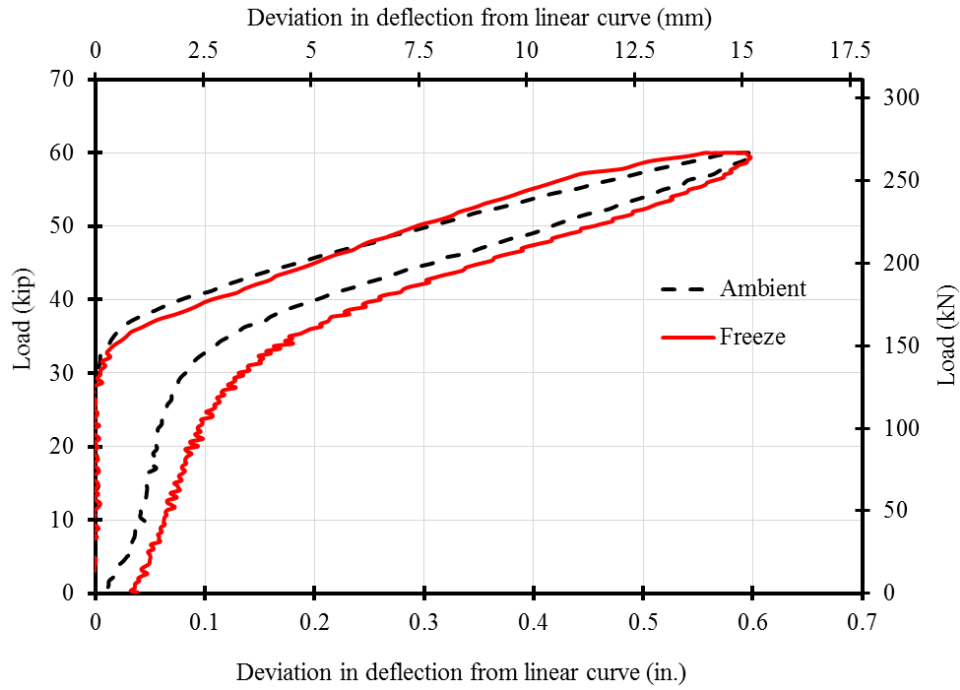


Figure 4.3-27 Deviation of load-deflection curves from the linear un-cracked curve in Beam F2 indicating the decompression loads at ambient and  $-40^{\circ}\text{F}$  ( $-40^{\circ}\text{C}$ )

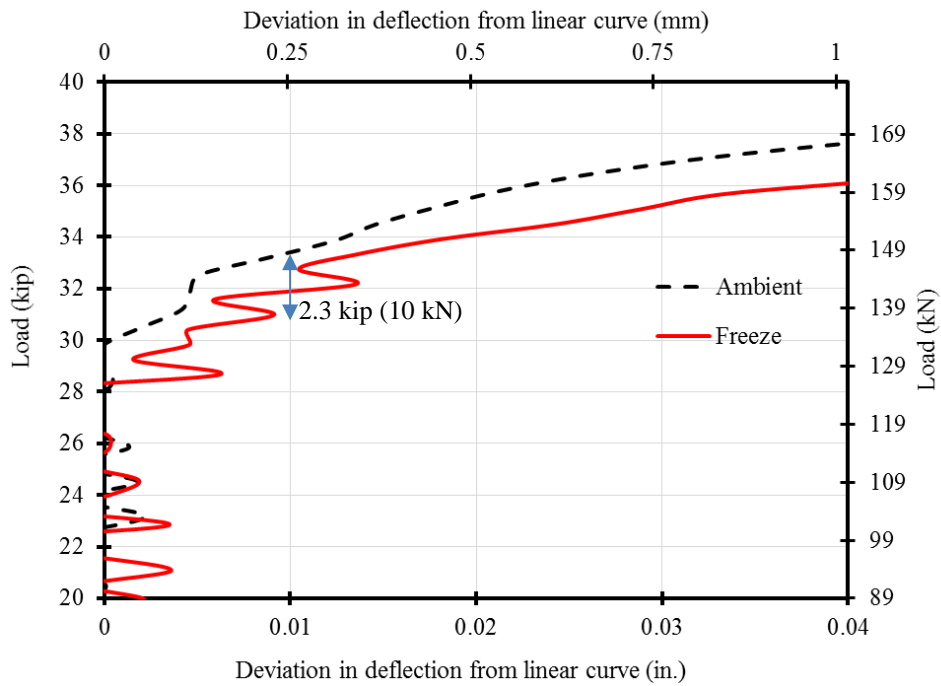


Figure 4.3-28 Close-up view showing the deviation of load-deflection curves from the linear un-cracked curves in Beam F2 and indicating the decompression loads at ambient &  $-40^{\circ}\text{F}$  ( $-40^{\circ}\text{C}$ )

#### 4.3.3.3 Beam H1

Beam H1 was tested in a similar manner to previous beams but at an elevated temperature of 176 °F (80 °C). The beam was allowed to saturate at this high temperature until the core temperature matched the surrounding air temperature. Thereafter, the beam was loaded under three-point loading in loading and unloading cycles to a maximum load of 60 kip (267 kN). The cracking load was observed from the load-deflection curves and was estimated between 35 and 40 kip (156 and 178 kN) as shown in Figure 4.3-29. After completing the load cycles, the beam was allowed to cool down until it reached the ambient temperature and the load cycles were performed again as shown in Figure 4.3-30. The load-deflection curves from the first set of load cycles were compared to those from the second set as shown in Figure 4.3-31 for the 60-kip (267-kN) load cycle. Similar to Beams F1 and F2, the difference in the decompression load between the heating and ambient load cycles was estimated by calculating the deviation of the load-deflection curve from the linear un-cracked curve as shown in Figure 4.3-32 and the close-up view in Figure 4.3-33. As shown in the figure, the decompression load observed while heating the beam was higher than that observed at ambient temperature with a difference of approximately 2.9 kip (13 kN). In other words, the increase in temperature results in an increase in the effective prestressing force.

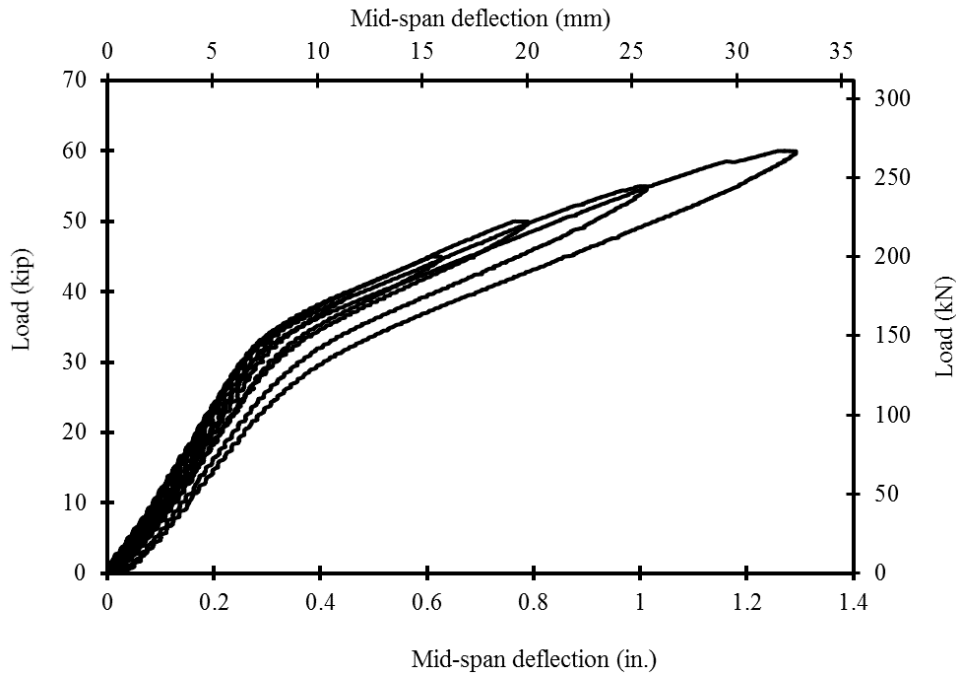


Figure 4.3-29 Load-deflection curves of Beam H1 due to loading at 176 °F (80 °C)

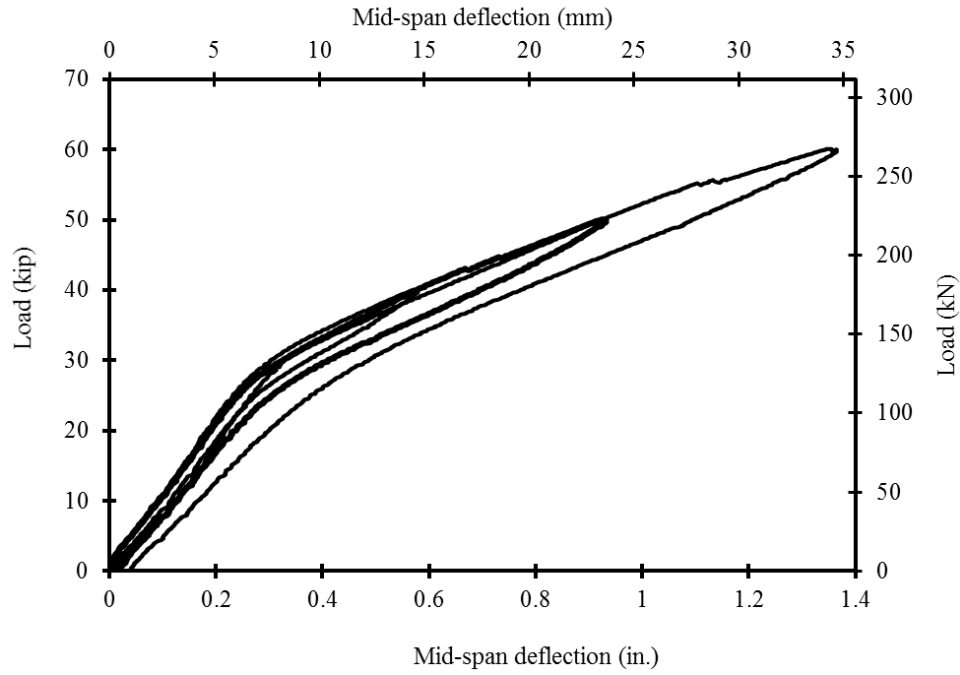


Figure 4.3-30 Load-deflection curves of Beam H1 due to loading at ambient temperature

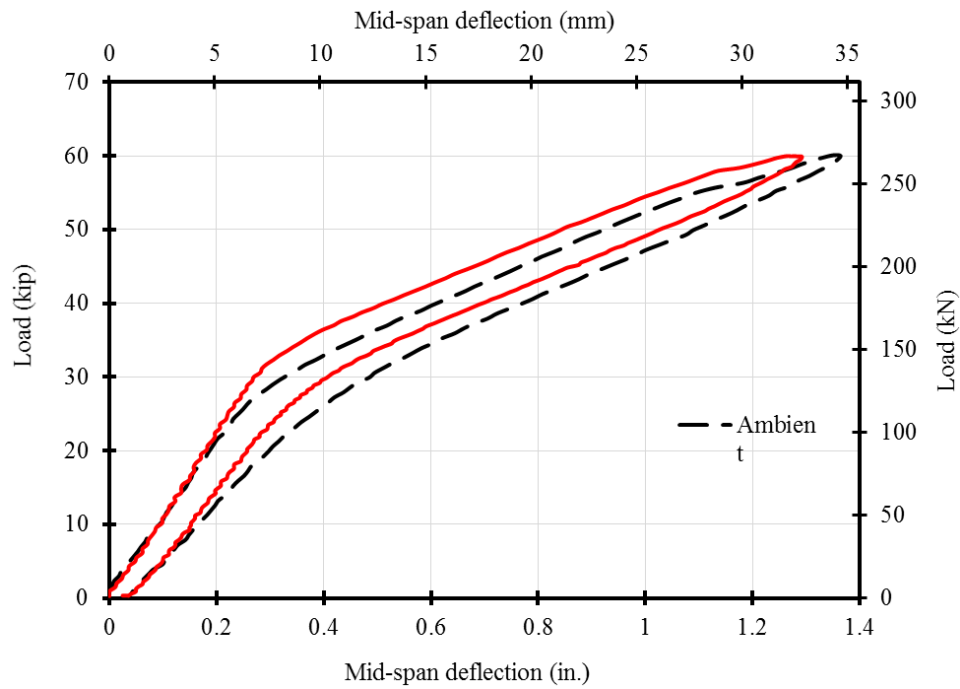


Figure 4.3-31 Load-deflection curves of Beam H1 during 60-kip (267-kN) load cycle at ambient and 176 °F (80 °C)

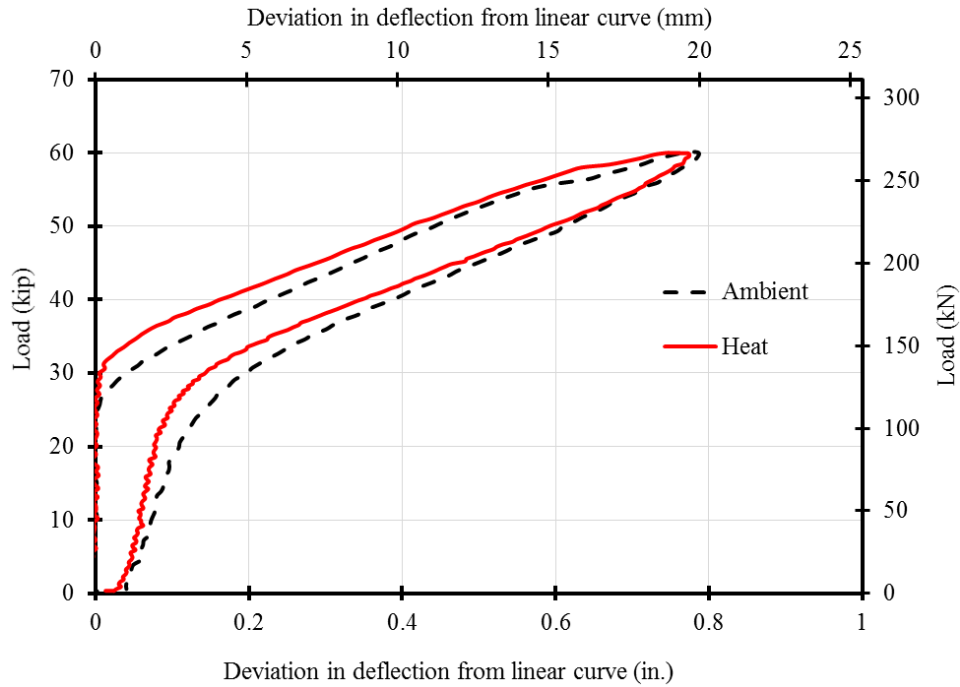


Figure 4.3-32 Deviation of load-deflection curves from the linear un-cracked curve in Beam H1 indicating the decompression loads at ambient and 176 °F

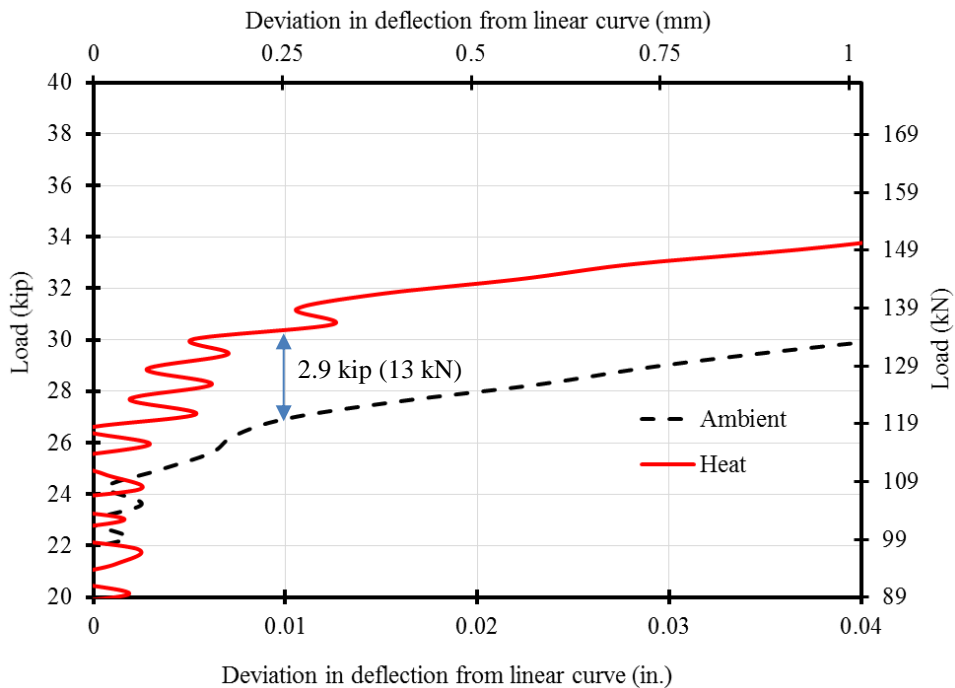


Figure 4.3-33 Close-up view showing the deviation of load-deflection curves from the linear un-cracked curves in Beam H1 and indicating the decompression loads at ambient & 176 °F (80 °C)

#### 4.3.3.4 Beam H2

Beam H2 was similar to Beam H1 in loading scenario and the load cycles at elevated and ambient temperatures are shown in Figure 4.3-34 and Figure 4.3-35, while the analysis for the decompression loads at both elevated and ambient temperatures are shown in Figure 4.3-36 through Figure 4.3-38. The figures confirm the findings from Beam H1 and showed a decompression load at elevated temperature approximately 3.9 kip (17 kN) higher than that at ambient temperature.

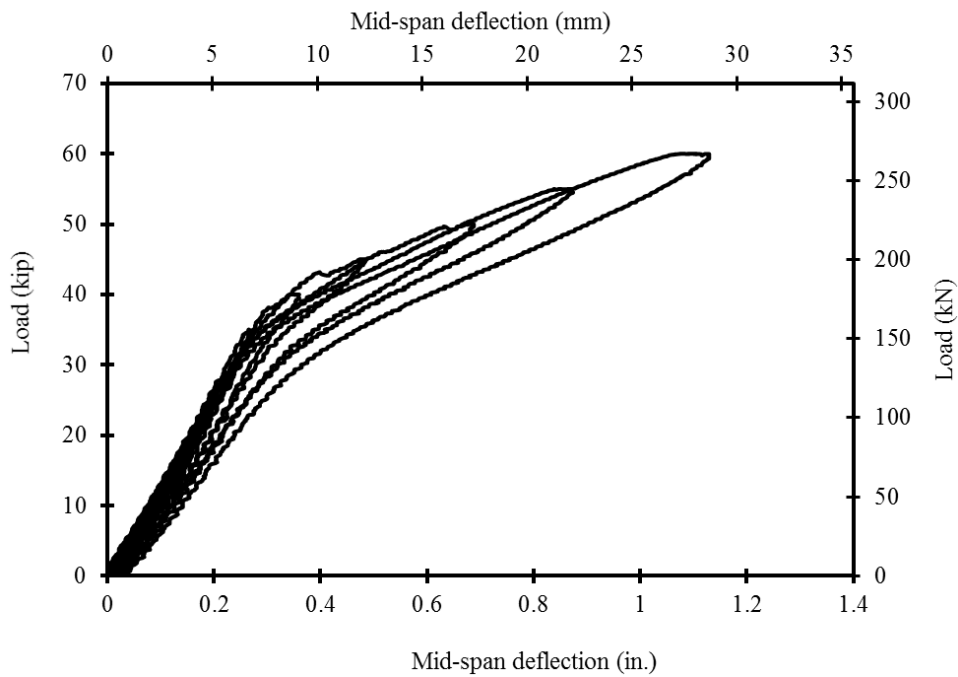


Figure 4.3-34 Load-deflection curves of Beam H2 due to loading at 176 °F (80 °C)

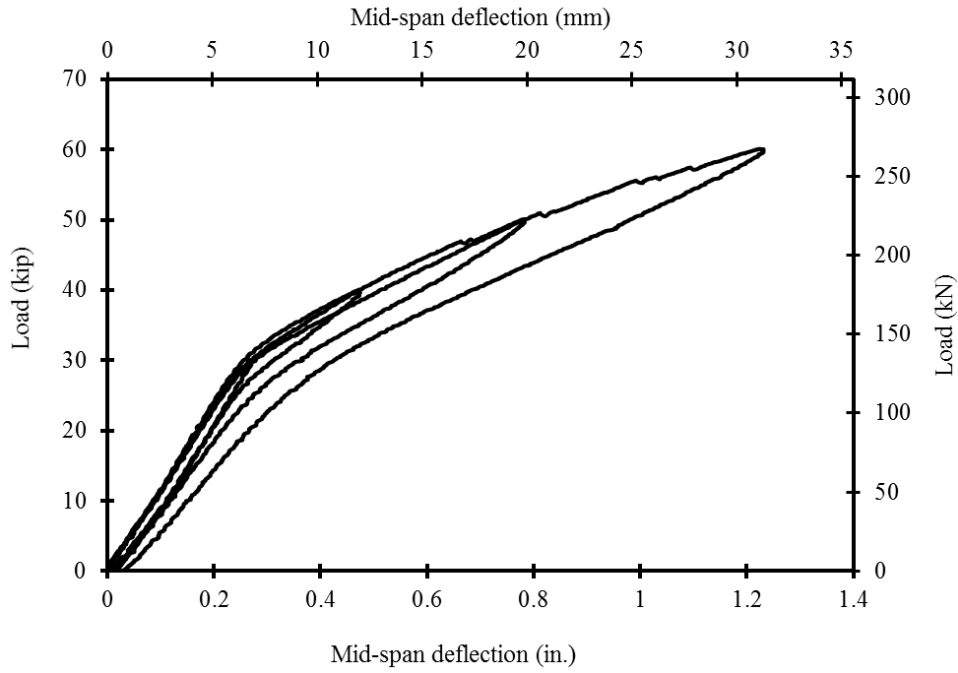


Figure 4.3-35 Load-deflection curves of Beam H2 due to loading at ambient temperature

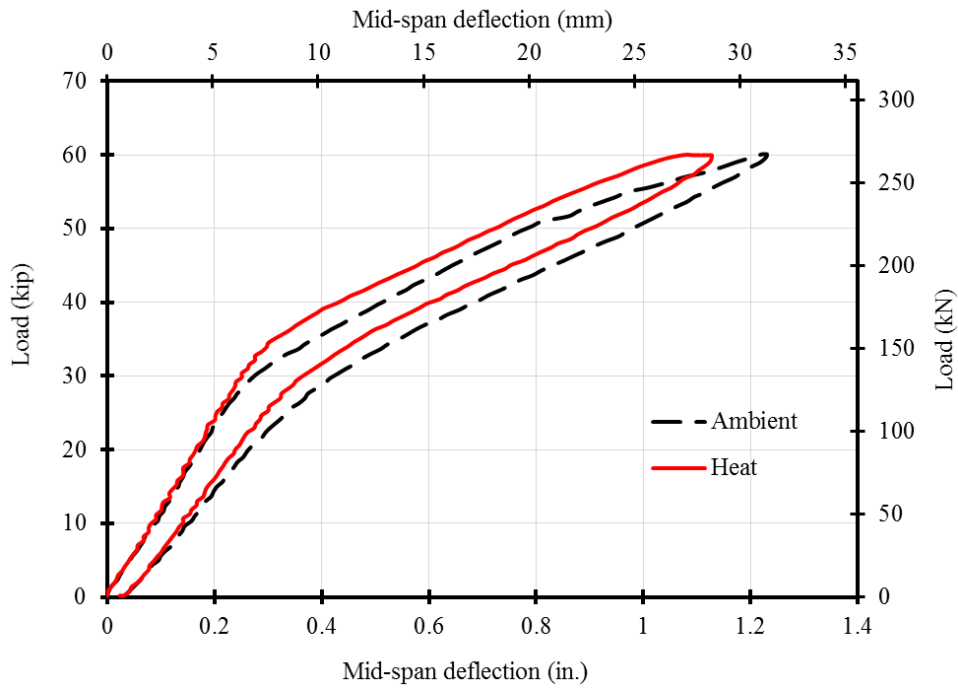


Figure 4.3-36 Load-deflection curves of Beam H2 during 60-kip (267-kN) load cycle at ambient and 176 °F (80 °C)

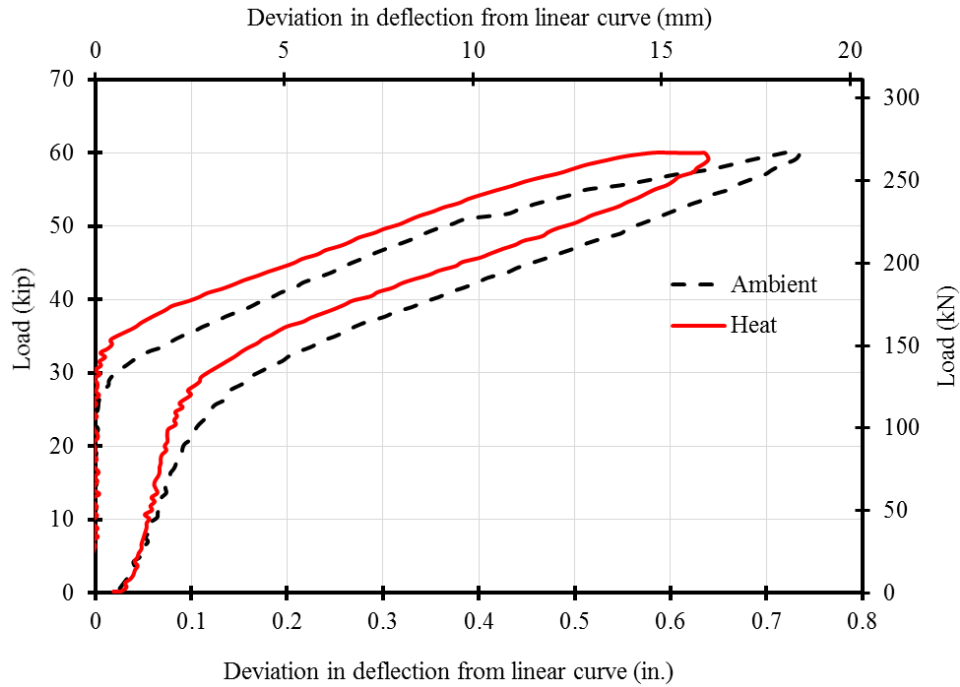


Figure 4.3-37 Deviation of load-deflection curves from the linear un-cracked curve in Beam H2 indicating the decompression loads at ambient and 176 °F (80 °C)

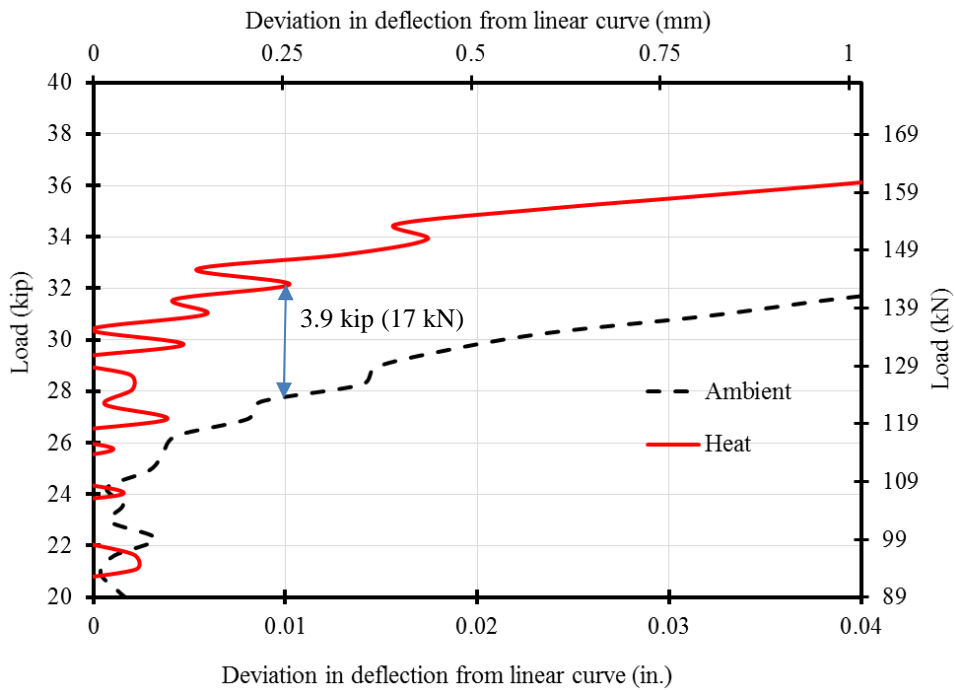


Figure 4.3-38 Close-up view showing the deviation of load-deflection curves from the linear un-cracked curves in Beam H2 and indicating the decompression loads at ambient & 176 °F (80 °C)

#### 4.3.3.5 Beam F2-R

The first phase of testing included loading Beam F2 in load cycles at ambient temperature. In second phase the beam was first saturated at a freezing temperature of  $-40\text{ }^{\circ}\text{F}$  ( $-40\text{ }^{\circ}\text{C}$ ) and then tested under the same loading and unloading pattern. Figure 4.3-39 shows the load-deflection curves for the 60-kip load cycles at both freezing and ambient temperatures. To estimate the difference in decompression load, the deviation of the experimental deflection curve from the linear un-cracked curve was calculated for both curves as shown in Figure 4.3-40 with the close-up view shown in Figure 4.3-41. Similar to beam F2, the decompression load at ambient temperature was higher than that at freezing temperature with a difference of approximately 2.1 kip (9 kN).

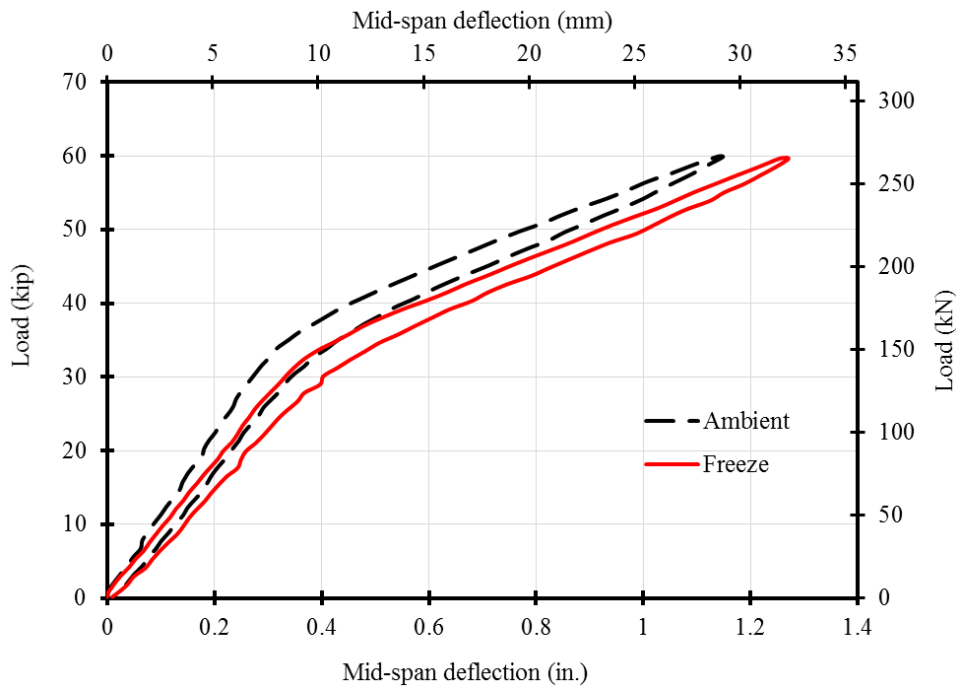


Figure 4.3-39 Load-deflection curves of Beam F2-R during 60-kip (267-kN) load cycle at ambient and  $-40\text{ }^{\circ}\text{F}$  ( $-40\text{ }^{\circ}\text{C}$ )

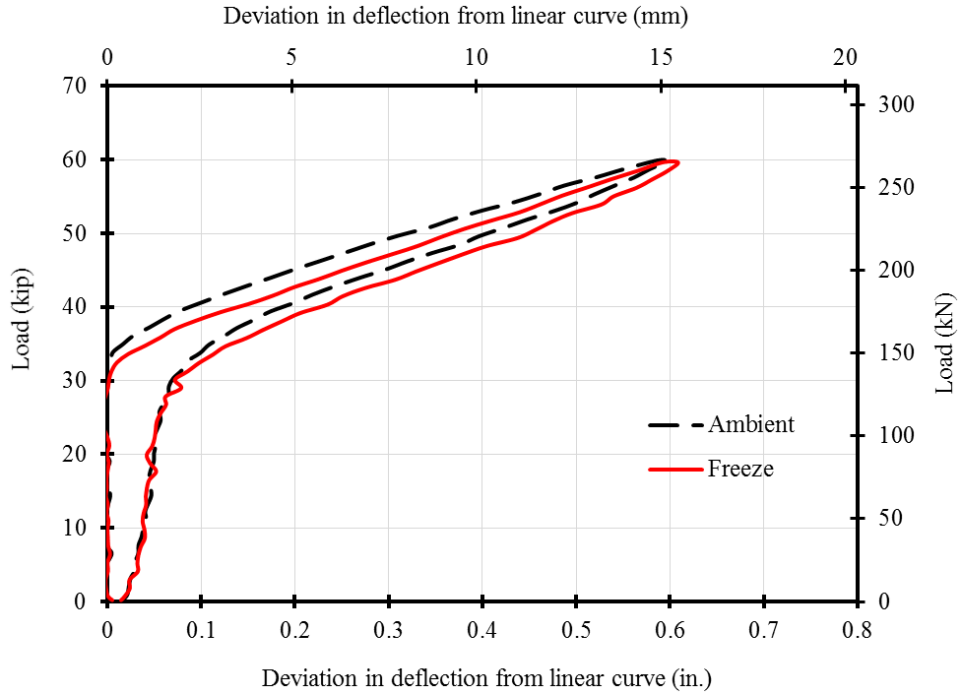


Figure 4.3-40 Deviation of load-deflection curves from the linear un-cracked curve in Beam F2-R indicating the decompression loads at ambient and -40 °F (-40 °C)

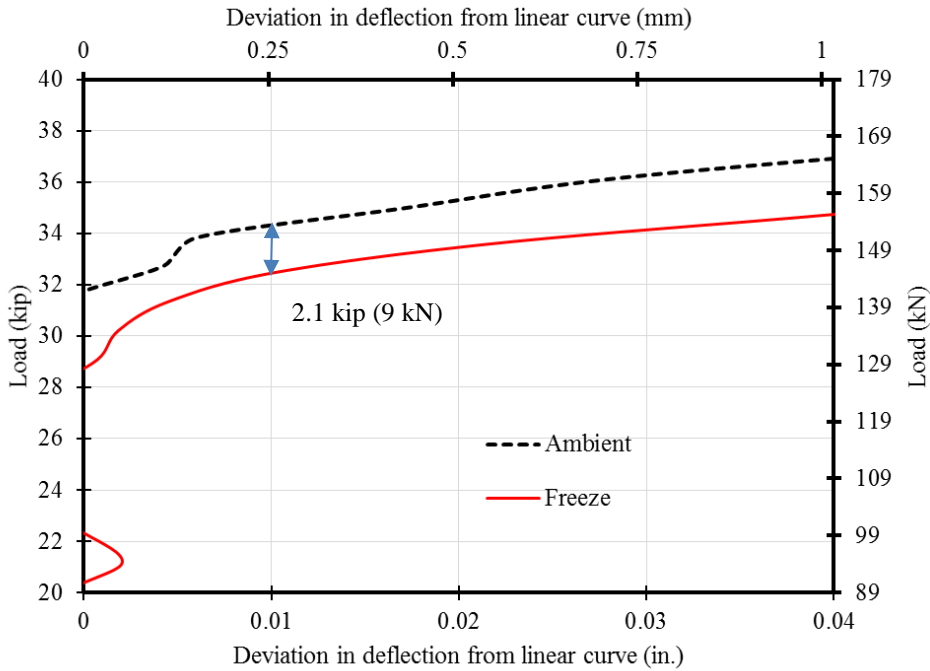


Figure 4.3-41 Close-up view showing the deviation of load-deflection curves from the linear un-cracked curves in Beam F2-R indicating the decompression loads at ambient & -40 °F (-40 °C)

#### 4.3.3.6 Beam H2-R

Beam H2-R was tested in the similar manner to beam F2-R but at an elevated temperature of 176 °F (80 °C). The first phase of testing was performed at ambient temperature followed by second phase of testing at an elevated temperature of 176 °F (80 °C). The analysis for decompression loads at both elevated and ambient temperatures are shown in Figure 4.3-42 through Figure 4.3-44 . The decompression load at elevated temperature was found to be approximately 2.3 kip (10 kN) higher than that at ambient temperature.

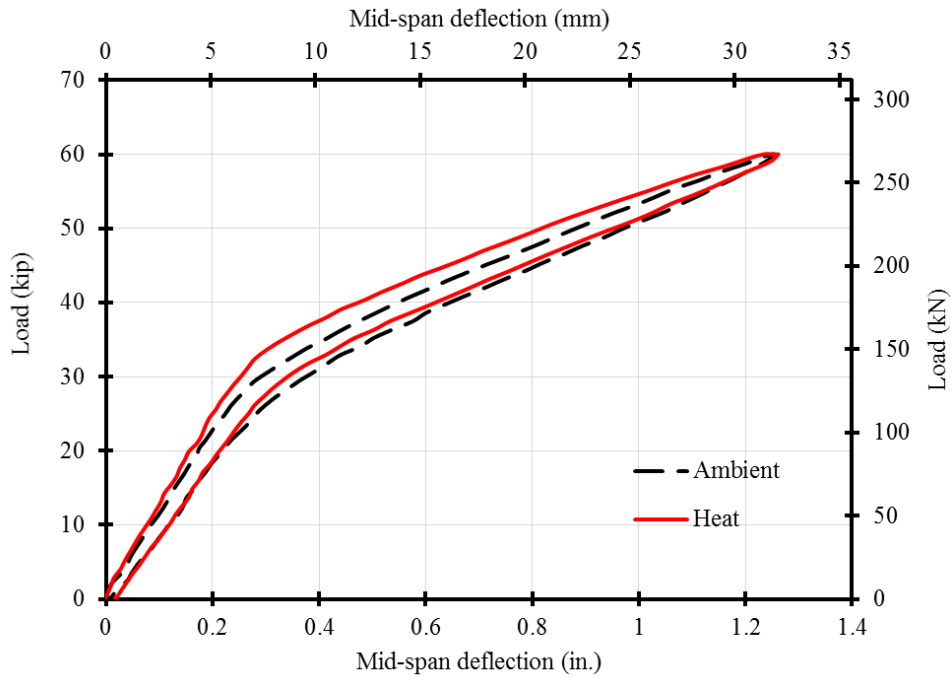


Figure 4.3-42 Load-deflection curves of Beam H2-R during 60-kip (267-kN) load cycle at ambient and 176 °F (80 °C)

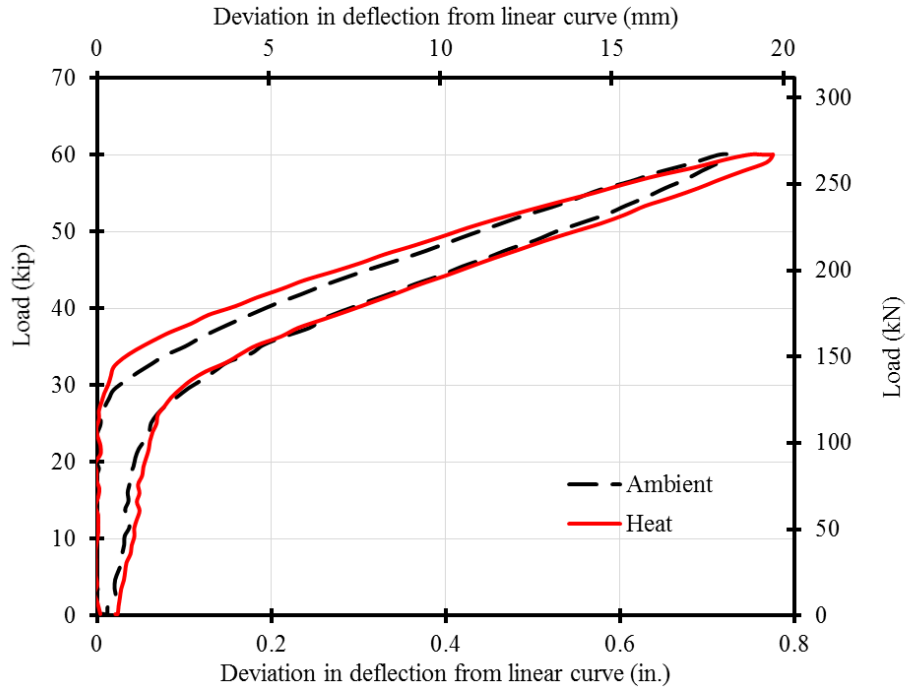


Figure 4.3-43 Deviation of load-deflection curves from the linear un-cracked curve in Beam H2-R indicating the decompression loads at ambient and 176 °F (80 °C)

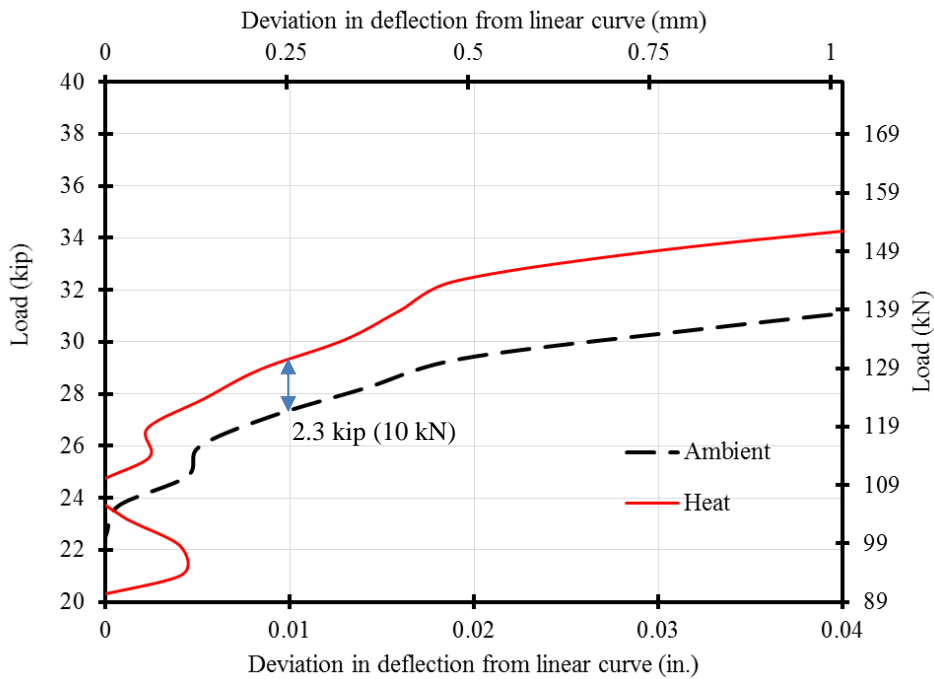


Figure 4.3-44 Close-up view showing the deviation of load-deflection curves from the linear un-cracked curves in Beam H2-R indicating the decompression loads at ambient & 176 °F (80 °C)

#### 4.3.3.7 Discussion

At the stage of decompression, the stress at the soffit of the beam at mid-span section ( $\sigma_{bot}$ ) is equal to zero. Therefore, the stress equation at the beam soffit can be written as:

$$\sigma_{bot} = -\frac{P_e}{A} - \frac{P_e \cdot e}{S_{bot}} + \frac{M_{DL}}{S_{bot}} + \frac{M_{decomp}}{S_{bot}} = 0 \text{ ksi or MPa} \quad (4.3-1)$$

where:

$P_e$	=	Effective prestressing force (kip or kN)
$M_{DL}$	=	Moment due to dead load = 44.35 kip.in. (5.0 kN.m)
$M_{decomp}$	=	Moment due to the decompression load = $\frac{P_{decomp} \cdot L}{4}$ (kip.in. or kN.m)
$P_{decomp}$	=	Decompression load (kip or kN)
$L$	=	Effective span of the beam = 15 ft (4.57 m)
$A$	=	Cross sectional area of the beam = 126.5 in. <sup>2</sup> (81,612 mm <sup>2</sup> )
$S_{bot}$	=	Section modulus = 468.8 in. <sup>3</sup> (7,682,255 mm <sup>3</sup> )
$e$	=	Eccentricity of prestressing, = 7.04 in. (179 mm)

By substituting the aforementioned values, the equation of the stress can be rearranged to represent a direct relationship between the effective prestressing force and the decompression load as follows:

$$0 = -P_e \left( \frac{1}{A} + \frac{e}{S_{bot}} \right) + \frac{M_{DL}}{S_{bot}} + \frac{P_{decomp} \cdot L/4}{S_{bot}} \quad (4.3-2)$$

$$P_e = \frac{\frac{M_{DL}}{S_{bot}} + \frac{P_{decomp} \cdot L/4}{S_{bot}}}{\left( \frac{1}{A} + \frac{e}{S_{bot}} \right)} = \frac{44.35 + 45 P_{decomp}}{11.11} = 4 + 4.05 P_{decomp} \quad (4.3-3)$$

The change in the effective prestressing force ( $\Delta P_e$ ) can also be directly related to the change in decompression load ( $\Delta P_{decomp}$ ) as:

$$\Delta P_e = 4.05 \Delta P_{decomp} \quad (4.3-4)$$

With the increase or decrease in temperature, it is expected that the effective prestressing force will increase or decrease accordingly due to the difference in thermal expansion between concrete and CFCC. For instance, assuming the difference in coefficient of thermal expansion between concrete and CFCC is  $6 \times 10^{-6} / ^\circ\text{F}$  ( $12 \times 10^{-6} / ^\circ\text{C}$ ), the increase in temperature from 68 to 176 °F (20 to 80 °C) or the decrease in temperature from 68 to -40 °F (20 to -40 °C) (that is an increase or decrease of 108 °F or 60 °C), would yield a strain increase or decrease of 0.000648. As the total area of prestressing ( $a_{frp}$ ) is 0.719 in.<sup>2</sup> (463 mm<sup>2</sup>) and approximate elastic modulus of CFCC ( $E_{frp}$ ) is 22,480 ksi (155 GPa), this increase or decrease in strain shall yield an increase or decrease in the effective prestressing force of approximately 10.43 kip (46 kN)/beam, or an increase/decrease in the decompression load by approximately 2.57 kip (11 kN).

By comparing this theoretical value with the experimentally obtained differences in the decompression loads in Beams F1, F2, H1, H2, F2-R and H2-R it can be concluded that there is reasonable agreement between the experimental and theoretical values and the gain or loss in the prestressing force due to seasonal temperature change can be accurately predicted by estimating the normal temperature range and calculating the prestressing gain/loss due to the temperature change.

#### 4.4 Discussion of Test Results

Temperature change seems to be a key element in the design of beams prestressed with CFRP strands. CFCC strands showed a slight decrease in the elastic modulus that was corresponding to a decrease in the prestressing force with the increase in temperature. The second-time heating did not result in any significant loss of the prestressing force or the elastic modulus. Besides, after CFCC strands were allowed to cool down and tested to failure at ambient temperature, their attained average tensile strength and average elastic modulus were matching, or even slightly exceeding, those of unheated specimens. Therefore, it can be concluded that the increase in temperature to 400 °F (204 °C) did not cause any permanent damage in the CFCC strands.

Based on the results from the experimental investigation of decked bulb T beams exposed to temperature change, it appears that beams prestressed with CFCC strands experience a loss in the

prestressing force with the decrease in temperature. However, this loss in prestressing is recovered when the temperature increases back to the normal range. Similarly, beams prestressed with CFCC strands experience gain in the effective prestressing force when the temperature increases but this gain in prestressing is lost once the temperature drops down to the normal range. The gain or loss in effective prestressing force conforms with a reasonable degree of accuracy to the theoretical calculations. In addition, beams subjected to multiple cycles of heating and cooling tend to experience loss and gain in prestressing force without any signs of slippage or delamination of CFCC strands.

## CHAPTER 5: FREEZE-THAW EFFECT

### 5.1 Introduction

Recent published data (NIST 2014) indicated that approximately 102 freezing and thawing cycles occur annually in Michigan. The freeze-thaw cycles have their documented detrimental effect on roads and bridges, but little is known about the effect of freeze-thaw cycles on highway bridge beams prestressed with CFRP materials. Earlier research studies showed conflicting results. For instance, on study on FRP material showed that extreme low temperatures can cause micro cracking in the fiber matrix and high residual stress due to discrepancies in coefficients of thermal expansion of the constituent elements (Dutta 1988). However, Karbhari and Pope (1994) showed that FRP strength increases due to hardening at low temperature. On the other hand, Cusson and Xi (2002) reported 10 % reduction in the tensile strength of CFRP bars after exposure to 250 freeze-thaw cycles for 750 hrs.

The performance of CFRP-concrete bond at low temperatures has been the subject of several experimental studies (Green et al. 1997 & 2000; El badry et al. 2000; Subramaniam et al. 2008; Kim et al. 2011). Some researchers reported increased bond strength between CFRP and concrete under certain conditions. Whereas, others highlighted the detrimental effect of freeze thaw cycle on CFRP-concrete bond strength. Part of the dilemma is that concrete itself loses strength with the exposure to extreme temperatures (Shoukry et al. 2011).

Fewer researchers focused on FRP behavior in prestressed members at different temperature conditions. Bryan and Green (1996) studied the short-term behavior of concrete beams prestressed with 8 mm diameter Leadline CFRP tendons at low temperature. Based on the results, the flexural behavior of the beams was unaffected by short-term exposure to low temperature. In addition, the ultimate stresses and strains in CFRP tendons exceeded those reported by the manufacturer. Sayed-Ahmed and Shrive (1998) investigated the thermal variation effect on post-tensioned CFRP prestressing tendons. In their experimental study, thermal and flexural tests were carried out on masonry diaphragm walls prestressed concentrically with CFRP Leadline tendons. It was reported that the level of prestressing force in the Leadline tendons increased with the rise in temperature and decreased with the decrease in temperature. El-Hacha et al. (2004) studied the behavior of precracked concrete beams strengthened with prestressed CFRP sheets at low temperature. It was

concluded that the decrease in temperature did not adversely affect the flexural behavior of beams strengthened with prestressed CFRP sheets. Saiedi et al. (2013) studied the behavior of concrete beams prestressed with CFRP Leadline rods under sustained load and low temperature environments. Results showed that the bond between CFRP rods and concrete was affected negatively by such exposure causing reduction in the strength of prestressed beams.

Many existing design codes and guidelines in USA, Canada and Japan have been developed to account for potential deterioration of CFRP material caused by environmental and long-term effects (Ceroni et al. 2006). This is achieved by multiplying the guaranteed strength of the CFRP material by an environmental reduction factor less than 1.0. However, it should be noted that an unjustified reduction of material strength often leads to multiple design issues and results in congested sections with potential for further construction and service concerns. Therefore, the experimental program outlined in this chapter was conducted to evaluate the effect of freeze-thaw exposure on unbonded prestressed CFRP strands and CFRP prestressed concrete beams.

Two sets of CFRP specimens were prepared and subjected to successive 300 cycles of freezing and thawing induced in a large-scale environmental chamber. The first set included the four decked bulb T beams F1, F2, H1, and H2, that were tested before to the post-cracking stage and presented in the last chapter. The other set included five new CFCC strands stressed to 50.1 kip (223 kN) representing 82.5 % of the guaranteed tensile capacity (60.7 kip or 270 kN). The freeze-thaw test was conducted in accordance with ASTM C666/C 666M-03: “Standard Test Method for Resistance of Concrete to Rapid Freezing and Thawing”. After completing the freeze-thaw test, the CFRP prestressed concrete beams were tested to failure under three-point-load test setup, whereas the post-tensioned CFCC specimens were tested through uniaxial tensile test to determine the impact of successive freeze-thaw cycles on the residual strength of the prestressed CFCC strands. The following sections describe the specimen’s preparation, instrumentation, testing program and main finding and results of freeze-thaw test, flexural test of decked bulb T beams, and uniaxial test of CFCC strands.

## 5.2 Decked Bulb T Beams

### 5.2.1 Test setup

A special tempering tank was constructed inside the environmental chamber to accommodate the four decked bulb beams so that the temperature along the beam surfaces is constant at each phase of the test. The tempering tank had a length of 17 ft (5.2 m), a width of 48 in. (1.22 m), and a depth of 35 in. (889 mm) and was placed on a wooden platform deck mounted on steel adjustable chairs spaced at 2 ft (610 mm) on center with a height of 10 in. (254 mm). The tank was designed with two access holes at the sides for installing conduits in order to transfer water from the storage reservoir in the thawing phase of the freeze-thaw test. After constructing the tempering tank, the four decked bulb T beams were instrumented with two thermocouples at the center of the bottom flange and were placed inside the tank. Meanwhile, four concrete cylinders of the same batch of concrete used to cast the beams were prepared, labelled and placed inside the tank to evaluate the effect of freeze-thaw cycles on the concrete compressive strength. Air ducts were arranged inside the chamber and the beams were covered with layers of Styrofoam to ensure constant temperature along the beam length. Figure 5.2-1 through Figure 5.2-7 show the environmental chamber, construction of the tank, and the preparation for the test.



Figure 5.2-1 Environmental Chamber at the CIMR



Figure 5.2-2 Building a steel tank for the freeze-thaw test of bulb T beams



Figure 5.2-3 Decked bulb T beam placed in the tank for freeze-thaw testing



Figure 5.2-4 Concrete cylinders from the same batch as the beams placed with the beams and exposed to freeze-thaw cycles. Other cylinders are stored at Lab. conditions



Figure 5.2-5 Duct work for air freezing and water thawing according to ASTM C666



Figure 5.2-6 Decked bulb T beams during freezing and thawing cycles

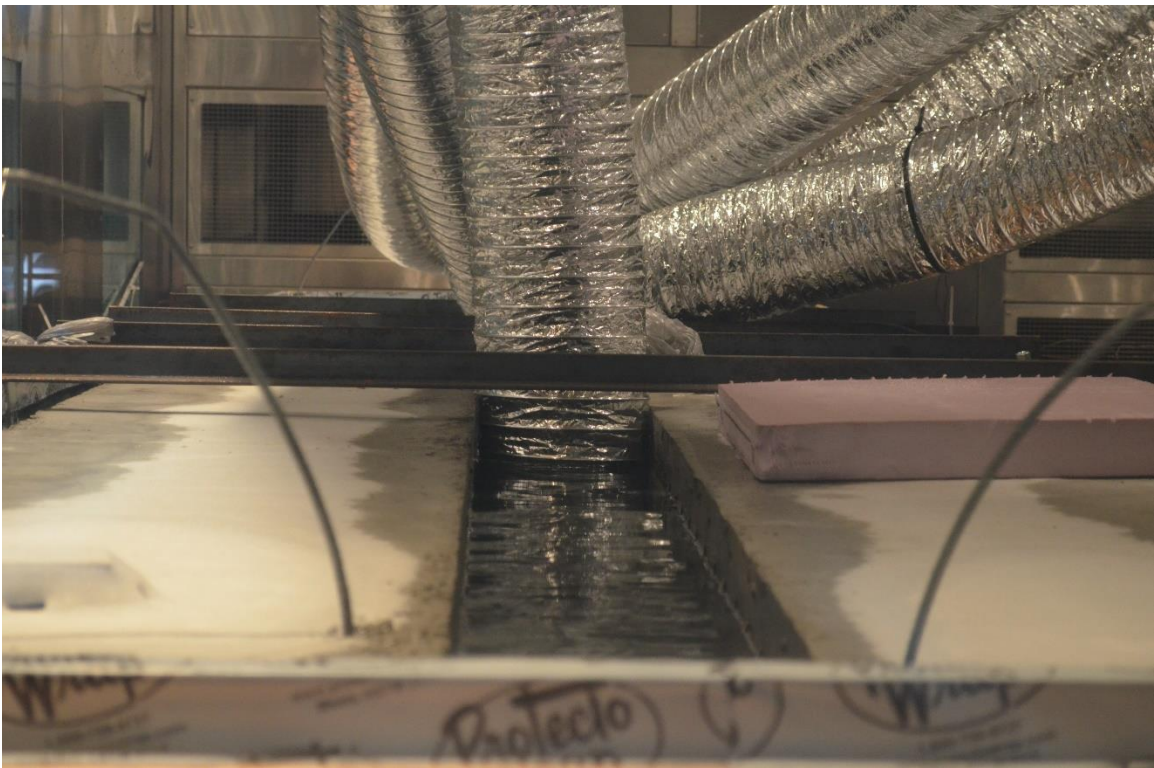


Figure 5.2-7 Water thawing of decked bulb T beams

The temperature profile of the freeze-thaw test for decked bulb T-beams followed the recommendations of ASTM C666-Procedure B, which states that specimens shall be completely surrounded by air during the freezing phase and by water during the thawing phase and that no less than 20 % of the time shall be used for thawing. Also, the temperature of the specimens should be lowered from 40 to 0 °F (4.4 to -18 °C) and then raised from 0 to 40 °F (-18 to 4.5°C) (in a time not less than 2 hrs. and more than 5 hrs. Therefore, the freezing phase of the test was conducted by lowering the air temperature of the environmental chamber to -50 °F (-45.5 °C) until the core temperature of the beams reached 0 °F (-18 °C) in 2 hrs. and 30 min. The thawing phase was executed by flooding the tempering tank with water and raising the air temperature in the chamber to 50 °F (10 °C) until the core temperature of the beams reached 40 °F (4.5 °C) in one hr. and 50 min. The total duration of each freeze-thaw cycle was set to 4 hours and 20 min. Figure 5.2-8 shows the time-temperature variations for freeze-thaw cycles for the prestressed beams. The 300 freeze-thaw cycles were executed in 54 days with a rate of 5.54 cycles per day. A temperature profile was created using VS-1 control system to follow the test program. The air temperature was set to change from -50 °F to 50 °F (-45.5 to 10 °C) in sequences to maintain the assigned core temperature. The control system was set to pump the water into the tempering tank with a proper water level in the thawing phase and continue to re-circulate the water through heat exchanger to maintain set water temperature of 40 °F (4.5 °C). After the beams were thawed, the system diverted the water back to the holding reservoir and maintained the water at 40 °F (4.5 °C) until the next thaw cycle is energized.

After completing 300 freeze-thaw cycles on the beams while monitoring their core temperatures at each cycle, the beams and the concrete cylinders were removed from the tank and were allowed to dry at the room temperature (Figure 5.2-9 and Figure 5.2-10). After proper drying, the four decked bulb T beams and the two control beams, preserved in controlled laboratory conditions, were moved to the testing facility and were loaded under three-point-load test setup to failure. The concrete cylinders were tested under uniaxial compression test to determine the residual concrete compressive strength.

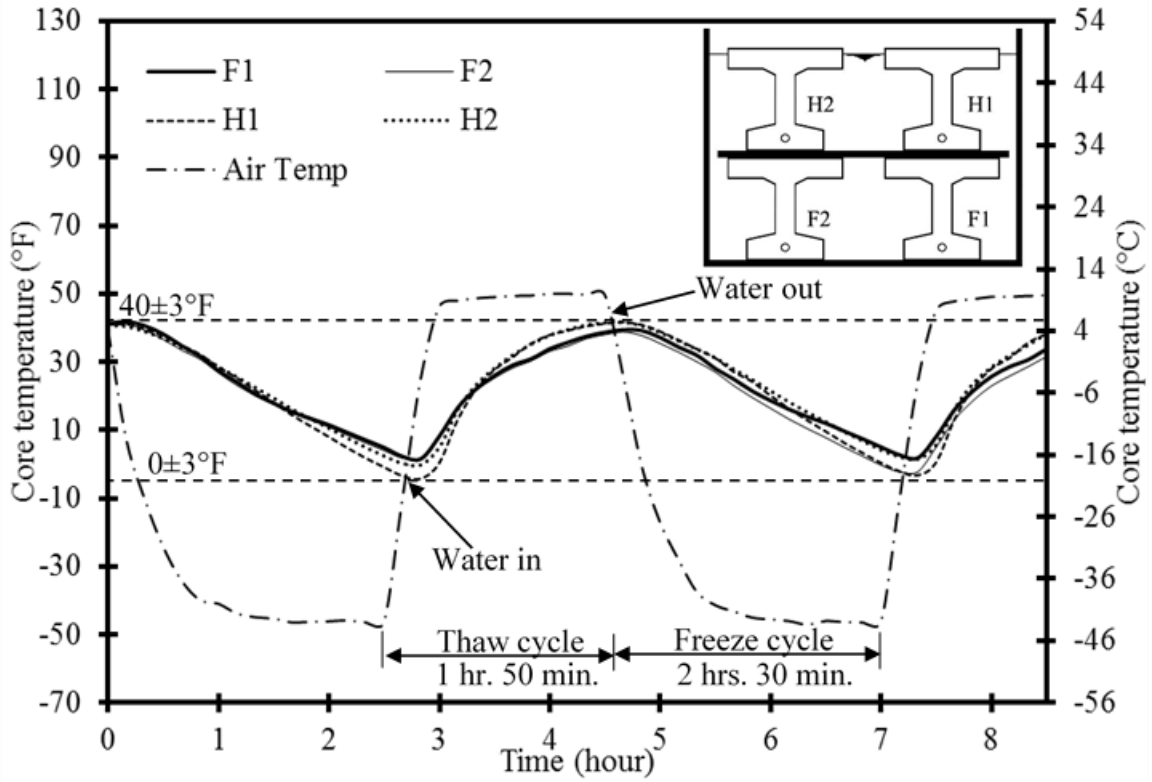


Figure 5.2-8 Air vs beam core temperature during the freezing and thawing cycles



Figure 5.2-9 Deterioration of decked bulb T beams after exposure to 300 freeze-thaw cycles



Figure 5.2-10 Concrete cylinders after exposure to 300 freeze-thaw cycles

The flexural test was conducted after 635 days of concrete casting. Test setup included supporting the beams on two elastomeric bearing pads, positioned on two steel stands spaced 15 ft (4.6 m). Two 2 in. (50 mm) linear strain gages were attached on the top concrete surface near the loading point to capture the concrete strain. Two linear motion transducers (LMTs) string pots were attached to the underside of the beam at mid-span to capture the deflection of the beams. Three linear variable differential transducers (LVDTs) were used to evaluate the strain at different depths at the mid-span section. A 220-kip (980-kN) MTS hydraulic actuator was programmed to apply a vertical concentrated load at the beam mid-span in a force-control mode with rate of 4 kip/min (100 kN/min). All sensors were connected to Mars Lab data acquisition system to collect the necessary data needed to perform a detailed analysis.

## 5.2.2 Test results

### 5.2.2.1 Uniaxial compressive test of concrete cylinders

Figure 5.2-11 through Figure 5.2-14 show the testing and failure of the concrete cylinders under a uniaxial test setup. The freeze-thaw cycles on the prestressed beams and concrete cylinders resulted in deterioration of concrete sections. Concrete spalling was observed at the top surface and at the corners of the decked bulb T beams. Similarly, concrete cylinders exhibited vertical cracks and fracture near the ends. This can be attributed to the water absorption and freeze-thaw cycling. During the thawing phase, the pores of concrete were filled with water and the concrete became fully saturated. In the freezing phase, this water in moist concrete froze and produced pressure on the voids that caused expansion, cracking, and scaling of concrete. The distress to critically saturated concrete from freezing and thawing commenced with the first freeze-thaw cycle and continued throughout the rest of the cycles. It resulted in concrete deterioration that was evident through testing the concrete cylinders in uniaxial compressive test setup. The results, presented in Table 5.2-1, showed a severe degradation in the concrete strength due to exposure to 300 freeze-thaw cycles. While average compressive strength of control cylinders was approximately 12,339 psi (85.1 MPa), the compressive strength of concrete cylinders exposed to freeze-thaw cycles averaged at 4,165 psi (28.7 MPa).



Figure 5.2-11 Testing and failure of cylinders after exposure to freeze-thaw cycles



Figure 5.2-12 Testing and failure of concrete cylinders after exposure to freeze-thaw cycles



Figure 5.2-13 Testing and failure of control cylinders



Figure 5.2-14 Typical failure mode of control cylinders not exposed to freeze-thaw cycles

Table 5.2-1 Results of uniaxial compressive test

Date of testing	Concrete compressive strength psi (MPa)	Average concrete compressive strength psi (MPa)
April 4, 2014 28 days after concrete pouring	10,800 (74.5)	11,100 (76.5)
	10,700 (73.8)	
	11,700 (80.7)	
	10,200 (70.3)	
	12,100 (83.4)	
Oct 16, 2015 Control cylinders	13,119 (90.5)	12,339 (85.1)
	11,925 (82.2)	
	11,973 (82.5)	
November 9, 2015 After freeze-thaw test	2,823 (19.5)	4,165 (28.7)
	4,559 (31.4)	
	5,112 (35.2)	

#### 5.2.2.2 Flexural test of decked bulb T beams

The decked bulb T-beams including the control beams were loaded to 60 kip (267 kN) during as discussed in the previous chapter. Therefore, all the beams were cracked before the start of the freeze-thaw test. After freeze-thaw cycles, the beams were loaded under three-point-load test setup in loading-unloading cycles to failure.

The theoretical analysis of the beam cross-section using the force equilibrium and strain compatibility method indicated a tension failure by rupture of prestressing CFCC tendons at theoretical load of 85 kip (378 kN). The first beam, control C1 failed at a load level of 94.8 kip (422kN) with a corresponding deflection of 3.3 in. (84 mm). The failure was characterized by rupture of CFCC strands followed by crushing of concrete at the top flange as shown in. Figure 5.2-15 through Figure 5.2-19. The maximum recorded concrete compressive strain before failure was approximately 2,144  $\mu\epsilon$ .

Control Beam C2 failed at a load of 93.3 kip (415 kN) with a corresponding midspan deflection of 2.74 in. (70 mm) and a concrete compression strain of 2,462  $\mu\epsilon$ . During the last load cycle, multiple popping sounds were heard while the beam was losing its structural integrity. After failure, the beam was inspected and it was found that there was spalling of concrete at multiple locations and the prestressing CFCC strands ruptured. Figure 5.2-20 through Figure 5.2-23 show the failure of control beam C2 due to rupture of CFCC strands.

Beam F1 was loaded to failure after 300 freeze-thaw cycles. The failure of the beam took place at a load level of 88.5 kip (394 kN) with a corresponding deflection of 2.64 in. (67 mm). The maximum recorded strain before failure was approximately 2,310  $\mu\epsilon$ . The failure was characterized by crushing of concrete at the top flange near the mid-span section as shown in Figure 5.2-24 through Figure 5.2-27. The change in the failure mode was attributed to the deterioration of the concrete due to the exposure to freeze-thaw cycles.

Beam F2 was identical in failure mode to Beam F1. Failure initiated by crushing of concrete in the top flange (Figure 5.2-28 through Figure 5.2-31) at a load level of 85.3 kip (380 kN) with a corresponding deflection of 2.47 in. (63 mm) and an extreme compression strain of 2,417  $\mu\epsilon$ . No popping sound was heard before failure. Prestressing tendons were checked after failure, and they were found intact.

Beam H1 failed at a load level of 84.3 kip (375kN) with a corresponding deflection of 2.84 in. (72 mm) and a maximum recorded concrete strain in the top flange of approximately 2,248  $\mu\epsilon$ . The failure took place by concrete crushing at the top flange near the mid-span section (Figure 5.2-32 through Figure 5.2-35), No rupture of CFCC strands was observed after failure.

Beam H2 experienced a failure mode similar to that of Beam H1. The beam failed at a load level of 89.8 kip (400 kN) with a corresponding deflection of 3.0 in. (76mm) and maximum compression strain at failure of 2,798  $\mu\epsilon$ . The failure was characterized by crushing of concrete in the top flange (compression failure) as shown in Figure 5.2-36 through Figure 5.2-39.

Based on the load-deflection curves from all load cycles including the ultimate load cycle, the total energy absorbed by each beam was calculated as the area under the load-deflection curve. For Beams C1 and C2, the total energy absorbed was estimated as 232.7 kip-in. (26.3 kN-mm) and 202.4 kip-in. (22.9 kN-mm), respectively. The freeze-thaw beams had lower energy-absorption capacities at failure compared to the control beams. The total absorbed energy for Beams F1, F2, H1, and H2 were calculated as 159.4 kip-in. (18 kN-m), 147.6 kip-in. (16.7 kN-m), 168.5 kip-in. (19 kN-m), and 185.3 kip-in. (20.9 kN-m) respectively.

The decompression loads for all beams at an age of 635 days, after freeze-thaw cycles were compared with the obtained values at an age of 270 days when the beams were tested at ambient temperature in the seasonal change temperature test. The decompression loads for all beams were

determined by estimating the deviation of the load-deflection curve from linearity as described earlier. For comparison purpose, the deviation from linearity for each test beam for the 60-kip (267-kN) load cycle were overlapped at both ages and the approximate difference in the decompression loads was determined. Using these decompression loads with the assumption that at decompression, there is no stress at the soffit of the beam, effective prestressing at the time of testing was evaluated by back calculation. The effective prestressing force was then used to estimate the prestressing loss from transfer to time of testing as listed in Table 5.2-2.

All beams experienced additional prestress loss at an age of 635 days compared with that at an age of 270 days. The decompression load for control beams, C1 and C2 at an age of 635 days was lower than that at an age of 270 days with a difference of approximately 1.5 kip (6.7 kN) and 0.9 kip (4 kN), respectively. This decrease in the decompression load reflects an additional prestress loss, which averaged approximately 3.6 % for the two control beams. This additional prestress loss in the control beams represent the long-term prestress loss in the beams between both ages as the beams were tested at ambient temperature without any exposure to freeze-thaw cycles. On the other hand, Beams F1, F2, H1 and H2 exhibited higher prestress loss compared to that of the control beams. The decompression load for the Beams F1, F2, H1, and H2 at the age of 635 days after 300 freeze-thaw cycles was lower than that at the age of 270 days with an approximate difference of 3.5 kip (15.6 kN), 2.5 kip (11.1 kN), 1.8 kip (8 kN), and 2 kip (8.9 kN) respectively. The estimated prestress loss from decompression loads for all four beams averaged 18.6 % at the age of 635 days and 11.45 % at the age of 270 days with a additional prestress loss of 7.15 %.

Comparing the load-deflection curves of the control beams with those of Beams F1, F2, H1, and H2 revealed that freeze-thaw exposure influenced the flexural test in multiple ways. For instance, the mode of failure shifted from CFCC rupture to concrete crushing. This shift resulted in 7.5 % to 10.3 % decrease in maximum load carrying capacity and corresponding deflection for freeze-thaw beams compared to Beams C1 and C2. Also, a decrease of 24 % in energy absorption capacity of freeze-thaw beams with respect to the control beams was observed.

Beams C1 and C2 failed due to CFRP rupture while the concrete strain in extreme compression fibers is small; 2,144  $\mu\epsilon$  and 2,462  $\mu\epsilon$  respectively. This matched the design and the anticipated failure mode of the beams. Whereas Beams F1, F2, H1 and H2 experienced compression failure at compression strains of 2,310  $\mu\epsilon$ , 2,417  $\mu\epsilon$ , 2,248  $\mu\epsilon$ , 2,798  $\mu\epsilon$  respectively.

Table 5.2-2 Summary of experimental results for decked bulb T-beams

Parameter		Control beams		Freeze-thaw beams			
		C1	C2	F1	F2	H1	H2
Experimental ultimate load, kip (kN)		94.8 (422)	93.3 (415)	88.5 (394)	85.3 (380)	84.3 (375)	89.8 (400)
Midspan deflection at failure, in. (mm)		3.30 (84)	2.74 (70)	2.64 (67)	2.47 (63)	2.84 (72)	3.00 (76)
Mode of failure		Tendon rupture	Tendon rupture	Concrete crushing	Concrete crushing	Concrete crushing	Concrete crushing
Extreme compression strain ( $\mu\epsilon$ )		2,144	2,462	2,310	2,417	2,248	2,798
Total energy absorbed kip-in. (kN.m)		232.7 (26.3)	202.4 (22.9)	159.4 (18)	147.6 (16.7)	168.5 (19)	185.3 (20.9)
Decompression load, kip (kN)	270 days age	32 (142.4)	31.2 (138.8)	31.5 (140.2)	31 (137.9)	27.8 (123.7)	28 (124.6)
	635 days age	30.5 (136)	30.3 (135)	28 (125)	27.5 (122)	26 (116)	26 (116)
Total prestress loss from transfer to time of testing, %	270 days age	3.5	5.8	5	5.7	15.8	15.2
	635 days age	8	8.5	15.2	16	21	21
Average increase in prestress loss, %		4.5	2.7	10.2	10.3	5.2	5.8

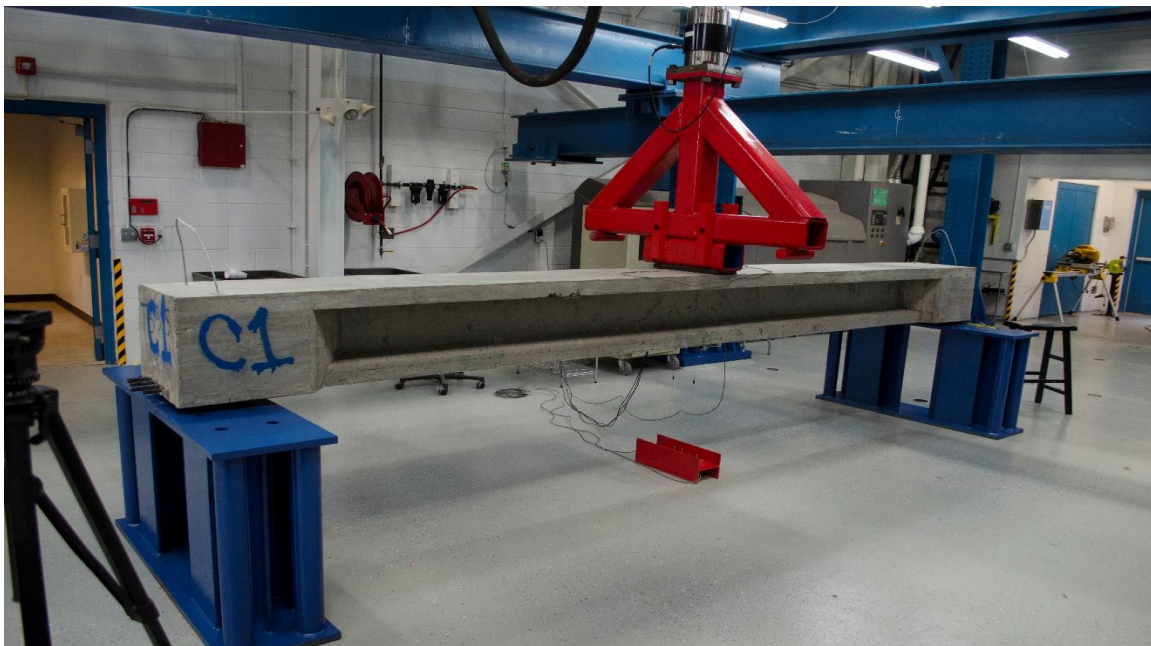


Figure 5.2-15 Flexural test setup for control beam C1



Figure 5.2-16 Instrumentation of Beam C1 for strain and deflection monitoring



Figure 5.2-17 Failure of Beam C1



Figure 5.2-18 Close-up view showing the rupture of CFCC strands in Beam C1

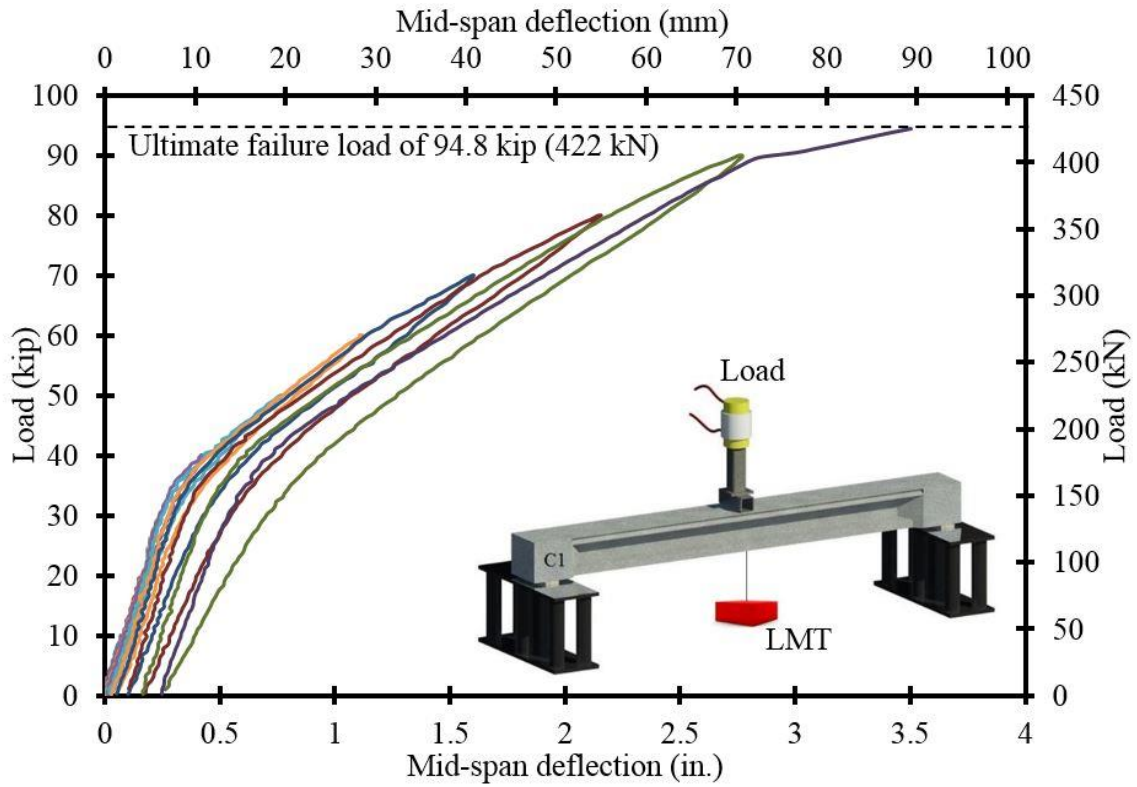


Figure 5.2-19 Load vs. deflection curves for Beam C1



Figure 5.2-20 Test setup of Beam C2

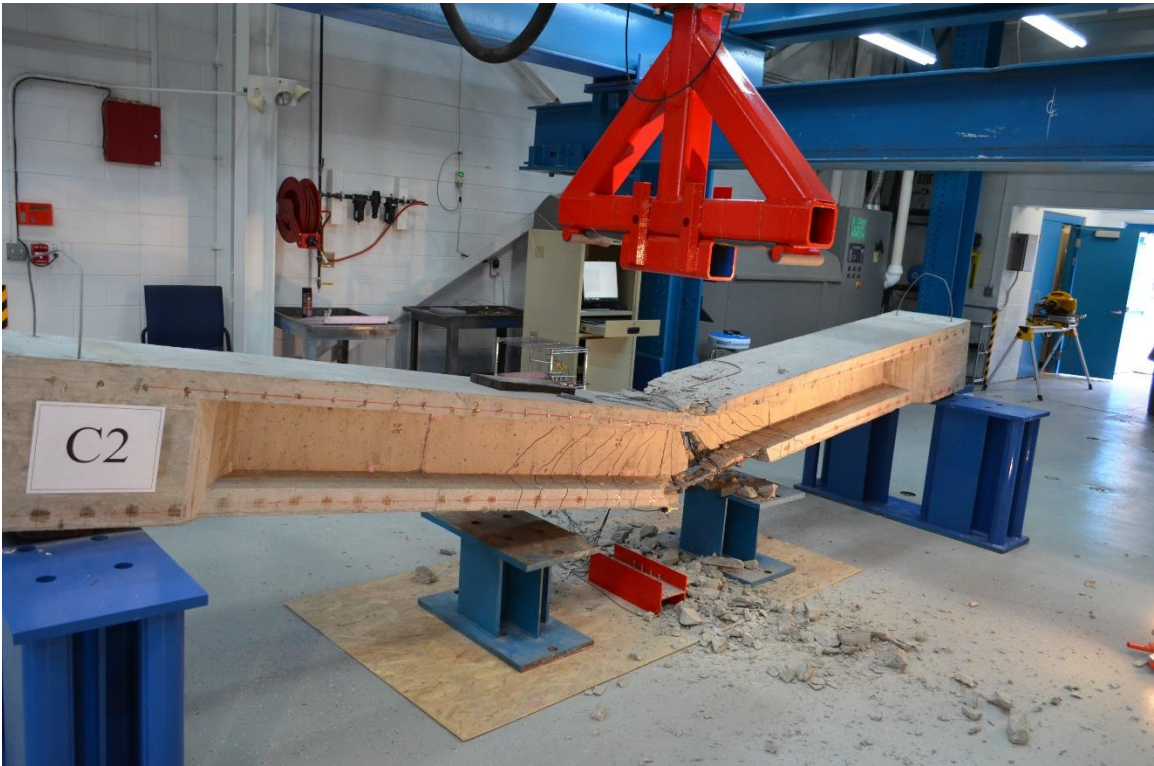


Figure 5.2-21 Failure of Beam C2



Figure 5.2-22 Rupture of strands and concrete spalling of Beam C2

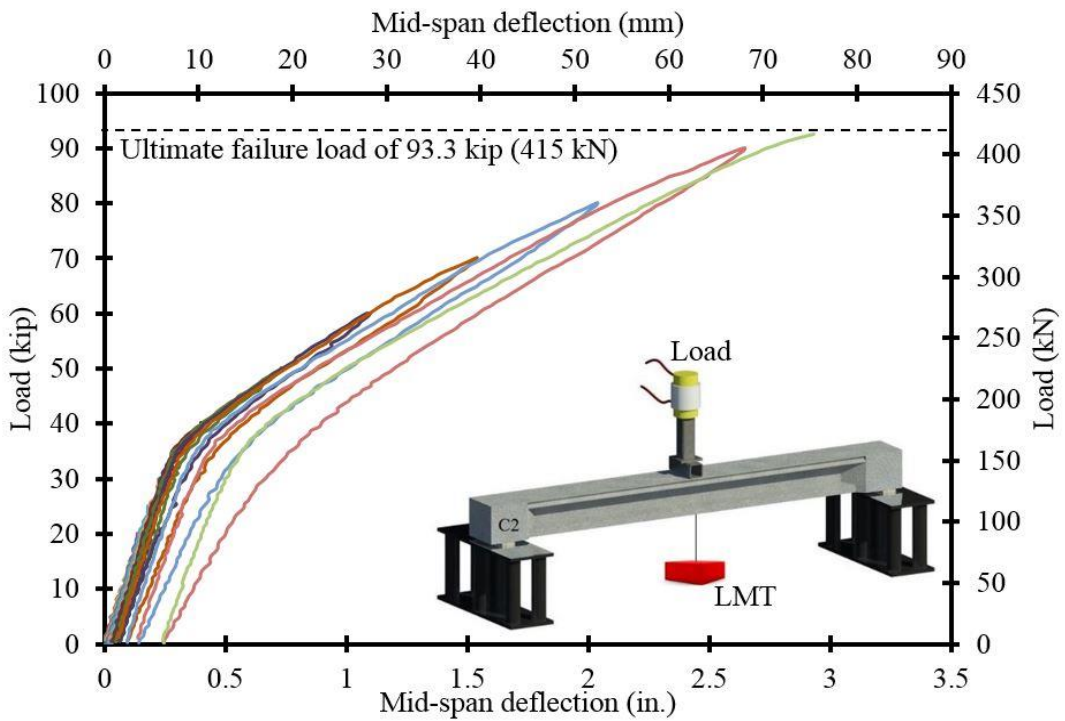


Figure 5.2-23 Load vs. deflection curves for Beam C2

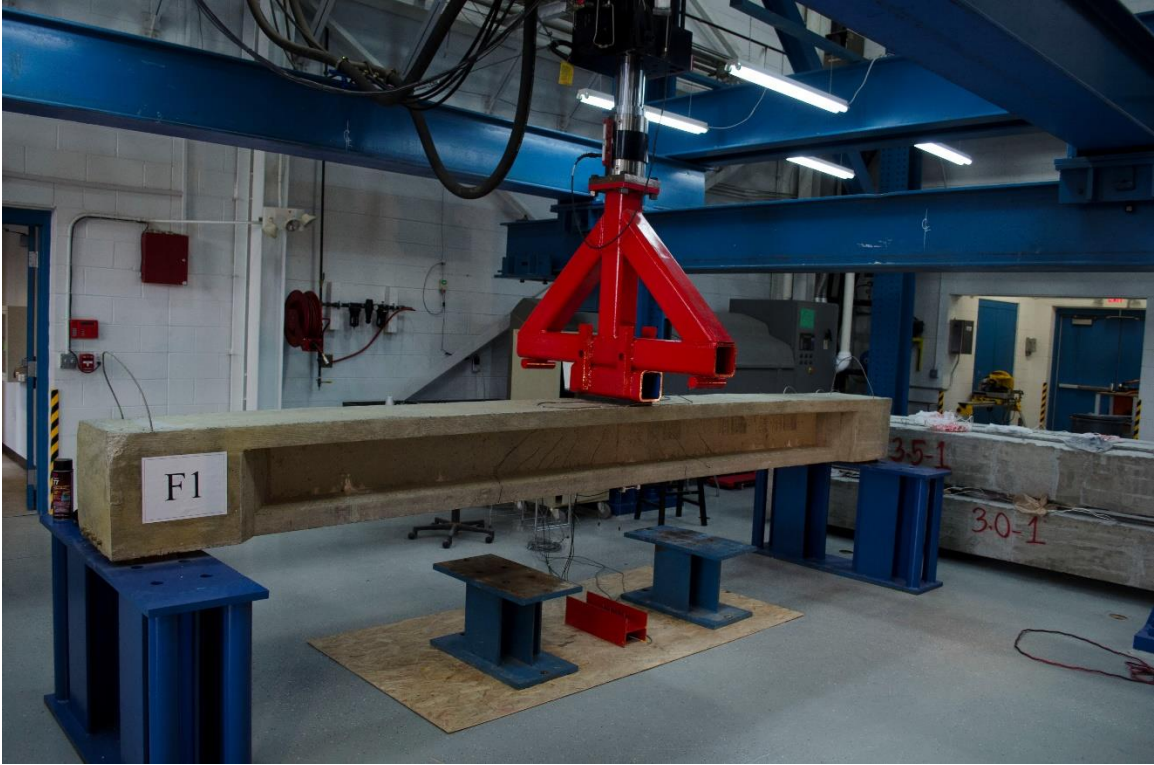


Figure 5.2-24 Test setup of Beam F1 after exposure to freeze-thaw cycles



Figure 5.2-25 Failure of Beam F1



Figure 5.2-26 Close-up picture for CFCC strands in Beam F1 after failure

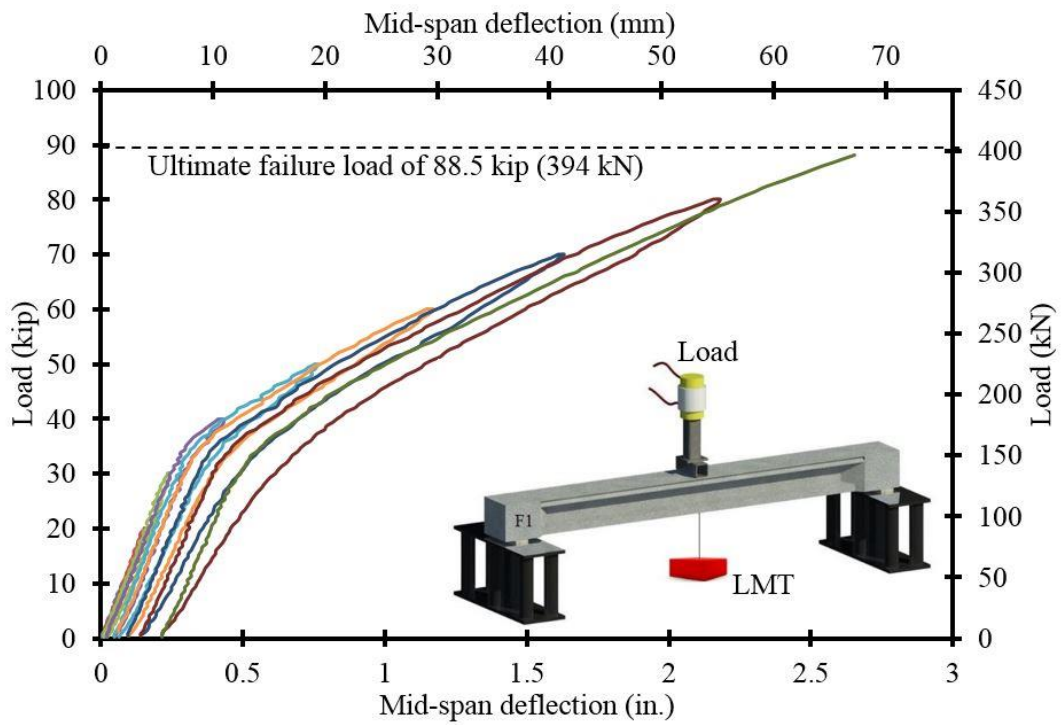


Figure 5.2-27 Load vs. deflection curves for Beam F1



Figure 5.2-28 Test setup for Beam F2 after exposure to freeze-thaw cycles



Figure 5.2-29 Failure of Beam F2



Figure 5.2-30 Close-up picture for CFCC strands in Beam F2 after failure

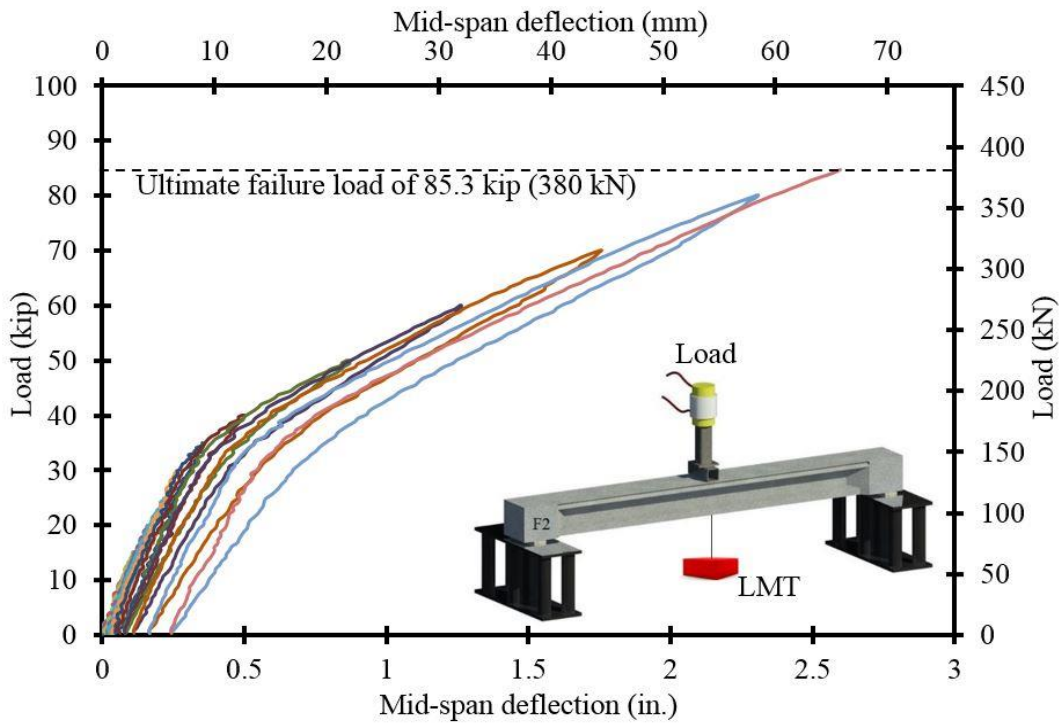


Figure 5.2-31 Load vs. deflection curves for Beam F2



Figure 5.2-32 Test setup for Beam H1 after exposure to freeze-thaw cycles



Figure 5.2-33 Failure of Beam H1



Figure 5.2-34 Close-up picture for CFCC strands in Beam H1 after failure

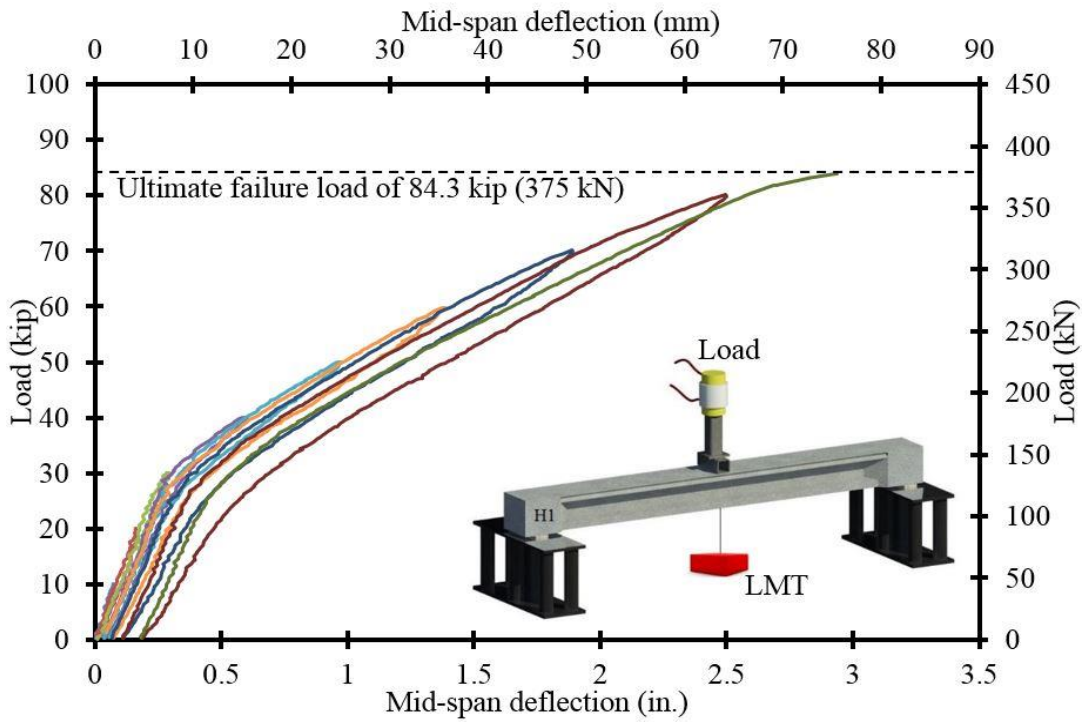


Figure 5.2-35 Load vs. deflection curves for Beam H1

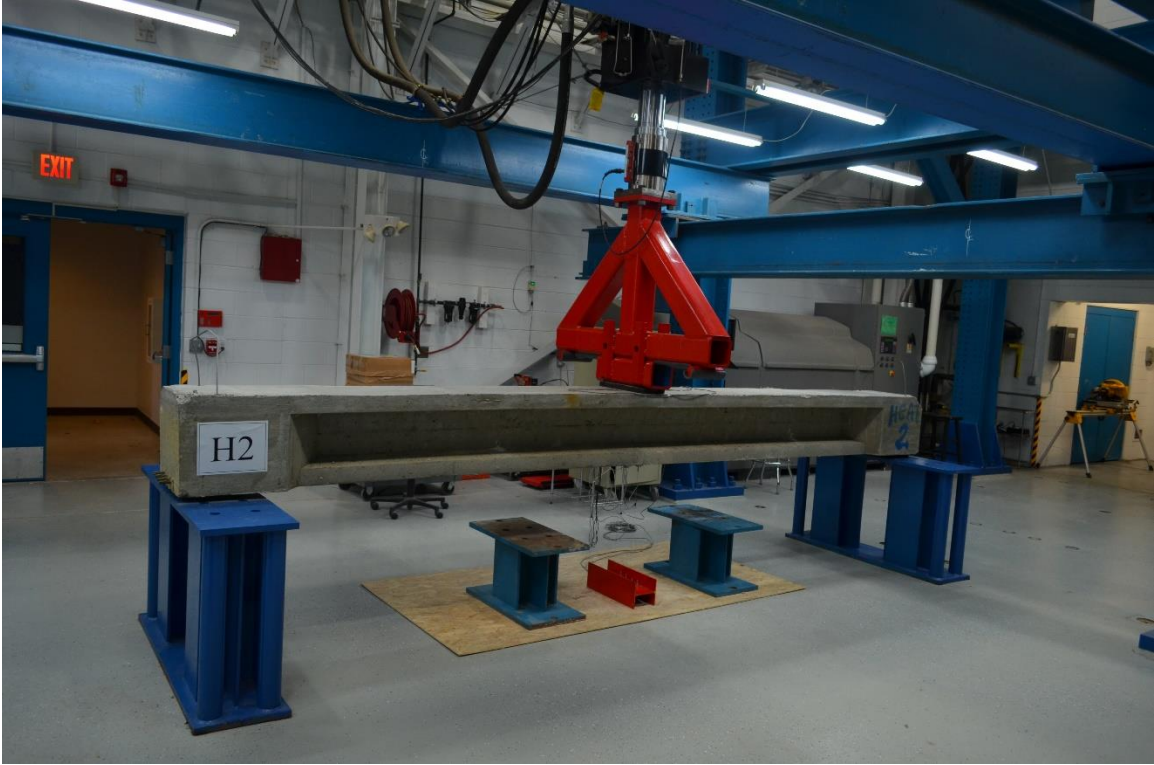


Figure 5.2-36 Test setup for Beam H2 after exposure to freeze-thaw cycles



Figure 5.2-37 Failure of Beam H2



Figure 5.2-38 Close-up picture for CFCC strands in Beam H2 after failure

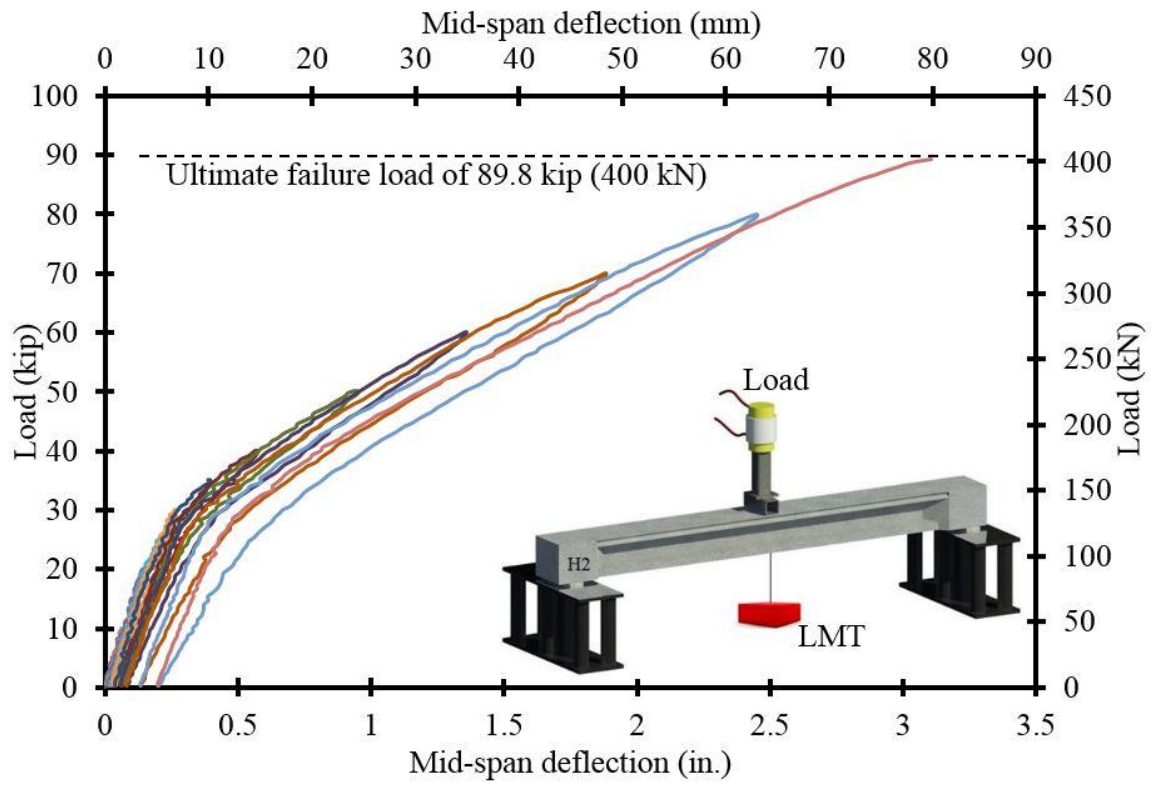


Figure 5.2-39 Load vs. deflection curves for Beam H2

## **5.3 Freeze-thaw cycles of CFCC specimens**

### **5.3.1 Test setup**

Five CFCC 4-ft (1.2-m) long specimens labelled as F/T-S1, F/T-S2, F/T-S3, F/T-S4 and F/T-S5 were constructed with sleeve anchorage at both ends as described earlier in the Report. The test specimens were loaded inside a custom-made high-strength steel frame and were connected to in-line load cells and threaded rods at one end (dead end) and fastened at the other end (live end) with a high-strength steel nut and a washer. The load cells were connected to a data acquisition system to monitor the prestressing force continuously. After installing the specimens inside the steel frame. Prestressing force was applied at the live end through a hydraulic jacking system at a rate of 6 kip/min (27 kN/min) and monitored through the installed load cells. The strands were prestressed in a prearranged sequence to avoid generating any eccentricity in the steel frame. The steel frame was then moved to the environmental chamber, where the specimens, along with the four decked bulb T beams, were subjected to 300 cycles of freezing and thawing. The load cells were covered with insulation layers to minimize the damage during the freeze-thaw cycles of the test. In addition, readings from the load cells were corrected according to the corresponding temperature. Figure 5.3-1 through Figure 5.3-4 document the preparation of the CFCC freeze-thaw test specimens, while Figure 5.3-5 show the change in the prestressing force with the change in temperature during a typical freeze-thaw cycle.

After completion of the freeze-thaw cycles, the test specimens were released from the steel frame as shown in Figure 5.3-6 through Figure 5.3-8 and were transported to the MTS four-post testing facility, where they were loaded in a uniaxial test setup to failure to estimate the residual CFCC strength after exposure to freeze-thaw cycles (Figure 5.3-9 and Figure 5.3-10).



Figure 5.3-1 Steel frame to accommodate 4-ft-long CFCC specimens



Figure 5.3-2 Prestressing CFCC strands and Inline load cell for force monitoring during the test



Figure 5.3-3 CFCC specimens in the Environmental Chamber along with the beams



Figure 5.3-4 CFCC specimens during freeze-thaw testing

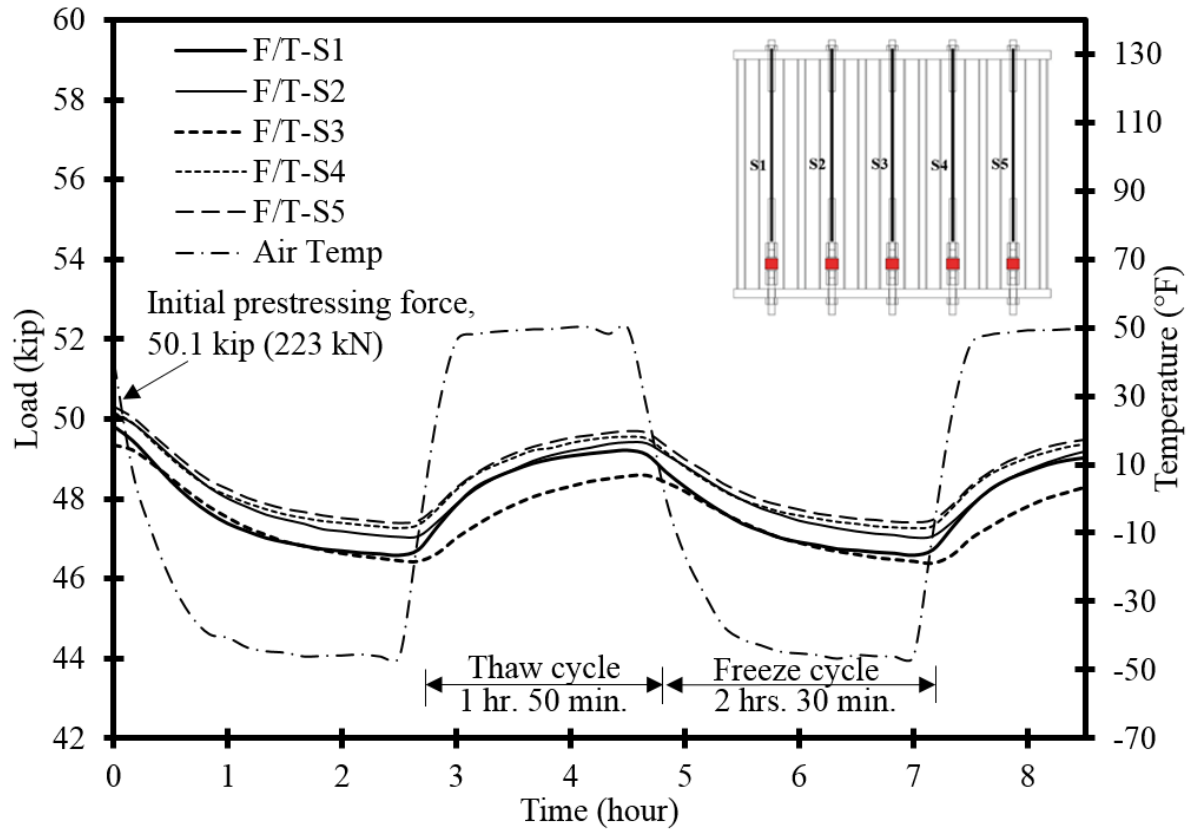


Figure 5.3-5 Change in prestressing force with the change in temperature in CFCC strands

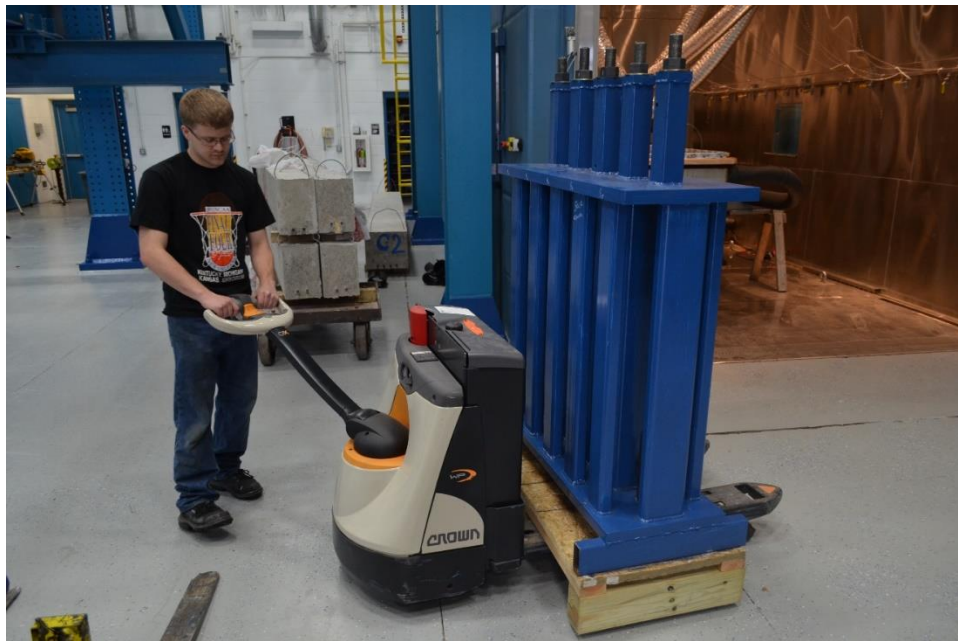


Figure 5.3-6 Removing the CFCC specimens after completion of 300 freeze-thaw cycles



Figure 5.3-7 Releasing CFCC strands after freeze-thaw exposure



Figure 5.3-8 Preparing CFCC strands for uniaxial tensile test to evaluate residual capacity

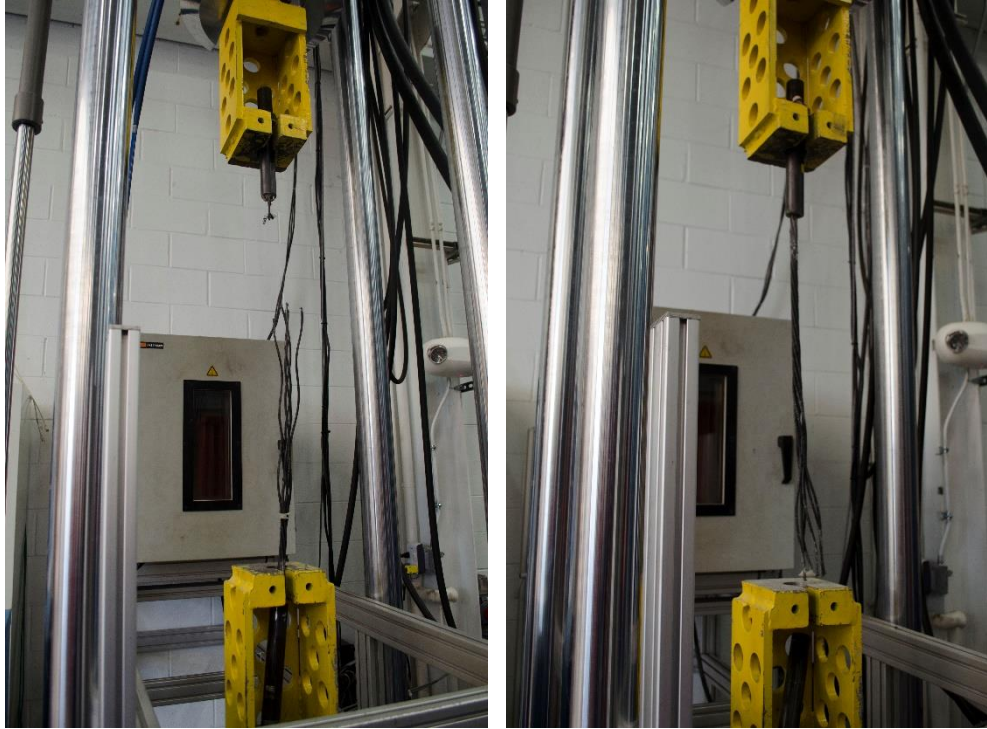


Figure 5.3-9 Loading and failure of CFCC strands



Figure 5.3-10 Failure of CFCC strands under uni-axial load test setup

### 5.3.2 Test results

Results of freeze-thaw test and uniaxial tensile test for post-tensioned CFCC specimens are provided in Table 5.3-1. Based on the results, the average loss in prestressing force was estimated as 3.6 % over 300 freeze-thaw cycles (54 days). This loss includes the loss due to strand relaxation as well as anchorage relaxation. The failure load of the test specimens averaged at 79.78 kip (355 kN). All specimens ruptured at failure, with no slippage within the anchors. The elastic of the test specimens averaged at 23,844 ksi (164 GPa). The experimental breaking load for all specimens after freeze-thaw exposure was approximately 15% higher than the failure loads from respective batch testing conducted at ambient temperature.

Table 5.3-1 Summary of experimental results for Post-tensioned CFCC strands

Specimen	Freeze-thaw Test			Uniaxial Tensile Test		
	Prestressing Force, kip (kN)		Prestressing Losses, (%)	Breaking Load, kip (kN)		Elastic modulus, ksi (Gpa)
	Before Freeze/thaw Cycles	After Freeze/thaw Cycles		Before Freeze/thaw Cycles	After Freeze/thaw Cycles	
F/T- S1	49.8 (222)	48.1 (214)	3.41	70.35 (313)	72.6 (323)	23,172 (160)
F/T- S2	49.4 (220)	47.7 (212)	3.41	70.35 (313)	82.7 (368)	24,375 (168)
F/T- S3	50.2 (223)	48.2 (215)	3.93	70.35 (313)	82.2 (366)	24,121 (166)
F/T- S4	50.3 (224)	48.4 (215)	3.82	68.61 (305)	78.3 (348)	23,910 (165)
F/T- S5	50.1 (223)	48.5 (216)	3.31	68.61 (305)	83 (370)	23,644 (163)

### 5.4 Discussion of Test Results

The test results show that freeze-thaw cycles have detrimental effect on concrete but not on CFCC. Concrete lost more than 60 % of its compressive strength, while CFCC gained additional 15 % of strength after exposure to freeze-thaw cycles. This change in strength altered the mode of failure of the test beams from tension-controlled to compression-controlled. The reduction of the nominal moment capacity was approximately 7.5 %, which was not significant because the beams were

designed as tension-controlled sections and therefore, concrete strength was not a significant parameter in establishing the nominal moment capacity. On the other hand, had the beams been designed as compression-controlled sections, the reduction in concrete strength would have led to a significant reduction in the nominal moment capacity since compression-controlled sections are sensitive to concrete strength.

From design perspective, it is strongly recommended to design bridge beam sections as tension-controlled sections. The compression in a bridge beam is resisted by the deck slab, which is the most vulnerable element to environmental conditions. A tension-controlled section will accommodate a reduction in the concrete strength without a significant reduction in the nominal moment capacity, unless the reduction in the concrete strength is severe and alters the mode of failure from tension-controlled to compression-controlled.

## CHAPTER 6: FIRE AND HEAT RESISTANCE

### 6.1 Introduction

Regardless of the material under consideration, loss in strength under high temperature is inevitable (Rafi et al. 2007; Williams et al. 2008; and Grace and Bebawy 2014). For instance, concrete loses 50 % of its compressive strength at approximately 1292 °F (700 °C). Note that different concrete constituents exhibit different thermal decomposition trends that result in a wide range in the behavior of concrete at high temperatures (Kodur et al. 2005). Steel is also susceptible to fire and is expected to lose 50 % of its tensile capacity at 932 °F (500 °C). Likewise, CFRP is susceptible to fire and extreme high temperature events as the polymer matrix in CFRP softens and deteriorates with the increase in temperature. CFRP loses approximately 50 % of its ambient strength at 392 °F (200 °C) according to Robert and Benmokrane (2010).

Precise data regarding the fire endurance of beams prestressed with CFRP strands are not available. However, it is generally accepted that prestressed concrete structures are more susceptible to fire than reinforced concrete structures, since the prestressing strands (whether steel or CFRP) are already stressed to a significant level of their ambient capacity. For instance, Zhang et al. (2017) showed that under hydrocarbon fire, prestressed box beams with higher level of prestressing force have higher ductility and creep and lower fire endurance than those with lower level of prestressing force. In addition, Maluk et al. (2010) studied the fire behavior of CFRP prestressed high strength concrete slabs and observed that when spalling of the concrete was avoided, the fire endurance of the prestressed slabs was influenced by the initial prestressing force as slabs with larger prestressing force achieved shorter fire endurance.

It should be noted that fire endurance of a beam prestressed with CFRP strands may not necessarily be dependent on the heat resistance of CFRP but rather on the ability of the prestressed beam to sustain a specific load at elevated temperatures (Abbasi and Hogg 2006). For instance, Maluk et al. (2010) suggested that the limiting factor for the fire endurance of CFRP reinforced or prestressed concrete is the deterioration in bond strength between CFRP and concrete at elevated temperatures rather than the flammability of the composite material or the deterioration of the epoxy matrix. This opinion is supported by earlier fire test results that showed 80 to 90 % reduction in the bond strength between concrete and CFRP as the temperature increased from 68 to 482 °F

(20 to 250 °C) compared to 38 % reduction in bond strength with conventional steel reinforcing bars (Katz et al. 1999; Kodur et al. 2005).

Another aspect of the fire resistance of prestressed concrete structures is the concrete cover and the potential for concrete cover spalling at high temperatures. According to Kodur et al. (2005), the strength of concrete in fire is governed by its moisture content. Test results by Saafi (2002) showed that too much moisture in the concrete generated high pressure in the beam that caused spalling in the concrete cover, which resulted in the premature exposure of the internal reinforcement to high temperature and overall reduction in the strength of the structural element. In addition, the shape of the structural element plays an important role in the fire resistance. For instance, in comparing rectangular-section to I-shape prestressed beams, it was found that the I-shape was more susceptible to spalling than the rectangular sections (Ashton and Malhotra 1953). Furthermore, the increase in concrete cover should provide a fire protection of the internal reinforcement and prestressing strands and extend the fire endurance of structural elements (Kodur et al. 2005; Yu and Kodur 2013). For instance, Terrasi et al. (2010) investigated the performance of CFRP and steel prestressed beams at elevated temperatures. Failure mode was either concrete spalling or deterioration of the bond between the strands and the concrete and consequently loss of prestressing force with evidences of increasing the fire endurance with the increase of concrete cover. It should be noted, however, that concrete cover thicker than 3.0 in. (7.5 mm) are deemed susceptible to spalling (Ashton and Malhotra 1953).

Through this part of the investigation, the performance of unprotected and protected CFCC strands at elevated temperature was evaluated. CFCC specimens with a length of 4 ft (1.2 m) were maintained at elevated temperatures for at least 30 minutes before they were loaded to failure under uni-axial tensile load to evaluate the reduction in the strength with the increase in temperature. In addition, to evaluate the performance of CFCC strands embedded in concrete under a fire event, another research investigation was carried out on a series of 16-ft (4.876-m) long decked bulb T beams prestressed with CFCC strands. The beams were subjected to fire event according to ASTM E119 while sustaining a central load representing the traffic load in real-scale bridge beams. Detailed discussion for both test setups, test results, and main conclusions are provided in the following sections.

## 6.2 Tensile Strength of CFRP at Elevated Temperatures

### 6.2.1 Test setup

Twelve test specimens were tested at high temperature to evaluate the effect of temperature increase on the tensile strength of CFCC strands. Each specimen had a length of 4 ft (1.2 m) and was provided with two sleeve anchorages at the ends.

The test setup included passing the test specimen through an INSTRON environmental chamber as shown in Figure 6.2-1 and Figure 6.2-2 and attaching its ends the fixed and moving heads of the MTS four-post testing facility. After the specimen was fixed in place, the environmental chamber was activated to heat the middle portion of the specimen to a predefined temperature. To ensure a uniform temperature throughout the heated length of the specimen, the chamber was maintained at the predefined the temperature for 30 minutes. After that, the MTS actuator was engaged, and the specimen was loaded in a uniaxial tensile test setup to failure with a loading rate of 6.5 kip/min (29 kN/min), while the temperature of the environmental chamber remained at the same predefined level. The specimens were tested at temperatures ranging from 302 °F (150 °C) to 662 °F (350 °C).

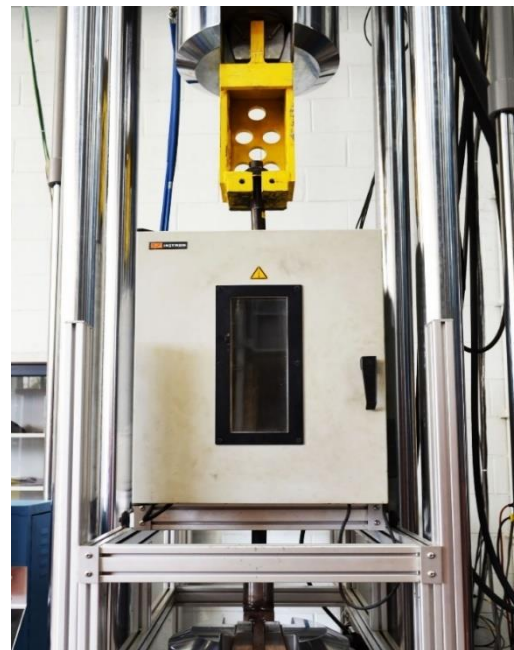
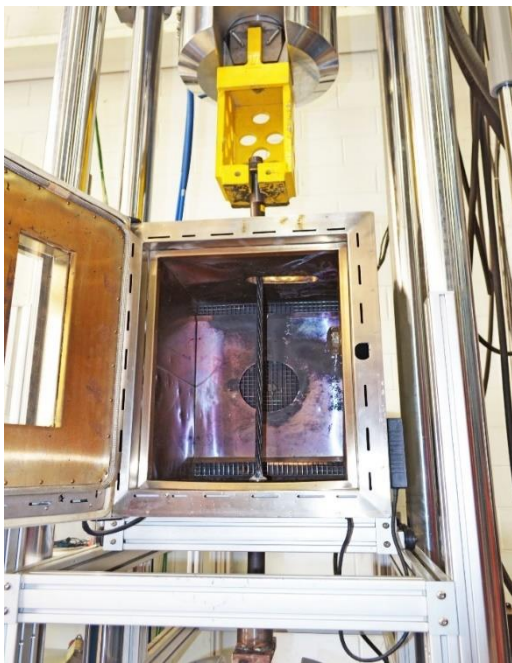


Figure 6.2-1 Test setup to establish tensile strength of CFCC at elevated temperatures



Figure 6.2-2 Anchorage device passing through a central opening in the heat chamber

### 6.2.2 Test results

Reduction of strength of CFCC strand with increasing the temperature was observed in all test specimens. The common mode of was rupture of stands within the heated length as shown in Figure 6.2-3 through Figure 6.2-11. The tensile strength of CFCC at 302 °F (150 °C) was approximately 54.79 kip (244 kN), while its tensile strength at 662 °F (350 °C) was 34.12 kip (152 kN). Table 6.2-1 shows the test result of all specimens, while Figure 6.2-12 shows a comparison between the test results and those obtained by the manufacturer on CFCC strands with different diameters.



Figure 6.2-3 Typical failure of test specimen at elevated temperature



Figure 6.2-4 Failure of CFCC specimen at 347 °F (175 °C)



Figure 6.2-5 Failure of CFCC specimen at 392 °F (200 °C)



Figure 6.2-6 Failure of CFCC specimen at 437 °F (225 °C)



Figure 6.2-7 Failure of CFCC specimen at 482 °F (250 °C)



Figure 6.2-8 Failure of CFCC specimen at 527 °F (275 °C)



Figure 6.2-9 Failure of CFCC specimen at 572 °F (300 °C)



Figure 6.2-10 Failure of CFCC specimen at 617 °F (325 °C)



Figure 6.2-11 Failure of CFCC specimen at 662 °F (350 °C)

Table 6.2-1 Summary of test results for tensile strength of CFCC at elevated temperature

Specimen ID	Temperature, °F (°C)	Failure Load, kip (kN)	Failure stress, ksi (MPa)	Ratio to guaranteed strength (60.7 kip or 270 kN) (%)
65-01	150 (65)	69 (306)	385 (2654)	1.13
150-01	302 (150)	54.79 (244)	306 (2110)	90
175-01	347 (175)	52.08 (232)	291 (2006)	86
200-01	392 (200)	52.37 (233)	293 (2020)	86
200-02	392 (200)	54.34 (242)	303 (2089)	89
225-01	437 (225)	52.14 (232)	291 (2006)	86
250-01	482 (250)	47.75 (212)	267 (1841)	79
275-01	527 (275)	45.82 (204)	256 (1765)	75
300-01	572 (300)	41.74 (186)	233 (1606)	69
325-01	617 (325)	36.16 (161)	202 (1393)	60
325-02	617 (325)	36.74 (163)	205 (1413)	60
350-01	662 (350)	34.12 (152)	191 (1317)	56
350-02	662 (350)	34.88 (155)	195 (1344)	57

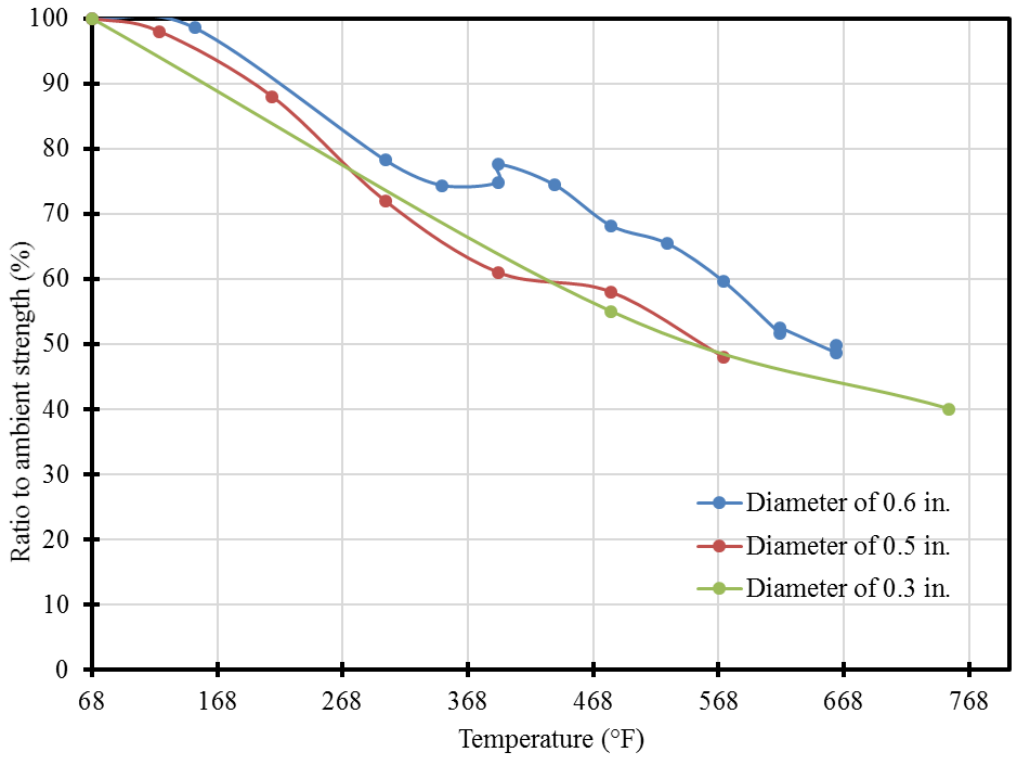


Figure 6.2-12 Decrease in tensile strength with increase in Temperature for CFCC strands

Table 6.2-2 Comparison with Manufacturer's test results

Temperature °F (°C)	Ratio to CFCC strength @ ambient (%)		
	0.6 in. (15.2 mm)*	0.5 in. (12.5 mm)**	0.3 in. (7.5 mm)**
68 (20)	100	100	100
122 (50)	-	98	-
212 (100)	-	88	-
302 (150)	79	72	-
392 (200)	76	61	-
482 (250)	69	58	55
572 (300)	61	48	-
662 (350)	49	-	-
752 (400)	-	-	40

\* Based on ultimate strength of 70 kip (311 kN) for 0.6 in. (15.2 mm) CFCC strands

\*\* Tokyo Rope Mfg. Co., Ltd. based on tensile strengths of : 38.2 kip (145 kN) for 0.5 in. (12.5 mm) CFCC, and 15 kip (67 kN) for 0.3 in. (10 mm) CFCC strands.

### **6.3 CFCC Prestressed Decked Bulb T Beams Under Fire/Loading Event**

Seven CFCC prestressed and one steel prestressed decked bulb T beams with varying prestressing force levels were tested under fire/loading events to evaluate the fire endurance of CFCC prestressed highway bridge beams in the case of fire. The beams had a total length of 16 ft (4.87 m) and cross section dimensions as shown in Figure 6.3-1.

Fire is an unlikely/unpredictable event that might happen anytime during the lifespan of the structure (Highway Bridge) or even during construction. However, the most critical time is when the bridge is in service and there is a traffic on the bridge when it engulfs in fire. The research investigation aimed at addressing this scenario by taking multiple key steps in specimen preparation and test setup.

First, to simulate the case of an aged structure that has been in service for many years and may have some level of deterioration, the beam specimens were not a freshly constructed specimen but were salvaged from an earlier shear research study that aimed at establishing the shear resistance of prestressed beams by applying loads near their ends (details and finding of the study is described later in the Report). The research team was therefore, able to salvage the middle portion of those test beams and recondition them for fire testing. At the time of fire testing, the beams were approximately three years old and they kept outdoors where they were exposed to different weather condition for at least two years. Originally, the beams had a length of 31 ft (9.5 m) but approximately a segment of 6 ft (1.82 m) from each end was damaged beyond repair. Nevertheless, the middle segment of each beam was in good conditions and was deemed a perfect fit for fire testing.

#### **6.3.1 Test setup**

The eight test beams, seven prestressed with CFCC strands. One with steel strand, were provided with CFCC stirrups through half of the span and steel stirrups through the other half. The steel stirrups were made of No.3 Grade 60 reinforcing bars, whereas the CFCC stirrups had a nominal diameter of 0.44 in. (10.5 mm) and effective cross-sectional area of 0.09 in.<sup>2</sup> (57.8 mm<sup>2</sup>). The stirrups were provided at a spacing of 4, 6 & 8 in. (101, 152, 203 mm). Both prestressing CFCC and steel strands had a nominal diameter of 0.6 in. (15.2 mm). The initial prestressing force per beam was 72 kip (320 kN) in one beam, 100 kip (445 kN) in five beams, and 132 kip (587 kN) in

two beams including steel prestressed beam. The average concrete strength was 6.4 ksi (44.1 MPa) and 9 ksi (62 MPa) at the time of prestress transfer and after 28 days, respectively. A clear cover to the outer edge of the stirrups of 0.75 in. (19 mm) was provided at the soffit and top of the beam, while a clear cover of 0.5 in. (13 mm) was provided at the sides.

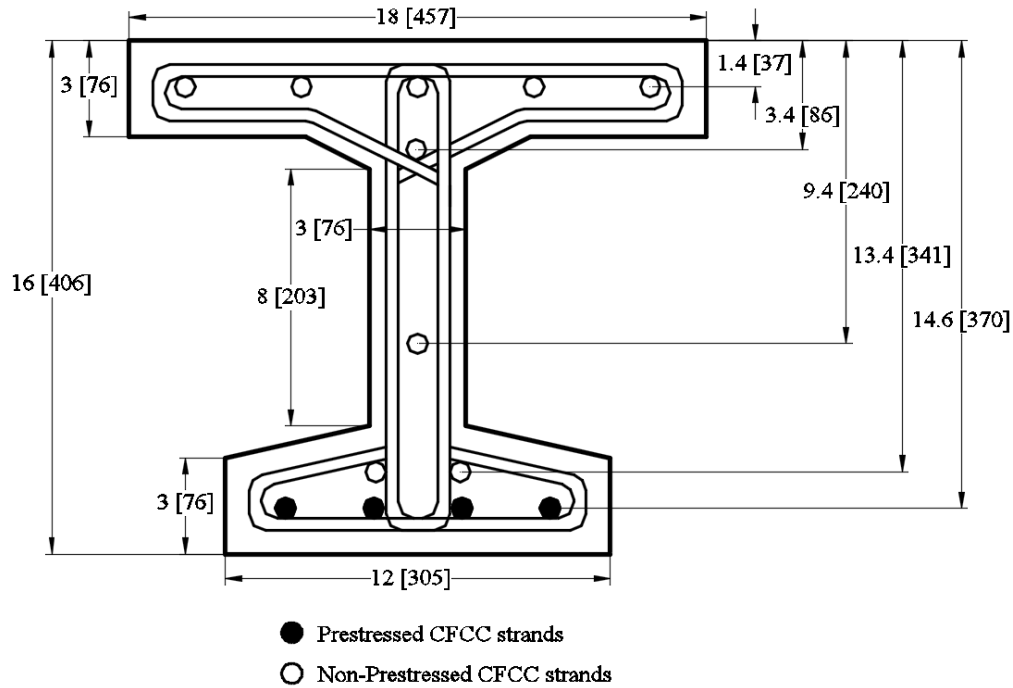


Figure 6.3-1 Cross-section of prestressed decked bulb T-beam, all dimensions are in in. [mm]

Each test beam was instrumented with 22 thermocouples Type-K. Eighteen thermocouples were placed at the mid-span and both quarter-span sections and four were placed at the end of the beam (Figure 6.3-2 through Figure 6.3-7). For the mid-span and quarter span sections, two thermocouples were placed at the top flange to measure concrete temperature, two in web and two in bottom flange at the level of prestressed strands to measure CFCC/steel temperature. The thermocouples were placed at their specified locations by drilling holes in the concrete section. The holes were sealed after placing the thermocouple using a thermal insulator. Six thermocouples were placed outside the beam to measure the air temperature of the fire chamber within 12 in. (305 mm) from the beam.

To simulate the traffic load in case of a fire event, all beams were simply supported and were loaded by a 110-kip (489-kN) MTS hydraulic actuator while conducting the fire test as shown in

Figure 6.3-7. The beams were loaded at their mid-span in a force control mode with a loading rate of 2 kip/minute (8.89 kN/minute) to a predetermined load. This predetermined load was maintained for the entire test until the failure of the beam. As this predetermined load represented typical service loads on the beams, it was taken slightly less than the anticipated cracking load of the beam, which was a function of the prestressing force. Predetermined load values of 14, 20, and 25 kip (62, 89, 111 kN) were applied on beams initially prestressed with prestressing forces of 72, 100, and 132 kip (320, 445, and 587 kN), respectively.

The testing scenario included loading the beam first before heating. After the load reached the assigned predetermined load level, the MTS actuator maintained the load level during the entire test in force-control mode.

After loading the beam, the door of the fire chamber was closed and the fire test started by heating the chamber following the time-temperature curve of ASTM E-119. The test continued until the beam was not able to support the applied load. After failure was confirmed, the fire testing ended and the fire chamber was allowed to cool down before the door was opened and the test specimen was inspected. The fire endurance for each beam was recorded as the time from the start of ASTM E119 temperature curve (start of the fire) to the failure of the beam. The nomenclature of each beam indicating the initial prestressing force, prestressing reinforcement, sustained load during testing and serial number of the beam is shown in Figure 6.3-8.

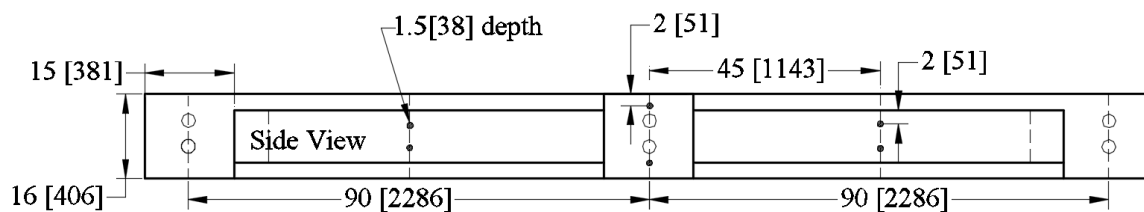


Figure 6.3-2 Side view of beam with thermocouple locations, all dimensions are in in. [mm]

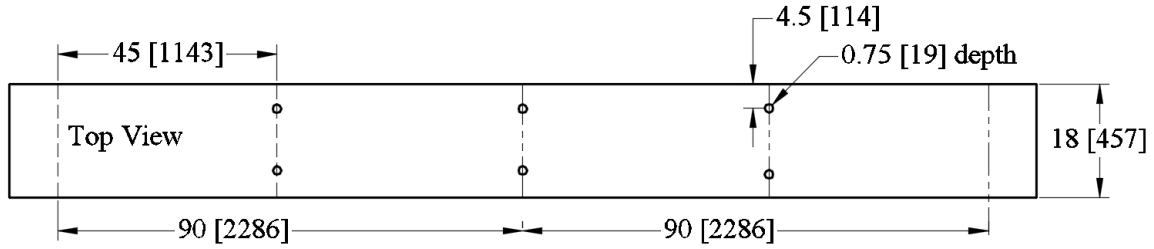


Figure 6.3-3 Thermocouple location in the beam, top view, all dimensions are in in. [mm]

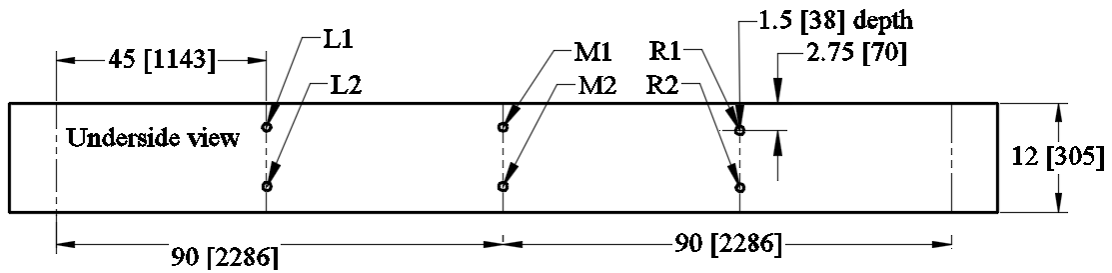


Figure 6.3-4 Thermocouple location in the beam, underside view, all dimensions are in in. [mm]

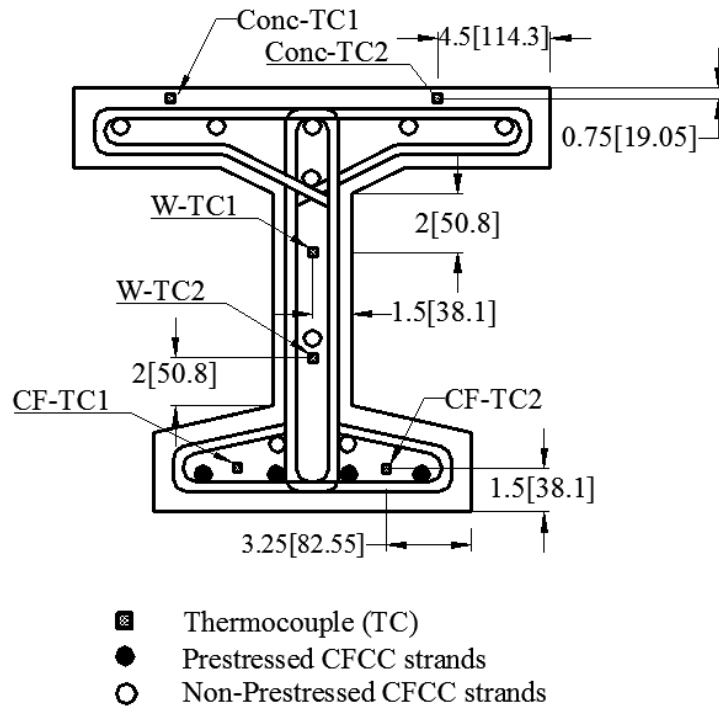


Figure 6.3-5 Thermocouple location in the quarter sections, all dimensions are in in. [mm]

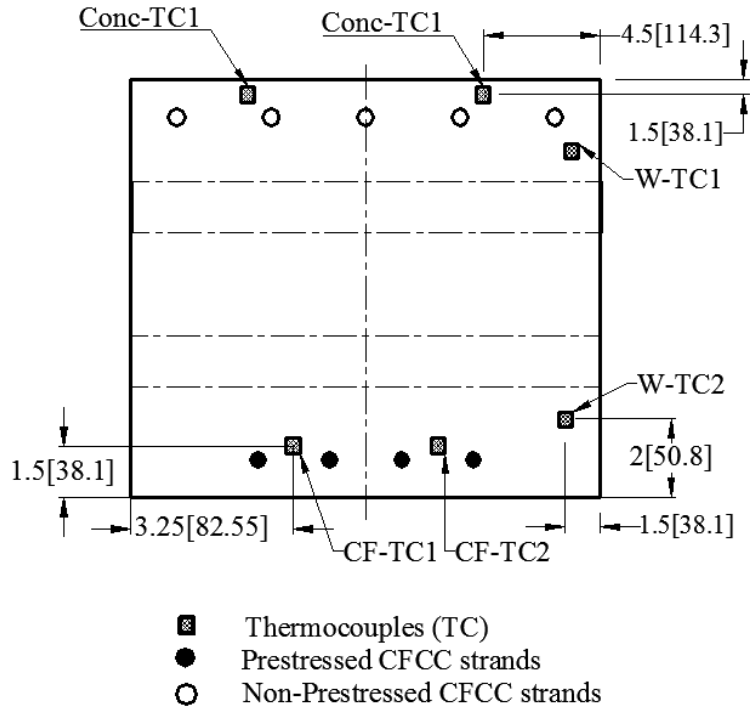


Figure 6.3-6 Thermocouple location in the mid-section, typical, all dimensions are in in. [mm]

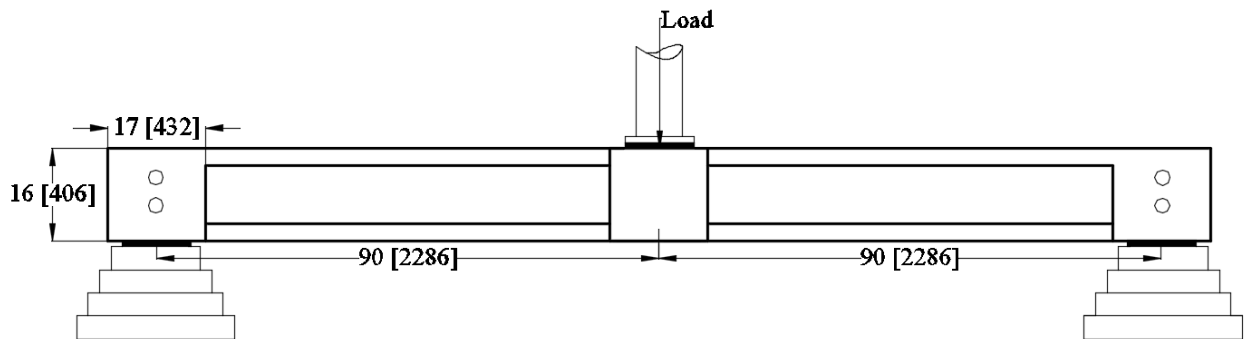


Figure 6.3-7 Sketch of test set-up, all dimensions are in in. [mm]

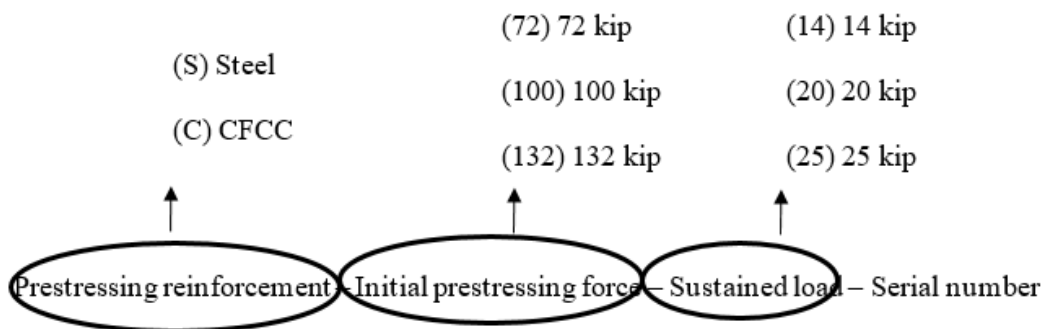


Figure 6.3-8 Beam notation

## 6.3.2 Test Results

### 6.3.2.1 Control beam S132-25-1

The first control beam (S132-25-1) was prestressed with steel strands. The initial prestressing force was 132 kip (587 kN) per beam and it was tested according to ASTM E119 with a central point load of 25 kip (111 kN). Linear transducer of hydraulic load actuator was connected to the data acquisition unit of the MTS to monitor the deflection of the beam. The beam was loaded to 25 kip (111 kN) with a rate of 2 kip/minute (8.9 kN/minute) in a force control mode. Since the applied load was less than the cracking load of the beam, no cracks were noticed under this load. The beam was exposed to fire (ASTM E119) to failure. The thermocouples were connected to the data acquisition unit to record the temperature.

First spalling of concrete was observed on the top flange of CFCC stirrup side of the beam. The beam started to lose stiffness and deflect after 50 minutes and failed completely after 98 minutes. The failure was detected by a sudden loss in the load carrying capacity. The mid-span deflection just before failure was 5.3 in. (136 mm). The side with CFCC stirrup was more effected by fire than the side with steel stirrup. At failure, the maximum recorded temperature of the prestressed steel strands was approximately 1082 °F (583 °C) and the maximum air temperature was 1827 °F (977 °C). At onset of deflection, these temperatures were 558 °F (292 °C) and 1655 °F (902 °C), respectively.

Figure 6.3-9 to Figure 6.3-10 show the test specimen before, during and after the fire test. In addition, and as shown in the time-deflection curve presented in Figure 6.3-13, the beam did not lose any stiffness during the first 50 minutes of the test, as there was no increase in deflection. Figure 6.3-14 shows the time-temperature curves for the six thermocouples placed at the mid-span section. The time-temperature curves for the six thermocouples placed at the level of prestressed steel strands are shown in Figure 6.3-15.



Figure 6.3-9 Beam S132-25-1 before fire



Figure 6.3-10 Beam S132-25-1 during fire



Figure 6.3-11 Beam S132-25-1 after fire



Figure 6.3-12 Rear view of Beam S132-25-1 after fire

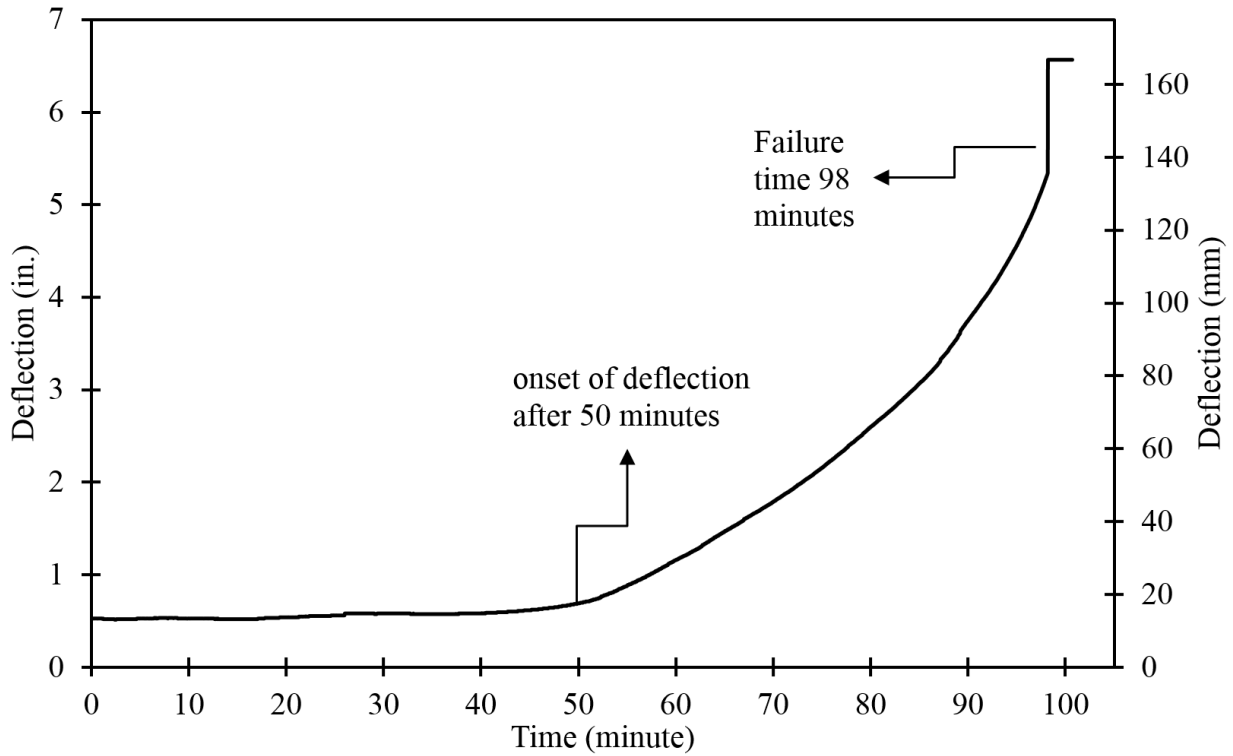


Figure 6.3-13 Time-deflection curve for Beam S132-25-1

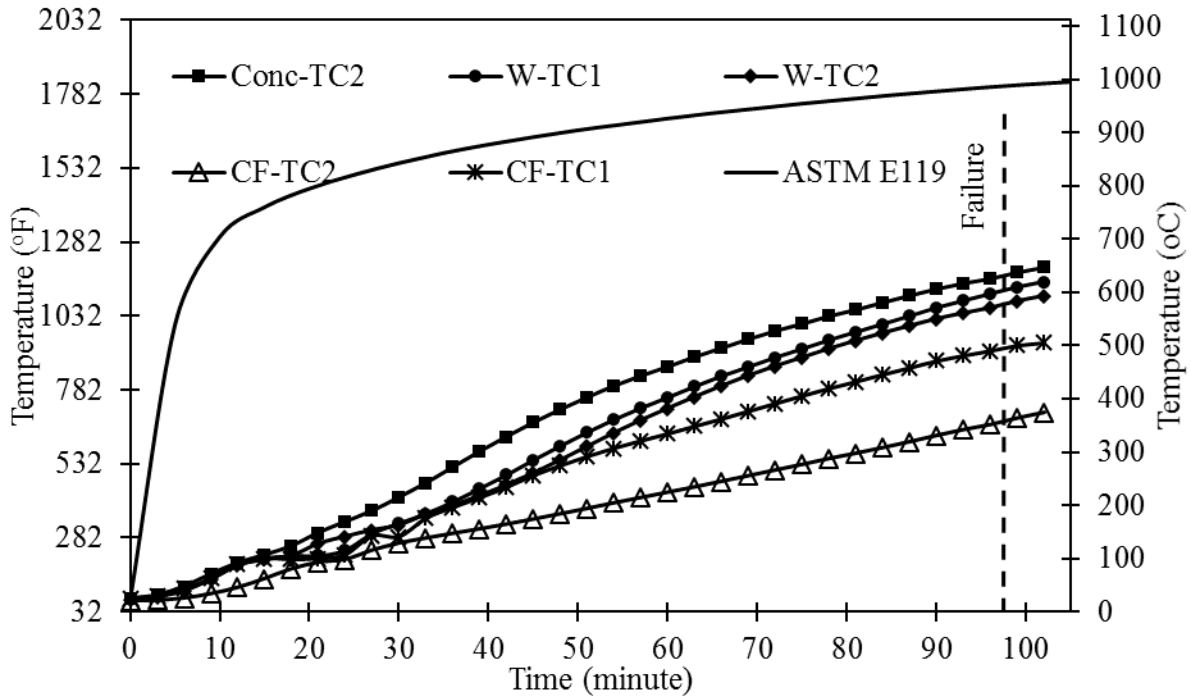


Figure 6.3-14 Time-temperature curves for Beam S132-25-1 at the mid-span

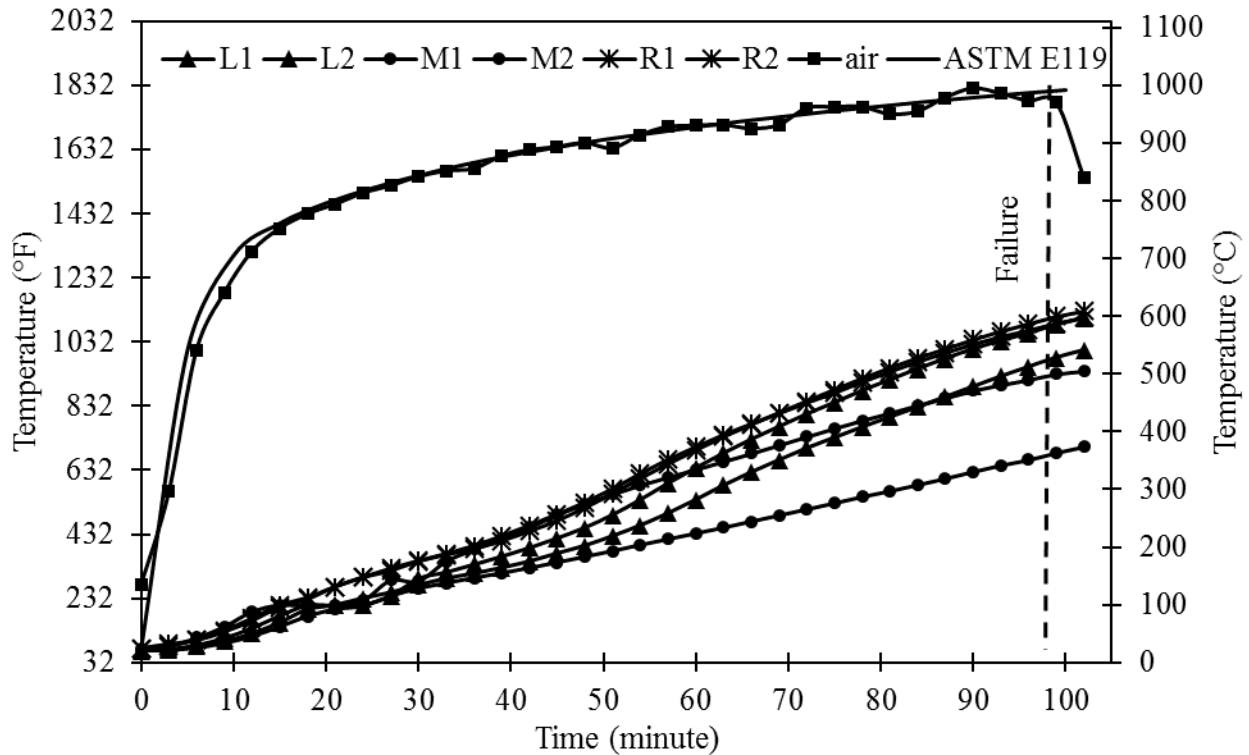


Figure 6.3-15 Time-temperature curves for Beam S132-25-1 at level of prestressed steel strands  
 6.3.2.2 Beam C72-14-1

Beam C72-14-1 was prestressed with CFCC strands. The initial prestressing force in the beam was 72 kip (320 kN) and it was tested according to ASTM E119 with a central point load of 14 kip (62 kN). Linear transducer of hydraulic load actuator was connected to the data acquisition unit of the MTS to monitor the deflection of the beam. Beam was loaded to 14 kip (62 kN) with a rate of 2 kip/minute (8.9 kN/minute) under force control. The thermocouples were connected to the data acquisition unit to record the temperature.

Figure 6.3-16 to Figure 6.3-20 show the test specimen before, during, and after the fire test. No deflection was noticed during the first 33 minutes after the start of the fire test. After 33 minutes, there was a gradual increase in deflection from 0.3 in. (8 mm) to 1.9 in. (48 mm). The failure took place after 69 minutes with a corresponding deflection of 6.3 in. (160 mm) (Figure 6.3-21). Figure 6.3-22 shows the temperature-time curve for the six thermocouples placed at the mid-span section. The temperature-time curve for the six thermocouples placed at the level of prestressed CFCC strands are shown in Figure 6.3-23.

No concrete crushing was observed near the mid span although slight spalling of concrete was observed on the top flange. At failure, the maximum temperature of the prestressed CFCC strand was 955 °F (513 °C) and the maximum air temperature was 1710 °F (932 °C). At onset of deflection, CFCC and air temperatures were 517 °F (269 °C) and 1560 °F (849 °C), respectively.



Figure 6.3-16 Beam C72-14-1 before fire



Figure 6.3-17 Beam C72-14-1 during fire



Figure 6.3-18 Burning of CFCC stirrups in Beam C72-14-1 during fire



Figure 6.3-19 Beam C72-14-1 after fire



Figure 6.3-20 Close-up view of Beam C72-14-1 after failure

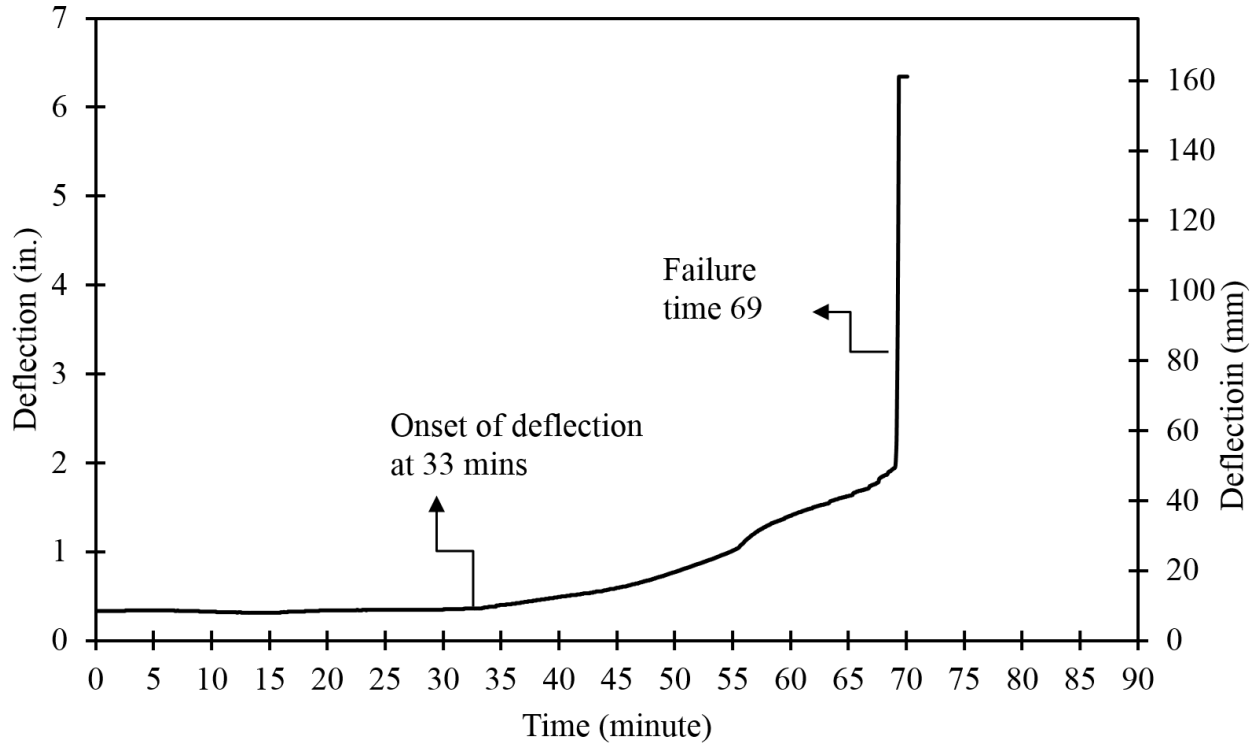


Figure 6.3-21 Time-deflection curve for Beam C72-14-1

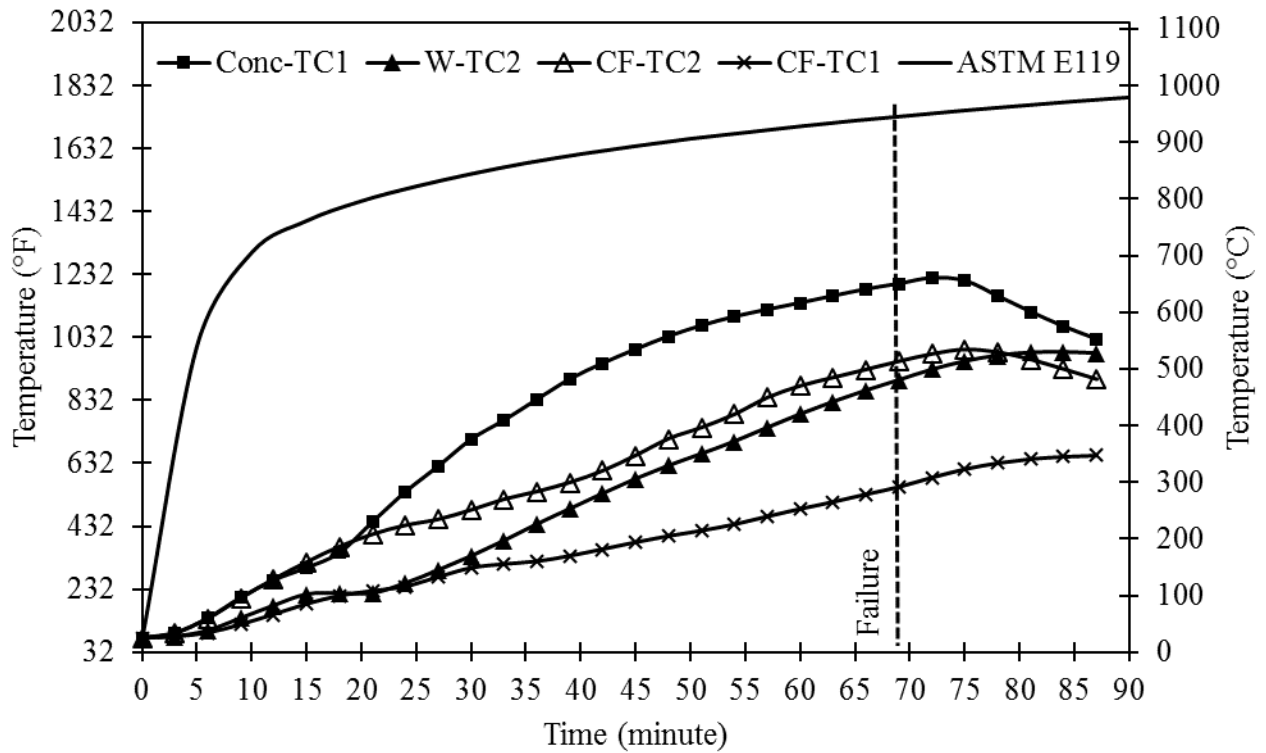


Figure 6.3-22 Time-temperature curves for Beam C72-14-1 at mid-span

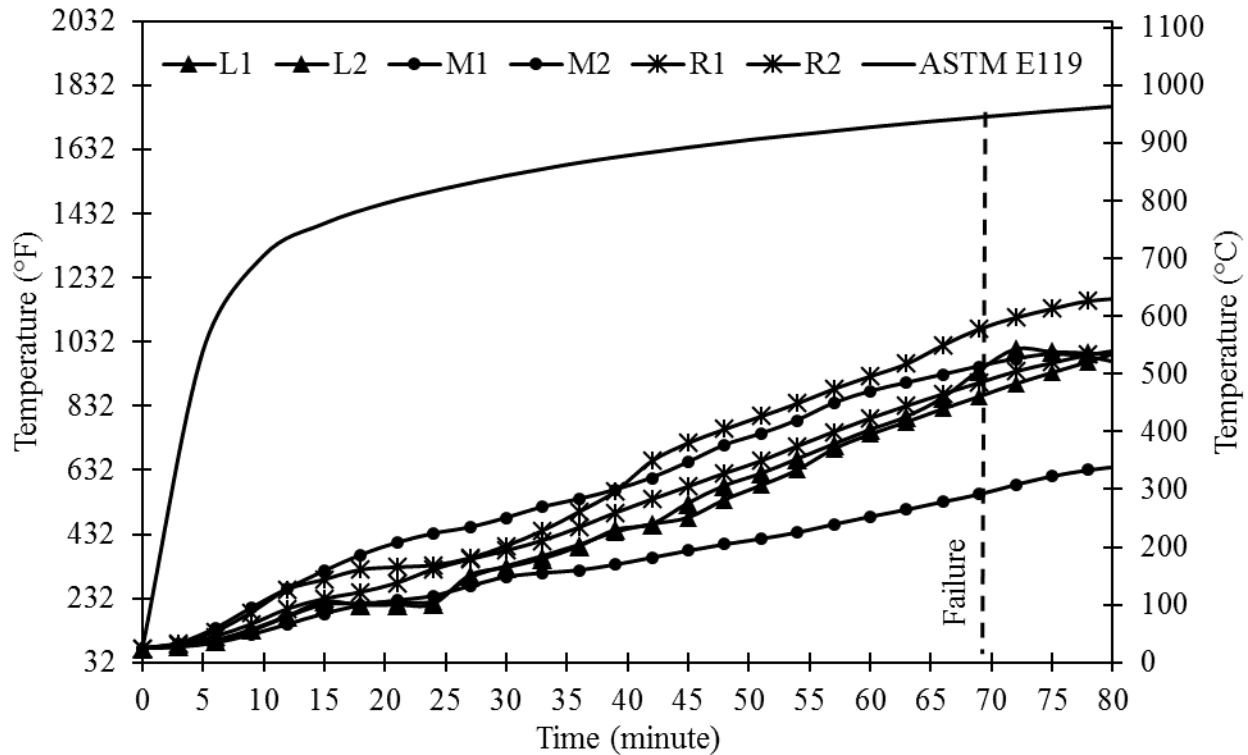


Figure 6.3-23 Time-temperature curves for Beam C72-14-1 at level of prestressed CFCC strands  
 6.3.2.3 Beam C100-20-1

Beam C100-20-1 was prestressed with CFCC strands. The initial prestressing force in the beam was 100 kip (445 kN) and it was tested according to ASTM E119 with a central point load of 20 kip (89 kN). Linear transducer of hydraulic load actuator was connected to the data acquisition unit of MTS to monitor the deflection of the beam. The beam was loaded to 20 kip (89 kN) with a rate of 2 kip/minute (8.9 kN/minute) under force control. The thermocouples were connected to the data acquisition unit to record the temperature.

Figure 6.3-24 to Figure 6.3-26 show the test specimen before and after the fire test. As shown in Figure 6.3-27, no deflection was noticed during the first 20 minutes at the start of the fire test. After 20 minutes, there was a gradual increase in the deflection from 0.6 in. (15 mm) to 1.7 in. (43 mm). The failure took place after 48 minutes with a corresponding deflection of 4.6 in. (117 mm). Heavy spalling of concrete was observed on the top flange. At failure, the maximum temperature of the prestressed CFCC strand was 956 °F (513 °C) and the maximum air temperature was 1650 °F (899 °C). At onset of deflection, CFCC and air temperatures were 595 °F (312 °C) and 1460 °F (793 °C), respectively. Figure 6.3-28 shows the temperature-time curve for the six thermocouples

placed at the mid-span section. The Time-temperature curves for the six thermocouples placed at the level of prestressed CFCC strands are shown in Figure 6.3-29.



Figure 6.3-24 Beam C100-20-1 before fire



Figure 6.3-25 Beam C100-20-1 after fire



Figure 6.3-26 Concrete spalling on CFCC stirrups side of Beam C100-20-1 after fire

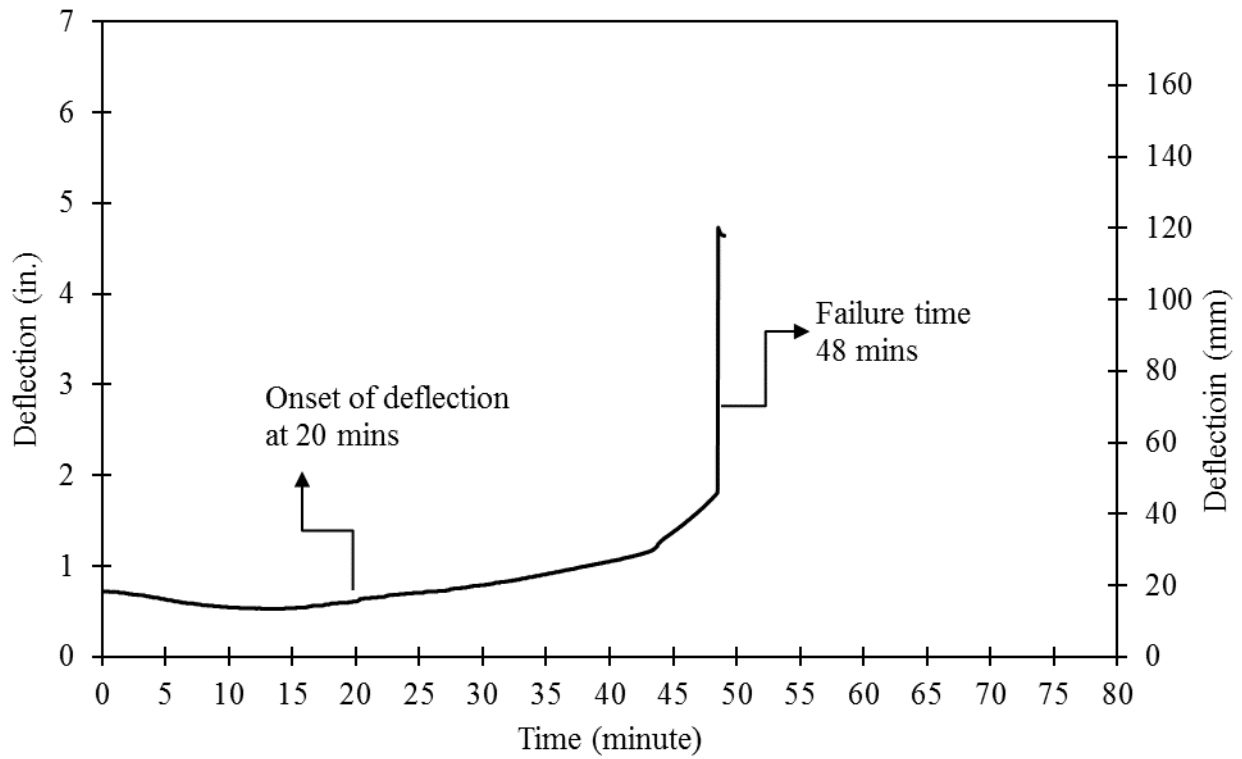


Figure 6.3-27 Time-deflection curve for Beam C100-20-1

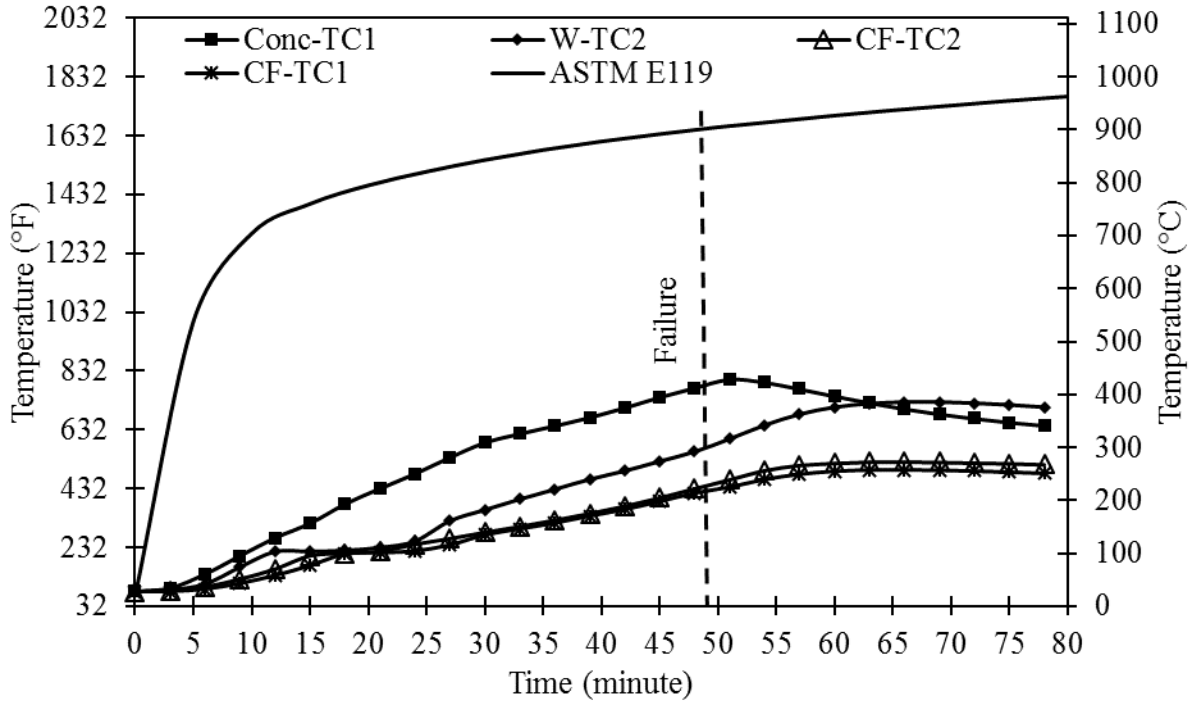


Figure 6.3-28 Time-temperature curves for Beam C100-20-1 at mid-span

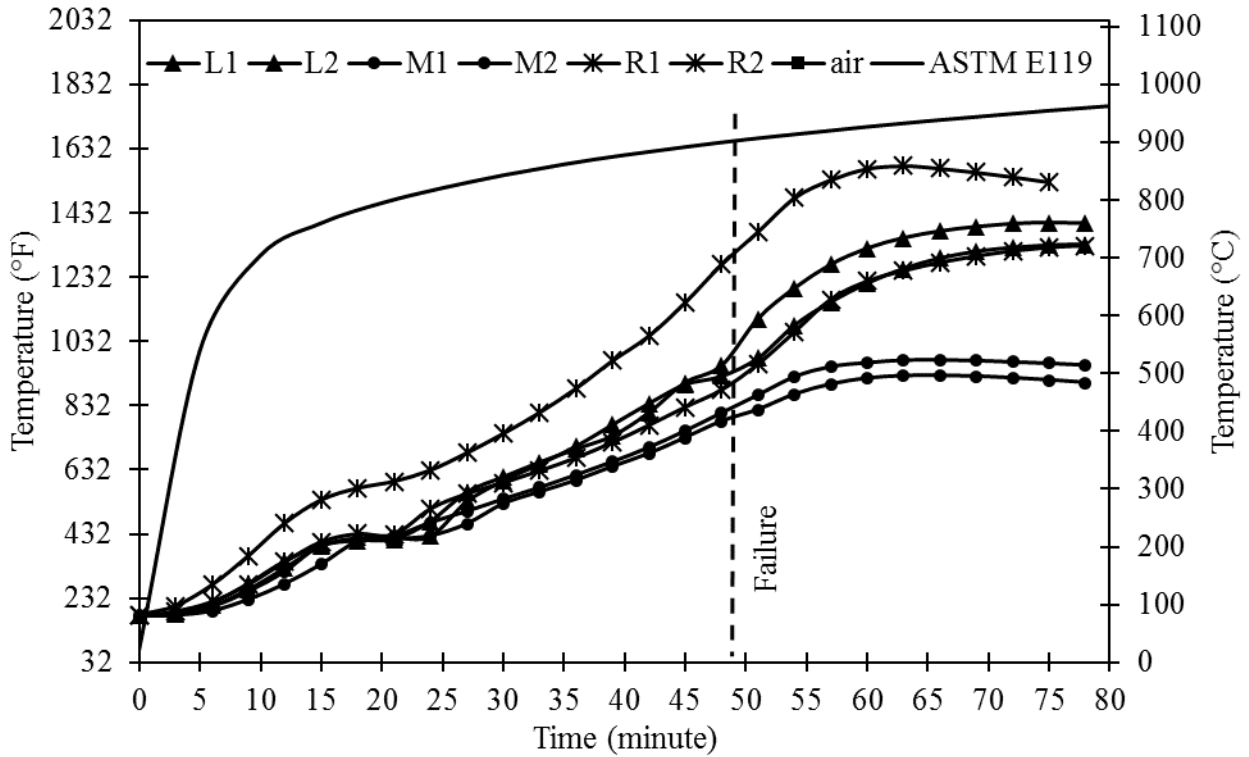


Figure 6.3-29 Time-temperature curves for Beam C100-20-1 at prestressed CFCC strands

#### 6.3.2.4 Beam C100-20-2

Beam C100-20-2 was prestressed with CFCC strands. The initial prestressing force in the beam was 100 kip (449 kN) and it was tested according to ASTM E119 with a central point load of 20 kip (89 kN). Linear transducer of hydraulic load actuator was connected to the data acquisition unit of MTS to monitor the deflection of the beam. The beam was loaded to 20 kip (89 kN) with a rate of 2 kip/minute (8.9 kN/minute) under force control. The thermocouples were connected to the data acquisition unit to record the temperature.

Figure 6.3-30 to Figure 6.3-32 show the test specimen before and after the fire test. Figure 6.3-33 shows time-deflection curve for the beam during the test. No deflection was noticed during the first 30 minutes at the start of the fire test. After 30 minutes, there was a gradual increase in the deflection from 0.6 in. (15 mm) to 2.4 in. (61 mm). The failure took place after 52 minutes with a corresponding deflection of 6.4 in. (153 mm). At failure, the maximum temperature of the prestressed CFCC strand was 686 °F (363 °C) and the maximum air temperature was 1671 °F (910 °C). At onset of deflection, CFCC and air temperatures were 396 °F (202°C) and 1552 °F (844 °C), respectively. Figure 6.3-34 shows the time-temperature curve for the six thermocouples placed at the mid-span section. The time-temperature curves for the six thermocouples placed at the level of prestressed CFCC strands are shown in Figure 6.3-35



Figure 6.3-30 Beam C100-20-2 before fire



Figure 6.3-31 Beam C100-20-2 after fire



Figure 6.3-32 Concrete spalling of bottom flange of Beam C100-20-2 after fire, bottom side view

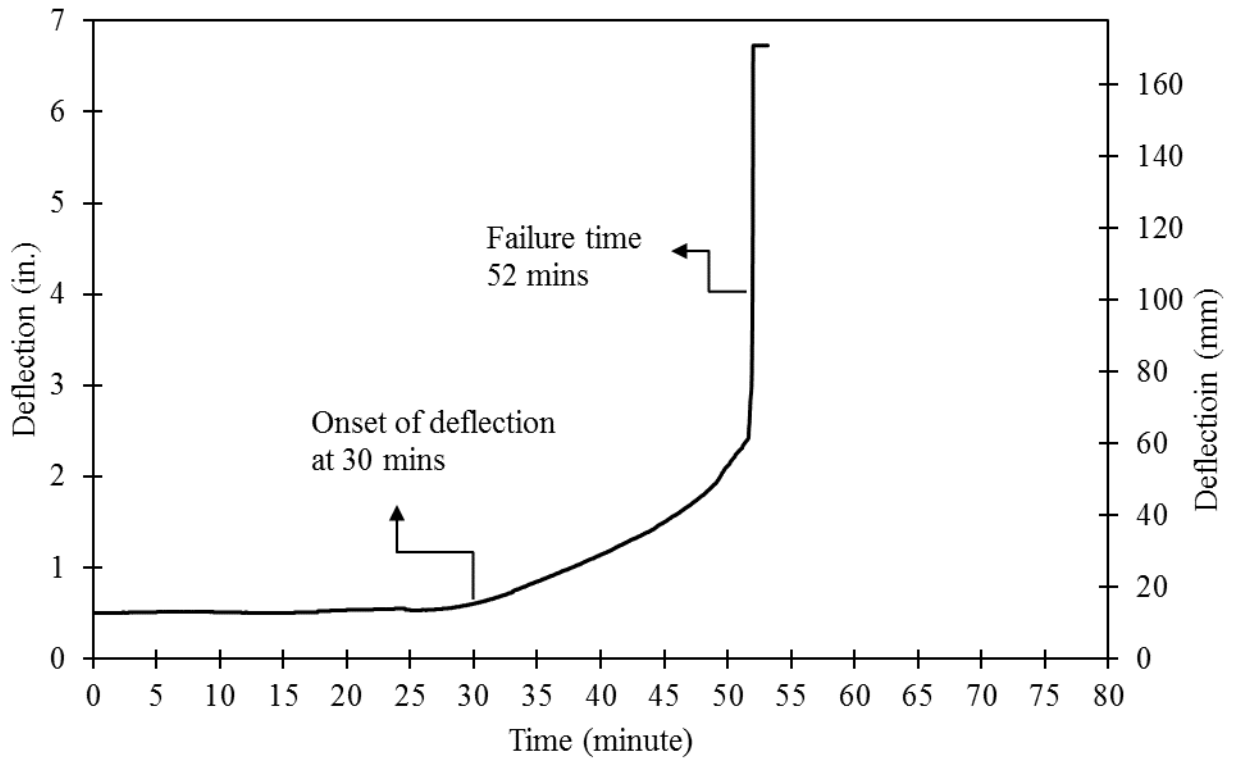


Figure 6.3-33 Time-deflection curve for Beam C100-20-2

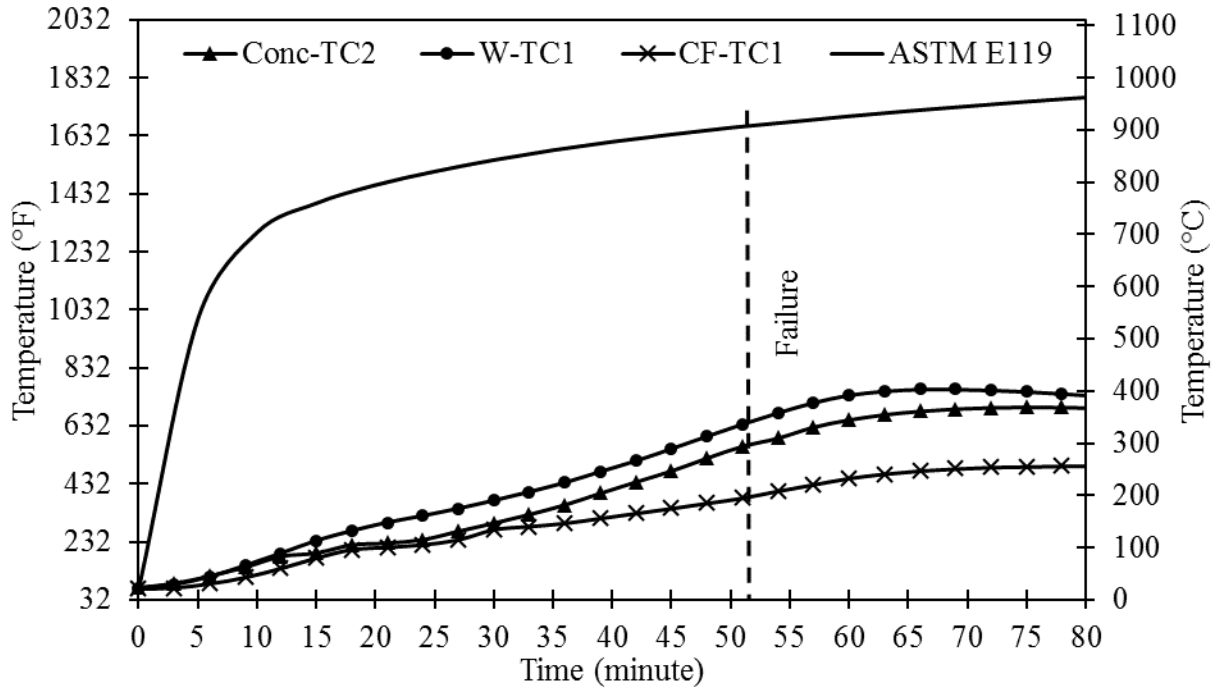


Figure 6.3-34 Time-temperature curves for Beam C100-20-2 at mid-span

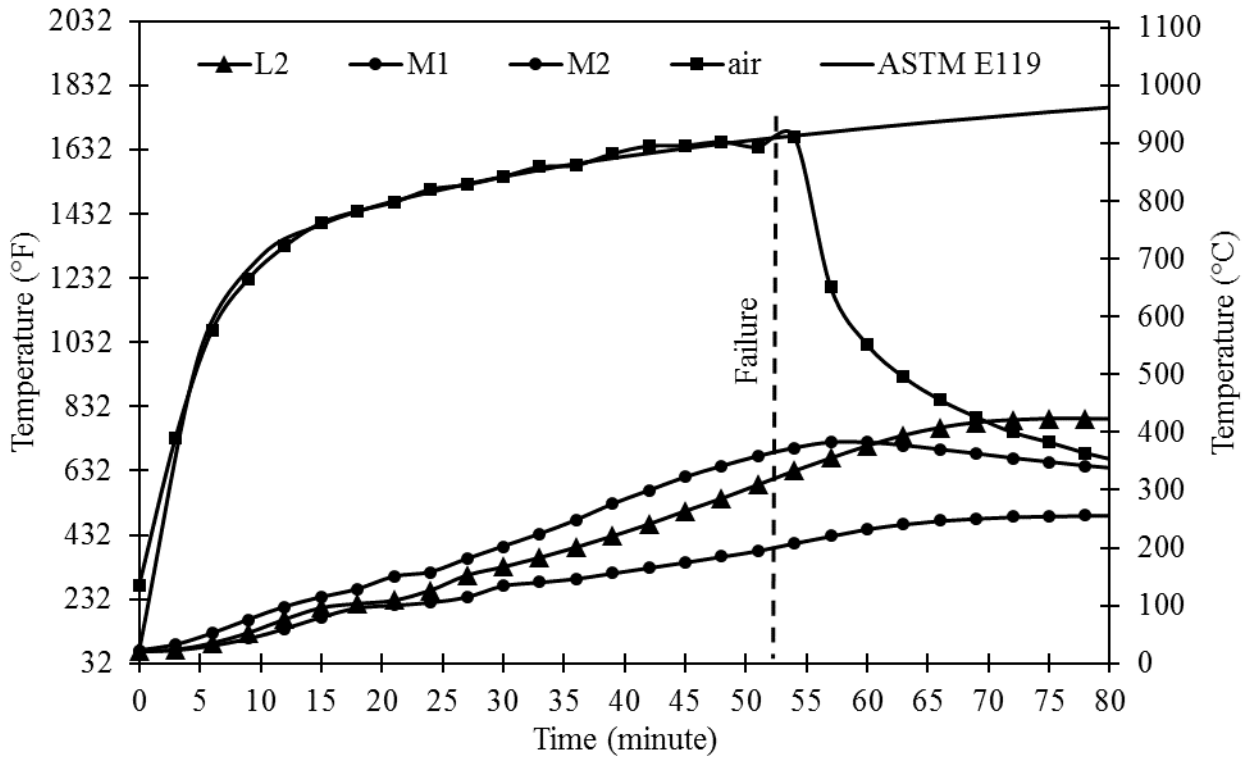


Figure 6.3-35 Time-temperature curves for Beam C100-20-2 at prestressed CFCC strands

#### 6.3.2.5 Beam C100-20-3

Beam C100-20-3 was prestressed with CFCC strands. The initial prestressing force in the beam was 100 kip (445 kN) and it was tested according to ASTM E119 with a central point load of 20 kip (89 kN). Linear transducer of hydraulic load actuator was connected to the data acquisition unit of MTS to monitor the deflection of the beam. The beam was loaded to 20 kip (89 kN) with a rate of 2 kip/minute (8.9 kN/minute) under force control. The thermocouples were connected to the data acquisition unit to record the temperature.

Figure 6.3-36 to Figure 6.3-38 show the test specimen before and after the fire test. Figure 6.3-39 shows time-deflection curve for the beam during the test. No deflection was noticed during the first 23 minutes at the start of the fire test. After 23 minutes, there was a gradual increase in the deflection from 0.5 in. (13 mm) to 1.8 in. (46 mm). The failure took place after 53 minutes with a corresponding deflection of 6.7 in. (171 mm). At failure, the maximum temperature of the prestressed CFCC strand was 678 °F (359 °C) and the maximum air temperature was 1680 °F (915 °C). At onset of deflection, CFCC and air temperatures were 277 °F (136 °C) and 1493 °F (812 °C), respectively.

Figure 6.3-40 shows the time-temperature curve for the six thermocouples placed at the mid-span section. The time-temperature curves for the six thermocouples placed at the level of prestressed CFCC strands are shown in Figure 6.3-41.



Figure 6.3-36 Beam C100-20-3 before fire



Figure 6.3-37 Beam C100-20-3 after fire



Figure 6.3-38 Carbon fiber filaments after burning of epoxy adhesive in Beam C100-20-3

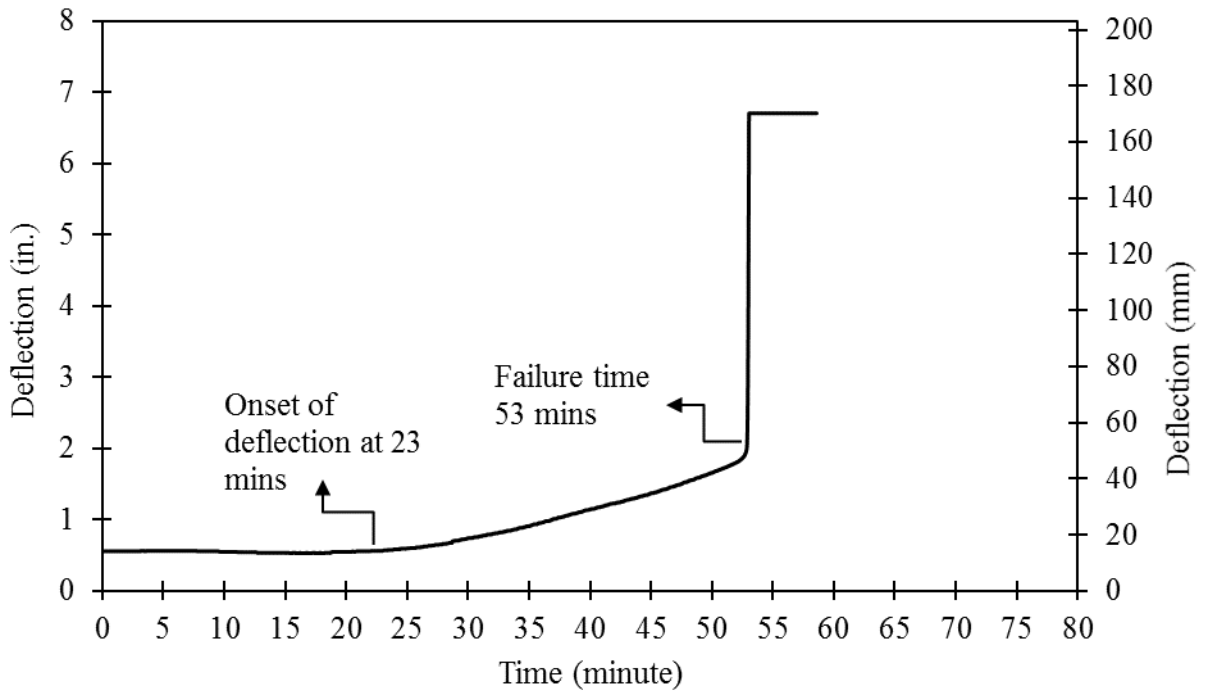


Figure 6.3-39 Time-deflection curve for Beam C100-20-3

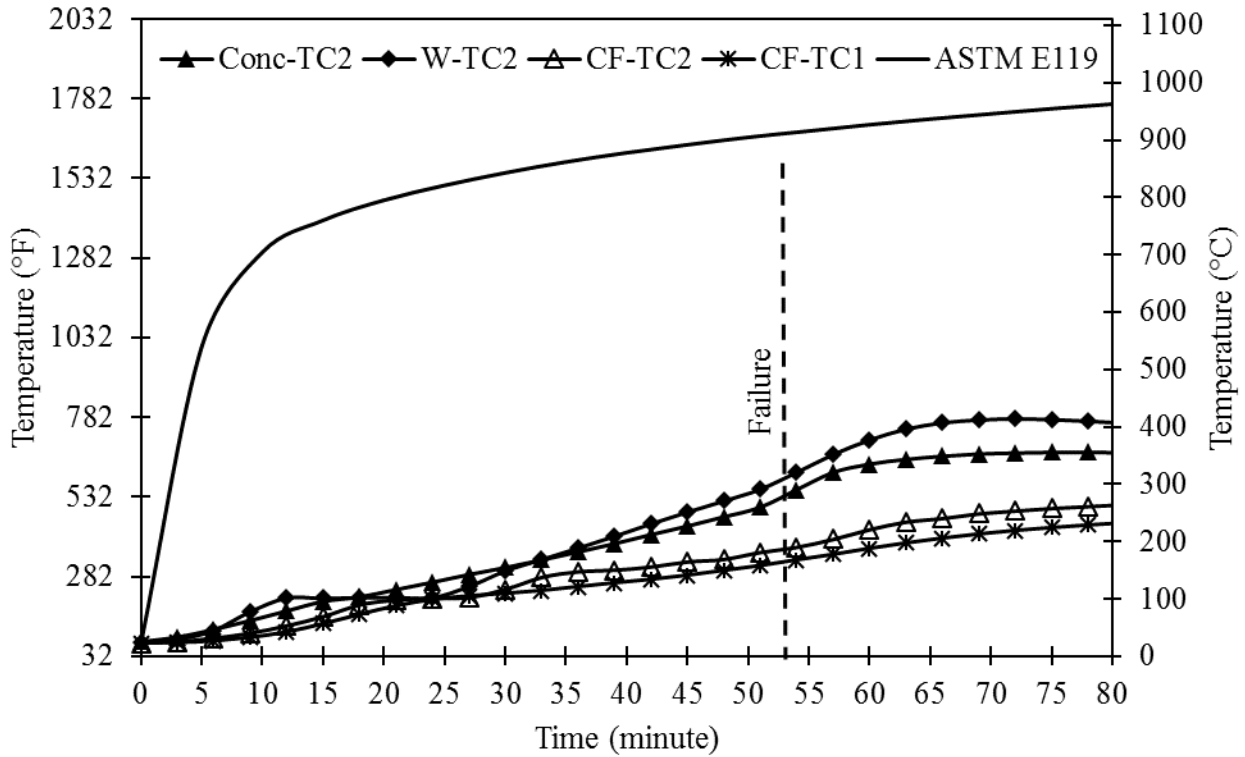


Figure 6.3-40 Time-temperature curve for Beam C100-20-3 at mid-span

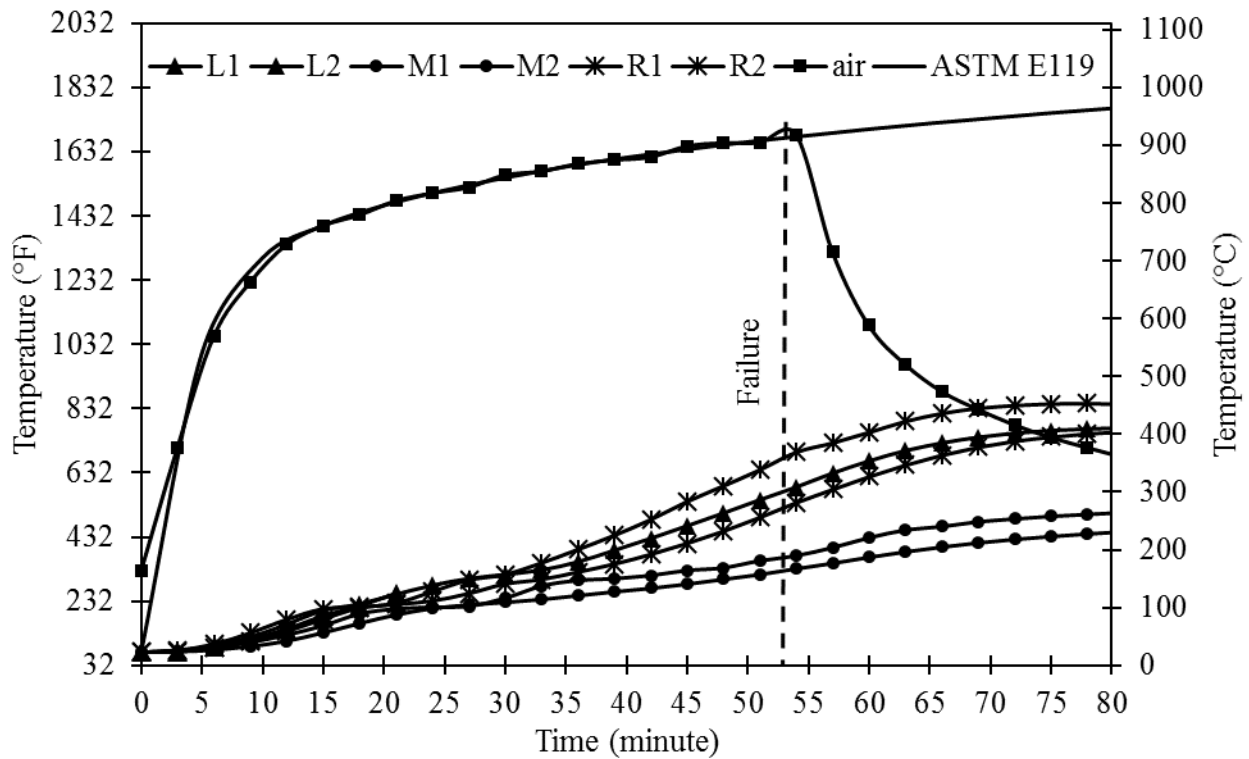


Figure 6.3-41 Time-temperature curves for Beam C100-20-3 at prestressed CFCC strands

#### 6.3.2.6 Beam C100-20-4

Beam C100-20-4 was prestressed with CFCC strands. The initial prestressing force in the beam was 100 kip (445 kN) and it was tested according to ASTM E119 with a central point load of 20 kip (89 kN). Linear transducer of hydraulic load actuator was connected to the data acquisition unit of MTS to monitor the deflection of the beam. The beam was loaded to 20 kip (89 kN) with a rate of 2 kip/minute (8.9 kN/minute) under force control. The thermocouples were connected to the data acquisition unit to record the temperature.

Figure 6.3-42 to Figure 6.3-44 show the test specimen before and after the fire test. Figure 6.3-45 shows deflection-time curve for the beam during the test. No deflection was noticed during the first 21 minutes at the start of the fire test. After 21 minutes, there was a gradual increase in the deflection from 0.5 in. (13 mm) to 1.9 in. (48 mm). The failure took place after 58 minutes with a corresponding deflection of 6.2 in. (157 mm). At failure, the maximum temperature of the prestressed CFCC strand was 771 °F (322 °C) and the maximum air temperature was 1706 °F (930 °C). At onset of deflection these temperatures were 293 °F (145 °C) and 1470 °F (799 °C), respectively.

Figure 6.3-46 shows the time-temperature curves for the six thermocouples placed at the mid-span section. The time-temperature curves for the six thermocouples placed at the level of prestressed CFCC strands are shown in Figure 6.3-47.



Figure 6.3-42 Beam C100-20-4 before fire



Figure 6.3-43 Beam C100-20-4 after fire



Figure 6.3-44 Concrete spalling of Beam C100-20-4 after fire

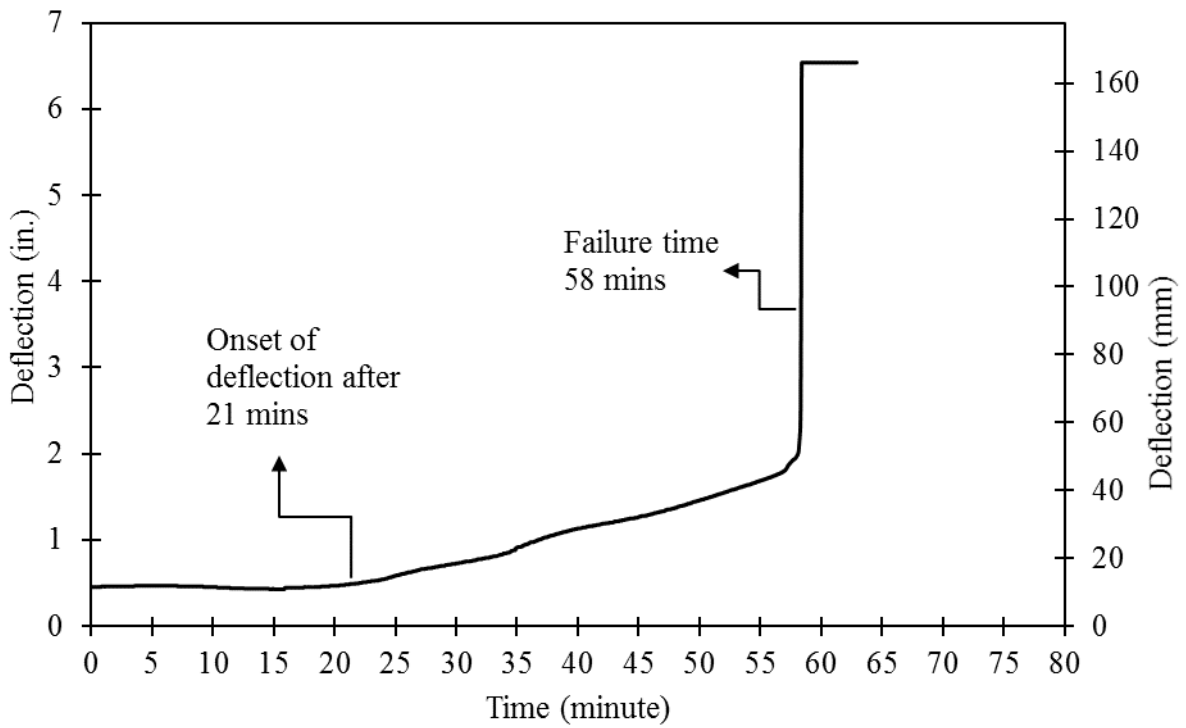


Figure 6.3-45 Time-deflection curve for Beam C100-20-4

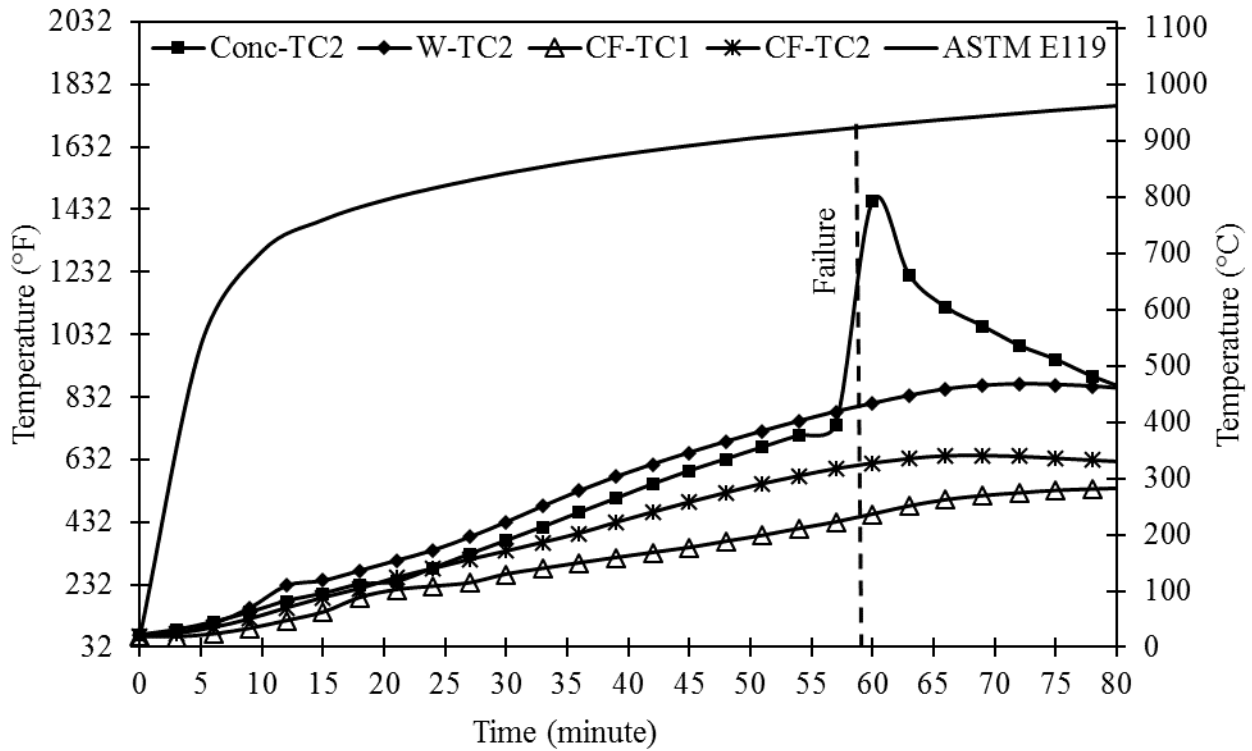


Figure 6.3-46 Time-temperature curves for Beam C100-20-4 in the mid-span

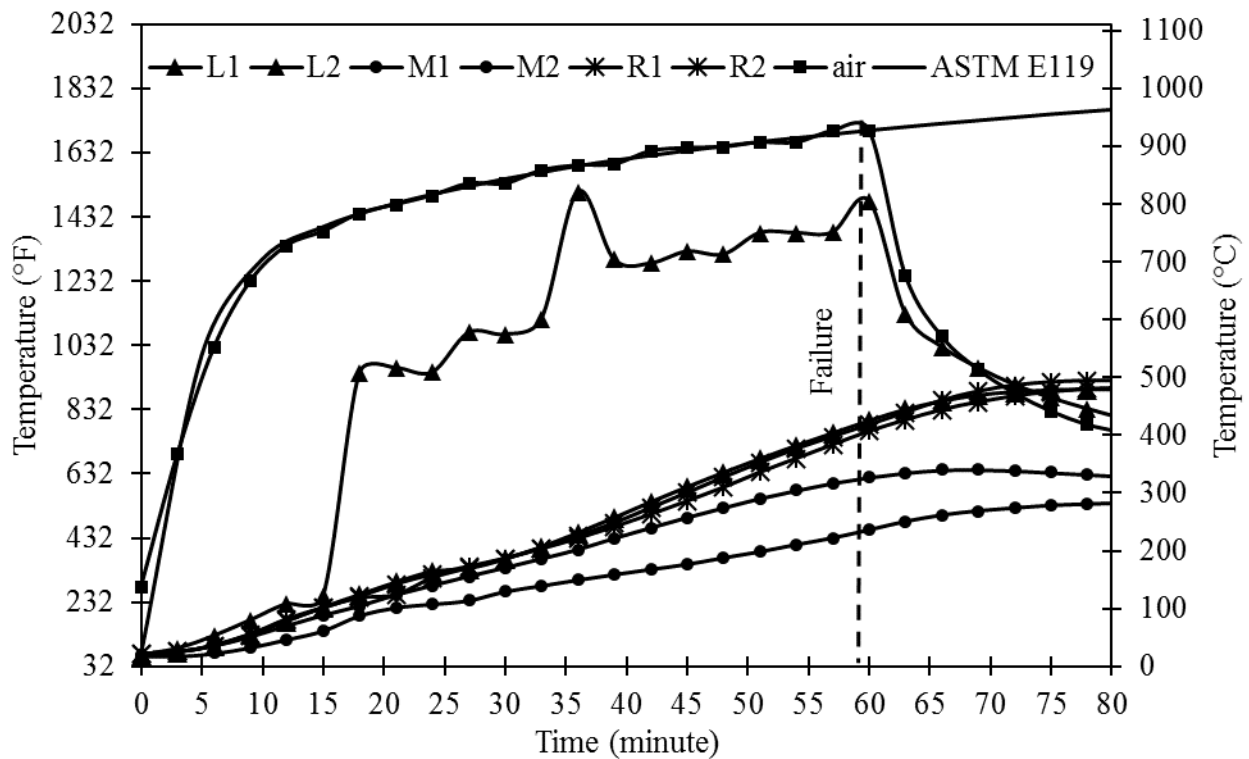


Figure 6.3-47 Time-temperature curves for Beam C100-20-4 at prestressed CFCC strands

#### 6.3.2.7 Beam C100-20-5

Beam C100-20-5 was prestressed with CFCC strands. The initial prestressing force in the beam was 100 kip (445 kN) and it was tested according to ASTM E119 with a central point load of 20 kip (89 kN). Linear transducer of hydraulic load actuator was connected to the data acquisition unit of MTS to monitor the deflection of the beam. The beam was loaded to 20 kip (89 kN) with a rate of 2 kip/minute (8.9 kN/minute) under force control. The thermocouples were connected to the data acquisition unit to record the temperature.

Figure 6.3-48 to Figure 6.3-49 show the test specimen before and after the fire test. Figure 6.3-51 shows deflection-time curve for the beam during the test. No deflection was noticed during the first 20 minutes at the start of the fire test. After 20 minutes, there was a gradual increase in the deflection from 0.4 in. (10 mm) to 1.6 in. (41 mm). The failure took place after 52 minutes with a corresponding deflection of 6.7 in. (170 mm). At failure, the maximum temperature of the prestressed CFCC strand was 623 °F (328 °C) and the maximum air temperature was 1665 °F (907 °C). At onset of deflection these temperatures were 254 °F (123 °C) and 1463 °F (795 °C), respectively.

Figure 6.3-52 shows the time-temperature curves for the six thermocouples placed at the mid-span section. The time-temperature curves for the six thermocouples placed at the level of prestressed CFCC strands are shown in Figure 6.3-53.



Figure 6.3-48 Beam C100-20-5 before fire



Figure 6.3-49 Beam C100-20-5 during fire



Figure 6.3-50 Beam C100-20-5 after fire

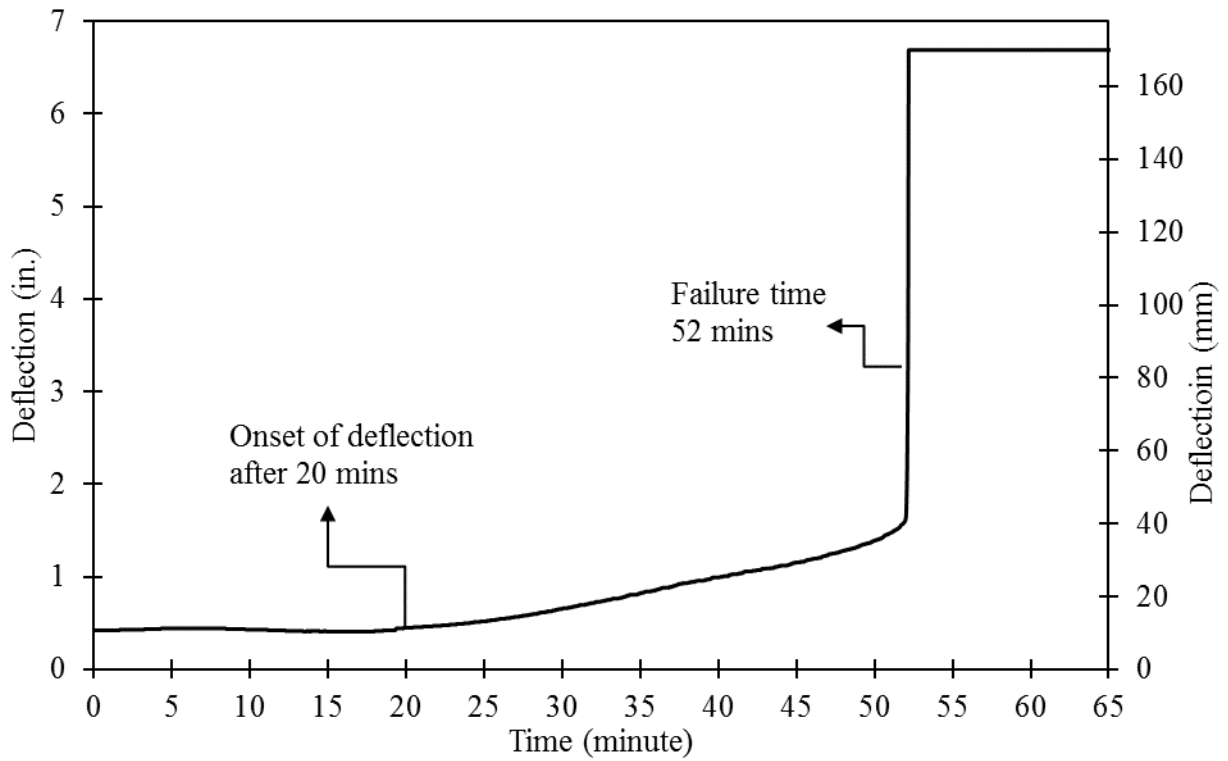


Figure 6.3-51 Time-deflection curve for Beam C100-20-5

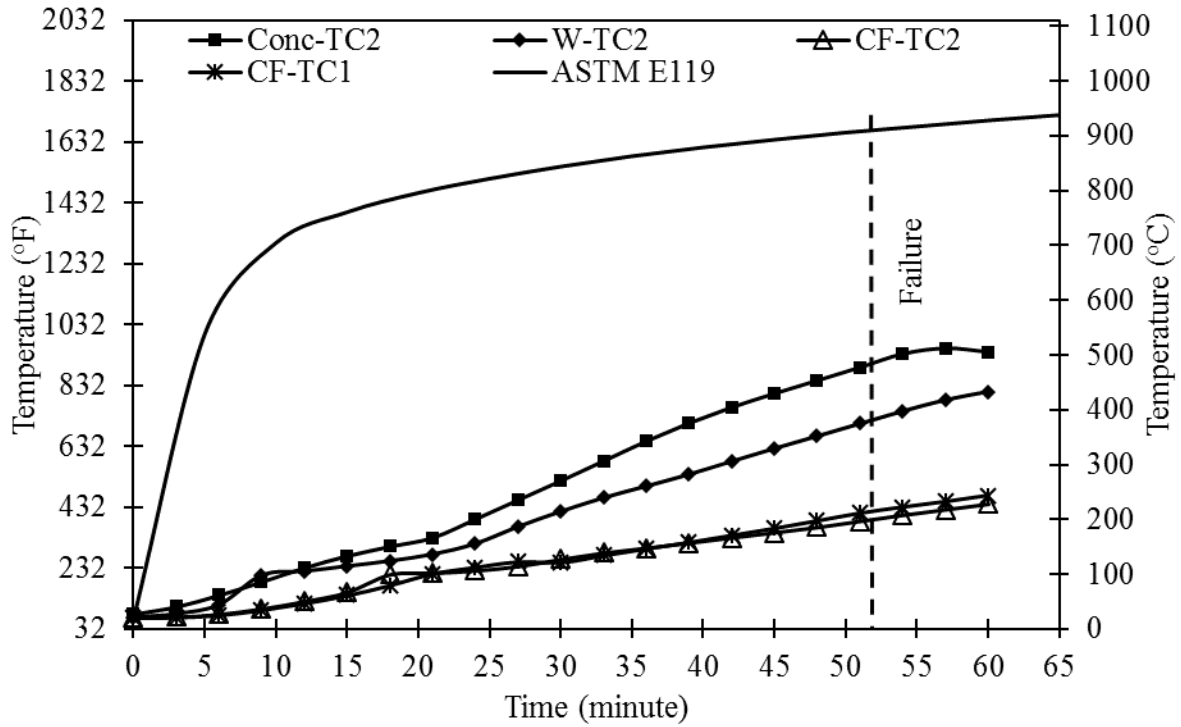


Figure 6.3-52 Time-temperature curves for Beam C100-20-5 at mid-span

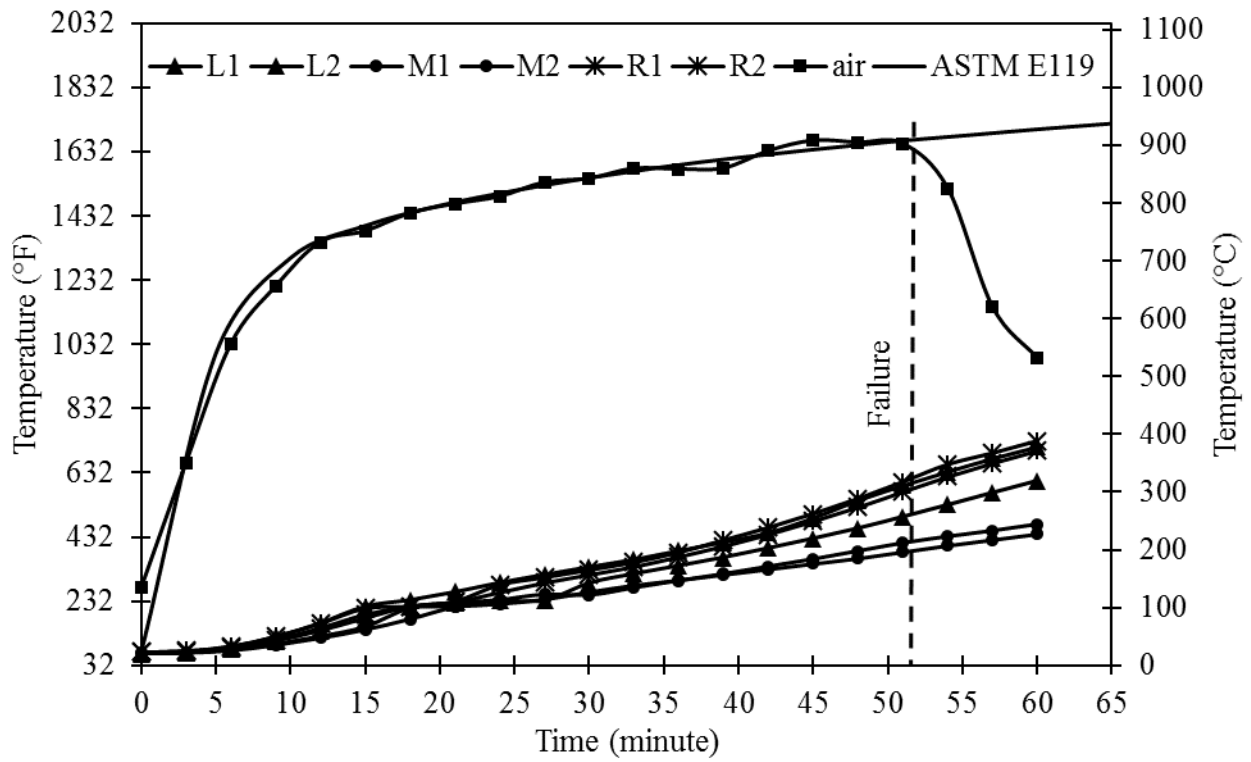


Figure 6.3-53 Time-temperature curves for Beam C100-20-5 at prestressed CFCC strands

#### 6.3.2.8 Beam C132-25-1

Beam C132-25-1 was prestressed with CFCC strands. The initial prestressing force in the beam was 132 kip (587 kN) and it was tested according to ASTM E119 with a central point load of 25 kip (111 kN). Linear transducer of hydraulic load actuator was connected to the data acquisition unit of MTS to monitor the deflection of the beam. The beam was loaded to 25 kip (111 kN) with a rate of 2 kip/minute (8.9 kN/minute) under force control. The thermocouples were connected to the data acquisition unit to record the temperature.

Figure 6.3-54 to Figure 6.3-56 show the test specimen before and after the fire test. Figure 6.3-57 shows time-deflection curve for the beam during the test. No deflection was noticed during the first 13 minutes at the start of the fire test. After 13 minutes, there was a gradual increase in the deflection from 0.7 in. (18 mm) to 2.7 in. (68 mm). The failure took place after 47 minutes with a corresponding deflection of 6.7 in. (170 mm). At failure, the maximum temperature of the prestressed CFCC strand was 803 °F (428 °C) and the maximum air temperature was 1664 °F (907 °C). At onset of deflection, these temperatures were 269 °F (132 °C) and 1357 °F (736 °C), respectively.

Figure 6.3-58 shows the time-temperature curves for the six thermocouples placed at the mid-span section. The time-temperature curves for the six thermocouples placed at the level of prestressed CFCC strands are shown in Figure 6.3-59.



Figure 6.3-54 Beam C132-25-1 before fire



Figure 6.3-55 Beam C132-25-1 after fire



Figure 6.3-56 Close up view of mid-section of Beam C132-25-1 just after failure

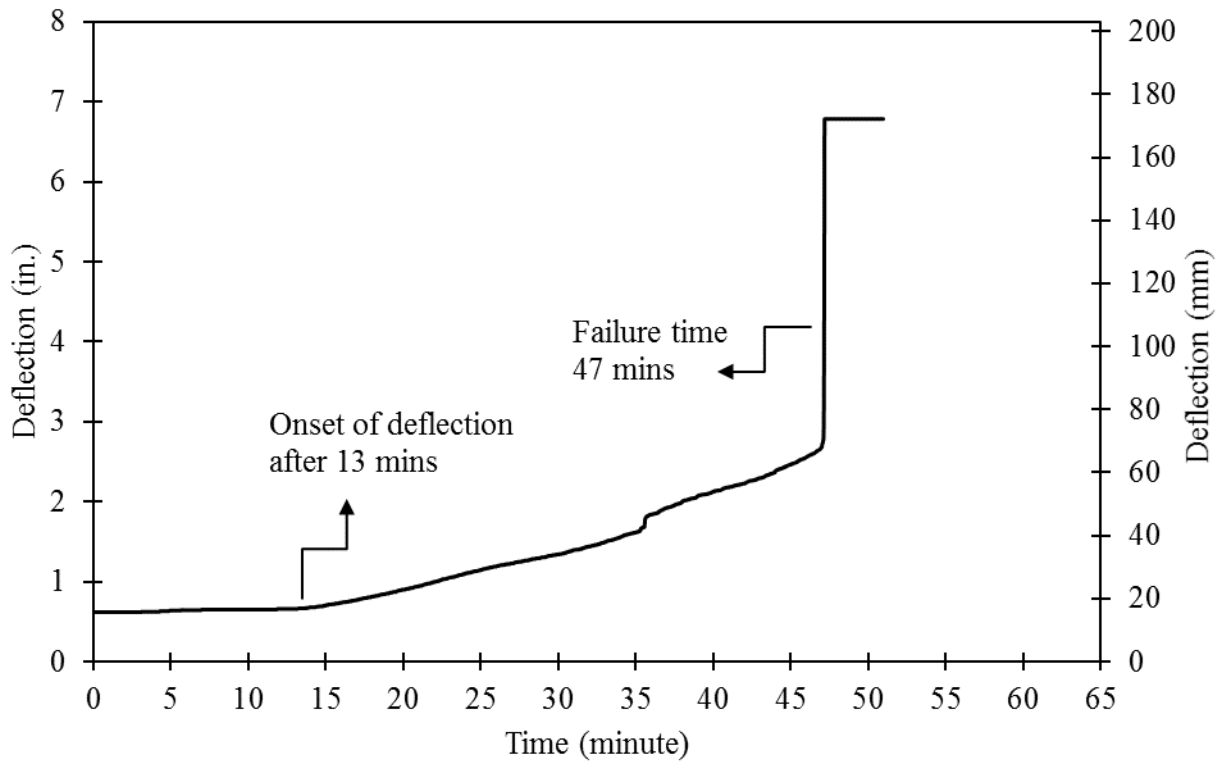


Figure 6.3-57 Time-deflection curve for Beam C132-25-1

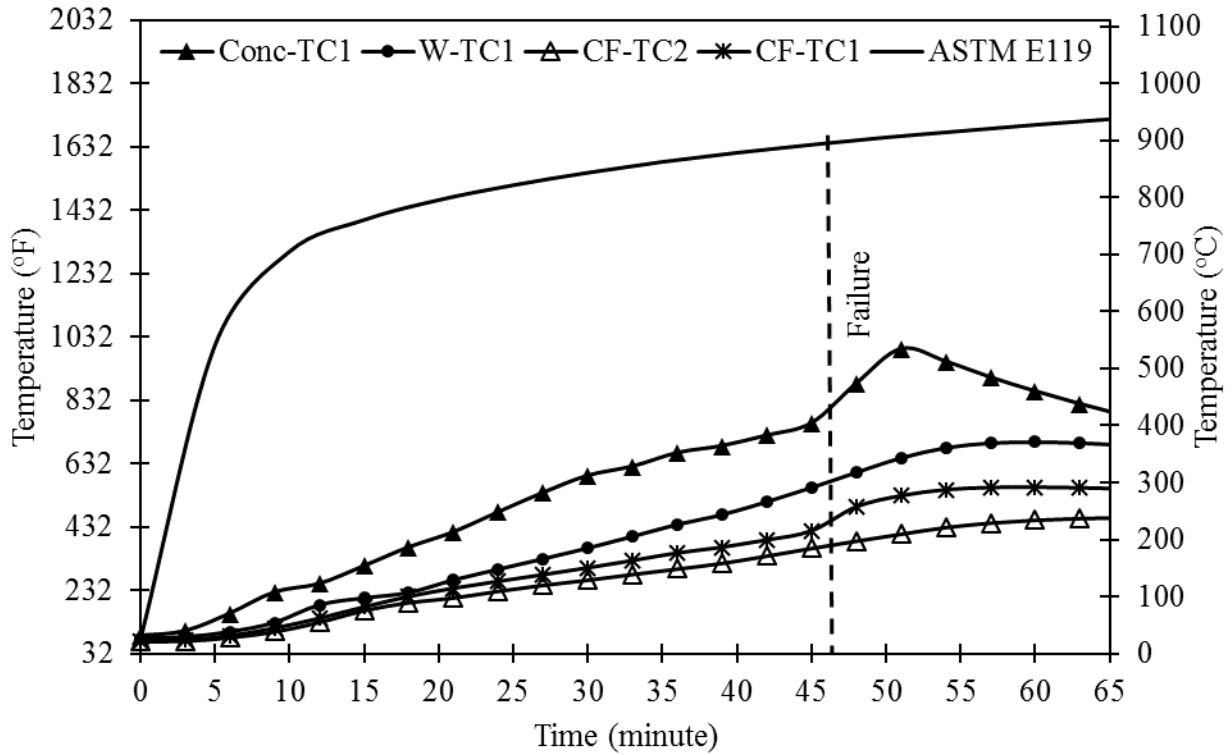


Figure 6.3-58 Time-temperature curves for Beam C132-25-1 at mid-span

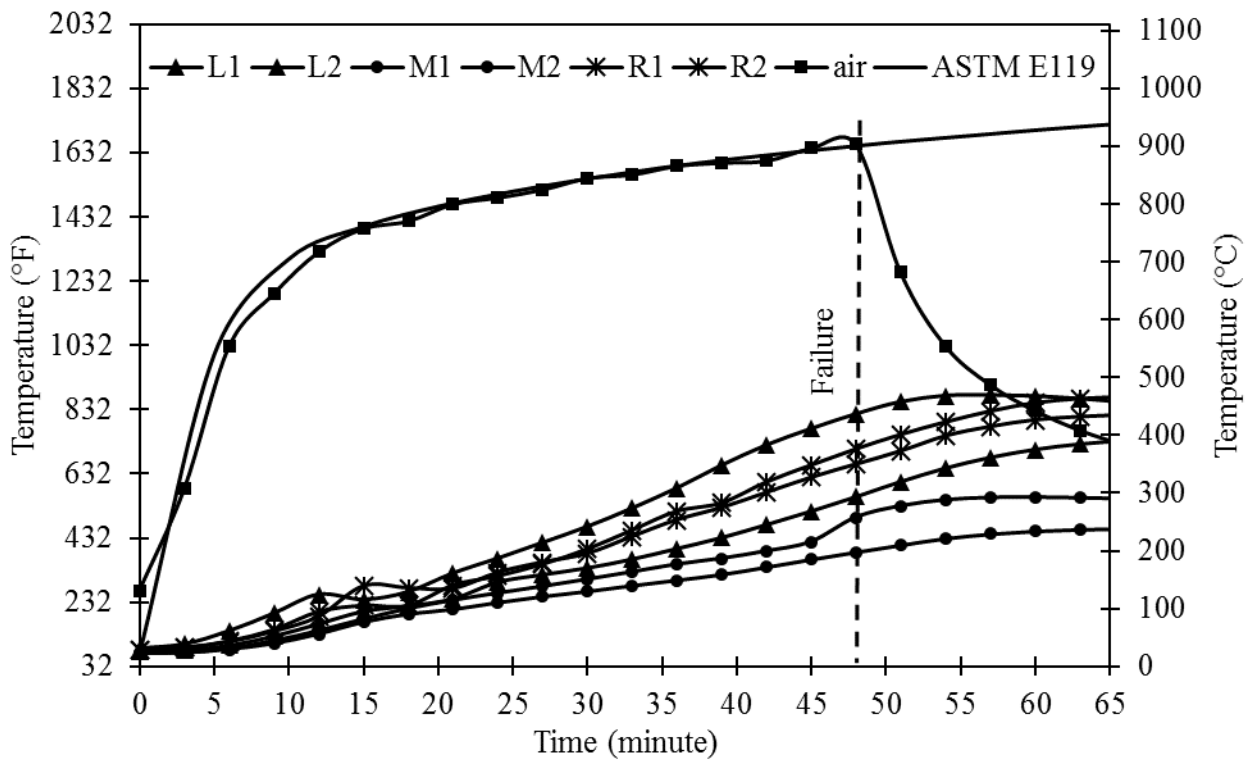


Figure 6.3-59 Time-temperature curves for Beam C132-25-1 at prestressed CFCC strands

#### **6.4 Discussion of Test Results**

The fire endurance of all test beams is shown in Table 6.4-1. As anticipated, the overall fire endurance of beams prestressed with CFCC strands is less than that of beam prestressed with steel strands. Comparing Beam C132-25-1 with S132-25-1 shows that CFCC prestressed beams can achieve approximately 50 % of fire endurance of steel prestressed beams. In addition, higher level of prestressing resulted in slightly lower fire endurance time. Similar result was observed for onset of deflection.

Stirrup spacing do not seem to have an influence on the fire endurance of the beams although it should be mentioned that in all beams, the side with CFCC stirrups experienced significantly more cracks and concrete spalling than the side with steel stirrups.

Temperature readings of the prestressing strands at failure spread over a wide range in all the beam. This can be attributed to the difference in cracks pattern and concrete spalling between the beams. When cracks develop near the location of the thermocouple, it can lead to higher temperature readings. But overall, it appears that Beam C72-14-1 achieved the highest CFCC temperature range among all beams with CFCC strands, mainly because of its extended fire endurance. Between Beams C100-20-1 through C100-20-5 and Beam C132-25-1, there is no significant difference in the fire endurance or the CFCC temperature at the time of failure. But there is a notable difference between Beam C132-25-1 and Beam S132-25-1 in both the fire endurance and the temperature of the prestressing strands at the time of failure.

Table 6.4-1 Fire resistance time of CFCC prestressed decked bulb T beam

Beam	Stress ratio of prestressing strand to guaranteed strength	Fire endurance	Time to onset of deflection	Stirrup Spacing,	Temp. range of strands @ failure (°F)
	(%)	minutes	minutes	in. (mm)	°F (°C)
C72-14-1	25	69	33	4 (102)	556-1073 (291-578)
C100-20-1	35	48	20	6 (152)	416-689 (213-365)
C100-20-2	35	52	30	4 (102)	390-686 (199-363)
C100-20-3	35	53	23	6 (152)	334-696 (168-369)
C100-20-4	35	58	21	6 (152)	440-759 (227-404)
C100-20-5	35	52	20	6 (152)	392-623 (200-328)
C132-25-1	44	47	13	4 (102)	381-803 (194-428)
S132-25-1	50	98	50	4 (102)	678-1103 (359-595)

## CHAPTER 7: SPLICING & BOND FATIGUE

### 7.1 Introduction

Bond between CFRP strands and surrounding concrete is the key in establishing the integrity of the section and achieving the design flexural and shear capacities especially in prestressing applications (Grace et al. 2000a). The bond can be achieved through chemical adhesion, shear resistance, and interlock mechanisms between the FRP bars and the concrete (Kanakubo et al. 1993).

Test standards that evaluate the bond strength between CFRP and concrete were developed and included in different design guides such as ACI. Pullout testing is considered the simplest and is commonly accepted. However, stress conditions during pullout experiments are rarely found in practice and bond strength values established under this test setup may vary considerably from those in practical circumstances (Achillides and Pilakoutas 2004). Other test standards are also available and different research teams developed multiple bond and bond-slip analytical models to estimate the bond strength between concrete and internal reinforcement. For instance, a bond slip model was developed by Alsiwat and Saatcioglu (1992), using the distribution and transfer of forces between steel rebars and concrete. Harajli (2009) studied on the impact of reinforced concrete and examined the bond slip relationship for different concrete cover and confinement conditions. Tastani and Pantazopoula (2010) also conducted detailed experiments that showed that the force distribution along the embedment length is not uniform along the rebar.

While the bond between steel reinforcement and concrete have been the focus of decades of research studies (Akbas et al, 2016), bond between CFRP and concrete lacks the experimental work and the corresponding analytical models. Nevertheless, it is widely accepted that, similar to steel, bond-slip relationship between CFRP and concrete depends on factors such as degree of confinement, bar size, bar composition, surface conditions, casting position, concrete cover, embedment length, and surface deformation (Achillides and Pilakoutas 2004; Malvar 1994). Current guidelines such as ACI 440 (2018) provides formula and equations to estimate the bond strength between CFRP and concrete but recent research work suggests that these formulae are too conservative (Harajli and Abouniaj 2010; Hao et al 2008).

Fatigue is described as the progressive deformation that occurs in a material that is subjected to cyclic stress and strains at elevated stress locations may result in cracks or complete fracture after enough fluctuations. While many studies focused on the fatigue of the composite material itself (Talreja 1987; Natarajan et al. 2005; and Akbas et al. 2016), the bond fatigue between CFRP and concrete has not drawn enough attention with few exceptions. For instance, Katz (2000) and Den-Ujil (1995) recorded a reduction in bond strength after cyclic loading. Curtis (1989) reported around 5 to 8 % reduction in the bond strength between concrete and CFRP due to cyclic loading per decade of logarithmic life. On the other hand, Wang and Belarbi (2010) reported an increase in bond stiffness and bond capacity after cyclic loading. They explained that this increase in bond stiffness and strength was due to the closing of micro voids between the concrete after cyclic loading. Ezeldin and Balaguru (1989) showed that the addition of fibers to concrete will change the bond performance due to the fact the concrete properties were altered.

This chapter presents a detailed experimental investigation that was executed with the main objective of establishing the characteristics of the bond strength between CFRP and concrete. The experimental investigation is composed of three test programs. The first test program included evaluating the bond strength between CFCC strands and uncracked concrete in a pull-out test setup. The second test program evaluated the bond strength in rectangular beams provided with different configurations of bottom lap-spliced CFCC reinforcement and loaded in a four-point-load setup to failure. The third test program evaluated different configurations of lap-spliced CFCC stirrups in precast prestressed box beams. Details of each test program and the main findings and conclusions are provided in the following sections.

## **7.2 Pull-out Test**

### **7.2.1 Test setup**

A total of 29 CFCC specimens were constructed according to ACI 440.3R-12-B.3: “Test Method for Bond Strength of FRP Bars by Pullout Testing”. Each specimen consisted of a single 0.6 in. (15.2 mm) CFCC strand with a sleeve anchorage on one side and embedded vertically at the center of a concrete cube with a side length of 8 in. (203 mm). The bonded length of CFCC strand was limited to five times the diameter or 3 in. (76 mm) according to the test method. The remaining embedded length was shielded against concrete bonding using a bond breaker Polyvinyl Chloride (PVC) pipe. Specimen configuration is shown in Figure 7.2-1. As shown on the figure, the strand

extended 0.5 in. (12.7 mm) beyond the concrete cube to facilitate monitoring the slippage of the CFCC strand when the specimen was loaded.

Figure 7.2-2 through Figure 7.2-4 show the construction of the test specimen. A wooden formwork was prepared with a side length of 8 in. (203 mm) and the CFCC specimen was passed through the formwork and protruded 0.5 in. (12.7 mm) from the bottom side. PVC pipe was provided for debonding,

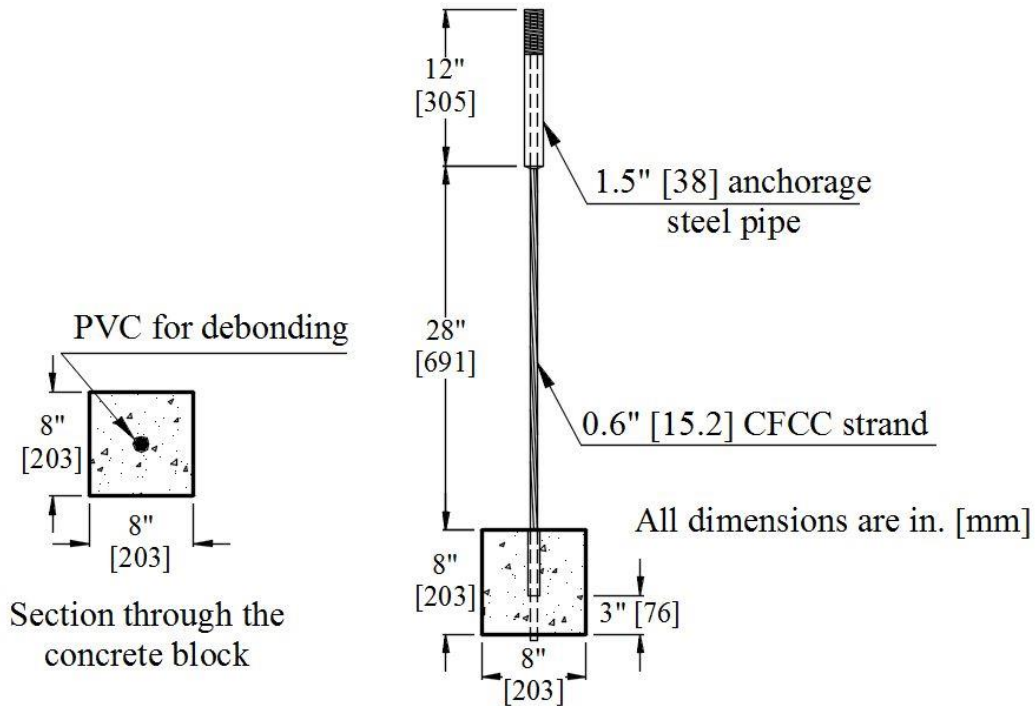


Figure 7.2-1 Specimen configuration of pull-out test



Figure 7.2-2 Formwork for pull-out test specimens



Figure 7.2-3 CFCC specimens in the formwork before pouring the concrete



Figure 7.2-4 Pouring concrete and completed pull-out specimen after removal of formwork

The concrete cube specimens were cast using a concrete mix with a design strength of 7000 psi (48 MPa). After casting the concrete, the specimens were covered with wet burlap and plastic sheets and were allowed to cure for 72 hours. The specimens were removed from formwork and testing was commenced 28 days after casting.

Pull-out test was conducted on two phases. Phase I included establishing the average static pull-out strength of the test specimens. This was achieved by testing to failure five test specimens in a test setup as shown in Figure 7.2-5. Phase II was similar to Phase I in the test setup, but the monotonic load was replaced by a cyclic load.



Figure 7.2-5 Test setup for bond specimens

As shown in the figure, the specimens were mounted in a two-post MTS uniaxial testing machine. The sleeve anchorage of the CFCC strand was threaded into the moving head of testing machine. A special high-strength steel head was prepared to accommodate and hold the concrete block. In addition, an LVDT was attached at the free end of the strand under the concrete block to capture the slippage of the strand. During Phase I, the specimens were loaded monotonically at a load rate of 4 kip/min (18 kN/min) to failure.

In Phase II, test standard ACI 440.3R-12-B.7: “Test Method for Tensile Fatigue of FRP Bars” was implemented to establish the cyclic load rate and amplitude. Based on the test standard, a total of 24 test specimens were loaded to load levels ranging from 60 % to 75 % of the average pull-out strength that was established in Phase I. The frequency of the cyclic load was 4 Hz with a ratio between the cycle lowest to the highest amplitudes of 10 %. Each specimen was tested under its assigned cyclic load to failure or 2 million cycles, which ever came first as recommended by ACI 440.3R-12.

### 7.2.2 Test results

In Phase I, the average pull-out strength was 12 kip (54 kN) and the minimum and maximum pull-out strengths were 10.4 kip (46 kN) and 14.4 kip (64 kN), respectively (Table 7.2-1). The pullout of the CFCC strand from the concrete cube was detected by a sudden drop in the load and a sudden increase in the reading from the LVDT attached to the free end of the specimen as shown in Table 7.4-2. Since the bonded length of CFCC strand was 76 mm (3 in.), the static average bond strength was approximately 4 kip/in. (0.7 kN/mm). In all cases, the failure was due to pure slippage of CFCC strand. No concrete splitting was observed.

Table 7.2-1 Pull-out test results

Specimen #	Failure Load kip (kN)
1	10.4 (46.4)
2	11.5 (51)
3	11.3 (50.2)
4	14.4 (64)
5	12.6 (56.1)
Average pullout load	12 (53.5)

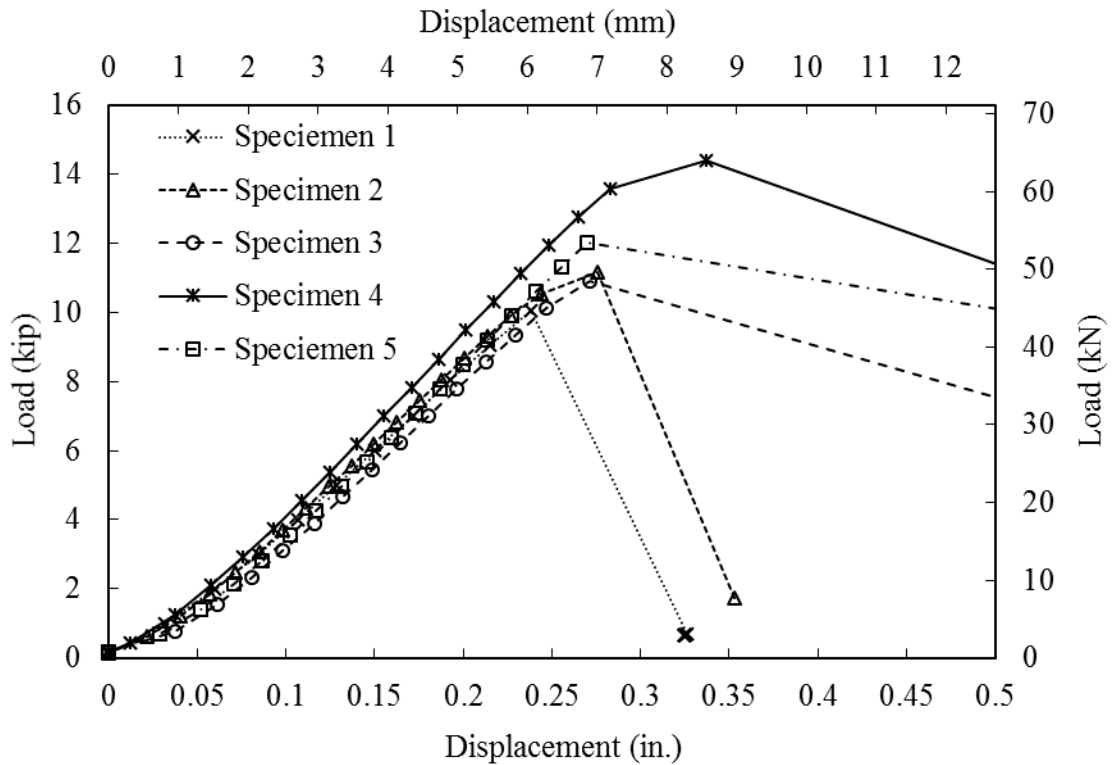


Figure 7.2-6 Load-displacement curve for static pullout test

Test results of Phase II are presented in Table 7.2-2. As shown in the table six load levels were selected for the testing. The selection of the load level aimed at achieving number of load-cycles-to-failure between 1000 and two million cycles, according to test standard. The minimum load ratio was limited to 60 % after one specimen survived two million cycles at this load ratio.

The S-N curve was plotted as shown in in Figure 7.2-7 to determine the pullout strength at 2 million cycles according to ACI 440.3R-12-B7. The stress ratio was represented on a linear scale on the vertical axis, and the number of cycles to failure was represented on a logarithmic scale on the horizontal axis. The S-N line was plotted as the trend line from the test results by the least-square method. The 2 million cycle pull-out strength was calculated by interpolation from the S-N curve and was found to be between 64 % of the static average pullout strength. In other words, to avoid pull-out failure due to cyclic loading, the bond strength shall not exceed 64 % of the average static pull-out strength. For instance, since pull-out strength of CFCC strands averaged at 4.0 kip/in. (0.7 kN/mm), the maximum bond strength to avoid pullout failure under static load is

approximately 2.56 kip/in. (0.45 kN/mm). This limit can be established by simply extending the development length of the CFCC strand by 56 %.

Table 7.2-2 Bond fatigue test results

Load/stress ratio to pull-out (%)	Specimen Identification	Cycles to Failure	Maximum stress ratio (%)	Minimum stress ratio (%)
60	A	2000000 »	69	50
65	A	142000	75	54
	B	2000000 »	75	54
	C	854700	75	54
	D	37200	75	54
	E	796900	75	54
67.5	A	2000000 »	78	56
	B	302800	78	56
	C	152620	78	56
	D	126867	78	56
	E	2000000 »	78	56
70	A	20000	81	59
	B	490000	81	59
	C	6475	81	59
	D	830	81	59
	E	246900	81	59
	F	1541	81	59
72.5	A	1290	84	61
	B	228400	84	61
	C	1914	84	61
	D	29261	84	61
	E	229650	84	61
75	A	85	86	63
	B	627	86	63
» No failure occurred by the end of 2000000 cycles				

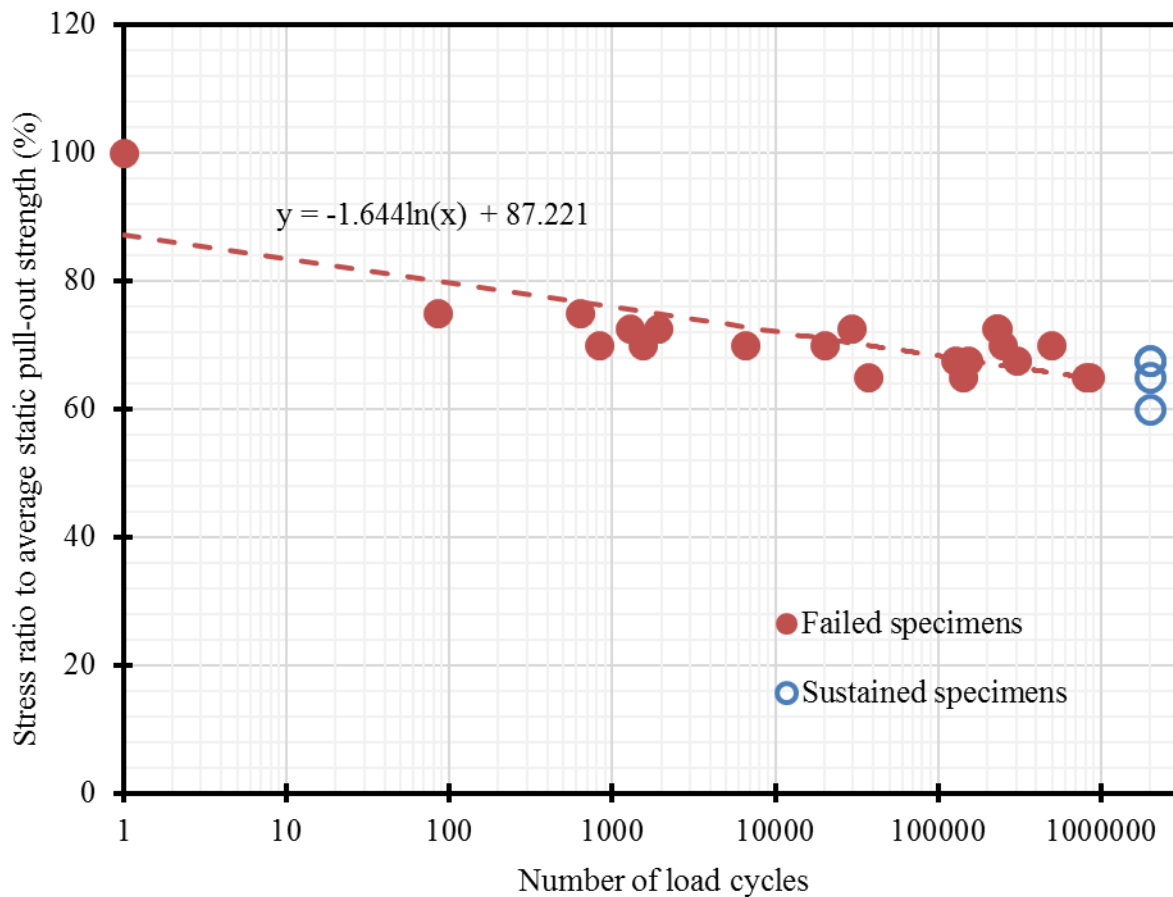


Figure 7.2-7 Stress ratio vs No. of load cycles to failure in CFCC specimens tested for bond fatigue strength

### 7.3 Flexural Bond Strength

The bond strength established by pullout test method is only valid if the concrete is uncracked and/or in compression. In case of cracked concrete or concrete in tension, the bond strength between the reinforcement and concrete typically depends on the amount of confinement provided by the concrete and the confinement provided by the lateral reinforcement.

This test program of the experimental investigation focused on establishing the bond strength between CFRP and cracked concrete or concrete subjected to tensile/flexural stresses. The test program included the design, construction, and testing of ten CFCC reinforced concrete beams under four-point-load test setup to failure. Continuous CFCC strands served as the bottom reinforcement for two control beams, while the remaining eight beams were reinforced with CFCC

strands that were lap-spliced within the constant moment region between the two points of load. Different splice lengths and different diameters of CFCC strands were investigated.

### 7.3.1 Test setup

All ten beam specimens had a width of 10 in. (254 mm), a depth of 14 in. (356 mm), and an effective span of 11 ft (3.35 m). All the beams were provided with 2 No. 4 (12 mm) top steel reinforcement and No. 3 (10 mm) steel stirrups every 4 in. (102 mm) except through the constant moment region as shown in Figure 7.3-1 and Figure 7.3-2 . Five beams were reinforced with two bottom CFCC strands with a diameter of 0.6 in. (15.2 mm). The other five beams were reinforced with two bottom CFCC strands with a diameter of 0.5 in. (12.5 mm). Out of the five beams in each group, one beam was provided with continuous CFCC strands, while the CFCC strands in the remaining four beams were spliced through the constant moment region with splice length of 1, 2, 3, and 4 ft (305, 610, 914, 1219 mm).

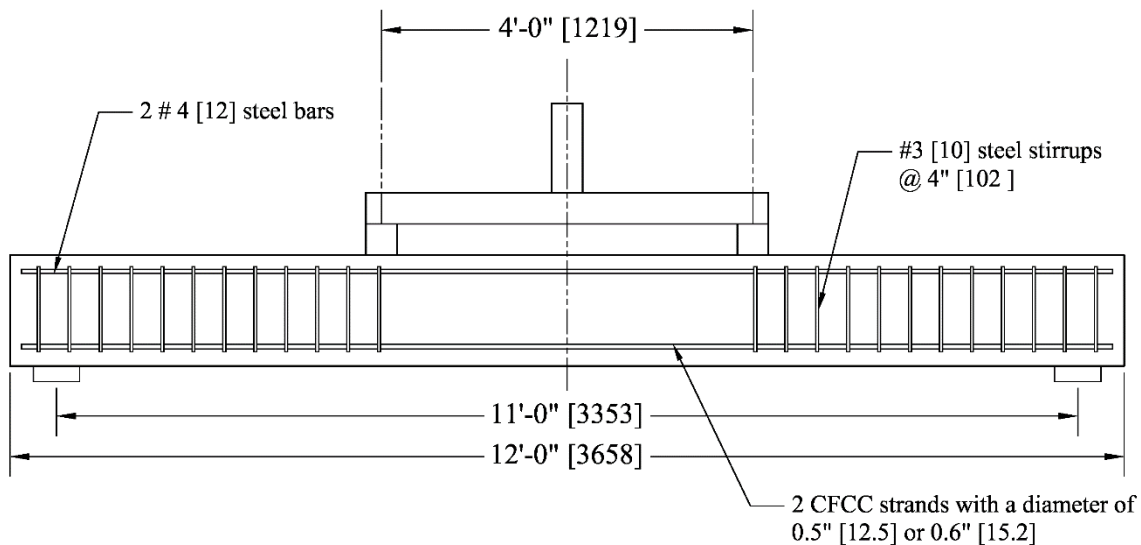


Figure 7.3-1 Test setup of evaluation of flexural bond splice length

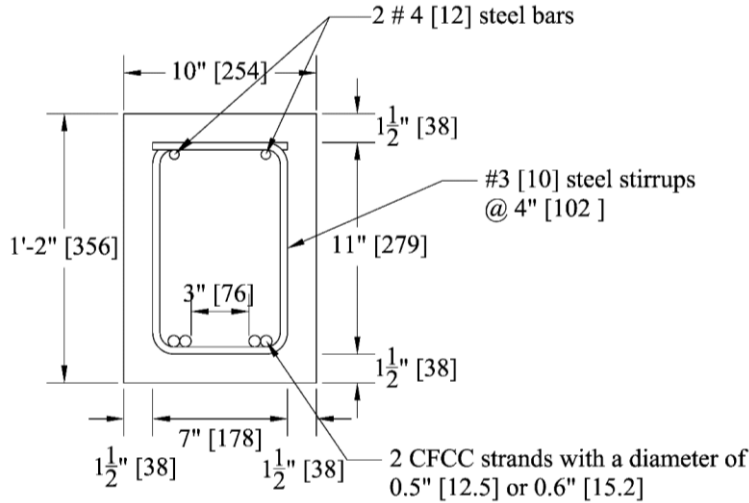


Figure 7.3-2 Cross section and dimensions of test beams

The nomenclature of the specimens is given as: “B- length of splice in ft-diameter of CFCC”. For instance, B4-0.5 is a beam reinforced with two bottom CFCC strands with a diameter of 0.5 in. (12.5 mm) spliced with a lap splice length of 4 ft (1219 mm) through the constant moment region. The control beams with continuous CFCC reinforcement were denoted BC-0.5 and BC-0.6 for CFCC diameter of 0.5 in (12.5 mm) and 0.6 in. (15.2 mm), respectively. The size and properties of all the different reinforcement are shown in Table 7.3-1 Properties of reinforcement, while Figure 7.3-3 through Figure 7.3-6 show the construction process of the test specimens. A ready-mix concrete was used to cast the beams. The concrete mix was designed to achieve a 28-day compressive strength of 7000 psi, and a desired slump of 8 in. (203 mm) to achieve the required workability. A slump of 8.25 in. (210 mm) was verified prior to pouring concrete in accordance with ASTM C143/C143M-15a specifications. Several test cylinders were prepared from the same concrete batch and were tested to determine concrete compressive strength at different ages (Figure 7.3-7). After concrete casting, the beams were cured by covering them with wet burlap sheets and spraying with water for 7 days.

Table 7.3-1 Properties of reinforcement

Material Properties	Flexural Reinforcement		Shear Reinforcement	
	CFCC		Steel No.4	Steel No.3
Diameter, in. (mm)	0.5 (12.5)	0.6 (15.2)	0.5 (12)	0.38 (10)
Effective cross-sectional area, in. <sup>2</sup> (mm <sup>2</sup> )	0.12 (77.5)	0.179 (115.6)	0.2 (129)	0.11 (71)
Breaking load, kip (kN)	46.09 (205)	64.3 (286)	18 (80)	9.9 (44)
Ultimate tensile strength, psi (MPa)	379,000 (2,613)	358,240 (2,470)	90,000 (621)	90,000 (621)
Modulus of elasticity, psi (MPa)	21.7×10 <sup>6</sup> (149,900)	20.9×10 <sup>6</sup> (144,000)	29×10 <sup>6</sup> (200,000)	29×10 <sup>6</sup> (200,000)
Yield strength, psi (MPa)	-----	-----	60,000 (414)	60,000 (414)
Elongation (%)	1.70	1.70	5.00	5.00



Figure 7.3-3 Assembling the reinforcement cages of the test beams



Figure 7.3-4 Completed reinforcement cage showing the location of the splice and stirrups

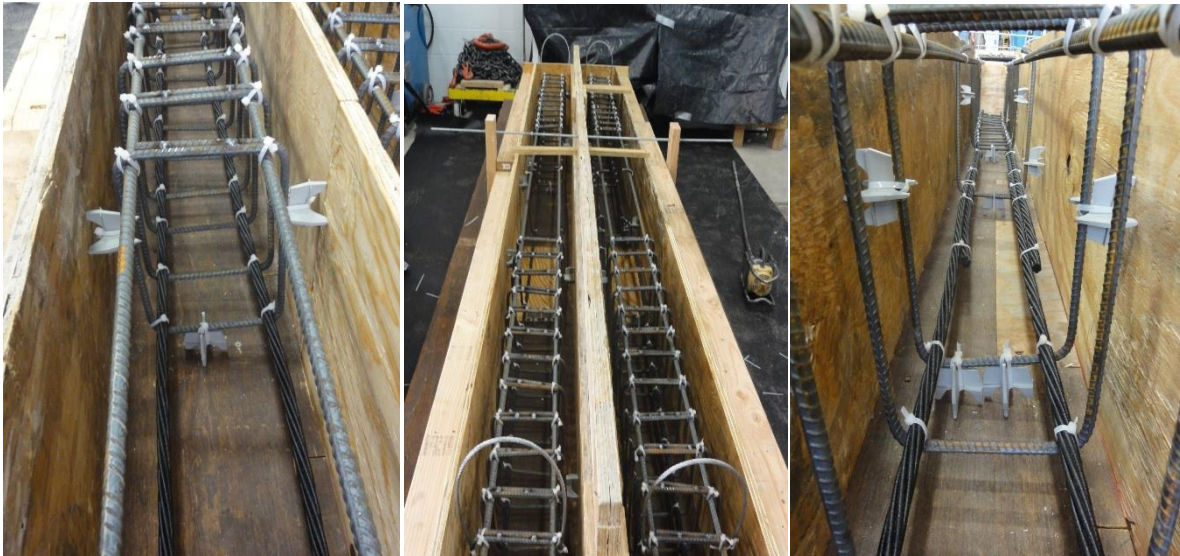


Figure 7.3-5 Placing the reinforcement cages in the formwork



Figure 7.3-6 Casting the concrete in the test specimens



Figure 7.3-7 Completed beams and preparing concrete cylinders for uniaxial testing

The uniaxial compressive strength of the concrete was determined according to ASTM C39/C39M-12 specifications, at 7, 14, 21, and 28 days after beams casting. Three concrete cylinders were tested each time and the average test results were taken to determine the average

concrete compressive strength. An average 28-day compressive strength of 10 ksi was achieved as shown in Figure 7.3-8.

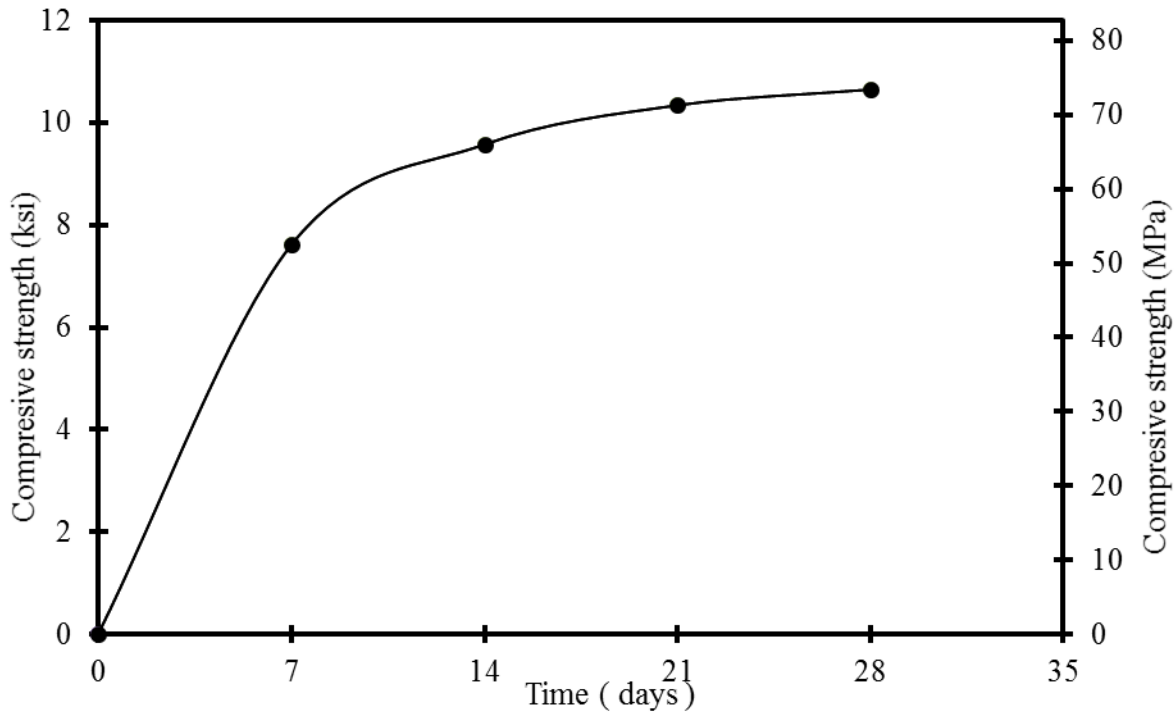


Figure 7.3-8 Average compressive strength of concrete over time

The beam specimens were instrumented with concrete strain gages, linear variable differential transducers (LVDTs), load cells, and linear motion transducers (LMTs). At mid-span section, two electric resistance strain gages were installed externally on the top concrete surface to monitor the concrete compression strain. In addition, Three LVDTs were attached to the side of the specimens to capture the strain through the depth of the beam. A load cell attached to the hydraulic actuator with a maximum capacity of 220 kips (1000 kN) was used to monitor the applied vertical load on the beam during testing. LMTs were attached to the underside of the beams to monitor the deflection. All sensors were connected to a computer with a data acquisition interface system to monitor and record test data.

The beam specimens were loaded in four-point-load flexural test in a displacement control mode with a loading rate of 0.1 in/min (2.54 mm/min). The distance between the two points of load (the constant moment region) was 4 ft (1.22 m). Beams were simply supported over a steel-reinforced elastomeric bearing pads with a thickness of 1.0 in. (25.4 mm).

### 7.3.2 Test results

Table 7.3-2 provides a summary for the test results of all beam specimens. In addition, Figure 7.3-9 through Figure 7.3-37 show the test setup, loading, and failure mode of failure for all test specimens. The cracking load for all beam was around 10 kip (44 kN). Control beam BC-0.5 failed by rupture of CFCC strands, while control beam BC-0.6 failed by crushing of the concrete. Other beam specimens failed by pullout of the lap splice that was accompanied by spalling and cracking (splitting) of the concrete at the splice location. In addition, in all beam specimens with a lap splice, a wide flexural crack developed at the end of the lap splice at the time of the failure as shown in the figures.

Figure 7.3-38 and Figure 7.3-39 show the load deflection curves for the test specimens. It should be noted that due to the size of the reinforcement relative to the size of the beam and due to the increased concrete cover in the test beams, the load deflection curves exhibited slight drops in the load with the development of the flexural cracks. The load level was quickly regained after the internal flexural reinforcement was engaged and carried the tensile force across the crack.

Table 7.3-2 Summary for test results of beam specimens in flexural bond test

Beam	Splice length	Failure load	Conc. strain	Mode of failure	Deflection @ failure	CFCC strain @ failure
	in. (mm)	lb (kN)	$\mu\epsilon$		in. (mm)	$\mu\epsilon$
B1-0.5	12 (305)	17,980 (80)	-890	Pullout/split	1.10 (28)	6,360
B2-0.5	24 (610)	35,360 (157)	-1570	Pullout/split	2.16 (55)	12,550
B3-0.5	36 (914)	35,211 (157)	-1557	Pullout/split	1.93 (49)	12,470
B4-0.5	48 (1219)	36,787 (164)	-1870	Pullout/split	2.58 (66)	12,950
BC-0.5	Cont.	46,838 (208)	-2601	Tension	3.42 (87)	16,600
B1-0.6	12 (305)	26,026 (116)	-1376	Pullout/split	1.09 (28)	6,490
B2-0.6	24 (610)	29,874 (133)	-1398	Pullout/split	1.51 (38)	7,400
B3-0.6	36 (914)	35,892 (160)	-1742	Pullout/split	1.68 (43)	8,910
B4-0.6	48 (1219)	47,312 (210)	-2738	Pullout/split	2.00 (51)	11,730
BC-0.6	Cont.	58,973 (262)	-2252	Compression	2.98 (76)	14,670

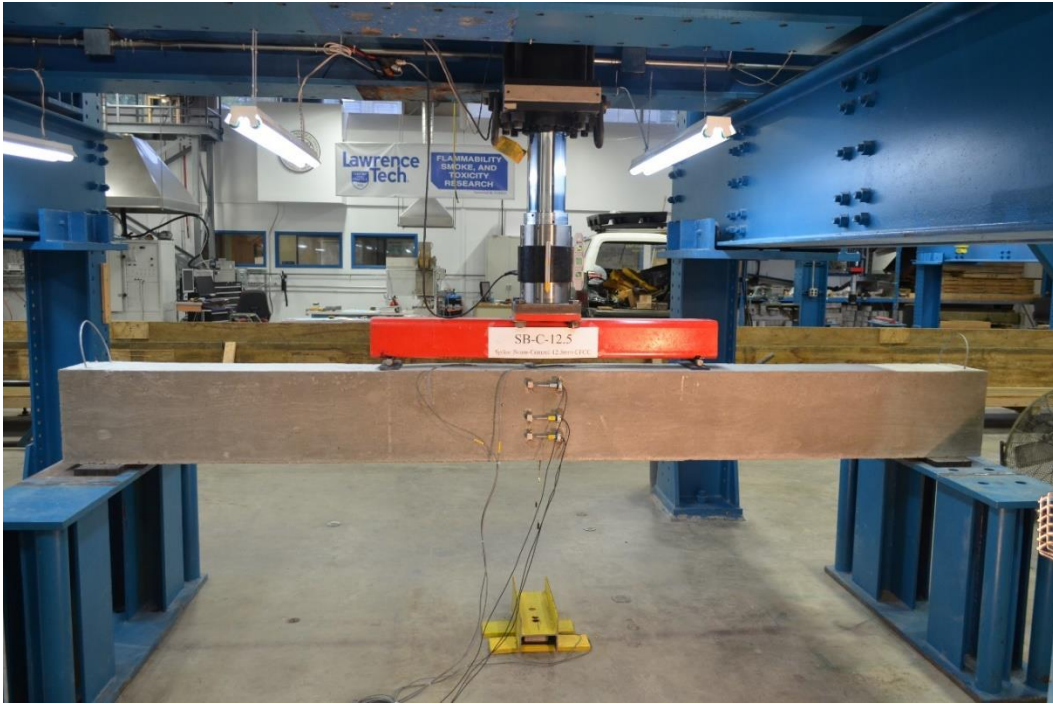


Figure 7.3-9 Setup and Testing of BC-0.5



Figure 7.3-10 Failure of BC-0.5



Figure 7.3-11 Close-up view of BC-0.5 showing the rupture of steel strands



Figure 7.3-12 Setup and testing of B1-0.5



Figure 7.3-13 Failure of B1-0.5



Figure 7.3-14 Close-up view of B1-0.5 showing a large crack at the end of splice



Figure 7.3-15 Setup and testing of B2-0.5



Figure 7.3-16 Failure of B2-0.5



Figure 7.3-17 Close-up view of B2-0.5 showing CFCC slippage at the end of splice

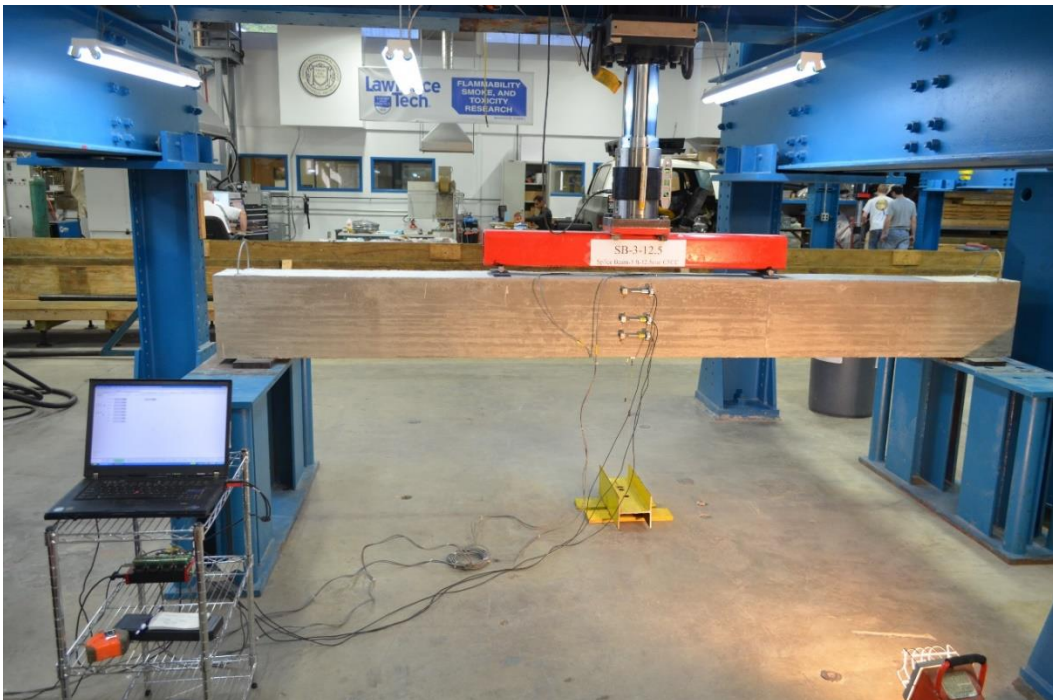


Figure 7.3-18 Setup and testing of B3-0.5



Figure 7.3-19 Failure of B3-0.5



Figure 7.3-20 Close-up view of B3-0.5 showing CFCC slippage at the end of splice

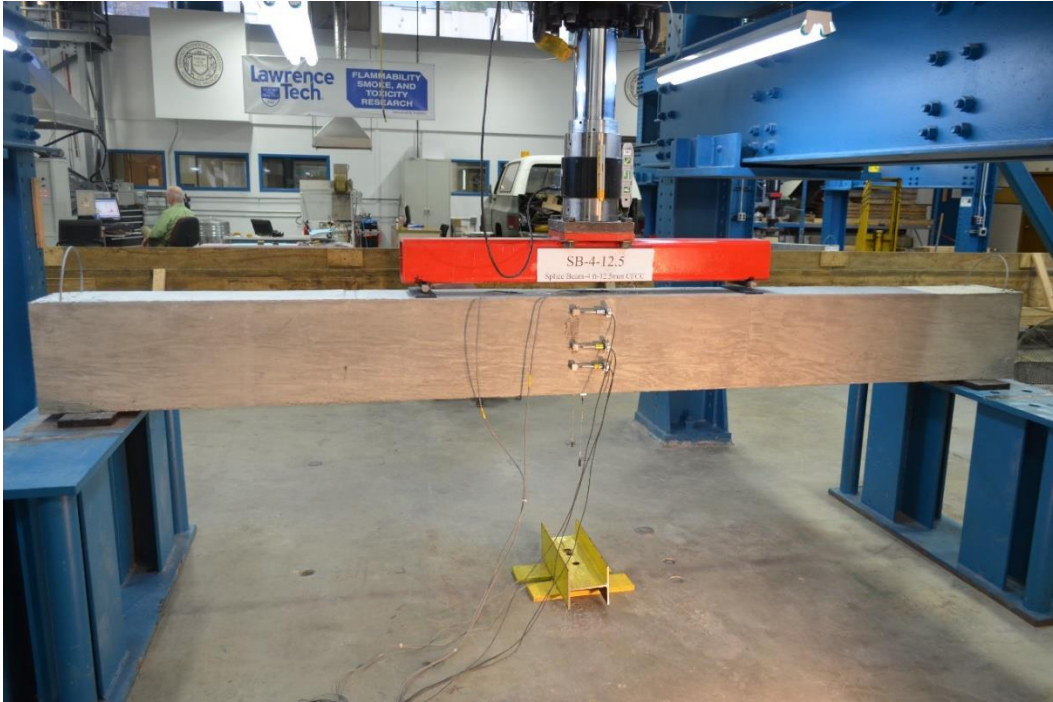


Figure 7.3-21 Setup and testing of B4-0.5

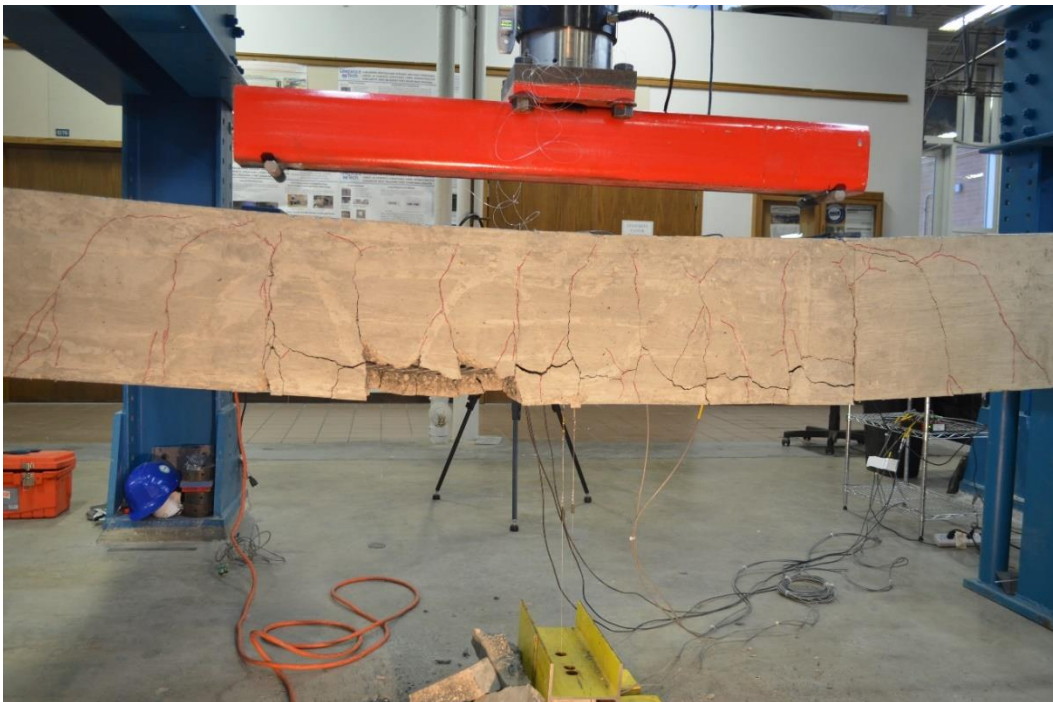


Figure 7.3-22 Failure of B4-0.5



Figure 7.3-23 Close-up view of B4-0.5 showing CFCC slippage at the end of the splice



Figure 7.3-24 Failure of BC-0.6



Figure 7.3-25 Crushing of concrete followed by rupture of CFCC strands in BC-0.6



Figure 7.3-26 Setup and testing of B1-0.6



Figure 7.3-27 Failure of B1-0.6



Figure 7.3-28 Close-up view of B1-0.6 showing the CFCC slippage at the end of the splice



Figure 7.3-29 Setup and testing of B2-0.6



Figure 7.3-30 Failure of B2-0.6



Figure 7.3-31 Close-up view of B2-0.6 showing CFCC slippage at the end of the splice



Figure 7.3-32 Setup and testing of B3-0.6



Figure 7.3-33 Failure of B3-0.6

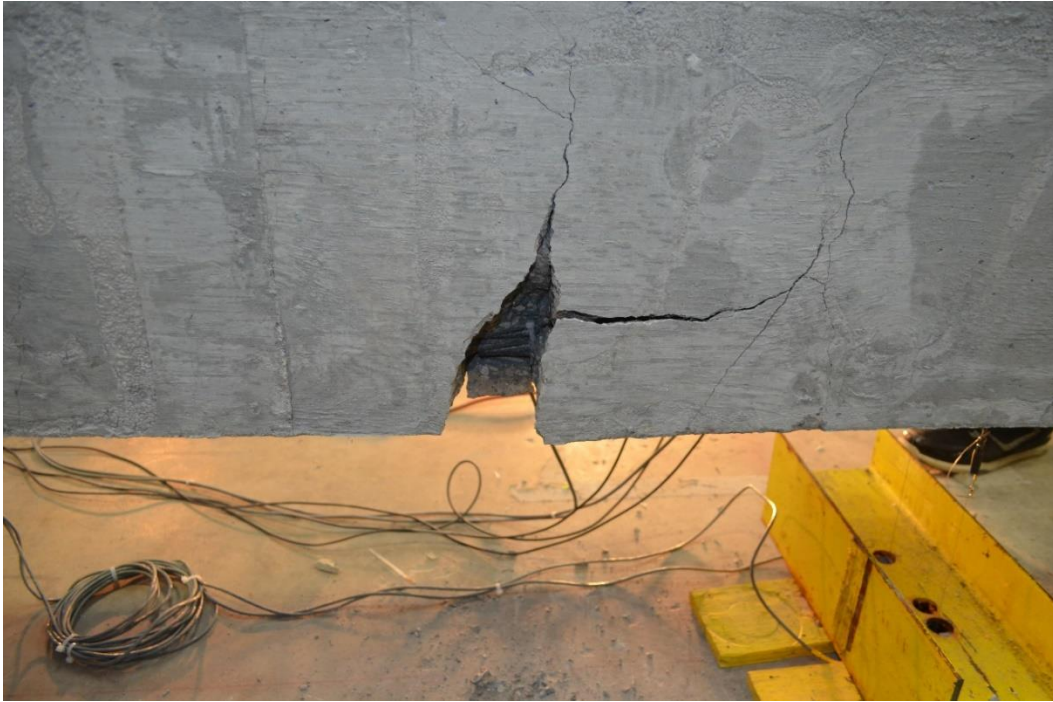


Figure 7.3-34 Cracking and failure of B3-0.6 at the end of the splice



Figure 7.3-35 Setup and testing of B4-0.6



Figure 7.3-36 Failure of B4-0.6



Figure 7.3-37 Close-up view of B4-0.6 showing CFCC slippage at splice end

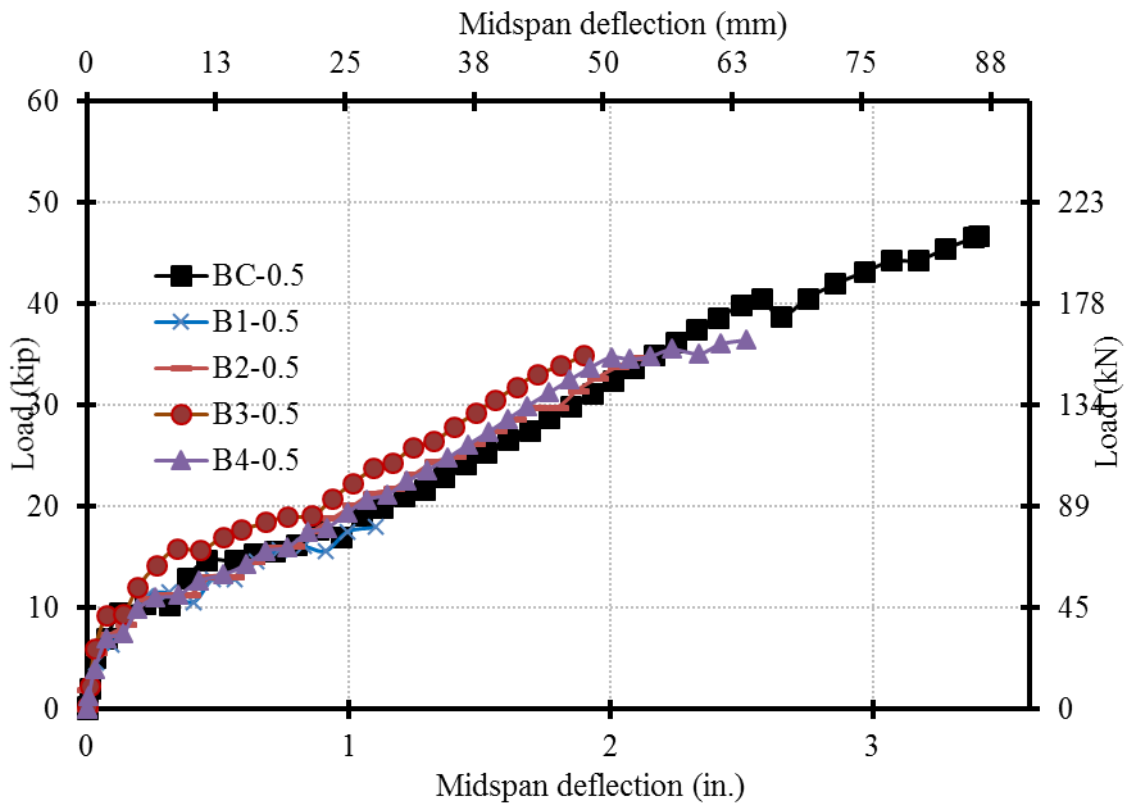


Figure 7.3-38 Load vs. mid-span deflection of beams with 0.5-in. (12.5-mm) CFCC strands

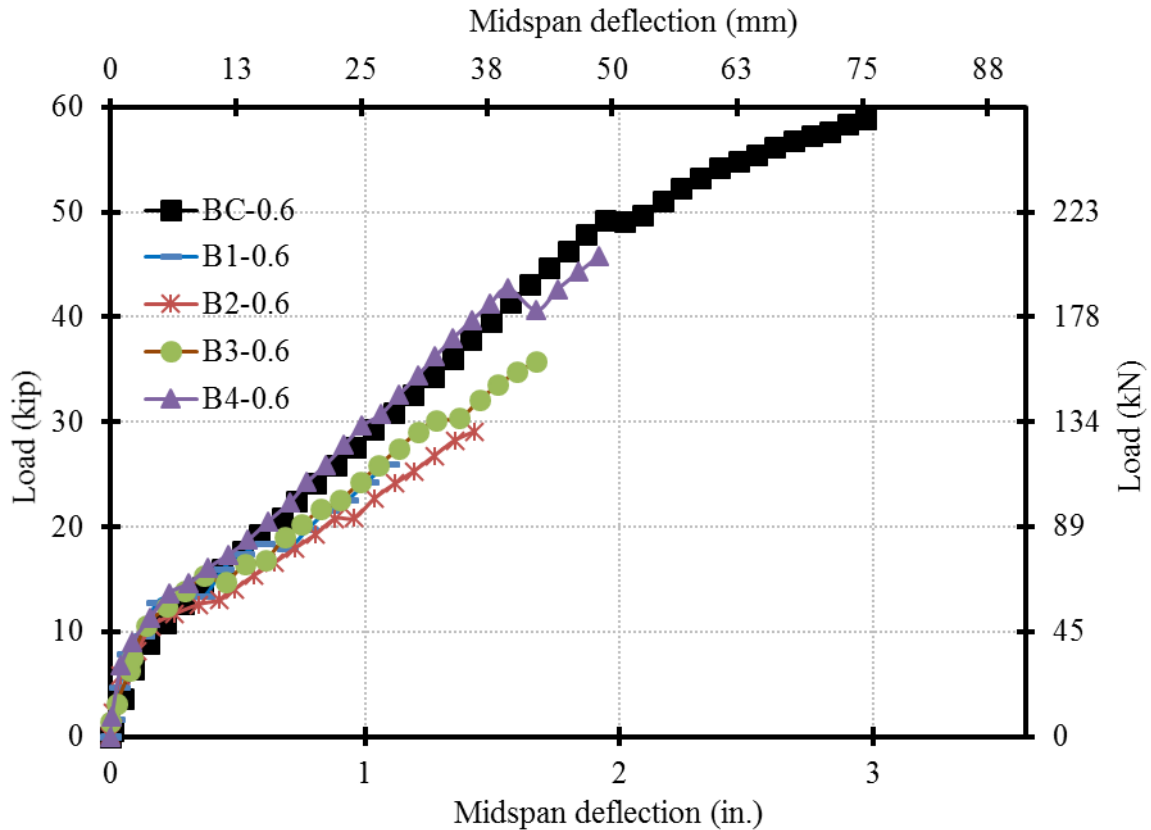


Figure 7.3-39 Load vs. mid-span deflection of beams with 0.6-in. (15.2-mm) CFCC strands

### 7.3.3 Discussion of test results

Failure by concrete splitting or reinforcement pullout are two widely recognized forms of bond and lap splice failure in case of steel reinforced concrete when the concrete is in tension. Concrete splitting dominates when there is not sufficient concrete cover or when there is not enough lateral reinforcement to provide confinement and control the longitudinal cracks. If enough concrete cover is provided along with enough lateral reinforcement, the pullout failure dominates. In this case, the failure can be delayed by increasing the bonded length until yield of reinforcement is achieved before the pullout failure.

The dimensions of the cross section and the concrete cover at the bottom and on the sides of the beams were selected to avoid typical splitting failure according the ACI-318 (2014). In addition, ACI 440.1R-06 reported that to avoid and concrete splitting a limit of at least 3.5 for the normalized cover  $c/d_b$  should be maintained, where  $c$  is the concrete cover and  $d_b$  is the diameter

of the strands. All beam specimens satisfied the minimum concrete cover requirements. Therefore, typical concrete splitting of the test specimens was unlikely.

Control Beam BC-0.5 exhibited a tension-controlled failure, while control beam BC-0.6 exhibited a compression-controlled failure. Difference in failure modes in control beams is attributed to the increased reinforcement ratio that was attained by increasing the diameter of CFCC strands from 0.5 in. (12.5 mm) to 0.6 in. (15.2 mm).

Beams with lap-spliced 0.6 in. (15.2 mm) CFCC strands showed a near-linear increase in the maximum load with the increase in the splice length as shown in Figure 7.3-40. On the other hand, beams with lap-spliced 0.5 in. (12.5 mm) CFCC strands, exhibited an increase in the maximum load when the lap splice length increased from 12 in. (305 mm) to 24 in. (610 mm) as the load nearly doubled. Further increase in the splice length did not yield any significant increase in the maximum load of the specimens.

Test results can be explained by examining the CFCC strain at the time of beam failure as shown in Figure 7.3-41. With a splice length of 12 in. (305 mm), the strain in CFCC strands exceeded  $6000 \mu\epsilon$  in both BC-0.5 and BC-0.6. This strain level was nearly three times the typical yield strain of steel reinforcing bars ( $2000 \mu\epsilon$ ). On the other hand and as mentioned earlier, the design criteria and equations that govern the design of lap splices in common steel design codes and guidelines such as ACI 318 are based on the yield strength of the steel reinforcement. In other words, those equations were developed to guard against failure of lap splice until the reinforcement achieves its yield strength. Since the minimum strain of the test specimens was much higher than the yield strain of the steel reinforcement, the failure mode of the test specimens was neither concrete splitting nor reinforcement pullout as defined by general steel design codes. Rather, the failure mode can be assumed as severe concrete cracking followed by bond loss and pullout of CFCC strands.

Beams B2-0.5, B3-0.5, B4-0.5 achieved the same failure load regardless of the splice length due to the significant concrete tensile strain (cracking) at the time of failure. The strain of the CFCC strands at the time of failure ranged from 12,500 to 13,000  $\mu\epsilon$  in those beams. At this strain level, the bond strength of the concrete surrounding the reinforcement had nearly diminished and that allowed the CFCC strands to pullout of the concrete that fell into pieces when the pullout took place.

The failure loads of B2-0.6, B3-0.6, and B4-0.6 test continued to increase with increasing the splice length, which indicated that degradation in the bond strength of the concrete due to increased strain was countered and surpassed by the increase in the splice bond length. However, it is not expected that the failure load would continue to increase with increasing the splice length. Every increase in the splice length leads to an increase in the maximum load and increase in the CFCC and surrounding concrete strain, which further degrades the bond strength and limits the increase in the maximum load. Therefore, the full strength of CFCC strand at the splice may not be achieved because the concrete, surrounding the strand, becomes severely cracked and can no longer develop adequate bond strength to the CFCC reinforcement.

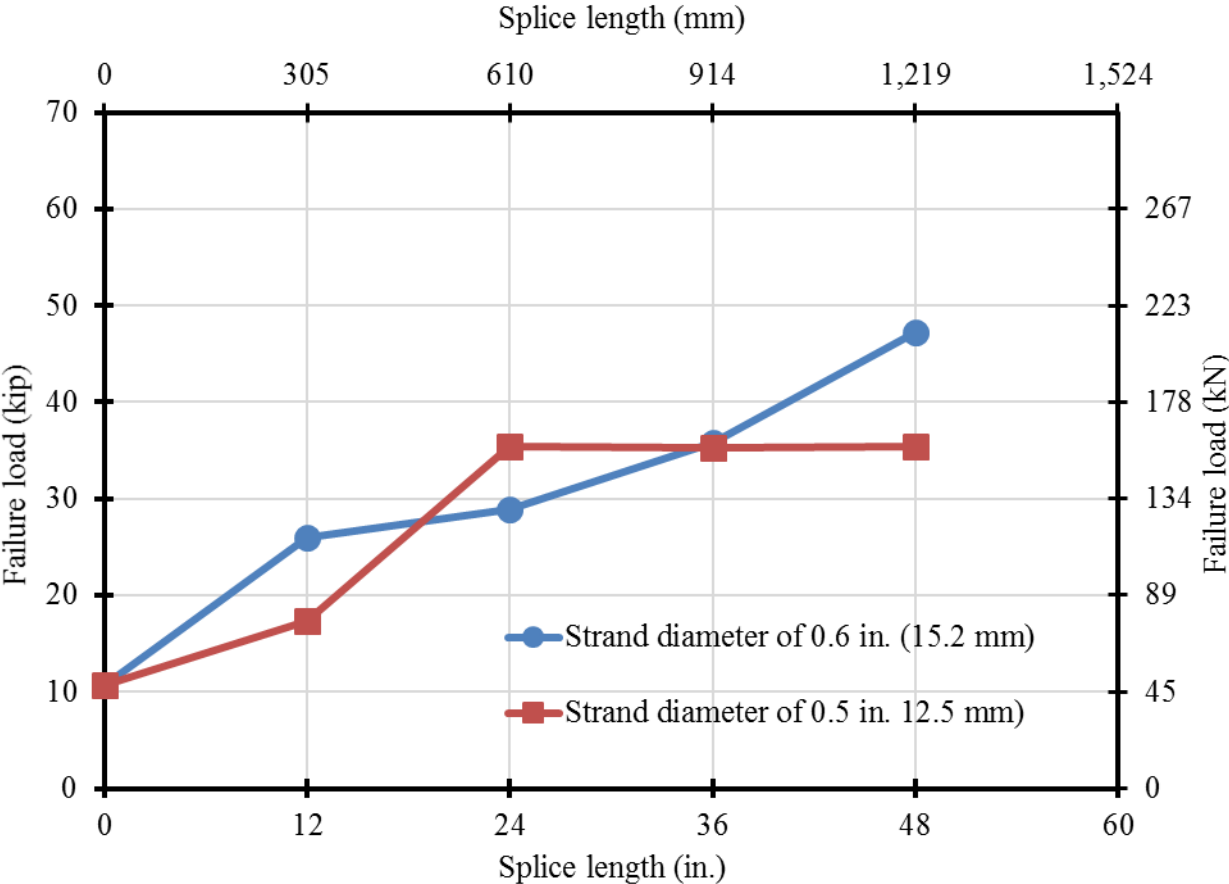


Figure 7.3-40 Splice length vs. Maximum load in all test beams

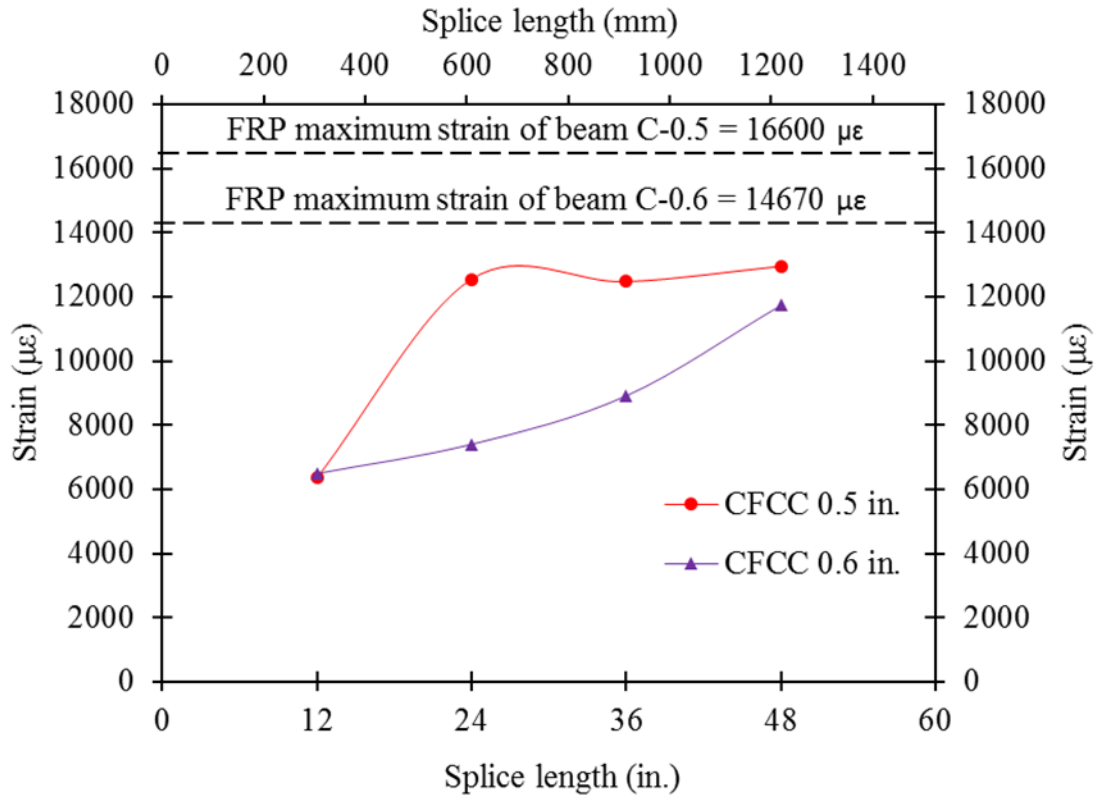


Figure 7.3-41 Strain versus splice length of the spliced CFCC strands

## 7.4 Lap-spliced CFRP Stirrups

The use of spliced U-shape stirrups in highway bridge box beams is a common construction practice that facilitates pouring the concrete and eliminates any potential for honeycombing in the bottom flange. The stirrup splice (overlap) extends through the full depth of the beam when stirrups are made of steel and this has been proven adequate through testing and construction. Nevertheless, enough data or test results are currently unavailable to support the same for spliced U-shape CFRP stirrups. Therefore, this test program focused on verifying the splice length in CFRP stirrups. Four CFCC prestressed concrete box beams with spliced U-shaped stirrups were designed, constructed, and tested to verify the use of spliced CFRP stirrups in bridge beam construction.

### 7.4.1 Test setup

As shown in Figure 7.4-1 and Figure 7.4-2, the box beams had a width of 17 in. (432 mm), a depth of 19 in. (483 mm), and a length of 24 ft (7.32 m), while the cavity inside the beams had a depth

of 10 in. (254 mm) and a width of 11 in. (279 mm). The beams were also provided with 12-in. (305-mm) thick end blocks and 10 in. (254 mm) thick interior diaphragms at the load location at a distance of 5ft (1524 mm) from each end.

All beams were reinforced in tension with four 0.6 in. (15.2 mm) prestressed CFCC strands and five 0.6 in. (15.2 mm), non-prestressed CFCC strands. In the transverse direction, the stirrups were provided at a center-to-center spacing of 8 in. (203 mm).

The beams were loaded in a three-point-load shear test setup and the shear load was placed at a distance of 4.91 ft (1.5 m) from the center of the end support as shown in Figure 7.4-3. The beam was loaded over a span of 18.083 ft (5.51 m) since one support was placed under an end block and the other support was placed under the interior diaphragm on the other side of the beam. The distance from the load to the nearest support presented the critical shear span of the beam. Each beam was loaded twice to evaluate the shear capacity of both ends.

Closed steel stirrups No.5 (16 mm) were provided between the interior diaphragms. In addition, CFCC stirrups with a diameter of 0.6 in. (15.2 mm) were provided on one end of each beam within the critical shear span, while the other end of each beam was provided with No.5 (16 mm) steel stirrups. The steel and CFCC stirrups that were provided within the shear span had four configurations in the four beams; one beam was provided with closed CFCC and steel stirrups at the ends. The other three beams were provided with U-shape spliced CFCC and steel stirrups with splice lengths of 4, 7, and 10.5 in. (102, 178, and 267 mm). It should be noted that the splice length of 10.5 in. (267 mm) represents the full-depth splice as shown in Figure 7.4-4. The nomenclature of the test beams is written as: “material of stirrups -splice length in inches”. Material do the stirrups is denoted C for CFCC and S for steel. In case of closed stirrups, the splice length was replaced with a letter C. For instance, C7 is a beam specimen with U-shape spliced CFCC stirrups on a splice length of 7 in. (178 mm). SC is a beam specimen with closed steel stirrups. Material properties of stirrups are shown in Table 7.4-1. All stirrups had a center to center spacing of 8 in. (203 mm). Figure 7.4-5 shows the general configuration and dimensions of the stirrups.



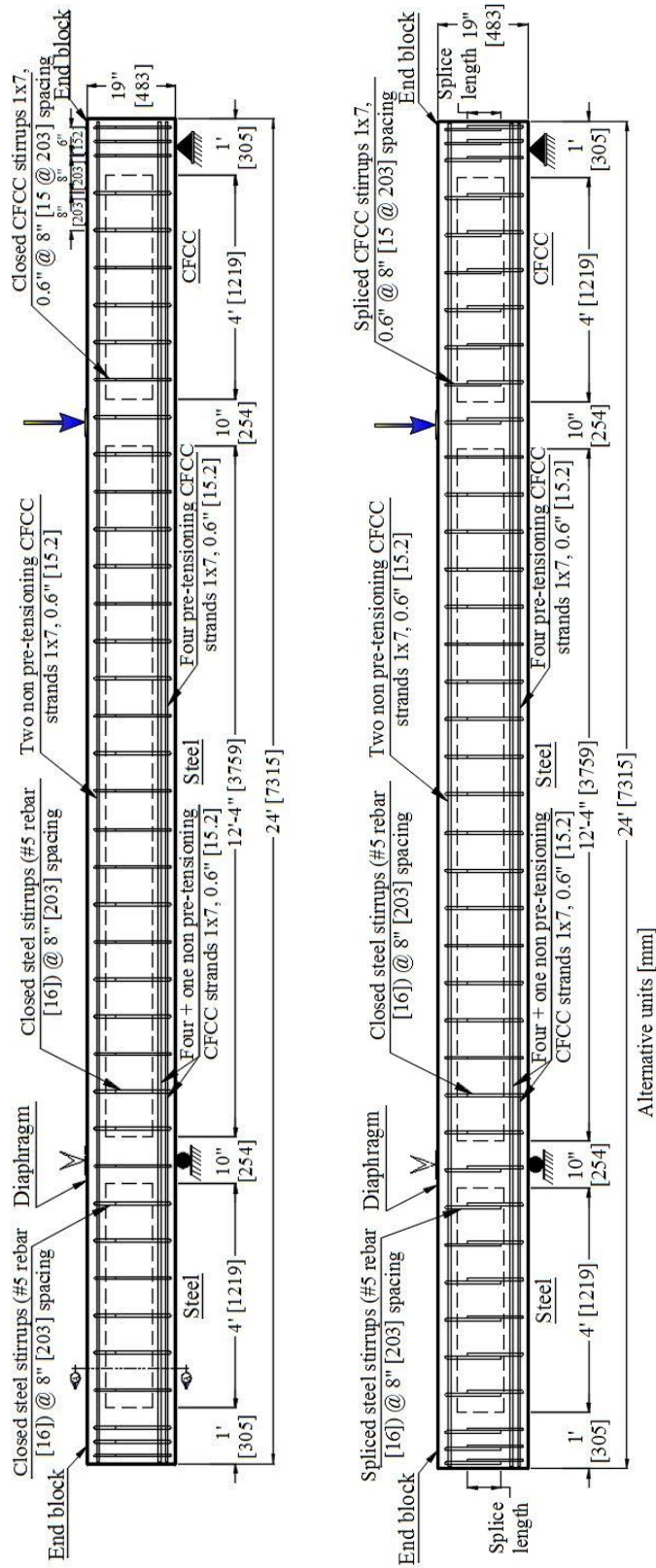


Figure 7.4-3 Longitudinal sections of prestressed concrete box-beams

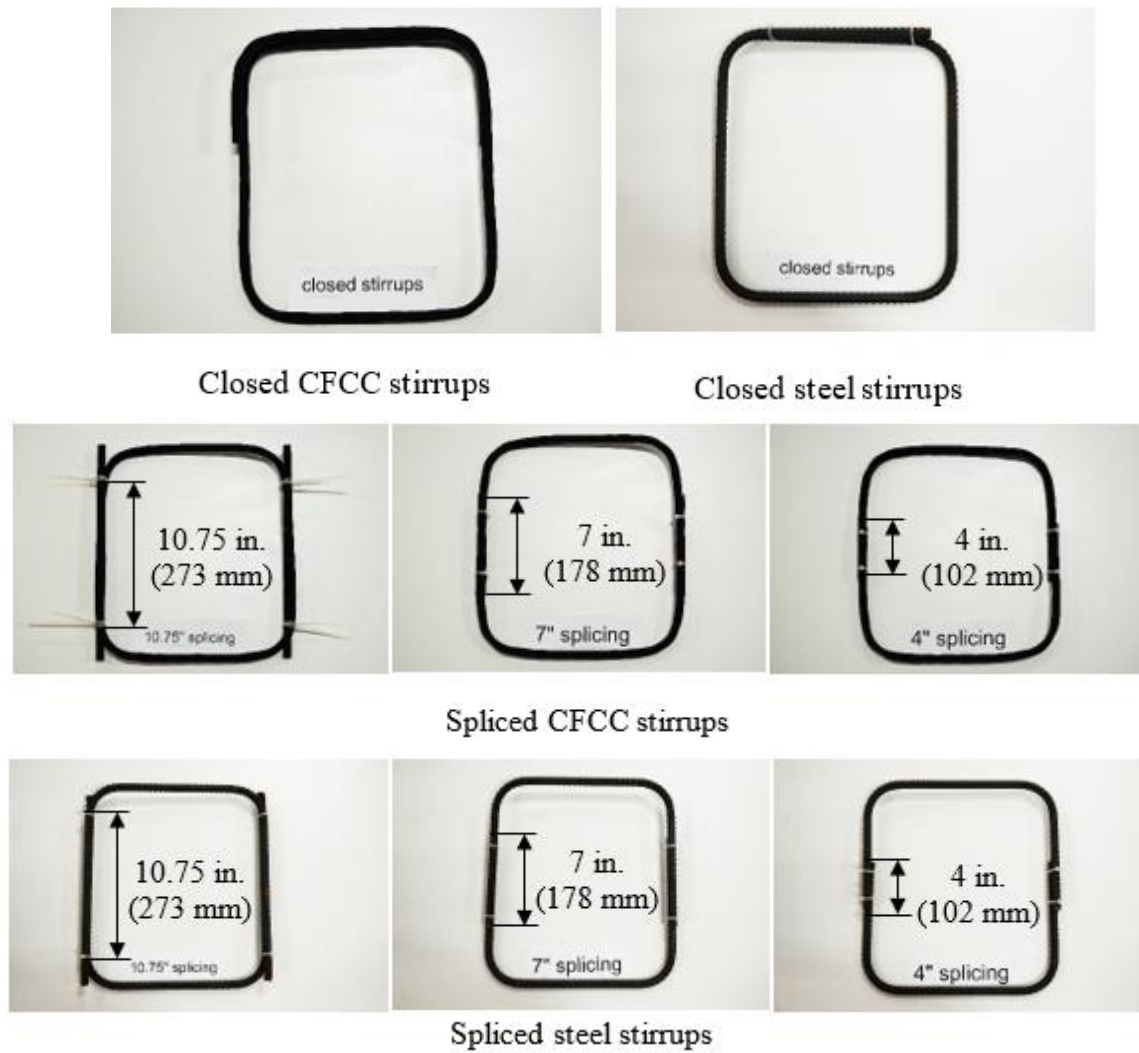


Figure 7.4-4 Configuration of stirrups in the beam specimens

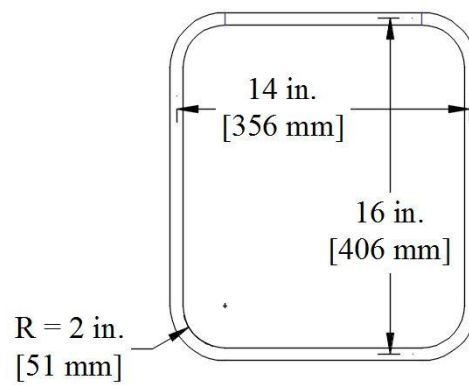


Figure 7.4-5 Stirrup dimensions

Table 7.4-1 Material properties of shear reinforcement

Material properties of stirrups	CFCC	No.5 steel
Diameter, in. (mm)	0.6 (15.28)	0.625 (16)
Effective cross-sectional area, in. <sup>2</sup> (mm <sup>2</sup> )	0.179 (115.6)	0.31 (200)
Average breaking load, kip (kN)	69.9 (311)	27.9 (124)
Ultimate tensile strength, ksi (MPa)	390 (2,690)	90 (621)
Modulus of elasticity, ksi (GPa)	21,320 (147)	29,000 (200)
Yield strength, ksi (MPa)	-----	60 (414)
Elongation (%)	1.8	≈ 5.00

The construction of the box-beams consisted of building the formwork, assembling the reinforcement cages, prestressing the CFCC strands, casting the box beams, and cutting the prestressed CFCC strands. All four box beams were cast at the same time from the same concrete batch with a design 28-day concrete strength of 7000 psi (48 MPa).

The formwork consisted of wooden platform, center walls, and side walls as shown in Figure 7.4-6 and Figure 7.4-7. The hollow portion inside the box beams was formed from 11-in. (279-mm) wide by 10-in. (254-mm) high Styrofoam blocks as shown in the figures. The stirrups in the critical shear spans at the ends of each beam were instrumented with strain gages attached to their vertical legs. Bottom prestressing strands were also instrumented with strain gages.

Each box beam was prestressed with four prestressing CFCC strands with a total average initial prestressing force of 120 kip (534 kN) per beam. The prestressing of the strands was carried out in a 50-ft (15.2 m) long reinforced concrete prestressing bed with two abutment-type bulk heads that were anchored to the bed. Figure 7.4-8 through Figure 7.4-11 show the process of prestressing the box beams. At the live end, CFCC strands were coupled with steel strands using a special mechanical anchorage system. The steel strands were anchored to the bulk head using conventional steel anchorage devices. At the dead end, the CFCC strands were coupled with high-strength steel threaded rods that were anchored to the bulkhead using high-strength steel nuts and washers. The dead-end couplers were provided with in-line load cells to monitor the prestressing force. Prestressing was executed using a hydraulic jack from the live end.

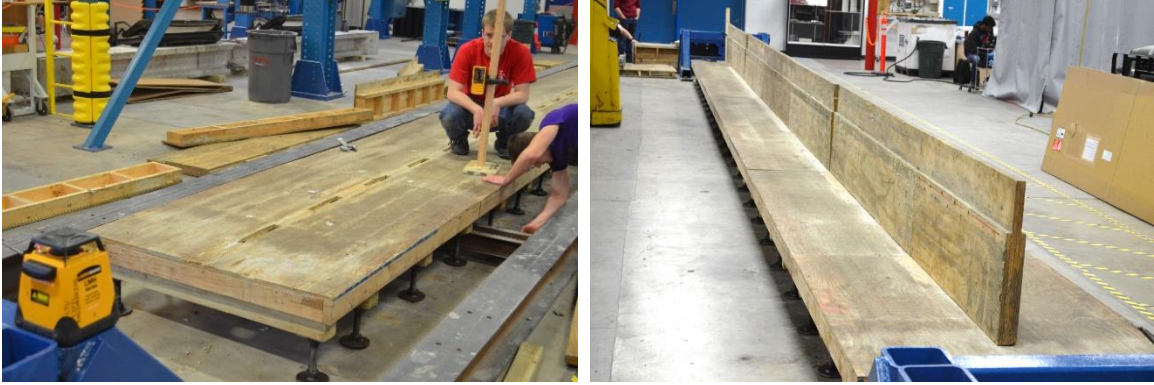


Figure 7.4-6 Construction of the formwork for the box beams



Figure 7.4-7 Preparing and instrumenting the reinforcement cages

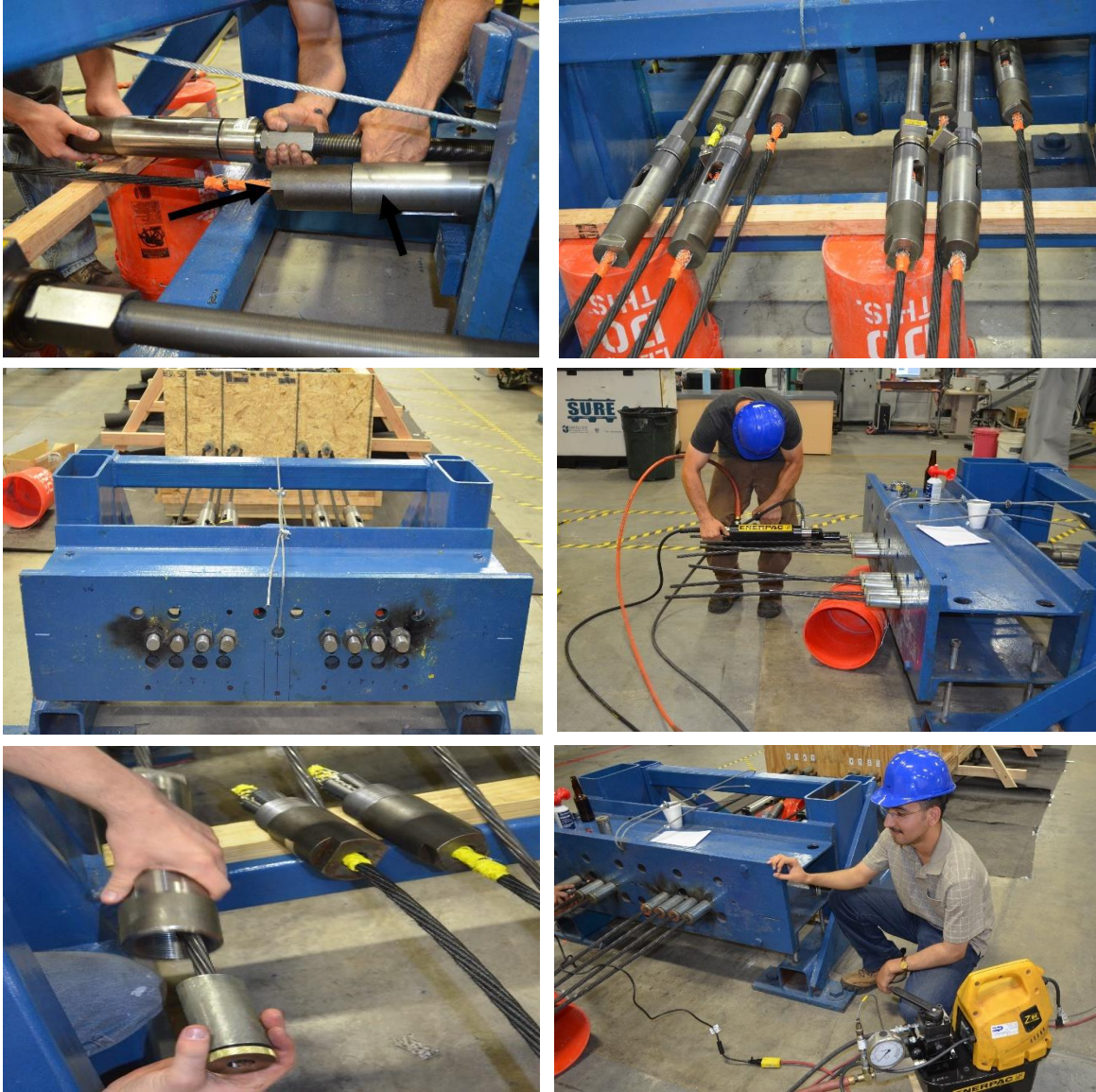


Figure 7.4-8 Prestressing CFCC strands from the live end with load cell on the dead end

To eliminate a possible rotation of the bulkhead during prestressing the CFCC prestressing strands were pulled in a specific order as illustrated in Figure 7.4-10. Couplers were staggered at both ends of the prestressing strands with 2 ft (0.61 m) spacing to avoid contacting while prestressing as shown in Figure 7.4-11.

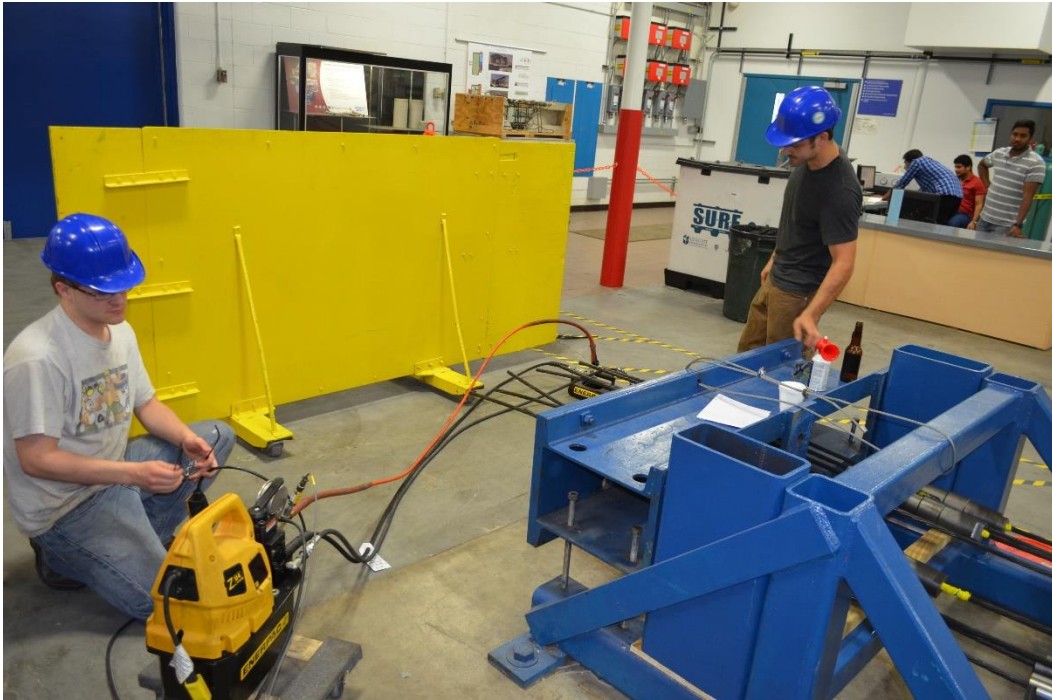


Figure 7.4-9 Prestressing CFCC strands from the live end

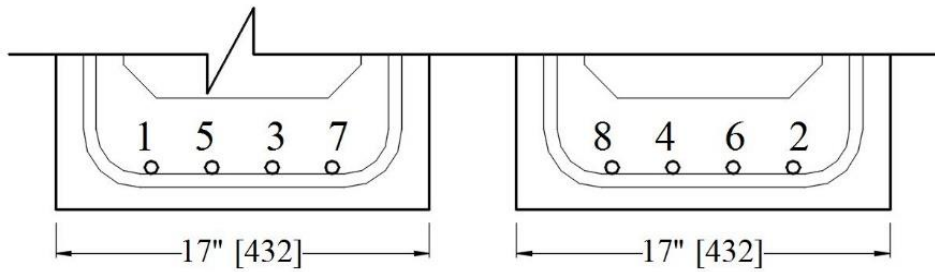


Figure 7.4-10 Prestressing order of CFCC strands

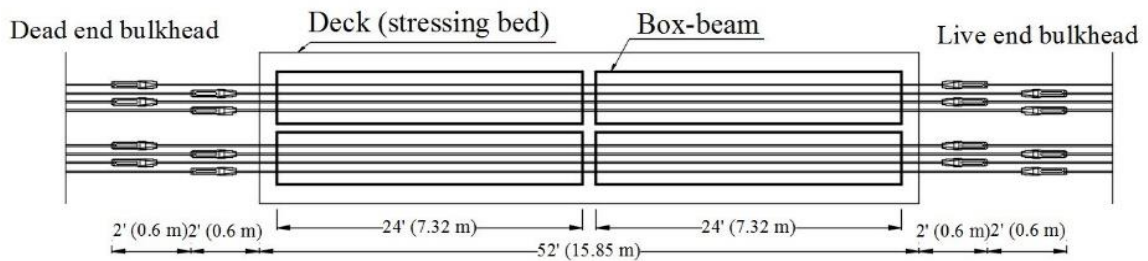


Figure 7.4-11 Couplers spacing

The box-beams were cast using a ready-mix concrete with a slump of 8 in. (203 mm) which was verified prior to pouring. In addition, twenty test cylinders were constructed from the same concrete batch to determine concrete compressive strength at different ages. After concrete casting, the beams were cured by covering them with wet burlap sheets and spraying water for 7 days (Figure 7.4-12).

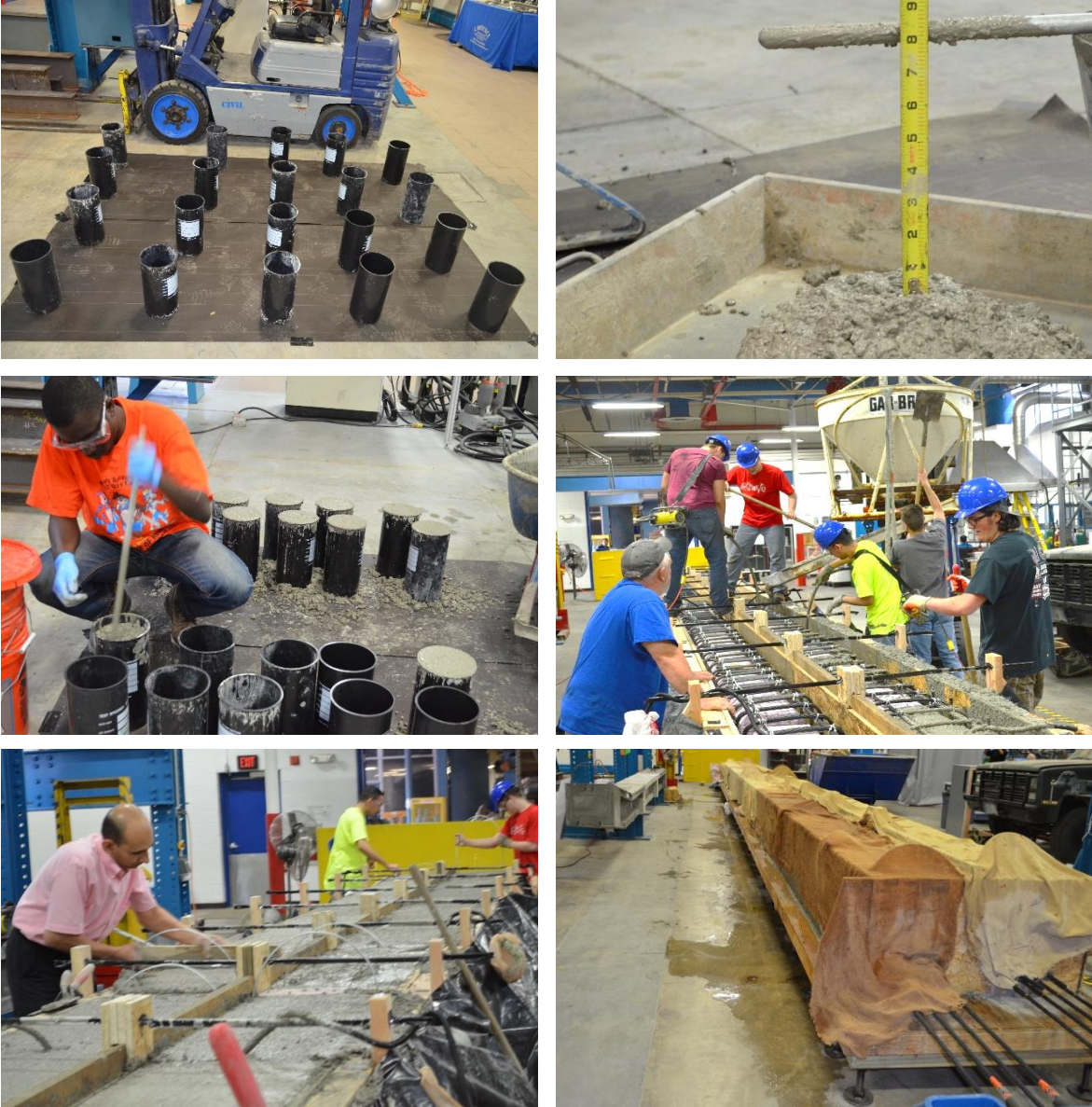


Figure 7.4-12 Casting the concrete of the box beams

The next day after casting the box-beams the side walls were removed from the formwork. After 13 days as the concrete gained the initial compressive strength, the prestressing force was transferred to the concrete by heating and cutting the steel strands coupled to the CFCC strands using oxy-acetylene torch as shown in Figure 7.4-13. As with prestressing, prestress release was executed in a proper sequence to avoid any possible rotation to the bulkheads. The beams were removed from the formwork and transferred to storage. The prestressing forces were recorded through the in-line load cells from the time of stressing until the release of strands as shown in Figure 7.4-14. In addition, the uniaxial compressive strength of the concrete was determined with an average concrete compressive strength of 11,305 psi after 28 days as shown in Figure 7.4-15.

After prestress release, the beams were moved to the testing facility and were externally instrumented for testing. Multiple sensors were installed externally including concrete strain gages, linear variable differential transducers (LVDTs), load cells, and linear motion transducers (LMTs). A computer with a data acquisition interface system was used to monitor and record test data.



Figure 7.4-13 Releasing of prestressed strands

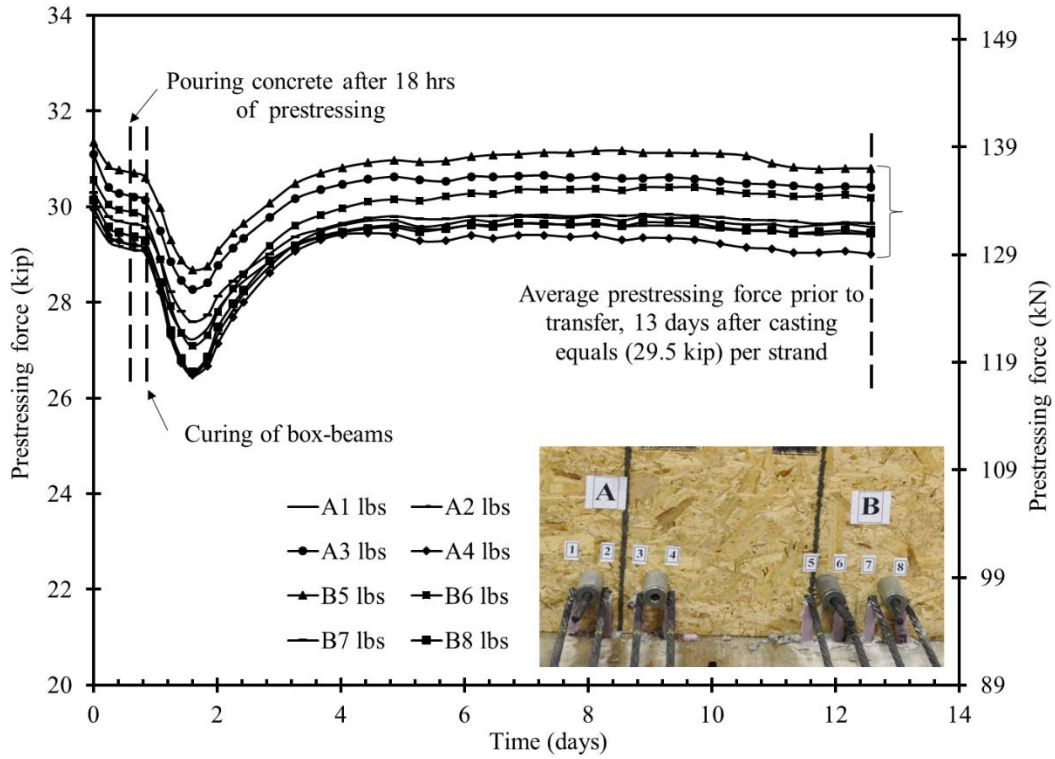


Figure 7.4-14 Prestressing force prior to transfer

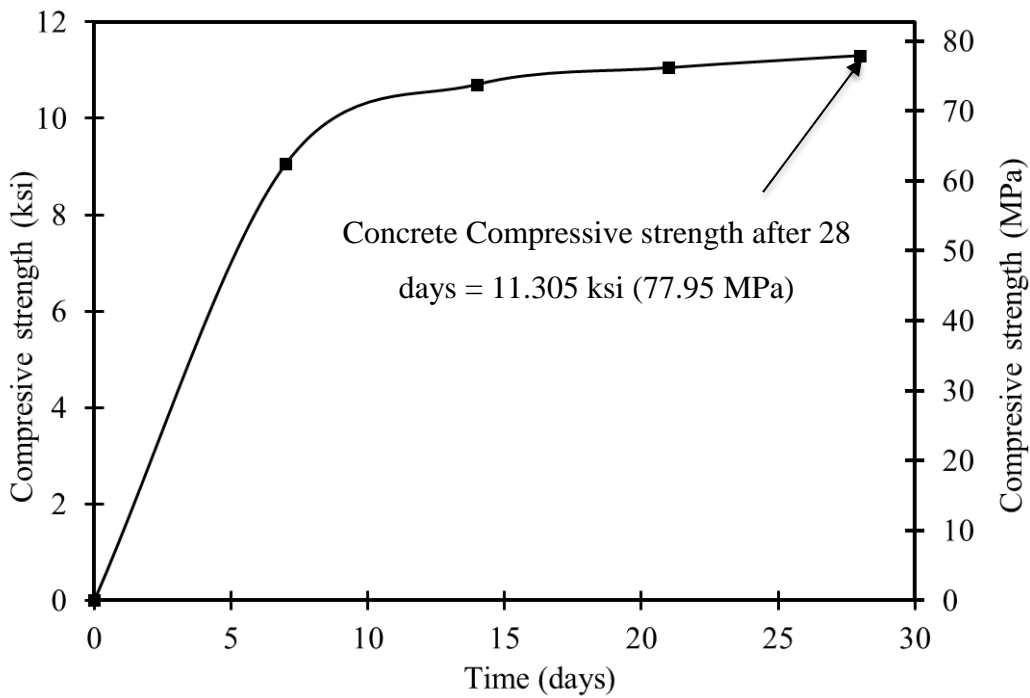


Figure 7.4-15 Concrete compressive strength

## 7.4.2 Test Setup

Box beams were simply supported over steel reinforced elastomeric bearing pads with a thickness of 1.0 in. (25.4 mm). Shear test in each beam started with testing beam end with CFCC stirrups then the end with steel stirrups. The beams were subjected to several loading/unloading cycles with a load increment of 5 kip (22.2 kN) to a load level of 40 kip (177.9 kN) then an increment of 10 kip (44.5 kN) to failure. The load was applied through a controlled actuator displacement rate of 0.1 in/min (2.54 mm/min). Crack development was inspected and marked by the end of each load cycle. Beam test setup and instrumentation are shown in Figure 7.4-16 and Figure 7.4-17.

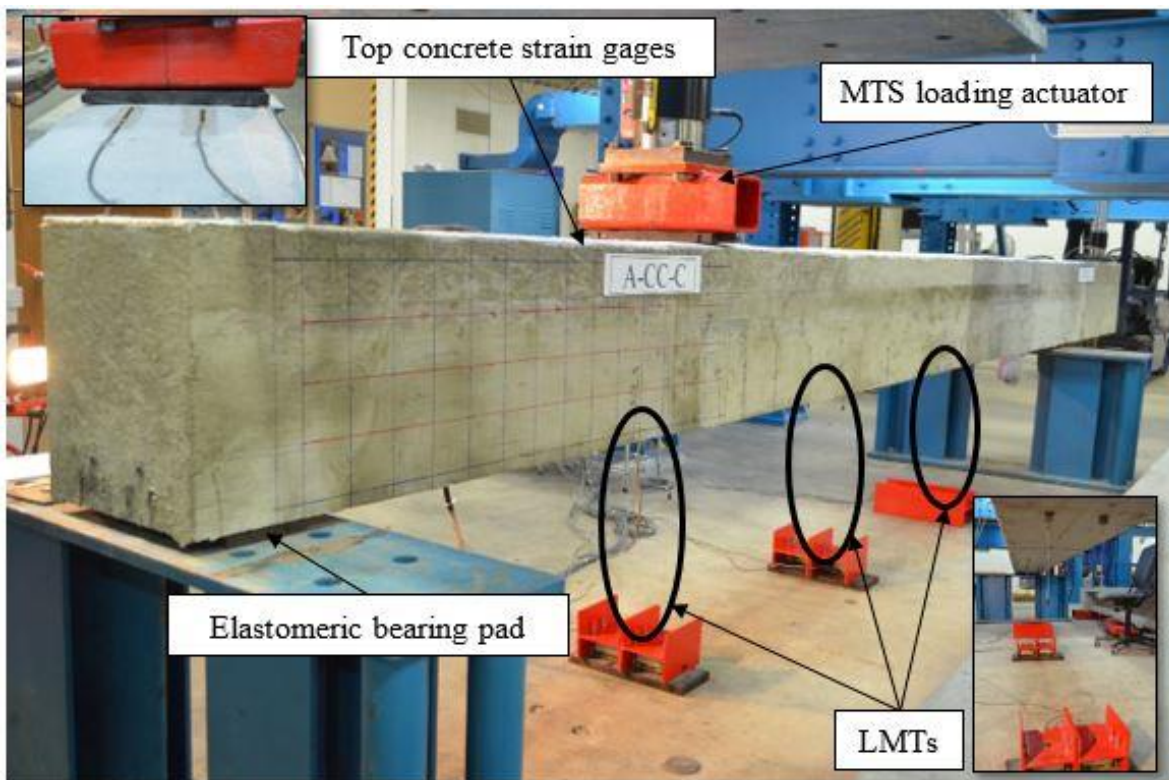


Figure 7.4-16 Instrumentation and test setup of the box beams

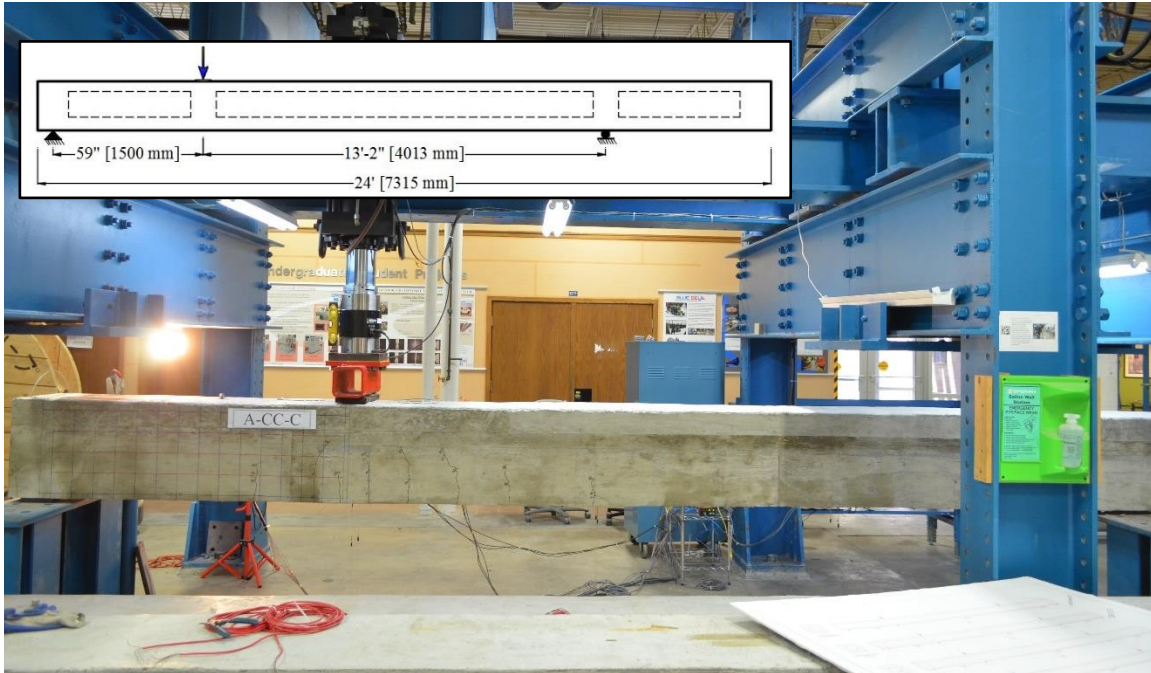


Figure 7.4-17 Shear test setup of box beams

### 7.4.3 Test results

#### 7.4.3.1 Control Box-Beam (C-C)

Beam C-C was a beam end provided with closed CFCC stirrups. The first observed flexural crack under the load developed at a shear force of 32.7 kip (145 kN). A decompression shear force of 19.5 kip (87 kN) was also observed in post-cracking load cycles. By increasing the load, the flexure cracks extended diagonally through the web. At a shear force of 43.7 kip (194 kN), the first web shear crack initiated on the side of the beam, while the existing flexure cracks propagated towards the point of loading, as shown in Figure 7.4-18. A sudden failure took place when the shear force approached 96 kip (427 kN). The failure took place through top concrete crushing in the compression zone under the load as shown in Figure 7.4-19. The shear force-deflection response for all load cycles is presented in Figure 7.4-20, while the shear force-deflection curve for the last load cycle is presented in Figure 7.4-21. The deflection under the loading point at failure was around 1.92 in. (49 mm). No rupture of the CFCC stirrups was observed at failure. No rupture or debonding of the longitudinal CFCC prestressing strands was observed either.



Figure 7.4-18 Crack pattern in beam C-C



a) Front side



b) Back side

Figure 7.4-19 Failure of beam C-C

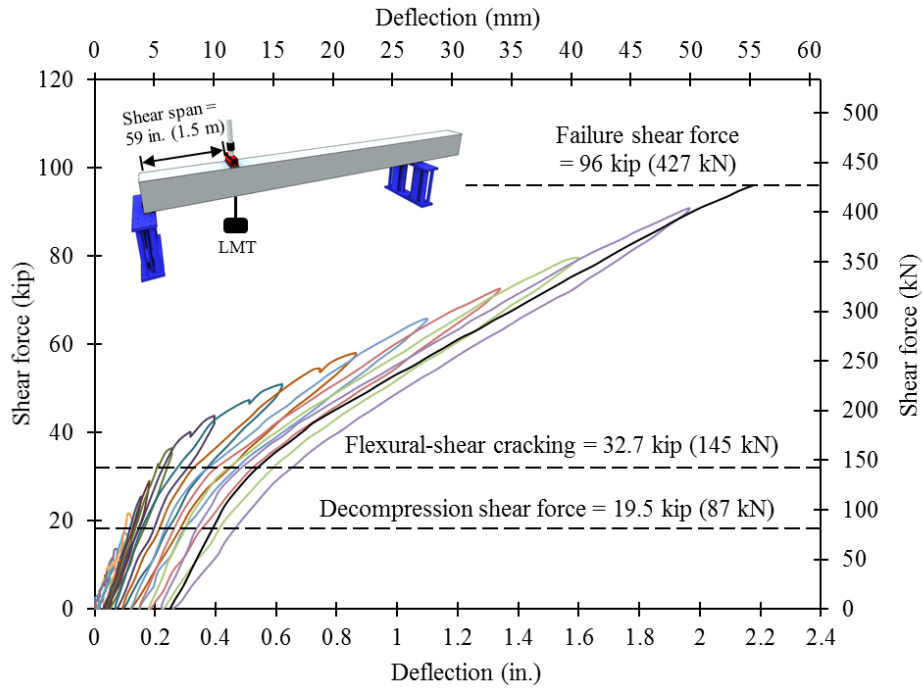


Figure 7.4-20 Shear force vs under-load-deflection in Beam C-C for all load cycles

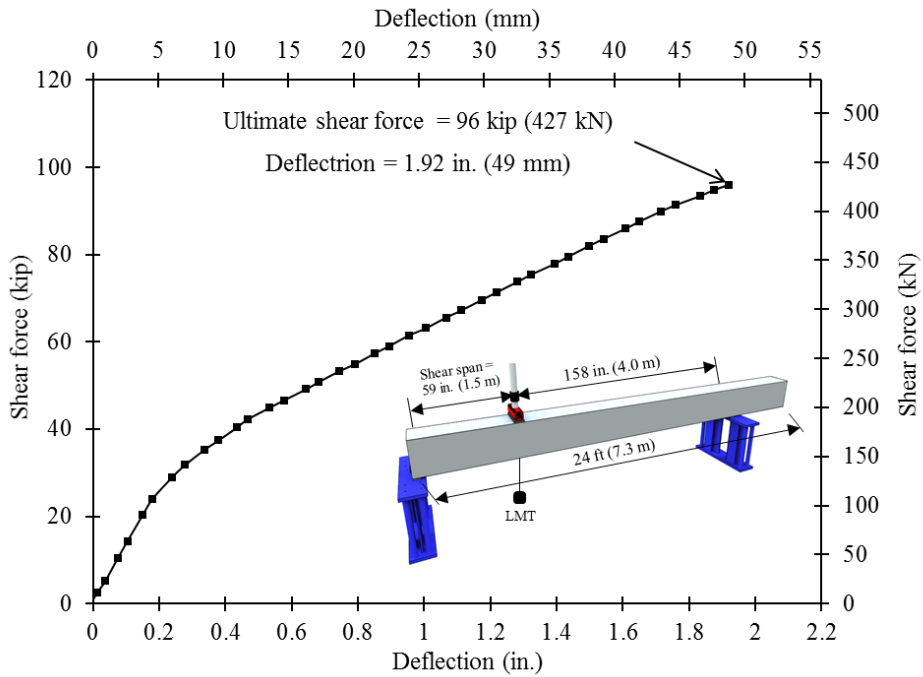


Figure 7.4-21 Shear force vs under-load-deflection in Beam C-C for last load cycle

#### 7.4.3.2 Beam (C-10.75)

Beam C-10.75 was a beam end provided with lap spliced CFCC stirrups with a splice length of 10.75 in. (273 mm). The first observed flexure-shear crack developed at a shear force of 32.3 kip (144 kN) in Bema C-10.75. In addition, a decompression shear force of 19.7 kip (88 kN) was observed in post-cracking load cycles. The flexural cracks extended diagonally through the web with increasing the load. At a shear force level of 58.2 kip (259 kN), the first web shear crack developd, while the existing flexure cracks propagated towards the point of loading, as shown in Figure 7.4-22. A sudden failure took place when the shear force approached 93.5 kip (416 kN). Failure took place through crushing and shearing of the concrete in the compression flange as shown in Figure 7.4-23. The shear force-deflection response for all load cycles is shown in Figure 7.4-24, while the shear force-deflection for last load cycle is shown in Figure 7.4-25. The deflection under the loading point at failure was around 1.84 in. (47 mm). No rupture or pullout of the CFCC stirrups was observed at failure. There was also no rupture or debonding of the longitudinal CFCC prestressing strands.

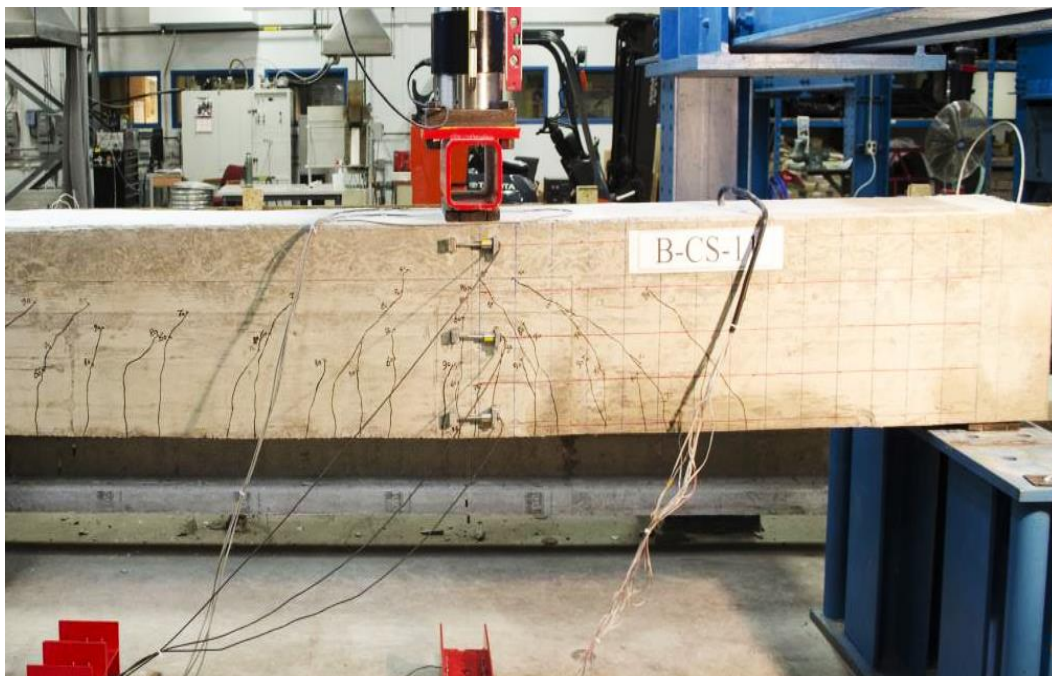


Figure 7.4-22 Crack pattern of beam C-10.75



Figure 7.4-23 Failure of beam C-10.75

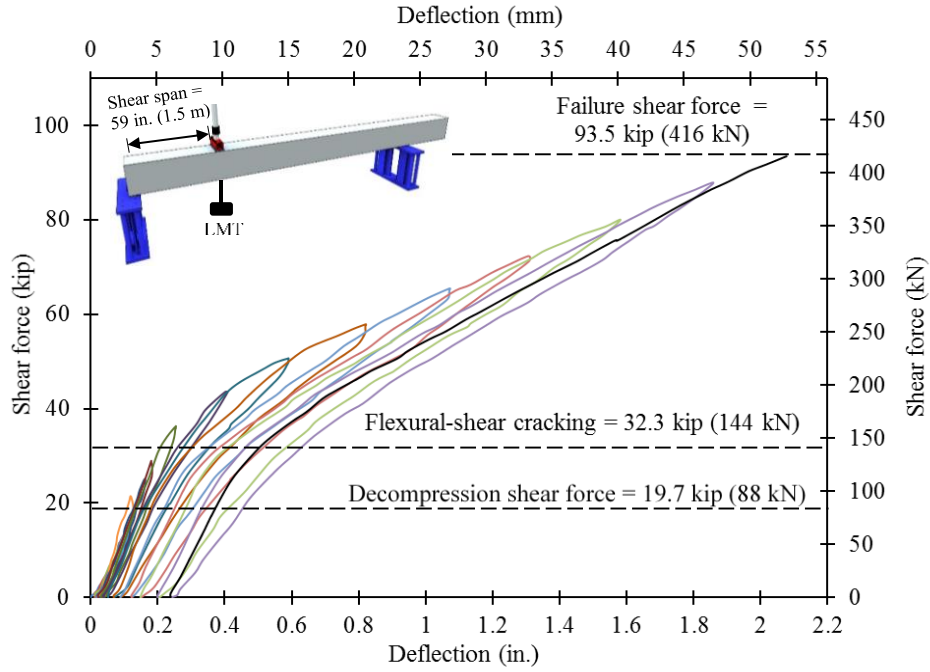


Figure 7.4-24 Shear force vs under-load-deflection in Beam C-10.75 for all load cycles

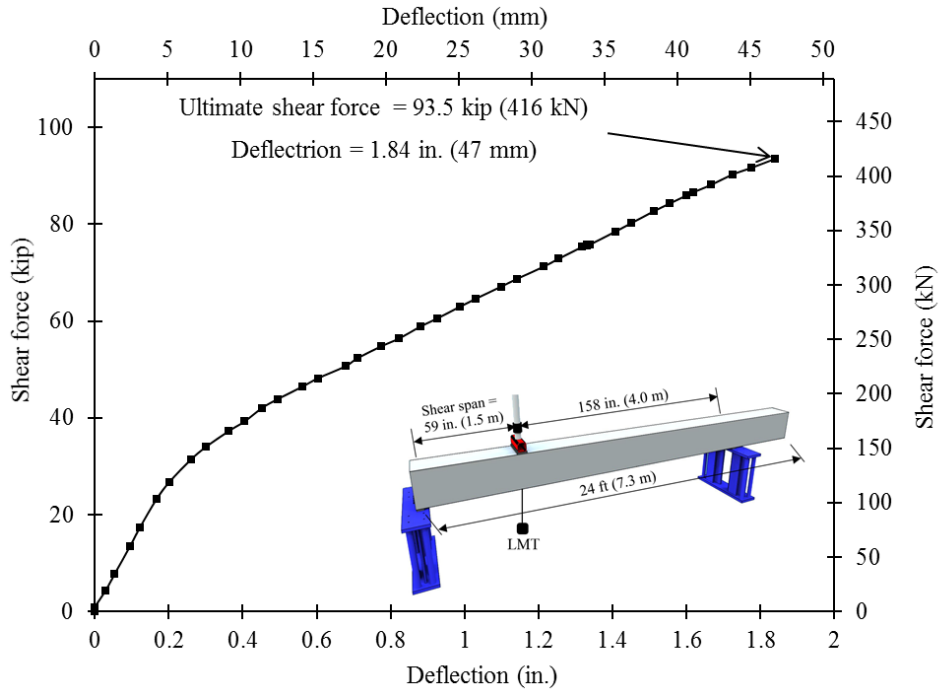


Figure 7.4-25 Shear force vs under-load-deflection in Beam C-10.75 for last load cycle

#### 7.4.3.3 Beam (C-7)

Beam C-7 was a beam end provided with lap spliced CFCC stirrups with a splice length of 7 in. (178 mm). The first observed flexure-shear crack in Beam C-7 developed at a shear force of 30.5 kip (136 kN). In addition, a decompression shear force of 18.6 kip (83 kN) was observed in post-cracking load cycles. At an average shear force of 51 kip (227 kN) three web shear cracks initiated simultaneously and crossed the spliced stirrups in the shear zone, while the existing flexure cracks propagated towards the point of loading, as shown in Figure 7.4-26. A sudden failure took place when the shear force approached 69.2 kip (308 kN). Failure was characterized by pullout of the CFCC stirrups followed by shear failure of the concrete at the major crack as shown in Figure 7.4-27. The shear force-deflection response for all load cycles is shown in Figure 7.4-28, while that for the last load cycle is shown in Figure 7.4-29. The deflection under the loading point at failure was around 1.14 in. (29 mm). No rupture of the CFCC stirrups was observed at failure. However, all the spliced stirrups pulled out of the concrete in the region where the inclined web crack crossed the lapped splice. There was also no rupture or debonding of the longitudinal CFCC prestressing strands.

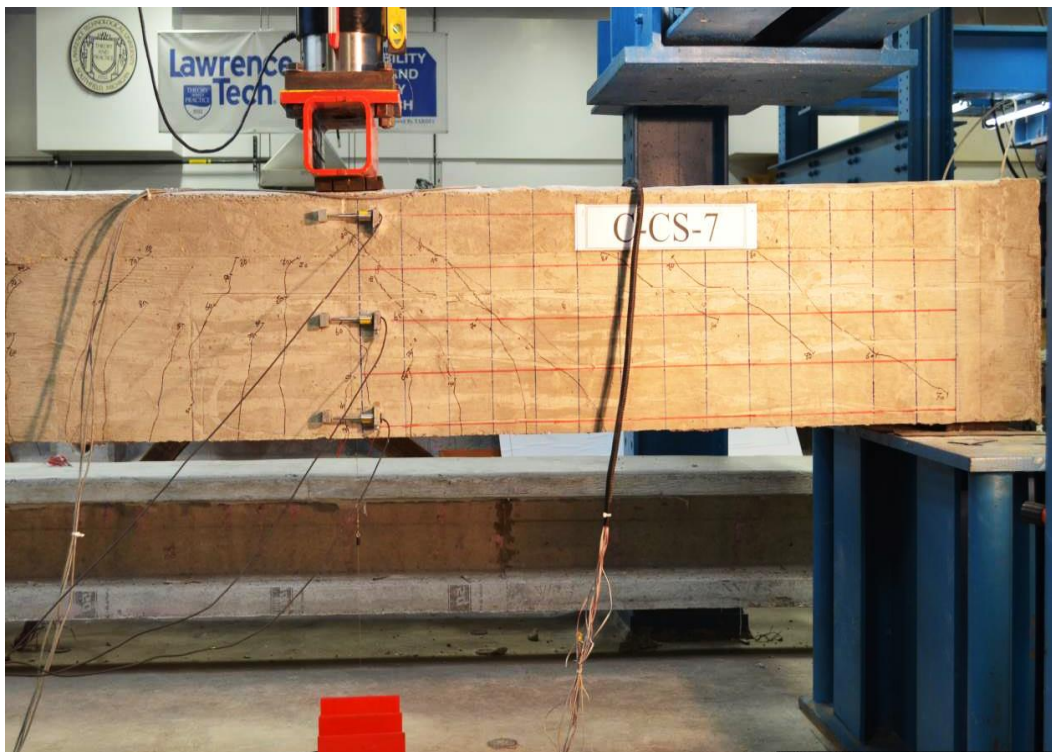


Figure 7.4-26 Crack pattern of beam C-7



a) Front side



b) Back side



c) Slippage of the 7 in. (178 mm) spliced stirrups

Figure 7.4-27 Failure of beam C-7

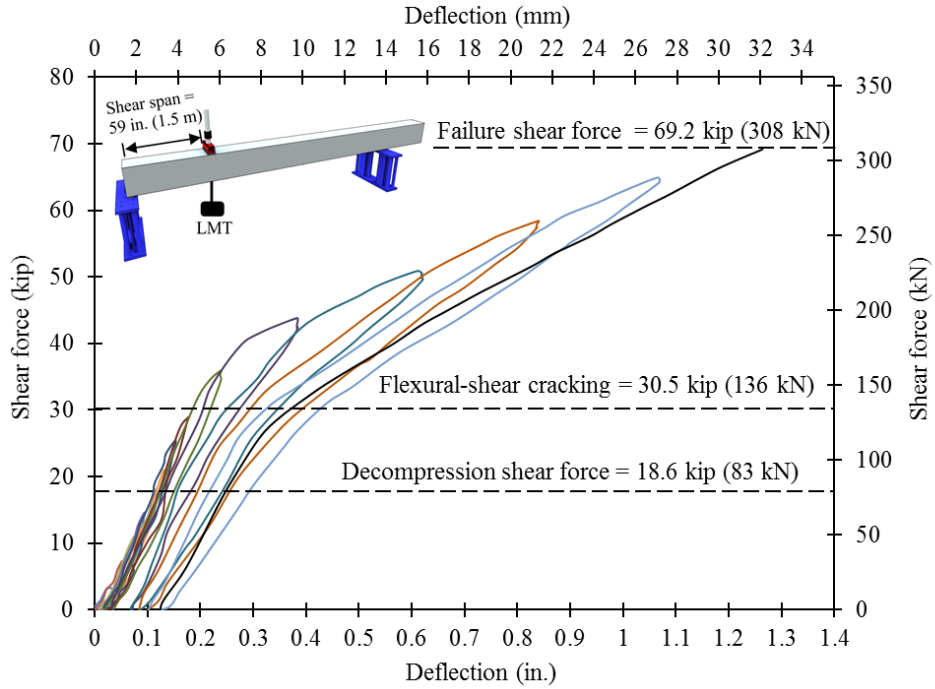


Figure 7.4-28 Shear force vs under-load-deflection in Beam C-7 for all load cycles

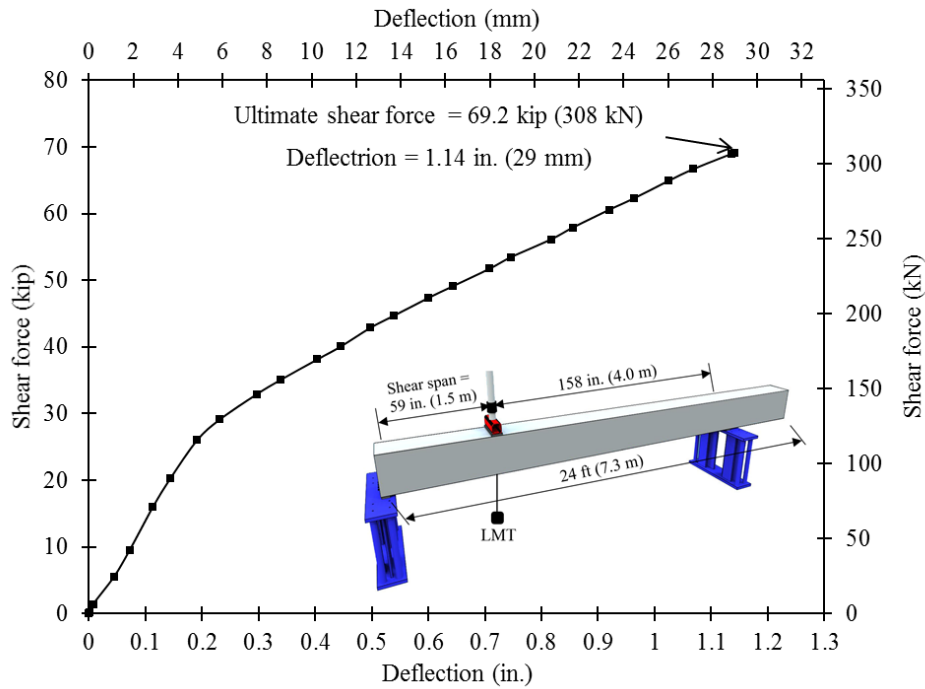


Figure 7.4-29 Shear force vs under-load-deflection in Beam C-7 for last load cycle

#### 7.4.3.4 Beam (C-4)

Beam C-4 was a beam end provided with lap spliced CFCC stirrups with a splice length of 4 in. (102 mm). The first observed flexure-shear crack developed at a shear force of 32.8 kip (146 kN). In addition, a decompression shear force of 20.8 kip (93 kN) was observed in post-cracking load cycles. At a shear force level of 51 kip (227 kN), the first web shear crack initiated, while the existing flexural cracks propagated towards the point of loading, as shown in Figure 7.4-30. A sudden failure took place when the shear force approached 63.6 kip (283 kN). Failure took place through a pullout of the CFCC stirrups followed by a shear failure of the concrete at the major crack as shown in Figure 7.4-31. The shear force-deflection response for all load cycles is shown in Figure 7.4-32, while the shear force-deflection curve for last load cycle is shown in Figure 7.4-33. The deflection under the loading point at failure was around 0.96 in. (24 mm). No rupture of the CFCC stirrups was observed at failure. However, all the spliced stirrups pulled out of the concrete in the region where the inclined web crack crossed the lapped splice. There was also no rupture or debonding of the longitudinal CFCC prestressing strands.

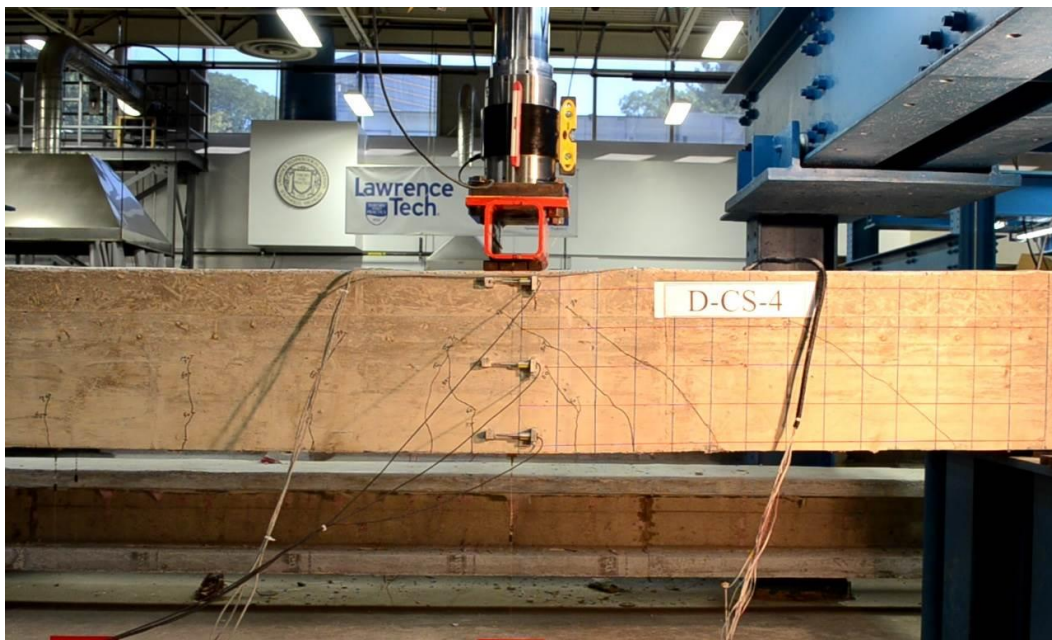


Figure 7.4-30 Crack pattern of beam C-4



a) Front side



b) Back side



c) Slippage of the 4 in. (102 mm) spliced stirrups

Figure 7.4-31 Failure of beam C-4

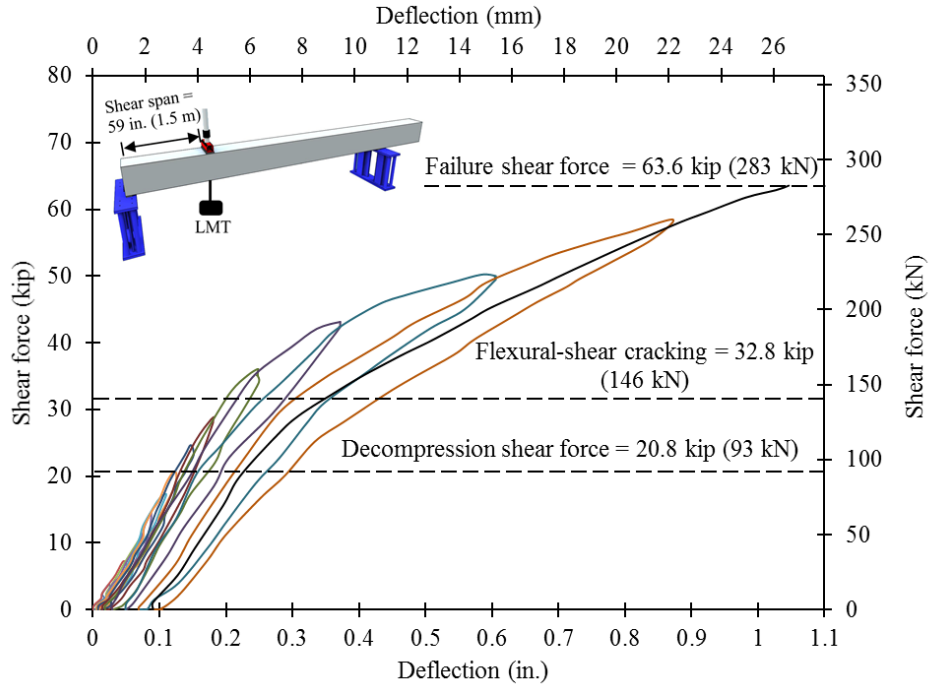


Figure 7.4-32 Shear force vs under-load-deflection in Beam C-4 for all load cycles

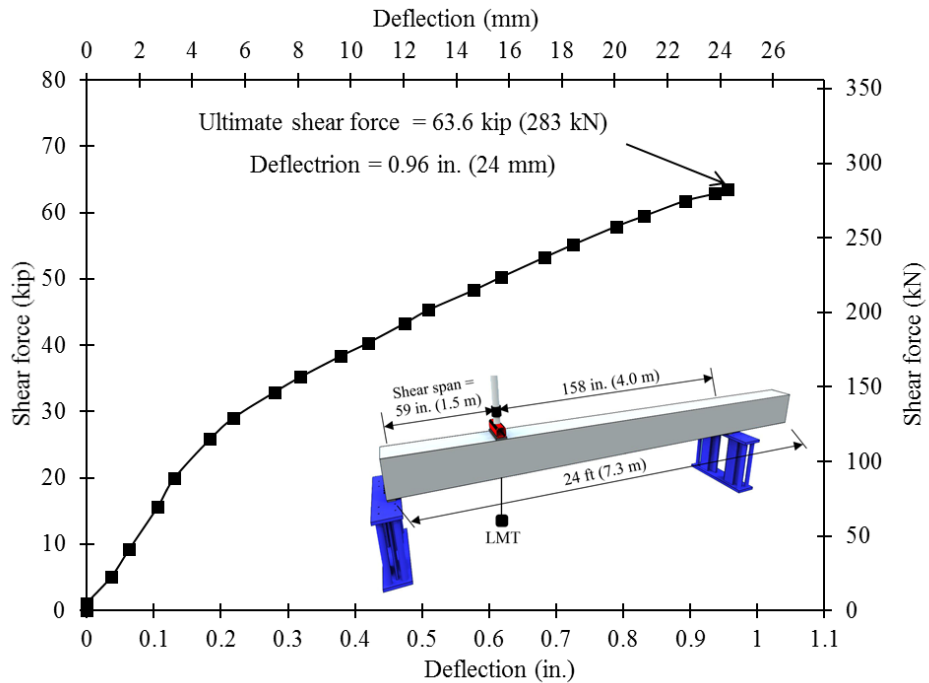


Figure 7.4-33 Shear force vs under-load-deflection in Beam C-4 for last load cycle

#### 7.4.3.5 Control Beam (S-C)

Beam S-C was a beam end provided with closed steel stirrups. The first observed shear crack under the load developed at a shear force of 31.4 kip (140 kN). In addition, a decompression shear force of 19.7 kip (88 kN) was observed in the post-cracking load cycles. At 43.7 kip (194 kN), the first web shear crack initiated, while the existing flexure cracks propagated towards the point of loading as shown in Figure 7.4-34. A sudden failure took place when the shear force approached 89.2 kip (397 kN). Failure took place through top concrete crushing in the compression zone under the load as shown in Figure 7.4-35. The shear force-deflection response for all load cycles is shown in Figure 7.4-36, while the shear force-deflection curve for the last load cycle is shown in Figure 7.4-37. The deflection under the loading point at failure was around 1.86 in. (47 mm). No rupture of the steel stirrups was observed at failure. There was no rupture or debonding of the longitudinal CFCC prestressing strands either.



Figure 7.4-34 Crack pattern of beam S-C



a) Front side



b) Back side

Figure 7.4-35 Failure of beam S-C

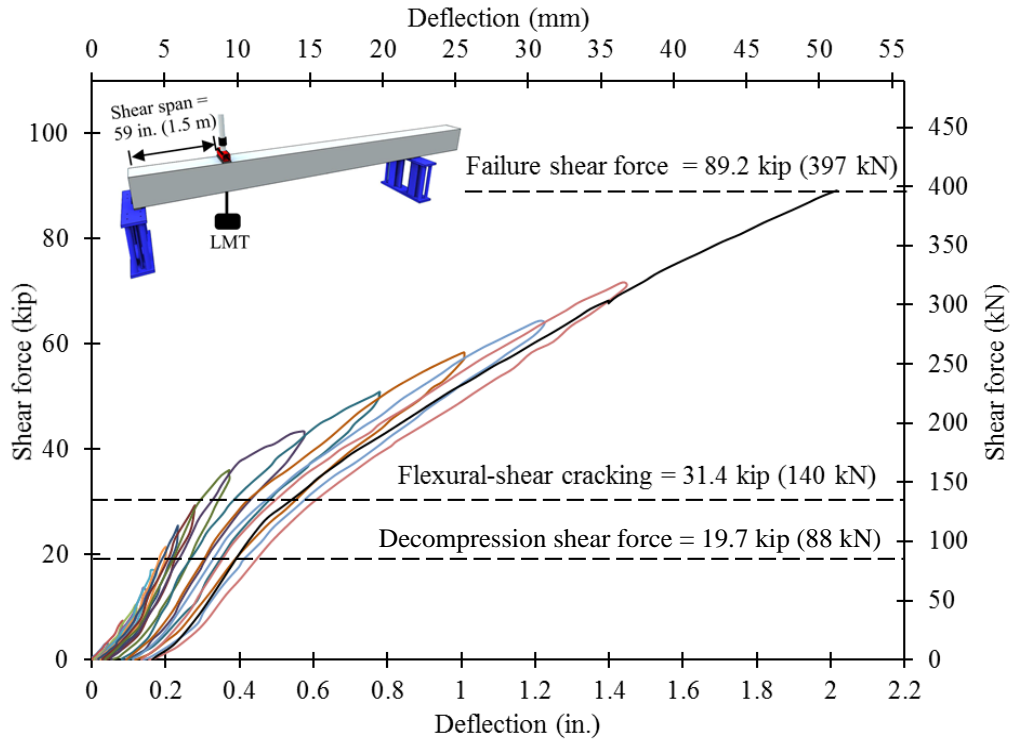


Figure 7.4-36 Shear force vs under-load-deflection in Beam S-C for all load cycles

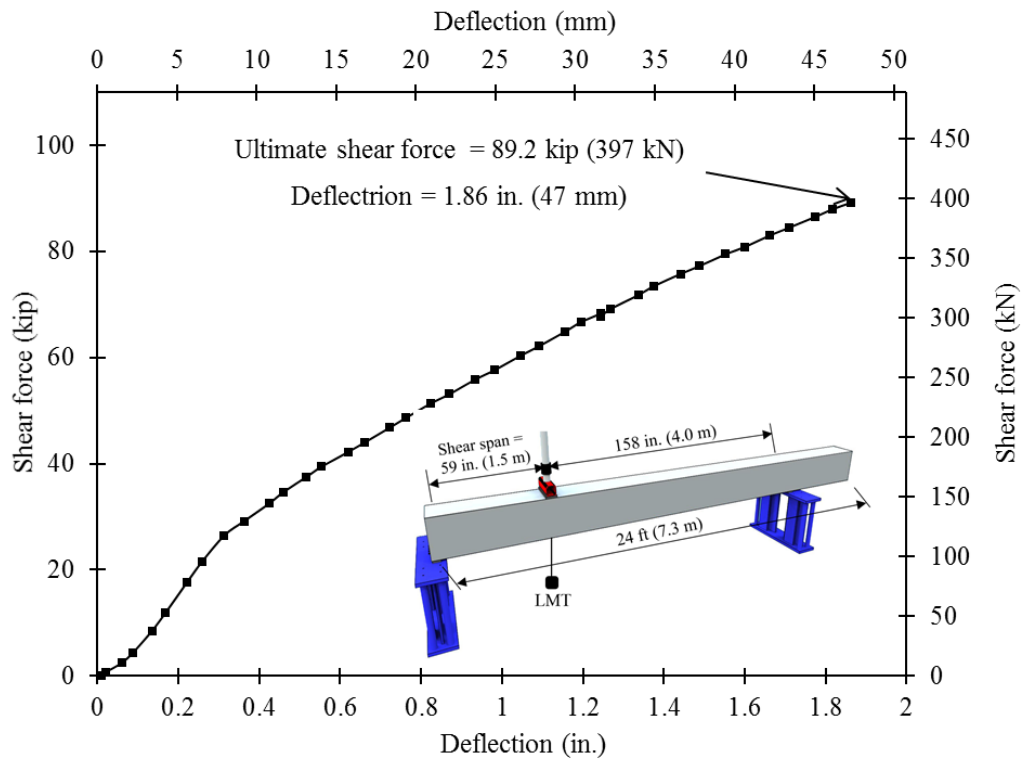


Figure 7.4-37 Shear force vs under-load-deflection in Beam S-C for last load cycle

#### 7.4.3.6 Beam (S-10.75)

Beam S-10.75 was a beam end provided with lap spliced steel stirrups with a splice length of 10.75 in. (273 mm). The first observed flexure-shear crack developed at a shear force of 32.5 kip (145 kN). In addition, a decompression shear force of 21.8 kip (97 kN) was observed during post-cracking load cycles. With further increase in the load, the flexure cracks extended diagonally through the web without any noticeable web shear crack, as shown in Figure 7.4-38. A sudden failure took place when the shear force approached 99.3 kip (442 kN). Failure took place through crushing and shearing of the concrete in the compression flange as shown in Figure 7.4-39. The shear force-deflection response for all load cycles is shown in Figure 7.4-40, while the shear force-deflection curve for the last load cycle is shown in Figure 7.4-41. The deflection under the loading point at failure was around 2.14 in. (54 mm). No rupture of the steel stirrups was observed at failure. Also, none of the stirrups pulled out of the concrete in the region where the inclined crack crossed the lap splice. There was no rupture or debonding of the longitudinal CFCC prestressing strands.



Figure 7.4-38 Crack pattern of beam S-10.75



a) Front side



b) Back side

Figure 7.4-39 Failure of beam S-10.75

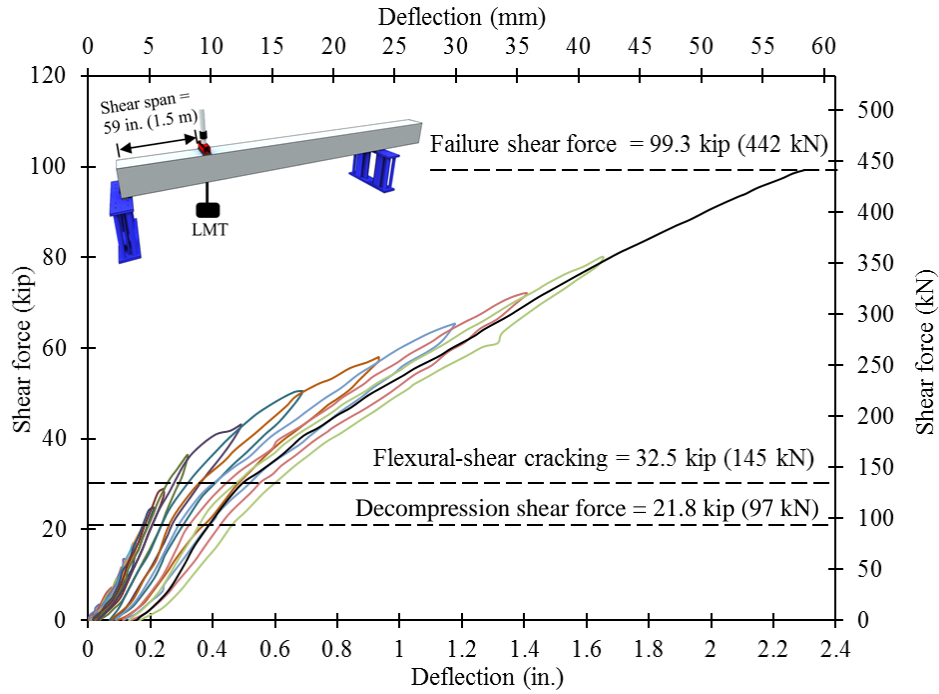


Figure 7.4-40 Shear force vs under-load-deflection in Beam S-10.75 for all load cycles

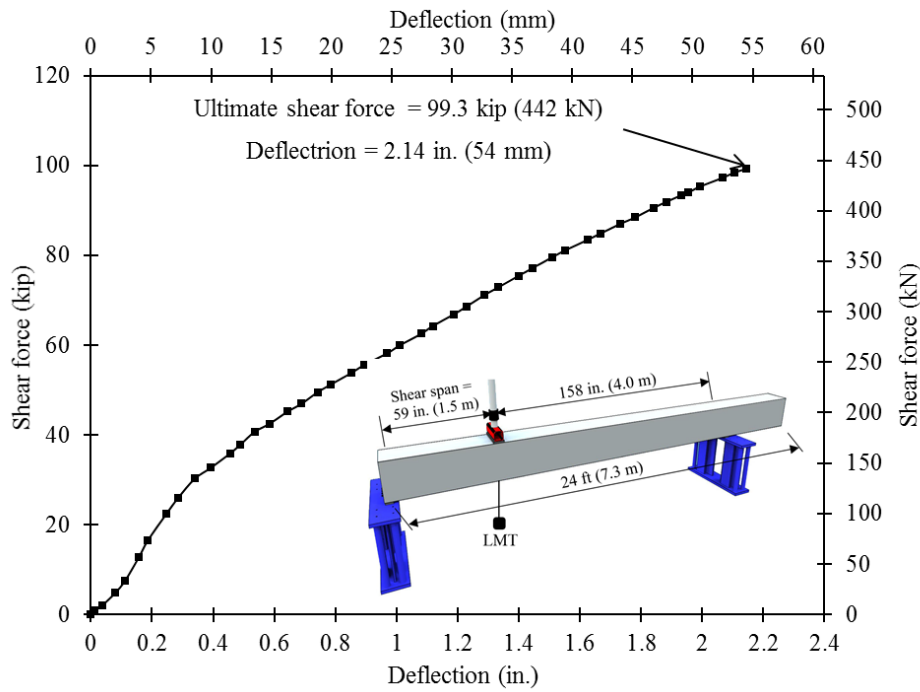


Figure 7.4-41 Shear force vs under-load-deflection in Beam S-10.75 for last load cycle

#### 7.4.3.7 Beam (S-7)

Beam S-7 was a beam end provided with lap spliced steel stirrups with a splice length of 7 in. (178 mm). The first observed flexure-shear crack developed at a shear force of 30.2 kip (134 kN). In addition, a decompression shear force of 20.1 kip (89 kN) was observed in the post-cracking load cycles. At an average shear force of 51 kip (227 kN), the first web shear crack initiated, while the existing flexural cracks propagated towards the point of loading, as shown in Figure 7.4-42. A sudden failure took place when the shear force approached 84.8 kip (377 kN). Failure took place through a pullout of the overlapped steel stirrups followed by a shear failure of the concrete at the major crack as shown in Figure 7.4-43. The shear force-deflection response for all load cycles is shown in Figure 7.4-44, while the shear force-deflection curve for last load cycle is shown in Figure 7.4-45. The deflection under the loading point at failure was around 1.53 in. (39 mm). No rupture of the steel stirrups was observed at failure. No rupture or debonding of the longitudinal CFCC prestressing strands was observed.



Figure 7.4-42 Crack pattern of beam S-7



a) Front side



b) Back side



c) Slippage of the 7 in. (178 mm) spliced stirrups

Figure 7.4-43 Failure of beam S-7

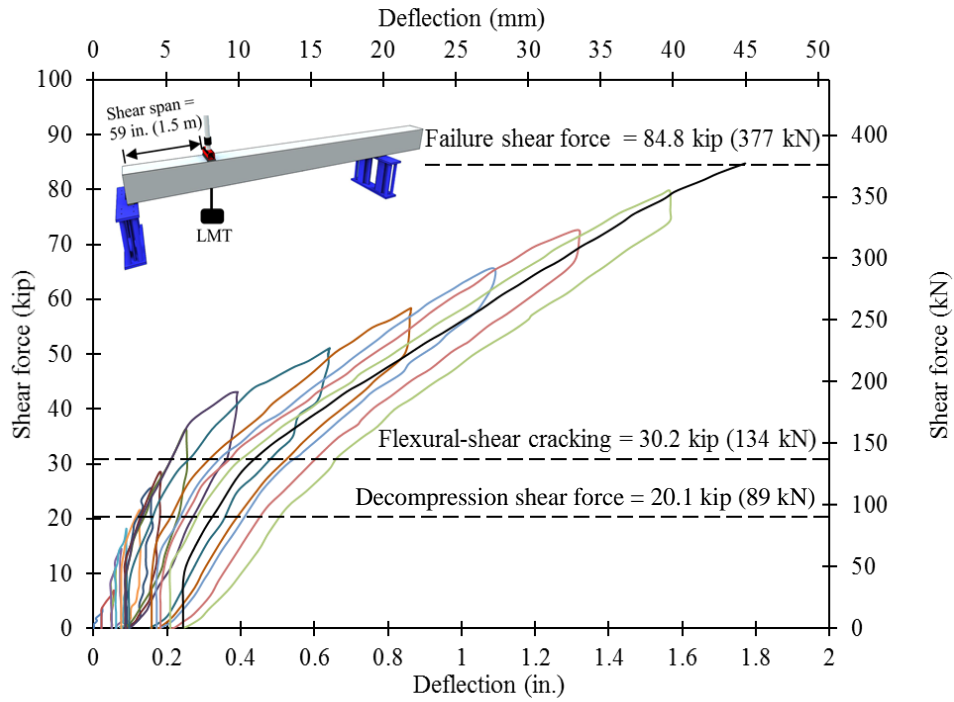


Figure 7.4-44 Shear force vs under-load-deflection in Beam S-7 for all load cycles

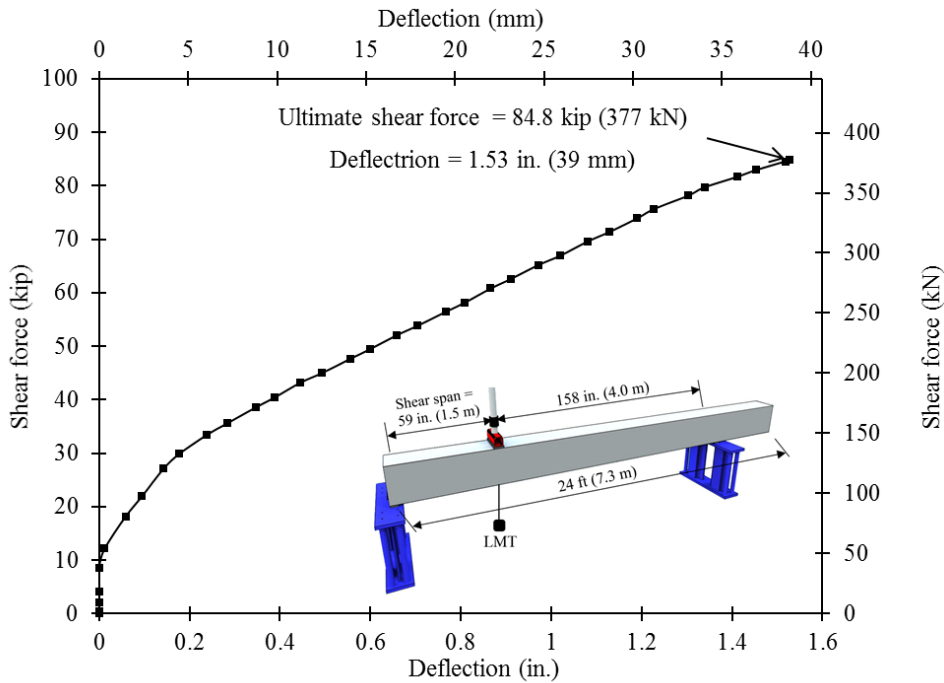


Figure 7.4-45 Shear force vs under-load-deflection in Beam S-C for last load cycle

#### 7.4.3.8 Beam (S-4)

Beam S-4 is a beam end provided with lap spliced steel stirrups with a splice length of 4 in. (102 mm). The first observed flexure-shear crack developed at a shear force of 32.1 kip (143 kN). In addition, a decompression shear force of 19.7 kip (9 kN) was observed in the post-cracking load cycles. At a shear force level of 36.4 kip (162 kN), two web shear crack initiated, while the existing flexure cracks propagated towards the point of loading, as shown in Figure 7.4-46. Sudden failure took place when the shear force approached 72.3 kip (322 kN). Failure took place through a pullout of the overlapped steel stirrups as shown in Figure 7.4-47. The shear force-deflection response for all load cycles is shown in Figure 7.4-48, while the shear force-deflection curve during last load cycle is shown in Figure 7.4-49. The deflection under the loading point at failure was around 1.43 in. (36 mm). No rupture of the steel stirrups was observed at ultimate failure. However, all the spliced stirrups pulled out of the concrete in the region where the inclined web crack crossed the lapped splice. There was no rupture or debonding of the longitudinal CFCC prestressing strands.

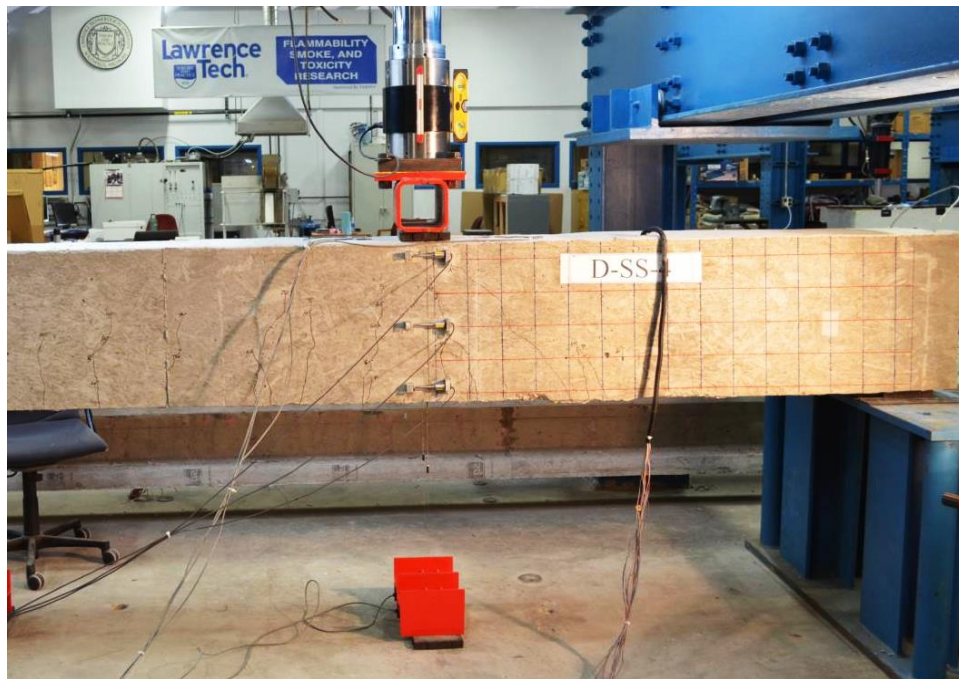
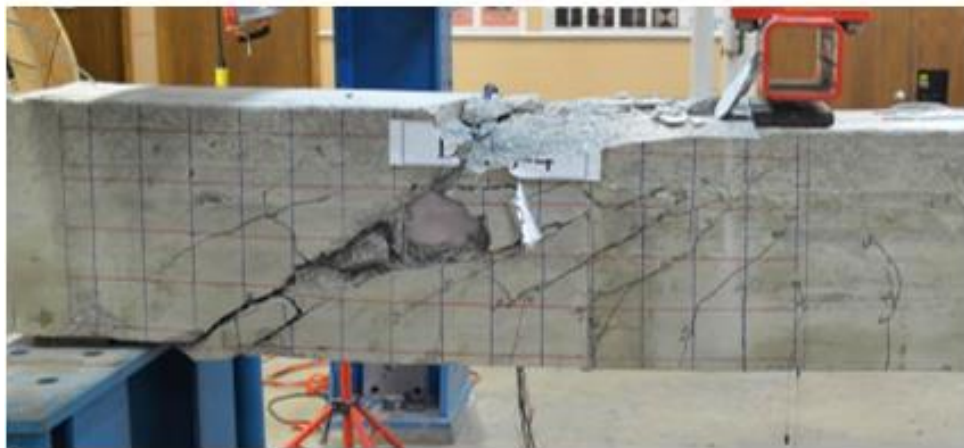


Figure 7.4-46 Crack pattern of beam S-4



a) Front side



b) Back side



c) Slippage of the 4 in. (102 mm) spliced stirrups

Figure 7.4-47 Failure of beam S-4

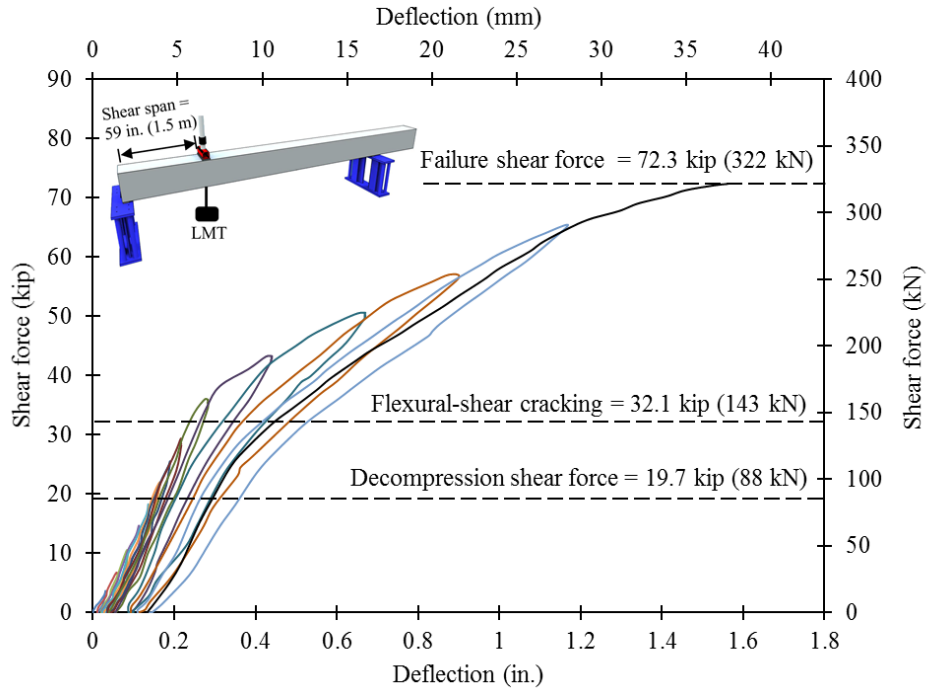


Figure 7.4-48 Shear force vs under-load-deflection in Beam S-4 for all load cycles

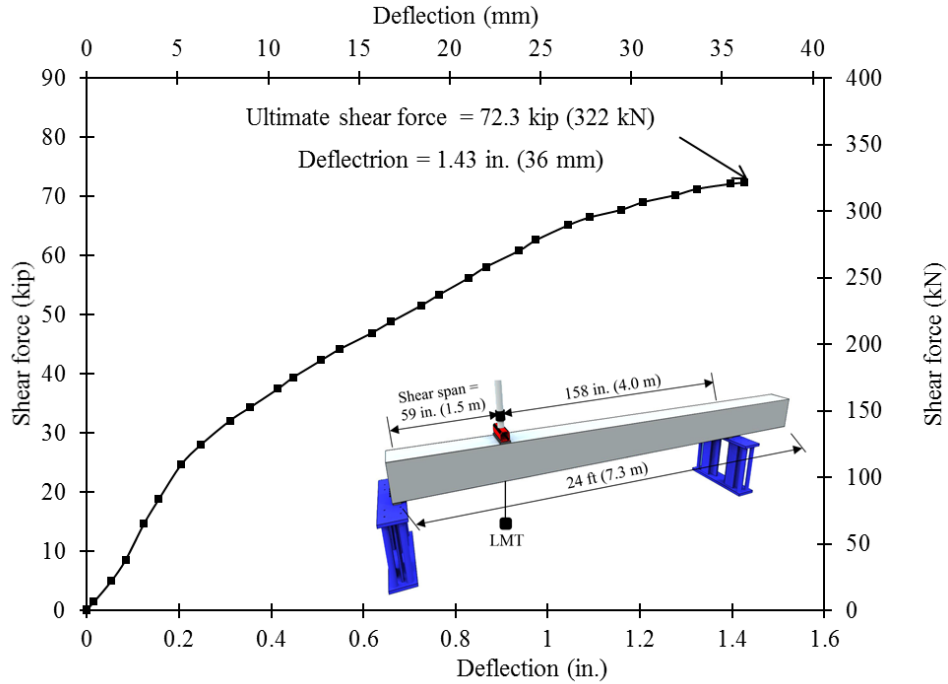


Figure 7.4-49 Shear force vs under-load-deflection in Beam S-C for last load cycle

#### 7.4.4 Discussion of test results

The failure mode of box beams was influenced by the flexure-shear effect at the shear span and the bond between the spliced stirrups and the surrounding concrete. The control beams C-C, S-C exhibited a flexure failure due to crushing of the top concrete in the compression flange upon reaching a top concrete strain at failure of  $-2663 \mu\epsilon$  and  $-2305 \mu\epsilon$ , respectively. Shear mode of failure was observed in beams C-10.75, and S-10.75. Pullout mode of failure was observed in beams C-7, C-4, and S-7, S-4, reinforced with spliced CFCC and steel stirrups, respectively. Prior failure shear cracks propagated diagonally through the web and was followed by slippage of the spliced stirrups, which was distinguished by loud intermittent sounds. Ultimately, a complete failure occurred and characterized by sudden drop in the recorded shear force. This was confirmed from the inspection of the failed portion. Summary of test results is shown in Table 7.4-2.

As shown in the Table, a full-length splice was as efficient in transferring the shear force as the closed stirrups. Besides, a splice of 4 in. (102 mm) in the CFCC or steel stirrups was sufficient to transfer approximately 66 % or 82 % of the shear force transfer by a closed stirrup, respectively.

Overall, it appears that sections with CFCC stirrups achieved slightly less shear carrying capacity than those with steel stirrups. This is understood in the light of the lower elastic modulus of CFCC compared to steel. A lower elastic modulus allowed for wider shear cracks and thereby a reduction in the aggregate interlock.

Table 7.4-2 Summary of test results of the shear bond test

ID	Decomp. shear force. kip (kN)	Cracking shear force $V_{cr}$ kip (kN)	Ultimate shear force $V_u$ kip (kN)	Maximum deflection under load $\delta_u$ in. (mm)	Top concrete strain $\epsilon_{cu}$ ( $\mu\epsilon$ )	Maximum stirrups strain $\epsilon_{stirrup}$ ( $\mu\epsilon$ )	Mode of failure
C-C	19.5 (86.7)	32.7 (145.5)	96.0 (427.0)	1.92 (48.8)	-2663	2143	Crushing
C-10.75	19.7 (87.6)	32.3 (143.7)	93.5 (415.9)	1.84 (46.7)	-2770	1563	Shear
C-7	18.6 (82.7)	30.5 (135.7)	69.2 (307.8)	1.14 (49.0)	-1868	1186	Pullout
C-4	20.8 (92.5)	32.8 (145.9)	63.6 (282.9)	0.96 (24.4)	-1801	1444	Pullout
S-C	19.7 (87.6)	31.4 (139.7)	89.2 (396.8)	1.86 (47.2)	-2305	2237	Crushing
S-10.75	21.8 (97.0)	32.5 (144.6)	99.3 (441.7)	2.14 (54.5)	-3273	1272	Shear
S-7	20.1 (89.4)	30.2 (134.3)	84.8 (377.2)	1.53 (38.9)	-2410	3076	Pullout
S-4	19.7 (87.6)	32.1 (142.8)	72.3 (321.6)	1.43 (36.3)	-2386	2933	Pullout

## CHAPTER 8: LONG-TERM PERFORMANCE OF BEAMS WITH CFRP

### 8.1 Introduction

After construction, bridge beams prestressed with CFRP strands are exposed to harsh weather along with traffic loads. The lifespan of the bridge and future rehabilitation work depend on the resistance of the CFRP materials to different environmental conditions. Some of Michigan earlier bridges with CFRP reinforcement are currently under continuous monitoring (Grace et al. 2005 and 2002b) and different studies were conducted on the lifecycle cost analysis of bridge beams considering the environmental effect (Grace et al. 2012b).

In order to evaluate the effect of temperature and environmental conditions on the prestress loss in CFRP pretensioned beams, five 26-ft. (7.92-m) long deck bulb T-beams were designed, constructed, and subjected to harsh Michigan weather for extended time before they were tested under four-point-load flexural test setup to failure. Each beam was prestressed initially to 88 kip (391 kN) and designed to fail in a balanced-failure mode (balanced reinforced section). Out of the five beams, one beam served as a control beam and was tested to failure after 28 days of construction. The remaining four beams were split into two groups: two indoor and two outdoor beams. The two indoor beams were kept indoors in a controlled laboratory environment, while the two outdoor beams were kept outdoors, where they were subjected to different environmental conditions such as seasonal temperature change, rain, and freezing rain. After one year, one indoor beam and one outdoor beam were brought to the testing facility and were instrumented and tested to failure in a load setup similar to that used in testing the control beam. After two years of construction, the remaining two beams were also instrumented and tested to failure under the same load setup.

Cracking loads, decompression loads, maximum concrete and CFRP strains, maximum loads, and corresponding maximum deflections were collected compared among the five beams. In addition, an estimate for prestress loss was calculated for each beam based on the test results. The prestress loss calculations took into account the creep and shrinkage of concrete that were evaluated experimentally for the concrete batch by testing concrete prisms and cylinders according to current ASTM standards. The best estimates for concrete creep and shrinkage were determined and compared to their mathematically determined values according to current codes and guidelines

such as AASHTO LRFD and PCI. Test details and results are provided in this Chapter. The test results showed that except for a slight change in concrete strength, there was no significant difference in the test results among the five beams. In addition, short and long-term prestress loss can be reasonably estimated using current design guidelines established for steel strands except for prestress relaxation, which is determined based on properties of CFRP strands.

**8.2 Decked Bulb T beams**

**8.2.1 Test setup**

Five decked bulb T-beams were tested under four-point flexural loading to determine their overall performance and the prestress losses with respect to age and exposure conditions. The nomenclature for the beams were; C, I-1, O-1, I-2, and O-2 representing control, 1 year indoor, 1 year outdoor, 2 years indoor, and 2 years outdoor beams, respectively. Figure 8.2-1 and Figure 8.2-2 show the longitudinal and cross sections of the decked bulb T-beams.

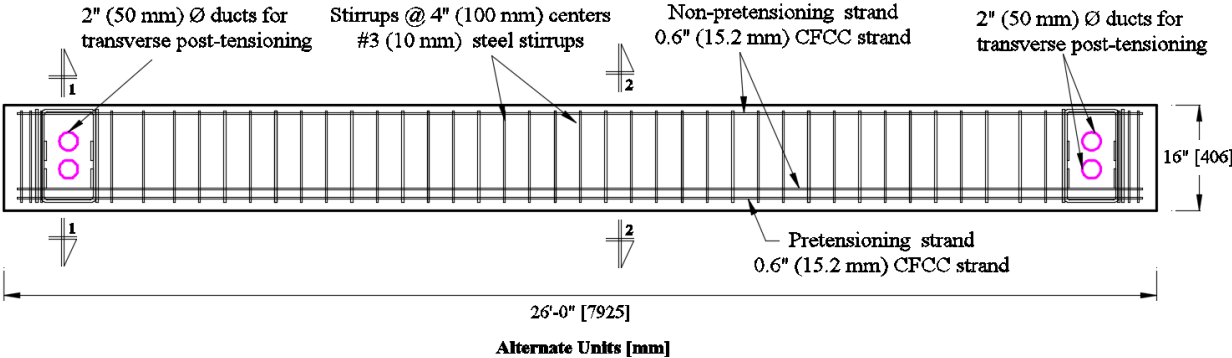


Figure 8.2-1 Longitudinal section of prestressed decked bulb T beam

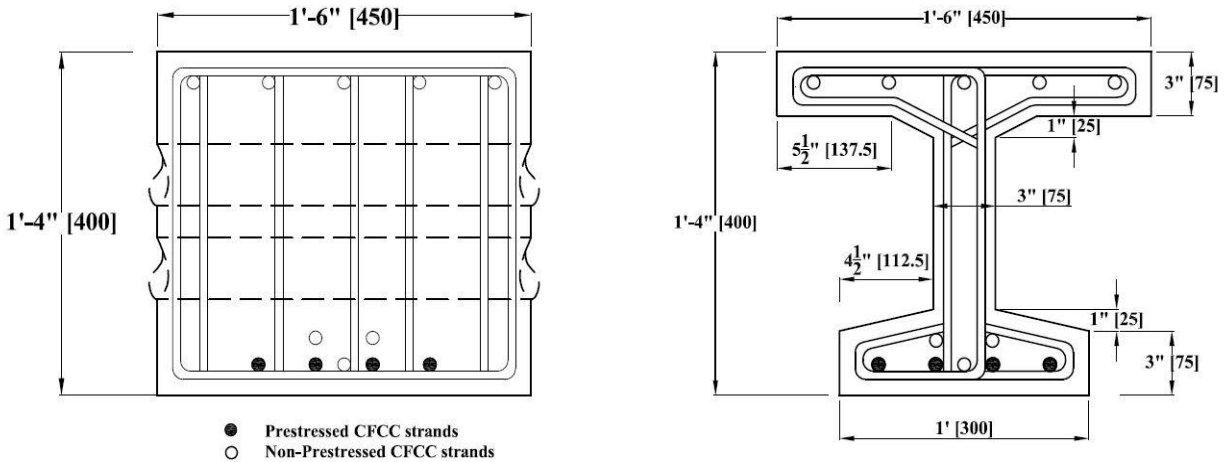


Figure 8.2-2 Details of cross section 1-1 (left) & 2-2 (right) of the beam specimen

The beams were reinforced with 4 prestressed and 3 non-prestressed 0.6 in. (15.2 mm) CFCC strands. Five similar non-prestressed strands were provided in the compression zone as a top reinforcement. The shear reinforcement in the beams consisted of 0.375 in. (10 mm) diameter Grade 60 deformed steel stirrups with three configurations as shown in Figure 8.2-3 and Figure 8.2-4 for the stirrups at the ends and middle of span respectively. The material properties for the shear reinforcement are summarized in Table 8.2-1. In addition, Two 3 in. (75 mm) diameter PVC pipes were installed in the end blocks to serve as conduits for typical post-tensioning as shown in Figure 8.2-5. The conduits were not used in this study since beams were tested individually.

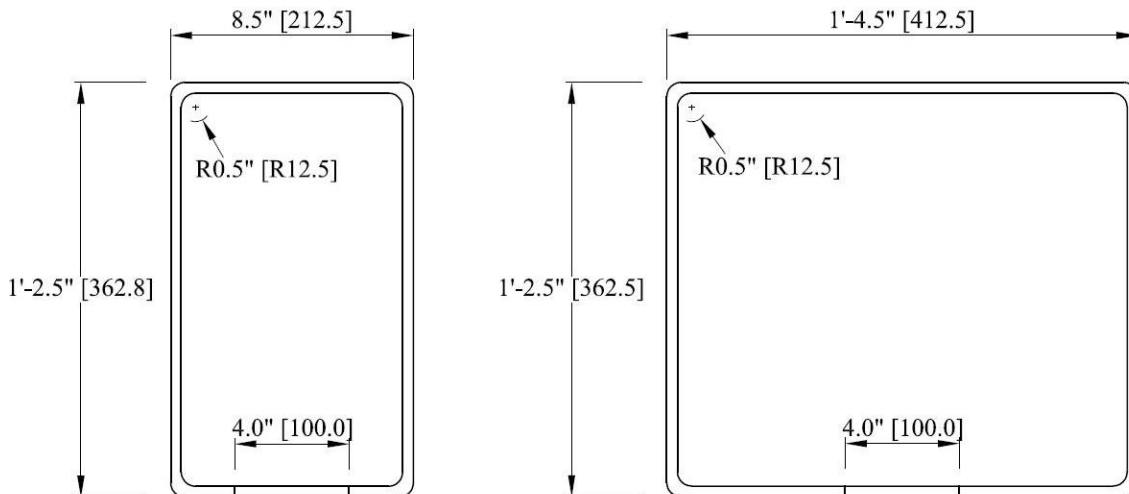


Figure 8.2-3 Steel shear reinforcement for end blocks

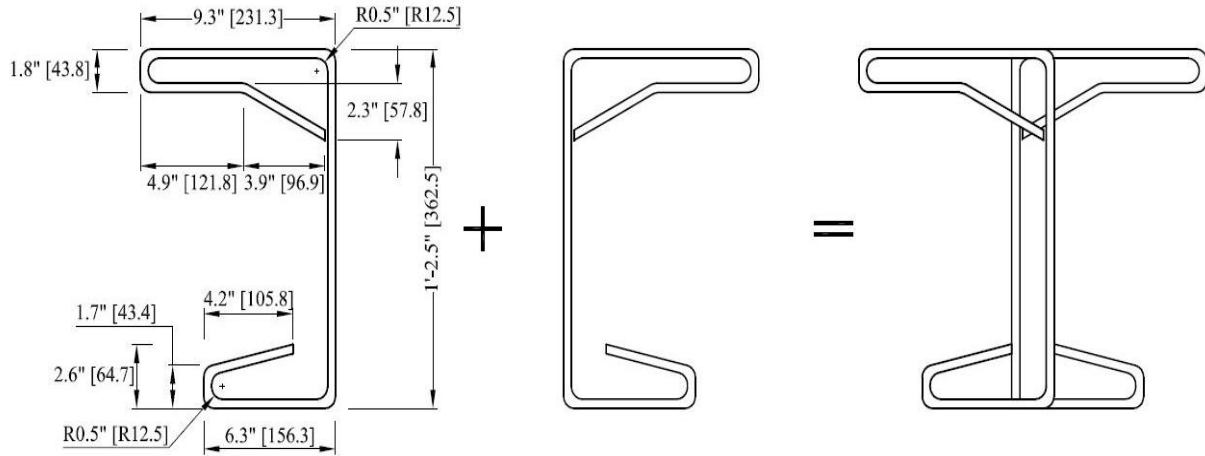


Figure 8.2-4 Steel shear reinforcement between end blocks

Table 8.2-1 Properties of steel shear reinforcement

Designation	# 3
Grade	60
Diameter, in. (mm)	0.375 (10)
Weight, lb/ft (N/m)	0.38 (5.64)
Cross-sectional area, in <sup>2</sup> (mm <sup>2</sup> )	0.11 (71)
Yield load, kip (kN)	6.6 (29.4)
Min. yield strength, ksi (MPa)	60 (414)
Breaking strength, kip (kN)	9.9 (44)
Min. tensile strength, ksi (MPa)	90 (621)
Modulus of elasticity, ksi (GPa)	29,000 (200)



Figure 8.2-5 Installing PVC conduits in the end block of the beams

The formwork consisted of the deck, center wall, side walls, and end plates. Wood was the major construction material for these groups with the exception of the side walls, which were made of a combination of wood and Styrofoam. The wooden deck (as shown in Figure 8.2-6) had a length of 52 ft (15.85 m) and a width of 4 ft (1.2 m). It was mounted on steel adjustable chairs spaced at 2 ft (0.6 m) on center, in rows of 2 along its length. Styrofoam with different thickness were cut to certain lengths and angles pertinent to the dimensions of the beam. The sheets were glued together and screwed to the wooden side and center walls (Figure 8.2-6 through Figure 8.2-8). All formwork in contact with concrete were smeared with oil to waterproof the surface and ensure easy deforming. To improve the stiffness of the formwork, a series of braces (wood and steel threaded rods) as shown in were used.

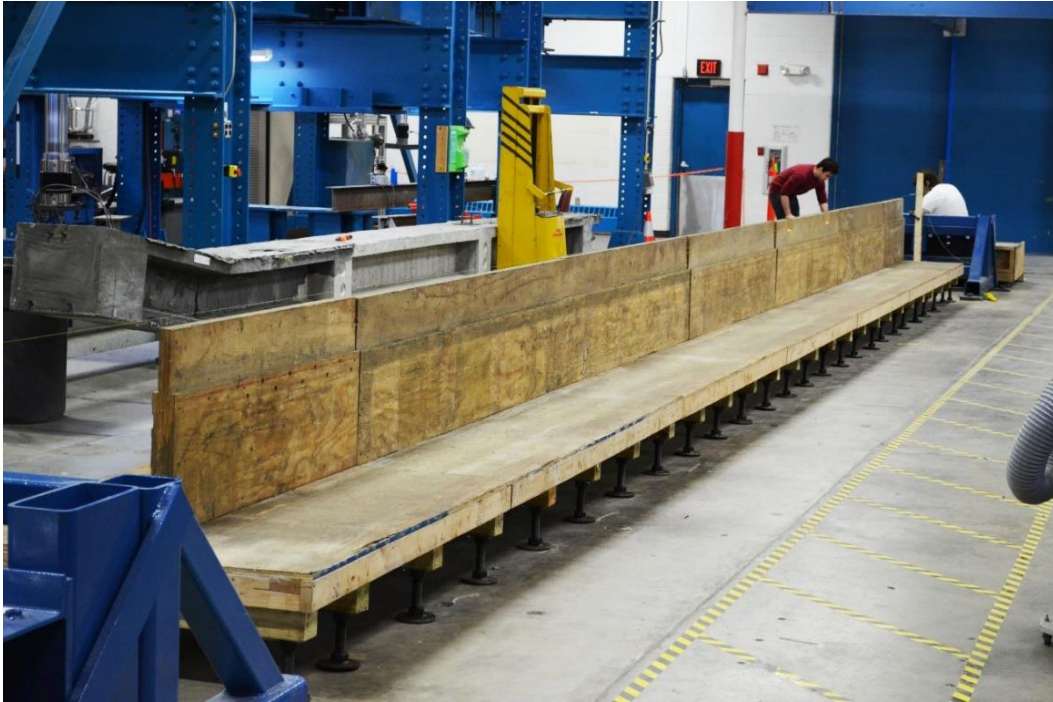


Figure 8.2-6 Wooden deck supported on adjustable steel chairs and center wall spanning between steel bulk heads



Figure 8.2-7 Leveling the platform using a laser level

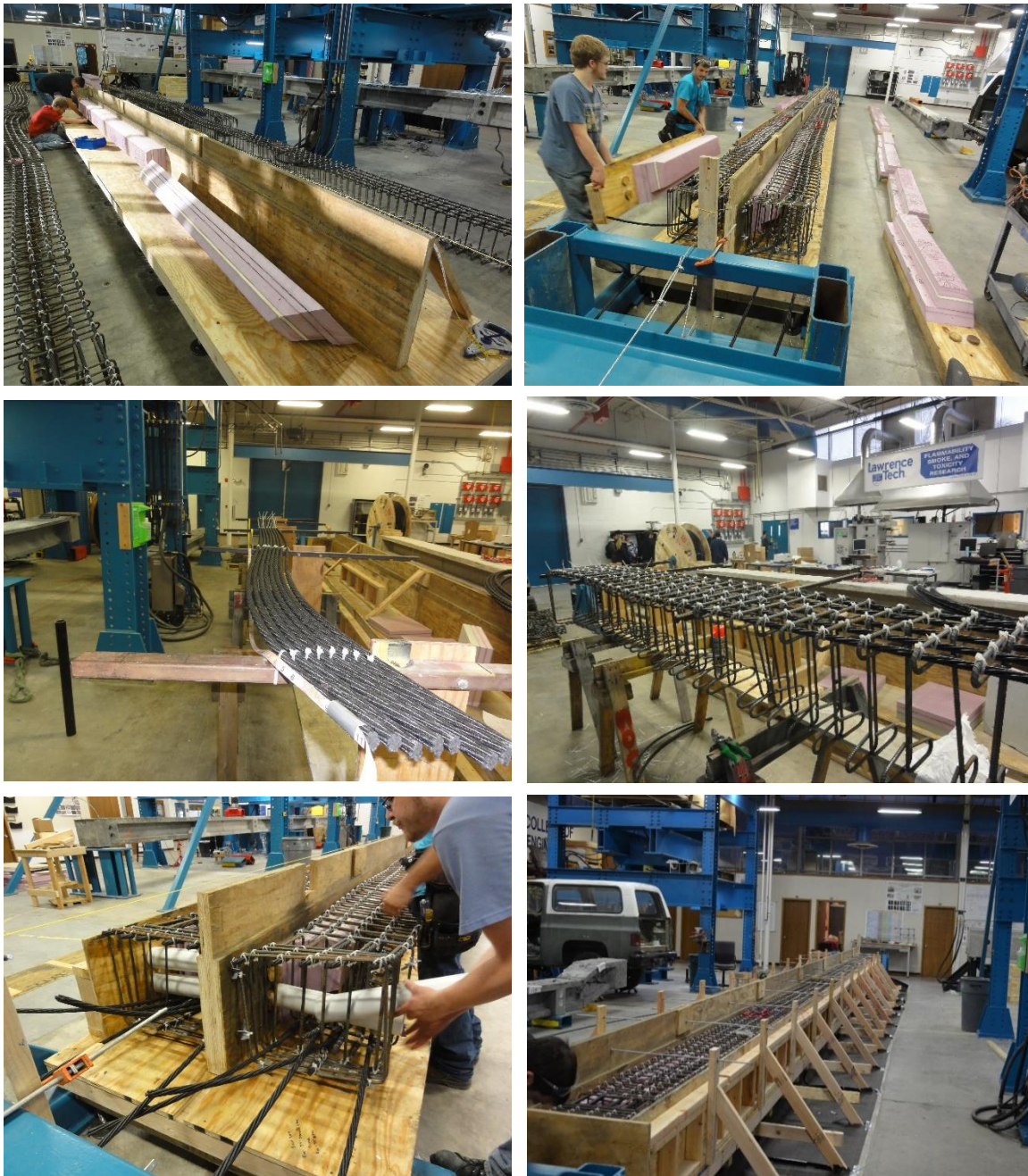


Figure 8.2-8 Different stages of formwork and cage construction

The reinforcement cage consisted of the flexural and shear reinforcements arranged. The process of construction of the reinforcement cage started by placing the compression reinforcement on stands and marking the positions of stirrups. The stirrups were placed in position and fastened with plastic ties. All other layers of non-prestressed reinforcement were passed through the stirrups and fastened into position. The cage was removed from the frame and placed on the deck and the

prestressing reinforcement spanning the full length of the deck were passed through as shown in Figure 8.2-9 . Plastic chairs with a height of  $\frac{3}{4}$  in. (19 mm) were installed on sides of the stirrups and the bottom longitudinal reinforcement to provide side and bottom cover respectively.

As shown in Figure 8.2-10, the formwork accommodated two beams side by side. Each beam was prestressed with four CFCC strands with a jacking force of 24 kip (106.75 kN) per strand. Prestressing was applied through two abutment-type steel bulk heads positioned at the ends of the deck. The CFCC prestressing strands were coupled with steel strands at the live and dead ends to facilitate anchorage (Figure 8.2-11). Threaded rods and nuts served as anchorage on the dead-end bulkhead. In-line load cells were installed at the dead ends on all eight prestressed strands. In addition, strain gages were attached to prestressed CFCC strands near the mid-span section (Figure 8.2-12).

Concrete with a design 28-day compressive strength of 7000 psi (48 MPa) and a slump of 8.0 in. (200 mm) was ordered and supplied. During placement, 6 in.  $\times$  12 in. (150 mm  $\times$  300 mm) concrete cylinders were prepared and cured under the same conditions as the beams, and were tested at ages 7, 14, 21, 28 days, 1 year, and 2 years to record the development of the compressive strength in accordance with ASTM C39/C39M-12: “Test Method for Compressive of Cylindrical Concrete Specimens”. Before placement, a slump test (Figure 8.2-13) was conducted and the slump was approximately 10 in. (254 mm).



Figure 8.2-9 Bottom prestressing installation

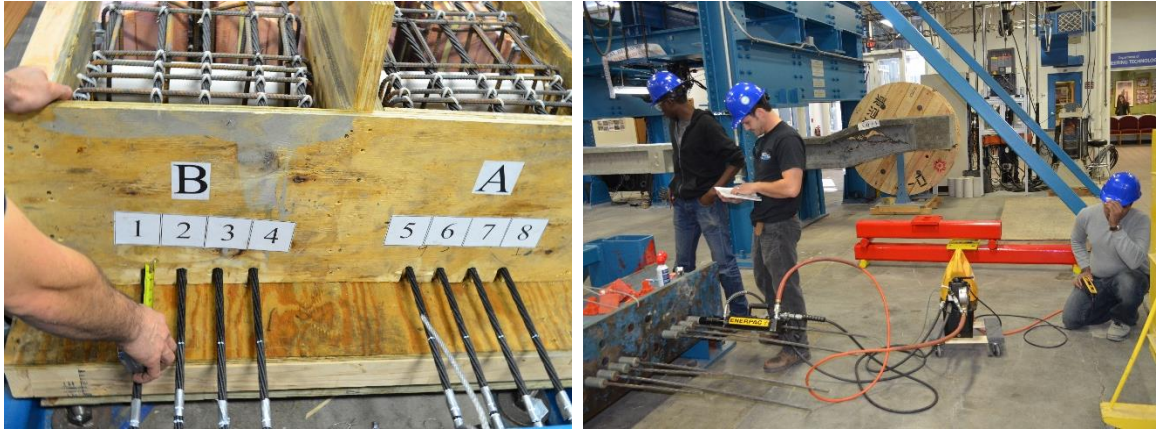


Figure 8.2-10 Layout and prestressing CFCC strands



Couplers with attached in-line load cells on the dead end

Couplers on the live end

Figure 8.2-11 Coupler connections



Figure 8.2-12 Installed strain gages on longitudinal reinforcement



Figure 8.2-13 Slump test

Concrete was placed manually in the formwork and was compacted using electric pencil vibrators. Care was taken during vibration to avoid damaging the installed internal strain gages. Figure 8.2-14 shows the stages of casting. After concrete placement, the specimens were covered with burlaps and moist cured for 7 days.

To record the core temperature of the decked bulb T-beams during curing, K-type thermocouple wires with a range of  $-325$  to  $+750$  °F ( $-200$  to  $+400$  °C) were embedded in the top and bottom flanges, and mid-web section at mid-span of the beams. Readings were taking off an OMEGA® HH509R handheld reader.

The sides of the formwork were removed 24 hours after concrete placement. Twenty-one days after casting, prestressing force was transferred to the beams by releasing the steel strands at the live end as shown in Figure 8.2-15 using a torch. As illustrated in Figure 8.2-16 and Figure 8.2-17, a total loss of 2 kip (8.9 kN) was recorded from the time of initial jacking to release. Immediately before prestress release, the prestressing force averaged at 22 kip (98 kN) A camber of 0.25 in. (6.35 mm) was recorded at release. After transfer of prestressing force, the beams were transferred to storage.

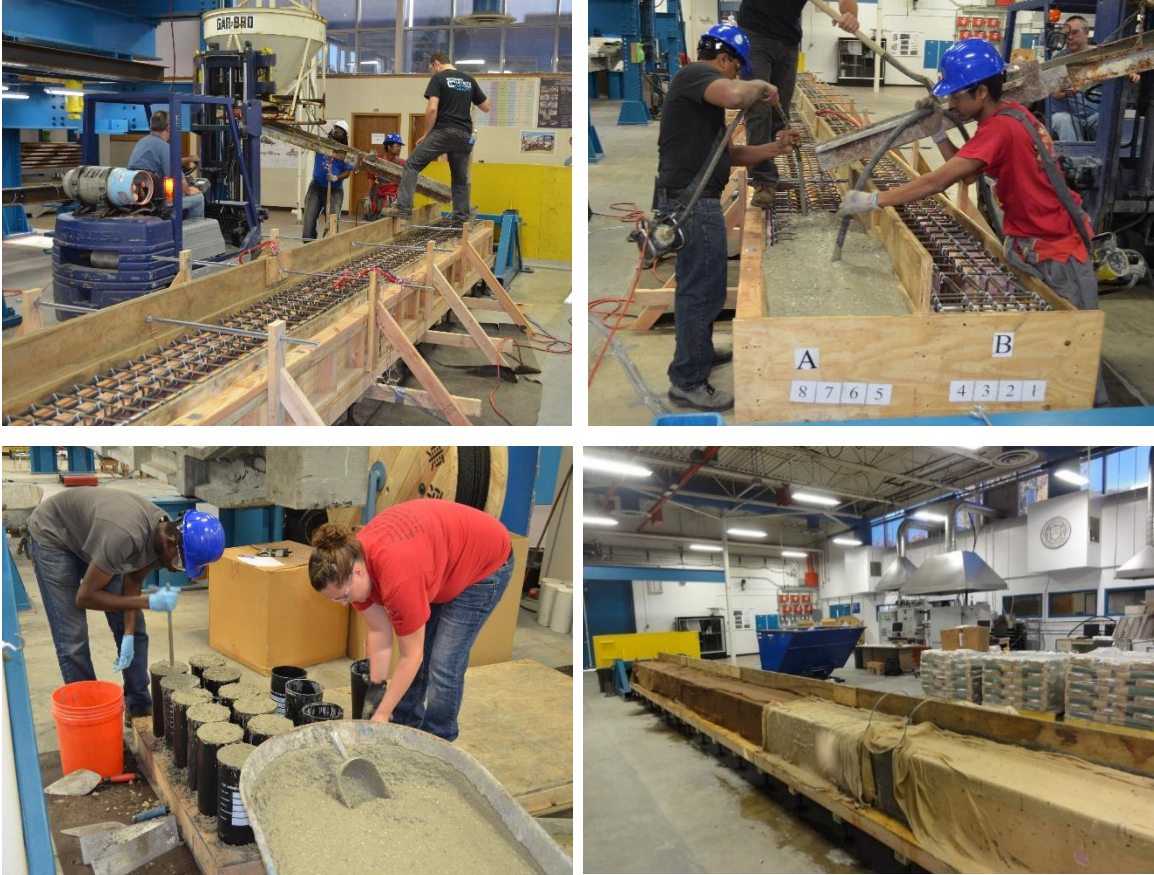


Figure 8.2-14 Placing and curing the concrete of the beams and cylinders



Figure 8.2-15 Release of steel strands at transfer

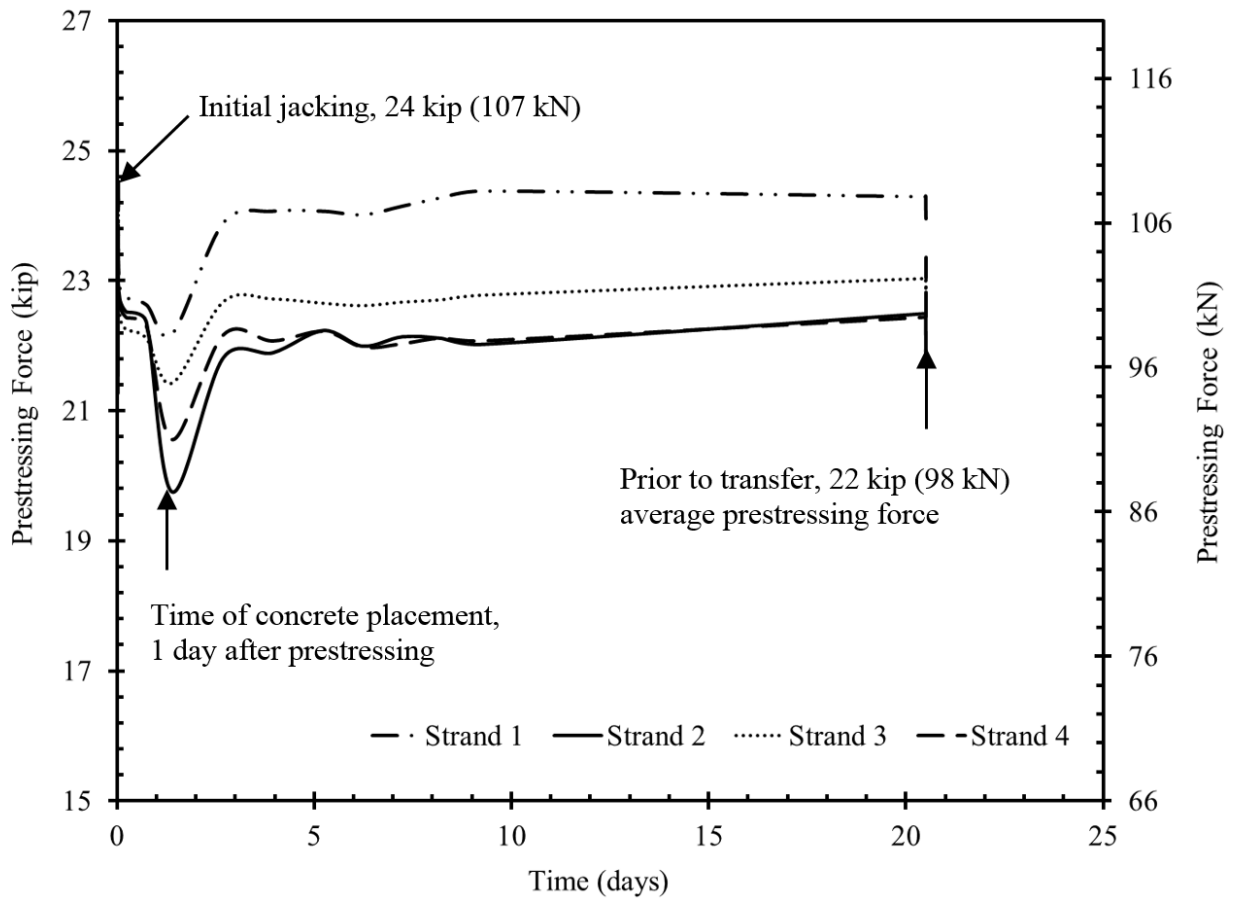


Figure 8.2-16 Prestress loss prior to transfer (Strand 1-4)

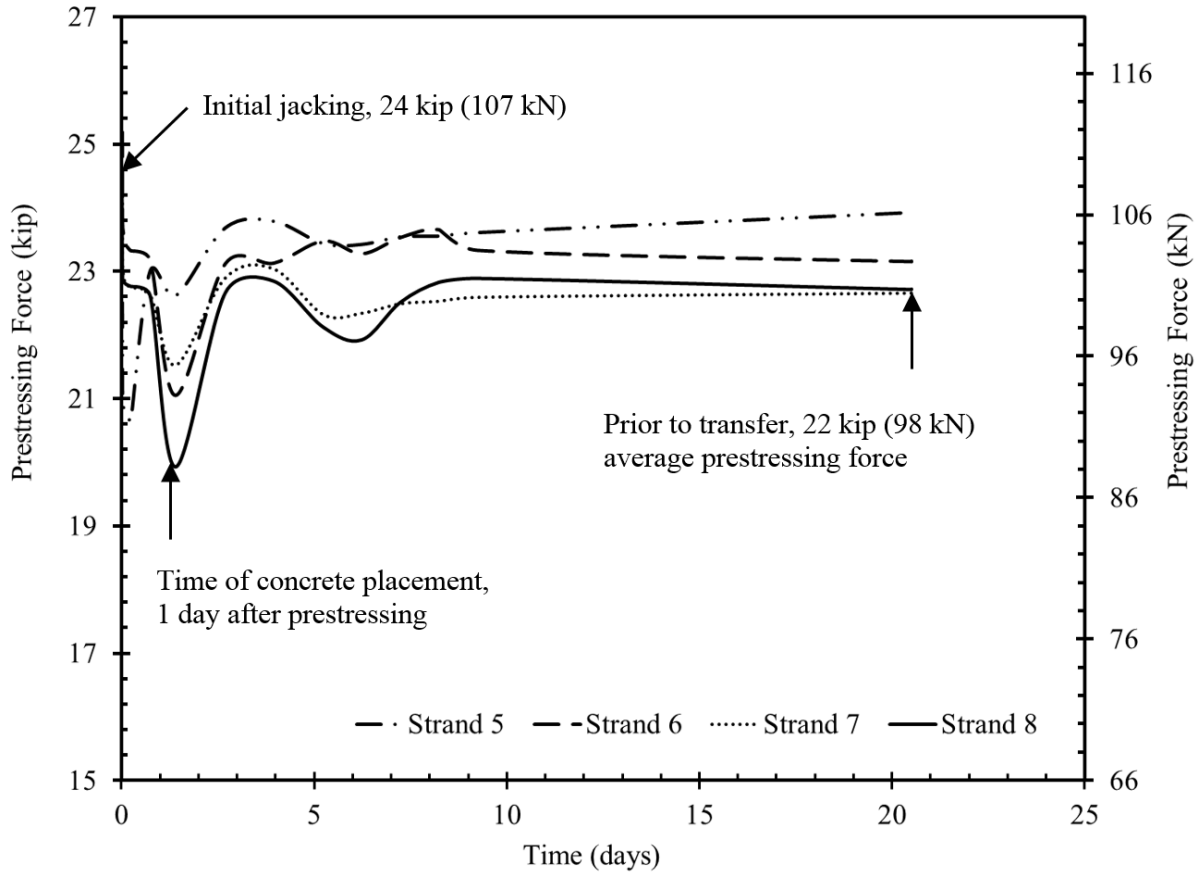


Figure 8.2-17 Prestress loss prior to transfer (Strand 5-8)

Geokon Model 4000 vibrating-wire strain gages (VWSG) (Figure 8.2-18 and Figure 8.2-19) were installed on the sides (top and bottom flanges, and web) of the beams at the mid-span to monitor the strain of the decked bulb T beams during their storage period. This type of strain gage has a temperature and working range of  $-4$  to  $+176$  °F ( $-20$  to  $+80$  °C) and  $\pm 1000$  to  $\pm 4000$   $\mu\epsilon$  respectively. It provides a temperature reading in tandem with strains.

LVDTs and electric strain gages were attached to the compression flange of the decked bulb T-beams at the time of testing to monitor and capture the strain under load cycles. In addition, displacements at mid-span of the decked bulb T beams were measured with LMT as shown in Figure 8.2-20. All sensors were connected to a data acquisition system except Geokon sensors that had a different data acquisition system that recorded the strain readings and temperature.



Figure 8.2-18 Smoothing the surface before installing strain gages

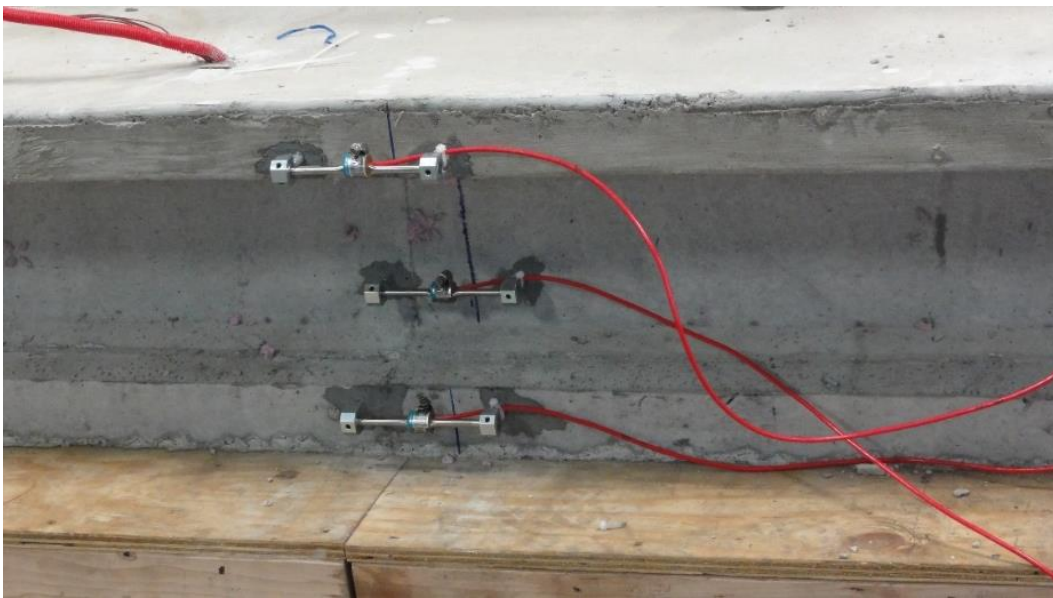


Figure 8.2-19 Installed VWSG on beams before prestress transfer

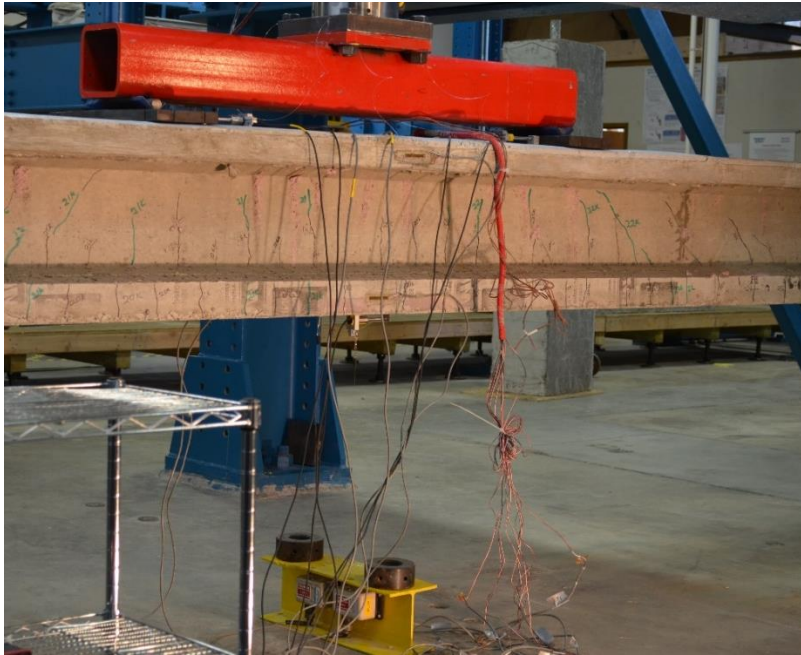


Figure 8.2-20 Instrumentation of decked bulb T beams at mid-span

The control beam was moved to the loading facility at age of 28 days, while other beams were stored either indoors or outdoors as shown in Figure 8.2-21 and Figure 8.2-22. A typical beam loading test setup is as shown in Figure 8.2-23. Load from a 220-kip (979-kN) capacity electronically controlled actuator was applied to the beams through a 4 ft (1.2 m) HSS spreader at mid-span. Load was applied through displacement-control mode with a loading rate ranging from 0.05 to 0.15 in./min (1.25 to 3.8 mm/min) for different load cycles. Beams were simply supported over 1.0- in. (25.4-mm) thick steel reinforced elastomeric bearing pads positioned on steel supports. The effective span from center-to-center of supports was 25 ft. (7.62 m). After the development of the first flexural crack, two strain gages were installed on the soffit of the beams at mid-span to confirm the decompression loads at the time of testing.



Figure 8.2-21 Outdoor beams



Figure 8.2-22 Indoor beams

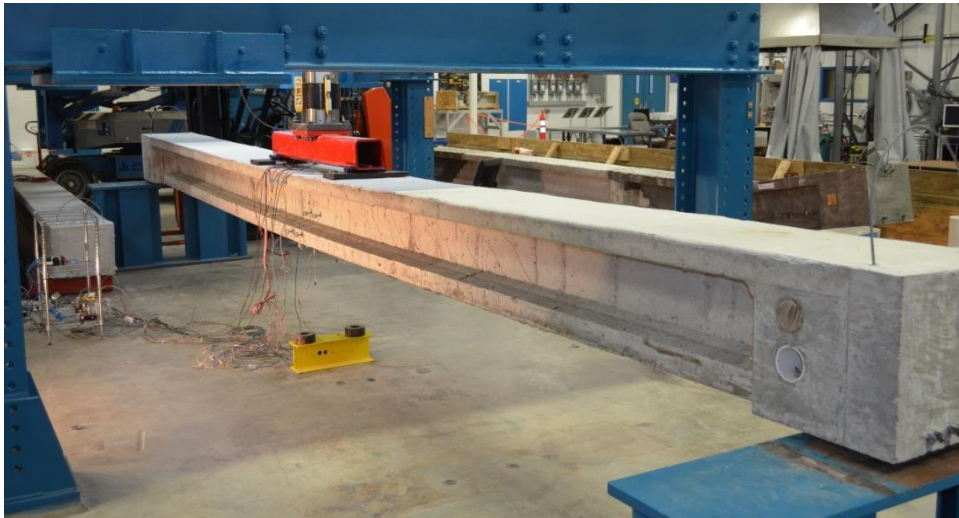


Figure 8.2-23 Test setup of decked bulb T beams

## 8.2.2 Test results

### 8.2.2.1 Monitoring of the test beams

Strain measured by the VWSG at the beginning and end of the monitoring period (prior to flexural testing) were extrapolated to the strand level. As shown in Figure 8.2-24, a line of best fit is plotted between the measured strains. The equation of the line of best fit was used to extrapolate the strain at the level of the strand. The change in strain at the strand level was then evaluated. It should be noted that the change in the strain level does not directly represent the prestress loss. For instance, both concrete creep and shrinkage result in negative strain readings. If this negative strain reading is translated to prestress force, it would indicate an increase not a decrease in the prestressing force. On the other hand, relaxation of CFCC strands results in an elongation of the strand that, by itself, leads to positive strain readings in a strain gage attached to the surface of the concrete. Nevertheless, when combining all three (concrete creep, shrinkage, and strand relaxation) together, this results in an equation with three unknowns that can't be solved. Therefore, a direct estimate for the prestress loss from strain readings was not obtained. Rather, the strains due to concrete creep, shrinkage, and strand relaxation were estimated using separate test protocols and the combined strain values were compared with those obtained from the VWSG. In addition, creep and shrinkage strains calculations according to available design guidelines such as AASHTO LRFD and PCI were estimated and compared with the values obtained experimentally and the readings from the VWSG after they were adjusted for temperature effects. The recorded VWSG strains over the monitoring period along with the recorded temperatures are shown in Figure 8.2-25 to Figure 8.2-34.

AASHTO LRFD equations in Section 2.5.3.1 were used to estimate theoretical losses due to elastic shortening, creep, and shrinkage of concrete. Total losses were the sum of the aforementioned losses and results from relaxation tests discussed earlier. Elastic shortening losses were estimated using AASHTO Eqn. C5.9.5.2.3a-1. Approximate estimate of time dependent creep and shrinkage losses (AASHTO Eqn. 5.9.5.3-1) was calculated with relative humidity values of 50% and 70% for indoor and outdoor beams respectively. AASHTO Eqn. 5.9.5.4.2a-1 and 5.9.5.4.2b-1 were used to estimate refined time dependent losses due to creep and shrinkage. Appropriate values of creep coefficient and shrinkage strain from creep and shrinkage tests were also used in the refined estimate equations. In all cases, a one-million-hour CFCC relaxation rate

of 1.92 % was used. Total prestress losses were also estimated using the PCI-Simplified method as specified in the PCI Design Handbook, 7<sup>th</sup> Edition.

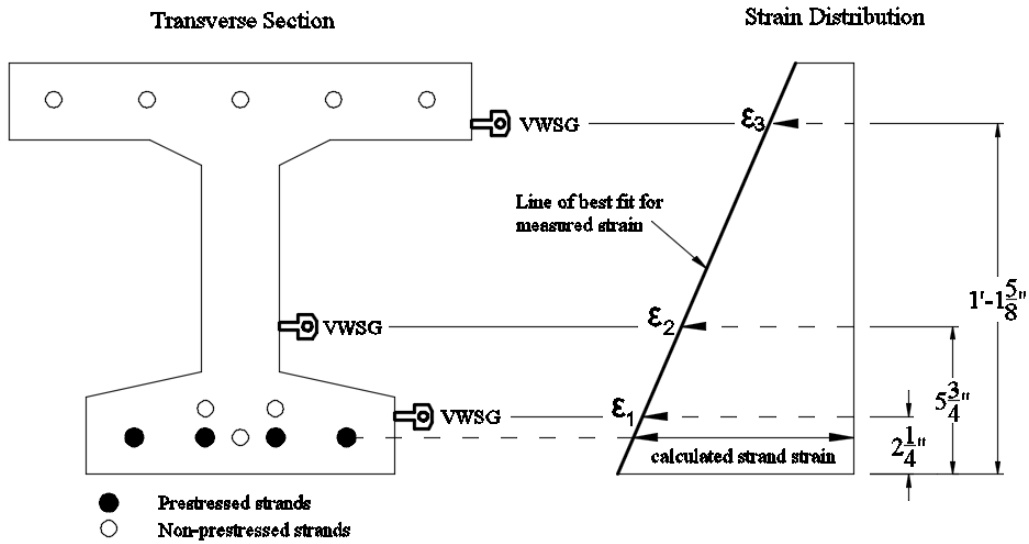


Figure 8.2-24 Line of best fit for VWSG strain measurements

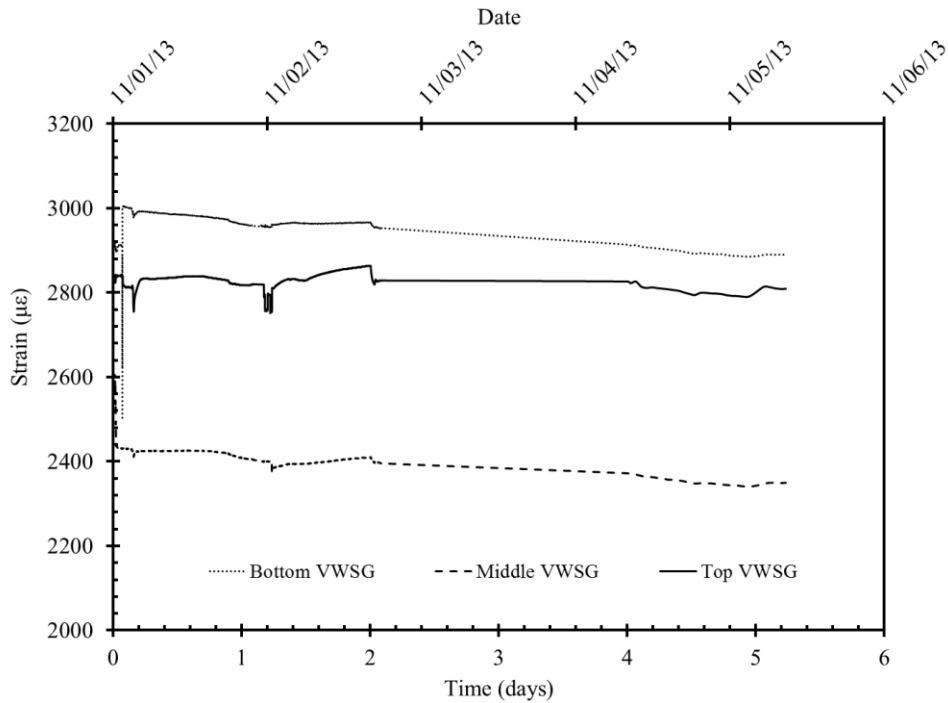


Figure 8.2-25 Recorded VWSG strain vs. time for Beam C

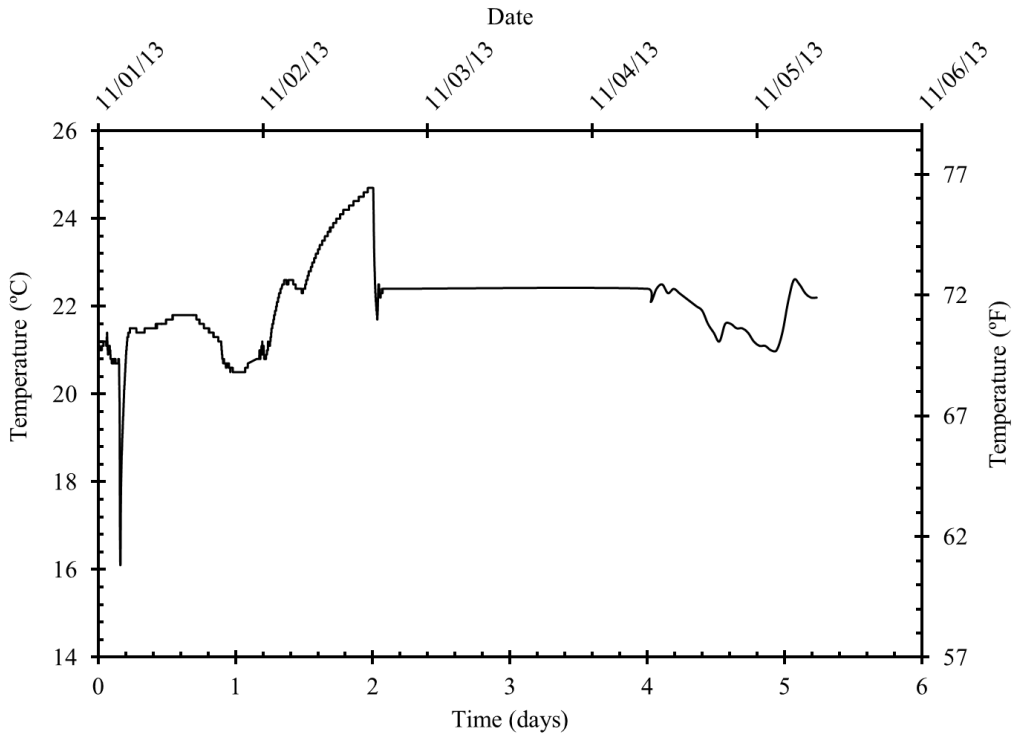


Figure 8.2-26 Recorded VWSG temperature vs. time for Beam C

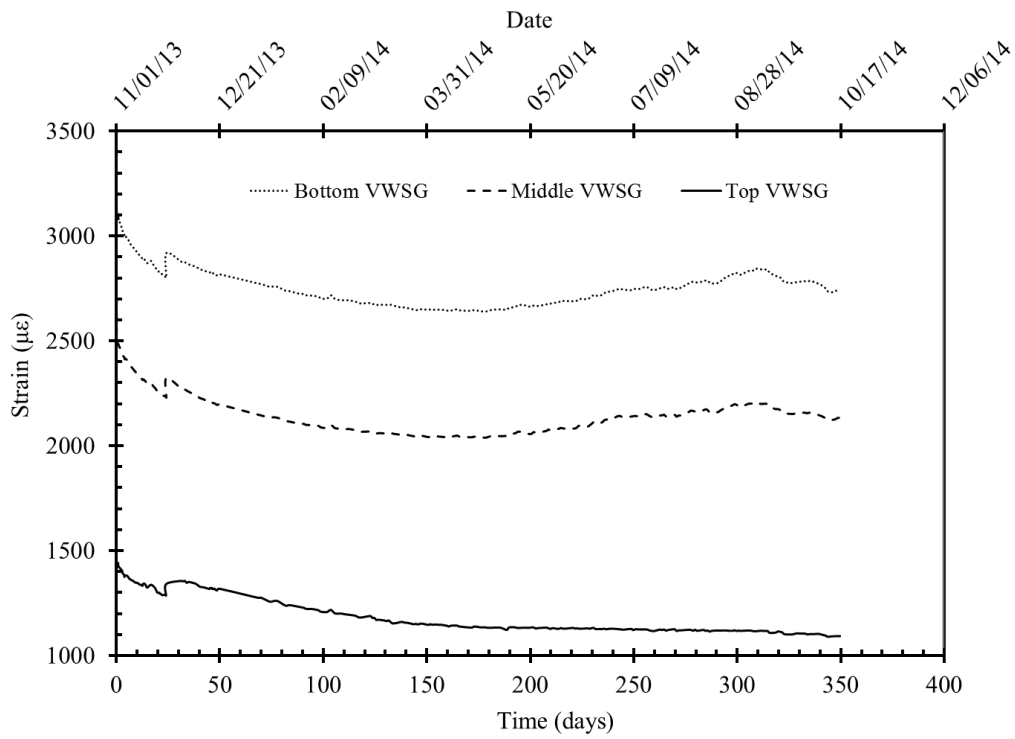


Figure 8.2-27 Recorded VWSG strain vs. time for Beam I-1

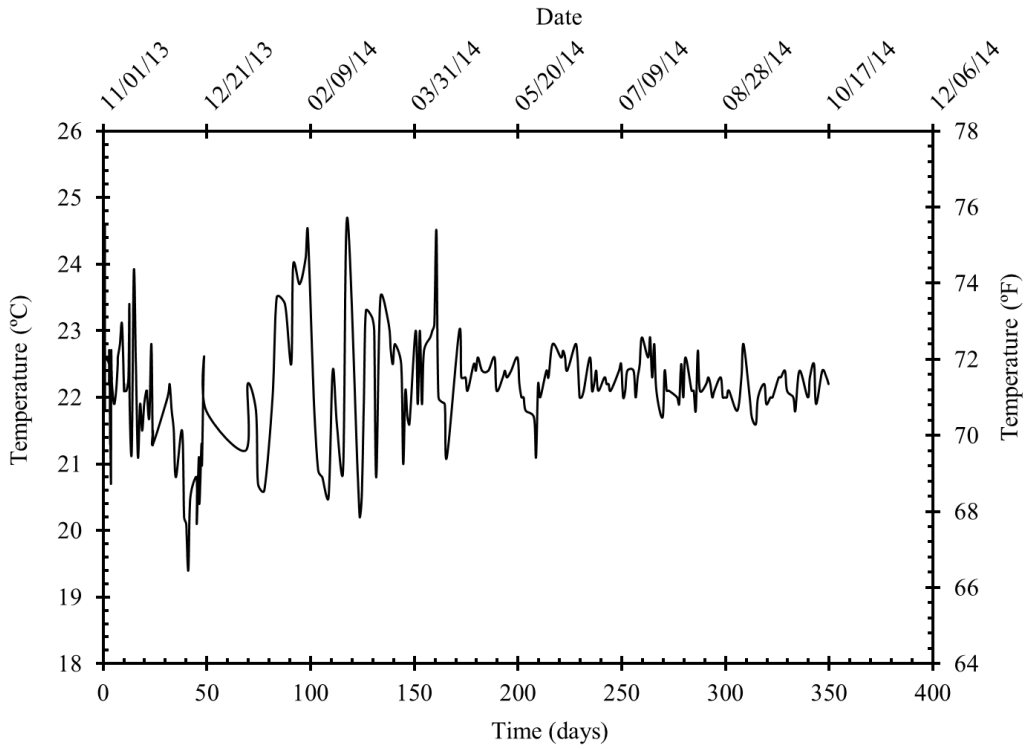


Figure 8.2-28 Recorded VWSG temperature vs. time for Beam I-1

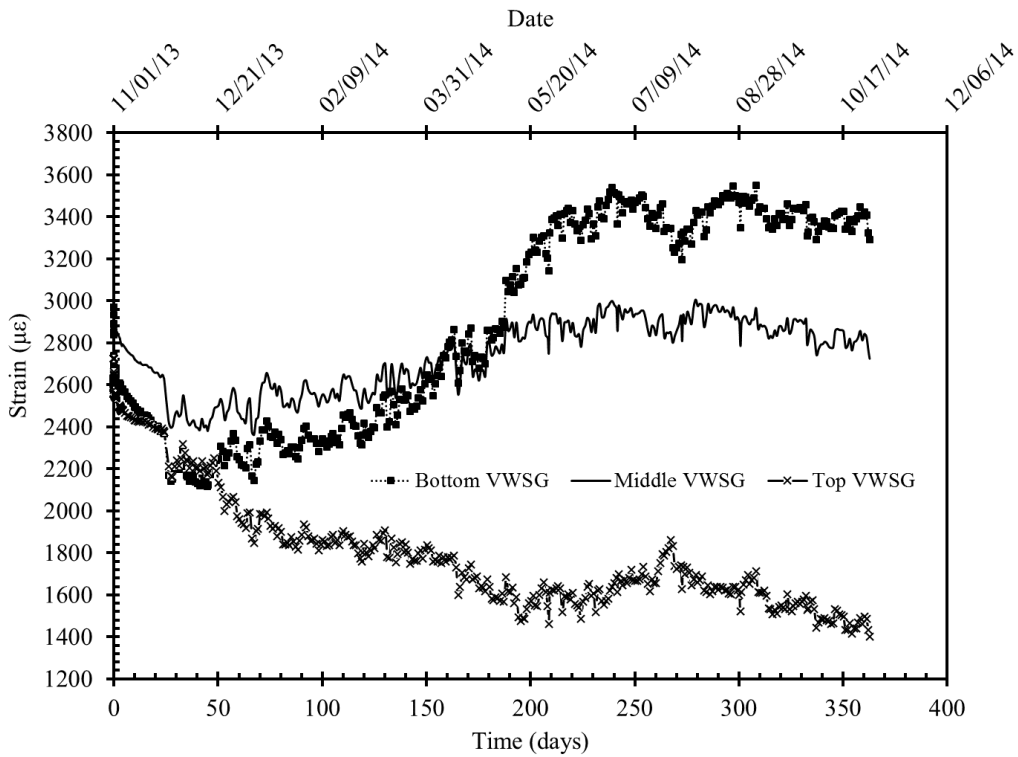


Figure 8.2-29 Recorded VWSG strain vs. time for Beam O-1

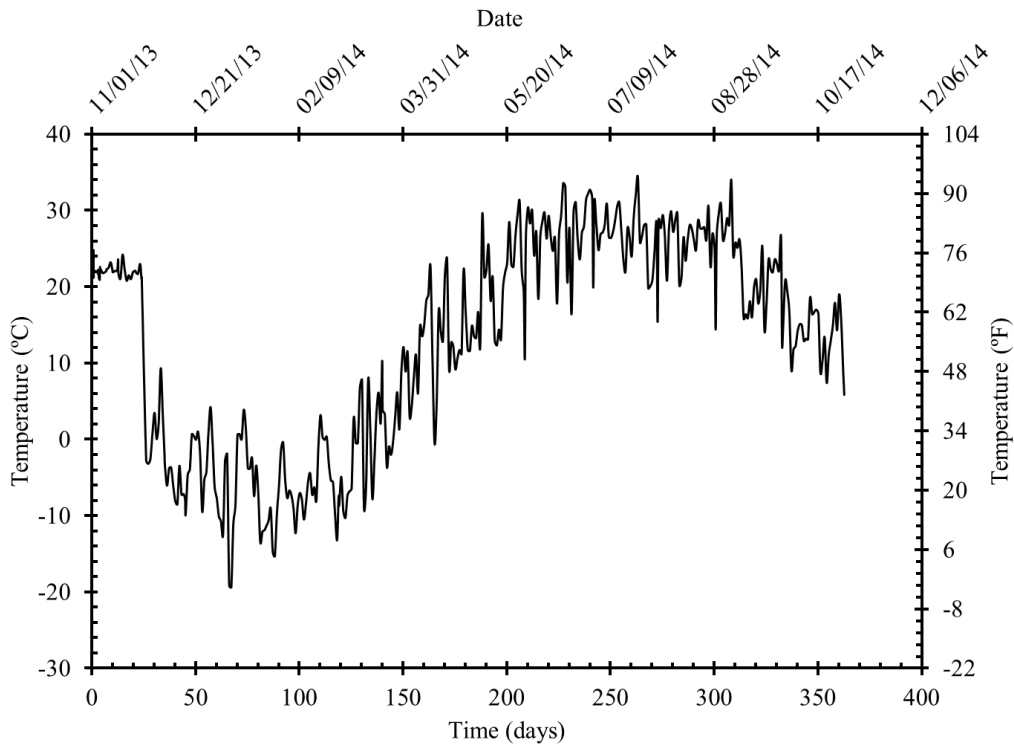


Figure 8.2-30 Recorded VWSG temperature vs. time for Beam O-1

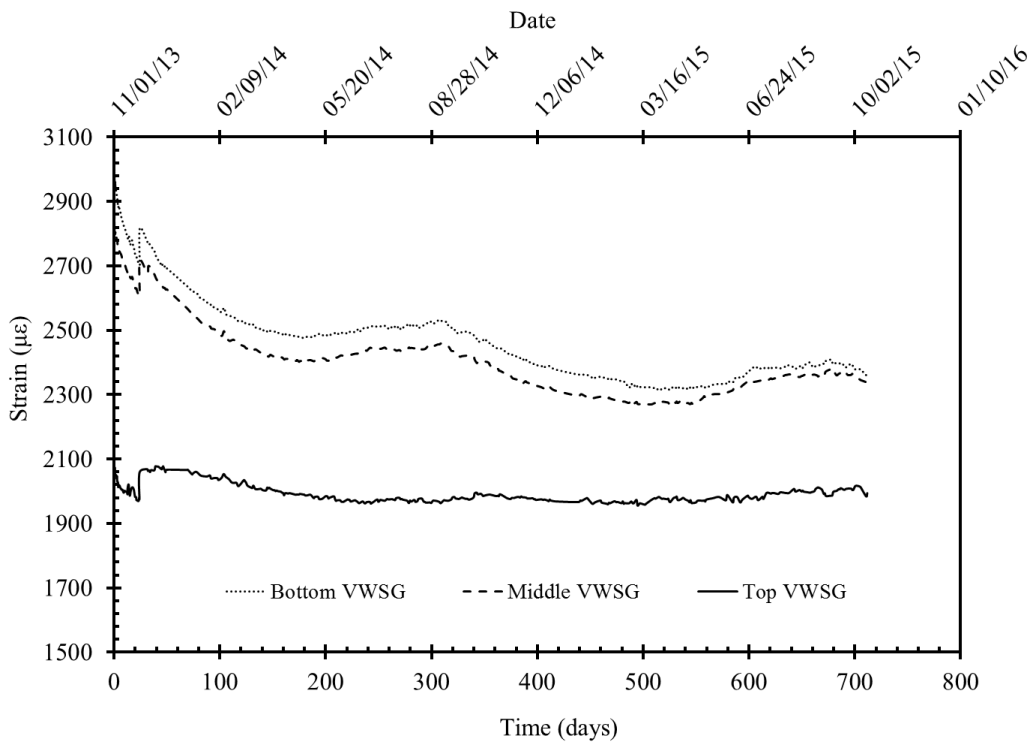


Figure 8.2-31 Recorded VWSG strain vs. time for Beam I-2

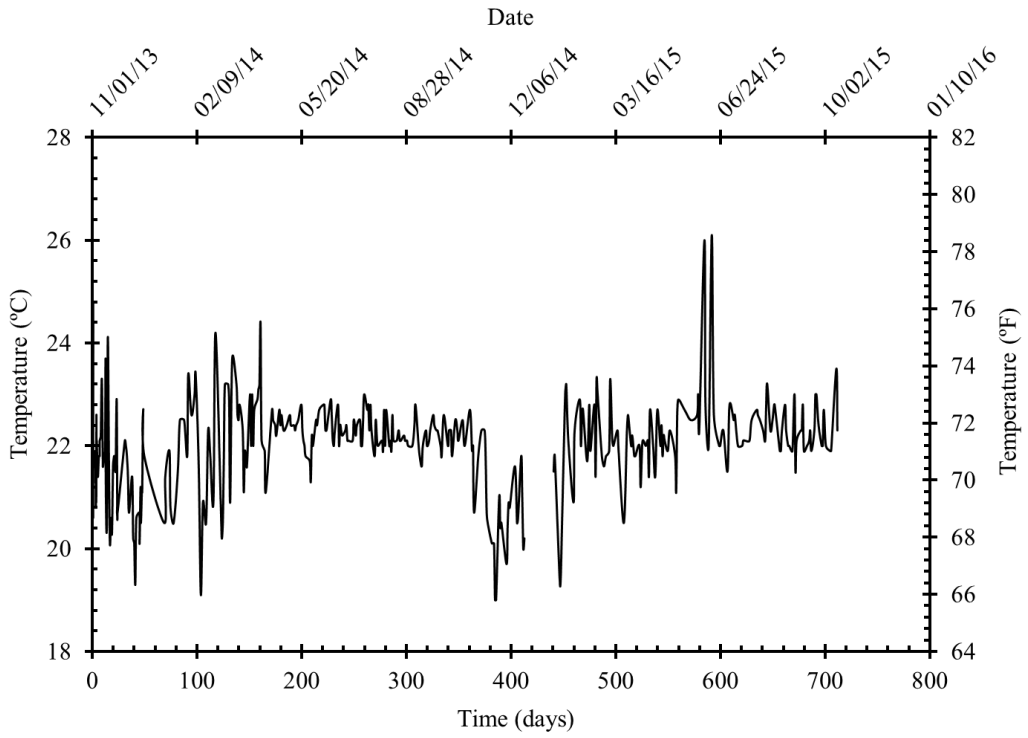


Figure 8.2-32 Recorded VWSG temperature vs. time for Beam I-2

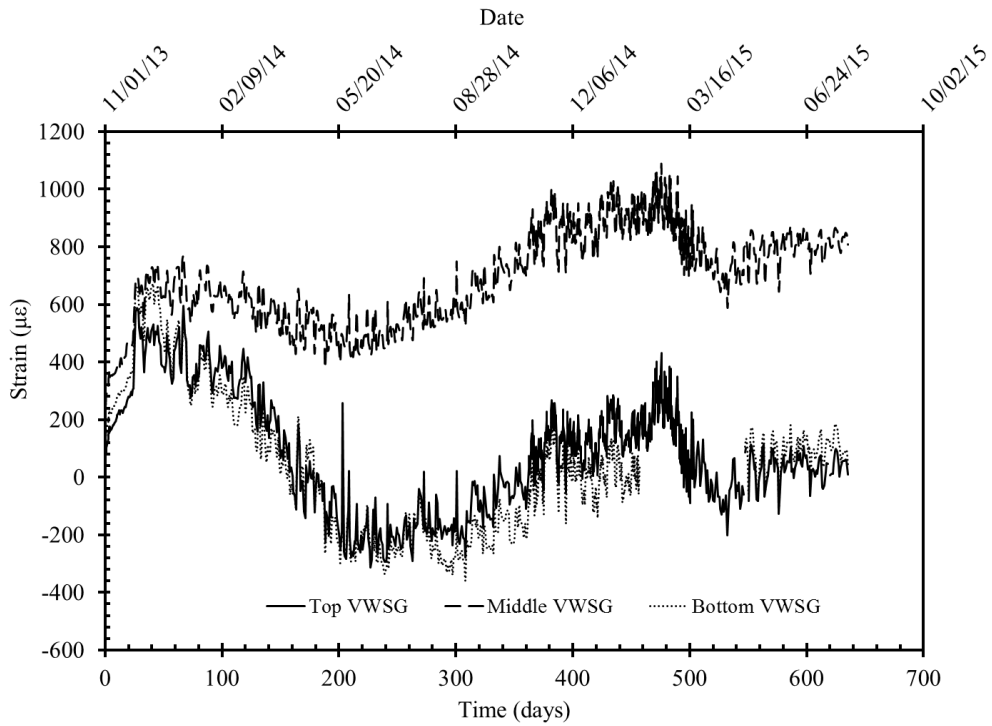


Figure 8.2-33 Recorded VWSG strain vs. time for Beam O-2

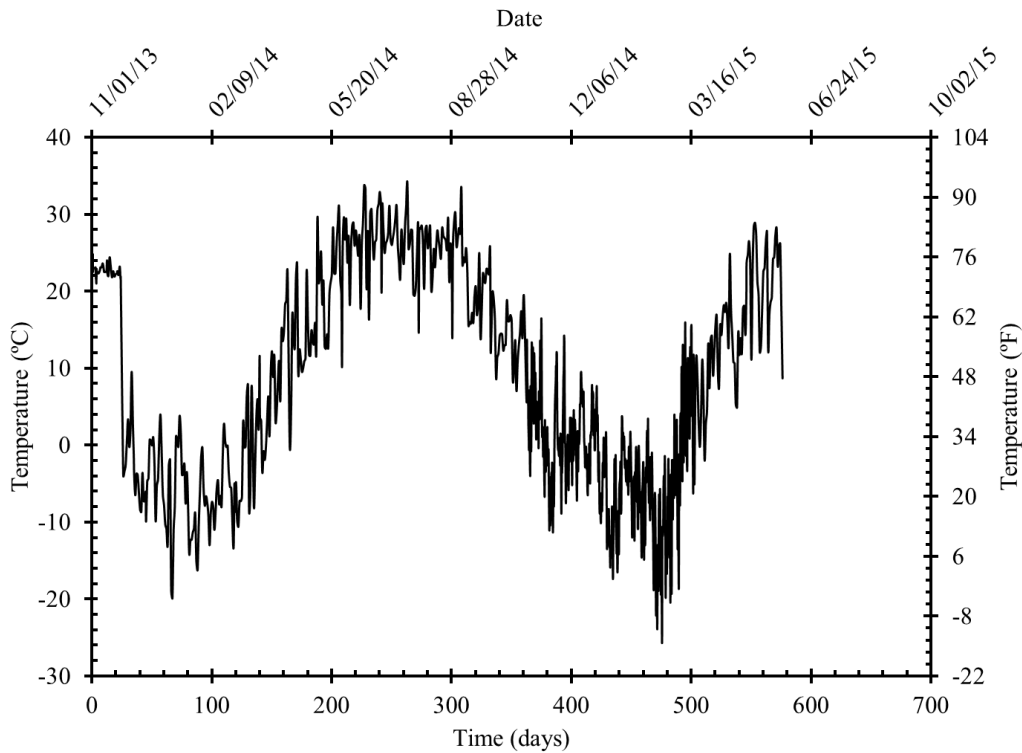


Figure 8.2-34 Recorded VWSG temperature vs. time for Beam O-2

### 8.2.2.2 Flexural test results

The service limit state represents the stage of loading where the beams remain uncracked. Cracking loads were estimated using the load-deflection inspection method (Figure 8.2-35). After cracking, the decompression load was determined and represented the load that caused zero stress in the extreme fiber in the pre-compressed tensile zone. The 50-kip (222-kN) load cycle was used to determine the decompression load of the beams. These decompression loads were converted to prestress loss. Figure 8.2-35 Figure 8.2-45 show the estimation of the decompression loads in all test beams. In addition, cracking loads, decompression loads, and the rest of the test results are summarized in Table 8.2-2.

All beams behaved in a similar manner after initiation of first crack. The crack widths and patterns and inelastic behaviors were also similar. First crack initiation occurred directly under one of the loading points of the 4-ft (1.22-m) spreader. After cracking, flexural cracks formed in the pure bending zone under the loading spreader and propagated vertically to the top flange as shown

in Figure 8.2-46. Additional flexural cracks developed outside the pure bending region and propagated diagonally to the top flange in the form of flexural shear cracks.

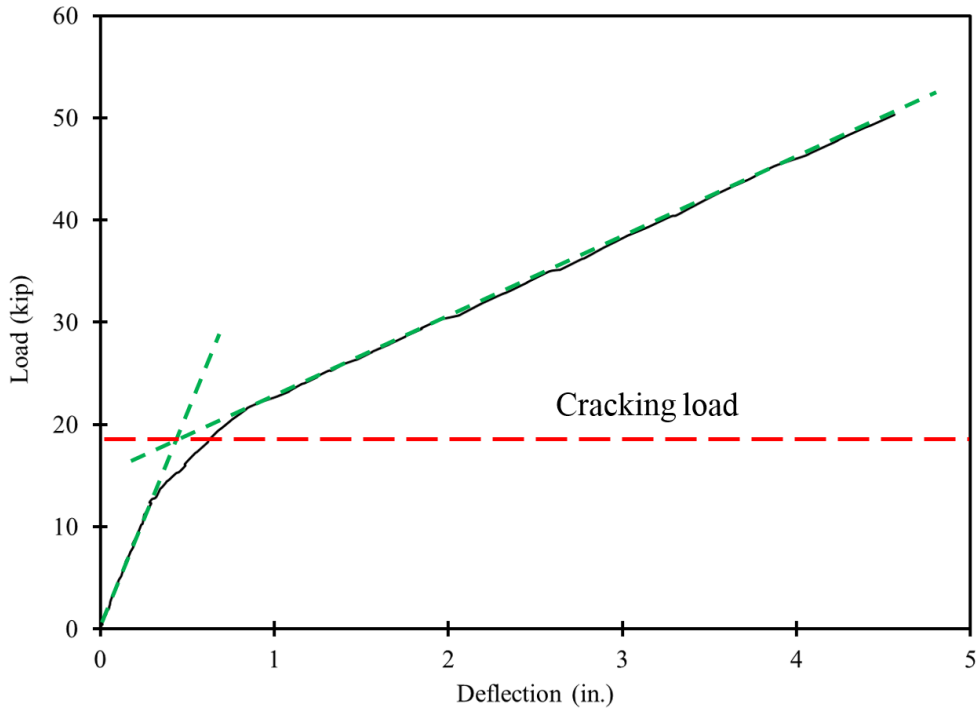


Figure 8.2-35 Cracking load from load deflection curve

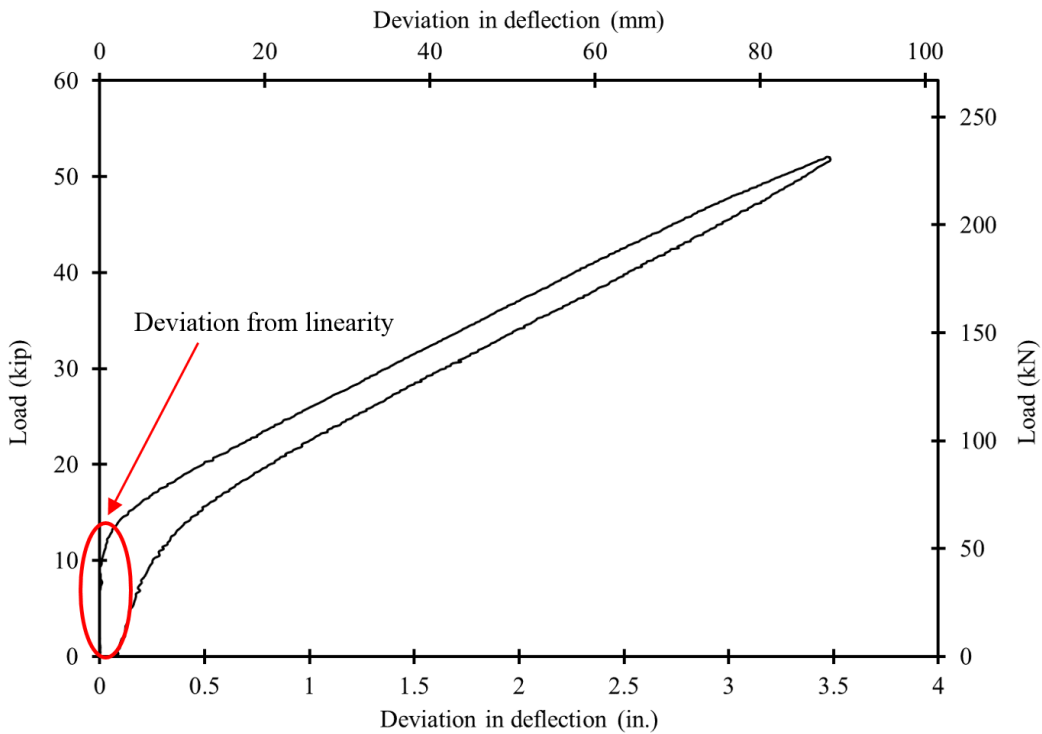


Figure 8.2-36 Load vs. deviation in deflection curve for Beam C

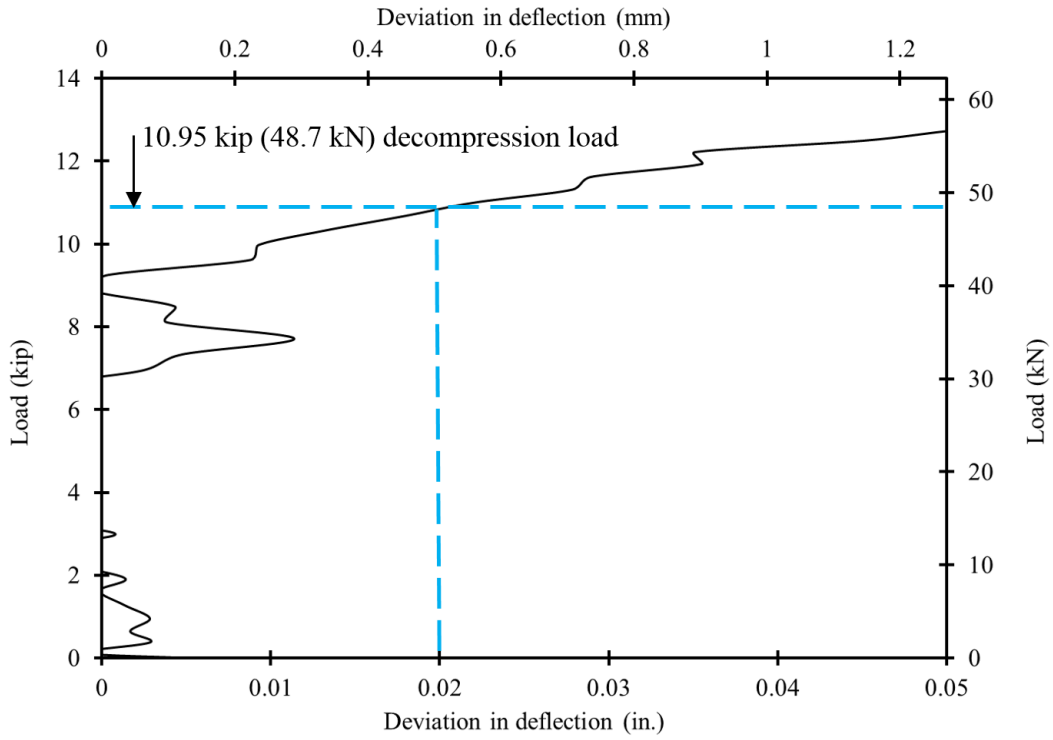


Figure 8.2-37 Deviation from linearity (Beam C)

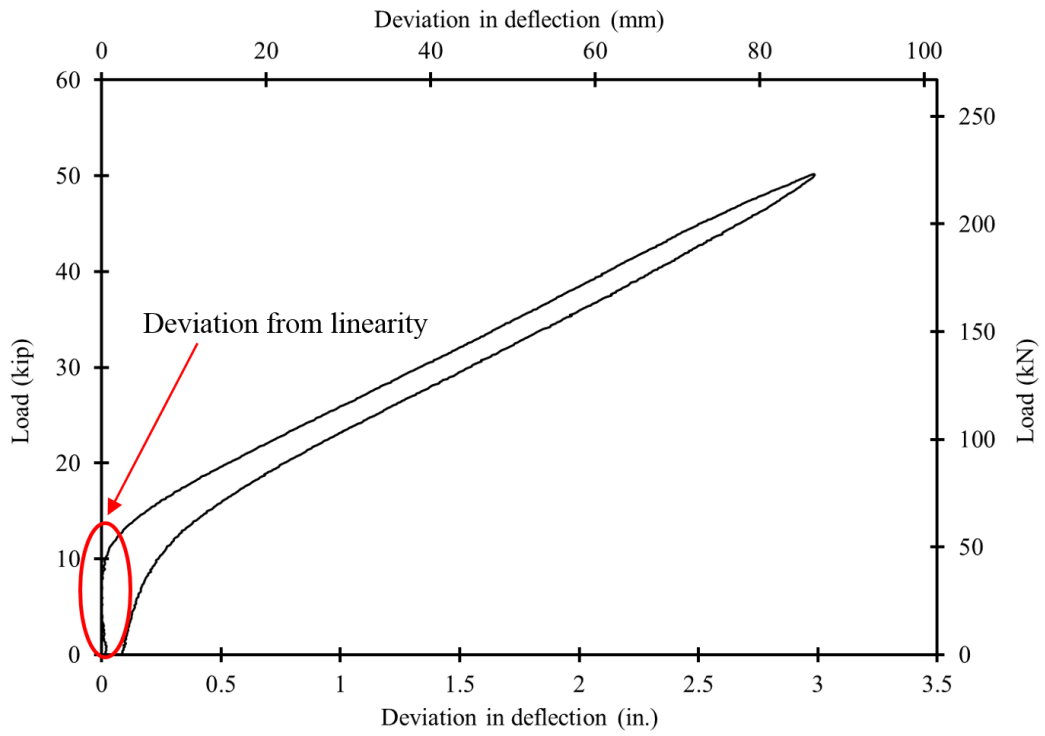


Figure 8.2-38 Load vs. deviation in deflection curve for Beam I-1

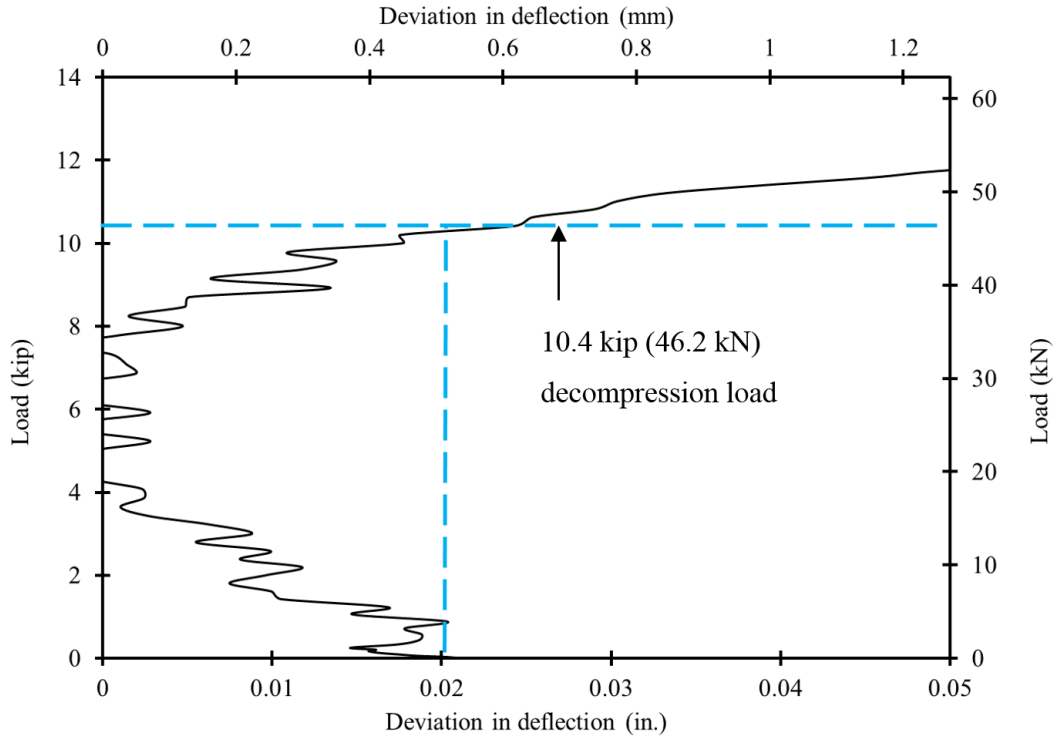


Figure 8.2-39 Deviation from linearity (Beam I-1)

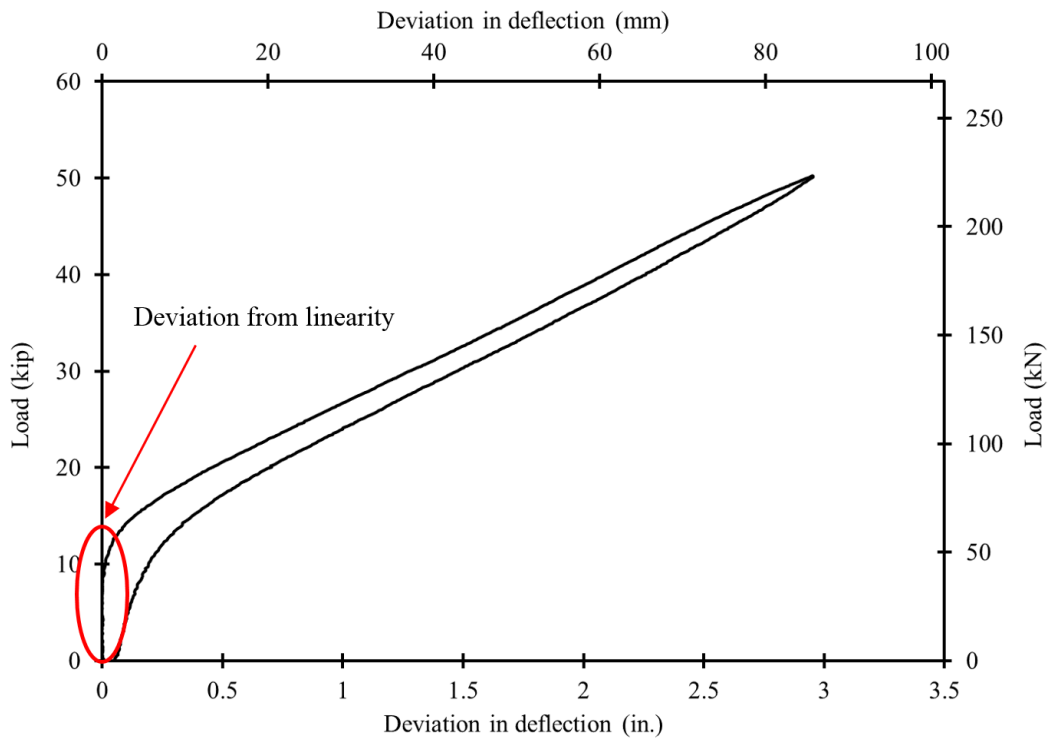


Figure 8.2-40 Load vs. deviation in deflection curve for Beam O-1

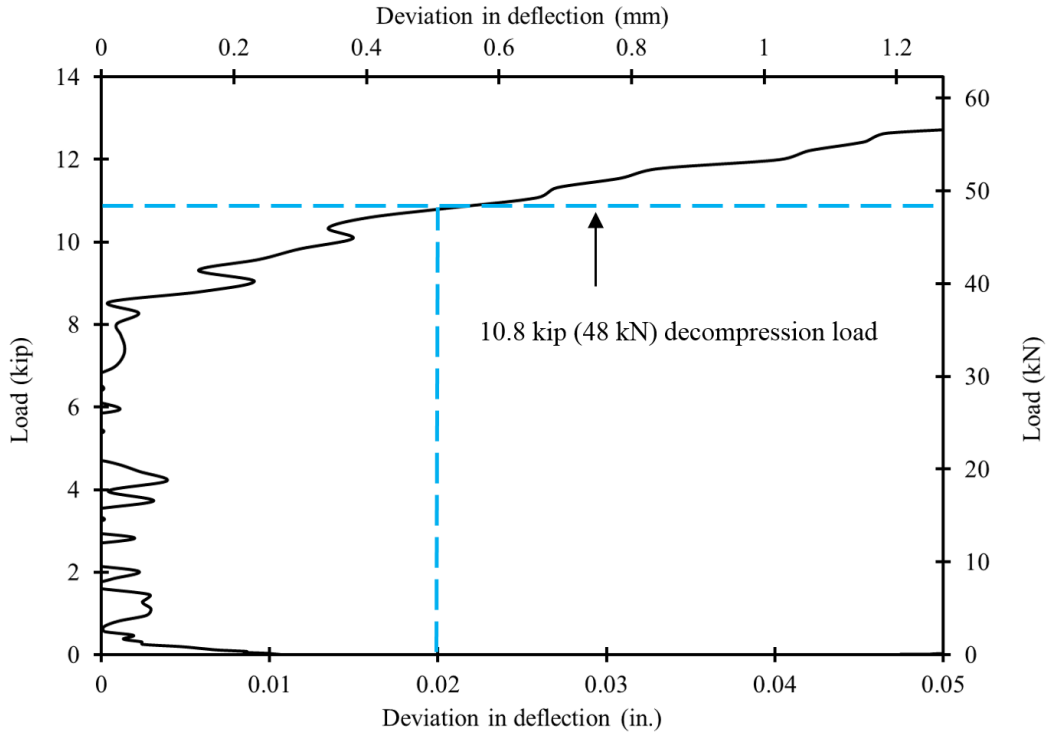


Figure 8.2-41 Deviation from linearity (Beam O-1)

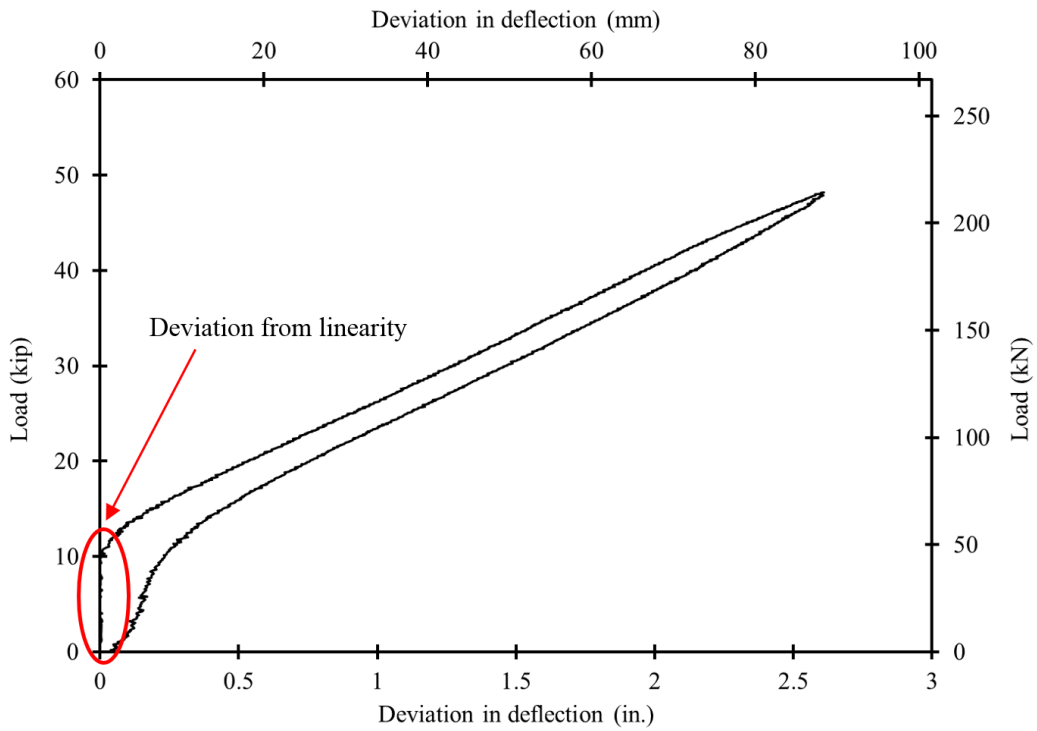


Figure 8.2-42 Load vs. deviation in deflection curve for Beam I-2

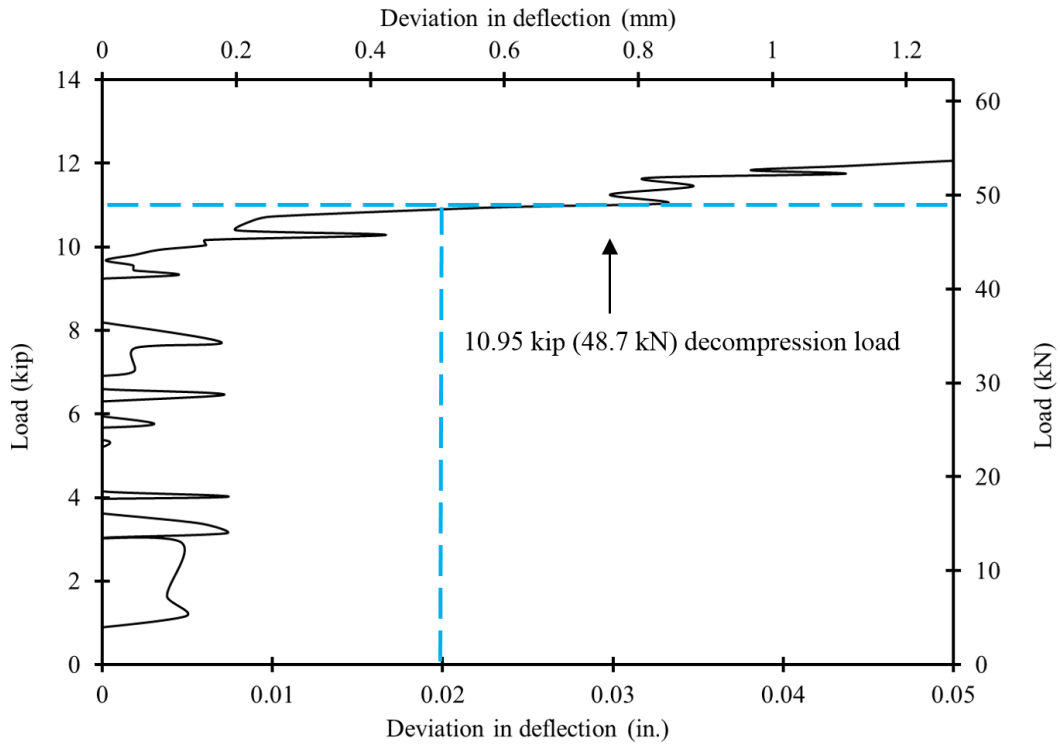


Figure 8.2-43 Deviation from linearity (Beam I-2)

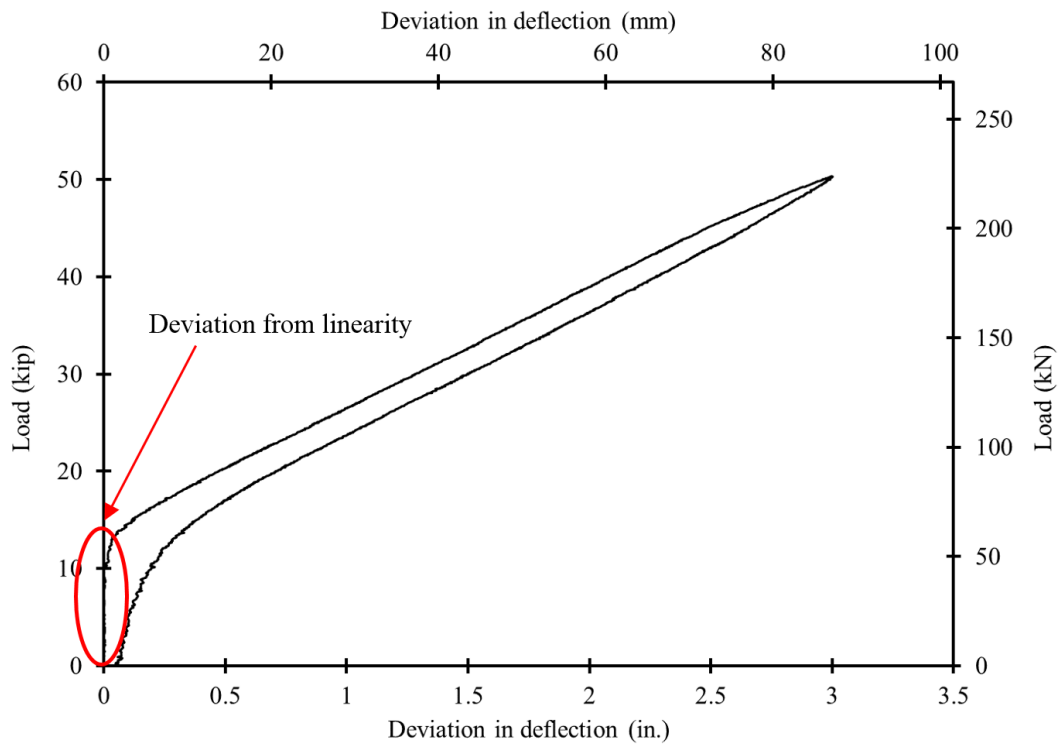


Figure 8.2-44 Load vs. deviation in deflection curve for Beam O-2

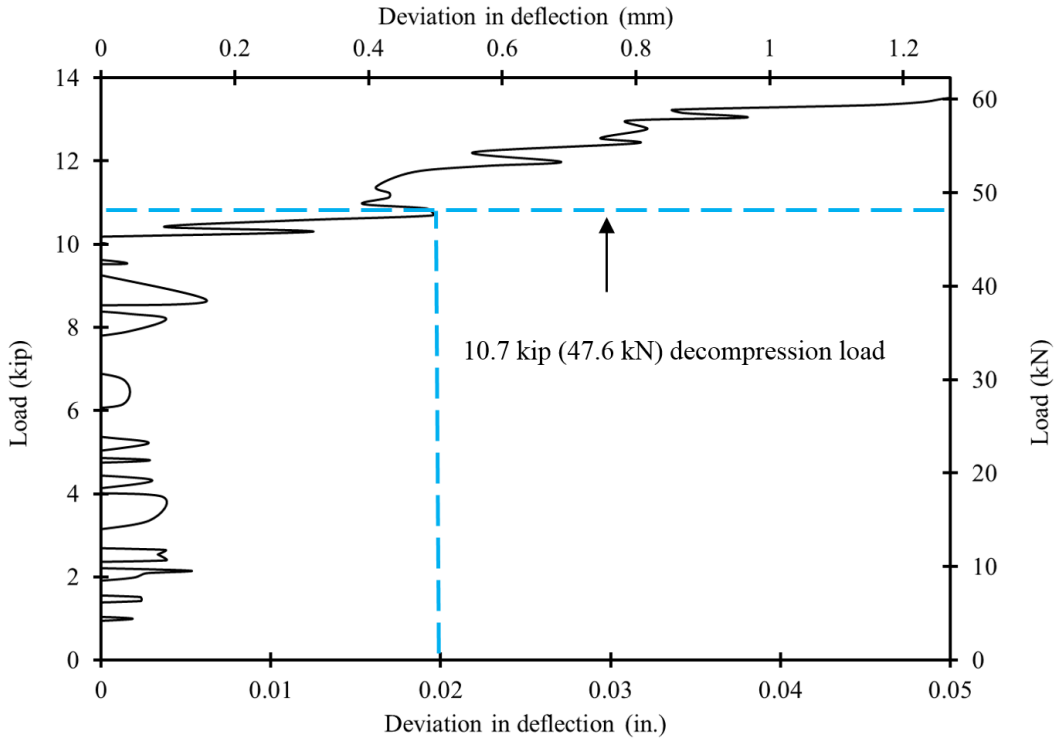


Figure 8.2-45 Deviation from linearity (Beam O-2)

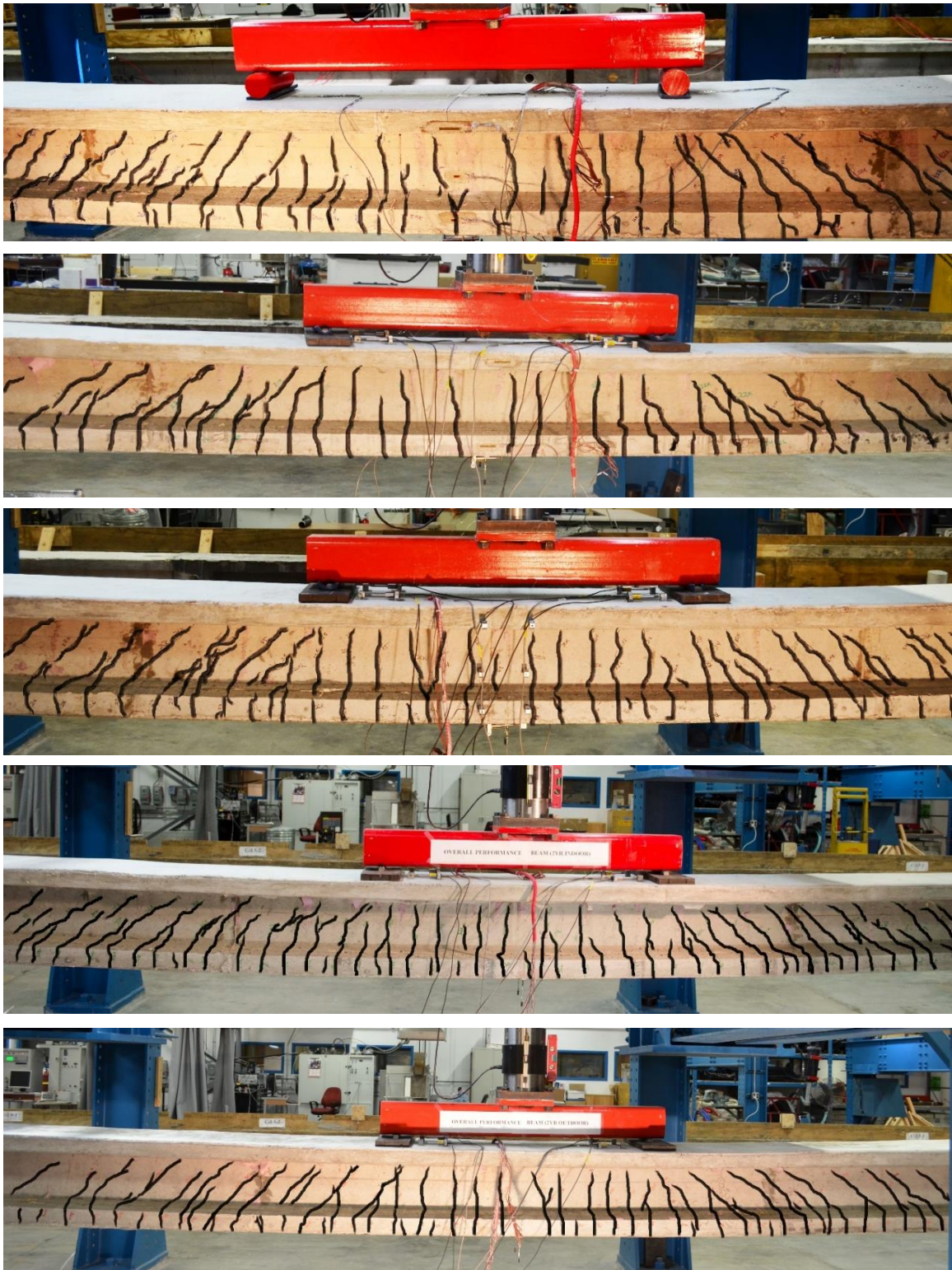


Figure 8.2-46 Cracking pattern of decked bulb T beams from the top: C, I-1, O-1, I-2, and O-2

Beam C, Beam I-1, Beam O-1, Beam I-2, and Beam O-2 exhibited accumulated residual mid-span deflections of 0.65 in. (16.5 mm), 0.54 in. (13.7 mm), 0.50 in. (12.7 mm), 0.55 in. (14.0 mm), and 0.38 in. (9.6 mm) respectively after the 60-kip (267-kN) load cycle. The failure mode of the fluctuated between a compression failure, where the concrete crushed but the CFCC strands remained intact and balanced failure, where both crushing of the concrete and rupture of CFCC happened nearly at the same time. All the beams exhibited the bilinear load-deflection curves. Figure 8.2-47 through Figure 8.2-59 show the failure of the five test beams along with the recorded load-deflection curves.

Beam C was loaded to in loading/unloading cycles after 28 days of concrete pouring but the last load cycle that led to beam failure was executed 71 days after concrete pouring. First crack was observed at 16.5 kip (73 kN), while failure took place by crushing of concrete in the top flange at a load of 66.4 kip (295 kN) with a corresponding mid-span deflection of 7.98 in. (203 mm) and an extreme concrete compression strain of 2970  $\mu\epsilon$ .

Beam I-1 was stored indoors and tested one year after concrete pouring. First crack was observed at 16.5 kip (73 kN), while failure took place by crushing of concrete in the top flange at a load of 74.3 kip (331 kN) with a corresponding mid-span deflection of 8.2 in. (208 mm) and an extreme compression strain of 3200  $\mu\epsilon$ .

Beam O-1 was stored outdoors and loaded to failure one year after concrete pouring. First crack was observed at 17 kip (76 kN). Failure was initiated by crushing of concrete in the top flange at a load of 76.7 kip (341 kN) with a corresponding deflection of 8.2 in. (208 mm) and an extreme compression strain of 3200  $\mu\epsilon$ . Rupture of the prestressing strands was observed after failure, which suggested a balanced failure, but this also could have been initiated by the energy released from the explosive crushing of concrete.

Beam I-2 was stored indoors and loaded to failure two years after concrete pouring. First crack was observed at 17 kip (75.6 kN). Failure took place by combined crushing of concrete in the top flange and rupture of prestressing strands at a load of 64.7 kip (288 kN) with a corresponding deflection of 7.5 in. (190 mm) and an extreme compression strain of 2830  $\mu\epsilon$ . It should be noted that the first attempt for last load cycle was interrupted by a power outage when the load level was approximately 62 kip (276 kN). The last load cycle was repeated after power was restored but it seems that the achieved failure load was affected by the first attempt.

Beam O-2 was tested two years after concrete pouring. First crack was observed at 18.0 kip (80 kN). Failure took place by crushing of concrete in the top flange at a load of 80.7 kip (359 kN) with a corresponding mid-span deflection of 8.7 in. (221.0 mm) and an extreme compression strain of 2960  $\mu\epsilon$ . Table 8.2-2 summarizes the results from the flexural testing of the decked bulb T-beams.



Figure 8.2-47 Failure of Beam C

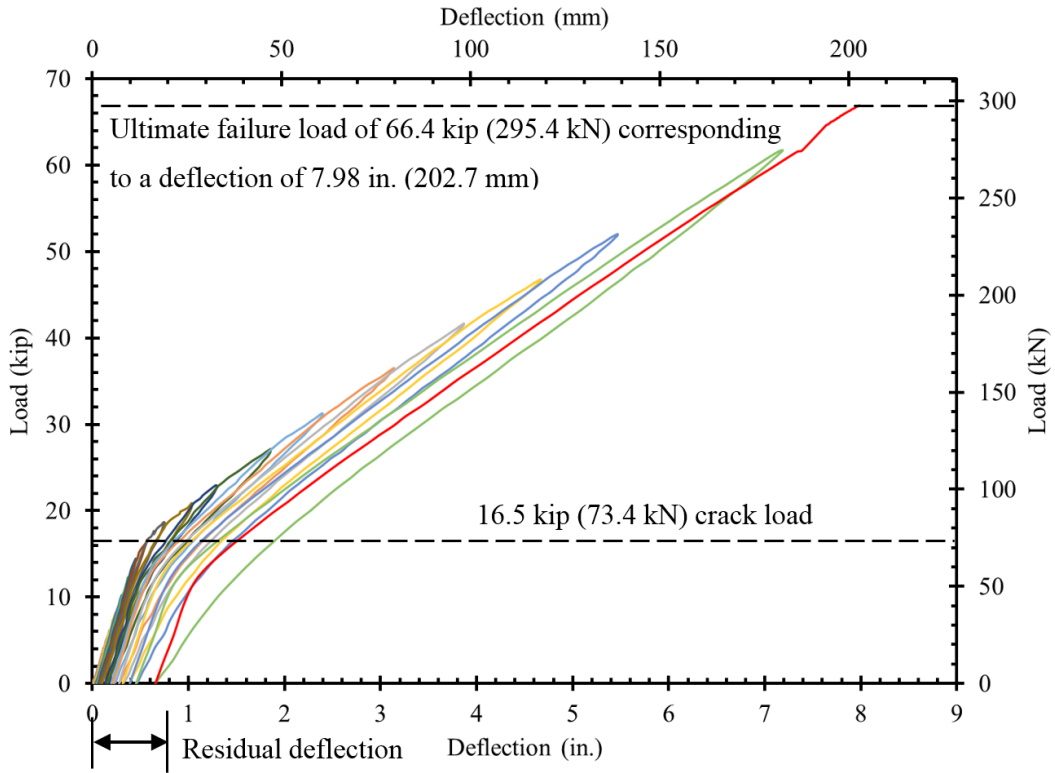


Figure 8.2-48 Load vs. deflection curves for Beam C



Figure 8.2-49 Failure of Beam I-1

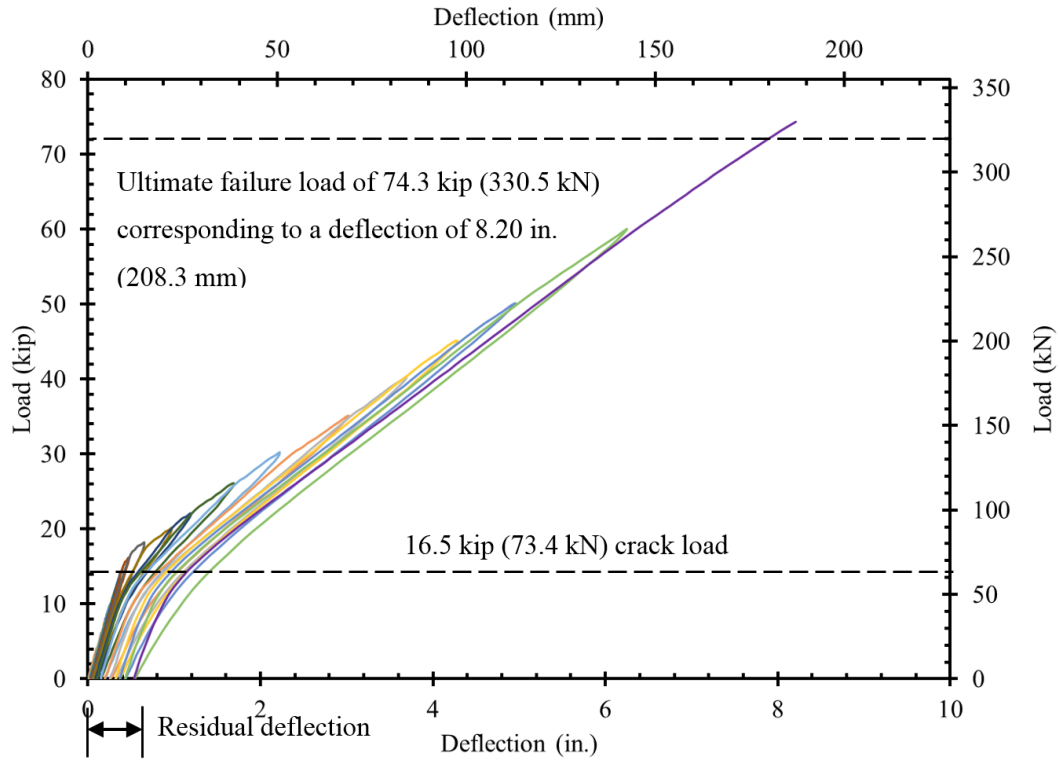


Figure 8.2-50 Load vs. deflection curves for Beam I-1

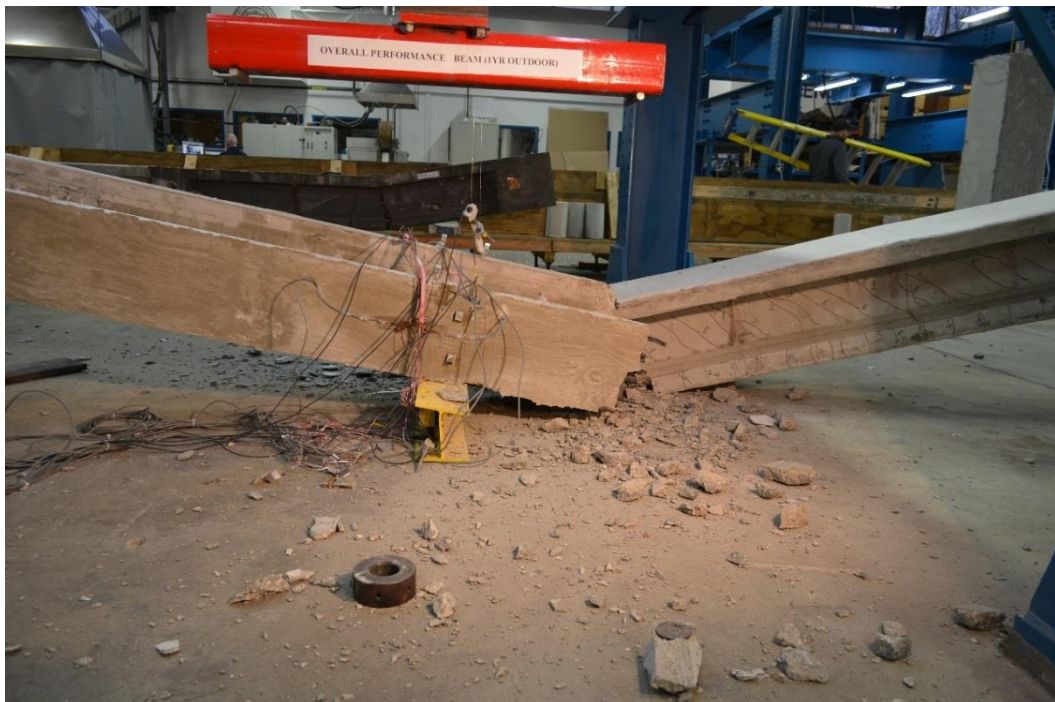


Figure 8.2-51 Failure of Beam O-1



Figure 8.2-52 Ruptured prestressing strands at failure of Beam O-1

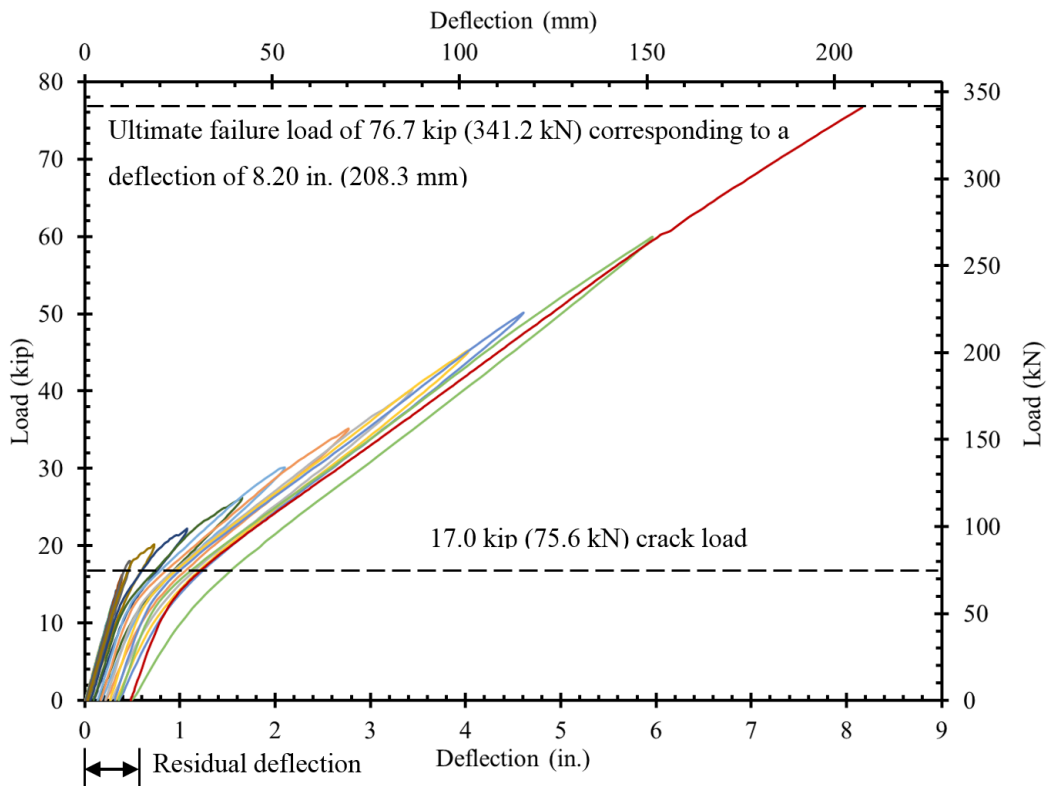


Figure 8.2-53 Load vs. deflection curves for Beam O-1



Figure 8.2-54 Failure of Beam I-2



Figure 8.2-55 Ruptured prestressing strands at failure of Beam I-2

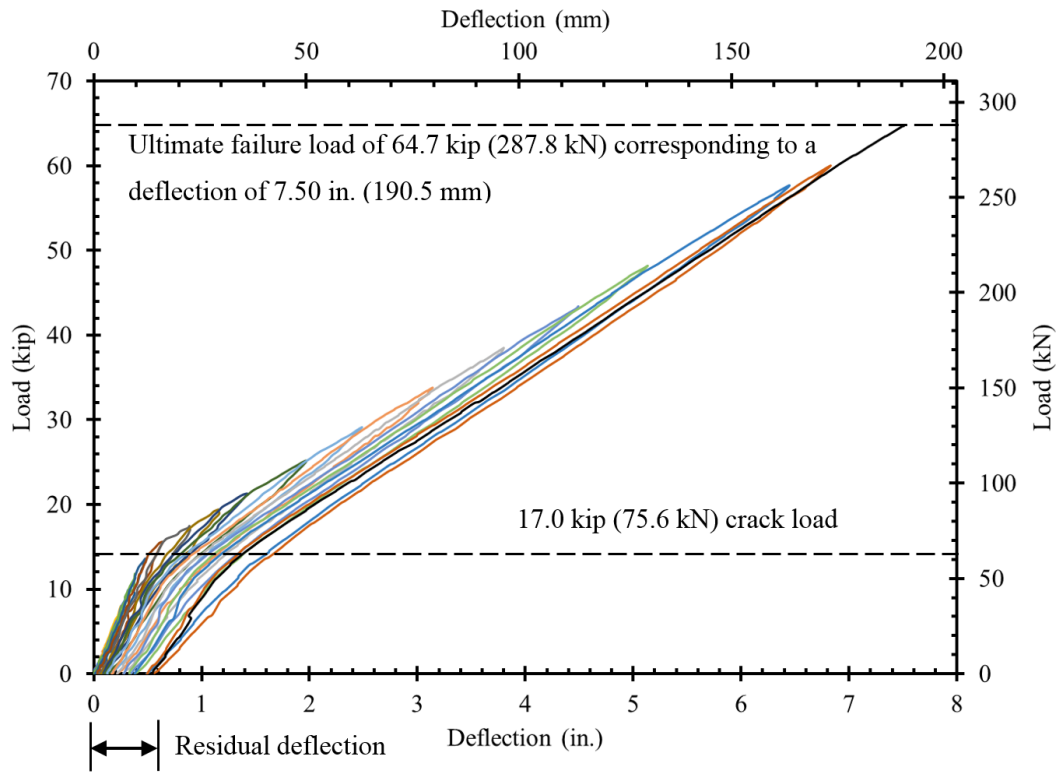


Figure 8.2-56 Load vs. deflection curves for Beam I-2



Figure 8.2-57 Failure of Beam O-2



Figure 8.2-58 Un-ruptured prestressing strands of Beam O-2 at failure

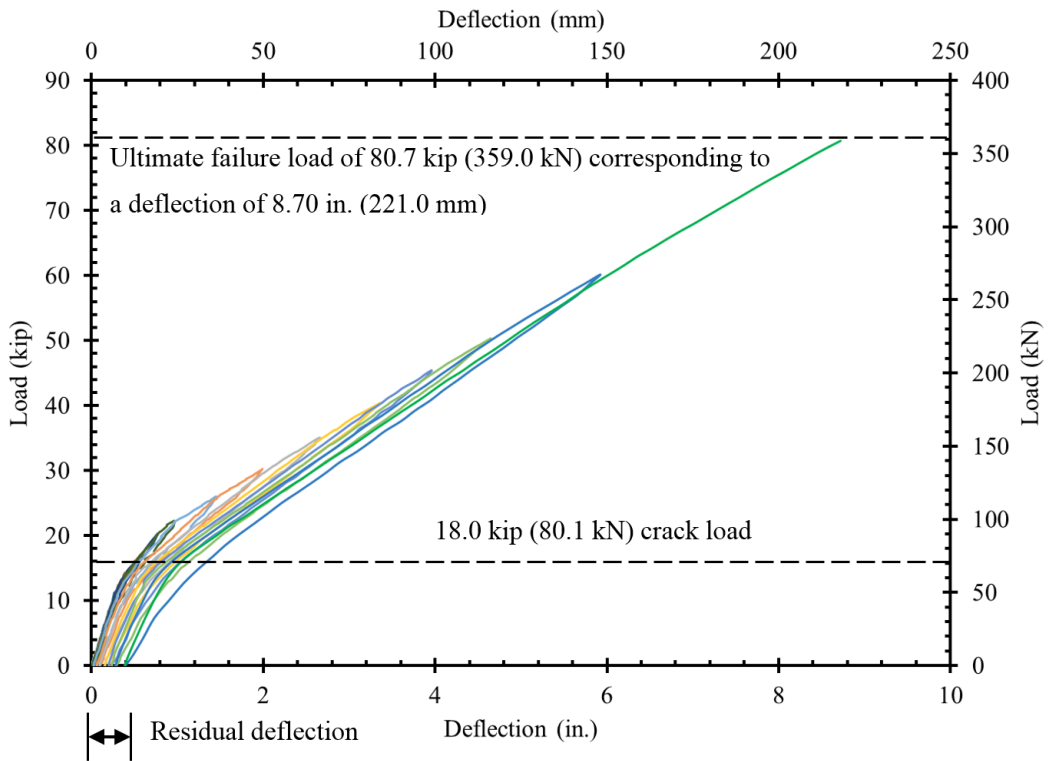


Figure 8.2-59 Load vs. deflection curves for Beam O-2

Table 8.2-2 Summary of experimental results for decked bulb T-beams

Parameter	Specimen ID				
	Beam C	Beam I-1	Beam O-1	Beam I-2	Beam O-2
Concrete compressive strength at testing psi (MPa)	10,700 (73.8)	10,300 (71.0)	11,900 (82.0)	10,100 (69.6)	12,000 (82.7)
Decompression load kip (kN)	10.95 (48.7)	10.4 (46.2)	10.8 (48)	10.95 (48.7)	10.7 (47.6)
Cracking load kip (kN)	16.5 (73.4)	16.5 (73.4)	17.0 (75.6)	17.0 (75.6)	18.0 (80.1)
Extreme compression strain ( $\mu\epsilon$ )	2470	2930	2950	2430	2830
Mid-span deflection at failure, in. (mm)	7.3 (185.4)	7.7 (195.6)	7.7 (195.6)	6.9 (175.3)	8.3 (210.8)
Experimental ultimate load, kip (kN)	66.4 (295.4)	74.3 (330.5)	76.7 (341.2)	64.7 (287.8)	80.7 (359.0)
Predicted ultimate load kip (kN)	69.0 (307.0)	67.2 (298.8)	73.2 (325.5)	67.2 (299.1)	73.9 (329.0)
Total energy absorbed kip-in (kNm)	325.0 (36.7)	355.7 (40.2)	367.2 (41.5)	282.6 (31.9)	409.7 (46.3)
Mode of failure	Concrete crushing	Concrete crushing	Balanced	Balanced	Concrete Crushing
Exp. prestress loss (%)	18.9	22.3	19.7	18.8	20.4
AASHTO LRFD prestress loss (%)	20.5	20.5	18.3	20.5	18.3
PCI prestress loss (%)	21.4	21.4	18.8	21.4	18.8

### 8.3 Discussion of Test Results

Data collected during the monitoring of the beams were adjusted and analyzed to evaluate the loss of prestressing force over the monitoring period. In addition, decompression loads from the flexural testing of the beams were captured and analyzed to back calculate the effective prestressing force. The test results of beams prestressed with CFCC strands over a testing period of two years showed insignificant change in the effective prestressing force that falls within the tolerance of collecting and analyzing the data. The differences in the ultimate load carrying capacities among the five beams is mainly attributed, and related to, the change in concrete strength over a period of two years.

Concrete prisms monitored for shrinkage and concrete cylinders loaded in creep rupture setup indoors and outdoors showed a typical concrete shrinkage and creep that can be conservatively estimated using currently available guidelines such as AAHTO LRFD. Elastic prestress loss and losses due to creep and shrinkage of the concrete showed a good agreement with values calculated theoretically according the AASHTO LRFD and PCI Design manual.

## CHAPTER 9: FLEXURAL AND SHEAR DESIGN OF CFRP PRESTRESSED BEAMS

### 9.1 Introduction

Once the loss in prestressing force is established, the analysis of a CFRP prestressed section becomes a straightforward process with few exceptions. For instance, steel reinforced/prestressed sections are classified as tension-controlled or compression-controlled according to the net tensile steel strain at the time the concrete in compression reaches its assumed crushing strain limit of 0.003. However, CFRP reinforced/prestressed sections are classified as tension or compression-controlled based on the actual failure mode whether it is crushing of the concrete or rupture of the CFRP reinforcement. If the concrete reaches a crushing strain of 0.003 while the net strain in the extreme CFRP remains less than net guaranteed tensile strain, the section is regarded as compression-controlled section. If the net extreme CFRP strain reaches the net guaranteed tensile strain, while the concrete compression strain remains less than 0.003, the section is regarded as tension controlled. The net guaranteed tensile strain is the net tensile strain in the reinforcement at balanced strain conditions. For all prestressed CFRP reinforcement, the net guaranteed strain limit may be taken as the specified guaranteed ultimate strain exclusive of the strain due to prestress, creep, shrinkage, and temperature.

Earlier studies and experimental work showed that the moment capacity of sections prestressed and reinforced with CFRP materials can be accurately estimated using the principles of strain compatibility and force equilibrium in the section (Grace et al. 2013a, 2013b, 2013c, 2012a, 2011a, 2011b, 2008, 2006a, and 2006b). ACI 440.4R-04 provides equations to calculate the depth of the neutral axis and nominal moment capacity of the section when the reinforcement or prestressing CFRP is provided in a single layer. In addition, several studies produced different design approaches with varying degrees of complexity (Grace et al. 2003a).

Due to the elastic nature of CFRP material, when the tension CFRP reinforcement is distributed over multiple layers, the failure of tension-controlled sections is usually governed by the failure of CFRP reinforcement at the extreme layer, which is the layer farthest from the compression fiber. CFRP reinforcements at layers closer to the compression fiber are likely to fail progressively once CFRP reinforcement at the extreme layer fails. It is therefore not recommended to sum the layers of CFRP reinforcement through their center of gravity. ACI 440.4R-04 Section

3.4.2 provides a set of equations to address this problem. Nevertheless, the equations in ACI 440 are based on the assumption that the stress distribution in concrete is linear and the section is tension-controlled and therefore, those equations are not applicable for compression-controlled sections or tension-controlled section with non-linear stress distribution on the concrete. That leaves the designer with the option of using basic strain compatibility and force equilibrium (Grace et al. 2003b). However, strain compatibility and force equilibrium in their raw format tend to be a lengthy iterative process, especially when the mode of failure is not known.

## 9.2 Flexural Design of CFRP reinforced/Prestressed section

To facilitate the flexural design and reduce the potential for error, a unified design approach is developed by converting the areas of CFRP reinforcement at different layers to equivalent areas at the level of the extreme CFRP layer using appropriate area reduction factors. The sum of equivalent reinforcement areas at the extreme layer is regarded as “The equivalent area of reinforcement,  $A_{fe}$ ” and is used to calculate the depth of the neutral axis and the nominal moment capacity of the section. In other words, the equivalent area of CFRP reinforcement is a discrete area of CFRP reinforcement positioned at the extreme CFRP layer that results in the same flexural capacity of n layers of reinforcement.

The area reduction factor needed to calculate the equivalent areas of reinforcement are obtained by assuming linear strain distribution through the depth of the section. Thereby, the area of CFRP reinforcement at the  $i$ th layer is reduced with a factor depending on the distance from the  $i$ th layer to the extreme layer. The area reduction factor can be calculated by evaluating the strain distribution through the section as follows:

The net tensile strain at any layer ( $i$ ) is related to the net tensile strain at the extreme CFRP layer by:

$$\varepsilon_i = \varepsilon_1 \left( \frac{d_i - c}{d_1 - c} \right) \quad (9.2-1)$$

where:

$\varepsilon_i$  = net tensile strain at the  $i$ th CFRP reinforcement layer

$\varepsilon_1$  = net tensile strain at the extreme CFRP layer

$d_i$  = depth of the  $i$ th CFRP layer from the extreme compression fiber (in. or mm)

$d_1$  = depth of the extreme CFRP layer from the extreme compression fiber (in. or mm)

$c$  = depth of neutral axis from the extreme compression fiber (in. or mm)

The tensile force,  $T_i$ , in any CFRP layer ( $i$ ) may be calculated as:

$$T_i = \varepsilon_i n_i a_f E_f = \varepsilon_1 \left( \frac{d_i - c}{d_1 - c} \right) n_i a_f E_f = \varepsilon_1 \left( \frac{d_i - c}{d_1 - c} n_i a_f \right) E_f = \varepsilon_1 A_{fe(i)} E_f \quad (9.2-2)$$

where:

$\varepsilon_i$  = net tensile strain at the  $i$ th CFRP reinforcement layer

$n_i$  = number of CFRP strands in the  $i$ th layer

$a_f$  = area of single CFRP strand in the  $i$ th layer (in.2 or mm2)

$E_f$  = elastic modulus of CFRP (ksi or MPa)

$d_i$  = depth of the  $i$ th CFRP layer from the extreme compression fiber (in. or mm)

$d_1$  = depth of the extreme CFRP layer from the extreme compression fiber (in. or mm)

$c$  = depth of neutral axis from extreme compression fiber (in. or mm)

where  $A_{fe(i)}$  is the area equivalent to the area of CFRP reinforcement at layer  $i$  and is calculated as:

$$A_{fe(i)} = \frac{d_i - c}{d_1 - c} (n_i a_f) \quad (9.2-3)$$

The equivalent area of reinforcement for the total reinforcement provided in the section,  $A_{fe}$  is calculated as:

$$A_{fe} = \sum_{i=1}^m A_{fe(i)} \quad (9.2-4)$$

Where

$m$  = number of layers (rows) of CFRP reinforcement

At this stage of analysis, the depth of the neutral axis from the extreme compression fiber,  $c$ , can be initially set equal to  $0.1d_1$ . The initial assumption of  $c = 0.1d_1$  is based on observations from multiple experimental flexural tests of CFRP prestressed beams and is only needed if calculations are performed by hand. This assumption usually yields accurate estimate for the depth of the neutral axis and the flexural capacity of the section. It needs not to be adjusted unless more refined calculations are required. In addition, if a Software tool is implemented in the design, there is no need to start with an initial assumption since a loop can be created in the software to calculate the exact depth of the N.A.

With  $c = 0.1d_1$ , Eq. 3 becomes:

$$A_{fe(i)} = \left(1 - \frac{s_i}{0.9d_1}\right) (n_i a_f) \quad (9.2-5)$$

where:

$$s_i = \text{Distance between } i\text{th CFRP layer and extreme CFRP layer (in.)} = d_1 - d_i$$

After establishing the equivalent area of reinforcement for the section, the exact depth of neutral axis shall be calculated from Eqs. 6 through 11, whichever is applicable:

For tension-controlled rectangular sections:

$$c = \frac{E_f A_{fe} (\varepsilon_{gu} - \varepsilon_{pe}) + P_e}{0.85 f'_c \beta_1 b} \quad (9.2-6)$$

For tension-controlled flanged sections:

$$c = \frac{E_f A_{fe} (\varepsilon_{gu} - \varepsilon_{pe}) + P_e - 0.85 f'_c h_f (b - b_w)}{0.85 f'_c \beta_1 b_w} \quad (9.2-7)$$

For tension-controlled double-flanged sections:

$$c = \frac{E_f A_{fe} (\varepsilon_{gu} - \varepsilon_{pe}) + P_e - 0.85 f'_c h_{f1} (b_{f1} - b_w) - 0.85 f'_c h_{f2} (b_{f2} - b_w)}{0.85 f'_c \beta_1 b_w} \quad (9.2-8)$$

For compression-controlled flanged sections:

$$0.85 f'_c \beta_1 b_w c + 0.85 f'_c h_f (b - b_w) = E_f A_{fe} \varepsilon_{cu} \left( \frac{d_1}{c} - 1 \right) + P_e \quad (9.2-9)$$

For compression-controlled rectangular sections:

$$0.85 f'_c \beta_1 b c = E_f A_{fe} \varepsilon_{cu} \left( \frac{d_1}{c} - 1 \right) + P_e \quad (9.2-10)$$

For compression-controlled double-flanged sections:

$$\begin{aligned} 0.85 f'_c \beta_1 b_w c + 0.85 f'_c h_{f1} (b_{f1} - b_w) + 0.85 f'_c h_{f2} (b_{f2} - b_w) \\ = E_f A_{fe} \varepsilon_{cu} \left( \frac{d_1}{c} - 1 \right) + P_e \end{aligned} \quad (9.2-11)$$

where:

$b$  = width of compression face of the member; for a flanged section in compression, the effective width of the flange (in. or mm)

$P_e$  = effective prestressing force in the section (kip or N)

$E_f$  = elastic modulus of CFRP (ksi or MPa)

$\varepsilon_{cu}$  = average concrete crushing strain, 0.003

$\varepsilon_{gu}$  = design guaranteed strain of CFRP including environmental and durability effects

$\varepsilon_{pe}$  = effective prestressing strain in CFRP after subtracting applicable prestress losses

$h_f$  = depth of compression flange (in. or mm)

$b_w$  = width of web (in. or mm)

$h_{f1}$  = depth of first compression flange (in. or mm) of double-flanged section (in. or mm)

$h_{f2}$  = depth of second compression flange in case of double-flanged section (in. or mm)

$b_{f1}$  = for a double-flanged section in compression, the effective width of the first flange (in. or mm)

$b_{f2}$  = for a double-flanged section in compression, the effective width of the second flange (in. or mm)

Equation 9.2-6 through 9.2-11 are developed by representing the natural relationship between concrete stress and strain by an equivalent rectangular concrete compressive stress block of  $0.85f'_c$  over a zone bounded by the edges of the cross-section and a straight line located parallel to the neutral axis at the distance  $a = \beta_1 c$  from the extreme compression fiber. The distance  $c$  is measured perpendicular to the neutral axis. The factor  $\beta_1$  is taken as 0.85 for concrete strengths not exceeding 4.0 ksi (28 MPa). For concrete strengths exceeding 4.0 ksi (28 MPa),  $\beta_1$  is reduced at a rate of 0.05 for each 1.0 ksi (6.89 MPa) of strength in excess of 4.0 ksi (28 MPa), except that  $\beta_1$  shall not be taken to be less than 0.65.

After calculating the depth of the neutral axis, the nominal moment capacity of the section can be calculated for flanged sections subjected to flexure about one axis and where the compression flange depth is less than  $a = \beta_1 c$  as follows:

$$M_n = \sum_{i=1}^m \left[ a_f n_i \varepsilon_i E_f \left( d_i - \frac{a}{2} \right) \right] + P_e \left( d_p - \frac{a}{2} \right) + 0.85 f'_c h_f (b - b_w) \left( \frac{a}{2} - \frac{h_f}{2} \right) \quad (9.2-12)$$

Or, for a double-flanged section:

$$M_n = \sum_{i=1}^m \left[ a_f n_i \varepsilon_i E_f \left( d_i - \frac{a}{2} \right) \right] + P_e \left( d_p - \frac{a}{2} \right) + 0.85 f'_c h_{f1} (b_{f1} - b_w) \left( \frac{a}{2} - \frac{h_{f1}}{2} \right) + 0.85 f'_c h_{f2} (b_{f2} - b_w) \left( \frac{a}{2} - h_{f1} - \frac{h_{f2}}{2} \right) \quad (9.2-13)$$

where:

$a_f$  = area of single CFRP strand in the  $i$ th layer (in.<sup>2</sup> or mm<sup>2</sup>)

$n_i$  = number of CFRP strands in the  $i$ th layer

$\varepsilon_i$  = net tensile strain at the  $i$ th layer of CFRP reinforcement determined from strain compatibility, taken equal to  $\varepsilon_1 \left( \frac{d_i - c}{d_1 - c} \right)$

$\varepsilon_1$  = net tensile strain at the extreme CFRP layer  
 $d_i$  = depth of the  $i$ th CFRP layer from the extreme compression fiber (in. or mm)  
 $d_1$  = depth of the extreme CFRP layer from the extreme compression fiber (in. or mm)  
 $f'_c$  = specified compressive strength of concrete at 28 days, unless another age is specified (ksi or MPa)  
 $P_e$  = effective prestressing force in the section (kip or N)  
 $d_p$  = distance from the extreme compression fiber to the centroid of prestressing strands (in. or mm)  
 $E_f$  = elastic modulus of CFRP (ksi or MPa)  
 $h_f$  = depth of compression flange (in. or mm)  
 $b$  = width of compression face of the member (in. or mm)  
 $b_w$  = width of web (in. or mm)  
 $a$  =  $\beta_1 c$ ; depth of the equivalent stress block (in. or mm)  
 $\beta_1$  = stress block factor  
 $c$  = depth of neutral axis from extreme compression fiber as determined from Eqs. 9.2-6 through 9.2-9, whichever is applicable (in. or mm)  
 $m$  = number of layers (rows) of CFRP reinforcement  
 $h_{f1}$  = depth of first compression flange in case of double-flanged section (in. or mm)  
 $h_{f2}$  = depth of second compression flange in case of double-flanged section (in. or mm)  
 $b_{f1}$  = for a double-flanged section in compression, the effective width of the first flange (in. or mm)  
 $b_{f2}$  = for a double-flanged section in compression, the effective width of the second flange (in. or mm)

For rectangular sections subjected to flexure about one axis, where the approximate stress distribution is used and where the compression flange depth is not less than  $a = \beta_1 c$  as determined in accordance with Eqs. 9.2-6 through 9.2-11, whichever is applicable, the nominal flexural resistance  $M_n$  may be determined by using Eq. 9.2-12, in which case  $b_w$  shall be taken as  $b$ .

In 2013 and 2014 two 45°-skewed simply supported highway bridges were constructed to carry M-102 over Plum Creek in Southfield, Michigan. Each bridge is composed of eight spread precast

prestressed box beams with a beam width of 48 in. (1219 mm), a depth of 33 in. (838 mm), and a length of 67.9 ft (20.7 m). Each beam is prestressed with 37 CFRP strands arranged in four rows. Each strand is prestressed with an initial prestressing force of 32.8 kip (146 kN).

The equivalent area method was used to calculate the nominal moment capacity of the bridge beams. The overall depth of the sections was taken as 42 in. (1067 mm) as the depth of the haunch between the deck slab and the haunch was ignored. The CFRP strands had a cross sectional area of  $0.179 \text{ in.}^2$  ( $115.2 \text{ mm}^2$ ), a modulus of elasticity of 21,000 ksi (144.8 GPa), and a guaranteed strength of 339 ksi (2237 MPa). Nevertheless, the design strength of the CFRP strands was taken as 90 % of the guaranteed strength to account for environmental conditions that might affect strand strength. Similar to steel strands, the spacing between CFRP strands was maintained at 2.0 in. (51 mm) in both directions. The deck slab had a design concrete strength of 4 ksi (28 MPa) and effective width of 8 ft (2438.8 mm). The estimated effective prestressing force after all losses was approximately 965 kip (4292 kN).

The equivalent area of reinforcement was calculated using Eqs. 9.2-3, 9.2-4, and 9.2-5 assuming a depth of neutral axis equal to 0.1 times the depth of the extreme CFRP layer (40 in. or 1016 mm). Then the actual depth of the neutral axis was calculated using Eq. 9.2-6 as the section was rectangular tension controlled. The depth of the neutral axis was calculated as 7.126 in. (181 mm) from the extreme compression fiber in the deck slab. Finally, the nominal moment capacity of the section was calculated according to Eq. 9.2-12 and was found to be 5836 kip.ft (7913 kN.m). It should be noted that the initial assumption for the depth of the neutral axis as 0.1 times the depth of the extreme CFRP layer had minimal effect on the rest of the calculations. For instance, other values for the depth of the neutral axis were assumed as shown in Table 9.2-1 and it can be shown that regardless of the initial assumption, Eq. 9.2-6 yielded nearly the same depth of the neutral axis and the change in the nominal moment capacity was negligible. On the other hand, when using strain compatibility and force equilibrium in their raw format, the exact depth of the neutral axis was found as 7.11 in. (180.6 mm) and the nominal moment capacity was 5837 kip.ft (7914). Those exact numbers can also be obtained by performing a second iteration of the equivalent area method and instead of assuming the depth of the neutral axis equal to 0.1 times the depth of the extreme CFRP layer in the second iteration, it can be assumed equal to the neutral axis depth obtained using Eq. 9.2-6 in the first iteration.

Table 9.2-1 Nominal moment capacity calculated using different assumptions for the depth of the neutral axis

Assumed value for the depth of the neutral axis, in. (mm)	Equivalent area of reinforcement according to Eqs.9.2-3 & 4, in. <sup>2</sup> (mm <sup>2</sup> )	Depth of the neutral axis according to Eq. 9.2-6, in. (mm)	Nominal moment capacity according to Eq. 9.2-12, kip.ft (kN.m)
0 (0)	6.372 (4111)	7.140 (181.4)	5834 (7910)
2 (50.8)	6.359 (4103)	7.134 (181.2)	5835 (7912)
4 (101.6)	6.345 (4094)	7.126 (181.0)	5836 (7913)
6 (152.4)	6.328 (4083)	7.116 (180.7)	5837 (7914)
8 (203.2)	6.310 (4071)	7.106 (180.5)	5837 (7914)
10 (254)	6.289 (4057)	7.094 (180.2)	5838 (7916)
12 (304.8)	6.265 (4042)	7.080 (179.8)	5839 (7917)
14 (355.6)	6.237 (4024)	7.064 (179.4)	5840 (7919)

### 9.3 Shear Design

This part of the report discusses a shear investigation that was conducted to evaluate the shear capacity of beams with CFRP stirrups (Grace et al. 2015). After executing the shear investigation, the beam specimens discussed herein were subjected to fire/loading events as discussed earlier in the report.

#### 9.3.1 Test setup

Eleven decked bulb T beams were constructed, instrumented, and tested under shear loading to failure. Nine beams were reinforced and prestressed with CFCC strands, while one beam was prestressed with conventional low-relaxation steel strands and one beam was reinforced with non-prestressed CFCC strands. Half the span of each beam was reinforced with CFCC stirrups, while the other half was reinforced with conventional steel stirrups. In addition, one of the CFCC prestressed beam was provided with no stirrups within the critical shear span. Both ends of each beam were tested to evaluate the performance of CFCC stirrups versus that of steel stirrups. The investigation addressed the shear performance with respect to several shear parameters including shear-span-to-depth ratio, stirrup spacing, prestressing force, and type of longitudinal and transverse reinforcement. All test beams failed by crushing of concrete in either the web or the top flange. No rupture of CFCC stirrups was experienced in any of the test beams. The performance of CFCC stirrups was analogous to that of steel stirrups with the exception that steel stirrups demonstrated a yield plateau before concrete failure. Beam ends with CFCC stirrups attained cracking and ultimate shear capacities similar to those attained in ends with steel stirrups. Results

from the experimental investigation were compared with the theoretical values predicted using some available shear design guidelines for steel and CFCC reinforcement. In addition, modifications for current AASHTO LRFD shear design equations and its possible implementation in the ACI 440 shear design guidelines are proposed based on the experimental results.

The shear test evaluated  $a/d$  ratios of 3, 4, 5 and 6, prestressing levels per beam of 0, 72, 100, and 132 kip (0, 320, 444, and 587 kN), and stirrup spacing of 4, 6, and 8 in. (102, 152, and 203 mm). The outcome of the experimental investigation was compared with the theoretical predictions according to available design guidelines (ACI 440.1R 2006, ACI 440.4R 2004, and AASHTO LRFD 2012) and a modification is proposed to update the current AASHTO LRFD and ACI 440 shear design equations to effectively predict the shear capacity.

Nine beams had an effective span of 31 ft. (9.45 m), while two beams had an effective span of 40 ft. (12.2 m). The longitudinal prestressed and non-prestressed CFCC strands had a nominal diameter of 15.2 mm (0.6 in.). The initial prestressing force per strand was adjusted to 18 kip (80 kN) in one beam, 25 kip (111 kN) in six beams, and 33 kip (147 kN) in two beams. These prestressing levels represented 30, 41, and 54 % of the guaranteed CFCC strand capacity, respectively. As each beam was prestressed with four prestressing strands, these prestressing levels corresponded to a total initial prestressing force per beam of 72, 100, and 132 kip (320, 444, and 587 kN), respectively. In addition, one more beam was reinforced with CFCC strands with no prestressing and another beam was prestressed with conventional low relaxation steel strands with a diameter of 0.6 in. (15.2 mm) to an initial prestressing level of (132 kip) 587 kN per beam or 33 kip (147 kN) per strand. The beams were provided with transverse CFCC stirrups with a nominal diameter of 0.4 in. (10.2 mm) and No. 3 (M10) steel stirrups at a spacing of 4, 6, or 8 in. (102, 152, or 203 mm).

The beam is referred with acronym indicating multiple characteristics. The acronym includes letters and numbers. The first letter and number refer to the type of the longitudinal reinforcement (S for steel and C for CFCC) and the level of prestressing force per beam in kips [0, 72, 100, or 132 kip (0, 320, 444, or 587 kN)], respectively. The second letter and number refer to the transverse reinforcement (S for steel stirrups and C for CFCC stirrups) and the stirrup spacing in inches [4, 6, or 8 in. (102, 152, or 203 mm)], respectively. The last number refers to the  $a/d$  ratio (3, 4, 5, or 6). For example, Beam C100-S6-4 is a beam prestressed longitudinally with CFCC strands to a

level of 100 kip, provided with steel stirrups at spacing of 6 in., and loaded at a distance equal to  $4d$  from the support, where  $d$  is the effective depth of the beam. Detailed prestressing, construction, and curing techniques of the beams can be found at Grace et al. (2012a) and Rout (2013). The concrete compressive strength averaged 6.4 ksi (44 MPa) at the time of prestress transfer and 9 ksi (62 MPa) after 28 days.

Each beam end was instrumented with approximately 60 strain and deflection sensors. Linear strain gages were attached to all longitudinal prestressing and non-prestressing strands under the loading point. Strain gages were also attached to the surfaces of the top and bottom flanges and to the flange sides as well. Linear and rosette strain gages were attached to the web of the beam within the shear span. Linear variable differential transducers (LVDTs) were mounted on the web within the shear span at angles of 0, 45, and 90 degrees. Linear motion transducers (LMTs) were attached to the soffit of the beam under the loading point and at the mid-span to record deflection. In addition, each stirrup in the shear span was instrumented with two strain gages on the vertical leg.

All beams were simply supported over two steel reinforced neoprene/elastomeric bearing pads and were loaded by a 220-kip (1000-kN) hydraulic actuator. The load was applied as a concentrated load at a distance  $a$  from the center of the support. The distance  $a$  was taken as 45, 60, 75 and 85 in. (1.1, 1.5, 1.9, and 2.2 m), which corresponded to approximate  $a/d$  ratios of 3, 4, 5, and 6, respectively.

The testing scenario for each beam was executed through two stages. First, beam end with CFCC stirrups was loaded under shear loading setup to failure. At this stage of testing, the beam was simply supported over its effective span either 31 ft or 40 ft (9.45 m or 12.2 m) and the load was applied at the distance  $a$  from the center of the support. After failure, the beam was rotated and the other end, with steel stirrups, was positioned under the loading actuator. To eliminate the already-failed portion of the beam, the far support was located under the first interior diaphragm rather than under the end of the beam. Therefore, the effective span was shortened to 23 ft or 33 ft (7 or 10 m) for beams with original effective spans of 31 ft and 40 ft (9.45 m or 12.2 m), respectively. The second beam end was then tested under the same shear loading setup, with the same  $a/d$  ratio to failure. In both stages of testing, the load was applied through incremental loading/unloading cycles and the crack map was plotted and updated at every load cycle.

### 9.3.2 Test results

To facilitate comparison with shear design guidelines, the results presented herein relates the response of the beams to the shear force rather than the applied load. The shear force is the reaction at the near-load support due to the applied load. The results of the investigation are summarized in Table 9.3-1, which shows: the cracking shear force, ultimate shear force with the corresponding under-load deflection, maximum recorded strain in the concrete top flange, the stirrups, and the longitudinal reinforcement.

The cracking shear force was obtained visually by inspecting the beam with every load cycle and was established through the load-deflection curves. A typical load deflection curve for the test beams was characterized by the change in slope with the onset of cracks. The cracking shear force was obtained by detecting the force level, where the two slopes of envelope for the load-deflection curves intersected.

Overall, the variation in the stirrup material (steel and CFCC) did not influence the cracking or maximum shear capacity of the test beams. The recorded concrete strain at failure at the top flange, on the stirrups, and on the longitudinal CFCC strands did not vary significantly between beam ends with steel stirrups and those with CFCC stirrups. It can be concluded that while the stirrups, either steel or CFCC, were actively participating in the shear loading mechanism, they did not govern the failure mode. Rather, the failure occurred due to the collapse of the concrete portion which led to the failure of the shear loading mechanism. This was confirmed from the inspection of stirrups after failure. The CFCC stirrups did not experience any rupture and while the steel stirrups yielded long before the failure, they continued to support the assigned load until the shear strain exceeded the strain required to maintain the integrity of the section and preserve a reasonable amount of the aggregate interlock.

The stirrups sustained a wide range of strain depending on their location relative to the load and support. In addition, the response of each stirrup was different during each load cycle depending on the development of diagonal cracks. The strain in the stirrups was negligible before the development of diagonal cracks but once cracks developed, there was a rapid increase in the strain. At the last load cycles, strain in the stirrups appeared to be proportional to the load with no further sudden increase, which indicted that cracking map fully developed at that region and no new cracks intersected this particular stirrup.

Table 9.3-1 Experimental results of test beams

Beam Designation	Cracking Shear Force ( $V_{cr}$ )	Ultimate Shear Force ( $V_u$ )	Ultimate - Cracking Shear Force ( $V_u - V_{cr}$ )	Deflection Under Load ( $\delta_u$ )	Top Concrete Strain ( $\epsilon_{cu}$ )	Max. Stirrups Strain ( $\epsilon_{stirrup}$ )	Prestressing Strain ( $\epsilon_{prestress}$ )
	kip	kip	kip	in.	$\mu\epsilon$	$\mu\epsilon$	$\mu\epsilon$
C100-C6-3	26.8	58.7	31.9	1.6	-1282	3588	9154
C100-C6-4	19.1	52.2	33.1	3.0	-1767	3575	9465
C100-C6-5	15.5	49.1	33.6	4.1	-2624	3467	7694
C100-C6-6	14.2	46.3	32.1	5.5	-2732	3426	12688
C100-S6-3	27.2	61.2	34.0	1.4	-1642	3730	8533
C100-S6-4	20.0	53.6	33.6	2.6	-2038	3349	9061
C100-S6-5	15.7	49.6	33.9	3.5	-2639	3652	9475
C100-S6-6	12.4	44.2	31.8	4.8	-2649	3782	11794
C100-C4-3	27.9	53.8	25.9	1.3	-1042	3023	6938
C100-C8-3	28.1	53.1	25.0	1.4	-1531	3999	7072
C100-S4-3	30.6	68.1	37.5	1.7	-1937	3538	6888
C100-S8-3	28.1	51.0	22.9	1.2	-1381	3283	6838
C000-C4-3	9.4	44.0	34.6	2.3	-1558	2394	2085
C072-C4-3	23.6	58.3	34.7	2.0	-1302	2802	6065
C132-C4-3	30.4	71.3	40.9	1.8	-1520	3478	10623
C000-S4-3	11.0	51.4	40.4	2.2	-1697	3255	3059
C072-S4-3	22.3	61.6	39.3	1.8	-1806	2392	5730
C132-S4-3	30.8	69.5	38.7	1.5	-1677	3222	11509
S132-S4-3	29.7	72.0	42.3	1.6	-1973	3310	5756
S132-C4-3	29.9	68.3	38.4	1.5	-1511	3041	4614
C132-00-3	-	33.4	-	0.6	-465	-	7893

Note: 1 in. = 25.4 mm    1 kip = 4.45 kN

## Theoretical shear capacity

The shear capacities of the test beams were evaluated theoretically using the simplified approach provided in ACI 440.4R-04 for prestressed concrete beams with CFRP stirrups and AASHTO LRFD 2012 for reinforced/prestressed beams with steel stirrups. The following subsections provide a detailed discussion for both provisions with their major assumptions.

### Nominal Shear Capacity According to ACI 440.4R-04

ACI 440.4R assumes that the nominal shear strength,  $V_n$ , is the summation of the shear resistance provided by concrete,  $V_c$ , and the shear resistance provided by the stirrups,  $V_{frp}$ . This is in addition to the shear strength provided by the vertical component of prestressing force in case of draped strands,  $V_p$ . Therefore, the nominal shear strength  $V_n$ , N (lb), can be written as:

$$V_n = V_c + V_{frp} + V_p \quad (9.3-1)$$

$V_c$  is taken as:

$$V_c = 0.17\sqrt{f'_c}b_wd \text{ (N)} \quad (9.3-2-SI)$$

or

$$V_c = 2\sqrt{f'_c}b_wd \text{ (lb)} \quad (9.3-2-US)$$

where,  $f'_c$  is the concrete compressive strength, psi (MPa),  $b_w$  is the effective width, in. (mm), and  $d$  is the effective depth of the section from the top fibers to the center of the longitudinal reinforcement, in. (mm).

The value of  $V_c$  considered in ACI 440.4R is the lower level of the concrete shear resistance as provided in ACI 318-02 (2002). ACI 440.4R outlines that due to the scarcity of test data for beams with CFRP stirrups, the concrete shear capacity cannot be extended beyond the minimum value mentioned in Eqn. 9-3-2 shown above. Similarly, the contribution of CFCC stirrups in the shear resistance was directly adopted from ACI 318-02 by replacing the yield strength of steel stirrups,  $f_y$ , (psi) MPa, with a corresponding permissible strength limit for CFCC stirrups,  $f_{fb}$ , psi (MPa). The shear resistance provided by the vertical CFCC stirrups,  $V_{frp}$ , lb (N), is given as:

$$V_{frp} = \frac{f_{fb}A_v d}{S} \quad (9.3-3)$$

where,  $A_v$  is the total cross-sectional area of the stirrups,  $in.^2$  ( $mm^2$ ),  $d$  is the effective depth, in. (mm), and  $S$  is the stirrup spacing, in. (mm).

The permissible strength of CFCC stirrups,  $f_{fb}$ , is taken as the minimum of the tensile strength of CFCC stirrups at the bend portion or the tensile strength of CFCC stirrups corresponding to a strain of 0.2 %. The choice of 0.2 % as a limiting strain is to ensure a shear performance similar to that exhibited by conventional steel stirrups with a yield strain of 0.2 % and to prevent excessive cracks that may lead to loss of aggregate interlock and loss of section integrity.

### **Nominal Shear Capacity According to AASHTO LRFD Simplified Approach**

The simplified approach follows the same technique of calculating the shear strength of the section by adding the concrete shear strength to the stirrup shear strength. However, a more detailed methodology was followed to accurately estimate the concrete contribution, which was empirically assumed equal to the cracking shear strength of the concrete.

The nominal shear capacity  $V_n$ , N (lb), is calculated according to AASHTO LRFD simplified approach as:

$$V_n = V_n + V_n \leq 0.25 f'_c b_v d_v \quad (9.3-4)$$

$V_c$  is the lesser of  $V_{ci}$  and  $V_{cw}$ , where  $V_{ci}$  is the nominal shear resistance provided by concrete when inclined cracking results from combined shear and moment and  $V_{cw}$  is the nominal shear resistance provided by concrete when inclined cracking results from excessive principal tension in the web. For instance, considering the case before the development of cracks, the principal stresses at any element through the depth of the section can be calculated using Mohr's circle as:

$$f_{1,2} = \frac{f_x + f_y}{2} \pm \sqrt{\left(\frac{f_x - f_y}{2}\right)^2 + \tau_{xy}^2} \quad (9.3-5)$$

Where,

$f_{1,2}$  = Principal stresses, psi (MPa)

$f_x$ = Normal stresses in the horizontal direction (the axis of the beam), psi (MPa)

$f_y$ = Normal stresses in the vertical direction (perpendicular to the axis of the beam), psi (MPa)

$\tau_{xy}$ = In-plane shear stresses, psi (MPa)

$f_y$  is theoretically negligible in case of beams subjected to bending and shear stresses only.

Therefore, the eqn. of principal stresses can be written as:

$$f_{1,2} = \frac{f_x}{2} \pm \sqrt{\left(\frac{f_x}{2}\right)^2 + \tau_{xy}^2} \quad (9.3-6)$$

And the maximum principal stresses shall be taken as:

$$f_1 = \frac{f_x}{2} + \sqrt{\left(\frac{f_x}{2}\right)^2 + \tau_{xy}^2} \quad (9.3-7)$$

Equation 9.3-7 is valid for any element through the depth of the beam and the first crack will develop when  $f_1$  exceeds the tensile strength of the concrete,  $f_t$ . If the tensile strength is exceeded in the web, the cracks will develop primarily as web-shear cracks, while if the tensile strength of concrete is exceeded first in the bottom flange, the cracks will develop as flexural-shear cracks. The value of  $f_x$  represents the effect of prestressing force in addition to the normal stresses due to the moment.

If an element is taken at the neutral axis (N.A.) of the beam, the normal stresses can be taken as the prestressing force divided by the area of the cross section  $f_{pc}$  (compressive stresses) and therefore, Eqn. 9.3-7 can be written as:

$$f_1 = \frac{-f_{pc}}{2} + \sqrt{\left(\frac{-f_{pc}}{2}\right)^2 + \tau_{xy}^2} \quad (9.3-8)$$

Equation 9.3-8 can be arranged to estimate the shear stress level required to develop the first shear crack at the N.A. as follows:

$$\tau_{xy} = f_1 \sqrt{1 + \frac{f_{pc}}{f_1}} \quad (9.3-9)$$

In AASHTO LRFD, Eqn. 9.3-9 was simplified and developed to estimate the web shear cracking load,  $V_{cw}$ , by multiplying  $\tau_{xy}$  by the width of the web and the effective shear depth. In addition,  $f_1$  was replaced by an estimated value for the tensile strength of concrete,  $f_t$ , and this yielded the expression for  $V_{cw}$ , which represents the shear force that causes the principal stresses at the neutral axis of the section to reach the tensile strength of the concrete.  $V_{cw}$  was expressed as:

$$V_{cw} = f_t \sqrt{1 + \frac{f_{pc}}{f_t} b_v d_v} + V_p \quad (9.3-10)$$

To develop a simplified equation for  $V_{cw}$ , the tensile strength of the concrete was taken as  $2.0\sqrt{f'_c}$  (psi) [ $0.16\sqrt{f'_c}$  (MPa)]. This limit of the tensile strength was considered as a lower bound and thus a conservative estimate for the shear cracking strength. After linearizing the equation,  $V_{cw}$  was given in AASHTO LRFD as:

$$V_{cw} = (0.16\sqrt{f'_c} + 0.3 f_{pc})b_v d_v + V_p \quad (N) \quad f'_c \text{ in MPa} \quad (9.3-11-SI)$$

or

$$V_{cw} = (2.0\sqrt{f'_c} + 0.3 f_{pc})b_v d_v + V_p \quad (lb) \quad f'_c \text{ in psi} \quad (9.3-11-US)$$

On the other hand, the flexural-shear cracking strength,  $V_{ci}$ , can also be estimated by considering Eqn. 9-3-7 for an element at the soffit of the beam. In that case,  $f_x$  is taken as the stresses due to the prestressing force in addition to the flexural stresses due to the applied loads including the self-weight of beam, both calculated at the soffit of the beam, while ignoring the shear stresses at the soffit of the beam.

It should be noted that the flexural shear-cracking strength was based on the assumption that the first shear crack will occur at a minimum distance of  $d/2$  from the loading point (Hawkins et al. 2005) but to simplify the equation, the term  $d/2$  was ignored. It was also assumed that the flexural-shear crack will occur at slightly higher shear force than flexural cracking and the margin between shear cracking and flexural cracking was evaluated empirically and was set to  $0.63\sqrt{f'_c}b_v d_v$  (lb) [ $0.053\sqrt{f'_c}b_v d_v$  (N)]. Furthermore, a minimum shear cracking force of  $1.9\sqrt{f'_c}b_v d_v$  (lb) [ $0.16\sqrt{f'_c}b_v d_v$  (N)] was introduced to provide minimum  $V_c$  contribution over the

length of the member independent of whether a web or flexure-shear cracking regions was being designed. The final equation for  $V_{ci}$  was given as:

$$V_{ci} = 0.053 \sqrt{f'_c} b_v d_v + V_d + \frac{V_i M_{cre}}{M_{max}} \geq 0.16 \sqrt{f'_c} b_v d_v \quad (N) \quad f'_c \text{ in MPa} \quad (9.3-12-SI)$$

or

$$V_{ci} = 0.63 \sqrt{f'_c} b_v d_v + V_d + \frac{V_i M_{cre}}{M_{max}} \geq 1.9 \sqrt{f'_c} b_v d_v \quad (lb) \quad f'_c \text{ in psi} \quad (9.3-12-US)$$

where,

$V_d$  = shear force at section due to un-factored dead load, lb (N)

$V_i$  = factored shear force at section due to externally applied loads occurring simultaneously with  $M_{max}$ , lb (N)

$M_{max}$  = maximum factored moment at section due to externally applied loads, lb-in. (N-mm)

$M_{cre}$  = moment causing flexural cracking at section due to externally applied loads, lb-in. (N-mm) and is calculated as:

$$M_{cre} = S_c (f_r + f_{cpe} - \frac{M_{dnc}}{S_{nc}}) \quad (9.3-13)$$

$f_{cpe}$  = compressive stress in concrete due to effective prestressing, psi (MPa)

$M_{dnc}$  = total un-factored dead load moment acting on the monolithic or non-composite section, lb-in. (N-mm)

$S_c$  = section modulus for the extreme fiber of the composite section where tensile stress is caused by externally applied loads, in.<sup>3</sup> (mm<sup>3</sup>)

$S_{nc}$  = section modulus for the extreme fiber of the monolithic or non-composite section where tensile stress is caused by externally applied loads, in.<sup>3</sup> (mm<sup>3</sup>)

$f_r$  = modulus of rupture of concrete,  $f_r = 6.32\sqrt{f'_c}$  (psi) [ $f_r = 0.6\sqrt{f'_c}$  (MPa)] (AASHTO LRFD)

The contribution of the stirrups was calculated based on an angle of compression strut,  $\theta$ , flatter than 45° when  $V_{cw}$  is less than  $V_{ci}$ . The angle  $\theta$  is calculated from Mohr's circle as:

$$\cot \theta = \sqrt{1 + \frac{f_{pc}}{f_t}} \quad (9.3-14)$$

The expression was later simplified to a linear equation and the tensile strength of the concrete  $f_t$  was conservatively taken as  $4.0\sqrt{f'_c}$  (psi) [ $0.32\sqrt{f'_c}$  (MPa)]. In addition, an upper bound of 1.8 was imposed on  $\cot \theta$  so that the strut angle cannot become flatter than  $29^\circ$  for design purposes. However, for high moment and high shear regions, diagonal cracking in flexural-shear zones was believed to occur at low shear stress and the cracks are steep, therefore  $\cot \theta$  was taken equal to 1.0 ( $\theta = 45^\circ$ ) when  $V_{ci} < V_{cw}$ .

In its simplified format, the shear resistance by steel stirrups  $V_s$  is given as:

$$V_s = \frac{A_v f_y \cot \theta}{S} \quad (9.3-15)$$

where,

$$\text{If, } V_{ci} < V_{cw}, \cot \theta = 1.0 \quad (9.3-16)$$

or

$$\cot \theta = 1.0 + 3 \left( \frac{f_{pc}}{\sqrt{f'_c}} \right) \leq 1.8 \quad , \text{ otherwise} \quad (9.3-17)$$

### **Experimental vs. Theoretical Shear Capacity**

The experimental shear capacities of beams with CFCC stirrups were compared with the nominal shear capacities according to the shear provision in ACI-440.4R-04. Similarly, the shear capacities of beams with steel stirrups were compared with the nominal shear capacities according to the simplified shear design method provided in AASHTO LRFD. The following subsections present a brief description for the comparison along with a proposed adjustment for both shear provisions.

### **Nominal Shear Capacity According to ACI 440.4R-04**

As shown in Table 9.3-2, according to ACI 440.4R-04, the concrete shear resistance  $V_c$  for the test beams was constant at 8.3 kip (37 kN). This is considering an average  $f'_c$  of 9000 psi (62 MPa), a web width  $b_w$  of 3 in. (76 mm) and a shear depth  $d$  of 14.6 in. (371 mm). On the other hand,  $V_{frp}$  was calculated based on stirrup strength of 43.4 ksi (300 MPa) (corresponding to a strain of 0.2%) as the strength of the bend portion was experimentally proven higher than this stress limit. The nominal shear capacity according to ACI-440.4R,  $V_n$ , was much less than the experimental shear capacity,  $V_u$ , in all test beams. The ratio  $V_u/V_n$  ranged between 1.2 and 2.4 with an average of 1.8 and a standard deviation of 0.313 (Beam C132-00-3 was excluded). It should be noted that the nominal shear resistance according to ACI-440.4R-04 accounts for the stirrup spacing but ignores both the  $a/d$  ratio and the prestressing level.

### **Nominal Shear Capacity According to AASHTO LRFD Simplified Approach**

Table 9.3-3 shows the nominal shear resistance  $V_n$  of the section according to the simplified approach. As shown in the Table,  $V_{cw}$  for all test beams was less than  $V_{ci}$ . Therefore  $V_{cw}$  was the governing concrete shear-cracking strength and the angle of compression strut was flatter than  $45^\circ$ . However, the nominal shear capacity of the section  $V_n$  was higher than the experimental shear capacity,  $V_u$ , in all test beams. The ratio  $V_u/V_n$  ranged between 0.68 and 0.98 with an average of 0.826 and a standard deviation of 0.097. Overall, the results of the simplified approach were better than those of the ACI 440.4R-04.  $V_{ci}$  in the simplified approach showed a good correlation to the experimental cracking shear force. In addition, the nominal shear capacity for the section  $V_n$  was, to some extent, responsive to the change in stirrup spacing and prestressing level, but not to the change in  $a/d$  ratio.

### **Nominal Shear Capacity According to Proposed AASHTO LRFD Simplified Approach**

Through the simplified approach provided by AASHTO LRFD, three different values for the tensile strength of concrete were used at three different equations: (1)  $f_r = 6.32 \sqrt{f'_c}$  (psi) [ $f_r = 0.6 \sqrt{f'_c}$  (MPa)] (AASHTO LRFD section 5.4.2.6) in calculating  $M_{cre}$  to calculate the flexural-shear cracking force  $V_{ci}$ , (2)  $f_t = 2.0 \sqrt{f'_c}$  (psi) [ $f_t = 0.16 \sqrt{f'_c}$  (MPa)] to calculate the web-shear cracking force  $V_{cw}$ , and (3)  $f_t = 4.0 \sqrt{f'_c}$  (psi) [ $f_t = 0.32 \sqrt{f'_c}$  (N)] to calculate the angle of

compression strut  $\theta$ . While it seems reasonable to use a lower bound for the web-shear cracking force, this approach resulted in an over estimation of the nominal shear resistance in the test beams. In current AASHTO LRFD,  $V_{cw}$  has been intentionally reduced by reducing  $f_t$  and thus it always controlled the concrete cracking shear force for the test specimens. Consequently,  $V_s$  was calculated using an angle of compression strut flatter than  $45^\circ$  (or  $\cot \theta > 1.0$ ).

Had the same value for  $f_t$  been used to calculate both  $V_{cw}$  and  $V_{ci}$ , the governing shear cracking force would have been  $V_{ci}$  and  $V_s$  would have been calculated with angle of compression strut equal to  $45^\circ$  (or  $\cot \theta$  of 1.0). Adding  $V_{cw}$  to the corresponding  $V_s$  (with  $\cot \theta > 1.0$ ) resulted in  $V_n$  larger than that when  $V_{ci}$  was added to the corresponding  $V_s$  (with  $\cot \theta = 1.0$ ). This was the chief reason for the consistently higher theoretical shear capacity when compared with the experimental capacity of the test beams.

Therefore, it is suggested that both  $V_{cw}$  and  $V_{ci}$  need to be calculated considering the same  $f_t$  or  $f_r$ . It is possible that the designer chooses a lower value for  $f_r$  than what is currently specified by AASHTO LRFD ( $7.6 \sqrt{f'_c}$  psi or  $0.63 \sqrt{f'_c}$  MPa) to be on the conservative side but the same reduced value needs to be implemented in calculating both  $V_{cw}$  and  $V_{ci}$ .

For the current investigation,  $V_{cw}$  and  $V_{ci}$  were calculated assuming a concrete modulus of rupture equal to the tensile strength of concrete and equal to  $7.6 \sqrt{f'_c}$  (psi) [ $0.63 \sqrt{f'_c}$  (MPa)]. In addition, the component that accounts for the difference between the flexural cracking and the flexural-shear cracking strength  $0.63 \sqrt{f'_c} b_v d_v$  (lb) [ $0.053 \sqrt{f'_c} b_v d_v$  (N)] was ignored. The value of  $V_{ci}$  was found to be always less than  $V_{cw}$ . In different words, all the specimens in the current investigation failed due to flexural-shear cracking rather than web-shear cracking. Further, the values of  $V_{ci}$  calculated using the proposed modified equations matched very well with the reported experimental cracking shear force. The prestress loss was taken as 15 % for all test beams.

As shown in Table 9.3-2 and Table 9.3-3, the simplified approach with the proposed modification predicts with good accuracy the ultimate shear strength of the test beams provided with either CFCC or steel stirrups. In case of beams with CFCC stirrups, the ratio  $V_u/V_{n\_mod}$  ranged between 0.74 and 1.07 with an average of 0.945 and a standard deviation of 0.107 and on exclusion of the prematurely failed beam (C100-C4-3), the average increases to 0.97 with a corresponding standard deviation of 0.088. The shear resistance provided by CFCC stirrups was

calculated based on a strain limit of 0.35 % as given by AASHTO LRFD (Section 5.8.2.5), which appears to be a reasonable estimate for the maximum allowable strain in CFRP stirrups. For sections with conventional steel stirrups, the use of the yield strength (with a yield strain of 0.2 %) as the limiting stirrup strength remains adequate as it yielded reasonable estimate for the nominal shear capacity of the test specimens. In case of beams with steel stirrups the ratio  $V_u/V_{n\_mod}$  ranged between 0.90 and 1.09 with an average of 1.00 and a standard deviation of 0.064. Overall,  $V_{n\_mod}$  in the proposed approach showed good correlation with the experimental results and it corresponded well to the shear parameters including stirrup spacing,  $a/d$  ratio, and prestressing level.

In the light of current experimental study, it was not possible to comment on the calculation of the angle of compression strut when  $V_{cw}$  is governing but it may remain as recommended by current AASHTO LRFD simplified approach until further evaluation is available.

It is worth noting that the research team faced a significant difficulty adopting a closer stirrup spacing than 102 mm (4 in.). As shown in Table 9.3-2 and Table 9.3-3, the shear strength of beams with stirrup spacing of 4 in. (102 mm) failed on the un-conservative side with respect to the calculated average shear capacity using the proposed simplified approach. The research team believe that the reduced shear capacity with stirrup spacing of 4 in. (102 mm) can be attributed to constructability issues; the thickness of the web in the test specimens was limited to 3 in. (76 mm). Further, every stirrup in the shear span was instrumented with two properly insulated strain gages. The tight spacing between the stirrups and the insulation of the strain gages resulted in a slight disturbance in the compression struts and slightly lowered the shear strength of the section. This is clearly manifested in the premature failure of beam C100-C4-3.

The simplified approach of AASHTO LRFD provides a limit for the maximum shear strength as  $0.25 f'_c b_v d_v$  to guard against crushing of the web or the diagonal compression failure. Hawkins et al. (2005) provided a detailed discussion for this limit and suggested a limit of  $0.18 f'_c b_v d_v$  to guard against horizontal shear failure along the interface between the web and the bottom flange for a beam without end block. These two limits correspond to average diagonal compressive stresses of  $0.6 f'_c$  and  $0.4 f'_c$ , respectively. Through the current investigation it was observed that a limit of  $0.25 f'_c b_v d_v$  yielded an ultimate shear strength of 90.8 kip (404 kN), while a limit of  $0.18 f'_c b_v d_v$  yields 65.4 kip (291 kN). The maximum experimental shear strength

obtained through the experimental investigation was 72 kip (320 kN) in Beam S132-S4-3, which corresponded to a limit of  $0.2 f'_c b_v d_v$ . It seems that the limit of AASHTO LRFD tends to be unattainable, at least for the current test specimens, where stirrup spacing less than 4 in. (102 mm) was not feasible to adopt and where premature failure already took place at a smaller stirrup spacing (Beam C100-C4-3).

Table 9.3-2 Experimental vs. calculated shear resistance in beams with CFCC stirrups

Beam	Exp. Shear Force (kip)		ACI-440.4R-04 (kip)				Modified AASHTO LRFD (kip)				
	$V_{cr}$	$V_u$	$V_c$	$V_{frp}$	$V_n$	$\frac{V_u}{V_n}$	$V_{ci}$	$V_{cw}$	$V_{frp}$	$V_{n\_mod}$	$\frac{V_u}{V_{n\_mod}}$
C100-C6-3	26.8	58.7	8.3	19.1	27.2	2.10	26.5	39.1	30.8	57.3	1.02
C100-C6-4	19.1	52.2	8.3	19.1	27.2	1.90	19.6	39.1	30.8	50.4	1.04
C100-C6-5	15.5	49.0	8.3	19.1	27.2	1.80	15.5	39.1	30.8	46.1	1.07
C100-C6-6	14.2	46.3	8.3	19.1	27.2	1.70	13.5	39.1	30.8	44.3	1.05
C100-C4-3	27.9	53.7	8.3	28.6	36.9	1.50	26.5	39.1	46.1	72.6	0.74
C100-C8-3	28.1	53.1	8.3	14.4	22.7	2.40	26.5	39.1	22.9	49.7	1.07
C000-C4-3	9.4	44.1	8.3	28.6	36.9	1.20	5.62	28.1	46.5	51.9	0.84
C072-C4-3	23.6	58.2	8.3	28.6	36.9	1.60	20.7	36.4	46.1	66.8	0.87
C132-C4-3	30.4	71.3	8.3	28.6	36.9	1.90	32.6	42.0	45.9	78.7	0.91
S132-C4-3	29.9	68.3	8.3	28.6	36.9	1.90	32.6	42.0	45.9	78.7	0.87
C132-00-3 <sup>2</sup>	--	32.4	8.3	----	8.3	3.90	32.6	42.0	---	32.6	0.99
Average						1.800					0.970 <sup>1</sup>
Standard Deviation						0.313					0.088 <sup>1</sup>

(1) Beam C100-C4-3 was excluded for premature failure.

(2) Beam C132-00-3 was excluded from the average and standard deviation

Note: 1 kip = 4.45 kN

Table 9.3-3 Experimental vs. calculated shear resistance in beams with steel stirrups

Beam	Exp. Shear Force (kip)		AASHTO LRFD 2012 (kip)					Modified AASHTO LRFD (kip)				
	$V_{cr}$	$V_u$	$V_{ci}$	$V_{cw}$	$V_s$	$V_n$	$\frac{V_u}{V_n}$	$V_{ci}$	$V_{cw}$	$V_s$	$V_{n\_mod}$	$\frac{V_u}{V_{n\_mod}}$
C100-S6-3	27.2	61.2	29.7	15.5	49.5	65.0	0.94	27.2	39.1	29.7	56.7	1.08
C100-S6-4	20.0	53.5	22.7	15.5	49.5	65.0	0.83	20.0	39.1	29.7	49.7	1.08
C100-S6-5	15.7	49.7	18.4	15.5	49.5	65.0	0.76	16.0	39.1	29.7	45.4	1.09
C100-S6-6	12.4	44.3	16.4	15.5	49.5	65.0	0.68	13.9	39.1	29.7	43.6	1.01
C100-S4-3	30.6	68.1	29.7	15.5	74.2	89.7	0.76	27.2	39.1	44.5	71.5	0.95
C100-S8-3	28.1	51.0	19.7	15.5	37.1	52.6	0.97	27.2	39.1	22.3	49.2	1.03
C000-S4-3	11.0	51.5	8.5	7.4	44.7	52.2	0.98	5.8	28.1	45.0	50.8	1.01
C072-S4-3	22.3	61.6	23.6	13.3	66.1	79.1	0.78	21.1	36.4	44.5	65.6	0.94
C132-S4-3	30.8	69.5	36.4	18.0	79.8	91.1 <sup>1</sup>	0.77	33.3	42.0	44.3	77.6	0.90
S132-S4-3	29.7	72.0	36.4	18.0	79.8	91.1 <sup>1</sup>	0.79	33.3	42.0	44.3	77.6	0.93
Average							0.826					1.000
Standard Deviation							0.097					0.064

(1) Governed by the maximum shear strength  $0.25 f'_c b_v d_v$

Note: 1 kip = 4.45 kN

**Modified compression field theory according to AASHTO LRFD 2014 (Section 5.8.3.3, General Procedure Subsection 5.8.3.4.2)**

, According to AASHTO LRFD and similar to the simplified approach, the shear strength in steel prestressed beams without draping is calculated through the general procedure by adding concrete shear strength to the shear strength provided by the stirrups:

$$V_n = V_c + V_s \tag{9.3-18}$$

Concrete shear strength is a function of a factor  $\beta$ , which in turn is a function of the bottom steel strain  $\epsilon_s$  that is developed due to the combined action of moment and shear force,  $M_u$  and  $V_u$ . Therefore, concrete contribution to the shear capacity of the section is calculated as:

$$V_c = 0.0316 \beta \sqrt{f'_c} b_v d_v \quad (9.3-19)$$

Contribution of stirrups in shear strength is a function of a factor  $\theta$ , which is also a function of the bottom steel strain  $\varepsilon_s$  that is developed due to the combined action of moment and shear force,  $M_u$  and  $V_u$ . Contribution of the shear reinforcement is expressed in AASHTO LRFD as:

$$V_s = \frac{A_v f_y d_v \cot \theta}{S} \quad (9.3-20)$$

Both factors  $\beta$  and  $\theta$  are calculated using empirical equations (as a function of  $\varepsilon_s$ ) that have been calibrated using experimental test results from testing steel prestressed beams.  $\beta$  and  $\theta$  are calculated as:

$$\beta = \frac{4.8}{(1 + 750 \varepsilon_s)} \quad (9.3-21)$$

$$\theta = 29 + 3500 \varepsilon_s \quad (9.3-22)$$

However, there is upper and lower limits for the strain value,  $\varepsilon_s$ . According to AASHTO LRFD:

$$-0.4 \times 10^{-3} \leq \varepsilon_s \leq 6.0 \times 10^{-3} \quad (9.3-23)$$

Therefore, the values for  $\beta$  and  $\theta$  can range from the minimum and maximum as given in Table 9.3-4. According to the equations, increasing  $\varepsilon_s$  results in decreasing both  $V_c$  and  $V_s$  and thereby, reducing the overall shear capacity of the section. Nevertheless, beams prestressed with CFRP strands experience higher bottom strain than that in beams prestressed with steel strands, especially, when comparing the strain at the same load level before the yield of reinforcement. Therefore, the theoretical shear capacity according to current general procedure of AASHTO LRFD for beams prestressed with CFCC strands tends to be remarkably low most of the time, considering the higher bottom CFCC strain.

Table 9.3-4 Limits for the shear factors  $\beta$  and  $\theta$  based on the limits of bottom strain,  $\varepsilon_s$

$\varepsilon_s$	$\beta$	$\theta$
$-0.4 \times 10^{-3}$	6.85	27.6
$6.0 \times 10^{-3}$	0.872	50

Table 9.3-5 shows a comparison between the experimental and the theoretical nominal shear capacities of the beams using the AASTHO LRFD general procedure. The strain at the level of bottom reinforcement was calculated according to AASTHO equations and the theoretical nominal shear capacity was calculated twice and presented in the tables as  $V_{n1}$  and  $V_{n2}$ : Nominal shear capacity  $V_{n1}$  was calculated without imposing the upper limit of 0.006 on the bottom strain, while nominal shear capacity  $V_{n2}$  was calculated based on the bottom strain with a maximum value of 0.006.

With the upper limit of  $\epsilon_s$  (0.006) in place, and based on the experimental test results for the CFCC prestressed decked bulb T beams with CFCC stirrups, it appears that current AASHTO equations are quite conservative with an average experimental to theoretical shear capacity of 1.58 (a maximum of 1.98 and minimum of 1.04) and a standard deviation of 0.33. Without enforcing the upper limit of  $\epsilon_s$  (0.006) and based on the experimental test results for the same beams, it appears that current AASHTO equations are also conservative with an average experimental to theoretical shear capacity of 1.74 (with a maximum of 2.2 and minimum of 1.1) and a standard deviation of 0.41.

Similarly, with the upper limit of  $\epsilon_s$  (0.006) in place, and based on the experimental test results for the CFCC prestressed decked bulb T beams with steel stirrups, it appears that current AASHTO equations are quite conservative with an average experimental to theoretical shear capacity of 1.71 (a maximum of 2.15 and minimum of 1.25) and a standard deviation of 0.25. Without enforcing the upper limit of  $\epsilon_s$  (0.006) and based on the experimental test results for the same beams, it appears that current AASHTO equations are also conservative with an average experimental to theoretical shear capacity of 1.93 (with a maximum of 2.28 and minimum of 1.59) and a standard deviation of 0.23.

Based on the shear testing of one steel prestressed decked bulb T beams provided with steel stirrups it appears that current AASHTO equations are conservative with an experimental to theoretical shear capacity of 1.30. In addition, based on the shear testing of one steel prestressed decked bulb T beams provided with CFCC stirrups it appears that current AASHTO equations are still conservative with an experimental to theoretical shear capacity of 1.14. In both cases the calculated strain at the level of reinforcement at the time of failure was less than the limit of 0.006.

Therefore, it can be concluded that current AASHTO eqn. are quite conservative when directly used in estimating the shear capacity of beams prestressed with CFCC strands regardless of the type of transverse reinforcement whether it is steel stirrups or CFCC stirrups. Current AASHTO equations can be recalibrated based on the current available test results to further reduce the factor of safety to a reasonable level. However, since the equations are mostly empirical, the calibration shall not be limited to a single test program and shall extend to include test results from multiple programs for beams with different cross sections and different reinforcement configuration. This, however, is beyond the scope of the current report. Therefore, it is recommended, based on available test results, to maintain current provision of the AASHTO LRFD for the shear design using the general procedure and apply it to CFRP prestressed beams using the same factors of  $\beta$  and  $\theta$  as recommended for steel prestressed beam.

Table 9.3-5 Nominal shear capacities of test beams using general procedure

Beam Designation	Ultimate shear force ( $V_u$ )	Calculated bottom strain ( $\epsilon_s$ )	Nominal shear force <sup>1</sup> ( $V_{n1}$ )	$\frac{V_u}{V_{n1}}$	Nominal shear force <sup>2</sup> ( $V_n$ )	$\frac{V_u}{V_{n2}}$
	kip	$\mu\epsilon$	kip		kip	
C100-C6-3	58.7	5503	30.9	1.89	30.9	1.89
C100-C6-4	52.2	(6585)	27.0	1.93	29.1	1.80
C100-C6-5	49.1	(7931)	22.7	2.16	29.1	1.69
C100-C6-6	46.3	(8501)	21.1	2.20	29.1	1.59
C100-S6-3	61.2	5905	28.5	2.15	28.5	2.15
C100-S6-4	53.6	(6857)	25.3	2.12	28.2	1.90
C100-S6-5	49.6	(8048)	21.7	2.28	28.2	1.76
C100-S6-6	44.2	(7954)	21.9	2.01	28.2	1.57
C100-C4-3	53.8	4760	49.0	1.10	49.0	1.10
C100-C8-3	53.1	4652	26.9	1.98	26.9	1.98
C100-S4-3	68.1	(6973)	35.9	1.89	40.6	1.68
C100-S8-3	51.0	4327	27.2	1.87	27.2	1.87
C000-C4-3	44.0	(6754)	38.5	1.14	42.4	1.04
C072-C4-3	58.3	(6434)	39.8	1.46	42.0	1.39
C132-C4-3	71.3	(6355)	40.0	1.78	41.8	1.71
C000-S4-3	51.4	(7890)	32.3	1.59	41.0	1.25
C072-S4-3	61.6	(6944)	36.2	1.70	40.7	1.51
C132-S4-3	69.5	(6076)	40.1	1.73	40.5	1.72
S132-S4-3	72.0	3503	55.5	1.30	55.5	1.30
S132-C4-3	68.3	3192	59.7	1.14	59.7	1.14

Note: 1 kip = 4.45 kN

## CHAPTER 10: SUMMARY & CONCLUSIONS

Based on the comprehensive investigation and test results that were presented in this report, the following conclusions can be drawn:

1. In a uniaxial tensile test of a CFRP specimen, points of anchorage represent the weakest points in the specimen. Failure at maximum load is likely to initiate near the anchorage points regardless of the type of anchorage. Therefore, tensile strength of CFRP is dependent on quality control of assembling and preparing the anchorage devices.
2. A properly assembled wedge anchorage device, following the manufacturer's guidelines, withstands a load higher than the guaranteed strength of the CFRP without slippage or failure.
3. Average tensile strength of CFCC strands with a diameter of 0.6 in. (15.2 mm) is 70 kip (311 kN), which is approximately 15 % higher than the recommended guaranteed strength by the manufacturer (60.7 kip or 270 kN).
4. Minimum estimate for one-million-hour creep rupture strength of CFCC strands with a diameter of 0.6 in. (15.2 mm) is not less than 86 % of the average CFCC tensile strength, or nearly equal to the CFCC guaranteed tensile strength as recommended by the manufacturer (60.7 kip or 270 kN). This estimate is based on available test results at the time of writing and submitting this report.
5. Under sustained load levels higher than 90 % of the average tensile strength of CFCC, test specimens either ruptured within the first 100 hours of loading or continued to sustain the load without signs of creep. For instance, five CFCC specimens with a diameter of 0.6 in. (15.2 mm) loaded to 92 % of their average tensile strength or 105 % of their guaranteed strength have been sustaining the applied load for 11,200 hours (468 days) at the time of writing this report. Similarly, CFCC specimens with a diameter of 0.7 in. (17.8 mm) loaded to 108 % of their guaranteed strength have been sustaining the applied load for 18,600 hours (775 days) at the time of writing this report.
6. The one-million-hour relaxation rate, defined as the expected percentage loss in the force in a CFRP strand over one million hours, of CFCC strands with a diameter of 0.6 in. (15.2

mm) is approximately 1.9 % based on available test results. Weather conditions do not seem to induce additional relaxation or permanently alter the prestress loss in unbonded CFCC strands. Nevertheless, high temperature seems to induce additional heat related relaxation. For instance, at a temperature similar to the heat curing temperature of the concrete (150 °F or 66 °C), it was observed that CFCC strands with a diameter of 0.6 in. (15.2 mm) experience additional relaxation of approximately 250  $\mu\epsilon$ , which in prestressing application represent a prestress loss of 5 to 6 ksi or 900 to 1000 lb (4 to 4.5 kN) per strand.

7. Average static bond strength between CFCC strands with a diameter of 0.6 in. (15.2 mm) and uncracked concrete with an average 28-day compressive strength of 10 ksi (69 MPa) is approximately 1.6 ksi (11 MPa). Nevertheless, cyclic loading affects the bond strength between CFCC and concrete.
8. To avoid bond failure in case of locations subjected to cyclic loading, the bond strength between concrete and CFCC shall be limited to approximately 64 % of the average static bond strength, which results in a bond strength of approximately 1.0 ksi (6.9 MPa) between concrete and CFCC strands with a diameter of 0.6 in. (15.2 mm).
9. Splice failure of CFRP may occur as a result of: (1) concrete splitting, (2) strand pullout, or (3) pullout from severely cracked concrete. Concrete splitting is a common mode of failure of both steel and CFRP and is attributed to an inadequate concrete cover or confinement. Strands pullout is also a common mode of failure in CFRP and steel and is attributed to an inadequate bond length of the reinforcement. Pullout from severely cracked concrete is a unique mode of failure that is noticed in CFRP at high strain level (much higher than the yield strain of steel). It occurs due to the lower elastic modulus of CFRP and higher maximum strain of CFRP compared to steel yield strain. It is attributed to the deterioration of the concrete-CFRP bond strength due to severe concrete cracking around the strand.
10. Tensile strength of CFCC strands is affected by the increase in temperature. At a temperature of 400 °F (204 °C), the tensile strength of CFCC is approximately 78 % of its ambient tensile strength. Nevertheless, prestressed CFCC specimens heated to 400 °F (204 °C) and then were allowed to cool down before they were tested at ambient temperature achieved their ambient average tensile strength.

11. Fire endurance for a prestressed beam is defined as the period of time at which the prestressed beam continues to effectively support service loads in case of a fire event before any major failure or collapse. Under a standard ASTM E-119 time-temperature curve, the fire endurance of simply supported half-scale CFCC prestressed decked bulb T beams under three-point-load setup was approximately 69, 53, and 47 minutes for prestress levels of 30, 41, and 54 % of the CFCC guaranteed strength.
12. An identical half-scale steel prestressed decked bulb T beam with a prestress level equal to 56 % of the steel ultimate strength lasted for 98 minutes under similar fire and loading conditions.
13. Average tensile strength of CFCC strands subjected to 300 cycles of freezing and thawing is approximately 15 % higher than the average strength of CFCC specimens not subjected to freeze-thaw cycles.
14. Due to the difference in thermal expansion between concrete and CFRP, beams prestressed with CFRP strands experience a loss in the prestressing force with the decrease in temperature. However, this loss in prestressing is recovered when the temperature increases back to the normal range. Similarly, they experience gain in the effective prestressing force when the temperature increases but this gain in prestressing is lost once the temperature drops down to the normal range. The gain or loss in effective prestressing force conforms with the theoretical thermal expansion and contraction calculations.
15. Freeze-thaw cycles do not seem to have any detrimental effect on CFCC strands. On the other hand, freeze-thaw cycles do cause significant deterioration and reduction in the concrete strength. Therefore, by weakening the concrete side, exposure to freeze-thaw cycles can alter the mode of failure from tension-controlled to compression-controlled and reduce the nominal moment capacity of a CFRP prestressed beam.
16. Environmental conditions seem to affect the concrete more than CFCC strands. Therefore, while an environmental reduction factor may not be necessary for CFRP strands, it shall be adjusted to address concrete deterioration especially in compression-controlled sections.
17. In a two-year test program, CFCC prestressed beams kept outdoors and exposed to different environmental conditions showed a slight increase in compressive strength and

maximum load capacity than those observed in identical beams stored indoors. The difference can be attributed to the extended exposure to rain and moist conditions, which resulted in extended concrete curing. This conclusion does not contradict the previous conclusion, since further extended exposure to weather conditions especially repeated freeze-thaw cycles will eventually lead to deterioration in concrete strength.

18. No significant change in prestress loss was observed over a period of two years between five identical CFCC prestressed bulb T beams stored either indoors or outdoors. In addition, all five beams experienced compression-controlled mode of failure with no evidence of any significant deterioration in the mechanical properties of CFCC strands.
19. Elastic prestress loss as well as long-term prestress loss due to concrete creep and shrinkage can be reasonably estimated in a CFRP prestressed beam using prestress loss equations developed for steel strands and provided in current codes and guidelines such as AASHTO LRFD and PCI. Prestress loss due to relaxation of CFRP strands is pertinent to the relaxation characteristics of the CFRP material. In addition, the temporary change in prestressing force due to seasonal temperature change shall be calculated and considered in the design of CFRP prestressed beams.
20. The depth of the neutral axis and the nominal moment capacity of a section prestressed with CFRP strands distributed over multiple rows of reinforcement can be calculated using conventional strain compatibility and force equilibrium approach by assuming an equivalent stress block distribution on the concrete. To facilitate the calculations and minimize the number of iterations, the strain compatibility approach may be rearranged in the form of an equivalent area method. The equivalent area method simply replaces area of CFRP at any row with a reduced discrete area at level of the extreme CFRP row to facilitate the calculations of the depth of the neutral axis and verify the mode of failure. After establishing the depth of the neutral axis, the strain and stress in each row of CFRP strands can be calculated using strain compatibility and the nominal moment capacity of the section can be accurately estimated.
21. A tension-controlled section in beams prestressed with CFRP strands is defined as a cross section in which the strain of concrete in compression at nominal resistance is less than

maximum usable concrete strain just as the net tensile strain in the extreme tension CFRP reaches its net guaranteed strain limit.

22. A compression-controlled section in beams prestressed with CFRP strands is defined as a cross section in which the net tensile strain in the extreme tension CFRP at nominal resistance is less than the net guaranteed strain limit just as the concrete in compression reaches its assumed maximum usable concrete strain.
23. Balanced strain conditions exist at a cross-section when tension CFRP reinforcement reaches the strain corresponding to its design guaranteed strength just as the concrete in compression reaches its assumed ultimate strain of 0.003.
24. The shear design of CFRP prestressed beams with either steel or CFRP stirrups can be performed using either a simplified approach or a general procedure. The simplified approach equations were calibrated and reproduced to ensure a proper shear design. The general procedure as defined in the current edition of AASHTO LRFD yields conservative estimates for the shear capacities of beams prestressed with CFRP strands. This is attributed to the fact that the general procedure considers the bottom strain, at the level of bottom reinforcement, in the shear design. As the bottom strain increases, the shear capacity of the section decreases and vice-versa. Due to the lower elastic modulus of CFRP, beams prestressed with CFRP exhibits larger bottom strain values, after cracking, than those prestressed with steel strands and therefore, their shear capacities according to the general procedure in its current format is less than those of beams prestressed with steel strands.

## REFERENCES

1. AASHTO, 2014, "AASHTO LRFD Bridge Design Specifications," 7<sup>th</sup> ed., American Association of State Highway and Transportation Officials, Washington, DC.
2. Abbasi, A & Hogg, Paul., 2006, "Fire Testing of Concrete Beams with Fibre Reinforced Plastic Rebar," *Composites Part A: Applied Science and Manufacturing*. Vol. 37, Issue No. 8, pp. 1142-1150
3. Achillides, Z. and Pilakoutas, K., 2004, "Bond Behavior of Reinforced Polymer Bars under Direct Loading," *Journal of Composites for Construction*, Vol. 8, Issue No. 2, pp. 173-181.
4. Akbas, T., Celik, O., Yalcin, C., and Ilki, A., 2016, "Monotonic and Cyclic Bond Behavior of Deformed Cfrp Bars in High Strength Concrete," *Polymers*, Vol. 8, Issue No. 6, doi: 10.3390/polym8060211.
5. Ali, A., Mohamed, H., Benmokrane, B., and Elsafty, A., 2018, "Effect of Applied Sustained Load and Severe Environments on Durability Performance of Carbon-Fiber Composite Cables," *Journal of Composite Materials*, Vol. 53, No. 5, pp. 677–692.
6. Alsiwat, J.M.; Saatcioglu, M., 1992, "Reinforcement anchorage slip under monotonic loading," *ASCE J. Struct. Eng.*, Vol. 118, issue No. 9, pp. 2421–2438
7. American Concrete Institute (ACI), 2015, "Guide for the Design and Construction of Structural Concrete Reinforced with FRP Bars," ACI 440.1R-15, Farmington Hills, MI.
8. American Concrete Institute (ACI), 2012, "Guide Test Methods for Fiber-Reinforced Polymer (FRP) Composites for Reinforcing or Strengthening Concrete and Masonry Structures," ACI 440.3R-12, Farmington Hills, MI.
9. American Concrete Institute (ACI), 2004, "Prestressing Concrete Structures with FRP Tendons," ACI 440.4R-04, Farmington Hills, MI.
10. American Concrete Institute (ACI), 2014, "Building code requirements for structural concrete and commentary," ACI 318-14, Farmington Hills, MI.
11. Ando, N., Matsukawa, H., Hattori, A., and Mashima, A., 1997, "Experimental Studies on the Long-term Tensile Properties of FRP Tendons," *Proceedings of the Third International*

Symposium on Non-Metallic (FRP) Reinforcement for Concrete Structures (FRPRCS-3), Sapporo, Japan, Vol. 2, 203-210.

12. Ashton, L. A., Malhotra, H. L., 1953, "The Fire Resistance of Prestressed Concrete Beams," *Fire Res. Notes* (1953), p. 65
13. ASTM Standard C666, 2008, "Test Method for Resistance of Concrete to Rapid Freezing and Thawing," ASTM International, West Conshohocken, PA, USA. DOI: 10.1520/C0666\_C0666M-03R08, [www.astm.org](http://www.astm.org).
14. Balazs, G.L. and Borosnyoi, A., 2001, "Long-Term Behavior of FRP." In: Cosenza E, Manfredi G, Nanni A, editors, *Proceedings of the international workshop "Composites in construction: a reality,"* American Society of Civil Engineers, Reston, pp. 84–91.
15. Barr, P. J., Stanton, J. F., and Eberhard, M. O., 2005 "Effects of Temperature Variations on Precast, Prestressed Concrete Bridge Girders." *Journal of Bridge Engineering*, Vol. 10, No. 2, pp. 186-194.
16. Bryan, P.E., Green, M. F., 1996, "Low Temperature Behavior of CFRP Prestressed Concrete Beams," *Canadian Journal of Civil Engineering*, V. 23, No. 2, Apr., pp. 464-470.
17. CAN/CSA-S6-06, 2006, "Canadian Standards Association Highway Bridge Design Code."
18. Canadian Standards Association (CAN/CSA-S806). (2002). "Design and construction of building components with fibre reinforced polymers," CSA International, Rexdale, Ontario, Canada.
19. Ceroni, Francesca, E. Cosenza, M. Gaetano, M. Pecce, 2006, "Durability Issues of FRP Rebars in Reinforced Concrete Members," *Cement and Concrete Composites*, vol. 28, No. 10, pp. 857–868.
20. Cusson, R., Xi, Y., 2002, "The Behavior of Fiber-Reinforced Polymer Reinforcement in Low Temperature Environmental Climates," Report No. CDOT-DTD-R-2003, *Colorado Department of Transportation*, 97p.
21. Curtis, P. T., 1989, "The Fatigue Behavior of Fibrous Composite Materials," *Journal of Strain Analysis*, V. 24, No. 4, pp. 235-244. doi: 10.1243/03093247V244235

22. Den Uijl, J. A. ,1995, “Bond and Fatigue Properties of Arapree,” Proc.,RILEM Int. Conf. on Non-Metallic (FRP) Reinforcement for Concrete Struct., L. Taerwe, ed., E & FN Spon, London, pp. 146-153.
23. Dutta, P. K., 1988, “Structural Fiber Composite Materials for Cold Regions,” *Journal of Cold Regions Engineering*, No. 3, pp. 124-132.
24. Elbadry, M. M., Abdalla, H., & Ghali, A., 2000, “Effects of Temperature on the Behaviour of Fiber Reinforced Polymer Reinforced Concrete Members: Experimental Studies,” *Canadian Journal of Civil Engineering*, 27(5), 993-1004.
25. El-Hacha, R., Wight, R. G., and Green, M. F., 2004, “Prestressed Carbon Fiber Reinforced Polymer Sheets for Strengthening Concrete Beams at Room and Low Temperatures,” *Journal of Composites for Construction*, V.8, No.1, pp. 3–13.
26. Enomoto, T., Harada, T., Ushijima, K., and Khin, M., 2009, “Long term relaxation characteristics of CFRP cables,” Proc., 4th Int. Conf. on Construction Materials (ConMat09), Japan Concrete Institute, Japan, pp. 1205–1210.
27. Ezeldin, A. and Balaguru, P., 1989, “Bond Behavior of Normal and High-strength Fiber Reinforced Concrete,” *ACI Materials Journal*, Vo. 86, Issue No. 5, pp. 515-524
28. Gerritse, A., and Den Uijl, J. A., 1995, “Long-term Behavior of Arapree.” Proc., 2nd Int. Symp. on Non-Metallic (FRP) Reinforcement for Concrete Structures, L. Taerwe, ed., E & FN Spon, London, pp. 57–66.
29. Grace, N., Ushijima, K., Rout, S., and Bebawy, M., 2015, “Performance of CFRP Stirrups in Prestressed Decked Bulb T Beams,” *ASCE Journal of Composites for Construction*, 1090-0268/04014061, May/June, Vol. 19, Issue 3.
30. Grace, N., and Bebawy, M., 2014, “Fire Protection for Beams with Fiber-Reinforced Polymer Flexural Strengthening Systems,” *ACI Structural Journal*, V. 111, Issue 3, pp. 537-548
31. Grace, N., Ushijima, K., Baah, P. and Bebawy, M., 2013a, “Behavior of CFRP Prestressed Decked Bulb-T Beam Bridge System,” *ASCE Journal of Composites for Construction*, Vol. 17, No. 4, July/Aug., pp. 497-506.

32. Grace, N., Ushijima, K. Matsagar, V., and Wu, C., 2013b, "Performance of AASHTO-type bridge model prestressed with carbon fiber-reinforced polymer reinforcement," *ACI Structural Journal*. Vol 110, Issue 3, pp. 491-501.
33. Grace, N., Jensen, E., Matsagar, V., and Penjendra, P., 2013c, "Performance of an AASHTO beam bridge prestressed with CFRP tendons," *Journal of Bridge Engineering*. 18. 110-121. 10.1061/(ASCE)BE.1943-5592.0000339.
34. Grace, N., Enomoto, T., Baah, P. and Bebawy, M., 2012a, "Flexural Behavior of CFRP Precast Prestressed Decked Bulb T Beams," *ASCE Journal of Composites for Construction*, Vol. 16, No. 3, May/June, pp. 225-234.
35. Grace, N., Jensen, E., Eamon, C, Shi, X., 2012b, "Life Cycle Cost Analysis of CFRP Reinforced Concrete Bridges," *ACI Str. Journal*, Vol. 109, Issue 5, pp. 697-704
36. Grace, N., Jensen, E., and Bebawy, M, 2012c, "Transverse post-tensioning arrangement for side-by-side box-beam bridges", *PCI Journal*, Vol. 57, Issue 2, Spring, pp 48-63.
37. Grace, N., Kapil, P., Soliman, I., and Hanson, J., 2011a, "Flexural Behavior of Side-by-Side Box Beam Bridges – a Comparative Study", *PCI Journal*, Vol 56, Issue 3, June, pp 94-112.
38. Grace, N., Jensen, E., and Noamesi, D., 2011b, "Flexural Performance of Carbon Fiber-Reinforced Polymer Prestressed Concrete Side-by-Side Box Beam Bridge," *Journal of Composites for Construction*. 15. 10.1061/(ASCE)CC.1943-5614.0000207.
39. Grace, N., Jensen, E, Matsagar, V, Soliman, E., Hanson, J., 2010a, "Use of Unbonded CFRP Strands in Transverse Post-Tensioning in Box Beam Bridges," *International Journal of Earth Sciences and Engineering*.
40. Grace, N., Jensen, E., Enomoto, T., Matsagar, V., Soliman, E., and Hanson, J., 2010b, "Transverse diaphragms and unbonded CFRP posttensioning in box-beam bridges," *PCI Journal*. 55. 109-122. 10.15554/pcij.03012010.109.122.
41. Grace, N. F., Enomoto, T., Abdel-Mohti, A., Tokal, Y., and Purayankara, S., 2008, " Flexural behavior of precast concrete box beams post-tensioned with unbonded, carbon-fiber-composite cables," *PCI* Vol. 53, Issue 4, pp. 62-82.

42. Grace, N., Singh, S., Puravankara, S. and Sachidanandan, S., 2006a, "Behavior of Prestressed Concrete Box-Beam Bridges Using CFRP Tendons," PCI Journal, Vol. 62, Issue 2, pp. 26-41. 10.15554/pcij.03012006.26.41.
43. Grace, N. F., Enomoto, T., Sachidanandan, S., and Purayankara, S., 2006b, "Use of CFRP/CFCC Reinforcement in Prestressed Concrete Box Beam Bridges," ACI Structural Journal, Vol. 103, No. 1, January/February, pp. 123-132.
44. Grace, N.F., Roller, J. J., Navarre, F. N., Nacey, R.B., and Bonus, W., 2005, "Truck Load Distribution Behavior of the Bridge Street Bridge, Southfield, Michigan," PCI Journal, Vol. 50, No. 2, March/April, pp.76-89.
45. Grace, Singh, Shenouda, and Sunup, 2004, "Flexural Response of CFRP Prestressed Concrete Box Beams for Highway Bridges," PCI Journal, Vol.49, No. 1, January/February.
46. Grace, and Singh, 2003a, "Design Approach for carbon Fiber –Reinforced Polymer Prestressed Concrete Bridge Beams," ACI Structural Journal, Vol. 100, No. 3, pp. 365-376.
47. Grace, Enomoto, Abdel-Sayed, Yagi, and Collavino, 2003b, "Experimental Study and Analysis of a Full-Scale CFRP/CFCC DT Beam," PCI journal, Vol. 48, No. 4, July/August.
48. Grace, Navarre, Nacey, Bonus, and Collavino, 2002a, "Design-Construction of Bridge Street Bridge-First CFRP Bridge in the United States," PCI Journal, Vol. 47, No. 5, September/October.
49. Grace, Enomoto, T., and Yagi, K., 2002b, "Behavior of CFCC and CFRP Leadline Prestressing Systems in Bridge Construction," PCI Journal, Vol. 47, No. 3, May/June.
50. Grace, 2000a, "Transfer Length of CFRP/CFCC Strands for Double-T Girders," PCI Journal, V. 45, No. 5, September/October.
51. Grace and Abdel-Sayed, 2000b, "Behavior of Carbon Fiber - Reinforced Prestressed Concrete Skew Bridges," ACI Structural Journal, V. 97, No. 1, Jan.-Feb.
52. Grace N., 1999, "Innovative CFRP Continuous Prestressed Concrete Bridges," ACI Concrete International, V. 21, No. 10, pp. 42-47.

53. Green, M. F., Bisby, L. A., Beaudoin, Y. and Labossiere, P., 2000, "Effect of Freeze-Thaw Cycles on the Bond Durability between Fiber Reinforced Polymer Plate Reinforcement and Concrete," *Canadian Journal of Civil Engineering*, V. 27, No. 5, pp. 949-959.
54. Hao, Q., Wang, Y., Ou, J., 2008, "Design Recommendations for Bond Between GFRP/steel Wire Composite Rebars and Concrete," *Eng. Struct.*, Vol. 30, pp. 3239-3246.
55. Harajli, M. and Abouniaj, M., 2010, "Bond Performance of GFRP Bars in Tension: Experimental Evaluation and Assessment of ACI 440 Guidelines," *ASCE Journal of Composites for Construction*, Vol. 14, Issue No. 6, pp. 659-668.
56. Harajli, M.H., 2009, "Bond Stress-Slip Model for Steel Bars in Unconfined or Steel, FRC, or FRP Confined Concrete under Cyclic Loading," *ASCE Journal of Composites for Construction*, Vol. 135, Issue No. 5, pp. 509-518.
57. Hollaway, L., 1993, "Polymer Composites for Civil and Structural Engineering," Blackie academic & Professional, Glasgow.
58. Japanese Society of Civil Engineers (JSCE), 1997, "Recommendations for design and construction of concrete structures using continuous fibre reinforced materials," JSCE, Tokyo, Japan.
59. Kanakubo, T., Yonemaru, K., Fukuyama, H., Fujisawa, M., and Sonobe, Y., 1993, "Bond Performance of Concrete Members Reinforced with FRP Bars," *Proc., Int. Symp. on Fiber Reinforced Plastic Reinforcement for Concrete Structures: ACI SP-138*, A. Nanni and C. W. Dolan, Eds.
60. Karbhari, V. M. and Gregory Pope, 1994, "Impact and Flexure Properties of Glass/Vinyl Ester Composites in Cold Regions," *Journal of Cold Regions Engineering*, No. 1, pp. 1-20.
61. Katz, A., 2000, "Bond to Concrete of FRP Rebars after Cyclic Loading," *ASCE Journal of Composites for Construction*. Vol. 4, Issue No. 3, pp. 137-144.
62. Katz, A., Berman, N. and Bank, L. C., 1999, "Effect of High Temperature on Bond Strength of FRP Rebars," *Journal of Composites for Construction*, Vol. 3, Issue No. 2, pp. 73-81.

63. Kim, Y. J., Hossain, M., & Chi, Y., 2011, "Characteristics of CFRP–concrete interface subjected to cold region environments including three-dimensional topography," *Cold Regions Science and Technology*, 67(1), pp. 37-48.
64. Kodur, V. K. R., and Bisby, L. A., 2005, "Evaluation of Fire Endurance of Concrete Slabs Reinforced with Fiber-Reinforced Polymer Bars," *Journal of Composites for Construction*, Vol. 131, Issue No. 1, pp. 73–81.
65. Kodur, V., Bisby, L., and Foo, S., 2005, "Thermal Behavior of Fire-Exposed Concrete Slabs Reinforced with Fiber-Reinforced Polymer Bars," *ACI structural Journal*, Vol. 102, issue no. 6, pp. 799–807.
66. Maluk C, Bisby L, Santa Maria H, Terrasi G and Green M., 2010, "Effects of Elevated Temperatures and Fire on Bond Strength of Prestressed Steel and Carbon FRP Bars in High Performance Self-Consolidating Concrete," *Proceedings of the 2<sup>nd</sup> Postgraduate Engineering Students' PUC Congress*, May 28, Pontificia Universidad Católica de Chile, Santiago, Chile.
67. Malvar, L.J., 1994, "Bond Stress-Slip Characteristics of FRP Rebars," Rep. TR-2013-SHR, Naval Fac. Engrg. Service Ctr., Port Hueneme, California
68. Natarajan, V., GangaRao, H.V.S., and Shekar, V., 2005, "Fatigue Response of Fabric Reinforced Polymeric Composites," *Journal of Composite Materials*, Vol. 39, Issue No. 17, pp. 1541-1559.
69. Oskouei, A.V. and Taleie, S.M., 2010, "Experimental Investigation on Relaxation of Fiber –reinforced Polymer Composites," *Journal of Reinforced Plastics and Composites*, Vol. 29, pp. 2705-2718.
70. Patrick, X. and Zou, W., 2003, "Long-Term Properties and Transfer Length of Fiber-Reinforced Polymers," *ASCE Journal of Composites for Construction*, Vol. 7, Issue No. 1, pp. 10-19.
71. Prestressed Concrete Institute (PCI), 2010, "PCI Design Handbook," 7th Edition, Chicago, Illinois.

72. Rafi, M. M., Nadjai, A., and Ali, F., 2007, "Fire Resistance of Carbon FRP Reinforced Concrete Beams," *Magazine of Concrete Research*, V. 59, No. 4, pp. 245–255.
73. Robert, M. and Benmokrane, B., 2010, "Behavior of GFRP Reinforcing Bars Subjected to Extreme Temperatures," *ASCE Journal of Composites for Construction*, Vol. 14, Issue No. 4, pp. 353-360.
74. Saadatmanesh, H. and Tannous, F., 1999, "Relaxation, Creep and Fatigue Behavior of Carbon Fiber Reinforced Plastic Tendons," *ACI Material Journal*, Vol. 96, Issue No. 2, pp. 143-53.
75. Saafi, M., 2002, "Effect of Fire on FRP Reinforced Concrete Members," *Composite Structures*, Elsevier, Vol 58, Issue no. 1, pp. 11–20.
76. Saiedi, R., Green, M. F. and Fam, A., 2013, "Behavior of CFRP-Prestressed Concrete Beams Under Sustained Load at Low Temperature," *Journal of Cold Regions Engineering*, V.27, No. 1, pp.1-27.
77. Sayed-Ahmed, E. Y., and Shrive, N. G., 1999, "Smart FRP prestressing tendons: Properties and prospects." *Proc., Second Middle East Symp. on Structural Composites for Infrastructure Applications*, A.H. Hosny, I. Mahfouz, and S. Sarkani, eds., pp. 80–93.
78. Shoukry, S. N., William, G. W., Downie, B., and Riad, M. Y., 2011, "Effect of moisture and temperature on the mechanical properties of concrete," *Construction and Building Materials*, V.25, No.2, pp. 688–696.
79. Swenson, T. and French, C., 2015, "Effect of Temperature on Prestressed Concrete Bridge Girder Strand Stress During Fabrication' Research Report No. MN/RC 2015-50, Minnesota Department of Transportation
80. Subramaniam, K. V., Ali-Ahmad, M, and Ghoson, M., 2008, "Freeze-Thaw Degradation of FRP-Concrete Interface: Impact on Cohesive Fracture Response," *Engineering Fracture Mechanics*, V. 75, pp. 3924-3940.
81. Talreja, R., 1987, "Fatigue of Composite Materials," Technomic Publishing Company, Lancaster, PA.

82. Tastani, S.P., and Pantazopoulou, S.J., 2010, "Direct Tension pullout test: Experimental results," *ASCE Journal of Structural Engineering*, Vol. 136, pp. 731–743.
83. The National Institute of Standards and Technology (NIST), 2014, "Freeze-Thaw Cycles: Expansions and Contractions Cause Potholes," <https://www.pothole.info/2014/12/freeze-thaw-cycles-expansions-and-contractions-cause-potholes/> (Dec 05, 2014).
84. Terrasi G.P., Stutz A., Barbezat M., and Bisby L., 2011, "Fire Behaviour of CFRP Prestressed High Strength Concrete Slabs," *Proceedings, CICE 2010 - The 5<sup>th</sup> International Conference on FRP Composites in Civil Engineering*, September 27-29, Beijing, China, pp. 423-427
85. Wang, H. and Belarbi, A., 2010, "Static and Fatigue Characteristics of FRP Rebars Embedded in Fiber-Reinforced Concrete," *Journal of Composite Materials*, Vol. 44, issue No. 13, pp. 1605-1622.
86. Williams, B., Kodur, V., Green, M. and Bisby, L., 2008, "Fire Endurance of Fiber-Reinforced Polymer Strengthened Concrete T-Beams," *ACI Structural Journal*, Vol. 105, Issue No. 1, pp. 60-67
87. Yu, B. and Kodur, V., 2013, "Factors Governing the Fire Response of Concrete Beams Reinforced with FRP Rebars," *Composite Structures*, Elsevier, Vol. 100, June, pp. 257–269.
88. Zhang, G., Kodur, V., Xie, J., He, S., and Hou, W., 2017, "Behavior of Prestressed Concrete Box Bridge Girders Under Hydrocarbon Fire Condition," *Procedia Engineering*. Elsevier, Vol. 210, pp. 449–455.
- Zhang, G. & Kodur, V., Hou, W. and He, S., 2017, "Evaluating Fire Resistance of Prestressed Concrete Bridge Girders," *Structural Engineering and Mechanics*, Vol. 62, pp. 663-674.

**Click below to access:**

**[APPENDIX A: DESIGN GUIDELINES IN LRFD FORMAT](#)**

**Click below to access:**

**[APPENDIX B: DESIGN EXAMPLE FOR BEAM WITH CFRP RESINFORCEMENT](#)**